

# Small-Molecule Activation Chemistry Catalyzed by Proton-Coupled Electron Transfer

by

Christopher J. Chang

B.S., Chemistry, California Institute of Technology (1997)

M.S., Chemistry, California Institute of Technology (1997)

SUBMITTED TO THE DEPARTMENT OF CHEMISTRY IN PARTIAL FULFILLMENT OF  
THE REQUIREMENTS FOR THE DEGREE OF

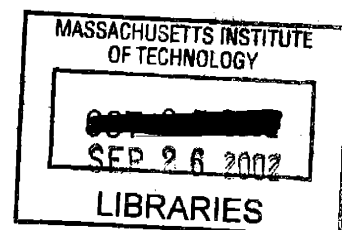
DOCTOR OF PHILOSOPHY IN CHEMISTRY  
AT THE  
MASSACHUSETTS INSTITUTE OF TECHNOLOGY

September 2002

© Massachusetts Institute of Technology, 2002

All Rights Reserved

ARCHIVES



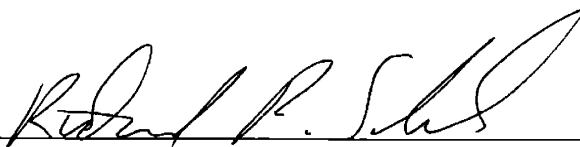
Signature of Author: Christopher J. Chang  
Department of Chemistry  
August 26, 2002

Certified by: Daniel G. Nocera  
Daniel G. Nocera  
W. M. Keck Professor of Energy and Professor of Chemistry  
Thesis Supervisor

Accepted by: Robert W. Field  
Robert W. Field  
Haslam and Dewey Professor of Chemistry  
Chairman, Departmental Committee on Graduate Studies

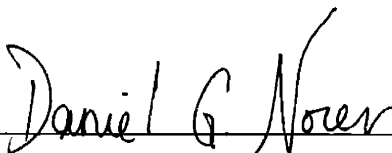
V.1

This doctoral thesis has been examined by a Committee of the Department of Chemistry as follows:



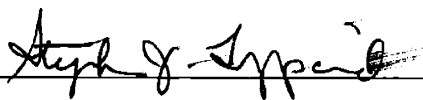
---

Richard R. Schrock  
Frederick G. Keyes Professor of Chemistry  
Committee Chairman



---

Daniel G. Nocera  
W. M. Keck Professor of Energy and Professor of Chemistry  
Thesis Supervisor



---

Stephen J. Lippard  
Arthur Amos Noyes Professor of Chemistry and Department Head

# Small-Molecule Activation Chemistry Catalyzed by Proton-Coupled Electron Transfer

by

Christopher J. Chang

Submitted to the Department of Chemistry on August 26, 2002, in partial fulfillment of the requirements for the Degree of Doctor of Philosophy.

## Abstract

Proton-coupled electron transfer (PCET) is the basic mechanism for bioenergetic conversion. Consummate examples include water oxidation in photosynthesis and oxygen reduction in respiration. Despite the importance of PCET in such catalytic bond-making and bond-breaking reactions, the underlying mechanisms of coupled proton and electron transport in these processes is not well understood. To address mechanistic issues surrounding the role of PCET in catalytic chemical transformations, we have begun characterizing PCET events at a molecular level in a broad spectrum of small-molecule activation reactions for the first time. Two distinct structural scaffolds have been elaborated to study the PCET chemistry of O—O bond forming and cleaving reactions. The first consists of platforms containing two redox sites linked face-to-face by a rigid xanthene (DPX) or dibenzofuran (DPD) spacer – Pacman porphyrins. A comparative structural study demonstrates that DPD has the unprecedented ability to open and close its binding pocket by a vertical distance of over 4 Å upon substrate binding, providing the first direct observation of the Pacman effect in a single cofacial platform. Moreover, efficient oxygen-activation chemistry is preserved when such cofacial motifs exhibit a large range of vertical motion; for example, dicobalt(II) complexes of both DPX and DPD are effective electrocatalysts for the direct four-electron reduction of oxygen to water despite their *ca.* 4 Å difference in metal-metal distances. The second scaffold consists of acid-base and redox functionalities affixed to a xanthene (HPX) or dibenzofuran (HPD) scaffold – Hangman porphyrins. HPX selectively encapsulates water between its acid-base and redox sites by hydrogen bonding, affording a minimalist model for the cytochrome P450 heme water channel assemblies. Comparative reactivity studies for the catalase-like disproportionation of hydrogen peroxide and the epoxidation of olefins by HPX and HPD platforms bearing acid and ester pendants reveal that the introduction of a proton-transfer network properly oriented to a redox-active platform can orchestrate catalytic O—O bond activation. For the catalase and epoxidation reaction types, a marked reactivity enhancement is observed for the xanthene-bridged platform with a pendant carboxylic acid, establishing that this approach can yield superior catalysts to analogs that do not control both proton and electron currencies.

Thesis Supervisor: Daniel G. Nocera

Title: W. M. Keck Professor of Energy and Professor of Chemistry

*To my dad*

## Acknowledgments

Getting to thank everybody who has helped me along this four-year journey is the best part of writing this thesis (and it's something that most people will actually read too). First and foremost, I'd like to thank God for peace and strength; faith is a wonderful thing. Thanks also to my advisor Dan Nocera, it's been a fun time. I've appreciated his energy, his vision, his generosity, and his honesty with me. He's always provided a great setting for helping me shape and chase the big picture, and I thank him for the training and insight that have made me better in many ways.

Dan has assembled a remarkable cast of scientists and characters, and I feel proud to have shared graduate school with such a dynamic team of people. Four people in the group deserve special mention. Yongqi Deng (aka Mr. Deng) was my mentor in the lab and he really took me under his wing when I first joined the group. Mr. Deng's legendary synthetic, culinary, and electrical skills, as well as his creativity and friendship have been a continuing inspiration to me. The original nightshift in 2-301 was headed by Al Barney, who knows how to make, fix, and move anything. He has been a fellow connoisseur of vast amounts of beer and single, double, or triple quarter-pounders with cheese at our favorite Scottish restaurant near Ghetto Star. Chen-Yu Yeh is the most efficient (and cleanest) synthetic chemist I've ever met, and I also thank him for showing me where to get the best (meaning cheapest) Chinese-cooked lobster. It's good to know that he's always having a nice day. I also thank Leng Leng Chng, who has been an amazing source of energy and knowledge during this past year. She really knows how to run those stairs.

It's also been a real treat to share science with a number of others in the group as well. I've enjoyed my conversations with Zhi-Heng Loh immensely and he has been an invaluable help with calculations and spectroscopy. I am confident that ZLoh's precocious analytical skills and work ethic will take him far. I would also like to acknowledge Brad Pistorio for his photochemical expertise and for introducing me to sweet potato fries at the former Deli Haus (nice!). It was always a Good Time to hang out with Erin Baker, friendly Canadian and fellow pyrrole maker. Thanks to the Scotts Carpenter and Miller for all their help on the laser systems, and may the data (and donut) dances of Carpenter live on from the magnet lab to the basement. I'd also like to thank Alan Heyduk and Dave Manke for their help in X-ray crystallography; special props to Dave for his enjoyment of Chinese restaurants if not Chinese food. Thanks to my favorite Rams fan from St. Louis, Bart Bartlett, who has gone through great efforts to keep the Nocera group networking. I'd also like to thank my deskmate Dave Krodel for just being himself. It's been quite exciting to see all the new people joining the PCET project this past year. Best of luck to Julien Bachmann, Niels Damrauer, Jeff Hirsch, Joel (Big JR) Rosenthal, and Jenny Yang in their respective endeavors. And I'd like to acknowledge all the other past and present Nocera group members that I have crossed paths with: Joshua Brown, Michael Casserly, Thomas Gray, Daniel Grohol, Darren (Hammy) Hamilton, Justin Hodgkiss, Steven Kaye, Yelena Koldobskaya, Huanqian Loh, Emily Meyer, Aaron Odom, Dimitris Papoutsakis, Christina Rudzinski, Matt Shores, Glen Walker, and Aetna Wun.

M.I.T. is a first-rate place to do science, and there are a number of the people that make it that way. Thanks to my thesis committee chair Dick Schrock and committee member Steve Lippard, as well as the rest of the inorganic faculty for their advice and help. Gretchen (G Money) Kappelmann has done a great job of keeping us in line, and I hope that she won't get grounded by Fred after our next unplanned trip to the casino. I've appreciated the sound advice and knowledge from Susan Brighton, and Kitty Valleli has made sure that payroll actually paid me. Thanks to Jeff Simpson, Mark Wall and the rest of the DCIF and Bill Davis in the X-ray laboratory for their experimental expertise.

Graduate school has brought some significant people and places into my life, and I'd like to acknowledge some of them here. Thanks to Bob and Em Hefty (and Jasper and Rookie) for their friendship, generosity, and love of California. From Monday Night to the Lake Show to Godzilla vs King Kong (or Time Bandits), it will always be fun to hang out. BTW, the porch is really nice. Dave Lahr has been my partner-in-crime and roommate from our first days at M.I.T. He is an expert in cruising in obscenely large American cars and eating food quickly with his hands. I hope that one day we'll both be able to either read a deck of cards in French or amass a full Ren and Stimpy collection together. Johann Chan (the Yo) has also been a great roommate and friend who eats, swiffs, and does chemistry like a big bowl of rice. And no acknowledgement would be complete without mentioning Old Speckled Hen and the Phoenix Landing, the 21<sup>st</sup> Amendment, the fine McDonald's and Wendy's restaurants of Central Square, and Aram's #2 as frequent places of respite.

I've also had the fortune of being with great scientists and people in other places. I'd like to thank Fred Anson and Chunnian Shi at Caltech for performing exquisite electrocatalytic studies, and I wish Fred the best in his recent retirement. Thanks to Jim Wishart and J.P. Kirby (a former Nocera-ite) for letting me hang out with them at Brookhaven to do pulse radiolysis experiments. It was always free, J.P. I thank Harry Gray for getting me interested in inorganic chemistry, and for the chance to work in his group as an undergraduate. Don Low was my first mentor in the lab. I've hung out with Jason Hong since my first days as an undergraduate at Caltech and am happy for our lasting friendship. Shouts to the DMT and the D12 as well. It was a pleasure to study in Jean-Pierre Sauvage's laboratory in Strasbourg, and thanks to Labo Sauvage for their hospitality. Thanks also to Mike and Amy Krische, James Bruce, and Karl Coleman for sharing those Thursday night pints at the Irish Times.

I send my love to Mom and Steve, Dad, Nick, and the rest of my family, and thank them for their continued love and support. Finally, I'd like to give a special thanks to my lovely wife Michelle. She's my favorite person and her love, caring, companionship, and support have made me happier than I've ever been. I look forward starting our new life together.

## Table of Contents

Abstract	3
Dedication	4
Acknowledgments	5
Table of Contents	7
List of Tables	12
List of Charts	14
List of Schemes	15
List of Figures	17

### Chapter 1. Protons, Electrons, and Catalytic Bond-Making and Bond-Breaking Chemistry

1.1.	Motivation and Specific Aims	25
1.2	Proton-Coupled Electron Transfer (PCET)	25
1.3	PCET in Biological Oxygen Production and Consumption	28
1.3.1	Oxygen Production in Photosynthesis: Photosystem II	28
1.3.2	Oxygen Consumption in Respiration: Cytochrome <i>c</i> Oxidase	31
1.3.3	Mechanistic Parallels for Biological O—O Bond Formation and Cleavage	32
1.4	Strategies for O—O Bond Formation/Activation Catalyzed by PCET	33
1.5	Organization and Scope of the Thesis	36
1.6	References and Notes	39

### Chapter 2. Pacman Porphyrins Based on Xanthene and Dibenzofuran Scaffolds

2.1	Motivation and Specific Aims	44
2.2	Background	44
2.3	Results and Discussion	47
2.3.1	Synthesis of a Xanthene-Bridged Cofacial Bisporphyrin (DPX) with Lateral and Vertical Preorganization	47
2.3.2	Transition-Metal Complexes of DPX	51
2.3.3	Structural Chemistry of DPX	52
2.3.4	Synthesis of a Dibenzofuran-Bridged Cofacial Bisporphyrin (DPD) with Lateral Preorganization and Vertical Flexibility	58
2.3.5	Transition-Metal Complexes of DPD	60
2.3.6	Structural Chemistry of DPD: Direct Observation of the “Pacman Effect”	61
2.4	Concluding Remarks	65

2.5	Experimental Section	67
2.6	References and Notes	84

### **Chapter 3. Comparison of Pacman Porphyrins Spanning a Large Range of Pocket Sizes**

3.1	Motivation and Specific Aims	90
3.2	Background	90
3.3	Results and Discussion	91
3.3.1	Structural Chemistry	91
3.3.2	EPR Spectroscopy	102
3.3.3	Steady-State Electronic Absorption and Emission Spectroscopy	103
3.3.4	Time-Resolved Electronic Absorption and Emission Spectroscopy	107
3.4	Concluding Remarks	108
3.5	Experimental Section	109
3.6	References and Notes	115

### **Chapter 4. Thermodynamic Characterization of the Pacman Effect**

4.1	Motivation and Specific Aims	118
4.2	Background	118
4.3	Results and Discussion	120
4.3.1	Dibenzofuran-Bridged Cofacial Bisporphyrin (DPD) as a Pyrimidine Receptor with Lateral Preorganization and Vertical Flexibility	120
4.3.2	Diphenylether-Bridged Cofacial Bisporphyrin (DPP) as a Pyrimidine Receptor with Lateral and Vertical Flexibility	128
4.4	Concluding Remarks	132
4.5	Experimental Section	132
4.6	References and Notes	138

### **Chapter 5. Catalytic Four-Electron Reduction of Oxygen to Water by Highly Flexible Dicobalt(II) Pacman Porphyrins**

5.1	Motivation and Specific Aims	144
5.2	Background	144
5.3	Results and Discussion	145
5.3.1	Synthesis and Structural Chemistry of Dicobalt(II) Cofacial Bisporphyrins	145
5.3.2	Redox Properties and Electrocatalytic Reduction of Oxygen to Water	150
5.4	Concluding Remarks	152
5.5	Experimental Section	153



5.6	References and Notes	157
-----	----------------------	-----

## **Chapter 6. Fine Tuning the Pocket Sizes of Cofacial Bisporphyrins: Molecular Teeth for the Pacman Jaws**

6.1	Motivation and Specific Aims	160
6.2	Background	160
6.3	Results and Discussion	162
6.3.1	Cofacial Bisporphyrin Derivatives Containing a Sterically-Demanding Aryl Group Opposite the Spacer	162
6.3.2	Transition-Metal Complexes of DPXM and DPDM	165
6.3.3	Structural Chemistry of DPXM	167
6.4	Concluding Remarks	175
6.5	Experimental Section	175
6.6	References and Notes	185

## **Chapter 7. Catalytic Oxygen Reduction by Dicobalt(II) Cofacial Bisporphyrins: The Proton Issue**

7.1	Motivation and Specific Aims	188
7.2	Background	188
7.3	Results and Discussion	190
7.3.1	Synthesis and Structural Chemistry	190
7.3.2	Electrochemistry	195
7.3.3	Electrocatalytic Reduction of Oxygen	196
7.3.4	Electronic Structure Calculations	198
7.3.5	Electronic Structure Contribution of Proton Coupling to the Selectivity for Four- or Two-Electron Oxygen Reduction Pathways	205
7.4	Concluding Remarks	206
7.5	Experimental Section	208
7.6	References and Notes	211

## **Chapter 8. Pacman Porphyrins for Catalytic PCET Oxidation Chemistry**

8.1	Motivation and Specific Aims	216
8.2	Background	216
8.3	Results and Discussion	217
8.3.1	Three-Branch Strategy for Sterically-Demanding Pacman Porphyrins	217
8.3.2	Suzuki Cross-Coupling Strategy for Meso-Tetraaryl Pacman Porphyrins	221

8.3.3	Peroxide Disproportionation Reactions with Meso-Tetraaryl Pacman Porphyrins	225
8.4	Concluding Remarks	226
8.5	Experimental Section	227
8.6	References and Notes	240
<b>Chapter 9. Hangman Porphyrins Based on Naphthalene, Xanthene, and Dibenzofuran Scaffolds</b>		
9.1	Motivation and Specific Aims	244
9.2	Background	244
9.3	Results and Discussion	246
9.3.1	Synthesis of Hanging Porphyrin Naphthalene (HPN) Architectures via Porphotrimethenes	246
9.3.2	Synthesis of Hanging Porphyrin Xanthene (HPX) Architectures using Lindsey Cyclizations	247
9.3.3	Synthesis of Hanging Porphyrin Dibenzofuran (HPD) and Xanthene (HPX) Architectures using Metal-Catalyzed Cross-Coupling Chemistry	250
9.4	Concluding Remarks	251
9.5	Experimental Section	252
9.6	References and Notes	263
<b>Chapter 10. Hydrogen-Bond Mediated Redox Chemistry of Naphthalene Hangman Porphyrins</b>		
10.1	Motivation and Specific Aims	266
10.2	Background	266
10.3	Results and Discussion	267
10.3.1	Synthesis and Reduction Chemistry of an Unusual Bisiron(III) Carboxylate-Bridged HPN Dimer	267
10.3.2	Synthesis and Reduction Chemistry of Biscyanide Iron(III) HPN Porphyrins	278
10.3.3	Oxidation Chemistry of Zinc(II) HPN Porphyrins	281
10.4	Concluding Remarks	285
10.5	Experimental Section	286
10.6	References and Notes	291

## **Chapter 11. Proton-Coupled O—O Bond Activation on a Synthetic Hydrogen-Bonding Redox Platform**

11.1	Motivation and Specific Aims	296
11.2	Background	296
11.3	Results and Discussion	300
11.3.1	Iron and Manganese Coordination Complexes of HPX and HPD	300
11.3.2	Iron(III) Hydroxide HPX Complex Yields a Heme/Water Channel Structure	302
11.3.3	Thermal Characterization of Water Channel Structure	305
11.3.4	Chemical Generation of High-Valent Ferryl HPX and HPD Derivatives	306
11.3.5	Catalase-Like Disproportionation of Hydrogen Peroxide	307
11.3.6	Olefin Epoxidation	309
11.3.7	Biological Relevance and Mechanistic Proposals	311
11.4	Concluding Remarks	314
11.5	Experimental Section	315
11.6	References and Notes	321

## **Chapter 12. Perspectives and Future Directions**

12.1	Perspectives	330
12.2	Future Directions	330
12.3	Experimental Section	334
12.4	References and Notes	339
	Biographical Note	342
	Curriculum Vitae	343

## List of Tables

<b>Table 2.1.</b>	Crystallographic Data for Zn <sub>2</sub> (DPX) ( <b>16</b> ), Cu <sub>2</sub> (DPX) ( <b>17</b> ), and Ni <sub>2</sub> (DPX) ( <b>18</b> ).	53
<b>Table 2.2.</b>	Selected Bond Lengths (Å) for Zn <sub>2</sub> (DPX) ( <b>16</b> ), Cu <sub>2</sub> (DPX) ( <b>17</b> ), and Ni <sub>2</sub> (DPX) ( <b>18</b> ).	56
<b>Table 2.3.</b>	Selected Bond Angles (deg) for Zn <sub>2</sub> (DPX) ( <b>16</b> ), Cu <sub>2</sub> (DPX) ( <b>17</b> ), and Ni <sub>2</sub> (DPX) ( <b>18</b> ).	56
<b>Table 2.4.</b>	Crystallographically Derived Intradimer Geometrical Features for Zn <sub>2</sub> (DPX) ( <b>16</b> ), Cu <sub>2</sub> (DPX) ( <b>17</b> ), and Ni <sub>2</sub> (DPX) ( <b>18</b> ).	57
<b>Table 2.5.</b>	Crystallographic Data for Zn <sub>2</sub> (DPD) ( <b>28</b> ) and Fe <sub>2</sub> O(DPD) ( <b>31</b> ).	64
<b>Table 2.6.</b>	Selected Bond Lengths (Å) and Angles (deg) for Zn <sub>2</sub> (DPD) ( <b>28</b> ).	65
<b>Table 2.7.</b>	Selected Bond Lengths (Å) and Angles (deg) for Fe <sub>2</sub> O(DPD) ( <b>31</b> ).	65
<b>Table 3.1.</b>	Crystallographic Data for H <sub>4</sub> (DPX) ( <b>15</b> ) and H <sub>4</sub> (DPD) ( <b>27</b> ).	92
<b>Table 3.2.</b>	Crystallographic Data for Pd <sub>2</sub> (DPX) ( <b>22</b> ) and Pd <sub>2</sub> (DPD) ( <b>34</b> ).	93
<b>Table 3.3.</b>	Selected Geometric Distances (Å) and Angles (deg) Calculated for Compounds <b>15</b> and <b>27</b> .	97
<b>Table 3.4.</b>	Selected Bond Lengths (Å) and Angles (deg) for Compounds <b>22</b> and <b>34</b> .	98
<b>Table 3.5.</b>	Crystallographically Derived Intradimer Geometrical Features for DPX and DPD Compounds.	99
<b>Table 3.6.</b>	Comparison of Geometric Intradimer Parameters Derived from EPR and X-ray Crystallography for Dicopper(II) Cofacial Bisporphyrins.	103
<b>Table 3.7.</b>	UV-Visible Absorption Data for DPX and DPD Complexes in Dichloromethane at 298 K, $\lambda_{\text{abs}} / \text{nm}$ ( $\epsilon / 1000 \text{ M}^{-1} \text{ cm}^{-1}$ ).	104
<b>Table 3.8.</b>	Emission Data and Singlet Excited State Parameters for DPX and DPD Complexes in Dichloromethane Solution at 298 K.	105
<b>Table 3.9.</b>	Emission Data and Triplet Excited State Parameters for DPX and DPD Complexes in Cyclohexane Solution at 298 K.	108
<b>Table 3.10.</b>	UV-Visible Absorption Data for Palladium(II) Porphyrin Complexes in Dichloromethane at 298 K, $\lambda_{\text{abs}} / \text{nm}$ ( $\epsilon / 1000 \text{ M}^{-1} \text{ cm}^{-1}$ ).	108
<b>Table 4.1.</b>	Crystallographic Data for Compounds <b>39</b> and <b>42</b> .	124
<b>Table 4.2.</b>	Selected Bond Lengths (Å) and Angles (deg) for Compounds <b>39</b> and <b>42</b> .	125
<b>Table 4.3.</b>	Association constants for binding of various pyridimines to Zn <sub>2</sub> (DPD) ( <b>28</b> ) at 25 °C.	127
<b>Table 5.1.</b>	Crystallographic Data for Co <sub>2</sub> (DPD)•2MeOH ( <b>43</b> ) and Co <sub>2</sub> (DPX) ( <b>44</b> ).	148
<b>Table 5.2.</b>	Selected Bond Lengths (Å) and Angles (deg) for Compounds <b>43</b> and <b>44</b> .	149

<b>Table 6.1.</b>	Crystallographic Data for H <sub>4</sub> (DPXM) ( <b>48</b> ), Zn <sub>2</sub> (DPXM) ( <b>55</b> ), and Mn <sub>2</sub> Cl <sub>2</sub> (DPXM) ( <b>59</b> ).	170
<b>Table 6.2.</b>	Selected Geometric Lengths (Å) for H <sub>4</sub> (DPXM) ( <b>48</b> ), Zn <sub>2</sub> (DPXM) ( <b>55</b> ), and Mn <sub>2</sub> Cl <sub>2</sub> (DPXM) ( <b>59</b> ).	171
<b>Table 6.3.</b>	Selected Geometric Angles (deg) for H <sub>4</sub> (DPXM) ( <b>48</b> ), Zn <sub>2</sub> (DPXM) ( <b>55</b> ), and Mn <sub>2</sub> Cl <sub>2</sub> (DPXM) ( <b>59</b> ).	172
<b>Table 6.4.</b>	Crystallographically Derived Intradimer Geometrical Features for DPX, DPD, and DPXM Compounds.	174
<b>Table 7.1.</b>	Crystallographic Data for Fe <sub>2</sub> O(DPXM) ( <b>66</b> ).	193
<b>Table 7.2.</b>	Selected Bond Lengths (Å) and Angles (deg) for Fe <sub>2</sub> O(DPXM) ( <b>66</b> ).	194
<b>Table 7.3.</b>	Crystallographically Derived Intradimer Geometrical Features for DPXM Compounds.	195
<b>Table 7.4.</b>	Cyclic Voltammetric and Electrocatalytic Data for Dicobalt(II) Pacman Porphyrins at 298 K.	196
<b>Table 7.5.</b>	Geometric Parameters for the Optimized Structures of the O <sub>2</sub> Adducts of Dicobalt Pacman Porphyrins.	204
<b>Table 7.6.</b>	Atomic Charges and Overlap Populations Obtained from Mulliken Population Analysis with Atomic Spin Densities for the Monocation Species Given in Parentheses.	205
<b>Table 10.1.</b>	Crystallographic Data for Compound <b>123</b> .	271
<b>Table 10.2.</b>	Selected Bond Distances (Å) and Angles (deg) for Compound <b>123</b> .	272
<b>Table 10.3.</b>	Spectroscopic Data for Dicyanoiron(III) Porphyrins in Dichloromethane at 298 K.	280
<b>Table 11.1.</b>	Crystallographic Data for Compound <b>132</b> .	303
<b>Table 11.2.</b>	Selected Bond Distances (Å) and Angles (deg) for <b>132</b> .	304
<b>Table 11.3.</b>	Epoxidation of Olefins Catalyzed by Manganese Hangman Complexes and MnCl(TMP).	310

## List of Charts

<b>Chart 2.1</b>	45
<b>Chart 2.2</b>	47
<b>Chart 2.3</b>	47
<b>Chart 2.4</b>	52
<b>Chart 2.5</b>	61
<b>Chart 3.1</b>	91
<b>Chart 4.1</b>	120
<b>Chart 5.1</b>	145
<b>Chart 6.1</b>	161
<b>Chart 6.2</b>	162
<b>Chart 6.3</b>	166
<b>Chart 6.4</b>	166
<b>Chart 7.1</b>	190
<b>Chart 8.1</b>	218
<b>Chart 8.2</b>	221
<b>Chart 8.3</b>	222
<b>Chart 9.1</b>	245
<b>Chart 11.1</b>	300
<b>Chart 12.1</b>	333

## List of Schemes

<b>Scheme 2.1.</b>	48
<b>Scheme 2.2.</b>	49
<b>Scheme 2.3.</b>	50
<b>Scheme 2.4.</b>	59
<b>Scheme 4.1.</b>	129
<b>Scheme 5.1.</b>	151
<b>Scheme 6.1.</b>	163
<b>Scheme 6.2.</b>	163
<b>Scheme 6.3.</b>	164
<b>Scheme 6.4.</b>	164
<b>Scheme 6.5.</b>	165
<b>Scheme 7.1.</b>	205
<b>Scheme 8.1.</b>	218
<b>Scheme 8.2.</b>	219
<b>Scheme 8.3.</b>	220
<b>Scheme 8.4.</b>	223
<b>Scheme 8.5.</b>	223
<b>Scheme 8.6.</b>	224
<b>Scheme 8.7.</b>	224
<b>Scheme 8.8.</b>	225
<b>Scheme 9.1.</b>	246
<b>Scheme 9.2.</b>	247
<b>Scheme 9.3.</b>	248
<b>Scheme 9.4.</b>	249
<b>Scheme 9.5.</b>	251
<b>Scheme 9.6.</b>	251
<b>Scheme 10.1.</b>	268
<b>Scheme 10.2.</b>	270
<b>Scheme 10.3.</b>	274
<b>Scheme 10.4.</b>	279
<b>Scheme 10.5.</b>	281
<b>Scheme 10.6.</b>	283
<b>Scheme 10.7.</b>	285
<b>Scheme 11.1.</b>	301

<b>Scheme 11.2.</b>	301
<b>Scheme 11.3.</b>	301
<b>Scheme 11.4.</b>	314
<b>Scheme 12.1.</b>	331
<b>Scheme 12.2.</b>	332
<b>Scheme 12.3.</b>	332



## List of Figures

<b>Figure 1.1.</b>	D—(amidinium-carboxylate)—A (left) and D—(carboxylate-amidinium)—A (right) salt bridge constructs for fundamental PCET studies.	27
<b>Figure 1.2.</b>	D—(amidinium-carboxylate)—A (left) and D—(carboxylate-amidinium)—A (right) salt bridge constructs based on ruthenium(II) polypyridine donors and nitroaromatic acceptors.	27
<b>Figure 1.3.</b>	Major components in PSII.	29
<b>Figure 1.4.</b>	Mechanistic proposals for the critical O—O bond-making step in water oxidation at the OEC in PSII by (a) radical coupling of bridging metal-oxo units and (b) nucleophilic attack of a metal-hydroxide on an electrophilic terminal metal-oxo.	30
<b>Figure 1.5.</b>	Simplified reaction scheme for oxygen reduction catalyzed by CcO.	32
<b>Figure 1.6.</b>	Babcock's mechanisms for conserved O—O bond formation and cleavage in (a) PSII and (b) CcO, respectively.	33
<b>Figure 1.7.</b>	Possible pathways for O—O bond formation from (a) radical-type coupling of metal-oxo units and (b) nucleophilic attack of hydroxide(oxide) on an electrophilic metal-oxo center.	34
<b>Figure 1.8.</b>	Mechanistic comparison of oxygen-element bond-forming reactions from metal-oxo platforms for (a) olefin epoxidation and (b) O—O coupling. Note that substrate attack occurs from an electronically-favored side-on geometry.	35
<b>Figure 1.9.</b>	Relationships of Salt Bridge, Pacman, and Hangman systems designed for the study of PCET.	36
<b>Figure 2.1.</b>	Standard reduction potentials for reduction of dioxygen to water. The number of electrons transferred is provided in parentheses.	44
<b>Figure 2.2.</b>	Crystal structure of Zn <sub>2</sub> (DPX) ( <b>16</b> ). Thermal ellipsoids are drawn at the 25% probability level. Hydrogen atoms and solvent molecules within the lattice have been omitted for clarity.	54
<b>Figure 2.3.</b>	Crystal structure of Cu <sub>2</sub> (DPX) ( <b>17</b> ). Thermal ellipsoids are drawn at the 25% probability level. Hydrogen atoms and solvent molecules within the lattice have been omitted for clarity.	55
<b>Figure 2.4.</b>	Crystal structure of Ni <sub>2</sub> (DPX) ( <b>18</b> ). Thermal ellipsoids are drawn at the 25% probability level. Hydrogen atoms and solvent molecules within the lattice have been omitted for clarity.	55

<b>Figure 2.5.</b>	Comparative views of the crystal structures of <b>16-18</b> : (a) top view, perpendicular to porphyrin planes, (b) side view, perpendicular to bridge plane, (c) side view, parallel to bridge plane. Side groups and hydrogen atoms have been omitted for clarity.	58
<b>Figure 2.6.</b>	Crystal structure of Zn <sub>2</sub> (DPD) ( <b>28</b> ). Thermal ellipsoids are drawn at the 25% probability level. Hydrogen atoms and solvent molecules within the lattice have been omitted for clarity.	63
<b>Figure 2.7.</b>	Crystal structure of Fe <sub>2</sub> O(DPD) ( <b>31</b> ). Thermal ellipsoids are drawn at the 25% probability level. Hydrogen atoms and solvent molecules within the lattice have been omitted for clarity.	63
<b>Figure 3.1.</b>	Crystal structure of H <sub>4</sub> (DPX) ( <b>15</b> ). Thermal ellipsoids are drawn at the 25% probability level. Hydrogen atoms and solvent molecules within the lattice have been omitted for clarity.	94
<b>Figure 3.2.</b>	Crystal structure of H <sub>4</sub> (DPD) ( <b>27</b> ). Thermal ellipsoids are drawn at the 25% probability level. Hydrogen atoms and solvent molecules within the lattice have been omitted for clarity.	95
<b>Figure 3.3.</b>	Crystal structure of Pd <sub>2</sub> (DPX) ( <b>22</b> ). Thermal ellipsoids are drawn at the 25% probability level. Hydrogen atoms and solvent molecules within the lattice have been omitted for clarity.	96
<b>Figure 3.4.</b>	Crystal structure of Pd <sub>2</sub> (DPD) ( <b>34</b> ). Thermal ellipsoids are drawn at the 25% probability level. Hydrogen atoms and solvent molecules within the lattice have been omitted for clarity.	96
<b>Figure 3.5.</b>	Comparative views of the crystal structures of H <sub>4</sub> (DPX) ( <b>15</b> ) and H <sub>4</sub> (DPD) ( <b>27</b> ): (a) top view; (b) side view, perpendicular to the bridge plane; (c) side view, parallel to the bridge plane. Hydrogen atoms omitted for clarity.	100
<b>Figure 3.6.</b>	Illustrated distances a–b and c–d for the cofacial bisporphyrin systems DPX (left) and DPD (right). Table 3.5 sub-caption defines the methods by which the crystallographically derived geometric features were measured.	102
<b>Figure 3.7.</b>	(a) Absorption and (b) emission spectra of Zn <sub>2</sub> (DPX) ( <b>16</b> ) (dotted line), Zn <sub>2</sub> (DPD) ( <b>28</b> ) (solid line), and Zn(Etio) (dashed line) in dichloromethane solution at room temperature. Spectra are normalized in intensities.	106
<b>Figure 4.1.</b>	Selected <sup>1</sup> H NMR spectra of <b>28</b> containing (a) 0, (b) 0.67 eq, (c) 1 eq and (d) 3 eq of 2-aminopyrimidine in CD <sub>2</sub> Cl <sub>2</sub>	121

solution at 25 °C. The spectral range captures the signals for the meso protons of free host **28** and host-guest complex **42**, which are found in the range of 9 to 10 ppm.

- Figure 4.2.** Job plot establishing the 1:1 stoichiometry for binding of 2-aminopyrimidine guest inside the cleft of host  $Zn_2(DPD)$  (**28**). 121
- Figure 4.3.** Crystal structure of  $Zn_2(DPD)(2\text{-aminopyrimidine})$  (**42**). Thermal ellipsoids are drawn at the 25% probability level. Hydrogen atoms have been omitted for clarity. 123
- Figure 4.4.** Absorption spectra of **28** in the presence of 0, 0.16, 0.32, 0.48, 0.64, 0.80, and 1.00 eq of 2-aminopyrimidine in toluene solution at 25 °C. The final spectrum does not change upon further additions of 2-aminopyrimidine. 126
- Figure 4.5.** Crystal structure of  $Zn_2(DPP)$  (**39**). Thermal ellipsoids are drawn at the 25% probability level. Hydrogen atoms and solvent molecules within the lattice have been omitted for clarity. 130
- Figure 4.6.** Comparative views of the crystal structures of  $Zn_2(DPD)$  (**28**),  $Zn_2(DPP)$  (**39**),  $Zn_2(DPD)(2\text{-aminopyrimidine})$  (**42**): (a) top view; (b) side view, perpendicular to the bridge plane. Hydrogen atoms omitted for clarity. 131
- Figure 5.1.** Crystal structure of  $Co_2(DPD)\cdot 2MeOH$  (**43**). Thermal ellipsoids are drawn at the 25% probability level. Hydrogen atoms and solvent molecules within the lattice have been omitted for clarity. 146
- Figure 5.2.** Crystal structure of  $Co_2(DPX)$  (**44**). Thermal ellipsoids are drawn at the 25% probability level. Hydrogen atoms and solvent molecules within the lattice have been omitted for clarity. 147
- Figure 5.3.** Cyclic voltammetric responses at an edge-plane graphite (EPG) electrode, covered with a thin layer of nitrobenzene containing (a) 0.17 mM  $Co_2(DPD)$  (**43**) or (b) 0.20 mM  $Co_2(DPX)$  (**44**). The EPG electrode was immersed in an aqueous supporting electrolyte containing 2 M  $HClO_4$ . Scan rate, 10 mV/s. 150
- Figure 5.4.** Rotating Pt ring-disk voltammograms for reduction of  $O_2$  at pyrolytic graphite disks coated with (a)  $Co_2(DPD)$  (**43**) or (b)  $Co_2(DPX)$  (**44**). Rotation rate, 100 rpm; disk current,  $S = 10 \mu A$ ; ring current,  $S = 5 \mu A$ ; supporting electrolyte, 0.5 M  $HClO_4/1.5$  M TFA saturated with air. 151
- Figure 5.5.** EPR spectrum of  $[Co_2(DPX)(\mu-O_2)(1,5\text{-Dicyclohexylimidazole})_2][PF_6]$  152

- taken in dichloromethane solution at 298 K.
- Figure 6.1.** Crystal structure of  $H_4(DPXM)$  (**48**). Thermal ellipsoids are drawn at the 25% probability level. Hydrogen atoms and solvent molecules within the lattice have been omitted for clarity. 168
- Figure 6.2.** Crystal structure of  $Zn_2(DPXM)$  (**55**). Thermal ellipsoids are drawn at the 25% probability level. Hydrogen atoms and solvent molecules within the lattice have been omitted for clarity. 168
- Figure 6.3.** Crystal structure of  $Mn_2Cl_2(DPXM)$  (**59**). Thermal ellipsoids are drawn at the 25% probability level. Hydrogen atoms and solvent molecules within the lattice have been omitted for clarity. 169
- Figure 6.4.** Illustrated distances a–b and c–d for the cofacial bisporphyrin systems DPXM (left) and DPDM (right). Table 6.4 sub-caption defines the methods by which the crystallographically derived geometric features were measured. 171
- Figure 6.5.** Comparative views of the crystal structures of  $Zn_2(DPX)$  (**16**),  $Zn_2(DPXM)$  (**55**), and  $Zn_2(DPD)$  (**28**): (a) side view, perpendicular to the bridge plane; (b) side view, parallel to the bridge plane. Alkyl side groups and hydrogen atoms omitted for clarity. 173
- Figure 7.1.** Crystal structure of  $Fe_2O(DPXM)$  (**66**). Thermal ellipsoids are drawn at the 25% probability level. Hydrogen atoms and solvent molecules within the lattice have been omitted for clarity. 192
- Figure 7.2.** Structural observation of the Pacman effect for the DPXM framework, depicting (a) open and (b) closed forms of the platform. Thermal ellipsoids are drawn at the 25% probability level. Hydrogen atoms and solvent molecules within the lattice have been omitted for clarity. 194
- Figure 7.3.** Cyclic voltammetric responses at an edge-plane graphite (EPG) electrode, covered with a thin layer containing (a) 0.07 mM  $Co_2(DPXM)$  (**64**) in tolunitrile or (b) 0.20 mM  $Co_2(DPDM)$  (**65**) in nitrobenzene. The EPG electrode was immersed in an aqueous supporting electrolyte containing 2 M  $HClO_4$ . Scan rate, 10 mV/s. 196
- Figure 7.4.** Rotating Pt ring-disk voltammograms for reduction of  $O_2$  at pyrolytic graphite disks coated with (a)  $Co_2(DPX)$  (**44**), (b)  $Co_2(DPD)$  (**43**), (c)  $Co_2(DPXM)$  (**64**), or (d)  $Co_2(DPDM)$  (**65**). Rotation rate, 100 rpm; disk current,  $S = 10 \mu A$ ; ring current,  $S = 5 \mu A$ ; supporting electrolyte for **43** and **44**, 0.5 M  $HClO_4$ /1.5 M TFA saturated with air; supporting electrolyte for **64** and **65**, 2 M  $HClO_4$  saturated with air. 197

<b>Figure 7.5.</b>	Optimized structures of the DPX-O <sub>2</sub> adducts (a) [Co <sub>2</sub> (DPX)(O <sub>2</sub> )] <sup>+</sup> and (b) [Co <sub>2</sub> (DPX)(O <sub>2</sub> )] <sup>2+</sup> .	200
<b>Figure 7.6.</b>	Optimized structures of the monocations (a) [Co <sub>2</sub> (DPX)(O <sub>2</sub> )] <sup>+</sup> and (b) [Co <sub>2</sub> (DPXM)(O <sub>2</sub> )] <sup>2+</sup> .	201
<b>Figure 7.7.</b>	Singly-occupied HOMOs of [Co <sub>2</sub> (DPX)(O <sub>2</sub> )] <sup>+</sup> (left) and [Co <sub>2</sub> (DPXM)(O <sub>2</sub> )] <sup>+</sup> (right). (a) Side view, perpendicular to the bridge plane, (b) top view, perpendicular to the porphyrin planes.	203
<b>Figure 7.8.</b>	HOMOs of (a) [Co <sub>2</sub> (DPX)(O <sub>2</sub> )] <sup>2+</sup> and (b) [Co <sub>2</sub> (DPXM)(O <sub>2</sub> )] <sup>2+</sup> .	204
<b>Figure 8.1.</b>	Turnover numbers (TON) for oxygen release from H <sub>2</sub> O <sub>2</sub> dismutation catalyzed by Mn <sub>2</sub> Cl <sub>2</sub> (DTMPX) ( <b>97</b> ) and Mn <sub>2</sub> Cl <sub>2</sub> (DTMPD) ( <b>98</b> ), their parent etio-type systems Mn <sub>2</sub> Cl <sub>2</sub> (DPX) ( <b>21</b> ) and Mn <sub>2</sub> Cl <sub>2</sub> (DPD) ( <b>33</b> ), and the monomer MnCl(TMP) (denoted as TMP). Error bars for the TON (not shown) are approximately ± 10%.	226
<b>Figure 10.1.</b>	Absorption spectra of ester <b>122</b> (solid line) and FeOH(TMP) (dotted line) in toluene.	268
<b>Figure 10.2.</b>	Absorption spectra of <b>123</b> (solid line) and Fe(1-naphthoate)(TMP) (dotted line) in toluene. The spectrum of the latter compound is multiplied by a factor of two.	269
<b>Figure 10.3.</b>	Crystal structure of Fe <sub>2</sub> (HPN-CO <sub>2</sub> <sup>-</sup> ) ( <b>123</b> ). Thermal ellipsoids are drawn at the 25% probability level. Hydrogen atoms and solvent molecules within the lattice have been omitted for clarity.	270
<b>Figure 10.4.</b>	Cyclic voltammogram of <b>123</b> in dichloromethane containing 0.1 M <i>n</i> -tetrabutylammonium perchlorate (TBAP) as supporting electrolyte. Scan rate = 100 mV/s, potentials reported vs Ag/AgCl.	273
<b>Figure 10.5.</b>	Thin-layer spectra recorded during the reduction of <b>123</b> at -0.6 V in dichloromethane containing 0.1 M tetra <i>n</i> -butylammonium perchlorate (TBAP) as supporting electrolyte.	273
<b>Figure 10.6.</b>	Transient absorption spectra obtained at 200 ns, 500 ns, 1 μs, and 4 μs after flash photolysis of an CH <sub>3</sub> CN solution containing <b>123</b> (90 μM), Ru(bpy) <sub>3</sub> <sup>2+</sup> (20 μM), and <i>p</i> -toluidine (20 mM) at 298 K.	274
<b>Figure 10.7.</b>	(a) Q-band region difference spectrum obtained from thin-layer spectroelectrochemistry at 298 K and (b) Q-band region transient absorption spectrum taken 5 μs after laser photolysis of an CH <sub>3</sub> CN solution containing <b>123</b> (100 μM), Ru(bpy) <sub>3</sub> <sup>2+</sup> (20 μM), and <i>p</i> -toluidine (20 mM) at 298 K.	275
<b>Figure 10.8.</b>	Single-wavelength transient absorption spectrum at 440 nm	276

- obtained after flash photolysis of an  $\text{CH}_3\text{CN}$  solution containing **123** (100  $\mu\text{M}$ ),  $\text{Ru}(\text{bpy})_3^{2+}$  (20  $\mu\text{M}$ ), and *p*-toluidine (20 mM) at 298 K.
- Figure 10.9.** Plot of observed pseudo-first-order rate constants for reduction of **123** with photogenerated  $\text{Ru}(\text{bpy})_3^+$  as a function of **[123]**. Line is best fit from least-squares fitting. 276
- Figure 10.10.** Q-band region transient absorption spectrum taken 300 ns after pulse photolysis. Sample consists of a 200  $\mu\text{M}$  solution of **123** in tetrahydrofuran at 298 K. 277
- Figure 10.11.** Plot of observed pseudo-first-order rate constants for radiolytic reduction of **123** as a function of **[123]**. Line is best fit from least-squares fitting. 278
- Figure 10.12.** Absorption spectra of ester **126** (dotted line) and **127** (solid line) in dichloromethane solution at 298 K. 279
- Figure 10.13.** Cyclic voltammograms of **126** (dotted line) and **127** (solid line) in dichloromethane containing 0.1 M *n*-tetrabutylammonium perchlorate (TBAP) as supporting electrolyte. Scan rate = 100 mV/s, potentials reported vs Ag/AgCl. 281
- Figure 10.14.** Cyclic voltammograms of (a) **128** and (b) **129** in dichloromethane containing 0.1 M *n*-tetrabutylammonium perchlorate (TBAP) as supporting electrolyte. Scan rate = 100 mV/s, potentials reported vs Ag/AgCl. 282
- Figure 10.15.** Thin-layer spectra recorded during the first oxidation of **129** at +0.9 V in dichloromethane containing 0.1 M tetra *n*-butylammonium perchlorate (TBAP) as supporting electrolyte. 283
- Figure 10.16.** Thin-layer spectra recorded during the first oxidation of **128** at +0.9 V in dichloromethane containing 0.1 M tetra *n*-butylammonium perchlorate (TBAP) as supporting electrolyte. 284
- Figure 11.1.** Comparison of proposed proton-activated O—O bond cleavage for iron-oxo heme formation in (a) peroxidases, (b) catalases, and (c) cytochrome P450 monooxygenases. 297
- Figure 11.2.** Crystal structure of  $\text{FeOH}(\text{HPX}-\text{CO}_2\text{H})\cdot\text{H}_2\text{O}$  (**132**). Thermal ellipsoids are drawn at the 25% probability level. Hydrogen atoms and solvent molecules within the lattice have been omitted for clarity. 302
- Figure 11.3.** Absorption spectral changes upon addition of  $[\text{NBu}_4][\text{OH}]$  to a toluene solution of **132**, showing conversion to product **132d**.  $[\text{NBu}_4][\text{OH}]$  added = 0, 0.33, 0.50, 0.67, 0.85, 1.0, 1.5, 2.0 equiv. 305

<b>Figure 11.4.</b>	Differential scanning calorimetry (DSC) scan of a solid sample of <b>132</b> under nitrogen.	306
<b>Figure 11.5.</b>	Absorption spectra of high-valent ferryl-HPX complexes analogous to Compounds I and II of heme oxygenases. Spectrum (a) was obtained by oxidation of FeCl(HPX-CO <sub>2</sub> H) ( <b>130</b> ) with PhIO in dichloromethane at -78 °C. Spectrum (b) was obtained by oxidation of FeOH(HPX-CO <sub>2</sub> H) ( <b>132</b> ) with mCPBA in THF at -61 °C.	307
<b>Figure 11.6.</b>	Oxygen release from H <sub>2</sub> O <sub>2</sub> dismutation catalyzed by <b>130</b> at 25 °C in a biphasic dichloromethane/pH 7 phosphate buffer medium.	308
<b>Figure 11.7.</b>	Turnover numbers (TON) for oxygen release from H <sub>2</sub> O <sub>2</sub> dismutation catalyzed by iron complexes <b>130</b> , <b>131</b> , <b>136</b> , and FeCl(TMP). In the graph, TMP denotes FeCl(TMP), and TMP* denotes FeCl(TMP) + 1 equiv benzoic acid.	309
<b>Figure 11.8.</b>	Time-course plot for the epoxidation of <i>cis</i> -cyclooctene with hydrogen peroxide catalyzed by <b>134</b> (triangles), <b>135</b> (squares), and <b>137</b> / MnCl(TMP) (circles). The addition of 1 equiv benzoic acid to MnCl(TMP) shows no detectible enhancement in catalytic epoxidation reactivity.	311
<b>Figure 12.1.</b>	Examples of Pacman and Hangman systems incorporating alternative ligand sets.	334

*Chapter 1*

**Protons, Electrons, and Catalytic Bond-Making  
and Bond-Breaking Chemistry**

A portion of the work presented in this chapter has been published:

Chang, C. J.; Brown, J. D. K.; Chang, M. C. Y.; Baker, E. A.; Nocera, D. G. In *Electron Transfer in Chemistry*, V. Balzani, Ed., Wiley-VCH, Weinheim, Germany, 2001, Vol. 3.2.4, p 409-461.



## 1.1 Motivation and Specific Aims

Aerobic life is predicated on the production and consumption of dioxygen. The interconversion of molecular oxygen and water in Nature forms the basis for the essential metabolic processes of photosynthesis and respiration. On a molecular scale, the chemical conversions attendant to the oxygen/water cycle require the coupled transport of four electrons and four protons to mediate the cleavage and formation of O—O bonds.

The research presented in this thesis is directed towards understanding the coupling between proton and electron motion in such catalytic bond-breaking and bond-making reactions, with a central focus on chemical conversions relevant to those that accompany oxygen reduction to water in oxygen-metabolizing metalloproteins and oxygen production from water in the photosynthetic process. Inorganic coordination chemistry is a vehicle for creating well-defined, homogeneous catalysts to effect these challenging chemical transformations involving reactive oxygen species (ROS). In an effort to deliver multiple electron and proton equivalents to a small-molecule substrate in a proficient manner, we have devised synthetic scaffolds that place dual redox or redox and acid-base sites in a face-to-face arrangement. Two general classes of compounds have been elaborated: (i) symmetric Pacman systems composed of two metalloporphyrin redox sites, and (ii) asymmetric Hangman systems containing a metalloporphyrin redox site with a pendant acid-base functionality.

The remainder of this chapter will introduce the fundamental concept of coupled proton and electron transport, a process we designate proton-coupled electron transfer (PCET). The contributions of PCET to biological O—O bond formation and cleavage chemistry will then be discussed briefly, followed by our strategy to use PCET as a framework for developing catalytic bond-making and bond-breaking reaction cycles based on synthetic Pacman and Hangman constructs. We will conclude by presenting the organization and scope of this thesis work.

## 1.2 Proton-Coupled Electron Transfer (PCET)

The interplay between proton and electron transfer has far-ranging implications in biology, chemistry, and physics. For instance, proton motion coupled to electron transfer is the basic mechanism of bioenergetic conversion. Oxidases and reductases have structures optimized to gather energy along charge-separating networks to drive proton translocation. The resultant proton gradient gives rise to a transmembrane chemical potential that provides energy for the activation of small molecules and the synthesis of complex biomolecules.<sup>1-3</sup> At the other end of the scientific spectrum, the coupling between proton and electron lies at the heart of the quintessential issues in electrochemistry such as hydrogen ion discharge at a platinum

electrode.<sup>4,5</sup> Recently, efforts in supramolecular solid-state chemistry have been directed toward the rational design of coupled electron-proton transfer systems with novel electronic or photonic properties.<sup>6-9</sup>

From a more fundamental standpoint, PCET steps beyond the simple electron transfer reactions treated by Marcus theory.<sup>10</sup> The concept of PCET encompasses both the synchronous and asynchronous coupling of proton and electron transport,<sup>11-22</sup> with the former more commonly known as hydrogen-atom transfer (HAT).<sup>14,15,23,24</sup> The making and breaking of chemical bonds, occurrences not originally considered in Marcus theory, typically attend electron transfer in many oxidation-reduction reactions.<sup>25-29</sup> The charge shift resulting from electron *and* proton motion couples to the polarization of the surrounding environment, thus providing a unique mechanism for PCET. For example, simple electron transfer (ET) is generally defined within the Marcus-Levich framework per equation 1.1,<sup>10,30,31</sup>

$$k_{\text{ET}} = V_{\text{el}}^2 \cdot FC_{\text{ET}} \quad (1.1)$$

where  $V_{\text{el}}$  is the electronic coupling and  $FC_{\text{ET}}$  is the Franck-Condon weighted density of states. PCET steps beyond this basic model because both the electron *and* the proton may affect  $V_{\text{el}}$  *and*  $FC$  (for this case we define a  $FC_{\text{PCET}}$ ).  $V_{\text{el}}$  will depend parametrically on the position of the proton in the reaction interface; extensive charge redistribution will lead to  $FC_{\text{PCET}}$  contributions.

To understand the origins of the  $FC_{\text{PCET}}$  factor, consider again a simple electron-transfer reaction. The electron tunnels through the potential barrier from donor to acceptor when the solvent fluctuates to a configuration where the energies of the reactants and products are essentially equal. For PCET, the electron *and* proton tunnel and now both events are induced by solvent fluctuations; coupling arises because the electron and proton influence each other thermodynamically and kinetically.<sup>11-22</sup> As the electron moves, the  $\text{p}K_{\text{a}}$ s of the donor and acceptor will change; but to predict kinetics, the driving force ( $\Delta G^{\circ}$ ) of the reaction is not sufficient. The  $FC_{\text{PCET}}$  factors will also be affected by changes in  $\Delta G^{\circ}$  and by the charge redistribution resulting from electron *and* proton motion. Thus any motion of the proton from its initial position will perturb  $V_{\text{el}}$  and  $FC_{\text{ET}}$ , thereby affecting the kinetics for electron transfer.

To investigate the basic mechanistic issues surrounding PCET, Nocera has begun examining photoinduced reactions of complementary donor-acceptor pairs that are mediated by an amidinium-carboxylate interface.<sup>13,32-39</sup> This salt bridge, which combines the dipole of an electrostatic ion-pair interaction with a hydrogen-bonding scaffold, allows for the rigorous investigation of how proton motion within a hydrogen-bond interface affects the charge,

energetics, and polarity of an electron transport chain. The systems depicted in Figure 1.1 display donor-acceptor motifs of this type, as the overall oxidation-reduction transformation may involve both electron transfer and bond-making/-breaking processes that accompany proton motion within the hydrogen-bond interface.

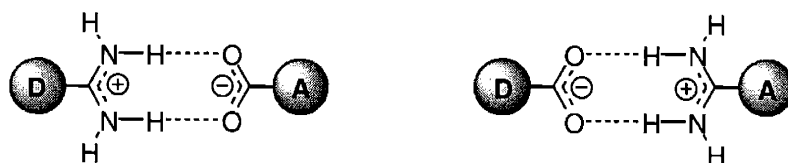


**Figure 1.1.** D—(amidinium-carboxylate)—A (left) and D—(carboxylate-amidinium)—A (right) salt bridge constructs for fundamental PCET studies.

A comparative kinetics study with ruthenium(II) polypyridine donors and nitroaromatic acceptors reveals that the rate of electron transfer depends significantly on the salt bridge and its orientation with respect to the electron transfer pathway (Figure 1.2).<sup>34</sup> Specifically, the rate of electron transfer through the D—(amidinium-carboxylate)—A salt bridge is ca.  $10^2$  times slower than that for the switched-interface system D—(carboxylate-amidinium)—A.

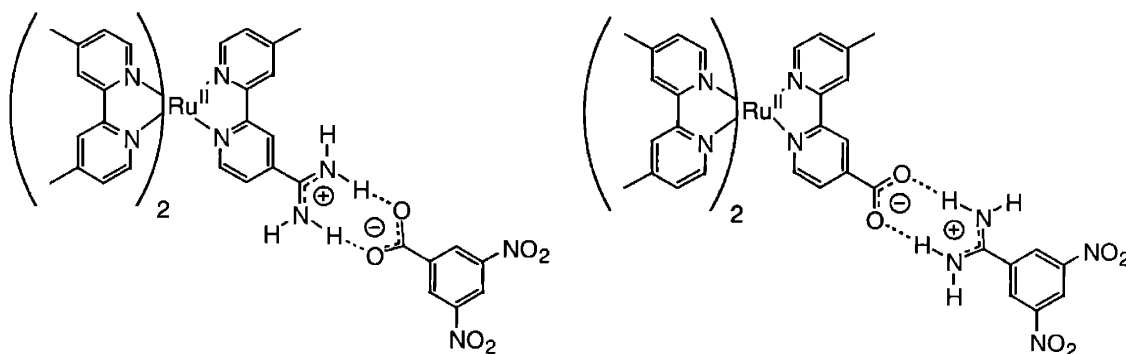


**Figure 1.2.** D—(amidinium-carboxylate)—A (left) and D—(carboxylate-amidinium)—A (right) salt bridge constructs based on ruthenium(II) polypyridine donors and nitroaromatic acceptors.

This rate disparity may have several origins. For D—(amidinium-carboxylate)—A, the permanent dipole of the salt bridge is in the direction of electron transfer. In contrast, the electron-transfer pathway in D—(carboxylate-amidinium)—A opposes the salt bridge dipole. Internal electrostatic fields affect the rates of electron transfer by altering the driving force of reaction relative to the isolated constituents. This feature results in an unfavorable energetic contribution in the case of D—(amidinium-carboxylate)—A and a favorable one in the case of D—(carboxylate-amidinium)—A. The thermodynamics may be further modified by

reorganization energies associated with the salt bridge. In D—(amidinium-carboxylate)—A, a proton shift from the ruthenium(II) amidinium donor to the carboxylate acceptor can stabilize the developing charge of the electron on the acceptor. Since the proton charge is strongly coupled to the solvent dipoles, charge shift within the salt bridge will be accompanied by significant solvent polarization, thereby giving rise to additional Franck-Condon factors. For D—(carboxylate-amidinium)—A, the proton already resides on the acceptor, and there it is likely to remain upon the arrival of the electron. Franck-Condon factors are thus minimized for D—(carboxylate-amidinium)—A. It should be emphasized that complete proton transfer in D—(amidinium-carboxylate)—A is not necessary for the PCET to be strongly perturbed; any shift of the proton from its initial state will affect the Franck-Condon factors for PCET.<sup>14,18</sup> Finally, differences in hydrogen-bond strengths in these asymmetric interfaces may play a role in the efficiencies of electronic coupling. The electron-withdrawing nitro groups on the acceptor will stabilize the negative charge on the carboxylate, resulting in a weaker hydrogen bond for D—(amidinium-carboxylate)—A than for D—(carboxylate-amidinium)—A and, hence, a correspondingly weaker electronic-coupling pathway.

The knowledge gained from studies of single-electron/single-proton PCET processes in well-defined model systems poises us to begin exploring small-molecule activation chemistry catalyzed by multiple PCET processes. The following section places PCET within the context of O—O bond formation and cleavage in natural systems. In particular, we highlight the seminal work of the late Gerald T. Babcock, whose vision has inspired our endeavors to study ROS activation chemistry catalyzed by PCET.

## **1.3 PCET in Biological Oxygen Production and Consumption**

### **1.3.1 Oxygen Production in Photosynthesis: Photosystem II**

Molecular oxygen is Nature's most versatile and useful metabolic oxidant. Virtually all of the dioxygen on earth is generated by the light-driven oxidation of water during photosynthesis in plants, algae, and cyanobacteria.<sup>40</sup> This remarkable process is carried out by Photosystem II (PSII), a 500 kDa multi-subunit complex that spans the thylakoid membrane in chloroplasts.<sup>41-47</sup> Inspection of the chemically balanced reaction catalyzed by PSII shows the reduction of two plastoquinone molecules per O<sub>2</sub> molecule produced. In addition, four protons are released that pass through the thylakoid membrane. The proton gradient created is used for ATP synthesis, and the electron equivalents stored by the plastoquinol product are eventually employed by Photosystem I (PSI) to reduce CO<sub>2</sub> during the Calvin cycle.<sup>40</sup>

The concomitant conversions of light to chemical energy and water to oxygen in PSII are specifically associated with four charge separation events across the thylakoid membrane (Figure 1.3). Light absorption by P680, the specialized chlorophyll complex embedded within protein subunits D1 and D2 of the PSII reaction center, generates a charge-separated state,  $P680^+Q_A^-$ , that lives for ca. 200  $\mu$ s. Subsequent electron transfer from  $Q_A$  to the secondary acceptor  $Q_B$  mobilizes the reduced plastoquinone for electron delivery to PSI. After each of the four successive, light-initiated charge separating steps,  $P680^+$  extracts an electron from a tetranuclear manganese cluster via a redox-active tyrosine  $Y_Z$  (Y161 of subunit D1) that prevents wasteful charge recombination of  $P680^+Q_A^-$ . In turn, the four positive charges accumulated by the tetramanganese cluster oxidize two molecules of water to oxygen and release four proton equivalents.

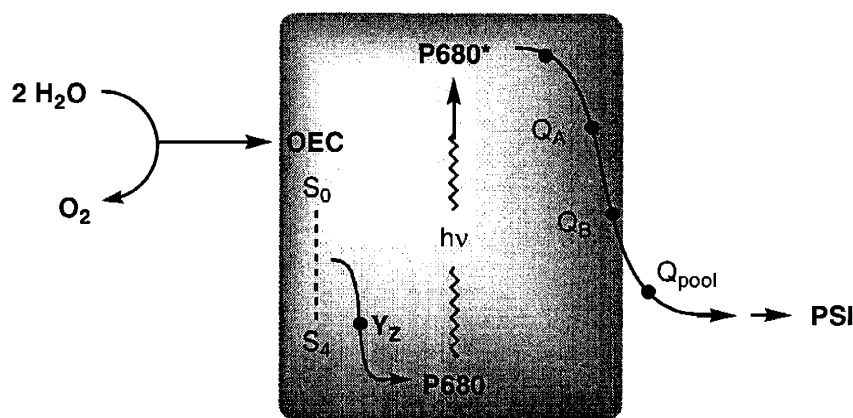


**Figure 1.3.** Major components in PSII.

The  $Mn_4$  cluster,  $Y_Z$ , and two non-redox cofactors,  $Ca^{2+}$  and  $Cl^-$ , comprise a single catalytic center known as the oxygen-evolving complex (OEC). Kok summarized the water-oxidation process by postulating the S-state notation (Kok cycle) in which the number of oxidizing equivalents stored in the OEC is denoted  $S_n$ .<sup>48</sup> The photochemistry/oxidizing equivalent accumulation process is described by equation 1.2. Only when the  $S_4$  state is reached does water oxidation occur.



Many speculative proposals have been made for the mechanism of photosynthetic water oxidation at the OEC over the past 30 years.<sup>49</sup> These mechanisms, which include structural rearrangements of cubane, adamantane, and butterfly clusters, have been reviewed previously

and will not be considered in detail here.<sup>50-53</sup> Notably, most of these proposals have not taken into account the role of the essential  $Y_Z$  residue.

More recently, two alternative classes of mechanisms have emerged that specifically employ two of the four manganese centers to carry out the O—O chemistry. The starting point for both proposals is the “dimer of dimers” structure first proposed by Sauer and Klein for the manganese cluster based on extensive EXAFS studies,<sup>43</sup> in addition, a recent low-resolution crystal structure<sup>54</sup> and EPR measurements<sup>55</sup> reveal the existence of a “3 + 1” form of the enzyme as well. Yachandra, Sauer, and Klein propose that the O—O bond-forming step occurs by radical coupling of bridging metal-oxo units in a highly-oxidized dimanganese core (Figure 1.4a).<sup>43</sup> Chemical precedent for O—O bond formation from such a unit is provided by the solvent-dependent interconversion of peroxo-dicopper(II) and bis( $\mu$ -oxo)-dicopper(III) complexes.<sup>56,57</sup> Alternatively, Babcock has put forth a model that postulates a direct role for the  $Y_Z$  radical in water oxidation (Figure 1.4b).<sup>42,58</sup> Terminal metal-oxo species are invoked here, as well as the participation of  $Y_Z$  for effecting PCET transformations. An attractive feature of this model is that the overall cluster maintains electroneutrality throughout the S-state cycle, which avoids the significant energetic penalties that would occur if uncompensated charges on the  $Mn_4$  core were allowed to accumulate. The key O—O bond-forming reaction is achieved by nucleophilic attack of a metal-hydroxide on a high-valent, electrophilic metal-oxo species. Variations of the nucleophilic partner, including a calcium(II)-hydroxide, have also been proposed.<sup>59,60</sup>

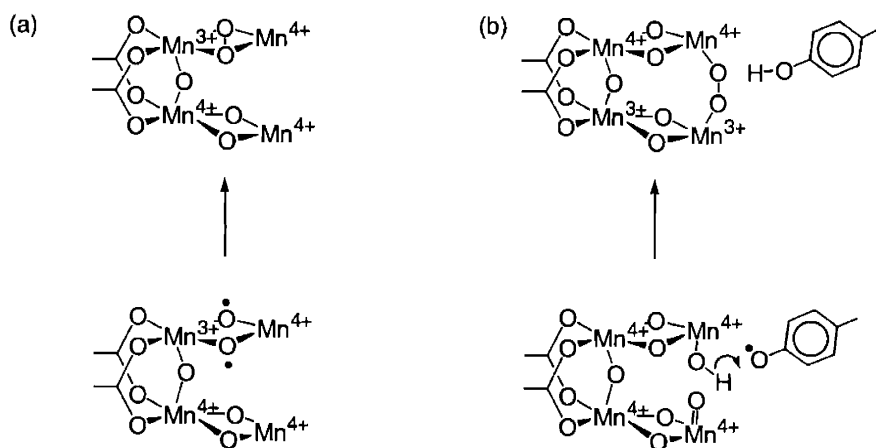


**Figure 1.4.** Mechanistic proposals for the critical O—O bond-making step in water oxidation at the OEC in PSII by (a) radical coupling of bridging metal-oxo units and (b) nucleophilic attack of a metal-hydroxide on an electrophilic terminal metal-oxo. Although dimer-of-dimers model for the  $Mn_4$  core is depicted here, a 3+1 form has been characterized recently by X-ray crystallography.

### 1.3.2 Oxygen Consumption in Respiration: Cytochrome *c* Oxidase

Despite its biological versatility, greater than 95% of the oxygen consumed in Nature is used for respiration.<sup>3,61</sup> High-energy electrons derived from food navigate the mitochondrial electron transport chain in a series of exergonic redox reactions. These energetically downhill electron transfers are used to drive a chemiosmotic proton gradient that leads to the production of ATP. Oxygen is the final electron acceptor in this respiratory cascade, and its proton-coupled reduction to water is used as a vehicle by which to clear the mitochondrial chain of low-energy, spent electrons. Cytochrome *c* oxidase (CcO), the terminal enzyme of the respiratory chain, binds, activates, and reduces oxygen and couples the energy released to translocate protons that contribute to the chemiosmotic gradient.<sup>3,61-68</sup>

CcO is a multisubunit integral membrane protein consisting of two major subunits.<sup>63,69-71</sup> Subunit I binds two heme *a* molecules and a copper ion. Subunit II binds a dimeric copper cluster known as Cu<sub>A</sub>. The immediate source of reducing equivalents for the conversion of dioxygen to water is cytochrome *c*; ultimately, the source is the oxidative catabolism of organic compounds. Protons are involved in the reaction of CcO, with eight taken up from one side and four released to the opposite side of the inner mitochondrial membrane. The proton gradient that results from this vectorial chemistry is used to drive the synthesis of ATP. Four of the protons involved are used to reduce dioxygen to water and are referred to as “chemical” or “scalar” protons. The other four protons are transported across the membrane and are referred to as “pumped” or “vectorial” protons.

Oxygen reduction occurs within subunit I at a binuclear site consisting of a heme (heme *a*<sub>3</sub>) and a copper center (Cu<sub>B</sub>) that are 4.5 to 5.2 Å apart. Three histidine residues, one of which is covalently crosslinked to a tyrosine residue by a post-translational modification (H240–Y244), ligate Cu<sub>B</sub>.<sup>70</sup> The tyrosine phenolic oxygen is approximately 5 Å from the heme *a*<sub>3</sub> Fe, and is ideally positioned to hydrogen bond to O<sub>2</sub> and other ROS substrates within the bimetallic cleft. Figure 1.5 depicts a simplified scheme for the reaction between CcO and O<sub>2</sub>, highlighting the key cofactors heme *a*<sub>3</sub>, Cu<sub>B</sub>, and Y244. Reduction and protonation of the oxidized form of the heme *a*<sub>3</sub>/Cu<sub>B</sub> center affords the reduced site, which subsequently binds O<sub>2</sub> to form the oxy species. The oxy species reacts further to produce P and F intermediates before regenerating the oxidized form of the enzyme. Notably, both P and F contain iron-oxo (ferryl) species that are derived from the cleavage of O—O bonds, and their reductions are limited by proton transfer reactions. In addition, the steps between P and the reduced form of the heme *a*<sub>3</sub>/Cu<sub>B</sub> site have been implicated in proton pumping processes. The stoichiometry of these steps is under current investigation, as up to four protons are pumped during the complete reduction cycle.<sup>65,72</sup>

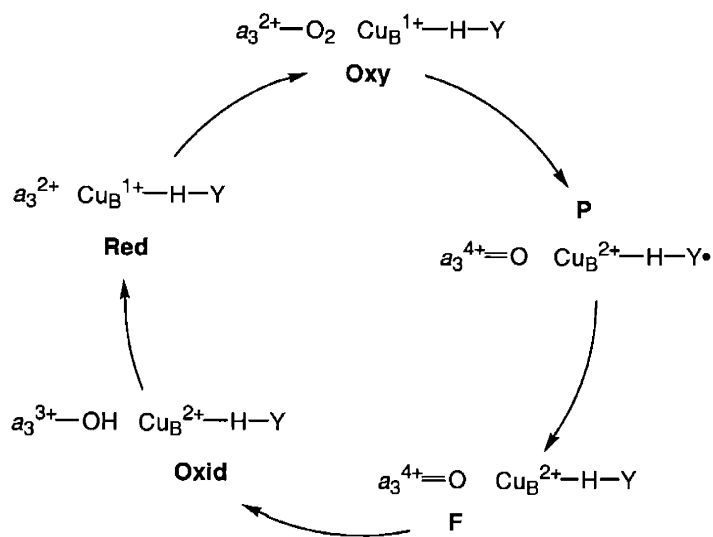


**Figure 1.5.** Simplified reaction scheme for oxygen reduction catalyzed by CcO.

### 1.3.3 Mechanistic Parallels for Biological O—O Bond Formation and Cleavage

PSII and CcO are responsible for practically all of the creation and consumption of dioxygen in Nature, with each enzyme carrying out the effective reverse chemical transformation of the other. Remarkably, these enzymatic machines perform parallel chemistry despite the disparity in their evolved active sites ( $\text{Mn}_4$  cluster for PSII, heme  $a_3/\text{Cu}_B$  for CcO). Not surprisingly, a comparison of PSII and CcO reveals striking chemical similarities. Both catalyze substrate conversion with rapid rates of turnover, up to several hundred cycles per second. The singly-bonded peroxy intermediates of PSII and CcO have escaped direct spectroscopic detection, consistent with their expected short lifetimes and the tight energetic constraints of species containing weak O—O bonds. In addition, a redox-active tyrosine proximate to the active site facilitates PCET reactions directed at metal-ligand bonds.

A enticing postulate arises from inspection of the critical O—O forming and cleaving step. Babcock suggested a beautifully symmetric mechanistic model for O—O bond-making and bond-breaking reactions in PSII and CcO, respectively (Figure 1.6).<sup>73</sup> Each process involves two transition metals and the redox-active tyrosine, and the O—O bond is made or broken through polar, electrophile/nucleophile pairs. The geometric arrangements of the two transition-metal cofactors and the tyrosine are similar, and the concerted reactions involve a chain of five atoms. The oxidation state of only one active-site metal ion is changed, and a single metal-oxygen bond is made or broken to offset concomitant O—O bond cleavage or formation. Notably, each



transformation maintains electroneutrality by the conservation in bond order and the concerted PCET (HAT) occurring between the substrate and proximate tyrosine.

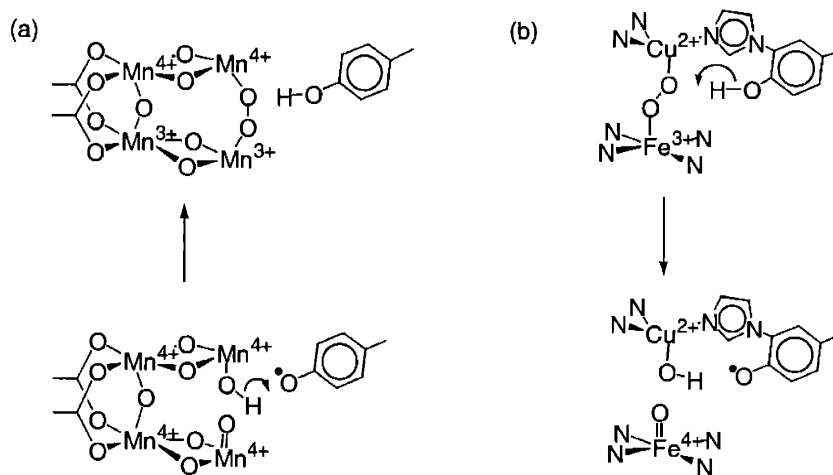
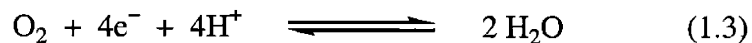


**Figure 1.6.** Babcock's mechanisms for conserved O—O bond formation and cleavage in (a) PSII and (b) CcO, respectively.

#### 1.4 Strategies for O—O Bond Formation/Activation Catalyzed by PCET

The biological interconversion of oxygen and water via PCET provides an underpinning for the design of synthetic systems to effect these chemical transformations. For bond-making and bond-breaking catalysis, PCET represents an interplay between the two most fundamental chemical reactivities, acid-base chemistry and oxidation-reduction (redox) chemistry. From a thermodynamic perspective, we can envision the effects of PCET on catalytic processes by posing these two simple questions: (i) How does proton transfer affect the redox potential of a given chemical system? (ii) And how does oxidation or reduction of a system affect its  $pK_a$ ? Conversely, the kinetic consequences of PCET on catalytic processes are both subtler and more complex. Such effects will arise in part from thermodynamic parameters, which will lead to changes in reaction driving force ( $\Delta G^\circ$ ), but electronic coupling between redox-active partners and accompanying Franck-Condon factors from charge redistribution will also weigh greatly in determining the rates of individual reaction steps within an overall catalytic cycle. With these issues in mind, we frame the parallel reactions of oxygen reduction to water and water oxidation to oxygen into a set of multiple PCET reactions that each involve four protons, four electrons, and the activation/formation of two formal O—O bonds. Per equation 1.3, the formal reduction potential for the direct four-electron, four-proton conversion of oxygen to water is 1.23 V vs NHE, or  $\Delta G^\circ = 56.8$  kcal/mol in bond-energy terms.



In an effort to simplify this complex problem and to build a solid mechanistic foundation on which to understand PCET-mediated O—O bond-based chemistry, we have directed our research towards addressing one question: *can we use PCET to learn how to make or break a single O—O bond?* From the principle of microscopic reversibility, studies approaching this chemical equilibrium from one direction will be applicable to the opposite direction as well. Accordingly, we will focus the remainder of this section on designs for the more difficult challenge of realizing O—O forming chemistry. Because the general field of synthetic water oxidation catalysts has been reviewed extensively,<sup>50,51,60</sup> we restrict our discussion to models that have directly inspired our PCET Pacman and Hangman templates.

The formation of an O—O bond catalyzed by transition-metal coordination complexes can be restricted to two limiting cases as depicted in Figure 1.7.

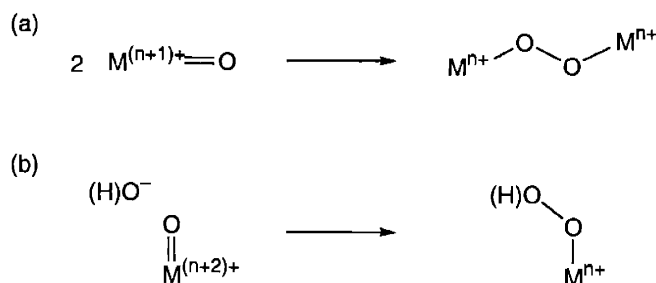


**Figure 1.7.** Possible pathways for O—O bond formation from (a) radical-type coupling of metal-oxo units and (b) nucleophilic attack of hydroxide(oxide) on an electrophilic metal-oxo center.

The first involves the homolytic combination of metal-oxo species bearing radical character, and the second entails heterolytic attack of a nucleophilic hydroxide/oxide on an electrophilic metal-oxo complex. The former has been invoked in the mechanism of the most well-characterized (and probably only) system for catalytic homogeneous water oxidation to oxygen, Meyer's  $[(\text{bpy})_2(\text{H}_2\text{O})\text{RuORu}(\text{H}_2\text{O})(\text{bpy})_2]^{4+}$  complex.<sup>74-77</sup> Oxidation of the bisruthenium(III)-aqua dimer at pH 1 to 7 with four equivalents of an outer-sphere oxidant generates a bisruthenium(V)-oxo species where the oxygen atoms of two  $d^3$  systems pair to form the O—O bond. The mechanism suggested for this bisruthenium system bears some resemblance to the aforementioned PSII proposals of Yachandra-Sauer-Klein for radical-based coupling of side-on bridging metal-oxo subunits,<sup>43</sup> and Babcock for the presence of high-valent terminal metal-oxo units.<sup>42,58</sup> Naruta suggested a dimer of manganese(V)-oxo adducts for a gable bisporphyrin that evolves oxygen from a complex mixture of acetonitrile/water/sulfolane upon the application of a very positive

potential ( $> 1.7$  V vs NHE);<sup>78</sup> however, neither this mechanistic claim nor the oxygen-evolution chemistry reported have been substantiated.<sup>50</sup>

In contrast, we sought to explore O—O bond-forming chemistry within the framework of the polar nucleophile/electrophile mechanism for the following reasons. First, this mechanism requires the formation of only one highly oxidizing species, simplifying PCET-directed activation to a single metal center. Moreover, chemical analogs of the proposed pathway are also observed in classic oxygen atom-transfer reactions between metal-oxo complexes and organic substrates (olefins, sulfides, phosphines), where direct attack of the substrate on the oxo ligand forms oxygen-element bonds (Figure 1.8a).<sup>79-83</sup> Finally, the polar formation and cleavage of O—O bonds, which is a formal two-electron transfer from a nucleophile to an electrophile, avoids nonselective one-electron radical pathways that typically plague high-oxidation state transition-metal chemistry.

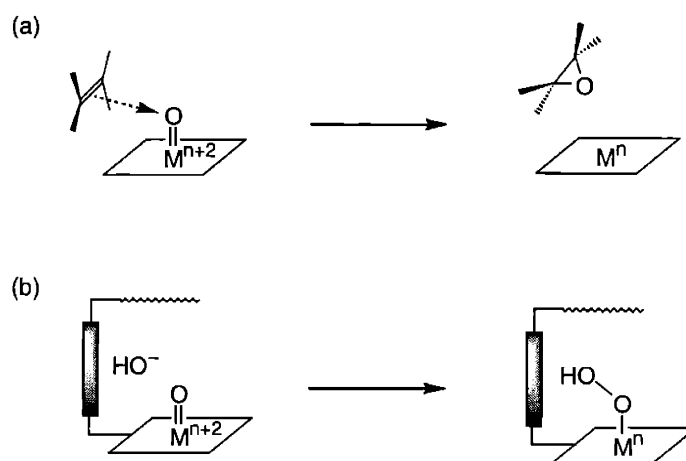


**Figure 1.8.** Mechanistic comparison of oxygen-element bond-forming reactions from metal-oxo platforms for (a) olefin epoxidation and (b) O—O coupling. Note that substrate attack occurs from an electronically-favored side-on geometry.

Figure 1.8b presents our working model for catalyzing the making and breaking of O—O bonds, and highlights the polar nature of the intermediates before and after bond activation/formation. We employ cofacial templates to create a matched microcavity that directs reactivity along the metal-ligand coordination axis. Substrate access and product release can, in principle, be controlled by the shape and flexibility supramolecular cleft. With particular regard to O—O bond-making and bond-breaking chemistry, oxygen-atom transfer from a high-valent transition-metal platform is preferred for the side-on approach of substrate to the metal-oxygen bond. This side-on model is consistent with a wide variety of reactivity patterns involving terminal metal-

oxo compounds.<sup>84-87</sup> Accordingly, these cofacial scaffolds dictate side-on reaction coordinates for oxygen-atom transfer. Metalloporphyrins are attractive platforms for both oxidative and reductive catalytic cycles as they provide a rich coordination chemistry with early and late transition metals in a myriad of oxidation states.<sup>88</sup> We anticipate that the concepts developed during PCET small-molecule activation studies will be valid for alternative ancillary ligand sets as well.

The designs of the particular Pacman and Hangman systems have their genesis in the donor-acceptor Salt Bridge constructs as illustrated in Figure 1.9. The Salt Bridge motif juxtaposes a hydrogen-bond pendant to a metalloporphyrin or other redox functionality in a side-to-side arrangement for the study of single-proton, single-electron PCET. The Pacman scaffold furnishes dual face-to-face metalloporphyrin sites to mediate multiple PCET events. The Hangman architecture combines features from both the Salt Bridge and Pacman constructs. This hybrid metalloporphyrin redox and acid-base hydrogen-bond pendant platform offers direct pathways for the introduction of proton and electron equivalents.

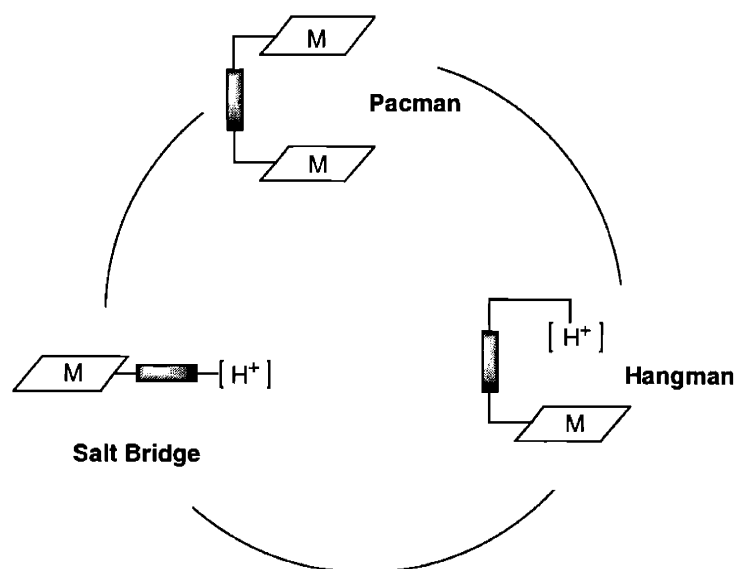


**Figure 1.9.** Relationships of Salt Bridge, Pacman, and Hangman systems designed for the study of PCET.

## 1.5 Organization and Scope of the Thesis

The thesis is arranged in two major sections describing the Pacman and Hangman strategies, respectively, for effecting ROS small-molecule activation chemistry catalyzed by PCET. The symmetric Pacman templates encompass chapters 2 to 8, and the asymmetric Hangman

constructs occupy chapters 9 to 11. Catalytic reduction chemistry is emphasized in chapters 2 to 7, and chapters 8 to 11 are largely directed towards oxidation reactivity.

Chapter 2 provides a starting point for our study of Pacman platforms by introducing novel cofacial bisporphyrin systems affixed to xanthene and dibenzofuran pillars. The resulting DPX (diporphyrin xanthene) and DPD (diporphyrin dibenzofuran) architectures furnish face-to-face complexes with minimal lateral displacements that span a large range of vertical pocket sizes. Remarkably, the DPD scaffold provides the first direct evidence for the Pacman effect in a single cofacial bisporphyrin platform. A comparative structural analysis establishes the ability of this system to open and close its binding pocket by over 4 Å in metal-metal distances in the presence of suitable exogenous ligands. Chapter 3 describes a thorough structural and spectroscopic comparison of a homologous set of coordination complexes for DPX and DPD. The resulting compilation of data for cofacial bisporphyrins exhibiting large differences in the vertical dimension sets a useful baseline for their application towards the multielectron transformation of small-molecule substrates. Chapter 4 presents a thermodynamic characterization of the Pacman effect. Analysis of supramolecular host-guest complexes formed from systems with vertical-only (DPD) versus vertical and horizontal flexibility (DPP = diporphyrin diphenylether) provides quantitative energetics for substrate binding. Restricting the Pacman motif to a single vertical degree of freedom leads to large enhancements in substrate inclusion by minimizing entropic contributions, thus presaging a rich reactivity for DPD-type platforms.

Chapter 5 probes the reactivity consequences for Pacman systems in PCET-mediated reductive catalysis. Dicobalt(II) complexes of both DPX and DPD are effective electrocatalysts for the direct four-electron, four-proton reduction of oxygen to water despite their ca. 4 Å in metal-metal distances, demonstrating that selective and efficient catalytic reactivity can be achieved with constructs that exhibit a large range of structural motion. Chapter 6 offers a novel approach for tuning the pocket sizes of the Pacman motif to complement the traditional method of changing the pillared bridge. Using sterically-demanding dipyrromethanes, aryl groups are installed *trans* to the spacer. These molecular “teeth” modulate the “bite” of the cofacial bisporphyrin superstructure. Examples based on both xanthene (DPXM = diporphyrin xanthene methoxyaryl, DPXB = diporphyrin xanthene bromoaryl) and dibenzofuran (DPDM = diporphyrin dibenzofuran methoxyaryl) scaffolds attest to the versatility of this synthetic method. With the ability to control the precise structural attributes of Pacman architectures, chapter 7 presents a comprehensive structure-function study of their dicobalt complexes for catalytic oxygen-reduction chemistry. Strikingly, the combined results from structural chemistry, electrochemistry, reactivity studies, and density functional calculations reveal that electronic-

induced differences in proton affinity for the  $[\text{Co}_2\text{O}_2]$  cores of Pacman- $\text{O}_2$  adducts track their catalytic selectivity for  $\text{H}_2\text{O}$  versus  $\text{H}_2\text{O}_2$  products.

Chapter 8 shifts the emphasis of PCET-catalyzed small-molecule studies toward oxidation chemistry. Two distinct synthetic methodologies are developed to create Pacman scaffolds to display enhanced electronic and steric stability to oxidizing media. In particular, the Suzuki cross-coupling reaction provides a modular strategy for assembling meso-tetraaryl cofacial bisporphyrins based on either xanthene (di-trimesitylporphyrin xanthene) or dibenzofuran (DTMPD = di-trimesitylporphyrin dibenzofuran). The suitability of these platforms for use in oxidizing conditions is demonstrated by their ability to effect the disproportionation of hydrogen peroxide to oxygen and water with catalytic activities greater than their etioporphyrin-based DPX and DPD counterparts.

Chapter 9 introduces three Hangman systems based on naphthalene, xanthene, and dibenzofuran scaffolds. The resulting HPN (hanging porphyrin naphthalene), HPX (hanging porphyrin xanthene), and HPD (hanging porphyrin dibenzofuran) constructs offer the ability to tune both the acid-base nature of the hydrogen-bond pendant and its orientation with respect to its cofacial metalloporphyrin redox partner. Strategies based on base-catalyzed ring opening of spiro-type macrocycles, high-dilution Lindsey reactions, and Suzuki cross coupling methods are employed to deliver these architectures. Chapter 10 explores the effects of proximate acid-base and redox sites by examining the reduction and oxidation chemistry of iron(III) and zinc(II) coordination complexes of HPN. Proton coupling is effective in modulating critical Fe(III)/Fe(II) heme redox potentials, as well as selecting oxidative conversion pathways of the porphyrin macrocycle itself. Chapter 11 presents the coordination chemistry and catalytic O—O bond activation reactivity of HPX and HPD Hangman porphyrin platforms. Comparative reactivity studies for the catalase-like disproportionation of hydrogen peroxide and the epoxidation of olefins by the HPX and HPD platforms with acid and ester hanging groups reveal that the introduction of a proton-transfer network properly oriented to a redox-active platform can orchestrate catalytic O—O bond activation. For the catalase and epoxidation reaction types, a marked reactivity enhancement is observed for the xanthene-bridged platform appended with a pendant carboxylic acid group, establishing that this approach can yield superior catalysts to analogs that do not control both proton and electron currencies. Chapter 12 briefly summarizes our findings and offers new directions to investigate small-molecule activation catalyzed by PCET.

## 1.6 References and Notes

1. Holm, R. H.; Solomon, E. I. *Chem. Rev.* **1996**, *96*, 2237 (Special Issue: Bioinorganic Enzymology).
2. Muller, A.; Ratajczaks, H.; Junge, W.; Diemann, E. *Stud. Phys. Theor. Chem. (Electron and Proton Transfer in Chemistry and Biology)*; Elsevier: Amsterdam, 1992; Vol. 78.
3. Babcock, G. T.; Wikström, M. *Nature* **1992**, *356*, 301-309.
4. Marcus, R. A. *Annu. Rev. Phys. Chem.* **1964**, *15*, 155-196.
5. Ulstrup, J. *Lecture Notes in Chemistry (Charge Transfer Processes in Condensed Media)*; Springer-Verlag: Berlin, 1979; Vol. 10.
6. Birge, R. R. *Annu. Rev. Phys. Chem.* **1990**, *41*, 683-733.
7. Durr, H.; Bouas-Laurent, H. *Studies in Organic Chemistry (Photochromism: Molecules and Systems)*; Elsevier: Amsterdam, 1990; Vol. 40.
8. Scherl, M.; Haarer, D.; Fischer, J.; DeCian, A.; Lehn, J.-M.; Eichen, Y. *J. Phys. Chem.* **1996**, *100*, 16175-16186.
9. Marks, T. J.; Ratner, M. A. *Angew. Chem. Int. Ed.* **1995**, *34*, 155-173.
10. Marcus, R. A.; Sutin, N. *Biochim. Biophys. Acta* **1985**, *811*, 265-322.
11. Cukier, R. I. *J. Phys. Chem.* **1995**, *99*, 16101-16115.
12. Cukier, R. I. *J. Phys. Chem.* **1996**, *100*, 15428-15443.
13. Cukier, R. I.; Nocera, D. G. *Annu. Rev. Phys. Chem.* **1998**, *49*, 337-369.
14. Cukier, R. I. *J. Phys. Chem. B* **2002**, *106*, 1746-1757.
15. Hammes-Schiffer, S. *ChemPhysChem* **2002**, *3*, 33-42.
16. Hammes-Schiffer, S. In *Electron Transfer in Chemistry*; Balzani, V., Ed.; Wiley-VCH: Weinheim, 2001; Vol. 1.1.5.
17. Rostov, I.; Hammes-Schiffer, S. *J. Chem. Phys.* **2001**, *115*, 285-296.
18. Hammes-Schiffer, S. *Acc. Chem. Res.* **2001**, *34*, 273-281.
19. Soudackov, A. V.; Hammes-Schiffer, S. *Chem. Phys. Lett.* **1999**, *299*, 503-510.
20. Soudackov, A.; Hammes-Schiffer, S. *J. Am. Chem. Soc.* **1999**, *121*, 10598-10607.
21. Fang, J.-Y.; Hammes-Schiffer, S. *J. Phys. Chem.* **1997**, *107*, 5727-5739.
22. Fang, J.-Y.; Hammes-Schiffer, S. *J. Chem. Phys.* **1997**, *107*, 8442-8454.
23. Roth, J. P.; Yoder, J. C.; Won, T.-J.; Mayer, J. M. *Science* **2001**, *294*, 2524-2526.
24. Mayer, J. M. *Acc. Chem. Res.* **1998**, *31*, 441-450.
25. Taube, H. *Angew. Chem. Int. Ed.* **1984**, *23*, 329-339.
26. Shaik, S.; Shurki, A. *Angew. Chem. Int. Ed.* **1999**, *38*, 587-625.
27. Bianco, R.; Hynes, J. T. *J. Phys. Chem. A* **1999**, *103*, 3797-3801.
28. Savéant, J.-M. *Acc. Chem. Res.* **1993**, *26*, 455-461.

29. Robert, M.; Savéant, J.-M. *J. Am. Chem. Soc.* **2000**, *122*, 514-517.
30. Sutin, N. *Acc. Chem. Res.* **1982**, *15*, 275-282.
31. Scott, R. A.; Mauk, A. G.; Gray, H. B. *J. Chem. Ed.* **1985**, *62*, 932-938.
32. Chang, C. J.; Brown, J. D. K.; Chang, M. C. Y.; Baker, E. A.; Nocera, D. G. In *Electron Transfer in Chemistry*; Balzani, V., Ed.; Wiley-VCH: Weinheim, Germany, 2001; Vol. 3.2.4, pp 409-461.
33. Yeh, C.-Y.; Miller, S. E.; Carpenter, S. D.; Nocera, D. G. *Inorg. Chem.* **2001**, *40*, 3643-3646.
34. Kirby, J. P.; Roberts, J. A.; Nocera, D. G. *J. Am. Chem. Soc.* **1997**, *119*, 9230-9236.
35. Roberts, J. A.; Kirby, J. P.; Wall, S. T.; Nocera, D. G. *Inorg. Chim. Acta* **1997**, *263*, 395-405.
36. Deng, Y.; Roberts, J. A.; Peng, S.-M.; Chang, C. K.; Nocera, D. G. *Angew. Chem. Int. Ed.* **1997**, *36*, 2124-2127.
37. Kirby, J. P.; van Dantzig, N. A.; Chang, C. K.; Nocera, D. G. *Tetrahedron Lett.* **1995**, *36*, 3477-3480.
38. Roberts, J. A.; Kirby, J. P.; Nocera, D. G. *J. Am. Chem. Soc.* **1995**, *117*, 8051-8052.
39. Turró, C.; Chang, C. K.; Leroi, G. E.; Cukier, R. I.; Nocera, D. G. *J. Am. Chem. Soc.* **1992**, *114*, 4013-4015.
40. Ort, D. R.; Yocum, C. F. *Oxygenic Photosynthesis: The Light Reactions*; Kluwer Academic: Dordrecht, 1996.
41. Tommos, C.; Babcock, G. T. *Biochim. Biophys. Acta* **2000**, *1458*, 199-219.
42. Tommos, C.; Babcock, G. T. *Acc. Chem. Res.* **1998**, *31*, 18-25.
43. Yachandra, V. K.; Sauer, K.; Klein, M. P. *Chem. Rev.* **1996**, *96*, 2927-2950.
44. Yocum, C. F.; Pecoraro, V. L. *Curr. Opin. Chem. Biol.* **1999**, *3*, 182-187.
45. Ananyev, G. M.; Zaltsman, L.; Vasko, C.; Dismukes, G. C. *Biochim. Biophys. Acta* **2001**, *1503*, 52-68.
46. Dismukes, G. C. *Science* **2001**, *292*, 447-448.
47. Vrettos, J. S.; Limburg, J.; Brudvig, G. W. *Biochim. Biophys. Acta* **2001**, *1503*, 229-245.
48. Kok, B.; Forbush, B.; McGloin, M. *Photochem. Photobiol.* **1970**, *11*, 457-475.
49. Volkov, A. G. *Bioelectrochem. Bioenerg.* **1989**, *21*, 3-24.
50. Yagi, M.; Kaneko, M. *Chem. Rev.* **2001**, *101*, 21-35.
51. Rüttinger, W.; Dismukes, G. C. *Chem. Rev.* **1997**, *97*, 1-24.
52. Brudvig, G.; Thorp, H. H.; Crabtree, R. H. *Acc. Chem. Res.* **1991**, *24*, 311-316.
53. Christou, G. *Acc. Chem. Res.* **1989**, *22*, 328-335.
54. Zouni, A.; Witt, H.-T.; Kern, J.; Fromme, P.; Kraut, N.; Saenger, W.; Orth, P. *Nature* **2002**, *409*, 739-743.



55. Britt, R. D.; Peloquin, J. M.; Campbell, K. A. *Annu. Rev. Biophys. Biomol. Struct.* **2000**, *29*, 463-495.
56. Halfen, J. A.; Mahapatra, S.; Wilkinson, E. C.; Kaderli, S.; Young Jr., V. G.; Que Jr., L.; Zuberbühler, A. D.; Tolman, W. B. *Science* **1996**, *271*, 1397-1400.
57. Tolman, W. B. *Acc. Chem. Res.* **1997**, *30*, 227-237.
58. Hoganson, C. W.; Babcock, G. T. *Science* **1997**, *277*, 1953-1956.
59. Pecoraro, V. L.; Baldwin, M. J.; Caudle, M. T.; Hsieh, W.-Y.; Law, N. A. *Pure Appl. Chem.* **1998**, *70*, 925-929.
60. Limburg, J.; Szalai, V. A.; Brudvig, G. W. *J. Chem. Soc. Dalton Trans.* **1999**, 1353-1361.
61. Malmström, B. G. In *Electron Transfer in Chemistry*; Balzani, V., Ed.; Wiley-VCH: Weinheim, Germany, 2001; Vol. 3.1.3, pp 39-55.
62. Ferguson-Miller, S.; Babcock, G. T. *Chem. Rev.* **1996**, *96*, 2889-2907.
63. Michel, H.; Behr, J.; Harrenga, A.; Kannt, A. *Annu. Rev. Biophys. Biomol. Struct.* **1998**, *27*, 329-356.
64. Schultz, B. E.; Chan, S. I. *Annu. Rev. Biophys. Biomol. Struct.* **2001**, *30*, 23-65.
65. Wikström, M. *Biochim. Biophys. Acta* **2000**, *1458*, 188-198.
66. Gennis, R. B. *Proc. Natl. Acad. Sci. USA* **1998**, *95*, 12747-12749.
67. Brzezinski, P. *Biochim. Biophys. Acta* **2000**, *1458*, 1-5.
68. Ramirez, B. E.; Malmström, B. G.; Winkler, J. R.; Gray, H. B. *Proc. Natl. Acad. Sci. USA* **1995**, *92*, 11949-11951.
69. Yoshikawa, S.; Shinzawa-Itoh, K.; Tsukihara, T. *J. Inorg. Biochem.* **2000**, *82*, 1-7.
70. Yoshikawa, S.; Shinzawa-ito, K.; Nakashima, R.; Yaono, R.; Yamashita, E.; Inoue, N.; Yao, M.; Fei, M. J.; Libeu, C. P.; Mizushima, T.; Yamaguchi, H.; Tomizaki, T.; Tsukihara, T. *Science* **1997**, *280*, 1723-1729.
71. Iwata, S.; Ostermeier, C.; Ludwig, B.; Michel, H. *Nature* **1995**, *376*, 660-669.
72. Rultenber, M.; Kannt, A.; Bamberg, E.; Fendler, K.; Michel, H. *Nature* **2002**, *417*, 99-102.
73. Hoganson, C. W.; Pressler, M. A.; Proshlyakov, D. A.; Babcock, G. T. *Biochim. Biophys. Acta* **1998**, *1365*, 170-174.
74. Binstead, R. A.; Chronister, C. W.; Ni, J.; Hartshorn, C. M.; Meyer, T. J. *J. Am. Chem. Soc.* **2000**, *122*, 8464-8473.
75. Gersten, S. W.; Samuels, G. J.; Meyer, T. J. *J. Am. Chem. Soc.* **1982**, *104*, 4029-4030.
76. Gilbert, J. A.; Eggleston, D. S.; Murphy Jr., W. R.; Geselowitz, D. A.; Gersten, S. W.; Hodgson, D. J.; Meyer, T. J. *J. Am. Chem. Soc.* **1985**, *107*, 3855-3864.
77. Geselowitz, D.; Meyer, T. J. *Inorg. Chem.* **1990**, *29*, 3894-3896.
78. Naruta, Y.; Sasayama, M.-a.; Sadaki, T. *Angew. Chem. Int. Ed.* **1994**, *33*, 1839-1841.

79. Holm, R. H. *Chem. Rev.* **1987**, *97*, 1401-1449.
80. Drago, R. S. *Coord. Chem. Rev.* **1992**, *117*, 185-213.
81. Griffith, W. P. *Chem. Soc. Rev.* **1992**, *21*, 179-185.
82. Sheldon, R. A. *Metalloporphyrins in Catalytic Oxidations*; Marcel Dekker: New York, 1994.
83. Meunier, B. *Struct. Bond. (Metal-Oxo and Metal-Peroxo Species in Catalytic Oxidations)*; Springer-Verlag: Berlin, 2000; Vol. 97.
84. Groves, J. T.; Myers, R. S. *J. Am. Chem. Soc.* **1983**, *105*, 5791-5796.
85. Jacobsen, E. N. *Acc. Chem. Res.* **2000**, *33*, 421-431.
86. Brock, S. L.; Mayer, J. M. *Inorg. Chem.* **1991**, *30*, 2138-2143.
87. Veige, A. S.; Slaughter, L. M.; Wolczanski, P. T.; Matsunaga, N.; Decker, S. A.; Cundari, T. R. *J. Am. Chem. Soc.* **2001**, *123*, 6419-6420.
88. Kadish, K. M.; Smith, K. M.; Guilard, R. *The Porphyrin Handbook*; Academic Press: San Diego, 2000.

*Chapter 2*  
**Pacman Porphyrins Based on Xanthene  
and Dibenzofuran Scaffolds**

Portions of the work presented in this chapter have been published:

Deng, Y.; Chang, C. J.; Nocera, D. G. *J. Am. Chem. Soc.* **2000**, *122*, 410-411.

Chang, C. J.; Deng, Y.; Heyduk, A. F.; Chang, C. K.; Nocera, D. G. *Inorg. Chem.* **2000**, *39*,  
959-966.

## 2.1 Motivation and Specific Aims

To initiate our program aimed at developing catalytic transformations mediated by coupled proton and electron transfer events, we sought to establish synthetic constructs that could participate in multielectron catalysis. Based on the rich redox properties of both multimetallic complexes and metalloporphyrin coordination compounds, we chose the symmetric cofacial bisporphyrin motif as a starting point for pursuing these ends. This chapter doubles the synthetic palette of available Pacman-type cofacial bisporphyrin platforms by introducing two novel systems derived from the cyclic ether pillars xanthene (DPX = diporphyrin xanthene) and dibenzofuran (diporphyrin dibenzofuran). The coordination chemistry and structural attributes of the DPX and DPD porphyrins have been thoroughly investigated. In particular, the DPD framework demonstrates a unique ability to open and close its binding pocket by over 4 Å in the presence of exogenous ligands, providing the first direct evidence for the Pacman effect. The bimetallic DPX and DPD face-to-face complexes thus present molecular clefts with unprecedented control of vertical pocket sizes for the exploration of small-molecule activation chemistry mediated by proton-coupled electron transfer (PCET).

## 2.2 Background

The activation and functionalization of small-molecule substrates is of central importance in biological and chemical catalytic transformations. Typically, these bond-making and bond-breaking processes encompass multiple oxidation-reduction (redox) events. The catalysis of multielectron redox reactions is a daunting task from a kinetic point of view, even though the thermodynamics of the overall transformation are generally favorable. This is due to the fact that summing uncoupled, single-electron steps to achieve a total multielectron reaction inevitably leads to an intermediate sink that requires an unfavorable step to complete the overall process. An exemplary catalytic reaction is the reduction of oxygen to water, the key chemical transformation in aerobic respiration that generates the energy needed for biological ATP synthesis.<sup>1-5</sup> Figure 2.1 depicts the standard reduction potentials connecting oxygen and its

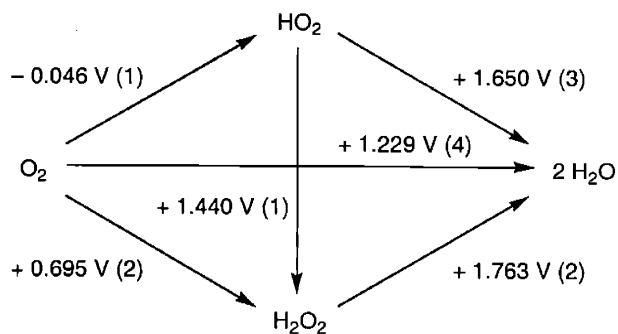
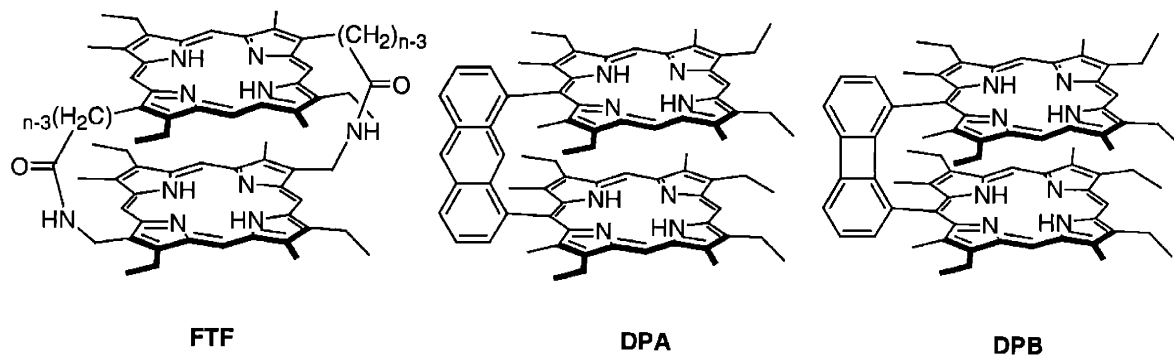


**Figure 2.1.** Standard reduction potentials for reduction of dioxygen to water. The number of electrons transferred is provided in parentheses.

chemical reduction products.<sup>6</sup> Both the four-electron, four-proton and the two-electron, two-proton pathways are thermodynamically favorable; however, if the reduction is carried out one electron and one proton at a time, a sink is reached at the change connecting dioxygen (O<sub>2</sub>) with hydroperoxide (HO<sub>2</sub>).

Natural systems have resolved the kinetic challenge of multielectron catalysis by utilizing two or more metals or other redox-active cofactors in close proximity to deliver cooperatively multiple oxidizing or reducing equivalents to a small-molecule substrate.<sup>7</sup> Thus, in our endeavors to uncover new synthetic catalysts for multielectron reactions, we turned our attention to the simplest unit of these motifs, binuclear transition-metal complexes, by reasoning that two metal centers working in concert could effectively promote multielectron chemistry via multielectron pathways. Of the various bimetallic complexes capable of supporting multielectron redox chemistry, porphyrins linked in a face-to-face arrangement – cofacial bisporphyrins – are distinguished by their ability to activate small molecules by more than one electron.<sup>8</sup> In this thesis, we note that the use of the term cofacial bisporphyrin denotes systems with the capability to participate in multielectron catalytic cycles; such bimetallic clefts are functionally distinct from related face-to-face constructs employed for photoinduced energy and electron transfer reactions.<sup>9-13</sup> Cofacial bisporphyrins fall into the two major classes depicted in Chart 2.1: (1) porphyrins linked by two or more flexible strapping units (FTF = face-to-face),<sup>14-39</sup> and (2) pillared bisporphyrins anchored by a single rigid bridge.<sup>11,40-65</sup>

**Chart 2.1**



Though limited to two different spacers, anthracene and biphenylene, the pillared systems DPA (diporphyrin anthracene) and DPB (diporphyrin biphenylene) have been prominent catalysts for the multielectron transformation of a variety of small-molecule substrates.<sup>8</sup> For example, cofacial bisporphyrin complexes of several metals, notably cobalt and iron, are electrocatalysts for the reduction of dioxygen by two and four electrons.<sup>16,18,66-72</sup> In addition, ruthenium and osmium cofacial bisporphyrins reduce protons to dihydrogen,<sup>48</sup> and dinitrogen by four and six

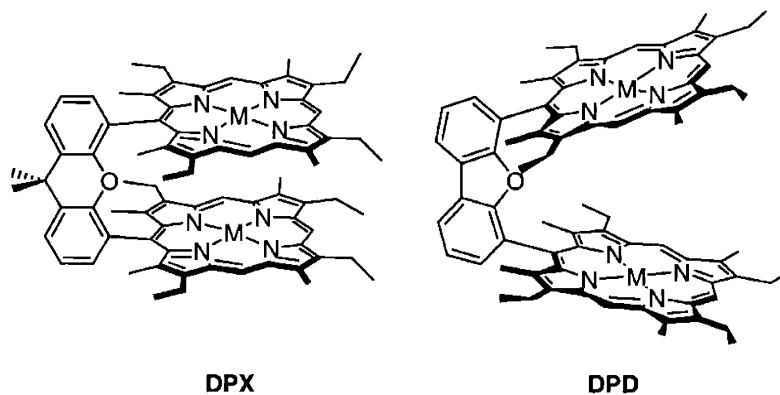
electrons.<sup>44,46,47</sup> In addition, electron-deficient congeners activate H—H and C—H bonds.<sup>49</sup> The exceptional multielectron reactivity of the pillared DPA and DPB bisporphyrins compared to their strapped FTF counterparts led Collman to first suggest that these molecules, which display small lateral shifts, have a vertical “Pacman” flexibility that allows the binding pocket to structurally accommodate reaction intermediates during catalysis.<sup>8</sup>

Despite these attractive reactivity properties, extensive examinations of existing Pacman bisporphyrin platforms are restricted by their formidable synthesis (> 20 steps); in particular, the prerequisite dialdehyde pillars are obtained through arduous multistep routes involving considerable time and effort.<sup>40,42</sup> Moreover, the DPA and DPB systems differ in vertical pocket size by only ca. 1 Å,<sup>51</sup> offering a limited range of conformational flexibility for examining structure/reactivity relationships. We thus became interested in testing the structural limits of vertical flexibility within the Pacman motif in order to expand the use of such platforms for multielectron catalysis, with specific interest in the activation of oxygen and other small molecules using proton-coupled electron transfer (PCET) as a mechanistic framework.<sup>73,74</sup> With the goal of increasing the structural breadth of the Pacman bite, we sought to develop methods for the facile assembly of new cofacial bisporphyrins that exhibit variable pocket sizes with minimal lateral displacements.

Inspired by the elegant work of Rebek<sup>75</sup> and Cram<sup>76</sup> on supramolecular clefts, we turned our attention to the cyclic ethers xanthene and dibenzofuran as new spacers for cofacial bisporphyrins. We now report that these pillars provide a convenient entry towards the construction of novel cofacial Pacman bisporphyrins DPX (DPX = diporphyrin xanthene) and DPD (DPD = diporphyrin dibenzofuran) that afford a unprecedented combination of synthetic availability and pocket size tunability.<sup>77-79</sup> The 4,5-substitution on xanthene affords a DPX cleft with lateral and vertical preorganization comparable to existing DPA and DPB systems. The introduction of porphyrinic substituents at the 4 and 6 positions of dibenzofuran imparts a significantly greater bite angle on the cofacial bisporphyrin motif to produce a DPD pocket with lateral preorganization and vertical flexibility. A remarkable finding is that the DPD system provides the first direct observation of the critical Pacman effect in a single cofacial bisporphyrin platform; a comparative structural analysis of biszinc and bisiron(III)  $\mu$ -oxo complexes demonstrates the unique ability of the DPD framework to open and close its binding pocket by a vertical distance of over 4 Å in the presence of exogenous ligands. In this chapter, we describe the ligand syntheses and coordination chemistry of DPX and DPD cofacial bisporphyrins (Chart 2.2). In addition, the synthetic results are bolstered by structural analysis of each of the Pacman

systems. The collected results provide a reliable backdrop for more detailed studies of their physical properties and catalytic applications.

**Chart 2.2**

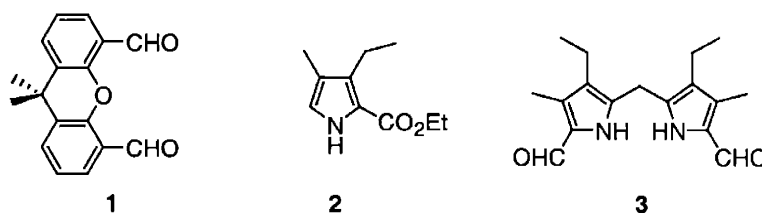


## 2.3 Results and Discussion

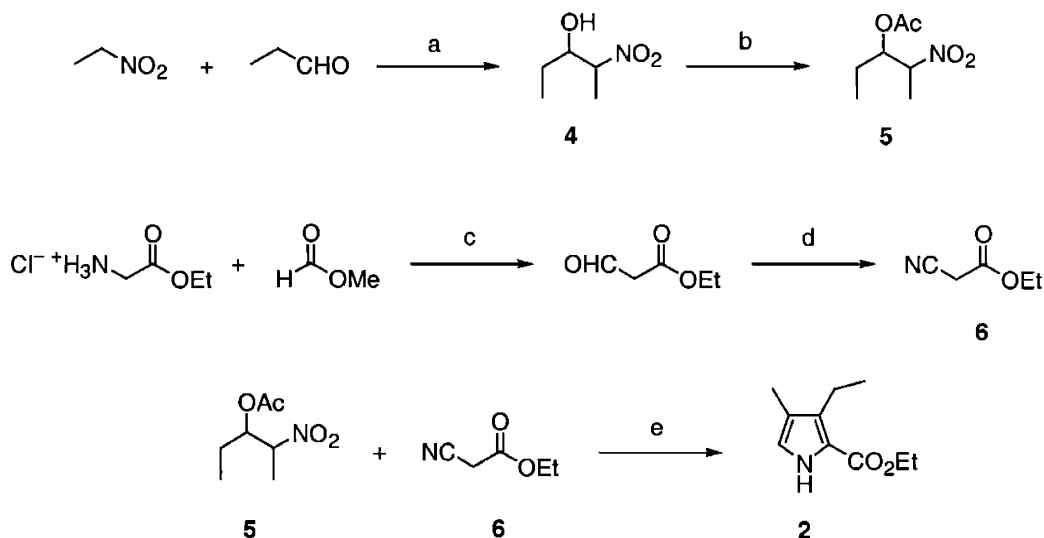
### 2.3.1 Synthesis of a Xanthene-Bridged Cofacial Bisporphyrin (DPX) with Lateral and Vertical Preorganization

The installation of a xanthene spacer into the pillared cofacial bisporphyrin motif affords a ditopic system with lateral and vertical preorganization. The xanthene-bridged cofacial bisporphyrin  $H_4$ (DPX) (**15**) (DPX = diporphyrin xanthene) is synthesized as outlined in Schemes 2.1 to 2.3. We employ the method originally developed by Chang<sup>40,42</sup> and elaborated by Collman<sup>45</sup> for the preparation of pillared bisporphyrins bridged by anthracene and biphenylene. This convergent route involves a three-branch coupling of a xanthene dicarboxaldehyde bridge **1**,  $\alpha$ -free pyrrole ethyl ester **2**, and dipyrromethanedialdehyde **3** to form the cofacial bisporphyrin (Chart 2.3).

**Chart 2.3**



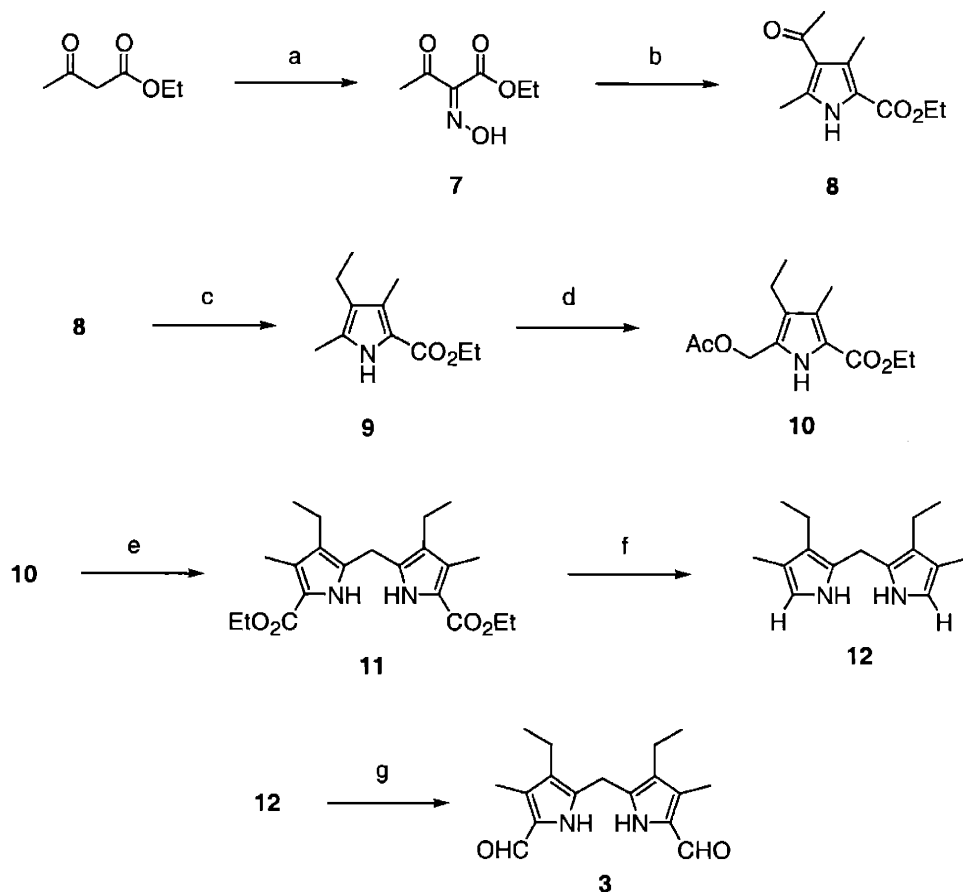
**Branch 1.** The  $\alpha$ -free pyrrole ethyl ester **2** is secured in five steps using a Barton-Zard strategy.<sup>80,81</sup> A Henry condensation of propionaldehyde and nitroethane catalyzed by KF affords nitroalcohol **4** in 70% yield. Acetylation delivers **5** in 92% yield.<sup>82,83</sup> Using the sterically-hindered base 1,8-diazabicyclo[5.4.0]undec-7-ene (DBU), compound **5** is converted to the nitroalkene *in situ* for subsequent reaction with ethyl isocyanoacetate **6** (available in two steps from glycine ethyl ester)<sup>84</sup> to yield the  $\alpha$ -free pyrrole **2** in 78% yield.



**Scheme 2.1.** (a) KF, isopropyl alcohol, < 40 °C; (b) Ac<sub>2</sub>O, < 60 °C; (c) Et<sub>3</sub>N, reflux; (d) POCl<sub>3</sub>, DMF, 40 °C; (e) THF/isopropyl alcohol, DBU, < 30 °C.

**Branch 2.** The dipyrrolylmethane dialdehyde **3** is prepared in seven total steps using an adapted synthesis of Chang.<sup>85</sup> The starting pyrrole **8** is synthesized using the standard Knorr method.<sup>86</sup> Ethyl acetoacetate is condensed with sodium nitrite to give oxime **7**, which is reacted directly with 2,4-pentanedione to deliver pyrrole **8** in 46% yield over two steps. Regioselective reduction of the pyrrole ketone affords **9** in 54% yield. Compound **9** is oxidized with lead(IV) acetate to give the acetoxy compound **10**, and acid-catalyzed dimerization delivers the ester-protected dipyrrolylmethane **11** in excellent yields (85% over two steps). Saponification and decarboxylation of **11** are carried out in a single transformation with sodium hydroxide in ethanol/water mixtures containing a trace amount of hydrazine hydrate (as a reducing agent) to yield the  $\alpha$ -free dipyrrolylmethane **12** in almost quantitative yield. Vilsmeier formylation of **12** using POCl<sub>3</sub>/DMF followed by base hydrolysis produces **3** in 75% yield.



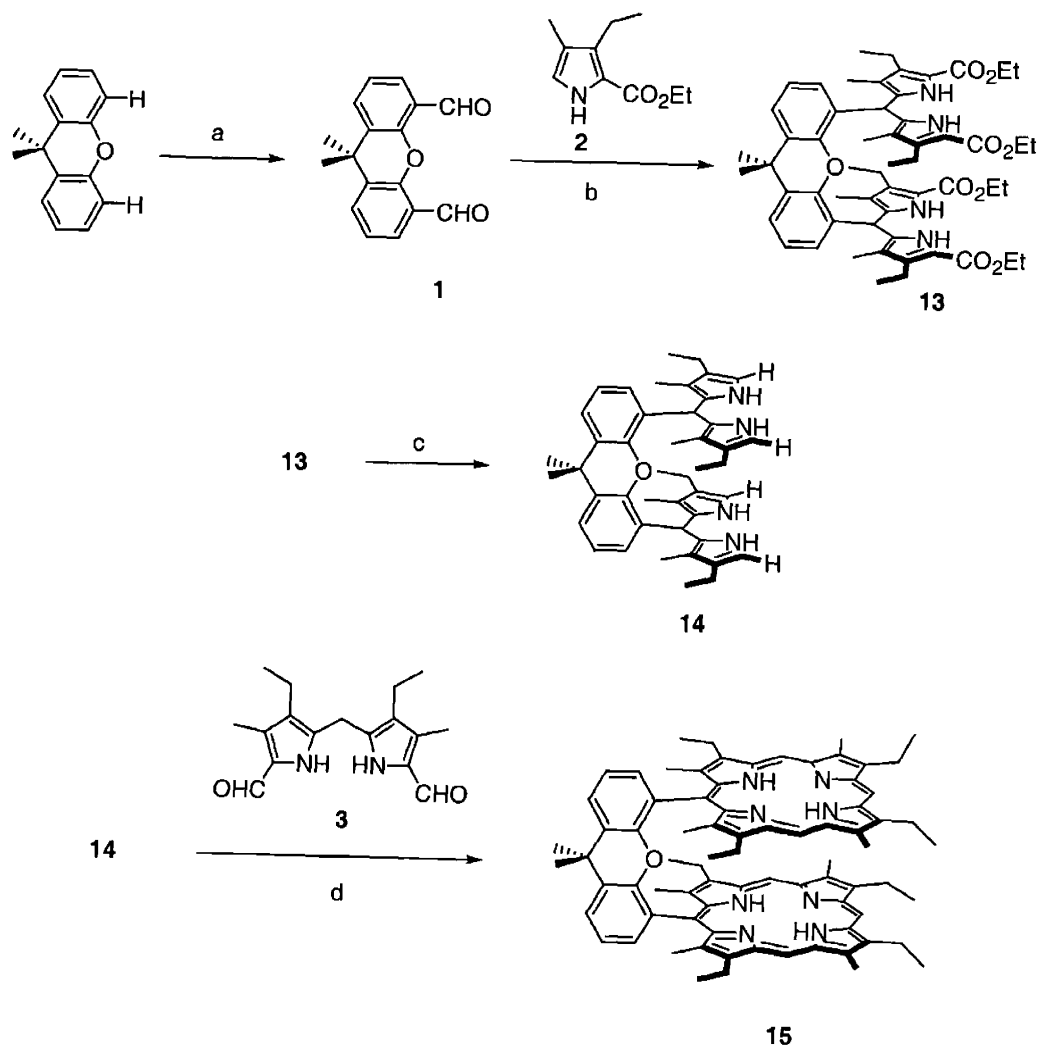


**Scheme 2.2.** (a)  $\text{NaNO}_2/\text{H}_2\text{O}$ ,  $< 180\text{ }^\circ\text{C}$ ; (b)  $\text{Zn}$ , 2,4-pentanedione,  $\text{HOAc}/\text{NaOAc}$ ,  $< 70\text{ }^\circ\text{C}$ ; (c)  $\text{NaBH}_4$ ,  $\text{BF}_3\cdot\text{OEt}_2$ ,  $0\text{ }^\circ\text{C}$ ; (d)  $\text{Pb}(\text{OAc})_4$ ,  $\text{HOAc}$ ,  $100\text{ }^\circ\text{C}$ ; (e)  $\text{HOAc}/\text{H}_2\text{O}$ , reflux; (f)  $\text{NaOH}$ ,  $\text{NH}_2\text{NH}_2\cdot\text{H}_2\text{O}$ ,  $\text{EtOH}/\text{H}_2\text{O}$ , reflux; (g) i.  $\text{POCl}_3$ ,  $\text{DMF}$ , ii.  $\text{Na}_2\text{CO}_3$ .

**Branch 3.** Xanthenone dialdehyde bridge **1** is obtained in 86% yield by the regioselective dilithiation of 9,9-dimethylxanthenone in the presence of  $\text{N,N,N',N'}$ -tetramethylethylenediamine (TMEDA) and dry DMF followed by hydrolysis of the intermediate imidate salt. Notably, the multigram availability of the xanthenone dialdehyde spacer in a facile one-pot reaction without purification by column chromatography or distillation offers a significant synthetic improvement over the DPA and DPB systems, which require five to eight synthetic steps to deliver the dialdehyde pillar.<sup>40,42,45,53</sup>

**Three-Branch Coupling.** Reaction of dialdehyde **1** with 4 equiv of pyrrole **2** in boiling ethanol affords the corresponding ester-protected bisdipyrromethane **13** in 88% yield. Subsequent saponification of the  $\alpha$ -ethyl esters of **13** with sodium hydroxide in ethylene glycol proceeds smoothly to produce the  $\alpha$ -free tetrapyrrole **14** (86% yield). Finally, cyclization of **14** with dipyrromethane dialdehyde **3** in the presence of a catalytic amount of *p*-toluenesulfonic acid

(PTSA) followed by oxidation with *o*-chloranil gives the corresponding bisporphyrin H<sub>4</sub>(DPX) (**15**) after workup and purification. The 23% yield for the final coupling step is comparable to the results obtained by the optimized procedure employed by Collman and co-workers for the synthesis of H<sub>4</sub>(DPB).<sup>45</sup> The free-base cofacial bisporphyrin H<sub>4</sub>(DPX) (**15**) is thus obtained in 16 steps in an overall yield of 3%. For comparison, the related anthracene- and biphenylene-bridged bisporphyrins H<sub>4</sub>(DPA) and H<sub>4</sub>(DPB) are synthesized in 20 and 23 steps, respectively.<sup>40,42,45,53</sup>



**Scheme 2.3.** (a) i. *n*-BuLi, TMEDA; ii. DMF; iii. H<sub>2</sub>O; (b) **2**, ethanol, HCl, reflux; (c) NaOH, ethylene glycol, reflux; (d) i. **3**, PTSA, methanol; ii. *o*-chloranil.

The cofacial disposition of rings in bisporphyrin **15** is revealed by <sup>1</sup>H NMR spectroscopy. The upfield shift of the internal NH-pyrrolic resonances in the <sup>1</sup>H NMR spectra of **15** (−6.42 and −6.80 ppm) compared to a monomeric counterpart (−3.10 and −3.29 ppm)<sup>87</sup> is characteristic of a

cofacial arrangement, due to a shielding effect caused by ring current interactions between the closely-associated porphyrin moieties.<sup>22,29</sup> The clean, sharp NMR peaks observed for the meso and methyl protons of **15** provide further support for a nonslipped, stacked conformation for the two adjoined porphyrin rings.

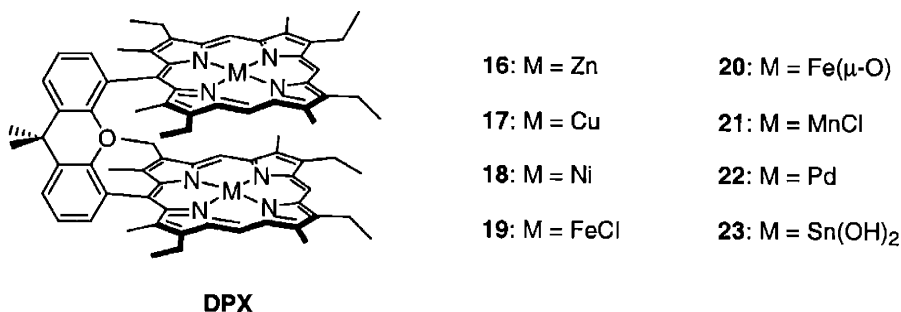
### 2.3.2 Transition-Metal Complexes of DPX

Homobimetallic complexes of  $H_4(DPX)$  (**15**) are readily secured by direct reaction with metal salts (Chart 2.4).<sup>88</sup> The coordination chemistry of **15** with first-row transition metals has been examined most extensively. For example, treatment of **15** with  $Zn(OAc)_2 \cdot 2H_2O$  in methanol/chloroform mixtures affords the corresponding binuclear zinc(II) complex  $Zn_2(DPX)$  (**16**) in quantitative yield. Complex **16** was identified using a combination of  $^1H$  NMR, high-resolution mass spectrometry, and elemental analyses. The homobimetallic complex  $Cu_2(DPX)$  (**17**) is obtained in excellent yield (94%) by reaction of **15** with  $Cu(OAc)_2 \cdot 2H_2O$  in methanol/chloroform mixtures. Complex **17** gave satisfactory mass spectral and elemental analyses. Magnetic susceptibility measurements over the temperature range 2 to 300 K verify the paramagnetic nature of **17**. The compound obeys the Curie law at high temperatures with a magnetic moment of 1.72 BM per metal center, though deviations from a simple paramagnet are observed at low temperature. A magnetic moment of 1.58 BM per metal center at 2 K indicates weak antiferromagnetic coupling. A fit of the molar susceptibility data to the Bleaney-Bowers model for dimers<sup>89</sup> gives an estimate for the exchange coupling constant  $J$  of  $-0.5 \text{ cm}^{-1}$ , a value that corresponds to the lower limit value obtained by EPR for a series of cofacial copper bisporphyrins.<sup>90</sup>  $Ni_2(DPX)$  (**18**) is prepared according to Adler's method<sup>91</sup> ( $NiCl_2$ /refluxing DMF) in good yield (83%). The diamagnetic complex was fully characterized by  $^1H$  NMR, high-resolution mass spectrometry, and elemental analyses. Bischloroiron(III) compound **19** is delivered in good yield (93%) from reaction of **15** with  $FeBr_2$  and 2,6-lutidine in a THF/benzene solvent system followed by anion exchange with aq HCl. The bisiron(III)  $\mu$ -oxo derivative **20** is obtained in 90% yield following similar metalation conditions but using a basic workup. A preliminary structural analysis using X-ray crystallography confirms that the intramolecular bisiron(III)  $\mu$ -oxo complex is selectively formed, and satisfactory high-resolution mass spectral data and elemental analyses accompanied iron complexes **19** and **20**. Lastly, bischloromanganese(III) complex **21** is afforded in high yield (90%) by an Alder reaction of **15** with  $Mn(OAc)_2 \cdot 4H_2O$  in DMF followed by anion exchange with aq NaCl/HCl. The complex was identified using high-resolution mass spectral and elemental analyses.

Insertions of heavier elements into the porphyrin cores of  $H_4(DPX)$  (**15**) proceed with similar success. Two examples are elaborated here, chosen for the attractive photophysical properties of

their metalloporphyrin coordination complexes.<sup>92</sup> Bispalladium(II) complex **22** is prepared in 68% yield from reaction of **15** with Pd(OAc)<sub>2</sub> in chloroform/methanol mixtures. Bisdihydroxytin(IV) derivative **23** is also synthesized from H<sub>4</sub>(DPX) (**15**) in 68% yield using SnCl<sub>2</sub> followed by workup with basic alumina. Both complexes were fully characterized using a combination of <sup>1</sup>H NMR and high-resolution mass spectrometry, and the palladium derivative gave satisfactory elemental analyses.

#### Chart 2.4



#### 2.3.3 Structural Chemistry of DPX

A systematic structural study of the DPX framework is provided by a homologous series of dinuclear zinc, copper, and nickel derivatives. The molecular structures of the homobimetallic zinc(II), copper(II), and nickel(II) complexes of DPX, **16-18**, are shown in Figures 2.2-2.4, respectively. Each atom of the porphyrin rings and the corresponding bridge is numbered in the standard fashion while auxiliary methyl and ethyl groups off the macrocycles are additionally identified with their connection to the porphyrin ring. Selected geometrical measurements are given in Tables 2.1-2.3.

Trends in bond lengths and angles of macrocyclic core structures and side chains agree well with those observed in related systems such as H<sub>4</sub>(DPA),<sup>51,53,93</sup> H<sub>4</sub>(DPB),<sup>45,51</sup> and 1,2-bis[5-(2,3,7,8-12,13,17,18-octaethylporphyrinato)]-*cis*-ethene porphyrins.<sup>94-96</sup> Structural highlights of the core structures for **16-18** are as follows:

**Zn<sub>2</sub>(DPX) (16).** Both tetracoordinate Zn(II) macrocycles (Figure 2.2) exhibit a wave conformation,<sup>97-99</sup> with a mean deviation of 0.3608 Å for the macrocyclic atoms from the porphyrin mean plane. Each macrocycle is positioned essentially in the N<sub>4</sub> plane (avg Zn—N<sub>4</sub> displacement = 0.0918 Å) with an average Zn—N bond length of 2.041 Å, which is in good agreement with related monomeric<sup>97-99</sup> and dimeric<sup>100,101</sup> Zn(II) porphyrins.

**Table 2.1.** Crystallographic Data for Zn<sub>2</sub>(DPX) (16), Cu<sub>2</sub>(DPX) (17), and Ni<sub>2</sub>(DPX) (18).

	16	17	18
Empirical formula	C <sub>79</sub> H <sub>77</sub> N <sub>8</sub> OZn <sub>2</sub>	C <sub>79</sub> H <sub>82</sub> Cu <sub>2</sub> N <sub>8</sub> O	C <sub>79</sub> H <sub>82</sub> N <sub>8</sub> Ni <sub>2</sub> O
Formula weight	1285.23	1286.61	1276.95
Temperature	183(2) K	183(2) K	183(2) K
Wavelength	0.71073 Å	0.71073 Å	0.71073 Å
Crystal system	Triclinic	Triclinic	Monoclinic
Space group	<i>P</i> $\bar{1}$	<i>P</i> $\bar{1}$	C2/c
Unit cell dimensions	<i>a</i> = 11.2671(2) Å <i>b</i> = 14.9809(2) Å <i>c</i> = 20.4852(2) Å $\alpha$ = 101.6680(10)° $\beta$ = 100.8890(10)° $\gamma$ = 101.8060(10)°	<i>a</i> = 11.21410(10) Å <i>b</i> = 14.9539(5) Å <i>c</i> = 20.6915(7) Å $\alpha$ = 101.810(2)° $\beta$ = 101.044(2)° $\gamma$ = 101.722(2)°	<i>a</i> = 24.1671(4) Å <i>b</i> = 10.669 Å <i>c</i> = 50.5080(9) Å $\beta$ = 99.553(2)°
Volume	12842.0(3) Å <sup>3</sup>	7549.5(4) Å <sup>3</sup>	12842.0(3) Å <sup>3</sup>
Z	2	2	8
Density (calculated)	1.327 Mg/m <sup>3</sup>	1.325 Mg/m <sup>3</sup>	1.321 Mg/m <sup>3</sup>
Absorption coefficient	0.800 mm <sup>-1</sup>	0.714 mm <sup>-1</sup>	0.641 mm <sup>-1</sup>
F(000)	1350	1356	5408
Crystal size	0.20 × 0.20 × 0.08 mm <sup>3</sup>	0.30 × 0.20 × 0.08 mm <sup>3</sup>	0.20 × 0.15 × 0.08 mm <sup>3</sup>
$\theta$ range for data collect	1.43 to 23.28°	1.54 to 21.50°	1.64 to 20.00°
Reflections collected	13185	11372	18577
Independent reflections	8982 (R <sub>int</sub> = 0.0300)	7353 (R <sub>int</sub> = 0.1015)	5996 (R <sub>int</sub> = 0.1005)
Data / restraints / param	8972 / 0 / 830	6093 / 0 / 812	5623 / 0 / 812
Goodness-of-fit on F <sup>2</sup>	1.116	1.036	1.173
Final R indices	R1 = 0.0570	R1 = 0.0909	R1 = 0.0768
[I > 2 $\sigma$ (I)]	wR2 = 0.1559	wR2 = 0.1994	wR2 = 0.1460
R indices (all data)	R1 = 0.0833 wR2 = 0.1973	R1 = 0.1940 wR2 = 0.2897	R1 = 0.1152 wR2 = 0.2051
Extinction coefficient	0.0029(8)	0.0000(3)	0.00000(2)
Largest diff peak	0.671 eÅ <sup>-3</sup>	0.788 eÅ <sup>-3</sup>	0.509 eÅ <sup>-3</sup>
Largest diff hole	-0.534 eÅ <sup>-3</sup>	-0.629 eÅ <sup>-3</sup>	-0.425 eÅ <sup>-3</sup>

**Cu<sub>2</sub>(DPX) (17).** The Cu(II) ions in Figure 2.3 are situated in an approximately N<sub>pyrrole</sub> square, as the N–Cu–N bond angles are 90 ± 1.5°. The average Cu–N bond length is 2.002 Å. A conformational analysis of the two macrocycles indicates inequivalent ring systems. The porphyrin ring containing Cu(1) exhibits a ruffled conformation with a mean deviation from planarity of 0.2176 Å; the meso carbons are alternately displaced above and below the mean porphyrin plane. In contrast, the ring with Cu(2) exhibits a wave conformation with a mean deviation from planarity of 0.3244 Å. Smith and co-workers have observed a similar effect in a related biscopper ethene-bridged bisporphyrin,<sup>94,95</sup> attributing this type of inequivalence to a “localized” macrocycle distortion<sup>102,103</sup> induced by the steric crowding of a large meso-substituent flanked by proximate alkyl groups.

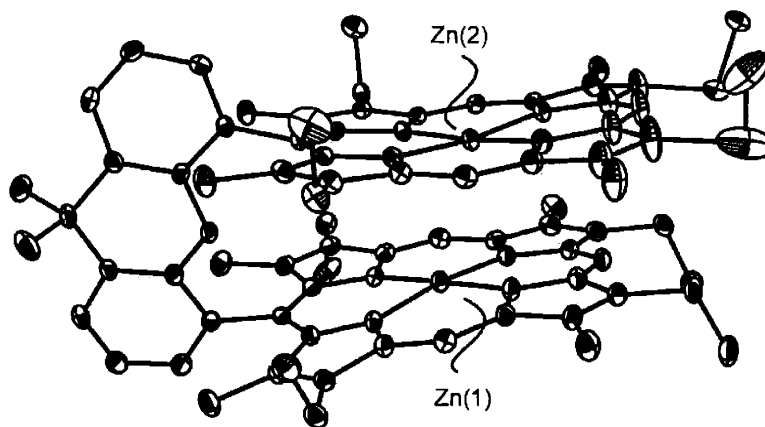


**Figure 2.2.** Crystal structure of Zn<sub>2</sub>(DPX) (16). Thermal ellipsoids are drawn at the 25% probability level. Hydrogen atoms and solvent molecules within the lattice have been omitted for clarity.

**Ni<sub>2</sub>(DPX) (18).** The square geometry for the Ni(II) cores in Figure 2.4 are confirmed by the average Ni–N<sub>4</sub> displacement of 0.0061 Å and N–Ni–N bond angles of 90 ± 1.7°. Deviation of Ni–N bond lengths from the 1.949 Å average (1.920(7) to 1.971(7) Å) typically are caused by aggregation and packing forces.<sup>99</sup> The shorter M–N bond lengths in **18** as compared to **17** result from the smaller radius of the Ni(II) ion.<sup>88</sup> As observed for the analog biscopper(II) complex **17**, the two ring systems of **18** are structurally inequivalent in the solid state. The macrocycle with Ni(1) exhibits a pronounced ruffled conformation with a mean deviation of 0.3502 Å for the macrocyclic atoms from the porphyrin mean plane. The meso carbons are alternately displaced from the mean porphyrin plane, ranging from 0.6304 Å above to 0.5829 Å below the 24-atom macrocycle unit. The S<sub>4</sub> ruffling of the porphyrin ring is typical of Ni(II) porphyrin complexes and results from the contraction of the metal coordination site owing to the small size and high electrophilicity of the Ni(II) ion.<sup>104,105</sup> The macrocycle containing Ni(2) has a less pronounced

ruffled structure. Although the mean deviation of 0.3250 Å from the porphyrin plane is similar to what was observed in the ring containing Ni(1), the meso carbons are displaced from only 0.0154 Å below to 0.4076 Å above the mean porphyrin plane.

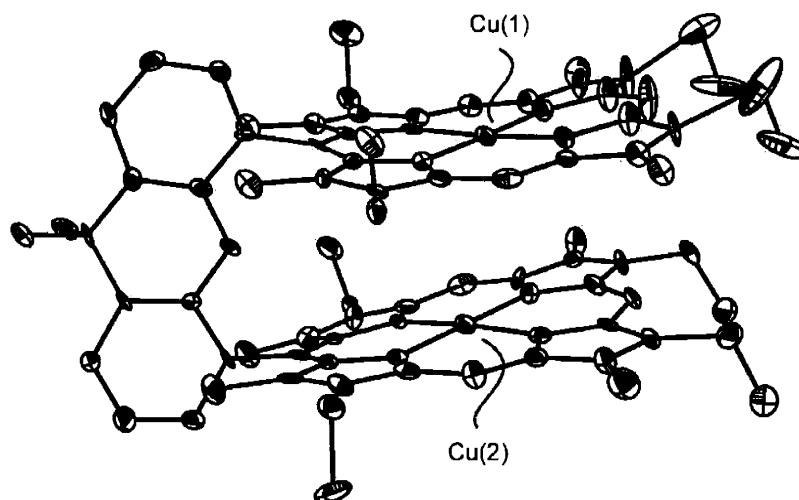


**Figure 2.3.** Crystal structure of Cu<sub>2</sub>(DPX) (17). Thermal ellipsoids are drawn at the 25% probability level. Hydrogen atoms and solvent molecules within the lattice have been omitted for clarity.

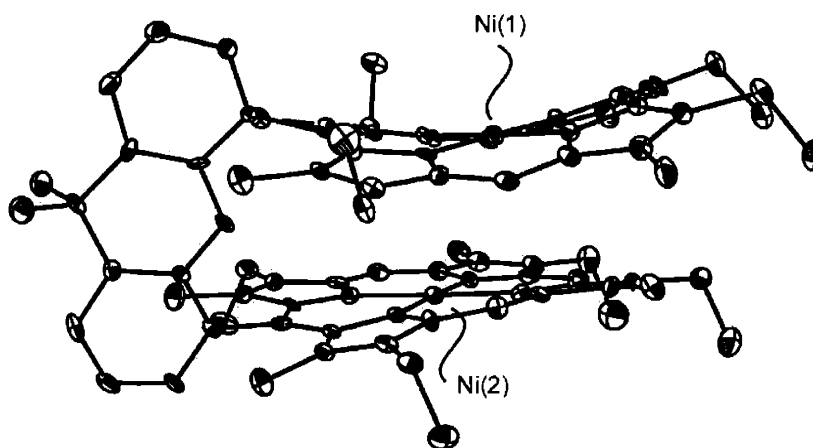


**Figure 2.4.** Crystal structure of Ni<sub>2</sub>(DPX) (18). Thermal ellipsoids are drawn at the 25% probability level. Hydrogen atoms and solvent molecules within the lattice have been omitted for clarity.

**Table 2.2.** Selected Bond Lengths (Å) for Zn<sub>2</sub>(DPX) (**16**), Cu<sub>2</sub>(DPX) (**17**), and Ni<sub>2</sub>(DPX) (**18**).

<b>16</b>		<b>17</b>		<b>18</b>	
Zn(1)–N(1)	2.031(4)	Cu(1)–N(1)	2.008(9)	Ni(1)–N(1)	1.942(7)
Zn(1)–N(2)	2.036(4)	Cu(1)–N(2)	2.016(9)	Ni(1)–N(2)	1.943(7)
Zn(1)–N(3)	2.040(4)	Cu(1)–N(3)	2.001(9)	Ni(1)–N(3)	1.948(7)
Zn(1)–N(4)	2.051(4)	Cu(1)–N(4)	2.011(9)	Ni(1)–N(4)	1.920(7)
Zn(2)–N(5)	2.047(4)	Cu(2)–N(5)	1.980(10)	Ni(2)–N(5)	1.968(7)
Zn(2)–N(6)	2.043(4)	Cu(2)–N(6)	1.995(9)	Ni(2)–N(6)	1.941(7)
Zn(2)–N(7)	2.040(4)	Cu(2)–N(7)	1.992(9)	Ni(2)–N(7)	1.958(7)
Zn(2)–N(8)	2.038(4)	Cu(2)–N(8)	2.013(9)	Ni(2)–N(8)	1.971(7)

**Table 2.3.** Selected Bond Angles (deg) for Zn<sub>2</sub>(DPX) (**16**), Cu<sub>2</sub>(DPX) (**17**), and Ni<sub>2</sub>(DPX) (**18**).

<b>16</b>		<b>17</b>		<b>18</b>	
N(1)–Zn(1)–N(2)	89.5(2)	N(3)–Cu(1)–N(1)	176.9(3)	N(4)–Ni(1)–N(1)	90.2(3)
N(1)–Zn(1)–N(3)	172.3(2)	N(3)–Cu(1)–N(4)	88.9(4)	N(4)–Ni(1)–N(2)	179.1(3)
N(2)–Zn(1)–N(3)	91.0(2)	N(1)–Cu(1)–N(4)	90.1(4)	N(1)–Ni(1)–N(2)	89.1(3)
N(1)–Zn(1)–N(4)	90.6(2)	N(3)–Cu(1)–N(2)	91.5(3)	N(4)–Ni(1)–N(3)	89.3(3)
N(2)–Zn(1)–N(4)	178.5(2)	N(1)–Cu(1)–N(2)	89.5(3)	N(1)–Ni(1)–N(3)	178.6(3)
N(3)–Zn(1)–N(4)	88.8(2)	N(4)–Cu(1)–N(2)	178.6(3)	N(2)–Ni(1)–N(3)	91.5(3)
N(7)–Zn(2)–N(8)	89.1(2)	N(5)–Cu(2)–N(6)	89.7(4)	N(6)–Ni(2)–N(7)	91.4(3)
N(7)–Zn(2)–N(6)	91.2(2)	N(5)–Cu(2)–N(7)	175.0(3)	N(6)–Ni(2)–N(5)	88.3(3)
N(8)–Zn(2)–N(6)	175.6(2)	N(6)–Cu(2)–N(7)	91.3(4)	N(7)–Ni(2)–N(5)	178.5(3)
N(7)–Zn(2)–N(5)	172.9(2)	N(5)–Cu(2)–N(8)	90.3(4)	N(6)–Ni(2)–N(8)	177.8(3)
N(8)–Zn(2)–N(5)	90.9(2)	N(6)–Cu(2)–N(8)	179.7(3)	N(7)–Ni(2)–N(8)	88.7(3)
N(6)–Zn(2)–N(5)	88.3(2)	N(7)–Cu(2)–N(8)	88.8(4)	N(5)–Ni(2)–N(8)	91.7(3)

The three approximately mutually perpendicular views of the molecular crystal structures of **16–18** shown in Figure 2.5 confirm the ability of the xanthene bridge to hold two porphyrin rings in a cofacial arrangement, akin to what is observed for anthracene and biphenylene systems. Pertinent geometrical parameters are summarized in Table 2.4. Scheidt and Lee's semiquantitative scheme for the pairwise overlap of the  $\pi$  systems of spatially oriented porphyrin



monomers within the crystalline lattice<sup>99</sup> provides a useful framework to analyze the structures of the xanthene bisporphyrins described here. The most important geometrical features of the aggregate dimer model are the lateral shift of the metal centers and the mean separation of the macrocycle planes, which are defined in Table 2.4. In this model, authentic  $\pi$ - $\pi$  interactions between aromatic macrocycles (as opposed to crystal packing effects) are signified by small lateral shifts ( $< 4$  Å).

**Table 2.4.** Crystallographically Derived Intradimer Geometrical Features for Zn<sub>2</sub>(DPX) (**16**), Cu<sub>2</sub>(DPX) (**17**), and Ni<sub>2</sub>(DPX) (**18**).<sup>a</sup>

	<b>16</b>	<b>17</b>	<b>18</b>
M—M distance (Å)	3.708	3.910	4.689
M—N <sub>4</sub> displacement (Å)	0.0918	0.0290	0.0061
Ct—Ct distance (Å)	3.863	3.978	4.698
MPS (Å)	3.417	3.611	3.666
Interplanar angle (deg)	4.4	2.3	1.9
Slip angle (deg)	27.8	24.8	38.7
Lateral shift (Å)	1.802	1.668	2.937

<sup>a</sup> Metrics were derived as follows. Macrocylic centers (Ct) were calculated as the centers of the four nitrogen planes (4-N plane) for each macrocycle. Interplanar angles were measured as the angle between the 4-N least squares planes. Plane separations were measured as the perpendicular distance from one macrocycle's 4-N least-square plane to the center of the other macrocycle; mean plane separations (MPS) were the average of the two plane separations. Slip angles ( $\alpha$ ) were calculated as the average angle between the vector connecting the two metal centers and the unit vectors normal to the two macrocyclic 4-N least squares planes ( $\alpha = \alpha_1 + \alpha_2/2$ ). The lateral shift was defined as  $[\sin(\alpha) \times (\text{Ct-Ct distance})]$ .

The data of Table 2.4 are unique insofar as lateral shifts are collected for a homologous series of cofacial bisporphyrins anchored by the same pillar. Owing to the inflexibility of the xanthene spacer, the lateral shifts of **16-18**, defined for the most part by the methine-methine direction perpendicular to the bridge, are small and similar. Of the three structures, **18** exhibits the least  $\pi$ -overlap, though the observed lateral shift is only moderately larger than that observed for related Ni(II) cofacial bisporphyrins (e.g., lateral shift of Ni<sub>2</sub>(DPA) is 2.40 Å).<sup>51</sup> The splayed structure of **18** suggests that the association of the nickel subunits is smaller than that of zinc and copper congeners. This finding is consonant with NMR investigations, which also show the same trend

for the aggregation of monomeric, asymmetric metalloporphyrins along this metal series.<sup>106-108</sup> The interplanar mean plane separations for **16-18** are similar, ranging from 3.4 to 3.6 Å.

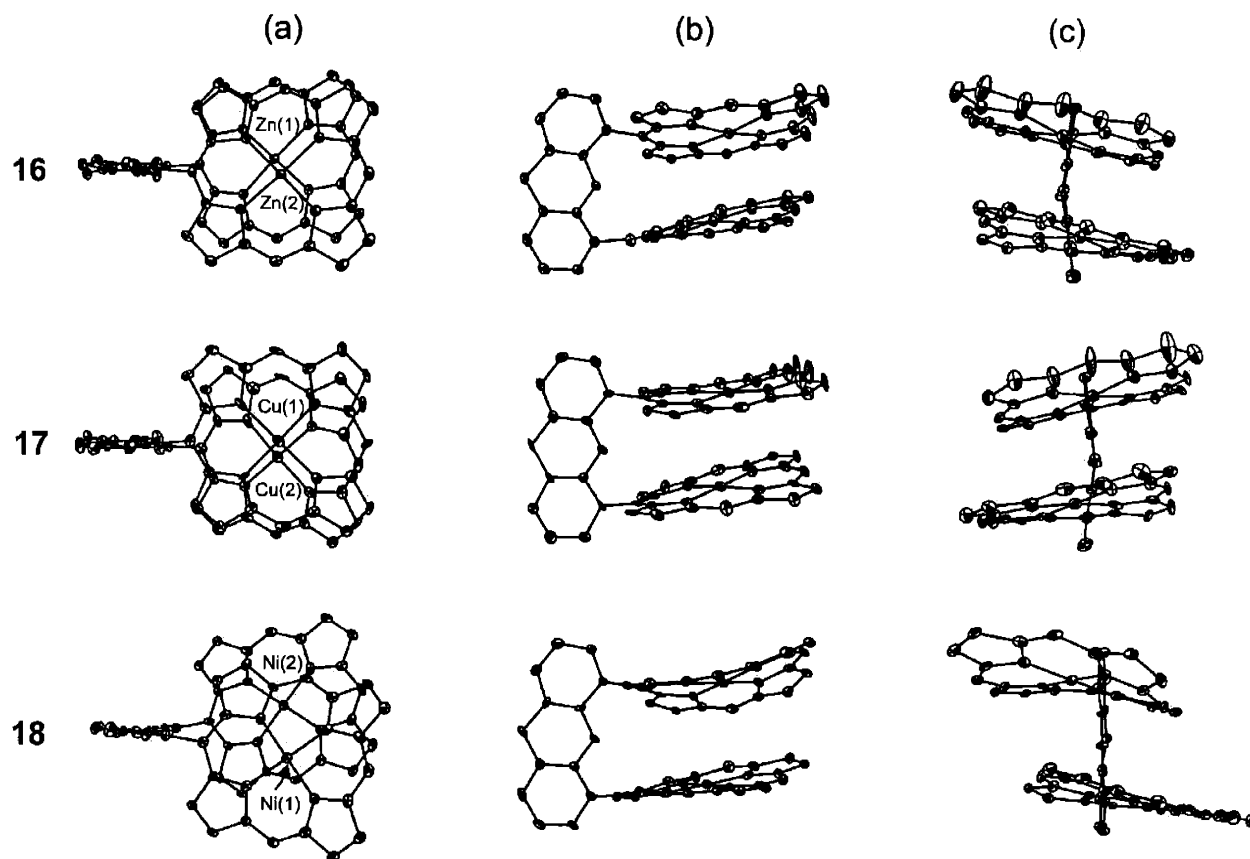
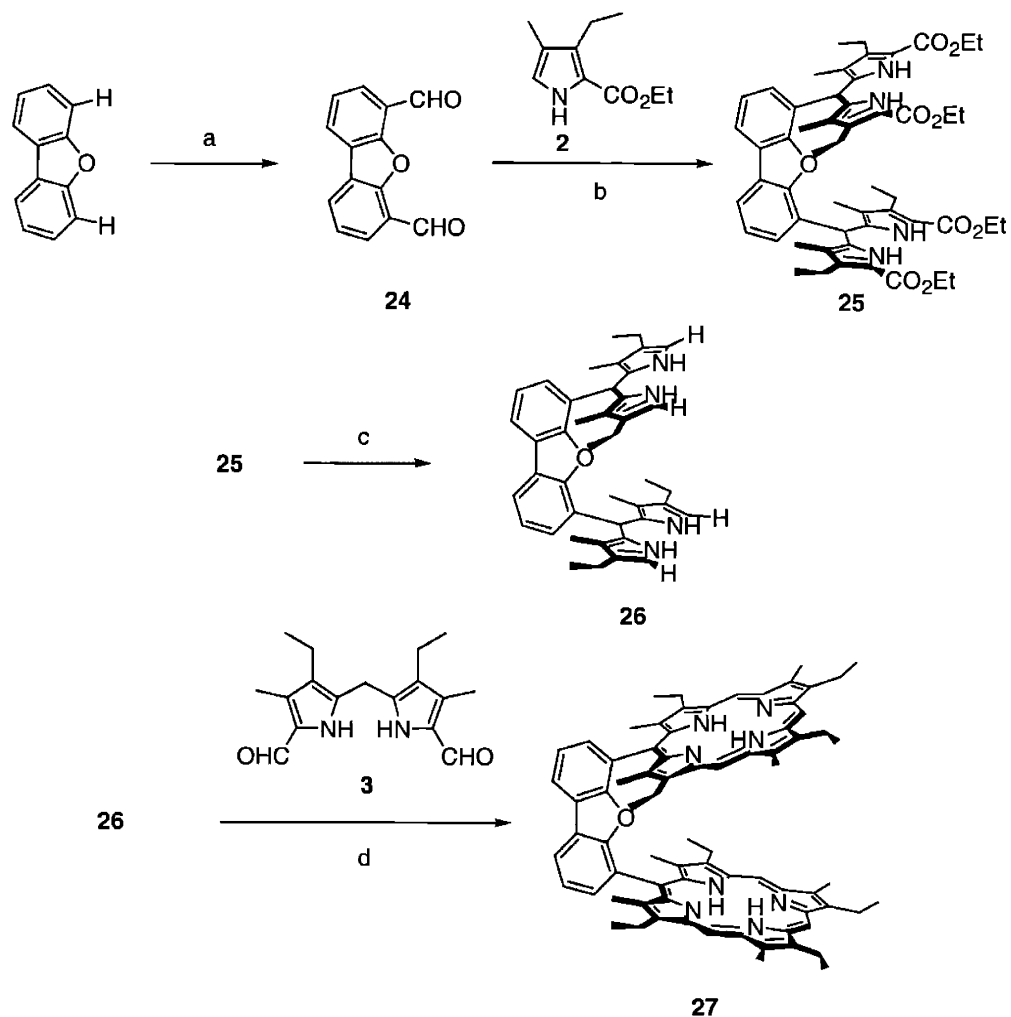


**Figure 2.5.** Comparative views of the crystal structures of **16-18**: (a) top view, perpendicular to porphyrin planes, (b) side view, perpendicular to bridge plane, (c) side view, parallel to bridge plane. Side groups and hydrogen atoms have been omitted for clarity.

### 2.3.4 Synthesis of a Dibenzofuran-Bridged Cofacial Bisporphyrin (DPD) with Lateral Preorganization and Vertical Flexibility

Substitution of the six-membered cyclic ether ring in xanthene for the five-membered one in dibenzofuran results in a pillared cofacial bisporphyrin platform exhibiting enhanced vertical flexibility while maintaining lateral preorganization. We employ the standard three-branch strategy<sup>40</sup> for the construction of the dibenzofuran-bridged cofacial bisporphyrin H<sub>4</sub>DPD (**27**) (DPD = diporphyrin dibenzofuran). The synthetic approach described in Scheme 2.4 is analogous to the route employed for the preparation of the xanthene-bridged cofacial bisporphyrin system DPX.



**Scheme 2.4.** (a) i. *n*-BuLi, TMEDA; ii. DMF; iii. H<sub>2</sub>O; (b) **2**, ethanol, HCl, reflux; (c) NaOH, ethylene glycol, reflux; (d) i. **3**, PTSA, methanol; ii. *o*-chloranil.

The dibenzofuran pillar branch for the DPD scaffold is delivered using a facile one-pot reaction in the same manner as described for the xanthene-based DPX system. Regioselective 4,6 dilithiation of dibenzofuran followed by the sequential addition of dry DMF and water yields dialdehyde **24** in 50% yield. Reaction of **24** with 2-(ethyloxycarbonyl)-3-ethyl-4-methylpyrrole (**2**) and subsequent hydrolysis and decarboxylation affords the  $\alpha$ -free tetrapyrrole **26** (> 90% over two steps). Condensation of tetrapyrrole **26** with 3,3'-diethyl-5,5'-diformyl-4,4'-dimethyl-2,2'-dipyrrylmethane **3** in the presence of *p*-toluenesulfonic acid (PTSA) followed by *o*-chloranil oxidation gives bisporphyrin H<sub>4</sub>(DPD) (**27**) in 20% yield after workup and purification. The convergent synthesis of the free-base DPD is achieved in 15 steps in an overall 3% yield. The <sup>1</sup>H NMR spectrum of **27** is consistent with a splayed structure in solution. The internal NH-pyrrolic resonances are only slightly upshifted (−3.85, −3.91 ppm) compared to monomeric porphyrins, in

contrast to the analogous xanthene bisporphyrin **15** which exhibits a marked upfield shift of these resonances due to the proximity of its macrocyclic rings.

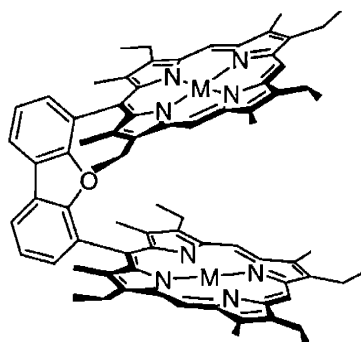
### 2.3.5 Transition-Metal Complexes of DPD

Homobimetallic complexes of  $H_4(DPD)$  (**27**) are produced by direct reaction with metal salts (Chart 2.5).<sup>88</sup> For example,  $Zn_2(DPD)$  (**28**) is obtained in quantitative yield from direct reaction of **27** with  $Zn(OAc)_2 \cdot 2H_2O$ . Complex **28** was fully characterized by  $^1H$  NMR spectroscopy and high-resolution mass spectral and elemental analyses. Treatment of  $H_4(DPD)$  (**27**) with  $Cu(OAc)_2 \cdot 2H_2O$  in methanol/chloroform mixtures affords the corresponding binuclear copper(II) complex  $Cu_2(DPD)$  (**29**) in excellent yield (90%). Complex **29** gave satisfactory high-resolution mass spectral and elemental analyses. Also,  $Ni_2(DPD)$  (**30**) was prepared according to Adler's method<sup>91</sup> ( $NiCl_2$ /refluxing DMF) in good yield (82%). The diamagnetic complex was characterized using  $^1H$  NMR, high-resolution mass spectrometry and elemental analyses. The successful preparation of compounds **28-30** completes a series of structurally homologous cofacial bisporphyrin complexes for both DPX and DPD containing zinc(II), copper(II) and nickel(II).

Other transition-metal derivatives are also available by direct reaction of  $H_4(DPD)$  (**27**) with metal salt precursors. Reaction of **27** with  $FeBr_2$  yields the corresponding diiron(II) complex. Exposure of this diiron(II) complex to air initially yields intra- and intermolecular  $\mu$ -oxo complexes as evidenced by TLC. The two products are equilibrated upon treatment with basic alumina to afford only the *intramolecular* bis-Fe(III)  $\mu$ -oxo complex  $Fe_2O(DPD)$  (**31**) in high yield (90%). Bischloroiron(III) compound **32** is delivered in good yield (91%) from reaction of **27** with  $FeBr_2$  and 2,6-lutidine in a THF/benzene solvent system followed by anion exchange with aq HCl. Lastly, bischloromanganese(III) complex **33** is afforded in high yield (86%) by an Alder reaction of **27** with  $Mn(OAc)_2 \cdot 4H_2O$  in DMF followed by anion exchange using aq NaCl/HCl. The complex was identified using high-resolution mass spectral and elemental analyses.

As observed for the DPX system, insertions of heavier elements into the porphyrin cores of  $H_4(DPD)$  (**27**) proceed with similar success. Bisplatinum(II) complex **34** is prepared in 90% yield by reaction of **27** with  $Pd(OAc)_2$  in chloroform/methanol mixtures. Bisdihydroxytin(IV) derivative **35** is synthesized from **27** in high yield (95%) using  $SnCl_2$  followed by workup with basic alumina. Both complexes were fully characterized using a combination of  $^1H$  NMR and high-resolution mass spectrometry, and the palladium complex gave satisfactory elemental analyses.

Chart 2.5



- |                       |                             |
|-----------------------|-----------------------------|
| 28: M = Zn            | 32: M = FeCl                |
| 29: M = Cu            | 33: M = MnCl                |
| 30: M = Ni            | 34: M = Pd                  |
| 31: M = Fe( $\mu$ -O) | 35: M = Sn(OH) <sub>2</sub> |

DPD

### 2.3.6 Structural Chemistry of DPD: Direct Observation of the “Pacman” Effect

The similar multielectron reactivity displayed by anthracene- and biphenylene-pillared cofacial bisporphyrins despite their ca. 1 Å difference in interplanar metal—metal distances led Collman to suggest that the DPA and DPB molecules have a vertical “Pacman” flexibility that allows the binding pocket to accommodate structurally reaction intermediates during catalysis.<sup>8</sup> Remarkably, the structural chemistry of the DPD system provides the *first direct support* for this crucial conformational change in a single cofacial platform. A comparative structural analysis of biszinc and bisiron(III)  $\mu$ -oxo complexes demonstrates the unprecedented ability of the DPD framework to open and close its binding pocket by a vertical distance of over 4 Å in the presence of exogenous ligands, thus validating the predicted Pacman effect for pillared cofacial porphyrin systems.

The molecular structures of the open and closed forms of the DPD scaffold, Zn<sub>2</sub>(DPD) (28) and Fe<sub>2</sub>O(DPD) (31), are shown in Figures 2.6 and 2.7, respectively. Each atom of the porphyrin rings and the corresponding bridge is numbered in the standard fashion while auxiliary methyl and ethyl groups off the macrocycles are additionally identified with their connection to the porphyrin ring. Selected geometrical measurements are given in Tables 2.5-2.7. Trends in bond lengths and angles of macrocyclic core structures and side chains agree well with those observed in related systems such as H<sub>4</sub>(DPX), H<sub>4</sub>(DPA),<sup>51,53,93</sup> H<sub>4</sub>(DPB),<sup>45,51</sup> and 1,2-bis[5-(2,3,7,8-12,13,17,18-octaethylporphyrinato)]-*cis*-ethene porphyrins.<sup>94-96</sup> Structural highlights of the open and closed forms of the DPD platform are as follows:

**Zn<sub>2</sub>(DPD) (28).** The introduction of porphyrinic substituents at the 4 and 6 positions of dibenzofuran imparts a significantly greater bite angle compared to other pillared bisporphyrins.

This fact is clearly established by the molecular structure of biszinc(II) **28**, which characterizes the relaxed form of the DPD system. Figure 2.6 depicts the natural wedge geometry of **28** with an interplanar angle of  $24.6^\circ$  and a large Zn—Zn distance of  $7.775 \text{ \AA}$  (Ct—Ct distance  $7.587 \text{ \AA}$ , mean plane separation  $7.356 \text{ \AA}$ ). For comparison, the analogous  $\text{Zn}_2(\text{DPX})$  (**16**) complex displays an interplanar angle of  $4.4^\circ$  and a compressed Zn—Zn distance of  $3.708 \text{ \AA}$  (Ct—Ct distance  $3.863 \text{ \AA}$ , mean plane separation  $3.417 \text{ \AA}$ ). The face-to-face arrangement of cofacial subunits is maintained, as illustrated by the small torsional twist of  $1.2^\circ$  (defined as the angle between the two meso-carbon to spacer bonds). The dibenzofuran bridge in **28** is planar (mean plane deviation  $0.016 \text{ \AA}$ ) and porphyrin macrocycles are essentially flat (avg deviation  $0.119 \text{ \AA}$ ). The Zn(II) ions of **28** are tetracoordinate with an average Zn—N bond length of  $2.042 \text{ \AA}$ .

*Fe<sub>2</sub>O(DPD)* (**31**). The structure of **31** (Figure 2.7) clearly demonstrates the dramatic ability of the DPD system to “bite” down on exogenous ligands. The porphyrin meso carbons connected to the bridge bend inward, forming a dihedral angle of  $12.8^\circ$ , while the macrocyclic cores tilt inward by  $10.1^\circ$ . As a result, the Fe—Fe distance is reduced to  $3.504 \text{ \AA}$ , with a Ct—Ct distance of  $4.611 \text{ \AA}$ . Average Fe—O ( $1.782 \text{ \AA}$ ) and Fe—N ( $2.104 \text{ \AA}$ ) bond lengths are normal for bisiron(III)  $\mu$ -oxo porphyrins.<sup>109-111</sup> The dibenzofuran bridge deviates from planarity, forming a dihedral angle of  $9.8^\circ$  between the two phenyl rings, and is positioned with dihedral angles of approximately  $84^\circ$  with the porphyrin cores.

Several other structural features of **31** merit comment. Conformational analysis indicates that the  $S_4$ -ruffled porphyrin cores are structurally inequivalent in the solid state, as core 1 displays a smaller displacement from planarity ( $d_{\text{avg}} = 0.0678 \text{ \AA}$ ) than core 2 ( $d_{\text{avg}} = 1.1063 \text{ \AA}$ ). The Fe atom displacements from the porphyrin mean planes ( $0.621 \text{ \AA}$  and  $0.678 \text{ \AA}$  for Fe(1) and Fe(2), respectively) are considerably larger than for related systems.<sup>110,112</sup> Unlike most other  $\mu$ -oxo bisiron bisporphyrins, where the rings align staggered to maximize  $\pi$  interactions,<sup>99</sup> the rigid dibenzofuran spacer restricts the porphyrin cores from rotation with respect to each other, resulting in a eclipsed conformation with an average N—Fe(1)—Fe(2)—N torsion angle of  $1.65^\circ$ . Perhaps the most striking feature of the structure of **31** is the small, bent Fe—O—Fe angle of  $158.7^\circ$ . For most iron  $\mu$ -oxo porphyrins, the Fe—O—Fe unit is nearly linear with angles ranging from  $172$ - $179^\circ$  to minimize the nonbonded interactions between the porphyrinic cores. For comparison, the smallest Fe—O—Fe angle reported thus far, in a urea-linked bisporphyrin ( $161.1^\circ$ ) was due to hydrogen bonding of the central oxygen to two solvent water molecules.<sup>113</sup>

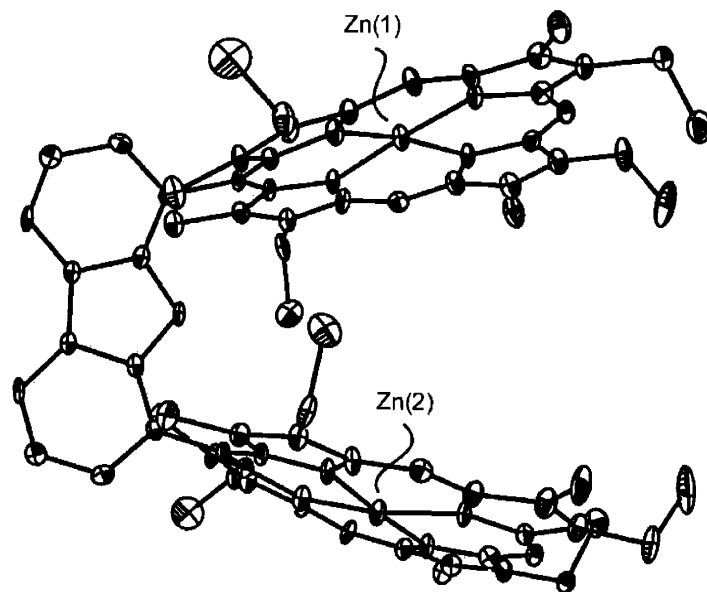


**Figure 2.6.** Crystal structure of Zn<sub>2</sub>(DPD) (28). Thermal ellipsoids are drawn at the 25% probability level. Hydrogen atoms and solvent molecules within the lattice have been omitted for clarity.

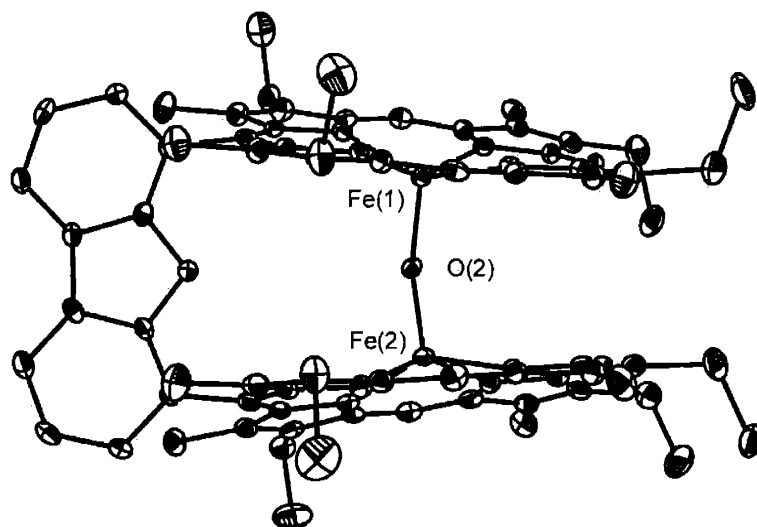


**Figure 2.7.** Crystal structure of Fe<sub>2</sub>O(DPD) (31). Thermal ellipsoids are drawn at the 25% probability level. Hydrogen atoms and solvent molecules within the lattice have been omitted for clarity.

**Table 2.5.** Crystallographic Data for Zn<sub>2</sub>(DPD) (**28**) and Fe<sub>2</sub>O(DPD) (**31**).

	<b>28</b>	<b>31</b>
Empirical formula	C <sub>79</sub> H <sub>86</sub> Cl <sub>2</sub> N <sub>8</sub> O <sub>3</sub> Zn <sub>2</sub>	C <sub>81</sub> H <sub>84</sub> Cl <sub>3</sub> Fe <sub>2</sub> N <sub>8</sub> O <sub>4</sub>
Formula weight	1397.20	1451.61
Temperature	183(2) K	183(2) K
Wavelength	0.71073 Å	0.71073 Å
Crystal system	Monoclinic	Orthorhombic
Space group	C2/c	P2 <sub>1</sub> 2 <sub>1</sub> 2 <sub>1</sub>
Unit cell dimensions	$a = 23.0808(2)$ Å $b = 25.9458(9)$ Å $c = 13.4593(5)$ Å	$a = 13.896(2)$ Å $b = 15.476(3)$ Å $c = 33.440(7)$ Å
	$\beta = 110.503(2)^\circ$	
Volume	7549.5(4) Å <sup>3</sup>	7192.0(2) Å <sup>3</sup>
Z	4	4
Density (calculated)	1.229 Mg/m <sup>3</sup>	1.341 Mg/m <sup>3</sup>
Absorption coefficient	0.757 mm <sup>-1</sup>	0.572 mm <sup>-1</sup>
F(000)	2936	3044
Crystal size	0.30 mm × 0.25 mm × 0.08 mm	0.5 mm × 0.5 mm × 0.25 mm
θ range for data collection	1.23 to 20.00°	1.22 to 20.00°
Reflections collected	11274	21224
Independent reflections	3522 (R <sub>int</sub> = 0.1109)	6699 (R <sub>int</sub> = 0.0322)
Data / restraints / parameters	3522 / 0 / 441	6699 / 0 / 897
Goodness-of-fit on F <sup>2</sup>	1.124	1.153
Final R indices [I > 2σ(I)]	$RI = 0.0890$ $wR2 = 0.2391$	$RI = 0.0420$ $wR2 = 0.1091$
R indices (all data)	$RI = 0.1439$ $wR2 = 0.2655$	$RI = 0.0455$ $wR2 = 0.1180$
Extinction coefficient	0.0028(4)	0.0035(3)
Largest diff peak	1.202 eÅ <sup>-3</sup>	0.511 eÅ <sup>-3</sup>
Largest diff hole	-0.691 eÅ <sup>-3</sup>	-0.364 eÅ <sup>-3</sup>



**Table 2.6.** Selected Bond Lengths (Å) and Angles (deg) for Zn<sub>2</sub>(DPD) (**28**).

<i>Bond Lengths (Å)</i>		<i>Bond Angles (deg)</i>	
Zn(1)-N(1)	2.041(8)	N(2)-Zn(1)-N(1)	89.6(3)
Zn(1)-N(2)	2.030(9)	N(2)-Zn(1)-N(4)	170.9(4)
Zn(1)-N(3)	2.059(9)	N(1)-Zn(1)-N(4)	91.1(4)
Zn(1)-N(4)	2.050(9)	N(2)-Zn(1)-N(3)	90.4(4)
		N(1)-Zn(1)-N(3)	176.4(4)
		N(4)-Zn(1)-N(3)	88.4(4)

**Table 2.7.** Selected Bond Lengths (Å) and Angles (deg) for Fe<sub>2</sub>O(DPD) (**31**).

<i>Bond Lengths (Å)</i>		<i>Bond Angles (deg)</i>			
Fe(1)-O(2)	1.783(3)	O(2)-Fe(1)-N(3)	103.25(16)	O(2)-Fe(2)-N(5)	106.34(16)
Fe(1)-N(3)	2.098(5)	O(2)-Fe(1)-N(4)	106.84(17)	O(2)-Fe(2)-N(7)	106.28(16)
Fe(1)-N(4)	2.105(4)	N(3)-Fe(1)-N(4)	84.95(17)	N(5)-Fe(2)-N(7)	147.39(17)
Fe(1)-N(2)	2.105(5)	O(2)-Fe(1)-N(2)	103.44(17)	O(2)-Fe(2)-N(6)	105.99(17)
Fe(1)-N(1)	2.117(4)	N(3)-Fe(1)-N(2)	87.40(17)	N(5)-Fe(2)-N(6)	83.67(18)
Fe(2)-O(2)	1.781(3)	N(4)-Fe(1)-N(2)	149.70(17)	N(7)-Fe(2)-N(6)	87.28(17)
Fe(2)-N(5)	2.101(5)	O(2)-Fe(1)-N(1)	107.79(15)	O(2)-Fe(2)-N(8)	104.55(17)
Fe(2)-N(7)	2.103(5)	N(3)-Fe(1)-N(1)	148.95(17)	N(5)-Fe(2)-N(8)	87.64(17)
Fe(2)-N(6)	2.105(5)	N(4)-Fe(1)-N(1)	86.83(17)	N(7)-Fe(2)-N(8)	84.45(17)
Fe(2)-N(8)	2.107(5)	N(2)-Fe(1)-N(1)	84.78(17)	N(6)-Fe(2)-N(8)	149.46(17)

## 2.4 Concluding Remarks

The success of pillared Pacman bisporphyrins in multielectron, small-molecule activation chemistry relies heavily on the choice of spacer.<sup>8</sup> The most crucial feature is the size and flexibility of the binding pocket provided by fixing two macrocyclic units in a cofacial arrangement. Traditionally, the pillared Pacman bisporphyrin motif has been limited to two spacers, anthracene and biphenylene. Biphenylene has been the bridge of choice in studies of the small-molecule activation chemistry of pillared bisporphyrins, providing a slightly tighter binding cavity than the more easily synthesized anthracene due to the fewer number of atoms separating the porphyrin subunits. However, the synthesis of the biphenylene pillar is particularly

arduous, involving multiple steps including a high-temperature vacuum pyrolysis (800 °C, 0.6 torr).<sup>45</sup>

We have developed two new Pacman cofacial bisporphyrin platforms based on the readily accessible cyclic ether spacers xanthene and dibenzofuran. The prerequisite xanthene and dibenzofuran pillars are prepared in multigram quantities in a convenient one-pot procedure without purification by column chromatography or distillation, offering a noteworthy synthetic improvement over both the anthracene- or biphenylene-pillared systems. The xanthene and dibenzofuran spacers are conveniently employed in the construction of the pillared cofacial bisporphyrins DPX and DPD, respectively. These new Pacman platforms allow for straightforward, systematic control of structural attributes pertaining to pocket size within a chemically similar ether-bridged series: DPX has both lateral and vertical preorganization, while DPD has lateral preorganization and vertical flexibility.

Structural analysis confirms the ability of the xanthene bridge with a six-membered center ring to hold two porphyrins in a face-to-face orientation. The homobimetallic zinc(II), copper(II), and nickel(II) complexes of DPX represent the first homologous series of pillared bisporphyrins examined by X-ray diffraction. Although the xanthene bridge contains the same number of atoms as anthracene, the presence of an  $sp^3$  oxygen in the wedge of the former gives the DPX scaffold enhanced vertical flexibility, allowing the binding pocket to span the dimensions of either the DPA or DPB system. Furthermore, the pocket size of the Pacman bisporphyrin may be further tuned by metal substitution, as the extent of  $\pi$ - $\pi$  interactions plays an important role in determining the lateral slip between the two porphyrin rings. Lastly, the central oxygen may provide a possible hydrogen-bonding site for proton-coupled redox processes in the bisporphyrin cavity.

The dibenzofuran bridge with a five-membered center ring produces a wedge-shaped DPD platform with unprecedented vertical flexibility while maintaining horizontal preorganization. The molecular structures of the open biszinc(II) (**28**) and closed bisiron(III)  $\mu$ -oxo (**31**) complexes reveal the significant vertical flexibility that the DPD system possesses. The preference of intramolecular  $\mu$ -oxo complex **31** over intermolecular products also suggests that the vertical open-to-closed conformational change for DPD is accompanied by a small energy. An accessible pocket that can collapse about a guest with minimized conformational energy should lower the transition state energy for substrate activation. Accordingly, DPD provides an attractive platform for our investigations of the proton-coupled, multielectron activation of small molecule substrates.

In closing, the cyclic ether pillars xanthene and dibenzofuran furnish two new Pacman bisporphyrin systems, and their structural chemistry demonstrates the ability to tune the vertical dimensions of the microcavity architecture. With these results in hand, we are now poised to investigate these and related cofacial bisporphyrin species for their physical properties and PCET-mediated small-molecule activation chemistry.

## 2.5 Experimental Section

### 2.5.1 Materials

Silica gel 60 (70-230 and 230-400 mesh, Merck) and aluminum oxide 60 (EM Science) were used for column chromatography. Analytical thin layer chromatography was performed using Merck 60 F254 silica gel (precoated sheets, 0.2 mm thick) or JT Baker IB-F aluminum oxide (precoated sheets, 0.2 mm thick). Solvents for synthesis were of reagent grade or better, and were dried according to standard methods.<sup>114</sup> 9,9-dimethylxanthene was obtained from xanthone as described by Rebek and co-workers.<sup>75</sup> All other reagents were used as received.

### 2.5.2 3-Hydroxy-2-nitropentane (4)

Propionaldehyde (174 g, 3 mol), isopropyl alcohol (450 mL), and ground potassium fluoride (25 g, 0.43 mol) were combined in a 3-necked round bottom flask equipped with a mechanical stirrer, a dropping funnel, and a drying tube. The mixture was cooled in an ice-water bath and nitroethane (225.21 g, 3 mol) was added dropwise to the reaction with stirring, keeping the temperature below 40 °C. The resulting lemonade-colored mixture was stirred at room temperature overnight and filtered. The isopropyl alcohol was removed by rotary evaporation, water (500 mL) was added, and the mixture was extracted with ether (3 × 300 mL). The organic extracts were dried over Na<sub>2</sub>SO<sub>4</sub> and the solvent was removed by rotary evaporation. Purification by vacuum distillation (50 torr) and collection of the fraction removed at 70-80 °C gave nitroalcohol **4** as a clear liquid (229 g, 70% yield). The product was used directly in the next step. GCMS (M+) calcd for C<sub>5</sub>H<sub>11</sub>NO<sub>3</sub> *m/z* 133, found 133.

### 2.5.3 3-Acetoxy-2-nitropentane (5)

Nitroalcohol **4** (110 g, 0.82 mol) was combined with conc H<sub>2</sub>SO<sub>4</sub> (0.5 mL) and mixture was cooled in an ice-water bath. Acetic anhydride (80 g, 0.82 mol) was added in portions over 30 min. The reaction was allowed to warm to room temperature and stirred for an additional hour. Vacuum distillation using a water aspirator under gentle heating (< 100 °C) removed acetic acid and acetic anhydride. Vacuum distillation using a vacuum pump and collection of the fraction boiling at 70-80 °C at 50 torr delivered 3-acetoxy-2-nitropentane **5** as a clear oil (132 g, 92%

yield). This product was used directly in subsequent reactions.  $^1\text{H}$  NMR (300 MHz,  $\text{CDCl}_3$ , 25  $^\circ\text{C}$ ):  $\delta$  = 5.27 (m, 1H, CH), 4.75 (m, 1H,  $\text{CHNO}_2$ ), 2.06 (m, 3H,  $\text{CH}_3$ ), 1.78 (m, 1H,  $\text{CH}_2$ ), 1.67 (m, 1H,  $\text{CH}_2$ ), 1.53 (m, 3H,  $\text{CH}_3$ ), 0.95 (m, 3H,  $\text{CH}_3$ ). GCMS (M+) calcd for  $\text{C}_7\text{H}_{13}\text{NO}_4$   $m/z$  175, found 175.

#### 2.5.4 Ethyl isocyanoacetate (6)

Glycine ethyl ester hydrochloride (69.5 g, 0.495 mol) and methyl formate (250 mL) were combined in an oven-dried, 3-necked round bottom flask equipped with a mechanical stirrer, an addition funnel, and a drying tube. The contents were brought to reflux and triethylamine (55 g) was added dropwise to the mixture over a period of 30 min. A white precipitate formed and the reaction was refluxed for an additional 21 h. The mixture was cooled to room temperature, filtered, and the solid was washed with an additional 250 mL methyl formate. Purification by vacuum distillation (50 torr) and collection of the fraction removed at 80-90  $^\circ\text{C}$  gave *N*-formyl glycine ethyl ester as a clear liquid (46.4 g, 71% yield). The product was used directly in the next step.

A combination of *N*-formyl glycine ethyl ester (92.3 g, 0.70 mol), dry triethylamine (176.1 g), and dry dichloromethane (705 mL) were added to a 3-necked round bottom flask equipped with a mechanical stirrer and an addition funnel. The resulting solution was cooled in an ice-acetone bath under nitrogen. Phosphorus oxychloride (107.8 g, 0.70 mol) was added dropwise to the reaction via the addition funnel over a period of 1 h. The melon-colored mixture was allowed to warm to room temperature and stirred for an additional hour. A solution of aq  $\text{Na}_2\text{CO}_3$  (140 g in 700 mL  $\text{H}_2\text{O}$ ) was added slowly to quench the reaction, keeping the temperature below 30  $^\circ\text{C}$ , and the reaction was left standing for 1 h. Water was added to bring the aqueous layer to ca. 1.5 L, the organic layer was decanted, and the aqueous phase was extracted with dichloromethane (2  $\times$  400 mL). The organic phases were combined and washed with brine (200 mL), dried over  $\text{Na}_2\text{SO}_4$ , and the solvent was removed by rotary evaporation with no heating. Vacuum distillation under low heat (< 70  $^\circ\text{C}$ , 50 torr) and collection of the product in a dry-ice acetone bath furnished compound **6** as a clear oil (65.6 g, 82%). The product, which has a phosphine-like smell, was stored at -20  $^\circ\text{C}$  under nitrogen.  $^1\text{H}$  NMR (300 MHz,  $\text{CDCl}_3$ , 25  $^\circ\text{C}$ ):  $\delta$  = 3.64 (q,  $J$  = 6.6 Hz, 2H,  $\text{CH}_2$ ), 2.96 (br s, 2H,  $\text{CH}_2$ ), 1.17 (t,  $J$  = 6.6 Hz, 3H,  $\text{CH}_3$ ).

#### 2.5.5 2-(Ethylloxycarbonyl)-3-ethyl-4-methylpyrrole (2)

Ethyl isocyanoacetate (**6**) (20 g, 0.177 mol) and 3-acetoxy-2-nitropentane (**5**) (44 g, 0.253 mol) were dissolved in a mixture of freshly distilled tetrahydrofuran (128 mL) and isopropyl alcohol (52 mL), and the contents were added to a dry round bottom flask equipped with an addition

funnel. The solution was cooled in an ice-acetone bath under nitrogen. 1,8-diazabicyclo[5.4.0]undec-7-ene (DBU) (60.8 g, 0.399 mol) was added dropwise to the solution, keeping the temperature below 30 °C. The reaction color changed from light yellow to orange, and a white precipitate formed. Stirring was continued at room temperature under nitrogen for an additional 14 h. The solvent was removed by rotary evaporation and warm water (200 mL) was added to the resulting orange oil. The biphasic mixture was allowed to cool to room temperature and extracted with ether (2 × 200 mL). The ether extracts were washed with 10% HCl (2 × 100 mL), dried over Na<sub>2</sub>SO<sub>4</sub>, and the solvent was removed by rotary evaporation. Recrystallization from methanol/water mixtures delivered  $\alpha$ -free pyrrole **2** as a flaky pale-yellow solid (25 g, 78% yield). <sup>1</sup>H NMR (300 MHz, CDCl<sub>3</sub>, 25 °C):  $\delta$  = 8.67 (br s, 1H, NH), 6.63 (d, *J* = 2.5 Hz, 1H, CH), 4.32 (q, *J* = 7.2 Hz, 2H, CH<sub>2</sub>), 2.75 (q, *J* = 7.5 Hz, 2H, CH<sub>2</sub>), 2.02 (s, 3H, CH<sub>3</sub>), 1.35 (t, *J* = 7.2 Hz, 3H, CH<sub>3</sub>), 1.12 (t, *J* = 7.5 Hz, 3H, CH<sub>3</sub>). GCMS (M+) calcd for C<sub>10</sub>H<sub>15</sub>NO<sub>2</sub> *m/z* 181, found 181.

#### 2.5.6 Ethyl $\alpha$ -oximinoacetoacetate (**7**)

Ethyl acetoacetate (185.6 g, 1.4 mol) and glacial acetic acid (300 mL) were added to a 3-necked round bottom flask equipped with a mechanical stirrer and an addition funnel. The resulting solution was cooled in an ice-acetone bath. A solution of sodium nitrite (103.8 g, 1.5 mol) in deionized water (140 mL) was added dropwise to the stirred ethyl acetoacetate solution, keeping the temperature < 18 °C. The reaction was left to warm to room temperature and stirred overnight to give a clear yellow solution of oxime **7**. This solution was used directly in the next manipulation.

#### 2.5.7 2-(Ethylloxycarbonyl)-3,5-dimethyl-4-acetylpyrrole (**8**)

Sodium acetate (450 g), glacial acetic acid (1.5 L), and 2,4-pentanedione (150 g, 154 mL, 1.5 mol) were combined in a 5-liter 3-necked round bottom flask equipped with a mechanical stirrer and an addition funnel. The resulting solution was cooled in an ice bath. The dual additions of zinc powder (1 g aliquots, 200 g total) and oxime **7** solution (1 to 2 mL aliquots, 440 mL total) to the stirred pentanedione solution were carried out over 1 to 2 h, keeping the temperature below 70 °C. The solution turned yellow-green, and the reaction was stirred in the ice bath for an additional three hours after completion of the dual additions. The reaction was then poured into ice-cold water (1 L), filtered, and washed with water. The remaining solid was redissolved in hot ethanol, filtered to remove excess zinc, and taken to dryness. Recrystallization from ethanol and water gave pyrrole **8** as a white solid (135 g, 46% yield over two steps). <sup>1</sup>H NMR (300 MHz, CDCl<sub>3</sub>, 25 °C):  $\delta$  = 10.26 (br s, 1H, NH), 4.35 (q, *J* = 7.5 Hz, 2H, CH<sub>2</sub>), 2.60 (s, 3H, CH<sub>3</sub>), 2.56 (s, 3H, CH<sub>3</sub>), 2.50 (s, 3H, CH<sub>3</sub>), 1.38 (t, *J* = 7.5 Hz, 3H, CH<sub>3</sub>).

### 2.5.8 2-(Ethylloxycarbonyl)-3,5-dimethyl-4-ethylpyrrole (9)

Under a nitrogen atmosphere, the ketopyrrole **8** (134.8 g, 0.64 mol) and sodium borohydride (48.8 g, 1.3 mol) were dissolved in freshly distilled tetrahydrofuran (400 mL). Dry  $\text{BF}_3 \cdot \text{OEt}_2$  (227 mL) was added dropwise to the ketopyrrole solution over a period of 90 min, and the reaction was stirred under nitrogen for an additional 2 h after completion of the last addition. The reaction was quenched with glacial acetic acid (2 to 5 mL) and poured over an ice-water mixture (500 mL). The resulting mixture was extracted with dichloromethane ( $3 \times 100$  mL), and the combined organic phases were washed with water ( $3 \times 100$  mL), dried over  $\text{Na}_2\text{SO}_4$ , and the solvent was removed to afford crude pyrrole **9** as a yellow solid. Recrystallization from ethanol and water furnishes pure pyrrole **9** as a crystalline white powder (67 g, 54% yield).  $^1\text{H}$  NMR (500 MHz,  $\text{CDCl}_3$ , 25 °C):  $\delta$  = 8.49 (br s, 1H, NH), 4.30 (q,  $J$  = 6.5 Hz, 2H,  $\text{CH}_2$ ), 2.39 (q,  $J$  = 6.5 Hz, 2H,  $\text{CH}_2$ ), 2.29 (s, 3H,  $\text{CH}_3$ ), 2.21 (s, 3H,  $\text{CH}_3$ ), 1.35 (t,  $J$  = 6.5 Hz, 3H,  $\text{CH}_3$ ), 1.06 (t,  $J$  = 6.5 Hz, 3H,  $\text{CH}_3$ ).

### 2.5.9 2-(Ethylloxycarbonyl)-3-methyl-4-ethyl-5-acetoxypyrrole (10)

Pyrrole **9** (135 g, 0.69 mol) was dissolved in glacial acetic acid (700 mL). Lead(IV) acetate was added in portions over a period of an hour (330 g total) to the stirred pyrrole mixture. The reaction was heated in air at 100 °C for 15 min, and poured directly into cold water (2 L). The resulting precipitate was filtered, washed with water ( $5 \times 100$  mL), and **10** was obtained as a fluffy tan solid that was used directly in the next step. Notably, the acetoxypyrrole **10** can be used moist without complete drying.

### 2.5.10 3,3'-Diethyl-5,5'-diethylloxycarbonyl-4,4'-dimethyl-2,2'-dipyrrylmethane (11)

Acetoxypyrrole **10** from the preceding reaction was dissolved in hot glacial acetic acid (1.5 L) and the resulting solution was brought to reflux in air. Water (300 mL) was added and the mixture was refluxed for an additional 15 min and poured into water (2.5 L). The mixture was left to sit overnight and the precipitate was isolated by vacuum filtration. Ester-protected dipyrromethane **11** was delivered as a beige solid (110 g, 85% yield over two steps).  $^1\text{H}$  NMR (300 MHz,  $\text{CDCl}_3$ , 25 °C):  $\delta$  = 8.95 (br s, 2H, NH), 6.35 (m, 2H, CH), 4.25 (q,  $J$  = 7 Hz, 4H,  $\text{CH}_2$ ), 3.85 (s, 2H,  $\text{CH}_2$ ), 2.40 (q,  $J$  = 7 Hz, 4H,  $\text{CH}_2$ ), 2.25 (s, 6H,  $\text{CH}_3$ ), 1.30 (t,  $J$  = 7 Hz, 6H,  $\text{CH}_3$ ), 1.05 (t,  $J$  = 7 Hz, 6H,  $\text{CH}_3$ ).

### 2.5.11 3,3'-Diethyl-4,4'-dimethyl-2,2'-dipyrrylmethane (12)

Ester-protected dipyrromethane **11** (100 g, 0.33 mol) was combined with ethanol (500 mL) and an aq NaOH solution (40 g in 100 mL) was added. The mixture was refluxed for 2 h under a

nitrogen atmosphere. The ethanol was removed under open heat with a nitrogen purge. Water (150 mL) and hydrazine hydrate (2 mL) were added and the mixture was refluxed under nitrogen for at least 5 h until a brown oil layer formed. The reaction was cooled to room temperature and the oil layer was decanted. The oil solidified upon standing in the refrigerator. The product **12** was isolated by filtration, washed with water until the washings were at neutral pH, and dried under high vacuum (quantitative yield). The product has a bone smell and was stored under nitrogen in a freezer at  $-20\text{ }^{\circ}\text{C}$ .  $^1\text{H}$  NMR (300 MHz,  $\text{CDCl}_3$ ,  $25\text{ }^{\circ}\text{C}$ ):  $\delta$  = 7.26 (br s, 2H, NH), 6.35 (m, 2H, CH), 3.79 (s, 2H,  $\text{CH}_2$ ), 2.47 (q,  $J$  = 7 Hz, 4H,  $\text{CH}_2$ ), 2.03 (s, 6H,  $\text{CH}_3$ ), 1.12 (t,  $J$  = 7 Hz, 6H,  $\text{CH}_3$ ).

#### 2.5.12 3,3'-Diethyl-5,5'-diformyl-4,4'-dimethyl-2,2'-dipyrrylmethane (**3**)

Under a nitrogen atmosphere, phosphorus oxychloride (12 mL) was added dropwise to a solution of **12** (9.2 g, 0.04 mol) in anhydrous DMF (60 mL) at  $-10\text{ }^{\circ}\text{C}$ . After stirring at  $-10\text{ }^{\circ}\text{C}$  for 30 min, the resulting mixture was allowed to warm to room temperature and stirred for an additional 2 h. The reaction was concentrated to half its original volume and methanol (200 mL) and  $\text{Na}_2\text{CO}_3$  (20 g) were added. The mixture was heated at  $60\text{ }^{\circ}\text{C}$  for 30 min and cooled to room temperature. The precipitate was filtered and washed with water until the washings became neutral. Recrystallization from ethanol afforded **3** as a khaki powder (8.6 g, 75% yield).  $^1\text{H}$  NMR (300 MHz,  $\text{CDCl}_3$ ,  $25\text{ }^{\circ}\text{C}$ ):  $\delta$  = 10.41 (br s, 2H, NH), 9.50 (s, 2H, CHO), 3.95 (s, 2H,  $\text{CH}_2$ ), 2.47 (q,  $J$  = 7 Hz, 4H,  $\text{CH}_2$ ), 2.30 (s, 6H,  $\text{CH}_3$ ), 1.08 (t,  $J$  = 7.2 Hz, 6H,  $\text{CH}_3$ ).

#### 2.5.13 4,5-Diformyl-9,9-dimethylxanthene (**1**)

*N*-Butyllithium (1.6 M in hexanes, 134 mL, 0.214 mol, 3 equiv) was added to 9,9-dimethylxanthene (15 g, 0.071 mol), dissolved in 80 mL of dry hexane containing *N,N,N',N'*-tetramethylethylenediamine (27 mL, 0.178 mol, 2.5 equiv). The mixture was refluxed under nitrogen for 10 min, cooled to  $0\text{ }^{\circ}\text{C}$ , and 30 mL of DMF was added. The stirred mixture was allowed to warm slowly to room temperature over a period of 2 h and then poured over ice. The precipitate was collected by filtration and recrystallized from hot methanol to afford dialdehyde **1** as an off-white solid (16.2 g, 86% yield).  $^1\text{H}$  NMR (300 MHz,  $\text{CDCl}_3$ ,  $25\text{ }^{\circ}\text{C}$ ):  $\delta$  = 10.68 (s, 2H, CHO), 7.82 (d, 2H, ArH), 7.75 (d, 2H, ArH), 7.25 (t, 2H, ArH), 1.69 (s, 6H,  $\text{CH}_3$ ).

#### 2.5.14 4,5-Bis[5,5'-bis(ethyloxycarbonyl)-4,4'-diethyl-3,3'-dimethyl-2,2'-dipyrrylmethyl] 9,9-dimethylxanthene (**13**)

A mixture of dialdehyde **1** (2.66 g, 0.01 mol) and pyrrole **2** (7.60 g, 0.042 mol) in absolute ethanol (65 mL) containing conc HCl (1.8 mL) was refluxed under nitrogen for 4 h and cooled in an ice-water bath. The precipitate was filtered and washed with cold methanol to give **13** as a

pale-pink powder (8.4 g, 88% yield).  $^1\text{H}$  NMR (300 MHz,  $\text{CDCl}_3$ , 25 °C):  $\delta$  = 8.19 (br s, 4H, NH), 7.40 (d, 2H, ArH), 7.03 (t, 2H, ArH), 6.67 (d, 2H, ArH), 5.59 (s, 2H, CH), 4.21 (q, 8H,  $\text{CH}_2$ ), 2.67 (q, 8H,  $\text{CH}_2$ ), 1.66 (s, 6H,  $\text{CH}_3$ ), 1.55 (s, 12H,  $\text{CH}_3$ ), 1.26 (t, 12H,  $\text{CH}_3$ ), 1.04 (t, 12H,  $\text{CH}_3$ ).

#### 2.5.15 4,5-Bis[4,4'-diethyl-3,3'-dimethyl-2,2'-dipyrrylmethyl]-9,9-dimethylxanthene (14)

Powdered NaOH (2 g) and **13** (4.2 g, 4.40 mmol) were suspended in 40 mL of ethylene glycol. The mixture was refluxed under nitrogen for 4 h. The precipitate was collected by suction filtration, washed with water until the washings became neutral, and dried under vacuum over  $\text{P}_2\text{O}_5$ . Product **14**, which was obtained as a goldenrod solid (2.52 g, 86% yield), was stored under nitrogen at -20 °C.  $^1\text{H}$  NMR (300 MHz,  $\text{CDCl}_3$ , 25 °C):  $\delta$  = 7.38 (d, 4H, ArH), 7.03 (t, 2H, ArH), 6.81 (br s, 2H, CH) 6.29 (s, 4H, NH), 5.68 (br s, 2H, CH), 2.38 (q, 8H,  $\text{CH}_2$ ), 1.62 (s, 18H,  $\text{CH}_3$ ), 1.13 (t, 12H,  $\text{CH}_3$ ).

#### 2.5.16 4,5-Bis[(5-(2,3,13,17-tetraethyl-3,7,12,18-tetramethylporphyrinyl)]-9,9-dimethylxanthene, $\text{H}_4(\text{DPX})$ (15)

A suspension of tetrapyrrole **14** (5.30 g, 8 mmol) and **3** (4.58 g, 16 mmol) in a mixture of THF (800 mL) and methanol (400 mL) was purged with nitrogen for 1 h. A solution of *p*-toluenesulfonic acid (3.56 g) in methanol (20 mL) was added dropwise over a period of 2 h. The resulting red mixture was stirred in the dark under nitrogen for 2 days. Solid *o*-chloranil (3.56 g) was added in one portion and stirring was continued in air for 24 h. The mixture was taken to dryness and the remaining solid redissolved in 500 mL of chloroform. A saturated methanolic solution of  $\text{Zn}(\text{OAc})_2 \cdot 2\text{H}_2\text{O}$  (25 mL) was added and the solution was refluxed for 15 min. The solvent was removed and the remaining residue was purified by flash column chromatography (silica gel, dichloromethane). The first band eluted was collected and vigorously stirred with 6 N HCl (15 mL) for 15 min. The solution was neutralized with a 10% aqueous sodium carbonate solution and the mixture was stirred for an additional 15 min. The organic phase was separated, washed with water (3  $\times$  50 mL), dried over  $\text{Na}_2\text{SO}_4$ , and taken to dryness. Purification by flash column chromatography (silica gel, dichloromethane to 1:1 methanol/dichloromethane) followed by recrystallization from dichloromethane/methanol afforded pure bisporphyrin **15** as a purple microcrystalline powder (2.1 g, 23% yield).  $^1\text{H}$  NMR (300 MHz,  $\text{CDCl}_3$ , 25 °C):  $\delta$  = 9.13 (s, 2H, meso), 8.29 (s, 4H, meso), 7.88 (d, 2H, ArH), 7.28 (t, 2H, ArH), 7.06 (d, 2H, ArH), 4.12 (m, 4H,  $\text{CH}_2$ ), 3.86 (m, 4H,  $\text{CH}_2$ ), 3.32 (m, 8H,  $\text{CH}_2$ ), 3.10 (s, 12H,  $\text{CH}_3$ ), 2.29 (s, 12H,  $\text{CH}_3$ ), 2.25 (s, 6H,  $\text{CH}_3$ ), 1.75 (t, 12H,  $\text{CH}_3$ ), 1.37 (t, 12H,  $\text{CH}_3$ ), -6.42 (br s, 2H, NH), -6.80 (br s, 2H, NH).



### 2.5.17 Zn<sub>2</sub>(DPX) (16)

A saturated methanolic solution of Zn(OAc)<sub>2</sub>•2H<sub>2</sub>O (1 mL) was added to a solution of **15** (20 mg, 0.017 mmol) in 5 mL chloroform. The reaction was refluxed for 30 min and taken to dryness. The solid residue was purified by flash column chromatography (silica gel, 3:1 dichloromethane/hexanes) followed by recrystallization from dichloromethane/methanol to yield analytically pure biszinc(II) **16** as a brick red solid in nearly essentially quantitative yield. <sup>1</sup>H NMR (300 MHz, CDCl<sub>3</sub>, 25 °C): δ = 9.13 (s, 2H, meso), 8.43 (s, 4H, meso), 7.85 (d, 2H, ArH), 7.21 (t, 2H, ArH), 6.95 (d, 2H, ArH), 4.15 (m, 4H, CH<sub>2</sub>), 3.87 (m, 4H, CH<sub>2</sub>), 3.56 (m, 4H, CH<sub>2</sub>), 3.32 (m, 4H, CH<sub>2</sub>), 3.21 (s, 12H, CH<sub>3</sub>), 2.29 (s, 12H, CH<sub>3</sub>), 2.24 (s, 6H, CH<sub>3</sub>), 1.74 (t, 12H, CH<sub>3</sub>), 1.40 (t, 12H, CH<sub>3</sub>). Anal. Calcd for C<sub>79</sub>H<sub>82</sub>N<sub>8</sub>OZn<sub>2</sub>: C, 73.54; H, 6.41; N, 8.68. Found: C, 73.69; H, 6.15; N, 8.35. HRFABMS (M<sup>+</sup>) calcd for C<sub>79</sub>H<sub>82</sub>N<sub>8</sub>OZn<sub>2</sub> *m/z* 1286.519, found 1286.520.

### 2.5.18 Cu<sub>2</sub>(DPX) (17)

To a 60-mL chloroform solution of bisporphyrin **15** (90 mg, 0.077 mmol) was added a solution of Cu(OAc)<sub>2</sub>•2H<sub>2</sub>O (200 mg) and potassium acetate (200 mg) in 15 mL of methanol. The resulting solution was refluxed for 4 h and solvent was removed by rotary evaporation. The solid was taken up in a 1:1 mixture of dichloromethane/water (120 mL). The organic layer was decanted, washed with water (3 × 50 mL), dried over Na<sub>2</sub>SO<sub>4</sub>, and taken to dryness. The crude material was purified by flash column chromatography (silica gel, 1:1 dichloromethane/hexanes) followed by recrystallization from dichloromethane/methanol to afford analytically pure **17** as a mulberry red solid (94 mg, 94% yield). Anal. Calcd for C<sub>79</sub>H<sub>82</sub>N<sub>8</sub>OCu<sub>2</sub>•2CH<sub>2</sub>Cl<sub>2</sub>: C, 66.85; H, 5.91; N, 7.70. Found: C, 67.25; H, 5.95; N, 7.41. HRFABMS (M<sup>+</sup>) calcd for C<sub>79</sub>H<sub>82</sub>N<sub>8</sub>OCu<sub>2</sub> *m/z* 1284.540, found 1284.519.

### 2.5.19 Ni<sub>2</sub>(DPX) (18)

A mixture of **15** (88 mg, 0.076 mmol) and NiCl<sub>2</sub> (123 mg) in 50 mL DMF was refluxed under nitrogen for 4 h. The solvent was removed under vacuum and the remaining solid was taken up in a 1:1 mixture of dichloromethane/water (150 mL). The organic layer was decanted, washed with water (3 × 50 mL), dried over Na<sub>2</sub>SO<sub>4</sub>, and taken to dryness. Purification by flash column chromatography (silica gel, 3:1 dichloromethane/hexanes) followed by recrystallization from dichloromethane/methanol gave analytically pure **18** as a plum red solid (80 mg, 83% yield). <sup>1</sup>H NMR (300 MHz, CDCl<sub>3</sub>, 25 °C): δ = 8.76 (s, 2H, meso), 8.00 (s, 4H, meso), 7.79 (d, 2H, ArH), 7.19 (t, 2H, ArH), 6.93 (d, 2H, ArH), 3.64 (m, 4H, CH<sub>2</sub>), 3.47 (m, 4H, CH<sub>2</sub>), 2.95 (m, 8H, CH<sub>2</sub>), 2.71 (s, 12H, CH<sub>3</sub>), 2.12 (s, 12H, CH<sub>3</sub>), 1.57 (t, 12H, CH<sub>3</sub>), 1.52 (s, 6H, CH<sub>3</sub>), 1.22 (t, 12H,

CH<sub>3</sub>). Anal. Calcd for C<sub>79</sub>H<sub>82</sub>N<sub>8</sub>ONi<sub>2</sub>•3H<sub>2</sub>O: C, 71.29; H, 6.61; N, 8.42. Found: C, 71.01; H, 6.65; N, 8.25. HRFABMS (M<sup>+</sup>) calcd for C<sub>79</sub>H<sub>82</sub>N<sub>8</sub>ONi<sub>2</sub> *m/z* 1274.532, found 1274.531.

#### 2.5.20 Fe<sub>2</sub>Cl<sub>2</sub>(DPX) (19)

In a dry box, a 100-mL flask equipped with a condenser was charged with **15** (90 mg, 0.077 mmol), 2,6-lutidine (0.2 mL), FeBr<sub>2</sub> (200 mg), THF (12 mL) and benzene (12 mL). The mixture was refluxed under nitrogen for 12 h, opened to air, and brought to dryness under vacuum. The residue was taken up in a 1:1 mixture of dichloromethane/water (50 mL). The organic layer was separated, washed with water (3 × 50 mL), and stirred with 3 N HCl (25 mL) for 90 min. The organic layer was decanted and solvent was removed under vacuum. The remaining solid was purified by column chromatography (silica gel, dichloromethane to 5% methanol/dichloromethane) and retreated with HCl as described above. The organic phase was separated, washed with water (3 × 50 mL), dried over Na<sub>2</sub>SO<sub>4</sub>, and taken to dryness. Recrystallization from dichloromethane and ether afforded pure **19** as a brown powder (96 mg, 93% yield). Anal. Calcd for C<sub>79</sub>H<sub>82</sub>Cl<sub>2</sub>Fe<sub>2</sub>N<sub>8</sub>O: C, 70.70; H, 6.16; N, 8.35. Found: C, 70.33; H, 6.43; N, 8.25. HRFABMS ([M-Cl]<sup>+</sup>) calcd for C<sub>79</sub>H<sub>82</sub>Cl<sub>2</sub>Fe<sub>2</sub>N<sub>8</sub>O *m/z* 1305.4999, found 1305.5023.

#### 2.5.21 Fe<sub>2</sub>O(DPX) (20)

In a dry box, **15** (20 mg, 0.017 mmol), pyridine (0.1 mL), FeBr<sub>2</sub> (60 mg), and THF (15 mL) were loaded in 50-mL flask equipped with a condenser. The mixture was refluxed under nitrogen for 5 h, opened to air, and brought to dryness under vacuum. The residue was purified using basic alumina (activity I, chloroform/ethyl acetate = 80/20) to give **20** as brown solid (18 mg, 90% yield). Anal. Calcd for C<sub>79</sub>H<sub>82</sub>Fe<sub>2</sub>N<sub>8</sub>O<sub>2</sub>: C, 73.71; H, 6.42; N, 8.70. Found: C, 73.77; H, 6.31; N, 8.68. HRFABMS ([M-O]<sup>+</sup>) calcd for C<sub>79</sub>H<sub>82</sub>Fe<sub>2</sub>N<sub>8</sub>O<sub>2</sub> *m/z* 1270.5310, found 1270.5316.

#### 2.5.22 Mn<sub>2</sub>Cl<sub>2</sub>(DPX) (21)

A solution of **15** (180 mg, 0.154 mmol) and Mn(OAc)<sub>2</sub>•4H<sub>2</sub>O (300 mg) in DMF (25 mL) was refluxed in air for 3 h. The reaction was cooled to room temperature and taken to dryness. The remaining was taken up in a 1:1 mixture of dichloromethane/water (50 mL). The organic layer was separated, washed with water (3 × 75 mL), and stirred with a 5:1 mixture of saturated aq NaCl and HCl (72 mL) for 90 min. The organic layer was decanted and solvent was removed under vacuum. The remaining solid was purified by column chromatography (silica gel, dichloromethane to 5% methanol/dichloromethane) and retreated with aq NaCl and HCl as described above. The organic phase was separated, washed with water (3 × 75 mL), dried over Na<sub>2</sub>SO<sub>4</sub>, and taken to dryness. Recrystallization from dichloromethane and ether afforded pure

**21** as a brown solid (186 mg, 90% yield). Anal. Calcd for  $C_{79}H_{82}N_8OCl_2Mn_2$ : C, 70.79; H, 6.17; N, 8.36; Cl, 5.29. Found: C, 70.26; H, 6.43; N, 8.13; Cl, 5.09. HRFABMS ( $[M-Cl]^+$ ) calcd for  $C_{79}H_{82}N_8OCl_2Mn_2$   $m/z$  1303.506, found 1303.506.

### 2.5.23 $Pd_2(DPX)$ (**22**)

To a 40-mL chloroform solution of  $H_4(DPX)$  (50 mg, 0.043 mmol) was added a solution of  $Pd(OAc)_2$  (200 mg) and potassium acetate (200 mg) in 12 mL of methanol. The resulting solution was refluxed for 11 h under nitrogen and the solvent was removed by rotary evaporation. The crude material was purified by flash column chromatography (silica gel, 1:1 hexanes/dichloromethane to dichloromethane) followed by recrystallization from dichloromethane/methanol to afford analytically pure **22** as a bright red solid (40 mg, 68% yield).  $^1H$  NMR (500 MHz,  $CDCl_3$ , 25 °C):  $\delta$  = 9.08 (s, 2H, meso), 8.46 (s, 4H, meso), 7.87 (d, 2H, ArH), 7.23 (t, 2H, ArH), 7.02 (d, 2H, ArH), 4.14 (m, 4H,  $CH_2$ ), 3.85 (m, 4H,  $CH_2$ ), 3.57 (m, 4H,  $CH_2$ ), 3.33 (m, 4H,  $CH_2$ ), 3.21 (s, 12H,  $CH_3$ ), 2.26 (s, 12H,  $CH_3$ ), 2.22 (s, 6H,  $CH_3$ ), 1.72 (t, 12H,  $CH_3$ ), 1.42 (t, 12H,  $CH_3$ ). Anal. Calcd for  $C_{79}H_{82}N_8OPd_2$ : C, 69.14; H, 6.02; N, 8.16. Found: C, 69.17; H, 5.98; N, 8.12. HRFABMS ( $M^+$ ) calcd for  $C_{79}H_{82}N_8OPd_2$   $m/z$  1370.468, found 1370.469.

### 2.5.24 $Sn_2(OH)_4(DPX)$ (**23**)

A combination of **15** (93 mg, 0.080 mmol) and  $SnCl_2 \cdot 2H_2O$  (298 mg) in pyridine (5.5 mL) was refluxed in air in the dark for 5 h. The reaction was cooled to room temperature and the solvent was removed under high vacuum. The remaining residue was redissolved in chloroform (100 mL) and the organic phase was washed with 3N HCl ( $2 \times 20$  mL) and water ( $4 \times 25$  mL). The organic layer was separated and dried over  $Na_2SO_4$ . In a separate 20-mL vial, basic alumina (10 g) and water (2 mL) were combined and shaken into a homogeneous powder (some warming occurred). The activated basic alumina powder was added to the chloroform solution containing the metalated porphyrin and the resulting mixture was stirred overnight in the dark. The reaction was filtered and solvent was removed by rotary evaporation. Recrystallization from chloroform and hexanes gave **23** as a bright red powder (80 mg, 68% yield).  $^1H$  NMR (500 MHz,  $CDCl_3$ , 25 °C):  $\delta$  = 9.61 (s, 2H, meso), 9.46 (s, 4H, meso), 8.11 (m, 2H, ArH), 7.53 (t, 2H, ArH), 7.37 (m, 2H, ArH), 4.66 (m, 4H,  $CH_2$ ), 4.33 (m, 4H,  $CH_2$ ), 4.16 (m, 4H,  $CH_2$ ), 3.87 (m, 4H,  $CH_2$ ), 3.81 (s, 12H,  $CH_3$ ), 2.46 (s, 12H,  $CH_3$ ), 2.34 (s, 6H,  $CH_3$ ), 1.81 (t, 12H,  $CH_3$ ), 1.67 (t, 12H,  $CH_3$ ). The hydroxide protons were not identified. HRFABMS ( $MH^+$ ) calcd for  $C_{79}H_{86}N_8O_5Sn_2$   $m/z$  1463.484, found 1463.490.

### 2.5.25 4,6-Diformyldibenzofuran (**24**)

Dibenzofuran (12 g, 0.071 mol) was dissolved in 70 mL of dry hexane containing *N,N,N',N'*-tetramethylethylenediamine (27 mL, 0.178 mol, 2.5 equiv). To this solution was added *n*-butyllithium (1.6 M in hexane, 134 mL, 3 equiv) and the mixture was refluxed under nitrogen for 10 min. The reaction was cooled to 0° C and 30 mL of DMF was added. The stirred mixture was allowed to slowly warm to room temperature over a period of 2 h and then poured over ice. The precipitate was collected by suction filtration and recrystallized from hot methanol to give **24** as a bone-white solid (8 g, 50% yield). <sup>1</sup>H NMR (300 MHz, CDCl<sub>3</sub>, 25 °C): δ= 10.72 (s, 2H, CHO), 8.25 (d, 2H, ArH), 8.05 (d, 2H, ArH), 7.57 (t, 2H, ArH). GCMS (M+) calcd for C<sub>14</sub>H<sub>8</sub>O<sub>3</sub> *m/z* 224, found 224.

### 2.5.26 4,6-Bis[5,5'-bis(ethyloxycarbonyl)-4,4'-diethyl-3,3'-dimethyl-2,2'-dipyrrylmethyl]dibenzofuran (**25**)

2-(Ethyloxycarbonyl)-3-ethyl-4-methylpyrrole (**2**) (5 g, 27.6 mmol, 4 equiv) and **24** (1.53 g, 6.9 mmol) and were added to absolute ethanol (50 mL) containing conc HCl (1.2 mL). The resultant mixture was refluxed under nitrogen for 4 h and cooled in an ice-water bath. The precipitate was filtered by suction and washed with cold methanol to afford **25** as a pink powder (5.2 g, 83% yield). <sup>1</sup>H NMR (300 MHz, CDCl<sub>3</sub>, 25 °C): δ= 8.62 (br s, 4H, NH), 7.86 (d, 2H, ArH), 7.29 (t, 2H, ArH), 7.08 (d, 2H, ArH), 5.89 (s, 2H, CH), 4.21 (q, 8H, CH<sub>2</sub>), 2.68 (m, 8H, CH<sub>2</sub>), 1.70 (s, 12H, CH<sub>3</sub>), 1.26 (t, 12H, CH<sub>3</sub>), 1.07 (t, 12H, CH<sub>3</sub>). FABMS (M+) calcd for C<sub>54</sub>H<sub>64</sub>N<sub>4</sub>O<sub>9</sub> *m/z* 912.5, found 912.3.

### 2.5.27 4,6-Bis[4,4'-diethyl-3,3'-dimethyl-2,2'-dipyrrylmethyl]dibenzofuran (**26**)

Powdered NaOH (3 g) and **25** (5.2 g, 5.7 mmol) were suspended in 40 mL of ethylene glycol, and the mixture was refluxed under nitrogen for 4 h. After cooling, the precipitate was collected by suction filtration, washed with water until the washings became neutral, and dried under vacuum over P<sub>2</sub>O<sub>5</sub>. The product **26** was obtained as a manila solid (3.2 g, 90% yield). It was stored under nitrogen at -20 °C. <sup>1</sup>H NMR (300 MHz, CDCl<sub>3</sub>, 25 °C): δ= 7.79 (d, 2H, ArH), 7.54 (s, 4H, NH), 7.24 (t, 2H, ArH), 6.30 (d, 2H, ArH), 6.29 (s, 2H, CH), 5.73 (s, 2H, CH), 3.71 (s, 2H, CH), 2.38 (q, 8H, CH<sub>2</sub>), 1.62 (s, 18H, CH<sub>3</sub>), 1.13 (t, 12H, CH<sub>3</sub>). FABMS (M+) calcd for C<sub>42</sub>H<sub>48</sub>N<sub>4</sub>O *m/z* 624.4, found 624.4.

### 2.5.28 4,6-Bis[(5-(2,3,13,17-tetraethyl-3,7,12,18-tetramethylporphyrinyl)]dibenzofuran, H<sub>4</sub>(DPD) (27)

A suspension of **26** (1.40 g, 2 mmol) and 3,3'-diethyl-5,5'-diformyl-4,4'-dimethyl-2,2'-dipyrrylmethane (**3**) (1.14 g, 4 mmol) in 300 mL methanol was purged with nitrogen for 1 h. A solution of *p*-toluenesulfonic acid (0.89 g) in methanol (10 mL) was added dropwise over a period of 30 min. The resulting dark red mixture was stirred in the dark under nitrogen for 2 days. Solid *o*-chloranil (0.89 g) was added in one portion and stirring was continued in air for 24 h. The mixture was taken to dryness and redissolved in 200 mL of chloroform. A saturated methanolic solution of Zn(OAc)<sub>2</sub>•2H<sub>2</sub>O (10 mL) was added and the mixture was refluxed for 15 min. The solvent was removed and the remaining residue was purified by flash column chromatography (silica gel, dichloromethane). The first band eluted was collected and vigorously stirred with 6 N HCl (8 mL) for 15 min. The solution was neutralized with a 10% aqueous solution of sodium carbonate and the mixture was stirred for an additional 15 min. The organic phase was separated, washed with water (3 × 25 mL), dried over Na<sub>2</sub>SO<sub>4</sub>, and taken to dryness. Purification by flash column chromatography (silica gel, dichloromethane to 5% methanol/dichloromethane) followed by recrystallization from dichloromethane/methanol yielded pure **27** as a purple microcrystalline powder (450 mg, 20% yield). <sup>1</sup>H NMR (300 MHz, CDCl<sub>3</sub>, 25 °C): δ = 9.70 (s, 4H, meso), 9.52 (s, 2H, meso), 8.64 (d, 2H, ArH), 7.79 (t, 2H, ArH), 7.76 (d, 2H, ArH), 3.78 (m, 20H, CH<sub>2</sub>), 3.33 (s, 12H, CH<sub>3</sub>), 2.36 (s, 12H, CH<sub>3</sub>), 1.59 (t, 12H, CH<sub>3</sub>), 1.51 (t, 12H, CH<sub>3</sub>), -3.85 (s, 2H, NH), -3.91 (s, 2H, NH). HRFABMS (M<sup>+</sup>) calcd for C<sub>76</sub>H<sub>80</sub>N<sub>8</sub>O *m/z* 1120.6455, found 1120.6447.

### 2.5.29 Zn<sub>2</sub>(DPD) (28)

A saturated methanolic solution of Zn(OAc)<sub>2</sub>•2H<sub>2</sub>O (1 mL) and a solution of **27** (50 mg, 0.045 mmol) in 15 mL chloroform were combined and refluxed for 20 min. The solvent was removed by rotary evaporation. The remaining solid was purified by flash column chromatography (silica gel, 3:1 dichloromethane/hexanes) followed by recrystallization from dichloromethane/methanol to yield analytically pure **28** as a ruby red solid in essentially quantitative yield. <sup>1</sup>H NMR (300 MHz, CDCl<sub>3</sub>, 25 °C): δ = 9.62 (s, 4H, meso), 9.56 (s, 2H, meso), 8.67 (d, 2H, ArH), 7.85 (t, 2H, ArH), 7.82 (d, 2H, ArH), 3.76 (m, 20H, CH<sub>2</sub>), 3.31 (s, 12H, CH<sub>3</sub>), 2.31 (s, 12H, CH<sub>3</sub>), 1.58 (t, 12H, CH<sub>3</sub>), 1.47 (t, 12H, CH<sub>3</sub>). Anal. Calcd for C<sub>76</sub>H<sub>76</sub>N<sub>8</sub>OZn<sub>2</sub>: C, 73.13; H, 6.14; N, 8.98. Found: C, 72.88; H, 6.20; N, 9.06. HRFABMS (M<sup>+</sup>) calcd for C<sub>76</sub>H<sub>76</sub>N<sub>8</sub>OZn<sub>2</sub> *m/z* 1244.472, found 1244.472.

### 2.5.30 Cu<sub>2</sub>(DPD) (29)

To a 20-mL chloroform solution of **27** (50 mg, 0.045 mmol) was added a solution of Cu(OAc)<sub>2</sub>•2H<sub>2</sub>O (100 mg) and potassium acetate (110 mg) in 15 mL of methanol. The resulting solution was refluxed for 4 h and solvent was removed by rotary evaporation. The solid was taken up in a 1:1 mixture of dichloromethane/water (40 mL). The organic layer was decanted, washed with water (3 × 15 mL), dried over Na<sub>2</sub>SO<sub>4</sub>, and taken to dryness. The crude material was purified by flash column chromatography (silica gel, 3:1 dichloromethane/hexanes) followed by recrystallization from dichloromethane/methanol to afford analytically pure **29** as a cherry red solid (50 mg, 90% yield). Anal. Calcd for C<sub>76</sub>H<sub>76</sub>N<sub>8</sub>OCu<sub>2</sub>•H<sub>2</sub>O: C, 72.30; H, 6.23; N, 8.88. Found: C, 72.49; H, 6.10; N, 8.78. HRFABMS (M<sup>+</sup>) calcd for C<sub>79</sub>H<sub>82</sub>N<sub>8</sub>OCu<sub>2</sub> *m/z* 1243.481, found 1243.481.

### 2.5.31 Ni<sub>2</sub>(DPD) (30)

A mixture of **27** (53 mg, 0.047 mmol) and NiCl<sub>2</sub> (110 mg) in 15 mL DMF was refluxed for 5 h. The solvent was removed under vacuum and the remaining solid was taken up in a 1:1 mixture of dichloromethane/water (100 mL). The organic layer was decanted, washed with water (3 × 50 mL), dried over Na<sub>2</sub>SO<sub>4</sub> and taken to dryness. Purification by flash column chromatography (silica gel, 3:1 dichloromethane/hexanes) followed by recrystallization from dichloromethane/methanol gave analytically pure **30** as a plum red solid (48 mg, 82% yield). <sup>1</sup>H NMR (500 MHz, CDCl<sub>3</sub>, 25 °C): δ = 9.33 (s, 4H, meso), 9.32 (s, 2H, meso), 8.51 (d, 2H, ArH), 7.62 (t, 2H, ArH), 7.27 (d, 2H, ArH), 3.68 (m, 16H, CH<sub>2</sub>), 3.25 (s, 12H, CH<sub>3</sub>), 2.32 (s, 12H, CH<sub>3</sub>), 1.58 (t, 12H, CH<sub>3</sub>), 1.51 (t, 12H, CH<sub>3</sub>). Anal. Calcd for C<sub>76</sub>H<sub>76</sub>N<sub>8</sub>ONi<sub>2</sub>: C, 73.92; H, 6.20; N, 9.07. Found: C, 74.15; H, 6.35; N, 8.68. HRFABMS (M<sup>+</sup>) calcd for C<sub>76</sub>H<sub>76</sub>N<sub>8</sub>ONi<sub>2</sub> *m/z* 1232.485, found 1232.492.

### 2.5.32 Fe<sub>2</sub>O(DPD) (31)

In a dry box, **27** (50 mg, 0.045 mmol), pyridine (0.1 mL), FeBr<sub>2</sub> (100 mg), and THF (15 mL) were loaded in 100-mL flask equipped with a condenser. The mixture was refluxed under nitrogen for 5 h, opened to air, and brought to dryness under vacuum. The residue was purified using basic alumina (activity I, chloroform/ethyl acetate = 85/15) to give **31** as brown solid (45 mg, 0.036 mmol) in 90% yield. Anal. Calcd for C<sub>76</sub>H<sub>76</sub>Fe<sub>2</sub>N<sub>8</sub>O<sub>2</sub>: C, 73.31; H, 6.15; N, 9.00. Found: C, 73.17; H, 6.21; N, 8.68. HRFABMS (MH<sup>+</sup>) calcd for C<sub>76</sub>H<sub>77</sub>Fe<sub>2</sub>N<sub>8</sub>O<sub>2</sub> *m/z* 1245.4868, found 1245.4861.

### 2.5.33 Fe<sub>2</sub>Cl<sub>2</sub>(DPD) (32)

In a dry box, a 100-mL flask equipped with a condenser was charged with **27** (50 mg, 0.045 mmol), 2,6-lutidine (0.1 mL), FeBr<sub>2</sub> (150 mg), THF (12 mL) and benzene (12 mL). The mixture was refluxed under nitrogen for 10 h, opened to air, and brought to dryness under vacuum. The residue was taken up in a 1:1 mixture of dichloromethane/water (50 mL). The organic layer was separated, washed with water (3 × 50 mL), and stirred with 3N HCl (35 mL) for 90 min. The organic layer was decanted and solvent was removed under vacuum. The remaining solid was purified by column chromatography (silica gel, dichloromethane to 5% methanol/dichloromethane) and retreated with HCl as described above. The organic phase was separated, washed with water (3 × 50 mL), dried over Na<sub>2</sub>SO<sub>4</sub>, and taken to dryness. Recrystallization from dichloromethane and ether afforded pure **32** as a brown powder (47 mg, 91% yield). Anal. Calcd for C<sub>76</sub>H<sub>76</sub>Cl<sub>2</sub>Fe<sub>2</sub>N<sub>8</sub>O: C, 70.21; H, 5.89; N, 8.62. Found: C, 70.43; H, 5.77; N, 8.35. HRFABMS ([M-Cl]<sup>+</sup>) calcd for C<sub>76</sub>H<sub>76</sub>Cl<sub>2</sub>Fe<sub>2</sub>N<sub>8</sub>O *m/z* 1263.453, found 1263.447.

### 2.5.34 Mn<sub>2</sub>Cl<sub>2</sub>(DPD) (33)

A solution of **27** (100 mg, 0.089 mmol) and Mn(OAc)<sub>2</sub>•4H<sub>2</sub>O (200 mg) in DMF (20 mL) was refluxed in air for 5 h. The reaction was cooled to room temperature and taken to dryness. The remaining was taken up in a 1:1 mixture of dichloromethane/water (50 mL). The organic layer was separated, washed with water (3 × 50 mL), and stirred with a 5:1 mixture of saturated aq NaCl and HCl (60 mL) for 90 min. The organic layer was decanted and solvent was removed under vacuum. The remaining solid was purified by column chromatography (silica gel, dichloromethane to 5% methanol/dichloromethane) and retreated with aq NaCl and HCl as described above. The organic phase was separated, washed with water (3 × 50 mL), dried over Na<sub>2</sub>SO<sub>4</sub>, and taken to dryness. Recrystallization from dichloromethane and ether afforded pure **33** as a brown solid (100 mg, 86% yield). Anal. Calcd for C<sub>76</sub>H<sub>76</sub>Cl<sub>2</sub>Mn<sub>2</sub>N<sub>8</sub>O: C, 70.31; H, 5.90; N, 8.63. Found: C, 70.45; H, 5.82; N, 8.54. HRFABMS ([M-Cl]<sup>+</sup>) calcd for C<sub>76</sub>H<sub>76</sub>Cl<sub>2</sub>Mn<sub>2</sub>N<sub>8</sub>O *m/z* 1261.459, found 1261.432.

### 2.5.35 Pd<sub>2</sub>(DPD) (34)

To a 50-mL chloroform solution of **27** (80 mg, 0.071 mmol) was added a solution of Pd(OAc)<sub>2</sub> (180 mg) and potassium acetate (200 mg) in 10 mL of methanol. The resulting solution was refluxed for 6 h under nitrogen and the solvent was removed by rotary evaporation. The crude material was purified by flash column chromatography (silica gel, 1:1 hexanes/dichloromethane to dichloromethane) followed by recrystallization from dichloromethane/methanol to afford analytically pure **34** as a cherry red solid (85 mg, 90% yield). <sup>1</sup>H NMR (500 MHz, CDCl<sub>3</sub>, 25

°C):  $\delta$  = 9.67 (s, 4H, meso), 9.51 (s, 2H, meso), 8.65 (d, 2H, ArH), 7.74 (t, 2H, ArH), 7.66 (d, 2H, ArH), 3.65-3.81 (m, 20H, CH<sub>2</sub>), 3.26 (s, 12H, CH<sub>3</sub>), 2.36 (s, 12H, CH<sub>3</sub>), 1.58 (t, 12H, CH<sub>3</sub>), 1.53 (t, 12H, CH<sub>3</sub>). Anal. Calcd for C<sub>76</sub>H<sub>76</sub>N<sub>8</sub>OPd<sub>2</sub>: C, 68.62; H, 5.76; N, 8.42. Found: C, 69.02; H, 5.90; N, 8.33. HRFABMS (M<sup>+</sup>) calcd for C<sub>76</sub>H<sub>76</sub>N<sub>8</sub>OPd<sub>2</sub>  $m/z$  1328.421, found 1328.422.

### 2.5.36 Sn<sub>2</sub>(OH)<sub>4</sub>(DPD) (35)

A combination of **27** (94 mg, 0.084 mmol) and SnCl<sub>2</sub>•2H<sub>2</sub>O (320 mg) in pyridine (5 mL) was refluxed in air in the dark for 8 h. The reaction was cooled to room temperature and the solvent was removed under high vacuum. The remaining residue was redissolved in chloroform (50 mL) and the organic phase was washed with 3N HCl (2 × 25 mL) and water (5 × 50 mL). The organic layer was separated and dried over Na<sub>2</sub>SO<sub>4</sub>. In a separate 20-mL vial, basic alumina (10 g) and water (2 mL) were combined and shaken into a homogeneous powder (some warming occurred). The activated basic alumina powder was added to the chloroform solution containing the metalated porphyrin and the resulting mixture was stirred overnight in the dark. The reaction was filtered and solvent was removed by rotary evaporation. Recrystallization from chloroform and hexanes gave **35** as a bright red powder (113 mg, 95% yield). <sup>1</sup>H NMR (500 MHz, CDCl<sub>3</sub>, 25 °C):  $\delta$  = 10.10 (s, 4H, meso), 9.98 (s, 2H, meso), 8.77 (d, 2H, ArH), 7.89 (t, 2H, ArH), 7.85 (d, 2H, ArH), 3.85-4.00 (m, 20H, CH<sub>2</sub>), 3.45 (s, 12H, CH<sub>3</sub>), 2.49 (s, 12H, CH<sub>3</sub>), 1.75 (t, 12H, CH<sub>3</sub>), 1.69 (t, 12H, CH<sub>3</sub>). The hydroxide protons were not identified. HRFABMS (MH<sup>+</sup>) calcd for C<sub>76</sub>H<sub>76</sub>N<sub>8</sub>O<sub>5</sub>Sn<sub>2</sub>  $m/z$  1421.437, found 1421.444.

### 2.5.37 General Details of X-ray Data Collection and Reduction

X-ray diffraction data were collected using a Siemens 3 circle diffractometer equipped with a CCD detector. Measurements were carried out at -90° C using Mo K $\alpha$  ( $\lambda$  = 0.71073 Å) radiation, which was wavelength selected with a single-crystal graphite monochromator. Four sets of data were collected using  $\omega$  scans and a -0.3° scan width. All calculations were performed using either a Silicon Graphics Indigo 2 or a PC workstation. The data frames were integrated to  $hkl$ /intensity, and final unit cells were calculated by using the SAINT v.4.050 program from Siemens. The structures were solved and refined with the SHELXTL v.5.03 suite of programs developed by G. M. Sheldrick and Siemens Industrial Automation, Inc., 1995.

### 2.5.38 X-ray Structure of Zn<sub>2</sub>(DPX) (16)

A 0.2 mm × 0.2 mm × 0.08 mm deep brick red crystal of plate morphology was obtained from a solution of the complex in a mixture of methanol and dichloromethane. The crystal was coated in Paratone N and mounted onto a glass fiber. A total of 13185 reflections were collected in the  $\theta$  range of 1.43° to 23.28°, of which 8982 were unique ( $R_{\text{int}}$  = 0.0300). The zinc atoms were



located by the Patterson method, and remaining atoms were located by standard difference Fourier techniques. Hydrogen atoms were placed in calculated positions using a standard riding model and were refined isotropically. A disordered ethyl group attached to C33 was assigned half occupancy in two different conformations. The largest peak and hole in the difference map were  $0.671 \text{ e}\text{\AA}^{-3}$  and  $-0.534 \text{ e}\text{\AA}^{-3}$ , respectively. The least squares refinement converged normally giving residuals of  $R = 0.0570$ ,  $wR^2 = 0.1559$ , and  $GOF = 1.116$ . The crystal data for  $C_{79}H_{77}N_8OZn_2$ : triclinic,  $P\bar{1}$ ,  $Z = 2$ ,  $a = 11.2671(2) \text{ \AA}$ ,  $b = 14.9809(2) \text{ \AA}$ ,  $c = 20.4852(2) \text{ \AA}$ ,  $\alpha = 101.6680(10)^\circ$ ,  $\beta = 100.8890(10)^\circ$ ,  $\gamma = 101.8060(10)^\circ$ ,  $V = 3217.57(8) \text{ \AA}^3$ ,  $\rho_{\text{calc}} = 1.327 \text{ g/cm}^3$ ,  $F(000) = 1350$ .

### 2.5.39 X-ray Structure of $Cu_2(DPX)$ (17)

A  $0.3 \text{ mm} \times 0.2 \text{ mm} \times 0.08 \text{ mm}$  mulberry red crystal of plate morphology was obtained from a solution of the complex in a mixture of methanol and dichloromethane. The crystal was coated in Paratone N and mounted onto a glass fiber. A total of 11372 reflections were collected in the  $\theta$  range of  $1.54^\circ$  to  $21.50^\circ$ , of which 7353 were unique ( $R_{\text{int}} = 0.1015$ ). The copper atoms were located by the Patterson method, the remaining atoms in the structure were located as peaks in the difference Fourier map. Hydrogen atoms were placed in calculated positions using a standard riding model and were refined isotropically. The largest peak and hole in the difference map were  $0.788 \text{ e}\text{\AA}^{-3}$  and  $-0.629 \text{ e}\text{\AA}^{-3}$ , respectively. The least squares refinement converged normally giving residuals of  $R = 0.0909$ ,  $wR^2 = 0.1994$ , and  $GOF = 1.036$ . The crystal data for  $C_{79}H_{82}Cu_2N_8O$ : triclinic,  $P\bar{1}$ ,  $Z = 2$ ,  $a = 11.21410(10) \text{ \AA}$ ,  $b = 14.9539(5) \text{ \AA}$ ,  $c = 20.6915(7) \text{ \AA}$ ,  $\alpha = 101.810(2)^\circ$ ,  $\beta = 101.044(2)^\circ$ ,  $\gamma = 101.722(2)^\circ$ ,  $V = 3225.7(2) \text{ \AA}^3$ ,  $\rho_{\text{calc}} = 1.325 \text{ g/cm}^3$ ,  $F(000) = 1356$ .

### 2.5.40 X-ray Structure of $Ni_2(DPX)$ (18)

A  $0.2 \text{ mm} \times 0.15 \text{ mm} \times 0.08 \text{ mm}$  plum red crystal of plate morphology was obtained from a solution of the complex in a mixture of methanol and dichloromethane. The crystal was coated in Paratone N and mounted onto a glass fiber. A total of 18577 reflections were collected in the  $\theta$  range of  $1.64^\circ$  to  $20.00^\circ$ , of which 5996 were unique ( $R_{\text{int}} = 0.1005$ ). The Patterson method was used to locate the nickel atoms, all remaining atoms were placed using the difference Fourier map. Hydrogen atoms were placed in calculated positions using a standard riding model and were refined isotropically. The largest peak and hole in the difference map were  $0.509 \text{ e}\text{\AA}^{-3}$  and  $-0.425 \text{ e}\text{\AA}^{-3}$ , respectively. The least squares refinement converged normally giving residuals of  $R = 0.0768$ ,  $wR^2 = 0.1460$ , and  $GOF = 1.173$ . The crystal data for  $C_{79}H_{82}N_8Ni_2O$ : monoclinic,  $C2/c$ ,  $Z = 8$ ,  $a = 24.1671(4) \text{ \AA}$ ,  $b = 10.669(0) \text{ \AA}$ ,  $c = 50.5080(9) \text{ \AA}$ ,  $\beta = 99.553(2)^\circ$ ,  $V = 12842.0(3) \text{ \AA}^3$ ,  $\rho_{\text{calc}} = 1.321 \text{ g/cm}^3$ ,  $F(000) = 5408$ .

### 2.5.41 X-ray Structure of Zn<sub>2</sub>(DPD) (28)

A single crystal of **28** was obtained by slow diffusion of methanol into a solution of the compound in dichloromethane. Empirical formula: C<sub>78</sub>H<sub>82</sub>Cl<sub>2</sub>N<sub>8</sub>O<sub>2</sub>Zn<sub>2</sub>, MW = 1397.20. monoclinic, C2/c, Z = 4, a = 23.0808(2) Å, b = 25.9458(9) Å, c = 13.4593(5) Å, β = 110.503(2)°, V = 7549.5(4) Å<sup>3</sup>, ρ<sub>calc</sub> = 1.229 g/cm<sup>3</sup>, F(000) = 2936. Crystal dimension: 0.3 mm × 0.25 mm × 0.08 mm. A total of 11274 reflections were collected in the θ range of 1.23° to 20.00°, of which 3522 were unique (R<sub>int</sub> = 0.1109). The structure was solved by direct methods in conjunction with standard difference Fourier techniques. Hydrogen atoms were placed in calculated positions using a standard riding model and were refined isotropically. One methanol molecule and one methylene chloride molecule were disordered in the bisporphyrin pocket. These solvent molecules were assigned half occupancy at two symmetry-equivalent positions. The largest peak and hole in the difference map were 1.202 eÅ<sup>-3</sup> and -0.691 eÅ<sup>-3</sup>, respectively. The least squares refinement converged normally giving residuals of R = 0.0890, wR<sup>2</sup> = 0.2391, and GOF = 1.124.

### 2.5.42 X-ray Structure of Fe<sub>2</sub>O(DPD) (31)

A single crystal of **31** was obtained by slowly diffusing ethyl acetate into a solution of the compound in chloroform. Empirical formula: C<sub>81</sub>H<sub>84</sub>Cl<sub>3</sub>Fe<sub>2</sub>N<sub>8</sub>O<sub>4</sub>, MW = 1451.61. orthorhombic, P2<sub>1</sub>2<sub>1</sub>2<sub>1</sub>, Z = 2, a = 13.896(2) Å, b = 15.476(3) Å, c = 33.440(7) Å, V = 7192(2) Å<sup>3</sup>, ρ<sub>calc</sub> = 1.341 g/cm<sup>3</sup>, F(000) = 3044. Crystal dimension: 0.5 mm × 0.5 mm × 0.25 mm. A total of 21224 reflections were collected in the θ range of 1.22° to 20.00°, of which 6699 were unique (R<sub>int</sub> = 0.0322). The structure was solved by direct methods in conjunction with standard difference Fourier techniques. Hydrogen atoms were placed in calculated positions using a standard riding model and were refined isotropically. One ethyl acetate molecule and one chloroform molecule were found in the crystal. The carbon atom as well as two chloride atoms of the chloroform molecule was found disordered and was assigned half occupancy at two positions. The largest peak and hole in the difference map were 0.511 eÅ<sup>-3</sup> and -0.364 eÅ<sup>-3</sup>, respectively. The least squares refinement converged normally giving residuals of R = 0.0420, wR<sup>2</sup> = 0.1180, and GOF = 1.153.

### 2.5.43 Physical Measurements

<sup>1</sup>H NMR spectra were collected in CDCl<sub>3</sub> or CD<sub>2</sub>Cl<sub>2</sub> (Cambridge Isotope Laboratories) at 25 °C at the MIT Department of Chemistry Instrumentation Facility (DCIF) using a Unity 300, a Mercury 300 or an Inova 500 spectrometer. All chemical shifts are reported using the standard δ notation in parts-per-million; positive chemical shifts are to higher frequency from the given reference. Absorption spectra were obtained using a Cary-17 spectrophotometer modified by On-

Line Instrument Systems (OLIS) to include computer control or a Spectral Instruments 440 Model spectrophotometer. Mass spectral analyses were carried out by the University of Illinois Mass Spectrometry Laboratory and the MIT DCIF. Elemental analyses were performed at H. Kolbe Mikroanalytisches Laboratorium, the University of Illinois Microanalysis Laboratory, or Quantitative Technologies, Inc (Whitehall, New Jersey). Magnetic measurements were performed using a SQUID susceptometer (Quantum Design MPMSR2 Susceptometer) within the 2 to 300 K temperature regime. The data were corrected for the diamagnetic contribution of the sample holder and for the diamagnetism of the compound, calculated using Pascal's constants.

## 2.6 References and Notes

1. Malmström, B. G. In *Electron Transfer in Chemistry*; Balzani, V., Ed.; Wiley-VCH: Weinheim, Germany, 2001; Vol. 3.1.3, pp 39-55.
2. Michel, H.; Behr, J.; Harrenga, A.; Kannt, A. *Annu. Rev. Biophys. Biomol. Struct.* **1998**, *27*, 329-356.
3. Schultz, B. E.; Chan, S. I. *Annu. Rev. Biophys. Biomol. Struct.* **2001**, *30*, 23-65.
4. Babcock, G. T.; Wikström, M. *Nature* **1992**, *356*, 301-309.
5. Ferguson-Miller, S.; Babcock, G. T. *Chem. Rev.* **1996**, *96*, 2889-2907.
6. Bard, A. J.; Parsons, R.; Jordan, J. *Standard Potentials in Aqueous Solution*; Marcel Dekker: New York, 1985.
7. Lippard, S. J.; Berg, J. M. *Principles of Bioinorganic Chemistry*; University Science Books: Mill Valley, CA, 1994.
8. Collman, J. P.; Wagenknecht, P. S.; Hutchison, J. E. *Angew. Chem. Int. Ed. Engl.* **1994**, *33*, 1537-1554.
9. Wasielewski, M. R. *Chem. Rev.* **1992**, *92*, 435-461.
10. Maruyama, K.; Osuka, A.; Mataga, N. *Pure Appl. Chem.* **1994**, *66*, 867-872.
11. Harriman, A.; Sauvage, J. P. *Chem. Soc. Rev.* **1996**, *25*, 41-49.
12. Holten, D.; Bocian, D. F.; Lindsey, J. S. *Acc. Chem. Res.* **2002**, *35*, 57-69.
13. Gust, D.; Moore, T. A.; Moore, A. L. In *Electron Transfer in Chemistry*; Balzani, V., Ed.; Wiley-VCH: Weinheim, Germany, 2001; Vol. 3.2.2, pp 272-336.
14. Collman, J. P.; Elliot, C. M.; Halbert, T. R.; Tovrog, B. S. *Proc. Natl. Acad. Sci. USA* **1977**, *74*, 18-22.
15. Collman, J. P.; Chong, A. O.; Jameson, G. B.; Oakley, R. T.; Rose, E.; Schmittou, E. R.; Ibers, J. A. *J. Am. Chem. Soc.* **1981**, *103*, 516-533.
16. Collman, J. P.; Anson, F. C.; Barnes, C. E.; Bencosme, C. S.; Geiger, T.; Evitt, E. R.; Kreh, R. P.; Meier, K.; Pettman, R. B. *J. Am. Chem. Soc.* **1983**, *105*, 2694-2699.
17. Collman, J. P.; Bencosme, C. S.; Barnes, C. E.; Miller, B. D. *J. Am. Chem. Soc.* **1983**, *105*, 2704-2710.
18. Collman, J. P.; Bencosme, C. S.; Durand Jr., R. R.; Kreh, R. P.; Anson, F. C. *J. Am. Chem. Soc.* **1983**, *105*, 2699-2703.
19. Kim, K.; Collman, J. P.; Ibers, J. A. *J. Am. Chem. Soc.* **1988**, *110*, 4242-4246.
20. Chang, C. K. *J. Am. Chem. Soc.* **1977**, *99*, 2819-2822.
21. Chang, C. K.; Kuo, M. S.; Wang, C. B. *J. Heterocycl. Chem.* **1977**, *14*, 943-945.
22. Chang, C. K. *J. Heterocycl. Chem.* **1977**, *14*, 1285-1288.
23. Chang, C. K. *J. Chem. Soc. Chem. Commun.* **1977**, 800-801.

24. Kagan, N. E.; Mauzerall, D.; Merrifield, R. B. *J. Am. Chem. Soc.* **1977**, *99*, 5484-5486.
25. Ogoshi, H.; Sugimoto, H.; Yoshida, Z. *Tetrahedron Lett.* **1977**, 169-172.
26. Paine III, J. B.; Dolphin, D.; Gouterman, M. *Can. J. Chem.* **1978**, *56*, 1712-1715.
27. Cowan, J. A.; Sanders, J. K. M. *J. Chem. Soc. Chem. Commun.* **1985**, 1213-1214.
28. Hunter, C. A.; Meah, M. N.; Sanders, J. K. M. *J. Am. Chem. Soc.* **1990**, *112*, 5773-5780.
29. Hunter, C. A.; Sanders, J. K. M. *J. Am. Chem. Soc.* **1990**, *112*, 5525-5534.
30. Anderson, H. L.; Hunter, C. A.; Meah, M. N.; Sanders, J. K. M. *J. Am. Chem. Soc.* **1990**, *112*, 5780-5789.
31. Anderson, S.; Anderson, H. L.; Sanders, J. K. M. *Acc. Chem. Res.* **1993**, *26*, 469-475.
32. Anderson, S.; Anderson, H. L.; Sanders, J. K. M. *J. Chem. Soc. Perkin Trans. 1* **1995**, 2255-2267.
33. Karaman, R.; Bruice, T. C. *J. Org. Chem.* **1991**, *56*, 3470-3472.
34. Karaman, R.; Blasko, A.; Almarsson, O.; Arasasingham, R.; Bruice, T. C. *J. Am. Chem. Soc.* **1992**, *114*, 4889-4998.
35. Karaman, R.; Jeon, S. W.; Almarsson, O.; Bruice, T. C. *J. Am. Chem. Soc.* **1992**, *114*, 4899-4905.
36. Karaman, R.; Almarsson, O.; Blasko, A.; Bruice, T. C. *J. Org. Chem.* **1992**, *57*, 2169-2173.
37. Karaman, R.; Almarsson, O.; Bruice, T. C. *J. Org. Chem.* **1992**, *57*, 1555-1559.
38. Bookser, B. C.; Bruice, T. C. *J. Am. Chem. Soc.* **1991**, *113*, 4208-4218.
39. Ichimura, K. *Chem. Lett.* **1977**, 641-644.
40. Chang, C. K.; Abdalmuhdi, I. *J. Org. Chem.* **1983**, *48*, 5388-5390.
41. Chang, C. K.; Liu, H. Y.; Abdalmuhdi, I. *J. Am. Chem. Soc.* **1984**, *106*, 2725-2726.
42. Chang, C. K.; Abdalmuhdi, I. *Angew. Chem. Int. Ed. Engl.* **1984**, *23*, 164-165.
43. Collman, J. P.; Kim, K.; Garner, J. M. *J. Chem. Soc. Chem. Commun.* **1986**, 1711-1713.
44. Collman, J. P.; Kim, K.; Leidner, C. R. *Inorg. Chem.* **1987**, *26*, 1152-1157.
45. Collman, J. P.; Hutchison, J. E.; Lopez, M. A.; Tabard, A.; Guillard, R.; Seok, W. K.; Ibers, J. A.; L'Her, M. *J. Am. Chem. Soc.* **1992**, *114*, 9869-9877.
46. Collman, J. P.; Hutchison, J. E.; Lopez, M. A.; Guillard, R. *J. Am. Chem. Soc.* **1992**, *114*, 8066-8073.
47. Collman, J. P.; Hutchison, J. E.; Ennis, M. S.; Lopez, M. A.; Guillard, R. *J. Am. Chem. Soc.* **1992**, *114*, 8074-8080.
48. Collman, J. P.; Ha, Y.; Wagenknecht, P. S.; Lopez, M. A.; Guillard, R. *J. Am. Chem. Soc.* **1993**, *115*, 9080-9088.
49. Collman, J. P.; Ha, Y. Y.; Guillard, R.; Lopez, M. A. *Inorg. Chem.* **1993**, *32*, 1788-1794.
50. Collman, J. P.; Fish, H. T. *Inorg. Chem.* **1996**, *35*, 7922-7923.

51. Fillers, J. P.; Ravichandran, K. G.; Abdalmuhdi, I.; Tulinsky, A.; Chang, C. K. *J. Am. Chem. Soc.* **1986**, *108*, 417-424.
52. Proniewicz, L. M.; Odo, J.; Goral, J.; Chang, C. K.; Nakamoto, K. *J. Am. Chem. Soc.* **1989**, *111*, 2105-2110.
53. Guilard, R.; Lopez, M. A.; Tabard, A.; Richard, P.; Lecomte, C.; Brandes, S.; Hutchison, J. E.; Collman, J. P. *J. Am. Chem. Soc.* **1992**, *114*, 9877-9889.
54. Guilard, R.; Brandes, S.; Tabard, A.; Bouhmaida, N.; LeComte, C.; Richard, P.; Latour, J. M. *J. Am. Chem. Soc.* **1994**, *116*, 10202-10211.
55. Guilard, R.; Brandes, S.; Tardieux, C.; Tabard, A.; L'Her, M.; Miry, C.; Guerac, P.; Knop, Y.; Collman, J. P. *J. Am. Chem. Soc.* **1995**, *117*, 11721-11729.
56. Ichihara, K.; Naruta, Y. *Chem. Lett.* **1998**, 185-186.
57. Naruta, Y.; Maruyama, K. *J. Am. Chem. Soc.* **1991**, *113*, 3595-3596.
58. Naruta, Y.; Sasayama, M.; Maruyama, K. *Chem. Lett.* **1992**, 1267-1270.
59. Naruta, Y.; Sasayama, M. *J. Chem. Soc. Chem. Commun.* **1994**, 2667-2668.
60. Naruta, Y.; Sawada, N.; Tadokoro, M. *Chem. Lett.* **1994**, 1713-1716.
61. Naruta, Y.; Sasayama, M. *Chem. Lett.* **1994**, 2411-2414.
62. Naruta, Y.; Sasayama, M.; Sasaki, T. *Angew. Chem. Int. Ed. Engl.* **1994**, *33*, 1839-1841.
63. Naruta, Y.; Sasayama, M.; Ichihara, K. *J. Mol. Cat. A* **1997**, *117*, 115-121.
64. Brun, A.; Harriman, A.; Heitz, V.; Sauvage, J. P. *J. Am. Chem. Soc.* **1991**, *113*, 8657-8663.
65. Chardon-Noblat, S.; Sauvage, J. P.; Mathis, P. *Angew. Chem. Int. Ed. Engl.* **1989**, *28*, 593-595.
66. Le Mest, Y.; L'Her, M.; Courtot-Coupez, J.; Collman, J. P.; Evitt, E. R.; Bencosme, C. S. *J. Chem. Soc. Chem. Commun.* **1983**, 1286-1287.
67. Le Mest, Y.; L'Her, M.; Hendricks, N. H.; Kim, K.; Collman, J. P. *Inorg. Chem.* **1992**, *31*, 835-847.
68. Le Mest, Y.; L'Her, M. *J. Chem. Soc. Chem. Commun.* **1995**, 1441-1442.
69. Le Mest, Y.; L'Her, M.; Saillard, J. Y. *Inorg. Chim. Acta* **1996**, *248*, 181-191.
70. Le Mest, Y.; Inisan, C.; Laouenan, A.; L'Her, M.; Talarmain, J.; El Khalifa, M.; Saillard, J. Y. *J. Am. Chem. Soc.* **1997**, *119*, 6905-6106.
71. Lui, H.-Y.; Abdalmuhdi, I.; Chang, C. K.; Anson, F. C. *J. Phys. Chem.* **1985**, *89*, 665-670.
72. Ni, C.-L.; Abdalmuhdi, I.; Chang, C. K.; Anson, F. C. *J. Phys. Chem.* **1987**, *91*, 1158-1166.

73. Chang, C. J.; Brown, J. D. K.; Chang, M. C. Y.; Baker, E. A.; Nocera, D. G. In *Electron Transfer in Chemistry*; Balzani, V., Ed.; Wiley-VCH: Weinheim, Germany, 2001; Vol. 3.2.4, pp 409-461.
74. Cukier, R. I.; Nocera, D. G. *Annu. Rev. Phys. Chem.* **1998**, *49*, 337-369.
75. Nowick, J. S.; Ballester, P.; Ebmeyer, F.; Rebek Jr., J. *J. Am. Chem. Soc.* **1990**, *112*, 8902-8906.
76. Schwartz, E. B.; Knobler, C. B.; Cram, D. J. *J. Am. Chem. Soc.* **1992**, *114*, 10775-10784.
77. Chang, C. J.; Deng, Y.; Heyduk, A. F.; Chang, C. K.; Nocera, D. G. *Inorg. Chem.* **2000**, *39*, 959-966.
78. Deng, Y.; Chang, C. J.; Nocera, D. G. *J. Am. Chem. Soc.* **2000**, *122*, 410-411.
79. Chang, C. J.; Baker, E. A.; Pistorio, B. J.; Deng, Y.; Loh, Z.-H.; Miller, S. E.; Carpenter, S. D.; Nocera, D. G. *Inorg. Chem.* **2002**, *41*, 3102-3109.
80. Barton, D. H. R.; Zard, S. Z. *J. Chem. Soc. Chem. Commun.* **1985**, 1098-1100.
81. Sessler, J. L.; Mozaffari, A.; Johnson, M. R. *Org. Synth.* **1992**, *70*, 68-78.
82. Tindall, J. B. *Ind. Eng. Chem.* **1941**, *33*, 65-66.
83. Sprang, C. A.; Egering, E. F. *J. Am. Chem. Soc.* **1942**, *64*, 1063-1064.
84. Harman, G. D.; Wenstock, L. M. *Organic Syntheses* **1988**, *VI*, 620-624.
85. Young, R.; Chang, C. K. *J. Am. Chem. Soc.* **1985**, *107*, 898-909.
86. Jones, R. A.; Bean, G. P. *The Chemistry of Pyrroles*; Academic Press: London, 1977; Vol. 34.
87. The chemical shifts obtained for the internal NH protons in a monomeric mono(meso-substituted porphyrin) xanthene are  $\delta$ -3.10 and -3.29 ppm.
88. Buchler, J. W. In *Porphyrins and Metalloporphyrins*; 2nd ed.; Smith, K. M., Ed.; Elsevier Scientific: Oxford, 1975, pp 157-232.
89. Carlin, R. L. *Magnetochemistry*; Springer-Verlag: Berlin, 1986.
90. Eaton, S. S.; Eaton, G. R.; Chang, C. K. *J. Am. Chem. Soc.* **1985**, *107*, 3177-3184.
91. Adler, A. D.; Longo, F. R.; Kampas, F.; Kim, J. *J. Inorg. Nucl. Chem.* **1970**, *32*, 2443-2445.
92. Kadish, K. M.; Smith, K. M.; Guillard, R. *The Porphyrin Handbook*; Academic Press: San Diego, 2000.
93. Harvey, P. D.; Proulx, N.; Martin, G.; Drouin, M.; Nurco, D. J.; Smith, K. M.; Bolze, F.; Gros, C. P.; Guillard, R. *Inorg. Chem.* **2001**, *40*, 4134-4142.
94. Senge, M. O.; Gerzevske, K. R.; Vicente, M. G. H.; Forsyth, T. P.; Smith, K. M. *Angew. Chem. Int. Ed. Engl.* **1993**, *32*, 750-753.
95. Senge, M. O.; Vicente, M. G. H.; Gerzevske, K. R.; Forsyth, T. P.; Smith, K. M. *Inorg. Chem.* **1994**, *33*, 5625-5638.

96. Clement, T. E.; Nurco, D. J.; Smith, K. M. *Inorg. Chem.* **1998**, *37*, 1150-1160.
97. Senge, M. O.; Forsyth, T. P.; Smith, K. Z. *Kristallogr.* **1996**, *211*, 176-185.
98. Scheidt, W. R.; Mondal, J. U.; Eigenbrot, C. W.; Adler, A.; Radonovich, L. J.; Hoard, J. L. *Inorg. Chem.* **1986**, *25*, 795-799.
99. Scheidt, W. R.; Lee, Y. J. *Struct. Bonding (Berlin)* **1987**, *64*, 1-70.
100. Osuka, A.; Nakajima, S.; Nagata, T.; Maruyama, K.; Toriumi, K. *Angew. Chem. Int. Ed. Engl.* **1991**, *30*, 582-584.
101. Paolesse, R.; Pandey, R. K.; Forsyth, T. P.; Jacquiod, L.; Gerzevske, K. R.; Nurco, D. J.; Senge, M. O.; Licoccia, S.; Boschi, T.; Smith, K. M. *J. Am. Chem. Soc.* **1996**, *118*, 3869-3882.
102. Furhop, J. H.; Witte, L.; Sheldrick, W. S. *Liebigs Ann. Chem.* **1976**, 1537-1559.
103. Hursthouse, M. B.; Neidle, S. *J. Chem. Soc. Chem. Commun.* **1972**, 449-450.
104. Fleischer, E. B. *J. Am. Chem. Soc.* **1963**, *85*, 146-148.
105. Kratzky, C.; Fassler, A.; Pfaltz, A.; Krautler, B.; Jaun, B.; Eschenmoser, A. *J. Chem. Soc. Chem. Commun.* **1984**, 1368-1371.
106. Abraham, R. J.; Barnett, G. H.; Hawkes, G. E.; Smith, K. M. *Tetrahedron* **1976**, *32*, 2949-2956.
107. Abraham, R. J.; Eivazi, F.; Pearson, H.; Smith, K. M. *J. Chem. Soc. Chem. Commun.* **1976**, 699-700.
108. Abraham, R. J.; Fell, S. C. M.; Pearson, H.; Smith, K. M. *Tetrahedron* **1979**, *35*, 1759-1766.
109. Anderson, O. P.; Schauer, C. K.; Caughey, W. S. *Am. Cryst. Assoc.* **1982**, *10*, 23.
110. Cheng, B. S.; Hobbs, J. D.; Debrunner, P. G.; Erlebacher, J.; Shelnut, J. A.; Scheidt, W. R. *Inorg. Chem.* **1995**, *34*, 102-110.
111. Hoffman, A. B.; Collins, D. M.; Day, V. W.; Fleischer, E. B.; Srivastava, T. S.; Hoard, J. L. *J. Am. Chem. Soc.* **1972**, *94*, 3620-3626.
112. Lay, K. L.; Buchler, J. W.; Kenny, J. E.; Scheidt, W. R. *Inorg. Chim. Acta* **1986**, *123*, 91-97.
113. Landrum, J. T.; Grimmett, D.; Haller, K. J.; Scheidt, W. R.; Reed, C. A. *J. Am. Chem. Soc.* **1981**, *103*, 2640-2650.
114. Armarego, W. L. F.; Perrin, D. D. *Purification of Laboratory Chemicals*; 4th ed.; Butterworth-Heinmann: Oxford, 1996.



*Chapter 3*

**Comparison of Pacman Porphyrins Spanning  
a Large Range of Vertical Pocket Sizes**

A portion of the work presented in this chapter has been published:

Chang, C. J.; Baker, E. A.; Pistorio, B. J.; Deng, Y.; Loh, Z.-H.; Miller, S. E.; Carpenter, S. D.;

Nocera, D. G. *Inorg. Chem.* **2002**, *41*, 3102-3109.

### 3.1 Motivation and Specific Aims

The development of a structure-function relation for cofacial Pacman bisporphyrins necessitates an understanding of the factors that govern pocket size variability and tunability. The xanthene- and dibenzofuran-bridged cofacial bisporphyrins introduced in chapter 2 span a large range of vertical pocket sizes while maintaining a face-to-face arrangement of porphyrinic subunits; DPX provides a cofacial cleft with vertical preorganization while DPD presents a platform with unprecedented vertical flexibility. Accordingly, these systems offer an ideal opportunity to probe the vertical dimension of the Pacman bite and its subsequent implications for catalysis. This chapter details a comprehensive structural and spectroscopic comparison of the DPX and DPD bisporphyrin scaffolds. The resulting compilation of data provides a foundation for the application of these and related platforms towards the proton-coupled activation of reactive oxygen species (ROS) and other small-molecule substrates.

### 3.2 Background

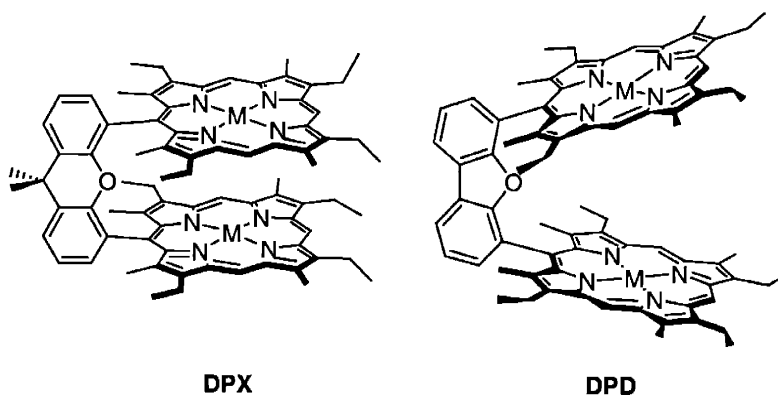
Ongoing investigations of cofacial bisporphyrins are motivated by their utility for the binding and multielectron activation of small-molecule substrates.<sup>1</sup> Over the past 25 years, the singly-bridged Pacman systems, which have been most successful in this regard, have featured two spacers, anthracene and biphenylene.<sup>2-21</sup> The exceptional activity of cofacial bisporphyrins anchored by anthracene (DPA = diporphyrin anthracene) and biphenylene (DPB = diporphyrin biphenylene) is based on their ability to impair a *lateral* slippage between porphyrin rings, allowing for efficient multielectron small-molecule transformations with little structural reorganization of juxtaposed subunits.<sup>1</sup> We became interested in testing the structural limits of the *vertical* flexibility within the Pacman motif in order to expand the use of such platforms for multielectron catalysis via proton-coupled electron transfer (PCET).<sup>22</sup> For the cases of the DPA and DPB scaffolds, a difference in the vertical pocket size of ca. 1 Å offers a limited range of conformational flexibility for examining structure/reactivity relationships derived from the Pacman effect.

With the goal of increasing the structural breadth of the Pacman bite, we recently introduced two novel cofacial bisporphyrins bearing the cyclic ether spacers xanthene (DPX = diporphyrin xanthene) and dibenzofuran (DPD = diporphyrin dibenzofuran).<sup>23-25</sup> The DPX and DPD systems afford an unprecedented range of vertical pocket sizes while maintaining a face-to-face arrangement of porphyrin subunits. In particular, the DPD platform provided direct structural evidence for the Pacman effect within a single pillared cofacial bisporphyrin motif. A comparative structural analysis of bizinc(II) and bisiron(III)  $\mu$ -oxo complexes of DPD

establishes the unique ability of this platform to open and close its binding pocket by a vertical distance of over 4 Å.<sup>24</sup>

To understand the effects of pocket size and flexibility on the multielectron reactivity of pillared cofacial bisporphyrins, we report here a systematic structural and spectroscopic comparison of the DPX and DPD platforms in Chart 3.1 using a homologous set of homobimetallic zinc(II), copper(II), and nickel(II) complexes. This chapter presents the most comprehensive study to date that compares and contrasts cofacial bisporphyrin systems with large differences in vertical tunability and flexibility, and the compiled results provide a useful benchmark for future structure-activity studies.

**Chart 3.1**



### 3.3 Results and Discussion

#### 3.3.1 Structural Chemistry

A direct structural comparison between DPX and DPD congeners is afforded by the molecular structures of the free-base porphyrins H<sub>4</sub>(DPX) (**15**) and H<sub>4</sub>(DPD) (**27**) and their bispalladium(II) complexes **22** and **34**. The palladium derivatives were chosen due to the proclivity of Pd(II) to attain a square geometry within the porphyrin macrocycle with no axial ligation.<sup>26,27</sup> The structures of free-base porphyrins **15** and **27** shown in Figures 3.1 and 3.2, respectively, and the structures of their bispalladium(II) complexes **22** and **34** are depicted in Figures 3.3 and 3.4, respectively. Each atom of the porphyrin rings and the corresponding bridge is numbered in the standard convention while auxiliary methyl and ethyl groups off the macrocycles are additionally identified according to their point of attachment to the porphyrin ring. Crystallographic data are given in Tables 3.1 and 3.2, and selected geometrical measurements are given in Tables 3.3 and 3.4. Trends in bond lengths and angles of macrocyclic core structures and side chains agree well

with those observed in related cofacial bisporphyrins.<sup>5,23-25,28</sup> Specific features of the core structures for **15**, **27**, **22**, and **34** are highlighted as follows.

**Table 3.1.** Crystallographic Data for H<sub>4</sub>(DPX) (**15**) and H<sub>4</sub>(DPD) (**27**).

	<b>15</b>	<b>27</b>
Empirical formula	C <sub>79</sub> H <sub>82</sub> N <sub>8</sub> O	C <sub>80</sub> H <sub>83</sub> N <sub>8</sub> O <sub>2</sub>
Formula weight	1252.52	1188.54
Temperature	183(2) K	183(2) K
Wavelength	0.71073 Å	0.71073 Å
Crystal system	Triclinic	Monoclinic
Space group	$P\bar{1}$	C2/c
Unit cell dimensions	$a = 13.5167(12)$ Å $b = 21.7008(18)$ Å $c = 23.8080(2)$ Å $\alpha = 80.1160(2)^\circ$ $\beta = 76.8320(2)^\circ$ $\gamma = 80.4070(10)^\circ$	$a = 22.6650(2)$ Å $b = 13.6749(14)$ Å $c = 42.0840(4)$ Å $\beta = 94.5540(2)^\circ$
Volume	6639.40(10) Å <sup>3</sup>	13 003(2) Å <sup>3</sup>
Z	4	8
Density (calculated)	1.253 Mg/m <sup>3</sup>	1.146 Mg/m <sup>3</sup>
Absorption coefficient	0.152 mm <sup>-1</sup>	0.068 mm <sup>-1</sup>
F(000)	2680	4800
Crystal size	0.52 mm × 0.24 mm × 0.10 mm	0.35 mm × 0.20 mm × 0.20 mm
θ range for data collection	2.25 to 20.00°	2.32 to 23.29°
Reflections collected	18992	25700
Independent reflections	12281 (R <sub>int</sub> = 0.0342)	9347 (R <sub>int</sub> = 0.0473)
Data / restraints / params	12281 / 0 / 1676	9347 / 0 / 874
Goodness-of-fit on F <sup>2</sup>	1.029	1.172
Final R indices [I > 2σ(I)]	R1 = 0.0552 wR2 = 0.1494	R1 = 0.0765 wR2 = 0.1727
R indices (all data)	R1 = 0.0715 wR2 = 0.1588	R1 = 0.0980 wR2 = 0.1816
Largest diff peak	0.395 eÅ <sup>-3</sup>	1.036 eÅ <sup>-3</sup>
Largest diff hole	-0.703 eÅ <sup>-3</sup>	-0.358 eÅ <sup>-3</sup>

**Table 3.2.** Crystallographic Data for Pd<sub>2</sub>(DPX) (**22**) and Pd<sub>2</sub>(DPD) (**34**).

	<b>22</b>	<b>34</b>
Empirical formula	C <sub>79.5</sub> H <sub>82</sub> N <sub>8</sub> OPd <sub>2</sub>	C <sub>80</sub> H <sub>86</sub> Cl <sub>6</sub> N <sub>8</sub> O <sub>2</sub> Pd <sub>2</sub>
Formula weight	1378.33	1617.07
Temperature	183(2) K	183(2) K
Wavelength	0.71073 Å	0.71073 Å
Crystal system	Triclinic	Monoclinic
Space group	<i>P</i> $\bar{1}$	<i>P</i> 2(1)
Unit cell dimensions	<i>a</i> = 11.1419(8) Å <i>b</i> = 14.9325(10) Å <i>c</i> = 20.8014(14) Å $\alpha$ = 100.6090(10)° $\beta$ = 100.9680(10)° $\gamma$ = 102.5440(10)°	<i>a</i> = 13.1958(7) Å <i>b</i> = 20.3976(11) Å <i>c</i> = 14.8663(8) Å $\beta$ = 108.9990(10)°
Volume	3223.5(4) Å <sup>3</sup>	3783.5(4) Å <sup>3</sup>
Z	2	2
Density (calculated)	1.420 Mg/m <sup>3</sup>	1.419 Mg/m <sup>3</sup>
Absorption coefficient	0.613 mm <sup>-1</sup>	0.739 mm <sup>-1</sup>
F(000)	1430	1665
Crystal size	0.16 mm × 0.19 mm × 0.61 mm	0.15 mm × 0.16 mm × 0.27 mm
$\theta$ range for data collection	2.38 to 23.26°	2.47 to 23.28°
Reflections collected	12860	15257
Independent reflections	8993 ( <i>R</i> <sub>int</sub> = 0.0699)	10 150 ( <i>R</i> <sub>int</sub> = 0.0236)
Data / restraints / params	8993 / 0 / 826	10150 / 0 / 901
Goodness-of-fit on <i>F</i> <sup>2</sup>	1.065	1.564
Final <i>R</i> indices [ <i>I</i> > 2 $\sigma$ ( <i>I</i> )]	<i>R</i> 1 = 0.0412 <i>wR</i> 2 = 0.1097	<i>R</i> 1 = 0.0413 <i>wR</i> 2 = 0.1292
<i>R</i> indices (all data)	<i>R</i> 1 = 0.0460 <i>wR</i> 2 = 0.1171	<i>R</i> 1 = 0.0447 <i>wR</i> 2 = 0.1366
Largest diff peak	0.937 eÅ <sup>-3</sup>	2.607 eÅ <sup>-3</sup>
Largest diff hole	-0.874 eÅ <sup>-3</sup>	-0.555 eÅ <sup>-3</sup>

***H*<sub>4</sub>(DPX) (15).** A conformational analysis of the two macrocycles reveals inequivalent ring systems. Ring 1, containing N(1) to N(4) exhibits a slightly ruffled *S*<sub>4</sub> conformation, with a mean deviation from planarity of 0.2885 Å. In contrast, the macrocycle containing N(5) to N(8) (ring 2) displays a saddle conformation with a mean deviation from planarity of 0.3548 Å. A similar ring inequivalence effect has been observed in a number of pillared bisporphyrin systems, and is attributable to a localized macrocycle distortion induced by the steric crowding of a large meso substituent flanked by proximate alkyl groups.<sup>29</sup> The hydrogen atoms inside the porphyrin rings are in their calculated positions, and are disordered over all nitrogen atoms. Lastly, a notable feature concerning the structure of free-base **15** is the severe butterfly fold of the xanthenone backbone along its center O(1)—C(47) axis. This bent distortion is best described in terms of an intraplanar angle through the center axis fold. For **15**, the butterfly angle is 36.1°. In contrast, metal derivatives of DPX typically display a flattened spacer with butterfly angles in the range of 6 to 15°, with smaller metal cations causing a greater distortion of the bridge from its naturally bent fold.<sup>23,25</sup>

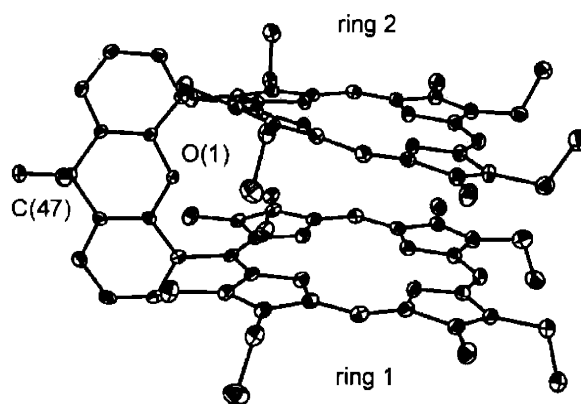


**Figure 3.1.** Crystal structure of *H*<sub>4</sub>(DPX) (**15**). Thermal ellipsoids are drawn at the 25% probability level. Hydrogen atoms and solvent molecules within the lattice have been omitted for clarity.

***H*<sub>4</sub>(DPD) (27).** As observed for **15**, the two ring systems of **27** are structurally inequivalent in the solid state. However, unlike **15**, both porphyrin subunits of **27** display a ruffled *S*<sub>4</sub> conformation. The macrocycle with N(1) to N(4) (ring 1) is nearly planar, with a mean deviation of 0.0553 Å for the macrocyclic atoms from the porphyrin mean plane. The meso carbons are alternately displaced from the mean porphyrin plane, ranging from 0.0758 Å above to 0.0822 Å below the 24-atom macrocyclic unit. Ring 2, containing N(5) to N(8), has a more pronounced ruffled structure. The mean deviation of 0.1639 Å from the porphyrin plane is greater than that observed in the ring containing N(1) to N(4), and the meso carbons are displaced from 0.3121 Å below to

0.3938 Å above the mean porphyrin plane. An acetone molecule modeled at 50% occupancy over two sites was located in the DPD pocket. Although the lengths of the two overlapping carbon-carbon bonds are longer than expected for acetone, the model was stable throughout the refinement. The hydrogen atoms inside the ring were located from the electron difference map, and their positions were also stable over the course of refinement.

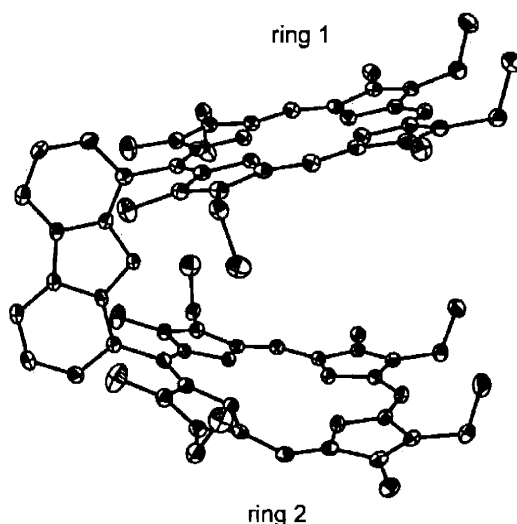


**Figure 3.2.** Crystal structure of  $H_4(DPD)$  (**27**). Thermal ellipsoids are drawn at the 25% probability level. Hydrogen atoms and solvent molecules within the lattice have been omitted for clarity.

**$Pd_2(DPX)$  (**22**).** The Pd(II) ions of **22** are situated in an approximately  $N_{pyrrole}$  square, as the N–Pd–N bond angles are  $90 \pm 2.2^\circ$ . The average Pd–N bond length is 2.017 Å. The two macrocycles of **22** are structurally inequivalent in the solid state. The ring with Pd(1) is nearly planar, with a mean deviation of 0.0925 Å from the 24-atom macrocyclic plane. The porphyrin displays a ruffled  $S_4$  conformation with meso carbons displaced from 0.1838 Å to 0.1982 Å above the mean plane. The macrocycle containing Pd(2) is also nearly planar, with a mean deviation of 0.0870 Å from the 24-atom plane; however, it exhibits a slight saddle conformation, with  $\beta$  carbons ranging from 0.2198 Å below to 0.1686 Å above the mean ring plane.

**$Pd_2(DPD)$  (**34**).** The square geometry for the Pd(II) core is confirmed by the average N–Pd–N bond angles of  $90 \pm 2.5^\circ$ . The relatively large deviation of Pd–N bond lengths from the 2.022 Å average (1.926(10) to 2.099(8) Å) are caused by aggregation and packing forces. For the ring containing Pd(1), the average Pd–N bond lengths are markedly shorter (1.984 Å) than for the core with Pd(2) (2.059 Å). As observed for the analog bispalladium(II) DPX complex **22**, the two ring systems of **34** are structurally inequivalent in the solid state. The macrocycle with Pd(1)

exhibits a pronounced dome conformation with a mean deviation of 0.2802 Å for the macrocyclic atoms from the porphyrin mean plane. The meso carbons directly connected to and *trans* to the spacer are slightly displaced from the porphyrin mean plane (−0.0509 Å and −0.1054 Å, respectively), while the β carbons span up to 0.3986 Å above the mean plane. The ring with Pd(2) displays a saddle geometry, with a mean deviation of 0.2946 Å from the 24-atom porphyrin mean plane. The meso carbons are alternately displaced from the mean porphyrin plane, ranging from 0.1706 Å above to 0.3514 Å below the 24-atom macrocycle unit.

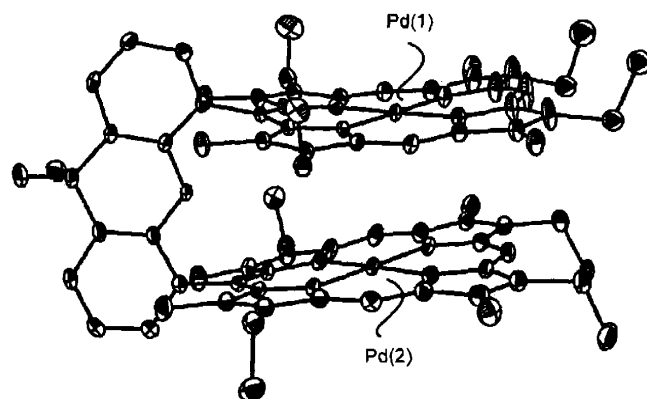


**Figure 3.3.** Crystal structure of Pd<sub>2</sub>(DPX) (22). Thermal ellipsoids are drawn at the 25% probability level. Hydrogen atoms and solvent molecules within the lattice have been omitted for clarity.

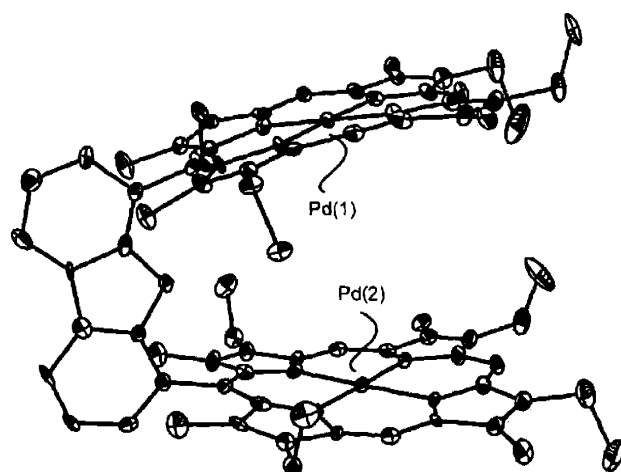


**Figure 3.4.** Crystal structure of Pd<sub>2</sub>(DPD) (34). Thermal ellipsoids are drawn at the 25% probability level. Hydrogen atoms and solvent molecules within the lattice have been omitted for clarity.



**Table 3.3.** Selected Geometric Distances (Å) and Angles (deg) Calculated for Compounds **15** and **27**.

<b>15</b>		<b>27</b>					
<i>Geometric Distances / Å</i>							
Ct(1)-N(1)	2.070	Ct(2)-N(5)	2.098	Ct(1)-N(1)	2.120	Ct(2)-N(5)	2.107
Ct(1)-N(2)	2.106	Ct(2)-N(6)	2.050	Ct(1)-N(2)	2.029	Ct(2)-N(6)	2.019
Ct(1)-N(3)	2.067	Ct(2)-N(7)	2.110	Ct(1)-N(3)	2.127	Ct(2)-N(7)	2.123
Ct(1)-N(4)	2.109	Ct(2)-N(8)	2.047	Ct(1)-N(4)	2.033	Ct(2)-N(8)	2.006
<i>Geometric Angles / deg</i>							
N(1)-Ct(1)-N(2)	88.4	N(7)-Ct(2)-N(8)	88.6	N(1)-Ct(1)-N(2)	85.3	N(7)-Ct(2)-N(8)	85.5
N(1)-Ct(1)-N(3)	177.5	N(7)-Ct(2)-N(6)	91.9	N(1)-Ct(1)-N(3)	178.5	N(7)-Ct(2)-N(6)	94.9
N(2)-Ct(1)-N(3)	91.6	N(8)-Ct(2)-N(6)	179.0	N(2)-Ct(1)-N(3)	94.6	N(8)-Ct(2)-N(6)	176.7
N(1)-Ct(1)-N(4)	91.5	N(7)-Ct(2)-N(5)	176.1	N(1)-Ct(1)-N(4)	94.8	N(7)-Ct(2)-N(5)	176.8
N(2)-Ct(1)-N(4)	179.5	N(8)-Ct(2)-N(5)	91.1	N(2)-Ct(1)-N(4)	178.5	N(8)-Ct(2)-N(5)	94.6
N(3)-Ct(1)-N(4)	88.3	N(6)-Ct(2)-N(5)	88.2	N(3)-Ct(1)-N(4)	85.3	N(6)-Ct(2)-N(5)	85.2

**Table 3.4.** Selected Bond Lengths (Å) and Angles (deg) for Compounds **22** and **34**.

		22	34
<i>Bond Lengths / Å</i>			
Pd(1)–N(1)	2.016(3)	Pd(2)–N(5)	2.005(3)
Pd(1)–N(2)	2.016(3)	Pd(2)–N(6)	2.021(3)
Pd(1)–N(3)	2.012(3)	Pd(2)–N(7)	2.011(3)
Pd(1)–N(4)	2.026(3)	Pd(2)–N(8)	2.027(3)
		Pd(1)–N(1)	2.004(10)
		Pd(1)–N(2)	1.984(10)
		Pd(1)–N(3)	2.022(10)
		Pd(1)–N(4)	1.926(10)
		Pd(2)–N(5)	2.042(10)
		Pd(2)–N(6)	2.055(10)
		Pd(2)–N(7)	2.041(11)
		Pd(2)–N(8)	2.099(8)
<i>Bond Angles / deg</i>			
N(1)–Pd(1)–N(2)	88.87(11)	N(7)–Pd(2)–N(8)	88.76(13)
N(1)–Pd(1)–N(3)	178.47(12)	N(7)–Pd(2)–N(6)	91.20(12)
N(2)–Pd(1)–N(3)	91.09(12)	N(8)–Pd(2)–N(6)	179.50(12)
N(1)–Pd(1)–N(4)	91.37(13)	N(7)–Pd(2)–N(5)	177.83(12)
N(2)–Pd(1)–N(4)	179.12(12)	N(8)–Pd(2)–N(5)	90.97(13)
N(3)–Pd(1)–N(4)	88.65(13)	N(6)–Pd(2)–N(5)	89.08(12)
		N(1)–Pd(1)–N(2)	89.7(4)
		N(1)–Pd(1)–N(3)	177.7(5)
		N(2)–Pd(1)–N(3)	91.8(4)
		N(1)–Pd(1)–N(4)	90.9(4)
		N(2)–Pd(1)–N(4)	179.3(4)
		N(3)–Pd(1)–N(4)	87.5(4)
		N(7)–Pd(2)–N(8)	90.3(4)
		N(7)–Pd(2)–N(6)	90.2(4)
		N(8)–Pd(2)–N(6)	179.1(5)
		N(7)–Pd(2)–N(5)	178.5(4)
		N(8)–Pd(2)–N(5)	91.1(4)
		N(6)–Pd(2)–N(5)	88.4(4)

**Table 3.5.** Crystallographically Derived Intradimer Geometrical Features for DPX and DPD Compounds.<sup>a</sup>

	M—M (Å)	Ct—Ct (Å)	MPS (Å)	interplanar angle (deg)	torsional twist (deg)	a—b dist (Å)	c—d dist (Å)
H <sub>4</sub> (DPX) (15)	NA	4.002	3.609	4.7	14.3	3.552	4.324
Zn <sub>2</sub> (DPX) (16)	3.708	3.863	3.417	4.4	7.9	4.619	4.272
Cu <sub>2</sub> (DPX) (17)	3.910	3.978	3.611	2.3	7.4	4.594	4.321
Ni <sub>2</sub> (DPX) (18)	4.689	4.698	3.666	1.9	22.2	4.657	4.466
Co <sub>2</sub> (DPX)	4.582	4.630	3.519	2.5	21.1	3.591	4.403
Pd <sub>2</sub> (DPX) (22)	3.970	4.002	4.058	3.9	14.6	4.613	4.318
H <sub>4</sub> (DPD) (27)	NA	8.220	8.220	23.0	1.9	4.853	5.654
Zn <sub>2</sub> (DPD) (28)	7.775	7.587	7.356	24.6	1.2	4.800	5.577
Co <sub>2</sub> (DPD)•2MeOH	8.624	8.874	8.794	56.5	9.3	4.826	5.730
Fe <sub>2</sub> O(DPD) (31)	3.504	4.611	4.871	21.1	1.9	4.763	5.082
Pd <sub>2</sub> (DPD) (34)	6.809	6.781	6.541	11.0	3.5	4.823	5.570

<sup>a</sup> Metrics were derived as follows. Macrocyclic centers (Ct) were calculated as the centers of the four nitrogen planes (4-N plane) for each macrocycle. Interplanar angles were measured as the angle between the 4-N least squares planes. Plane separations were measured as the perpendicular distance from one macrocycle's 4-N least-square plane to the center of the other macrocycle; mean plane separations (MPS) were the average of the two plane separations. Torsional twists were measured as the angle between the two meso-carbon to spacer bonds. The a-b and c-d distances were obtained according to the convention shown in Figure 3.6.

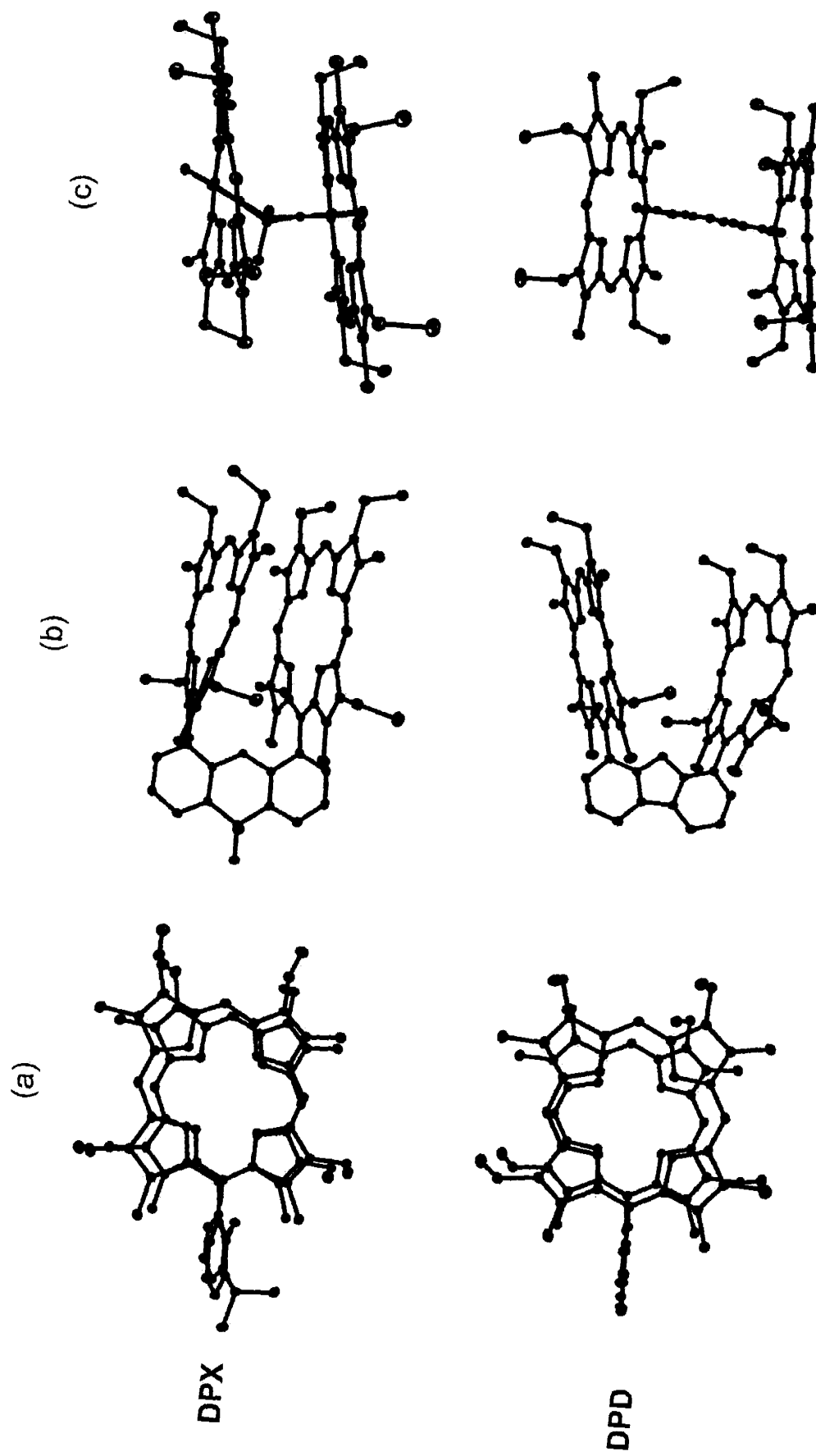


**Figure 3.5.** Comparative views of the crystal structures of  $H_4(DPX)$  (15) and  $H_4(DPD)$  (27): (a) top view; (b) side view, perpendicular to the bridge plane; (c) side view, parallel to the bridge plane. Hydrogen atoms omitted for clarity.

The structures of the parent free-base bisporphyrins and their bispalladium(II) complexes add to the rapidly growing body of structural data for the DPX and DPD systems. The three mutually perpendicular views of the molecular structures of free-base bisporphyrins **15** and **27** shown in Figure 3.5 confirm the ability of the xanthene and dibenzofuran bridges to confine the two porphyrin rings to a face-to-face arrangement while producing molecular clefts with a wide range of vertical pocket sizes. Pertinent geometrical intradimer features for DPX and DPD complexes characterized by X-ray crystallography are summarized in Table 3.5. Definitions for geometric measurements are given in Table 3.5 and Figure 3.6.

The collected data illustrate the significant effect of substituting a single six-membered ether ring (DPX) for a five-membered one (DPD). For example, in the absence of axial ligands, the center-to-center distances vary from 3.8 to 4.7 Å for the DPX platforms to 7.6 to 8.2 Å for the DPD compounds. The vertical range of almost 4 Å observed for DPX and DPD is in stark contrast to DPA and DPB, which differ by only ca. 1 Å in vertical size. Even more notable is the vast array of interplanar angles between the two macrocyclic subunits. The ring-parallel DPX complexes exhibit interplanar angles of less than 5°, while their ring-splayed DPD congeners display angles between 20 to 25°, all without the influence of axial ligands. For comparison, the corresponding values for unligated DPA and DPB complexes lie between 2 and 7°. Lastly, the cofacial geometry of DPX and DPD is displayed in their small torsional angles, which are all less than 25°. The DPD complexes are especially notable in this regard, with torsion angles of less than 10° in all cases.

A number of structural features can be used to tune the critical metal-metal distances, not the least of which is axial ligation. This fact is especially evident for DPD, where extremely compressed or splayed geometries can be achieved by the addition of axial ligands. With external ligation, the metal-metal distances of DPD can range from 3.504 Å for Fe<sub>2</sub>O(DPD) (**31**), which clamps its Pacman bite around a bridging oxo ligand, to 7.775 Å for Zn<sub>2</sub>(DPD) (**28**), which allows the DPD platform to attain its natural conformation. More subtle structural changes are available through metal substitution, which can influence the  $\pi$  overlap between porphyrin subunits. Within the DPX series, Ni<sub>2</sub>(DPX) (**18**) exhibits the least  $\pi$  overlap, giving the largest torsional twist (ca. 20°) and metal-metal separations (ca. 4.6 Å) in the absence of any external axial ligands.

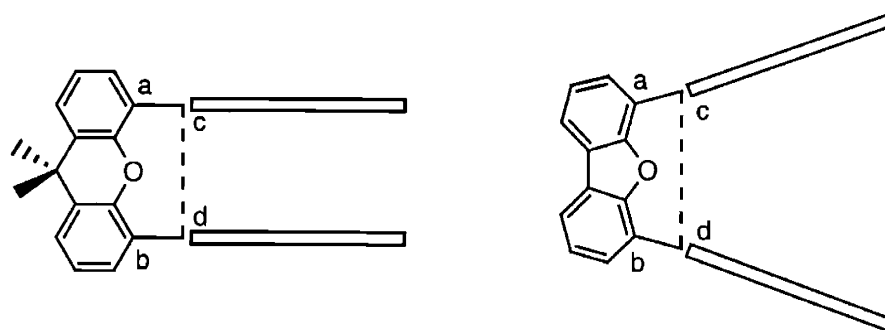


**Figure 3.6.** Illustrated distances a–b and c–d for the cofacial bisporphyrin systems DPX (left) and DPD (right). Table 3.5 sub-caption defines the methods by which the crystallographically derived geometric features were measured.

### 3.3.2 EPR Spectroscopy

The EPR spectra of homobimetallic copper(II) derivatives  $\text{Cu}_2(\text{DPX})$  (**17**) and  $\text{Cu}_2(\text{DPD})$  (**29**) in frozen solution provide a useful complement to the crystallographic studies. Previous studies by Eaton, Eaton and Chang have demonstrated the validity of such methods for structure determination of related cofacial bisporphyrins.<sup>30</sup> The interspin geometry of the two paramagnetic Cu(II) centers can be obtained by examining their triplet spectrum, and the interspin distance,  $r$ , can be determined from the ratio of the intensity of the half-field transitions to the intensity of the allowed transitions. The dipolar splitting of both the copper parallel and perpendicular lines in **17** and **29** are clearly resolved with no evidence of aggregation. Simulation gives  $r$  values of 4.2 Å and 8.0 Å for **17** and **29**, respectively. The separations between the copper parallel lines (2D values) give Cu—Cu distances that agree with those obtained from the dipolar splitting simulations. The spectra of the half-field transitions of **17** and **29** provide another estimate of metal-metal separation. The ratio of the intensity of the half-field transitions to the intensity of the allowed transitions are  $4.8 \times 10^{-3}$  for **17** and  $8.7 \times 10^{-5}$  for **29**, giving interspin distances of 4.0 and 7.8 Å, respectively. The data in Table 3.6 are generally consistent with crystallographic results, with EPR providing a systematically higher value for metal-metal and interplanar separations owing presumably to the absence of crystal packing effects and  $\pi$ - $\pi$  stacking in frozen solution.<sup>31</sup>

**Table 3.6.** Comparison of Geometric Intradimer Parameters Derived from EPR and X-ray Crystallography for Dicopper(II) Cofacial Bisporphyrins.

	$r_{\text{exp}}$ (Å) <sup>a</sup>	$r_{\text{sim}}$ (Å) <sup>b</sup>	M—M (Å) <sup>c</sup>	interplanar (Å) <sup>d</sup>	MPS (Å) <sup>c</sup>
Cu <sub>2</sub> (DPX) ( <b>17</b> )	4.00	4.20	3.90	4.00	3.60
Cu <sub>2</sub> (DPD) ( <b>29</b> )	7.80	8.00	—	7.30	—
Cu <sub>2</sub> (DPA)	4.90	4.90	4.57	4.60	3.90
Cu <sub>2</sub> (DPB)	4.14	4.13	3.81	3.90	3.50
Cu <sub>2</sub> (FTF-4)	4.04	4.15	—	4.00	—
Cu <sub>2</sub> (FTF-5)	4.12	4.15	—	3.90	—
Cu <sub>2</sub> (FTF-7)	5.00	4.95	5.22	3.80	3.52
Cu <sub>2</sub> (slip-4)	5.70	5.50	—	3.90	—

<sup>a</sup> Determined from the ratio of the intensities of the half-field to allowed EPR transitions. <sup>b</sup> Estimated from dipolar splitting simulations. <sup>c</sup> From X-ray crystal structures. <sup>d</sup> Interplanar distances determined from EPR simulation.

### 3.3.3 Steady-State Electronic Absorption and Emission Spectroscopy

The absorption and emission properties of H<sub>4</sub>(DPX) (**15**) and H<sub>4</sub>(DPD) (**27**) and their metal complexes are consistent with the structural geometries observed in the solid state and in solution. Electronic absorption and emission data for H<sub>4</sub>(DPX) (**15**) and H<sub>4</sub>(DPD) (**27**) and their homobimetallic zinc, copper and nickel complexes **16-18** and **28-30** are collected in Tables 3.7 and 3.8, respectively. Soret (B) and Q absorption bands arising from the standard Gouterman four-orbital model for porphyrin spectra<sup>32,33</sup> undergo varying degrees of perturbation upon cofacially disposing two porphyrin rings using xanthene or dibenzofuran.

The spectra of the biszinc(II) derivatives Zn<sub>2</sub>(DPX) (**16**) and Zn<sub>2</sub>(DPD) (**28**), shown in Figure 3.7, are exemplary of each series. Figure 3.7a compares the electronic absorption spectra of Zn<sub>2</sub>(DPX) (**16**), Zn<sub>2</sub>(DPD) (**28**), and their monomer analog Zn(Etio) (Etio = Etioporphyrin-I) in dichloromethane solution. Characteristic of strongly interacting porphyrin subunits,<sup>33,34</sup> the B band of Zn<sub>2</sub>(DPX) (**16**) is blue-shifted ( $\lambda_{\text{abs}} = 389$  nm,  $\epsilon = 290,000$  M<sup>-1</sup>cm<sup>-1</sup>) and broadened relative to that of both Zn<sub>2</sub>(DPD) (**28**) ( $\lambda_{\text{abs}} = 400$  nm,  $\epsilon = 512,000$  M<sup>-1</sup>cm<sup>-1</sup>) and the monomer ( $\lambda_{\text{abs}} = 400$  nm,  $\epsilon = 200,000$  M<sup>-1</sup>cm<sup>-1</sup>), while the Q(1,0) ( $\lambda_{\text{abs}} = 541$  nm,  $\epsilon = 14,300$  M<sup>-1</sup>cm<sup>-1</sup>) and Q(0,0) ( $\lambda_{\text{abs}} = 576$  nm,  $\epsilon = 13,200$  M<sup>-1</sup>cm<sup>-1</sup>) maxima are shifted to the red ( $\lambda_{\text{abs}} = 534$  and 571 nm for **28**, 529 and 567 nm for Zn(Etio)). In contrast, the absorption characteristics of Zn<sub>2</sub>(DPD)

(**28**) more closely approximate the monomer. The observed spectral differences are consistent with the enlarged distance between the two porphyrin chromophores imparted by the dibenzofuran backbone of DPD. The increased separation decreases  $\pi$ - $\pi$  overlap and exciton coupling between the porphyrin subunits. Similar trends are observed for DPA and DPB, where the exciton coupling in the latter series is greater due to its more compressed cofacial structure.<sup>35</sup>

**Table 3.7.** UV-Visible Absorption Data for DPX and DPD Complexes in Dichloromethane at 298 K,  $\lambda_{\text{abs}}$  / nm ( $\epsilon$ / 1000 M<sup>-1</sup> cm<sup>-1</sup>).<sup>a</sup>

	Soret (B)	Q region			
H <sub>4</sub> (DPX) ( <b>15</b> )	382 (202)	509 (11.6)	541 (6.4)	578 (7)	631 (2.9)
Zn <sub>2</sub> (DPX) ( <b>16</b> )	389 (290)	541 (14.3)		576 (13.2)	
Cu <sub>2</sub> (DPX) ( <b>17</b> )	387 (265)	534 (16.7)		571 (19.8)	
Ni <sub>2</sub> (DPX) ( <b>18</b> )	388 (305)	526 (13.6)		564 (23)	
H <sub>4</sub> (DPD) ( <b>27</b> )	397 (276)	501 (25)	536 (13.5)	571 (11.8)	625 (5.2)
Zn <sub>2</sub> (DPD) ( <b>28</b> )	400 (512)	534 (30.6)		571 (29.6)	
Cu <sub>2</sub> (DPD) ( <b>29</b> )	397 (400)	528 (17.6)		565 (23.4)	
Ni <sub>2</sub> (DPD) ( <b>30</b> )	395 (411)	521 (20.6)		560 (39.4)	

<sup>a</sup> Extinction coefficients ( $\epsilon$ ) are reported per molecule.

The absorption spectra for compounds **15** and **27** show a phyllo-type splitting pattern that is typical for mono meso-substituted free base porphyrins,<sup>27,36</sup> with the intensity of the Q-bands displaying the following pattern:  $Q_y(1,0) > Q_y(0,0) > Q_x(1,0) > Q_x(0,0)$ . The spectra of the homobimetallic copper(II) and nickel(II) derivatives are of the hypso type, due to the overlap between the filled  $d_{xz}$  and  $d_{yz}$  orbitals and the empty porphyrin  $\pi^*$  levels.

The B band maximum in the absorption spectrum of Cu<sub>2</sub>(DPX) (**17**) appears at 387 nm ( $\epsilon = 265,000 \text{ M}^{-1} \text{ cm}^{-1}$ ), with the Q(1,0) and Q(0,0) transitions occurring at 534 ( $\epsilon = 16,700 \text{ M}^{-1} \text{ cm}^{-1}$ ) and 571 nm ( $\epsilon = 19,800 \text{ M}^{-1} \text{ cm}^{-1}$ ), respectively, and the B band maximum in the absorption spectrum of Cu<sub>2</sub>(DPD) (**29**) appears at 397 nm ( $\epsilon = 400,000 \text{ M}^{-1} \text{ cm}^{-1}$ ), with the Q(1,0) and Q(0,0) transitions occurring at 528 ( $\epsilon = 17,600 \text{ M}^{-1} \text{ cm}^{-1}$ ) and 565 nm ( $\epsilon = 23,400 \text{ M}^{-1} \text{ cm}^{-1}$ ), respectively. The B absorption in the absorption spectra of Ni<sub>2</sub>(DPX) (**18**) and Ni<sub>2</sub>(DPD) (**30**) are centered at 388 nm ( $\epsilon = 250,000 \text{ M}^{-1} \text{ cm}^{-1}$ ) and 395 nm ( $\epsilon = 411,000 \text{ M}^{-1} \text{ cm}^{-1}$ ), respectively. The Q bands of **18** and **30** are shifted to higher energy with respect to their biscopper(II) counterparts, appearing at 526 ( $\epsilon = 13,600 \text{ M}^{-1} \text{ cm}^{-1}$ ) and 564 nm ( $\epsilon = 23,000 \text{ M}^{-1} \text{ cm}^{-1}$ ) for **18** and 521 ( $\epsilon = 20,600 \text{ M}^{-1} \text{ cm}^{-1}$ ) and 560 nm ( $\epsilon = 39,400 \text{ M}^{-1} \text{ cm}^{-1}$ ) for **30**. The relative energies



of the Q bands of the DPX and DPD derivatives follow the trend biszinc(II) > biscopper(II) > bisnickel(II), which is expected from Gouterman's four-orbital model analysis.<sup>32</sup>

Both Zn<sub>2</sub>(DPX) (**16**) and Zn<sub>2</sub>(DPD) (**28**) produce strong fluorescence typical of Q(0,0) and Q(1,0) excitation. As with the Q-band absorption profile, a correspondent red-shift of these emission bands relative to monomer is observed for **16** ( $\lambda_{em} = 591$  and 640 nm for **16**,  $\lambda_{em} = 572$  and 625 nm for monomer), while **28** ( $\lambda_{em} = 578$  and 631 nm) is similar to the monomer (Figure 3.7b). The free-base porphyrins **15** and **27** also exhibit fluorescence that follow the trend of their biszinc(II) congeners. The fluorescence maxima for free base porphyrin H<sub>4</sub>(DPX) (**15**), centered at  $\lambda_{em} = 637, 671,$  and 703 nm, are red-shifted in comparison to H<sub>2</sub>(Etio-I) ( $\lambda_{em} = 623, 649, 674,$  and 689 nm). The phyllo-type splitting pattern ( $\lambda_{abs}(Q_y(1,0)) = 509$  nm,  $\epsilon = 10,100$  M<sup>-1</sup>cm<sup>-1</sup>;  $\lambda_{abs}(Q_y(0,0)) = 543$  nm,  $\epsilon = 5800$  M<sup>-1</sup>cm<sup>-1</sup>;  $\lambda_{abs}(Q_x(1,0)) = 579$  nm,  $\epsilon = 6200$  M<sup>-1</sup>cm<sup>-1</sup>;  $\lambda_{abs}(Q_x(0,0)) = 631$  nm,  $\epsilon = 2400$  M<sup>-1</sup>cm<sup>-1</sup>), which is characteristic of mono-meso substituted porphyrins,<sup>27</sup> though observed in the absorption profile of **15**, is not apparent in the fluorescence spectrum. H<sub>4</sub>(DPD) (**16**) also displays a strong fluorescence with maxima at  $\lambda_{em} = 628, 658,$  and 694 nm; these values are comparable to the monomer.

**Table 3.8.** Emission Data and Singlet Excited State Parameters for DPX and DPD Complexes in Dichloromethane Solution at 298 K.

	$\lambda_{em}$ (nm) <sup>a</sup>	$\Phi_f$ <sup>b</sup>	$\tau_f$ (ns) <sup>c</sup>
H <sub>4</sub> (DPX) ( <b>15</b> )	637, 671, 703	0.0298 ± 0.009	10.55 ± 0.01
Zn <sub>2</sub> (DPX) ( <b>16</b> )	591, 640	0.0084 ± 0.001	1.35 ± 0.01
H <sub>4</sub> (DPD) ( <b>27</b> )	628, 658, 694	0.0870 ± 0.010	10.70 ± 0.10
Zn <sub>2</sub> (DPD) ( <b>28</b> )	578, 631	0.0541 ± 0.001	1.50 ± 0.02
H <sub>2</sub> (Etio)	623, 649, 674, 689	0.1200 ± 0.008	11.50 ± 0.10
Zn(Etio)	572, 625	0.0298 ± 0.009	1.45 ± 0.01

<sup>a</sup>  $\lambda_{em}$  is the corrected emission fluorescence energy maximum. <sup>b</sup>  $\Phi_f$  is the quantum yield for emission fluorescence. <sup>c</sup>  $\tau_f$  is the observed fluorescence lifetime.

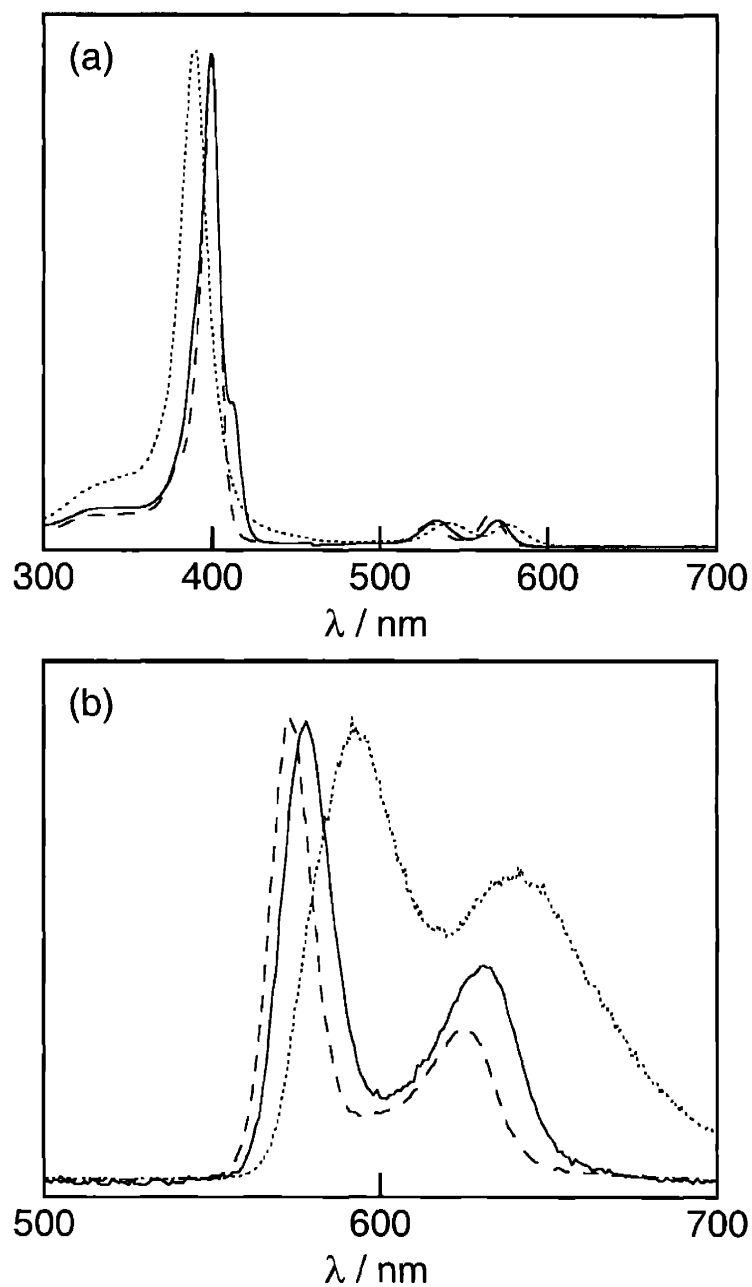


**Figure 3.7.** (a) Absorption and (b) emission spectra of Zn<sub>2</sub>(DPX) (**16**) (dotted line), Zn<sub>2</sub>(DPD) (**28**) (solid line), and Zn(Etio) (dashed line) in dichloromethane solution at room temperature. Spectra are normalized in intensities.

### 3.3.4 Time-Resolved Electronic Absorption and Emission Spectroscopy

Time-resolved spectroscopic measurements are also in agreement with the notion that the compressed, parallel arrangement of the porphyrin chromophores of DPX compared to the splayed, wedge geometry of the DPD porphyrins leads to greater exciton coupling in the former. The singlet excited-state properties of the free base and biszinc(II) derivatives are in accord with the steady-state electronic absorption and emission measurements; data are collected in Table 3.8. For example,  $\text{Zn}_2(\text{DPX})$  (**16**) has a shortened singlet excited-state lifetime ( $\tau_{\text{fl}} = 1.35 \pm 0.01$  ns) and reduced fluorescence quantum yield ( $\Phi_{\text{fl}} = 0.0084 \pm 0.001$ ) compared to  $\text{Zn}_2(\text{DPD})$  (**28**) ( $\tau_{\text{fl}} = 1.50 \pm 0.02$  ns,  $\Phi_{\text{fl}} = 0.0541 \pm 0.001$ ). The free base porphyrins also follow the same trend, with  $\text{H}_4(\text{DPX})$  (**15**) ( $\tau_{\text{fl}} = 10.55 \pm 0.05$  ns and  $\Phi_{\text{fl}} = 0.0298 \pm 0.009$ ) having a shorter singlet excited-state lifetime and reduced fluorescence quantum yield compared to  $\text{H}_4(\text{DPD})$  (**27**) ( $\tau_{\text{fl}} = 10.70 \pm 0.10$  ns,  $\Phi_{\text{fl}} = 0.0870 \pm 0.001$ ).

The situation is more complex for the triplet excited states for the DPX and DPD frameworks. A comprehensive description of the dynamics for these excited states is provided by examination of the bispalladium(II) complexes  $\text{Pd}_2(\text{DPX})$  (**22**) and  $\text{Pd}_2(\text{DPD})$  (**34**);<sup>39</sup> the heavy metal cores promote efficient crossover from singlet to triplet excited states by spin-orbit coupling.<sup>36</sup> Data are collected in Table 3.9. In contrast to trends observed for the singlet excited states of the free base and biszinc(II) DPX and DPD complexes, the phosphorescence quantum yield ( $\Phi_{\text{p}} = 1.07(54) \times 10^{-3}$ ) and lifetime ( $\tau_{\text{p}} = 0.53$   $\mu\text{s}$ ) of  $\text{Pd}_2(\text{DPD})$  (**34**) are significantly attenuated compared to its  $\text{Pd}_2(\text{DPX})$  (**22**) congener ( $\Phi_{\text{p}} = 35.2(3) \times 10^{-3}$  and  $\tau_{\text{p}} = 262$   $\mu\text{s}$ ). However, electronic absorption and emission spectroscopy of  $\text{Pd}_2(\text{DPX})$  (**22**) and  $\text{Pd}_2(\text{DPD})$  (**34**) establish that the porphyrin rings of the DPX cofacial analogue are in closer proximity than the porphyrin rings of the DPD analogue in fluid solution (Table 3.10). These results suggest that the enhanced triplet excited state decay of the DPD system in comparison to DPX is not a consequence of simple interplanar interactions such as exciton coupling, but rather arises from the increased conformational flexibility of the more widely spaced porphyrin macrocycles to rotate about the aryl ring of the wedge-shaped dibenzofuran pillar. In support of this contention, the photophysical properties of the monomer compounds  $\text{Pd}(\text{Etio})$  (**42**) and  $\text{Pd}(\text{PhEtio})$  (**45**) (PhEtio = 5-(4'-bromophenyl)-2,8,13,17-tetraethyl-3,7,12,18-tetramethylporphyrin) have been examined and been found to be similar to  $\text{Pd}_2(\text{DPX})$  (**22**) and  $\text{Pd}_2(\text{DPD})$  (**34**), respectively. In addition, nonlocal density functional calculations on  $\text{Pd}(\text{PhEtio})$  confirm the possibility of ring rotation about the C(meso)—C(aryl) bond, and show that such torsional motions are accompanied by non-planar distortions of the porphyrin ring with a decrease in the  $\text{T}_1\text{—S}_0$  energy gap.

**Table 3.9.** Emission Data and Triplet Excited State Parameters for DPX and DPD Complexes in Cyclohexane Solution at 298 K.

	$\lambda_{\text{em}}$ (nm) <sup>a</sup>	$\Phi_{\text{p}}$ <sup>b</sup>	$\tau_{\text{p}}$ ( $\mu\text{s}$ ) <sup>c</sup>
Pd <sub>2</sub> (DPX) ( <b>22</b> )	678	$35.2(3) \times 10^{-3}$	262(12)
Pd <sub>2</sub> (DPD) ( <b>34</b> )	673	$0.993(108) \times 10^{-3}$	0.52(1)
Pd(Etio) ( <b>42</b> )	668	$67.3(48) \times 10^{-3}$	203(7)
Pd(PhEtio) ( <b>45</b> )	672	$0.598(49) \times 10^{-3}$	0.46(1), 0.16(1)

<sup>a</sup>  $\lambda_{\text{em}}$  is the corrected emission phosphorescence energy maximum. <sup>b</sup>  $\Phi_{\text{p}}$  is the quantum yield for emission phosphorescence. <sup>c</sup>  $\tau_{\text{p}}$  is the observed phosphorescence lifetime.

**Table 3.10.** UV-Visible Absorption Data for Palladium(II) Porphyrin Complexes in Dichloromethane at 298 K,  $\lambda_{\text{abs}}$  / nm ( $\epsilon$  /  $1000 \text{ M}^{-1} \text{ cm}^{-1}$ ).<sup>a</sup>

	Soret (B)	Q region	
Pd <sub>2</sub> (DPX) ( <b>22</b> )	386 (223)	521 (16)	552 (30)
Pd <sub>2</sub> (DPD) ( <b>34</b> )	391 (256)	515 (23)	548 (49)
Pd(Etio) ( <b>42</b> )	391 (60)	511 (4.4)	546 (14)
Pd(PhEtio) ( <b>45</b> )	397 (176)	515 (14)	548 (31)

<sup>a</sup> Extinction coefficients ( $\epsilon$ ) are reported per molecule.

### 3.4 Concluding Remarks

The multielectron reactivity of pillared cofacial bisporphyrins toward small-molecule substrates is predicated on the ability of the spacer to provide a bimetallic cleft of proper size and flexibility for efficient accommodation of reaction intermediates during catalysis. Traditional systems based on anthracene (DPA) and biphenylene (DPB) exhibit notable activity, but their restrictions in vertical pocket size variability (ca. 1 Å) limit their use for systematic explorations of structure/activity relationships pertaining to the Pacman effect. In contrast, crystallographic analysis confirms the ability of the DPX and DPD platforms to provide cofacial pockets with an array of vertical sizes that can be tuned by axial ligation and/or metal substitution. Especially noteworthy is the ability of the DPD system to span a vertical range of metal-metal distances of over 4 Å. The structural studies are supported by EPR spectroscopy of the biscopper(II) derivatives, which directly probe metal-metal interactions in frozen solution. In addition, a series

of steady-state and time-resolved absorption and emission experiments reveal the general trend that the more compressed DPX complexes exhibit a greater degree of exciton coupling compared to their splayed DPD counterparts in fluid solution. In closing, our results show that the DPX and DPD systems afford a unique combination of synthetic availability and vertical flexibility. Future studies of these and related platforms for the catalytic transformation of small-molecule substrates should prove intriguing.

### 3.5 Experimental Section

#### 3.5.1 Materials

Silica gel 60 (70-230 and 230-400 mesh, Merck) was used for column chromatography. Analytical thin-layer chromatography was performed using Merck 60 F254 silica gel (precoated sheets, 0.2 mm thick). Solvents for synthesis were of reagent grade or better, and were dried according to standard methods. H<sub>2</sub>(Etio) and Zn(Etio) were purchased from Frontier Scientific. The porphyrin Pd(Etio) (**42**)<sup>26</sup> and the dipyrromethane 5-(4'-bromophenyl)-3,3'-dimethyl-4,4'-diethyl-2,2'-dipyrromethane (**43**)<sup>37</sup> were obtained using modification of literature procedures. The dipyrromethane precursor 3,3'-diethyl-5,5'-diformyl-4,4'-dimethyl-2,2'-dipyrromethane (**3**) and the cofacial bisporphyrins H<sub>4</sub>(DPX) (**15**), Zn<sub>2</sub>(DPX) (**16**), Cu<sub>2</sub>(DPX) (**17**), Ni<sub>2</sub>(DPX) (**18**), Pd<sub>2</sub>(DPX) (**19**), H<sub>4</sub>(DPD) (**27**), Zn<sub>2</sub>(DPD) (**28**), Cu<sub>2</sub>(DPD) (**29**), Ni<sub>2</sub>(DPD) (**30**), and Pd<sub>2</sub>(DPD) (**34**) were prepared as described in chapter 2. Spectroscopic experiments employed dichloromethane (spectroscopic grade, Burdick & Jackson), which was stored over 4 Å molecular sieves under high vacuum or in a glovebox. All other reagents were used as received.

#### 3.5.2 5-(4'-Bromophenyl)-2,8,13,17-tetraethyl-3,7,12,18-tetramethylporphyrin [H<sub>2</sub>(PhEtio)] (**44**)

A suspension of 5-(4'-bromophenyl)-3,3'-dimethyl-4,4'-diethyl-2,2'-dipyrromethane (**43**) (3.85 g, 10 mmol) and 3,3'-diethyl-5,5'-diformyl-4,4'-dimethyl-2,2'-dipyrromethane (**3**) (2.86 g, 10 mmol) in methanol (500 mL) was purged with nitrogen for 1 h. A solution of *p*-toluenesulfonic acid (2.5 g) in methanol (20 mL) was added dropwise over a period of 1 h. The resulting red mixture was stirred in the dark under nitrogen for 24 h. Solid *o*-chloranil (2.5 g) was added in one portion and stirring was continued in air for 24 h. The mixture was taken to dryness and the remaining solid redissolved in 400 mL of chloroform. A saturated methanolic solution of Zn(OAc)<sub>2</sub>•2H<sub>2</sub>O (20 mL) was added and the solution was refluxed for 1 h. The solvent was removed and the remaining residue was purified by flash column chromatography (silica gel, dichloromethane). The first band eluted was collected and vigorously stirred with 6 N HCl (15 mL) for 15 min. The solution was neutralized with a 10% aqueous sodium carbonate solution

and the mixture was stirred for an additional 15 min. The organic phase was separated, washed with water (3 × 50 mL), dried over Na<sub>2</sub>SO<sub>4</sub>, and taken to dryness. Purification by flash column chromatography (silica gel, dichloromethane) followed by recrystallization from dichloromethane/methanol afforded pure H<sub>2</sub>(PhEtio) as a grape purple powder (3.25 g, 51% yield). <sup>1</sup>H NMR (500 MHz, CDCl<sub>3</sub>, 25 °C): δ = 10.18 (s, 2H, meso), 9.97 (s, 1H, meso), 7.97 (d, 2H, ArH), 7.89 (d, 2H, ArH), 4.08 (m, 4H, CH<sub>2</sub>), 4.02 (m, 4H, CH<sub>2</sub>), 3.65 (s, 6H, CH<sub>3</sub>), 2.51 (s, 6H, CH<sub>3</sub>), 1.89 (t, 6H, CH<sub>3</sub>), 1.77 (t, 6H, CH<sub>3</sub>), -3.239 (br s, 1H, NH), -3.323 (br s, 1H, NH). HRFABMS (M<sup>+</sup>) calcd for C<sub>38</sub>H<sub>41</sub>N<sub>4</sub>Br *m/z* 632.252, found 632.255.

### 3.5.3 Pd(PhEtio) (45)

To a 50-mL chloroform solution of H<sub>2</sub>(PhEtio) (**44**) (50 mg, 0.079 mmol) was added a solution of Pd(OAc)<sub>2</sub> (100 mg) and potassium acetate (100 mg) in 8 mL of methanol. The resulting solution was refluxed for 3 h under nitrogen and the solvent was removed by rotary evaporation. The crude material was purified by flash column chromatography (silica gel, dichloromethane) followed by recrystallization from dichloromethane/methanol to afford analytically pure Pd(PhEtio) (**45**) as a brick red solid (49 mg, 86% yield). <sup>1</sup>H NMR (500 MHz, CDCl<sub>3</sub>, 25 °C): δ = 10.11 (s, 2H, meso), 10.05 (s, 1H, meso), 7.95 (d, 2H, ArH), 7.89 (d, 2H, ArH), 4.06 (m, 4H, CH<sub>2</sub>), 3.96 (m, 4H, CH<sub>2</sub>), 3.60 (s, 6H, CH<sub>3</sub>), 2.47 (s, 6H, CH<sub>3</sub>), 1.89 (t, 6H, CH<sub>3</sub>), 1.74 (t, 6H, CH<sub>3</sub>). HRFABMS (M<sup>+</sup>) calcd for C<sub>38</sub>H<sub>39</sub>N<sub>4</sub>BrPd<sub>2</sub> *m/z* 736.139, found 736.140.

### 3.5.4 General Details of X-ray Data Collection and Reduction

X-ray diffraction data were collected using a Siemens 3 circle diffractometer equipped with a CCD detector. Measurements were carried out at -90° C using Mo Kα (λ = 0.71073 Å) radiation, which was wavelength selected with a single-crystal graphite monochromator. Four sets of data were collected using ω scans and a -0.3° scan width. All calculations were performed using either a Silicon Graphics Indigo 2 or a PC workstation. The data frames were integrated to *hkl*/intensity, and final unit cells were calculated by using the SAINT v.4.050 program from Siemens. The structures were solved and refined with the SHELXTL v.5.03 suite of programs developed by G. M. Sheldrick and Siemens Industrial Automation, Inc., 1995.

### 3.5.5 X-ray Structure of H<sub>4</sub>(DPX) (15)

A 0.52 mm × 0.24 mm × 0.10 mm purple red crystal of plate morphology was obtained from slow evaporation of a methanol/dichloromethane solution of the compound. The crystal was coated in Paratone N and mounted onto a glass fiber. A total of 18992 reflections were collected in the θ range 2.25 to 20.00°, of which 12281 were unique (R<sub>int</sub> = 0.0342). Hydrogen atoms were placed in calculated positions using a standard riding model and were refined isotropically. The

largest peak and hole in the difference map were  $0.395 \text{ e}\text{\AA}^{-3}$  and  $-0.703 \text{ e}\text{\AA}^{-3}$ , respectively. The least squares refinement converged normally giving residuals of  $R1 = 0.0552$  and  $wR2 = 0.1494$ , with  $GOF = 1.029$ . Crystal data for  $\text{C}_{80}\text{H}_{92}\text{Cl}_2\text{N}_8\text{O}$ : triclinic,  $P\bar{1}$ ,  $Z = 4$ ,  $a = 13.5167(12) \text{ \AA}$ ,  $b = 21.7008(18) \text{ \AA}$ ,  $c = 23.808(2) \text{ \AA}$ ,  $\alpha = 80.116(2)^\circ$ ,  $\beta = 76.832(2)^\circ$ ,  $\gamma = 80.4070(10)^\circ$ ,  $V = 6639.4(10) \text{ \AA}^3$ ,  $\rho_{\text{calc}} = 1.253 \text{ g/cm}^3$ ,  $F(000) = 2680$ .

### 3.5.6 X-ray Structure of $\text{H}_4(\text{DPD})$ (27)

A  $0.35 \text{ mm} \times 0.20 \text{ mm} \times 0.20 \text{ mm}$  brick red crystal of block morphology was obtained from vapor diffusion of pentane into an acetone solution of the compound. The crystal was coated in STP and mounted onto a glass fiber. A total of 25700 reflections were collected in the  $\theta$  range  $2.32$  to  $23.29^\circ$ , of which 9347 were unique ( $R_{\text{int}} = 0.0534$ ). Hydrogen atoms bound to nitrogen in the porphyrin ring were located, and their positions were stable. Other hydrogen atoms were placed in calculated positions using a standard riding model and were refined isotropically. The largest peak and hole in the difference map were  $1.036 \text{ e}\text{\AA}^{-3}$  and  $-0.358 \text{ e}\text{\AA}^{-3}$ , respectively. The least squares refinement converged normally giving residuals of  $R1 = 0.0763$  and  $wR2 = 0.1708$ , with  $GOF = 1.148$ . Crystal data for  $\text{C}_{80}\text{H}_{83}\text{N}_8\text{O}_2$ : monoclinic,  $C2/c$ ,  $Z = 8$ ,  $a = 22.666(2) \text{ \AA}$ ,  $b = 13.6749(14) \text{ \AA}$ ,  $c = 42.084(4) \text{ \AA}$ ,  $\beta = 94.554(2)^\circ$ ,  $V = 13003(2) \text{ \AA}^3$ ,  $\rho_{\text{calc}} = 1.214 \text{ g/cm}^3$ ,  $F(000) = 5080$ .

### 3.5.7 X-ray Structure of $\text{Pd}_2(\text{DPX})$ (22)

A  $0.16 \text{ mm} \times 0.19 \text{ mm} \times 0.61 \text{ mm}$  ruby red crystal of rod morphology was obtained from slow diffusion of methanol into a dichloromethane solution of the compound. The crystal was coated in STP and mounted onto a glass fiber. A total of 12860 reflections were collected in the  $\theta$  range  $2.38$  to  $23.26^\circ$ , of which 8993 were unique ( $R_{\text{int}} = 0.0699$ ). The Patterson method was used to locate the palladium atoms, all remaining atoms were placed using the difference Fourier map. Hydrogen atoms were placed in calculated positions using a standard riding model and were refined isotropically. The largest peak and hole in the difference map were  $0.937 \text{ e}\text{\AA}^{-3}$  and  $-0.874 \text{ e}\text{\AA}^{-3}$ , respectively. The least squares refinement converged normally giving residuals of  $R1 = 0.0412$  and  $wR2 = 0.1097$ , with  $GOF = 1.065$ . Crystal data for  $\text{C}_{79}\text{H}_{82}\text{N}_8\text{OPd}_2$ : triclinic,  $P\bar{1}$ ,  $Z = 2$ ,  $a = 11.1419(8) \text{ \AA}$ ,  $b = 14.9325(10) \text{ \AA}$ ,  $c = 20.8014(14) \text{ \AA}$ ,  $\alpha = 100.6090(10)^\circ$ ,  $\beta = 100.9680(10)^\circ$ ,  $\gamma = 102.5440(10)^\circ$ ,  $V = 3223.5(4) \text{ \AA}^3$ ,  $\rho_{\text{calc}} = 1.420 \text{ g/cm}^3$ ,  $F(000) = 1430$ .

### 3.5.8 X-ray Structure of $\text{Pd}_2(\text{DPD})$ (34)

A  $0.15 \text{ mm} \times 0.16 \text{ mm} \times 0.27 \text{ mm}$  mighty red crystal of plate morphology was obtained from slow diffusion of methanol into a dichloromethane solution of the compound. The crystal was coated in STP and mounted onto a glass fiber. A total of 15257 reflections were collected in the

$\theta$  range 2.47 to 23.28°, of which 10150 were unique ( $R_{\text{int}} = 0.0236$ ). The Patterson method was used to locate the palladium atoms, all remaining atoms were placed using the difference Fourier map. Hydrogen atoms were placed in calculated positions using a standard riding model and were refined isotropically. The largest peak and hole in the difference map were 2.607 eÅ<sup>-3</sup> and -0.555 eÅ<sup>-3</sup>, respectively. The least squares refinement converged normally giving residuals of  $R1 = 0.0413$  and  $wR2 = 0.1292$ , with  $GOF = 0.564$ . Crystal data for C<sub>80</sub>H<sub>86</sub>N<sub>8</sub>O<sub>2</sub>Pd<sub>2</sub>: monoclinic, P2(1),  $Z = 2$ ,  $a = 13.1958(7)$  Å,  $b = 20.3976(11)$  Å,  $c = 14.8663(8)$  Å,  $\beta = 108.9990(10)^\circ$ ,  $V = 3783.5(4)$  Å<sup>3</sup>,  $\rho_{\text{calc}} = 1.419$  g/cm<sup>3</sup>,  $F(000) = 1664$ .

### 3.5.9 Physical Measurements

<sup>1</sup>H NMR spectra were collected in CDCl<sub>3</sub> (Cambridge Isotope Laboratories) at the MIT Department of Chemistry Instrumentation Facility (DCIF) using a Unity 300, a Mercury 300 or an Inova 500 spectrometer at 25 °C. All chemical shifts are reported using the standard  $\delta$  notation in parts-per-million; positive chemical shifts are to higher frequency from the given reference. Mass spectral analyses were carried out by the University of Illinois Mass Spectrometry Laboratory and the MIT DCIF. Elemental analyses were performed at H. Kolbe Mikroanalytisches Laboratorium, Michigan State University, the University of Illinois Microanalysis Laboratory, or Quantitative Technologies, Inc (Whitehall, New Jersey). X-band EPR spectra were recorded in toluene glass (between 120 and 160 K) in 4 mm quartz tubes using a Bruker 300 EMX EPR spectrometer. Data manipulation was carried out using the Win-EPR program. Absorption spectra were obtained using a Cary-17 spectrophotometer modified by On-Line Instrument Systems (OLIS) to include computer control or a Spectral Instruments 440 Model spectrophotometer.

Samples for all photochemical and photophysical measurements were contained within a cell equipped with a solvent reservoir and a 1-cm clear fused-quartz cell (Starna Cells, Inc.). The two chambers were isolated from each other by a high-vacuum Teflon valve and from the environment with a second high-vacuum Teflon valve. Samples were subject to at least three freeze-pump-thaw cycles (10<sup>-6</sup> torr). Emission spectra were recorded using a high-resolution instrument described previously.<sup>38</sup> The emission produced upon excitation at 546 nm was collected with a red-sensitive Hamamatsu R316-02 photomultiplier tube over a wavelength range of 565 – 860 nm. Integrated emission fluorescence and phosphorescence quantum yields ( $\Phi_{\text{fl}}$ ) were determined relative to Zn(TPP) (TPP = 5,10,15,20-tetraphenylporphyrin) as a standard ( $\Phi_{\text{fl}} = 0.04$  in methylcyclohexane). Optical densities of solutions used in quantum yield measurements were adjusted to be nearly identical and a correction formula was employed to correct for the different solvents used.



Time-resolved absorption and emission experiments in two different time regimes were carried out using the systems described in the following paragraphs. The system we refer to as a nanosecond laser system consists of a Coherent Infinity-XPO laser. The third harmonic of the 1064-nm fundamental is used to pump an optical parametric oscillator (OPO) that is tunable throughout the visible (420 – 700 nm). The OPO produces laser pulses at a repetition rate of 20 Hz with pulse energies of  $\sim 200 \mu\text{J}$  and pulse widths of 5 ns. Transient absorption is performed by exciting the sample at 550 nm (pump pulse) and probing with white light continuum generated by a 75 W xenon arc lamp (probe pulse). The probe pulse is electronically delayed relative to the pump pulse by a DG535 delay generator from Stanford Research Systems, Inc.; the shutters used are Vincent Associates Uniblitz T132 fast shutters. The probe pulse passes through the sample into a SPEX Triax 320 spectrometer and is detected with a Andor Technology DH520-25F-01 ICCD camera thermoelectrically cooled to  $-40^\circ\text{C}$ . In this study, transient spectra were collected over a wavelength range of 374 – 638 nm. Time-resolved emission is performed by exciting the sample at 550 nm and collecting the emission at either 650 nm or 670 nm. The emission signal is amplified in a Hamamatsu R928 photomultiplier tube attached to the lateral exit of the spectrometer. The output from the photomultiplier tube is channelled into a Lecroy 9384 CM digital oscilloscope. All instruments and electronics in this laser system are controlled by software written in Labview (National Instruments).

The system we refer to as the sub-picosecond laser system consists of a Coherent/BMI Comet-400S two-stage optical parametric amplifier (OPA). The OPA generates laser pulses at a repetition rate of 1 kHz and offers wavelength tunability from 475 – 710 nm with pulse energies greater than  $20 \mu\text{J}$ . The OPA is pumped by a Coherent/BMI Alpha-1000 chirped pulse regenerative amplifier, which in turn is pumped by a 10 W, 1 kHz Nd:YLF laser and seeded by a Coherent Mira femtosecond Ti:sapphire oscillator. The oscillator is pumped by a 5 W, *cw* Coherent Verdi solid-state, frequency-doubled Nd:YVO<sub>4</sub> laser. The modular design allows access to the low power (nanjoules per pulse) oscillator pulses at 76 MHz, as well as the more powerful (near-millijoule per pulse) output from the regenerative amplifier (800 nm, 1 kHz). Pulses from the regenerative amplifier are frequency doubled to give pulses at 400 nm. UV pulses are routinely generated from the OPA output to make the effective range for excitation from less than 240 nm to more than 800 nm. The pulses from the regenerative amplifier can be characterized in real time by a Positive Light SSA single-shot autocorrelator, and they have been measured to be  $\sim 100$  fs in duration. Emission lifetimes are measured on a Hamamatsu C4334 Streak Scope streak camera, which is controlled from the High Performance Digital Temporal Analyzer (HPDTA) software provided by Hamamatsu Photonics. This system allows for measurements of lifetimes with a resolution of  $\sim 10$  ps in a time window up to 1 ms limited by

the laser repetition rate. Delays involving long time windows ( $\geq 100$  ns) are generated by a Stanford Research Systems DG535 delay generator, whereas delays for short time windows ( $< 100$  ns) are generated by a Hamamatsu C1097-04 delay unit. The streak camera is capable of measuring the rise and decay of fluorescence at every wavelength in a 100 nm window simultaneously, allowing direct comparison of the kinetics of different spectral features.

### 3.6 References and Notes

1. Collman, J. P.; Wagenknecht, P. S.; Hutchison, J. E. *Angew. Chem. Int. Ed. Engl.* **1994**, *33*, 1537-1554.
2. Chang, C. K.; Abdalmuhdi, I. *J. Org. Chem.* **1983**, *48*, 5388-5390.
3. Chang, C. K.; Liu, H. Y.; Abdalmuhdi, I. *J. Am. Chem. Soc.* **1984**, *106*, 2725-2726.
4. Chang, C. K.; Abdalmuhdi, I. *Angew. Chem. Int. Ed. Engl.* **1984**, *23*, 164-165.
5. Fillers, J. P.; Ravichandran, K. G.; Abdalmuhdi, I.; Tulinsky, A.; Chang, C. K. *J. Am. Chem. Soc.* **1986**, *108*, 417-424.
6. Lui, H.-Y.; Abdalmuhdi, I.; Chang, C. K.; Anson, F. C. *J. Phys. Chem.* **1985**, *89*, 665-670.
7. Ni, C.-L.; Abdalmuhdi, I.; Chang, C. K.; Anson, F. C. *J. Phys. Chem.* **1987**, *91*, 1158-1166.
8. Collman, J. P.; Hutchison, J. E.; Lopez, M. A.; Tabard, A.; Guilard, R.; Seok, W. K.; Ibers, J. A.; L'Her, M. *J. Am. Chem. Soc.* **1992**, *114*, 9869-9877.
9. Collman, J. P.; Hutchison, J. E.; Lopez, M. A.; Guilard, R. *J. Am. Chem. Soc.* **1992**, *114*, 8066-8073.
10. Collman, J. P.; Hutchison, J. E.; Ennis, M. S.; Lopez, M. A.; Guilard, R. *J. Am. Chem. Soc.* **1992**, *114*, 8074-8080.
11. Collman, J. P.; Ha, Y.; Wagenknecht, P. S.; Lopez, M. A.; Guilard, R. *J. Am. Chem. Soc.* **1993**, *115*, 9080-9088.
12. Collman, J. P.; Ha, Y. Y.; Guilard, R.; Lopez, M. A. *Inorg. Chem.* **1993**, *32*, 1788-1794.
13. Collman, J. P.; Fish, H. T. *Inorg. Chem.* **1996**, *35*, 7922-7923.
14. Collman, J. P.; Tyvoll, D. A.; Chng, L. L.; Fish, H. T. *J. Org. Chem.* **1995**, *60*, 1926-1931.
15. Guilard, R.; Lopez, M. A.; Tabard, A.; Richard, P.; Lecomte, C.; Brandes, S.; Hutchison, J. E.; Collman, J. P. *J. Am. Chem. Soc.* **1992**, *114*, 9877-9889.
16. Guilard, R.; Brandes, S.; Tabard, A.; Bouhmaida, N.; LeComte, C.; Richard, P.; Latour, J. M. *J. Am. Chem. Soc.* **1994**, *116*, 10202-10211.
17. Guilard, R.; Brandes, S.; Tardieux, C.; Tabard, A.; L'Her, M.; Miry, C.; Gouerac, P.; Knop, Y.; Collman, J. P. *J. Am. Chem. Soc.* **1995**, *117*, 11721-11729.
18. Le Mest, Y.; L'Her, M.; Saillard, J. Y. *Inorg. Chim. Acta* **1996**, *248*, 181-191.
19. Le Mest, Y.; Inisan, C.; Laouenan, A.; L'Her, M.; Talarmain, J.; El Khalifa, M.; Saillard, J. Y. *J. Am. Chem. Soc.* **1997**, *119*, 6905-6106.
20. Harvey, P. D.; Proulx, N.; Martin, G.; Drouin, M.; Nurco, D. J.; Smith, K. M.; Bolze, F.; Gros, C. P.; Guilard, R. *Inorg. Chem.* **2001**, *40*, 4134-4142.

21. Naruta, Y.; Sasayama, M.; Ichihara, K. *J. Mol. Cat. A* **1997**, *117*, 115-121.
22. Chang, C. J.; Brown, J. D. K.; Chang, M. C. Y.; Baker, E. A.; Nocera, D. G. In *Electron Transfer in Chemistry*; Balzani, V., Ed.; Wiley-VCH: Weinheim, Germany, 2001; Vol. 3.2.4, pp 409-461.
23. Chang, C. J.; Deng, Y.; Heyduk, A. F.; Chang, C. K.; Nocera, D. G. *Inorg. Chem.* **2000**, *39*, 959-966.
24. Deng, Y.; Chang, C. J.; Nocera, D. G. *J. Am. Chem. Soc.* **2000**, *122*, 410-411.
25. Chang, C. J.; Baker, E. A.; Pistorio, B. J.; Deng, Y.; Loh, Z.-H.; Miller, S. E.; Carpenter, S. D.; Nocera, D. G. *Inorg. Chem.* **2002**, *41*, 3102-3109.
26. Buchler, J. W. *Static Coordination Chemistry of Metalloporphyrins*; 2nd ed.; Smith, K. M., Ed.; Elsevier Scientific: Oxford, 1975, pp 157-232.
27. Kadish, K. M.; Smith, K. M.; Guillard, R. *The Porphyrin Handbook*; Academic Press: San Diego, 2000.
28. Bolze, F. G., Claude P.; Drouin, M.; Espinosa, E.; Harvey, P. D.; Guillard, R. *J. Organomet. Chem.* **2002**, *643-644*, 89-97.
29. Senge, M. O.; Forsyth, T. P.; Smith, K. *Z. Kristallogr.* **1996**, *211*, 176-185.
30. Eaton, S. S.; Eaton, G. R.; Chang, C. K. *J. Am. Chem. Soc.* **1985**, *107*, 3177-3184.
31. Scheidt, W. R.; Lee, Y. J. *Struct. Bonding (Berlin)* **1987**, *64*, 1-70.
32. Gouterman, M. *J. Mol. Spectrosc.* **1961**, *6*, 138-163.
33. Gouterman, M.; Holten, D.; Lieberman, E. *Chem. Phys.* **1977**, *25*, 139-153.
34. Chang, C. K. *J. Heterocycl. Chem.* **1977**, *14*, 1285-1288.
35. Le Mest, Y.; L'Her, M.; Hendricks, N. H.; Kim, K.; Collman, J. P. *Inorg. Chem.* **1992**, *31*, 835-847.
36. Kalyanasundaram, K. *Photochemistry of Polypyridine and Porphyrin Complexes*; Academic Press: London, 1992.
37. Deng, Y., Ph.D. Thesis, Michigan State University: East Lansing, MI, 1997.
38. Rudzinski, C. M.; Engebretson, D. S.; Hartmann, W. K.; Nocera, D. G. *J. Phys. Chem. A* **1998**, *102*, 7442-7446.
39. Loh, Z.-H.; Miller, S. E.; Chang, C. J.; Carpenter, S. D.; Nocera, D. G., submitted for publication.

*Chapter 4*

**Thermodynamic Characterization  
of the Pacman Effect**

## 4.1 Motivation and Specific Aims

Chapters 2 and 3 initiated studies to build a structure-function relationship for the Pacman porphyrins anchored by xanthene and dibenzofuran. Detailed structural analyses establish that the DPX and DPD systems span an unprecedented range of pocket sizes. In particular, the DPD platform is distinguished by its ability to open and close its binding cavity by over 4 Å in metal-metal distances via the Pacman effect. To probe further the nature of dynamic flexibility within the cofacial bisporphyrin motif and its consequences for catalytic applications, we wished to assess the relative energetics of the Pacman effect. The supramolecular host-guest chemistry exhibited by the flexible cores of enzymatic active sites prompted us to employ a molecular receptor approach for these investigations. In this chapter, we evaluate the thermodynamics of substrate recognition within the Pacman cleft DPD that exhibits lateral preorganization and vertical flexibility. A novel cofacial bisporphyrin platform bridged by a diphenylether spacer (DPP = diporphyrin diphenylether) affords a Pacman system exhibiting both lateral and vertical flexibility. Binding studies of DPD and DPP with pyrimidine-based guests reveal that substrate affinity can be tuned solely by entropic control, and that the large vertical Pacman flexibility of the DPD system can yield highly stable inclusion complexes. Taken together, the results suggest a rich catalytic chemistry for DPD and related cofacial systems with directed flexibility for substrate binding and product release.

## 4.2 Background

Natural enzymes are unrivaled in their capacity to perform multielectron redox reactions and other sophisticated chemical functions.<sup>1</sup> The substantial structural flexibility of these biological machines is vital to their molecular reactivity and specificity. The ability of enzymatic systems to exquisitely modulate their physical shape allows them to direct substrate binding, activation, and/or product release; such dynamic host-guest interactions lead to an induced fit of reaction intermediates to deliver efficient catalytic turnover.<sup>2,3</sup>

The elaborate host-guest chemistry exhibited by these complex biological supramolecules provides motivation for the creation of simple synthetic constructs to catalyze new chemical transformations of substrates docked at an active site.<sup>4,5</sup> One such construct consists of two porphyrins linked in a face-to-face arrangement – cofacial bisporphyrins – to form molecular clefts for the binding and activation of small molecules.<sup>6</sup> Working in concert, facially disposed subunits can provide the oxidizing or reducing equivalents needed to effect the overall multielectron activation of small-molecule substrates. The two major classes of cofacial bisporphyrins are those linked by two or more flexible strapping units<sup>7-33</sup> and Pacman bisporphyrins anchored by a single rigid anthracene or biphenylene spacer.<sup>34-49</sup> The pillared

Pacman DPA and DPB systems have been prominent electrocatalysts for the reduction of a variety of small molecules (e.g., O<sub>2</sub>, N<sub>2</sub>, and H<sub>2</sub>); their exceptional reactivity is based on their ability to impair a lateral displacement of the porphyrin rings, allowing for efficient multielectron small-molecule transformations with little structural reorganization of juxtaposed subunits.<sup>35,36,40-43,48,50-55</sup>

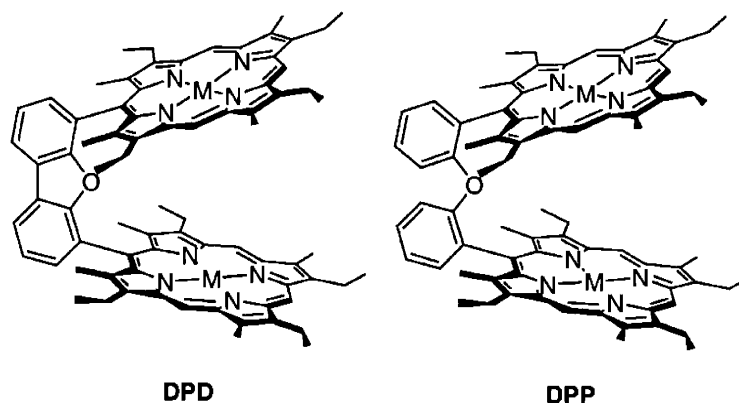
In order to expand the use of such platforms for multielectron catalysis via proton-coupled electron transfer (PCET),<sup>56,57</sup> we became interested in testing the structural limits of pocket flexibility within the Pacman motif. For the cases of the DPA and DPB platforms, a difference in the vertical pocket size of only ca. 1 Å offers a limited range of conformational flexibility for examining structure/reactivity relationships derived from the Pacman effect.<sup>37</sup> Thus, we have recently developed methods for the facile assembly of new cofacial bisporphyrins based on xanthene and dibenzofuran pillars; DPX and DPD afford an unprecedented range of vertical pocket sizes and flexibilities while maintaining a face-to-face arrangement of macrocyclic subunits.<sup>58-60</sup> In particular, the DPD system provided the first direct support for the crucial Pacman effect in a single framework. A comparative structural analysis of biszinc(II) and bisiron(III)  $\mu$ -oxo complexes of DPD demonstrated the remarkable ability of this platform to open and close its binding pocket by a vertical distance of over 4 Å,<sup>59</sup> mimicking the structural induced fit observed in enzymatic catalysis.

To assess further the structure-reactivity contributions of the Pacman effect on multielectron catalysis, we sought to develop the host-guest chemistry of the DPD platform by using stable adducts that are amenable to structural and spectroscopic scrutiny. An attractive starting point is the Lewis acid-base complexes formed between zinc(II) porphyrins and neutral nitrogen donors,<sup>61-63</sup> where multifunctional porphyrin hosts can lead to exceptionally stable inclusion complexes.<sup>23-27,64-77</sup> Especially noteworthy with regard to chemical catalysis is the work of Sanders toward the design of synthetic porphyrin receptors for the templated acceleration of Diels-Alder and other catalytic reactions.<sup>4,27,78-81</sup> For our purposes, we selected pyrimidine-based guests for investigation. Although this basic moiety is ubiquitous in nucleotide chemistry, few artificial receptors based on organometallic derivatives have been synthesized to encapsulate pyrimidine and its derivatives.<sup>82,83</sup> These heterocycles also provide an excellent geometric match for the wedge-shaped DPD framework with their 1,3-nitrogen substitution pattern.

A related Pacman system to DPD is afforded by using a diphenylether bridge (DPP), which is flexible in both horizontal and vertical directions. In this chapter, we now report that dizinc(II) complexes of both DPD and DPP (Chart 4.1) are efficient receptors for pyrimidines. Comparative binding studies of the two platforms suggest that pyrimidine encapsulation by the

DPD framework is accompanied by a reduced entropic penalty compared to DPP and other flexible cofacial bisporphyrin systems, giving rise to a smaller conformational energy cost upon substrate binding while maintaining its unusual vertical Pacman flexibility. These findings support the ability of DPD and related cofacial platforms to accommodate structurally reaction intermediates during multielectron catalysis, and provide a useful framework in which to design additional cofacial bisporphyrin derivatives for small-molecule activation chemistry.

**Chart 4.1**



## 4.3 Results and Discussion

### 4.3.1 Dibenzofuran-Bridged Cofacial Bisporphyrin (DPD) as a Pyrimidine Receptor with Lateral Preorganization and Vertical Flexibility.

Cofacial bisporphyrins anchored by a single dibenzofuran spacer (DPD) are available using the standard three-branch strategy originally developed by Chang<sup>34</sup> and elaborated by Collman,<sup>40</sup> and zinc insertion proceeds in a quantitative manner using standard conditions<sup>84</sup> to give the previously reported Zn<sub>2</sub>DPD (**28**).<sup>59</sup> The regioselective attachment of porphyrin macrocycles at the 4 and 6 positions of dibenzofuran yields a splayed DPD system that displays large vertical pocket sizes (>7.5 Å in metal-metal distances) with minimal lateral displacements of the porphyrin subunits; this architecture provides a complementary host structure for pyrimidine-based guests. For example, the complexation of 2-aminopyrimidine by **28** is readily monitored using <sup>1</sup>H NMR spectroscopy as highlighted in Figure 4.1.

In the presence of up to 1 equiv of the guest, two distinct sets of chemical shifts are observed between 9 and 10 ppm, corresponding to the meso protons of free host **28** ( $\delta = 9.67, 9.71$  ppm) and a single host-guest complex (**42**) ( $\delta = 9.58, 9.63$  ppm). For the latter complex, the proton signals of the guest exhibit significant upfield shifts ( $\delta = -3.7, -0.72$  ppm, 2.4 ppm) compared to



those of the free guest ( $\delta = 4.90, 6.62, 8.30$  ppm), consistent with coordination of the bidentate pyrimidine within the cleft of dimer **28**. The formation of a single complex is observed when the host-guest ratio reaches 1:1, and upon addition of excess guest signals for free guest are only observed in the spectrum. In addition, no changes in signal for the host-guest complex  $\text{Zn}_2(\text{DPD})(2\text{-aminopyrimidine})$  (**42**) are detected in temperature range from  $-20$  to  $40$  °C. Furthermore, a Job plot<sup>85</sup> of the  $^1\text{H}$  NMR titration data (Figure 4.2) shows that the complex is optimally formed at equimolar concentrations of porphyrin host and pyrimidine guest (i.e., a 0.5 mole fraction). Taken together, the data establish the formation of a stable 1:1 complex of **28** and 2-aminopyrimidine.

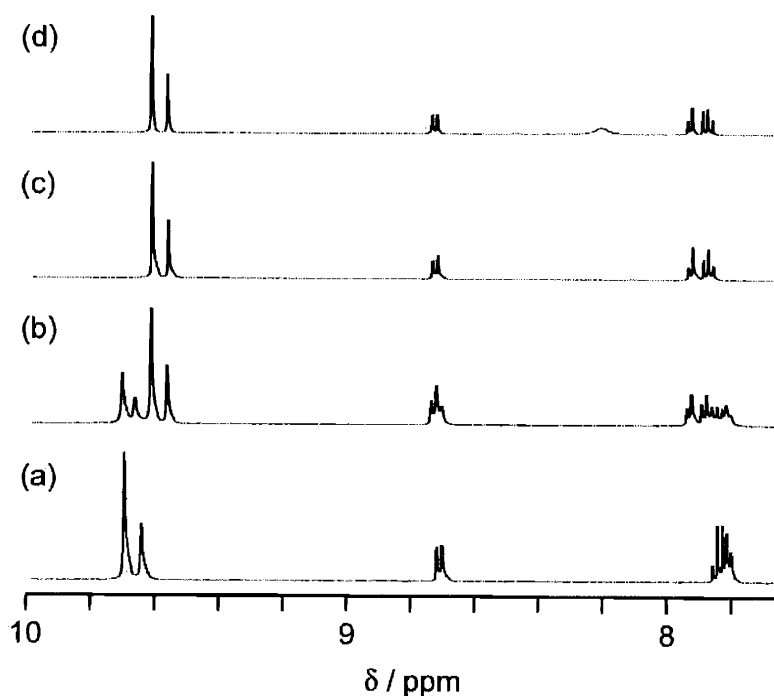


**Figure 4.1.** Selected  $^1\text{H}$  NMR spectra of **28** containing (a) 0, (b) 0.67 eq, (c) 1 eq and (d) 3 eq of 2-aminopyrimidine in  $\text{CD}_2\text{Cl}_2$  solution at  $25$  °C. The spectral range captures the signals for the meso protons of free host **28** and host-guest complex **42**, which are found in the range of 9 to 10 ppm.

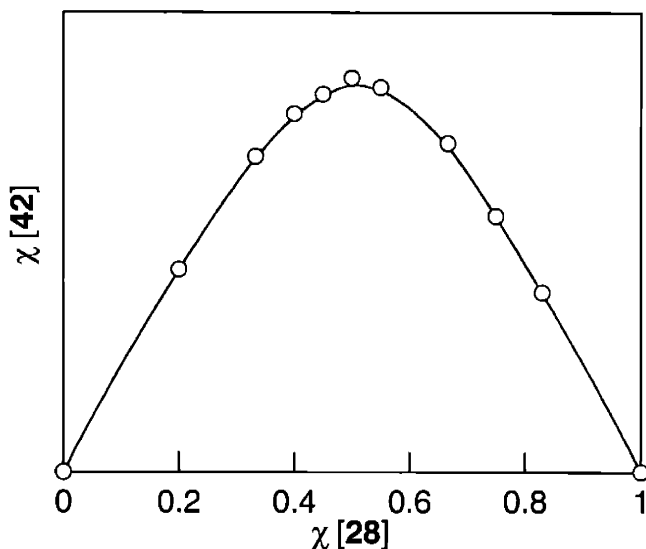


**Figure 4.2.** Job plot establishing the 1:1 stoichiometry for binding of 2-aminopyrimidine guest inside the cleft of host  $\text{Zn}_2(\text{DPD})$  (**28**).

The stability of the host-guest complex  $\text{Zn}_2(\text{DPD})(2\text{-aminopyrimidine})$  (**42**) allows for its facile isolation as an analytically pure solid on a preparative scale in good yield (85%), and material suitable for single-crystal X-ray analysis can be obtained from chloroform/methanol solutions. The structure of complex **42** depicted in Figure 4.3 confirms the encapsulation of 2-aminopyrimidine inside the cavity of bisporphyrin **28**. The structure of free host **28** has been reported previously.<sup>59</sup> The molecular structures of **28** and **42** offer a direct structural comparison for the Pacman effect upon substrate complexation. Crystallographic data are given in Table 4.1, and selected geometrical measurements are given in Table 4.2. Trends in bond lengths and angles of macrocyclic core structures and side chains agree well with those observed in related cofacial bisporphyrins. Specific features of the core structure of  $\text{Zn}_2(\text{DPD})(2\text{-aminopyrimidine})$  (**42**) in relation to  $\text{Zn}_2(\text{DPD})$  (**28**) are highlighted as follows.

The framework of free host  $\text{Zn}_2(\text{DPD})$  (**28**) undergoes a number of noteworthy conformational changes upon ligation of the pyrimidine guest to produce  $\text{Zn}_2(\text{DPD})(2\text{-aminopyrimidine})$  (**42**). The binding of guest triggers a closure of the molecule along a single longitude, affording a complex with a reduced Zn—Zn distance of 6.684 Å (Zn—Zn = 7.775 Å in free host **28**). The tightened conformation also results in compressed distances between the cofacial porphyrin meso carbons connected to the spacer (5.577 Å in **28**, 5.444 Å in **42**). For **42**, the five-coordinate Zn(II) ions adopt a square pyramidal geometry with an average Zn—N<sub>pyrrole</sub> bond length of 2.076 Å. Inequivalent Zn—N<sub>guest</sub> bond distances are observed in solid state (2.257 and 2.346 Å), and the corresponding zinc atoms are displaced towards the guest by 0.3341 and 0.2361 Å,

respectively, from the corresponding  $N_4$  macrocyclic planes. The guest is locked in a coplanar arrangement with the dibenzofuran spacer (dihedral angle =  $0.4^\circ$ ), placing the amino nitrogen of the pyrimidine guest  $3.380 \text{ \AA}$  from the oxygen atom of the dibenzofuran bridge and  $3.398 \text{ \AA}$  from the nearest porphyrinic nitrogen. The key structural feature of **42** in relation to free host **28** is the small torsional twist ( $4.6^\circ$  for **28**,  $1.2^\circ$  for **42**, defined as the torsion angle between the two meso-carbon to spacer bonds) between porphyrinic subunits, giving a host-guest complex in which the only notable conformational change from the free host is in the vertical direction. Taken together,  $Zn_2(DPD)$  (**28**) and  $Zn_2(DPD)(2\text{-aminopyrimidine})$  (**42**) represent a rare pair of structurally homologous biszinc(II) diporphyrin host and host-guest complexes to be characterized by single-crystal X-ray diffraction.<sup>78,79</sup>

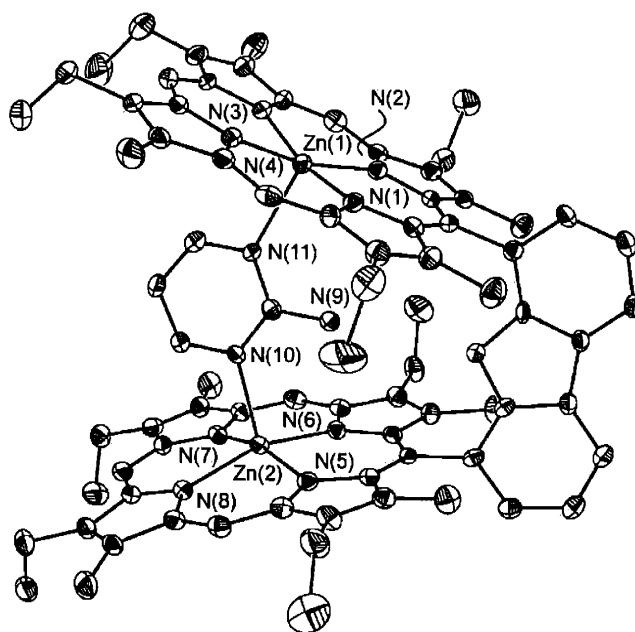


**Figure 4.3.** Crystal structure of  $Zn_2(DPD)(2\text{-aminopyrimidine})$  (**42**). Thermal ellipsoids are drawn at the 25% probability level. Hydrogen atoms have been omitted for clarity.

**Table 4.1** Crystallographic Data for Compounds **39** and **42**.

	<b>39</b>	<b>42</b>
Empirical formula	C <sub>80</sub> H <sub>83</sub> N <sub>11</sub> OZn <sub>2</sub>	C <sub>83</sub> H <sub>84</sub> Cl <sub>9</sub> N <sub>11</sub> OZn <sub>2</sub>
Formula weight	1345.31	1701.40
Temperature	183(2) K	183(2) K
Wavelength	0.71073 Å	0.71073 Å
Crystal system	Monoclinic	Monoclinic
Space group	C2/c	P2(1)/n
Unit cell dimensions	$a = 24.9702(18)$ Å $b = 14.9651(11)$ Å $c = 20.5660(15)$ Å  $\beta = 125.3260(10)^\circ$	$a = 17.9742(3)$ Å $b = 19.1934(3)$ Å $c = 26.1291(10)$ Å  $\beta = 102.1760(10)^\circ$
Volume	6270.1(8) Å <sup>3</sup>	8811.4(2) Å <sup>3</sup>
Z	4	4
Density (calculated)	1.425 Mg/m <sup>3</sup>	1.283 Mg/m <sup>3</sup>
Absorption coefficient	0.825 mm <sup>-1</sup>	0.866 mm <sup>-1</sup>
F(000)	2832	3520
Crystal size	0.25 × 0.23 × 0.13 mm <sup>3</sup>	0.28 × 0.42 × 0.50 mm <sup>3</sup>
θ range for data collection	2.39 to 23.29°	1.54 to 20.00°
Reflections collected	12425	25903
Independent reflections	4513 (R <sub>int</sub> = 0.0686)	8209 (R <sub>int</sub> = 0.0433)
Data / restraints / params	4513 / 0 / 401	8209 / 6 / 993
Goodness-of-fit on F <sup>2</sup>	1.048	1.107
Final R indices [I > 2σ(I)]	RI = 0.0364 wR2 = 0.1013	RI = 0.0863 wR2 = 0.2434
R indices (all data)	RI = 0.0387 wR2 = 0.1034	RI = 0.0943 wR2 = 0.2503
Largest diff peak	0.368 eÅ <sup>-3</sup>	1.384 eÅ <sup>-3</sup>
Largest diff hole	-0.611 eÅ <sup>-3</sup>	-0.708 eÅ <sup>-3</sup>

**Table 4.2a.** Selected Bond Lengths (Å) and Angles (deg) for Compound **39**.

<i>Bond Lengths (Å)</i>		<i>Bond Angles (deg)</i>			
Zn(1)–N(1)	2.041(2)	N(1)–Zn(1)–N(2)	91.57(8)	C(1)–N(1)–Zn(1)	128.5(2)
Zn(1)–N(2)	2.034(2)	N(1)–Zn(1)–N(4)	88.86(8)	C(6)–N(2)–Zn(1)	125.9(2)
Zn(1)–N(3)	2.052(2)	N(2)–Zn(1)–N(4)	178.6(7)	C(9)–N(2)–Zn(1)	128.3(2)
Zn(1)–N(4)	2.027(2)	N(1)–Zn(1)–N(3)	176.7(7)	C(11)–N(3)–Zn(1)	127.4(2)
O(1)–C(26)	1.373(3)	N(2)–Zn(1)–N(3)	88.49(8)	C(14)–N(3)–Zn(1)	126.3(2)
N(2)–C(6)	1.378(3)	N(3)–Zn(1)–N(4)	90.99(8)	C(16)–N(4)–Zn(1)	125.3(2)
N(2)–C(9)	1.368(3)	C(4)–N(1)–Zn(1)	124.1(2)	C(19)–N(4)–Zn(1)	127.9(2)
N(4)–C(16)	1.372(3)				
N(4)–C(19)	1.382(3)				

**Table 4.2b.** Selected Bond Lengths (Å) and Angles (deg) for Compound **42**.

<i>Bond Lengths (Å)</i>		<i>Bond Angles (deg)</i>			
Zn(1)–N(1)	2.064(6)	N(1)–Zn(1)–N(2)	87.4(2)	N(4)–Zn(1)–N(3)	87.0(3)
Zn(1)–N(2)	2.067(6)	N(1)–Zn(1)–N(4)	90.0(2)	N(1)–Zn(1)–N(11)	101.7(2)
Zn(1)–N(3)	2.105(6)	N(2)–Zn(1)–N(4)	163.0(2)	N(2)–Zn(1)–N(11)	101.8(2)
Zn(1)–N(4)	2.090(7)	N(1)–Zn(1)–N(3)	160.3(2)	N(4)–Zn(1)–N(11)	95.2(2)
Zn(1)–N(11)	2.262(6)	N(2)–Zn(1)–N(3)	89.8(3)	N(3)–Zn(1)–N(11)	98.0(2)
Zn(1)–N(1)	2.064(6)	N(5)–Zn(2)–N(6)	87.8(3)	N(5)–Zn(2)–N(8)	90.7(3)
Zn(2)–N(5)	2.064(6)	N(5)–Zn(2)–N(7)	166.7(2)	N(6)–Zn(2)–N(8)	167.3(2)
Zn(2)–N(6)	2.065(6)	N(6)–Zn(2)–N(7)	91.0(3)	N(7)–Zn(2)–N(8)	87.6(3)
Zn(2)–N(7)	2.069(7)				
Zn(2)–N(8)	2.084(7)				
Zn(2)–N(10)	2.345(6)				

The binding between Zn<sub>2</sub>(DPD) (**28**) and 2-aminopyrimidine can also be conveniently studied by using absorption spectroscopy. The addition of 2-aminopyrimidine results in significant red shifts for the Soret (399 to 406 nm) and Q band (533 and 570 to 539 and 575 nm, respectively) manifolds (Figure 4.4), indicative of axial nitrogen coordination to a zinc(II) porphyrin.

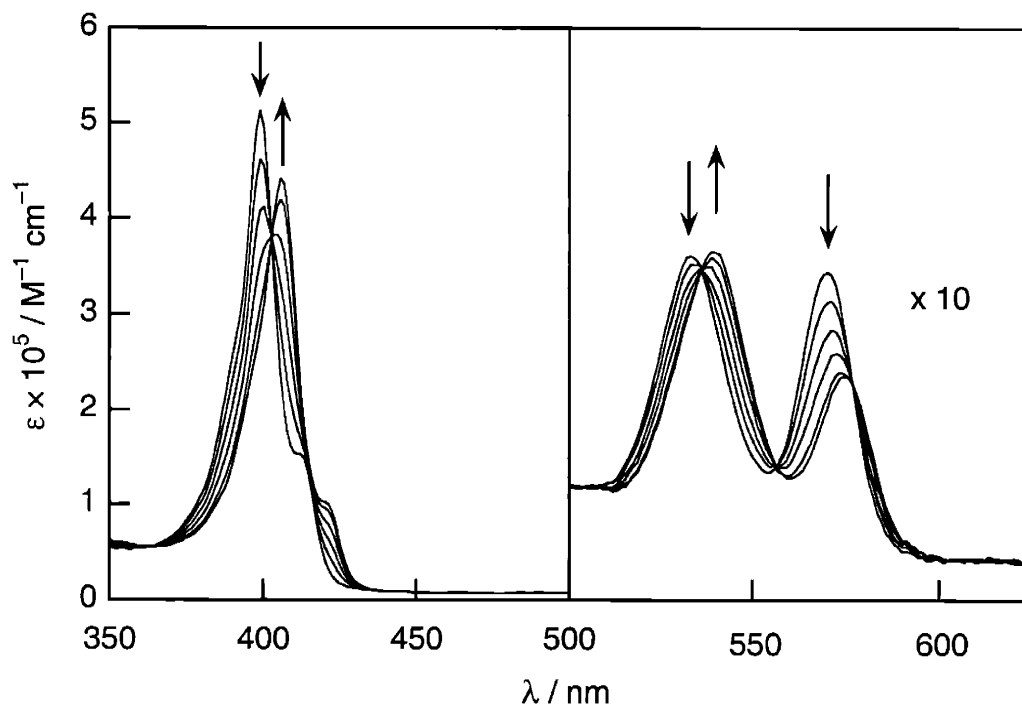


**Figure 4.4.** Absorption spectra of **28** in the presence of 0, 0.2, 0.4, 0.6, 0.8, and 1.0 eq of 2-aminopyrimidine in toluene solution at 25 °C. The final spectrum does not change upon further additions of 2-aminopyrimidine.

Well anchored isosbestic points over the entire range of binding isotherms indicate the existence of an equilibrium between the host and the 1:1 host-guest complex. Furthermore, a Hill plot<sup>86</sup> of  $\ln[(A_I - A)/(A - A_F)]$  yields a slope of  $1.00 \pm 0.03$ , indicating a simple binding process with no cooperativity. The high association constant,  $K_A = 9.6 (7) \times 10^7 \text{ M}^{-1}$ , is among the highest observed for the binding of nitrogen heterocycles to zinc(II) porphyrin-based hosts<sup>26,27,76</sup> and is unprecedented for coordination of the relatively weak pyrimidine base ( $\text{p}K_a = 3.5$ ),<sup>87</sup> attesting to the efficacy of the complementary wedge shape provided by the DPD cleft and its facile vertical Pacman closure to provide a stable host-guest adduct. Related dibasic heterocycles such as pyrazine and pyrimidines with increased steric hinderance at the 2-position (e.g. NMe<sub>2</sub>, OMe) show marginal affinity for the DPD cleft. A standard van't Hoff plot of temperature dependent

data give the thermodynamic parameters  $\Delta H^\circ = -63 \pm 6$  kJ/mol and  $\Delta S^\circ = -61 \pm 12$  J/mol·K. Notably, the entropic penalty associated with formation of host-guest complex  $\text{Zn}_2(\text{DPD})(2\text{-aminopyrimidine})$  (**42**) via a single, vertical Pacman motion is small in comparison to binding ditopic ligands to doubly-strapped biszinc(II) porphyrin receptors ( $\Delta S^\circ \sim -100$  to  $130$  J/mol·K) with multiple degrees of freedom.

A series of 2-substituted pyrimidines coordinate within the pocket of  $\text{Zn}_2(\text{DPD})$  (**28**), with association constants ranging over 5 orders of magnitude; the data are given in Table 4.3. The results reveal the general trend that more basic pyrimidines associate more strongly to host **28**, although no strict linear relationship was found between guest  $\text{p}K_a$  and binding affinity to **28**. In fact, it is interesting to note the significant differences in binding affinity (*ca.* 1400-fold) between 2-aminopyrimidine and its 5-isomer despite comparable  $\text{p}K_a$  values (3.5 for the 2-isomer, 2.8 for the 5-isomer). As the structure of **36** shows that the 2-amino group is not within standard hydrogen-bonding distances ( $< 3$  Å) of either the dibenzofuran bridge oxygen (3.380 Å) or the porphyrin nitrogens (3.398 Å), the data suggest that more subtle polar cavity effects or solvation may play a role in this host-guest stabilization.

**Table 4.3.** Association constants for binding of various pyrimidines to  $\text{Zn}_2(\text{DPD})$  (**28**) in  $\text{CH}_2\text{Cl}_2$  at 25 °C.

Guest	$K_A / \text{M}^{-1}$
2-aminopyrimidine	$9.6(7) \times 10^7$
pyrimidine	$4.0(2) \times 10^4$
2-chloropyrimidine	$6.2(1) \times 10^2$
2-bromopyrimidine	$7.0(1) \times 10^2$
5-aminopyrimidine	$7.0(1) \times 10^4$

Density functional theory (DFT) calculations were carried out to further probe the origin of the stability of host-guest complex  $\text{Zn}_2(\text{DPD})(2\text{-aminopyrimidine})$  (**42**). Surprisingly, Mulliken population analysis reveals the absence of significant overlap population along the internuclear axis of the 2-amino guest group and the dibenzofuran bridge oxygen, despite their proximity (3.380 Å). Instead significant overlap is present between the 2-aminopyrimidine nitrogen and the two proximal meso carbons C(5) and C(25) directly connected to the spacer, as well as the adjacent  $\alpha$ -pyrrolic carbons C(4), C(6), C(24), and C(26). The sum of the Mulliken overlap populations between 2-aminopyrimidine nitrogen and the aforementioned carbon atoms is 0.108 e; for comparison, the average Zn—N<sub>guest</sub> overlap population is 0.218 e. These data suggest that

the origin of the thermodynamically favorable host-guest interaction is a strong non-covalent interaction between the 2-aminopyrimidine nitrogen and the proximal carbons of the bisporphyrin framework. In addition, the strong non-covalent host-guest interaction could in turn be attributed to an increase in electronic charge of the porphyrinic subunits upon binding of the guest ( $-0.188$  e in **28**,  $+0.171$  e in **42**). Since binding of the pyrimidine guest to the bisporphyrin host leads to further stabilization of the host-guest complex, the host-guest interaction can be seen as being a synergistic one.

### 4.3.2 Diphenylether-Bridged Cofacial Bisporphyrin (DPP) as a Pyrimidine Receptor with Lateral and Vertical Flexibility

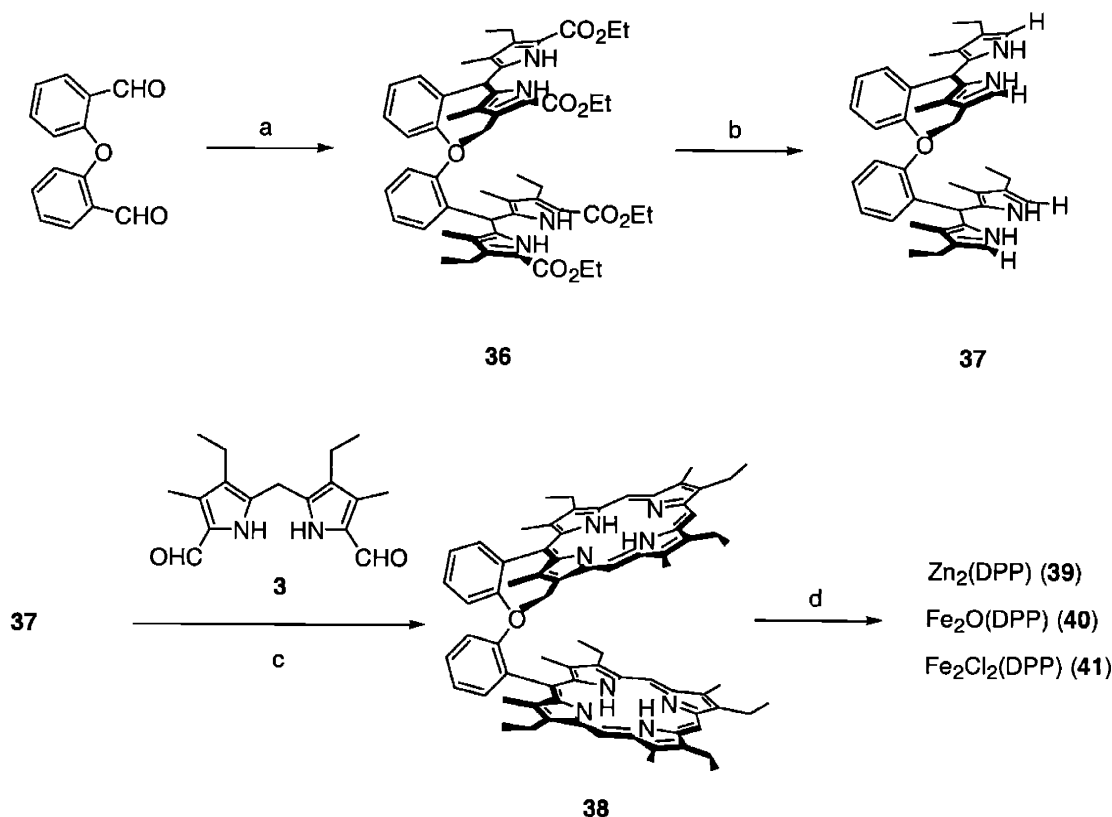
We wished to compare the host-guest chemistry of  $\text{Zn}_2(\text{DPD})$  (**28**) to a chemically similar dizinc(II) cofacial complex where the bite size of the cleft is not vertically preorganized for substrate binding. Bisporphyrins bearing a diphenylether (DPP = diporphyrin diphenylether) spacer are suitable in this regard, as this bridge provides the same chemical connectivity as dibenzofuran while yielding a Pacman system with both horizontal and vertical flexibility. Although the steric hinderance of the 6,6' protons of diphenylether precludes a planar structure and hence a strict quantitative comparison of binding energetics for DPD and DPP, the relative affinities for substrate inclusion can provide a basis for predicting multielectron reactivity.

The synthesis of a DPP cofacial bisporphyrin containing a diphenylether spacer follows the traditional three-branch strategy as outlined in Scheme 4.1. The acid-catalyzed reaction of bis(2-formylphenyl) ether with 4 equiv of pyrrole **2** in boiling ethanol affords the corresponding ester-protected bis(pyrryl)methane **36** in 86% yield. Removal of the  $\alpha$ -ethyl esters of **36** with sodium hydroxide in ethylene glycol delivers the  $\alpha$ -free tetrapyrrole **37** in 85% yield. The MacDonald-type condensation of **37** with dipyrromethane dialdehyde **3** in the presence of *p*-toluenesulfonic acid (PTSA) followed by oxidation with *o*-chloranil provides bisporphyrin  $\text{H}_4(\text{DPP})$  (**38**) in 19% yield. Free-base porphyrin **38** gave satisfactory high-resolution mass spectral and elemental analyses. The  $^1\text{H}$  NMR spectrum of **38** is consistent with a flexible, splayed structure in solution; the internal NH pyrrolic resonances of **38** are only slightly upshifted ( $-3.49$ ,  $-4.37$  ppm) compared to monomeric porphyrins. In addition, the broad NMR peaks for the meso protons of **38** are also indicative of a freely rotating structure.

Bimetallic complexes of the DPP framework are synthesized by reaction of the free-base porphyrin **38** with metal salt precursors. For example,  $\text{Zn}_2(\text{DPP})$  (**39**) is obtained in quantitative yield from reaction of **38** with  $\text{Zn}(\text{OAc})_2 \cdot 2\text{H}_2\text{O}$ .  $^1\text{H}$  NMR spectroscopy and high-resolution mass spectral and elemental analyses characterized the formation of **39**. Reaction of free base **38** with



FeBr<sub>2</sub> followed by treatment with basic alumina yields the corresponding bis-Fe(III)  $\mu$ -oxo complex Fe<sub>2</sub>O(DPP) (**40**) in high yield (84%). The bischloroiron(III) compound Fe<sub>2</sub>Cl<sub>2</sub>(DPP) (**41**) is prepared in 83% yield using a similar procedure as **40** but with an acidic workup. Iron complexes **40** and **41** were characterized using high-resolution mass spectrometry.



**Scheme 4.1.** (a) **2**, HCl, ethanol, reflux; (b) NaOH, ethylene glycol, reflux; (c) i. **3**, PTSA, methanol; ii. *o*-chloranil; iii. Zn(OAc)<sub>2</sub>•2H<sub>2</sub>O/methanol; iv. HCl; (d) MX<sub>2</sub>.

Additional structural characterization of the DPP platform is provided by a single-crystal X-ray diffraction analysis of the biszinc(II) compound Zn<sub>2</sub>(DPP) (**39**) (Figure 4.5). Crystallographic data are provided in Table 4.1, and geometric parameters are displayed in Table 4.2. The flexible diphenylether bridge allows the porphyrin subunits to stack in a parallel fashion to maximize  $\pi$ -overlap, giving a mean interplanar distance of 3.630 Å with a small interplanar angle of 1.2°. The structure confirms that the DPP framework exhibits little lateral preorganization. In contrast to the analogous DPD complex Zn<sub>2</sub>(DPD) (**28**), the porphyrin rings in DPP compound **39** are not arranged in a face-to-face manner, as evidenced by the large torsional twist for the latter (63.2° for **39**, 1.2° for **28**). The significant lateral displacement results an expanded metal—metal

distance of 6.185 Å. The porphyrin cores display normal structural parameters. The zinc(II) ions are four-coordinate, with an average Zn—N<sub>pyrrole</sub> bond lengths of 2.038 Å. The Zn is raised 0.1252 Å out of 24-atom macrocyclic plane, which has a mean deviation of 0.1672 Å.

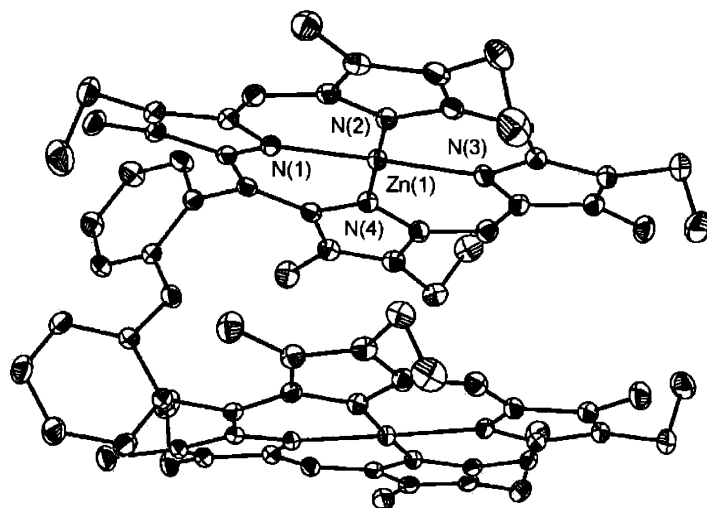


**Figure 4.5.** Crystal structure of Zn<sub>2</sub>(DPP) (**39**). Thermal ellipsoids are drawn at the 25% probability level. Hydrogen atoms and solvent molecules within the lattice have been omitted for clarity.

With this structural information in hand, we set out to evaluate the DPP system as a pyrimidine receptor. UV-visible spectroscopy reveals a simple binding process for the association of 2-aminopyrimidine to dizinc(II) host Zn<sub>2</sub>(DPP) (**39**). A 1:1 complex forms with no cooperativity between the two binding sites (Hill plot slope = 0.99 ± 0.02). Remarkably, the association constant  $K_A = 3.5 (1) \times 10^4 \text{ M}^{-1}$  is more than *3 orders of magnitude smaller* than that found for Zn<sub>2</sub>(DPD) (**28**). The thermodynamic nature of this dramatic change in binding affinity is revealed by temperature dependent experiments ( $\Delta H^\circ = -62 \pm 2 \text{ kJ/mol}$  and  $\Delta S^\circ = -125 \pm 8 \text{ J/mol}\cdot\text{K}$ ). The comparable enthalpic terms indicate that the ca. 3000-fold difference in host-guest complex stabilities between DPD and DPP is due solely to a substantial variation (~60 J/mol·K) in entropic energies. The structural studies are in support of this contention; for comparison, Figure 4.6 depicts two mutually perpendicular views of the molecular structures of the free hosts **28** and **39** and the host-guest complex **42**. These data establish that substrate binding to yield a 1:1 adduct within the DPD pocket requires a simple vertical Pacman closure, while substrate complexation to the DPP cleft most likely involves significant lateral and vertical rearrangement.

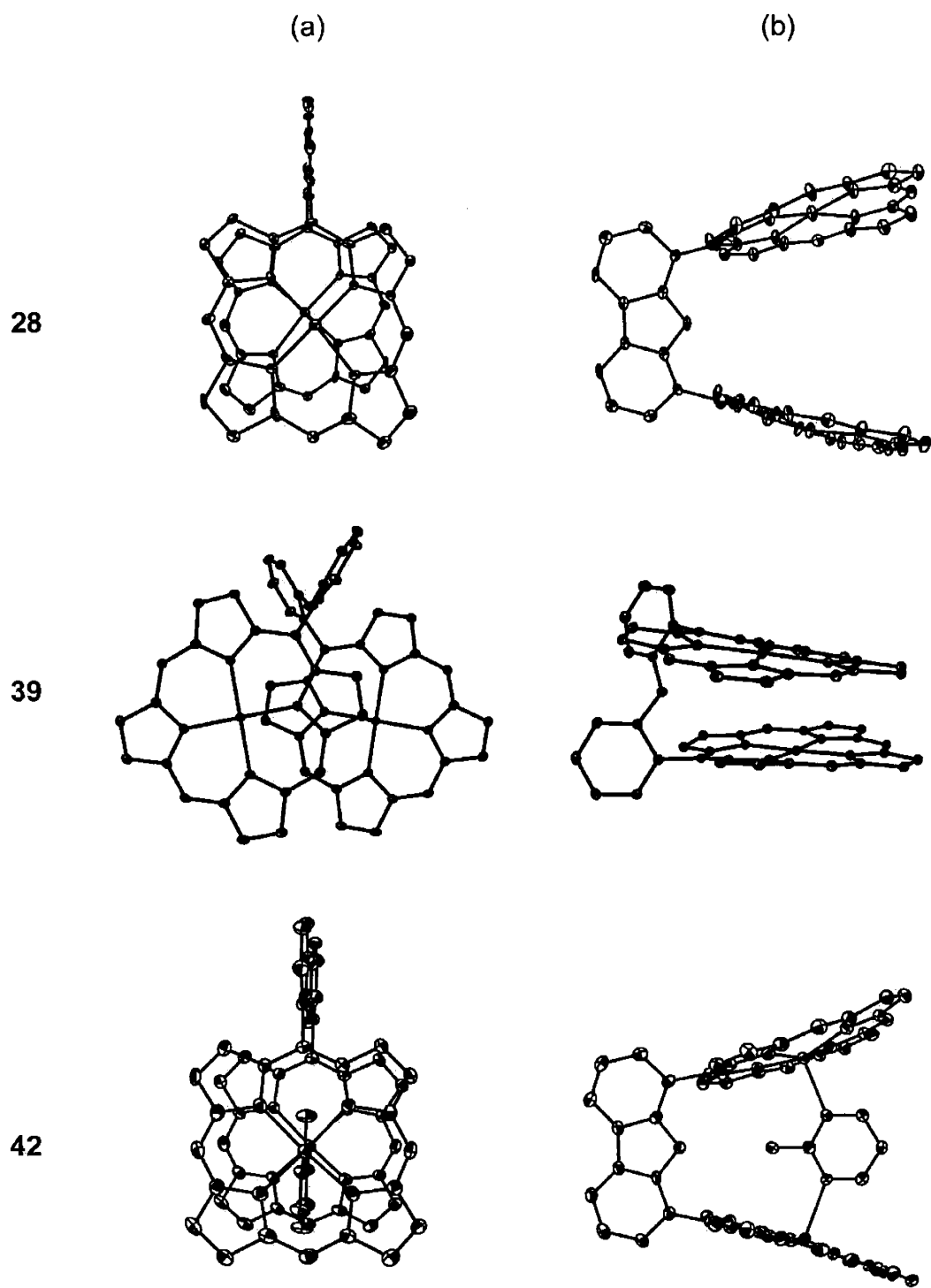


**Figure 4.6.** Comparative views of the crystal structures of Zn<sub>2</sub>(DPD) (**28**), Zn<sub>2</sub>(DPP) (**39**), Zn<sub>2</sub>(DPD)(2-aminopyrimidine) (**42**): (a) top view; (b) side view, perpendicular to the bridge plane. Hydrogen atoms omitted for clarity.

## 4.4. Concluding Remarks

The multielectron reactivity of the cofacial bisporphyrin motif is dictated by the capacity of the spacer to create a suitable microenvironment for mediating dynamic host-guest chemistry during catalysis.<sup>6</sup> The DPD architecture has unprecedented vertical flexibility for a pillared cofacial system while preserving a face-to-face arrangement of macrocyclic subunits, a unique structural attribute that promises a rich catalytic chemistry. In this study, we have explored the energetic virtues towards such a structure-function synergy by elaborating the host-guest chemistry of DPD and related Pacman platforms using zinc(II) derivatives and basic nitrogen donors.

We find that the vertical Pacman flexibility of DPD is accompanied by a relatively small conformational energy, and that substrate binding within the cofacial pocket can be tuned solely by entropic contributions. By confining the diporphyrin host to a single, vertical degree of freedom, the entropic gain of DPD over flexible cofacial counterparts is observed to be *ca.* 60 J/mol•K with negligible differences in enthalpy, leading to overall binding affinities that differ by over 3 orders of magnitude. These results presage a notable bimetallic reactivity for the DPD platform toward small molecule substrates owing to its unique ability to undergo a substantial Pacman rearrangement along a single longitudinal coordinate upon ligation, while maintaining a cofacial presentation of porphyrin subunits. In a more general sense, this work proposes directed host flexibility as an important structural feature in the design of architectures for catalytic reaction chemistry. Efforts to exploit the unique properties of the DPD system and related complexes in multielectron catalysis are in progress.

## 4.5 Experimental Section

### 4.5.1 Materials

Silica gel 60 (70-230 and 230-400 mesh, Merck) was used for column chromatography. Analytical thin layer chromatography was performed using Merck 60 F254 silica gel (precoated sheets, 0.2 mm thick). Solvents for synthesis were of reagent grade or better, and were dried according to standard methods.<sup>88</sup> Spectroscopic experiments employed toluene or dichloromethane (spectroscopic grade, Burdick & Jackson), which were stored over 4 Å molecular sieves. The starting materials 2-(ethyloxycarbonyl)-3-ethyl-4-methylpyrrole (**2**), 3,3'-diethyl-5,5'-diformyl-4,4'-dimethyl-2,2'-dipyrrylmethane (**3**), and the porphyrin Zn<sub>2</sub>(DPD) (**28**) were synthesized as described in chapter 2. All other reagents were used as received.

#### 4.5.2 2,2'-Bis[5,5'-bis(ethyloxycarbonyl)-4,4'-diethyl-3,3'-dimethyl-2,2'-dipyrrylmethyl]diphenylether (36)

Bis(2-formylphenyl) ether (1.13 g, 5 mmol) and pyrrole 2 (3.6 g, 20 mmol, 4 equiv) were added to absolute ethanol (75 mL) containing conc HCl (1.2 mL). The resultant mixture was refluxed under nitrogen for 5 h and cooled in an ice-water bath. Water (25 mL) was added and the precipitate was filtered by suction and washed with cold methanol to afford crude **36** as a pink powder (4.1 g, 86% yield), which was used without further purification. <sup>1</sup>H NMR (500 MHz, CDCl<sub>3</sub>, 25 °C):  $\delta$  = 8.51 (br s, 4H, NH), 7.01-7.07 (m, 6H, ArH), 6.24 (d, 2H, ArH), 5.74 (s, 2H, CH), 4.25 (q, 8H, CH<sub>2</sub>), 2.69 (q, 8H, CH<sub>2</sub>), 1.70 (s, 12H, CH<sub>3</sub>), 1.30 (t, 12H, CH<sub>3</sub>), 1.05 (t, 12H, CH<sub>3</sub>).

#### 4.5.3 2,2'-Bis[4,4'-diethyl-3,3'-dimethyl-2,2'-dipyrrylmethyl]diphenylether (37)

Powdered NaOH (4 g) and **36** (4 g, 4.4 mmol) were suspended in 40 mL of ethylene glycol and 4 mL of distilled water, and the mixture was refluxed under nitrogen overnight. The reaction was cooled to room temperature and water (100 mL) was added. The precipitate was collected by suction filtration, washed with water until the washings became neutral, and dried under vacuum over KOH. The product **37** was obtained as a goldenrod solid (2.33 g, 85% yield). It was stored under nitrogen at -20 °C. <sup>1</sup>H NMR (500 MHz, CDCl<sub>3</sub>, 25 °C):  $\delta$  = 7.38 (br s, 4H, NH), 6.96-7.08 (m, 6H, ArH), 6.38 (d, 2H, ArH), 6.26 (br s, 4H, CH), 5.62 (s, 2H, CH), 2.38 (q, 8H, CH<sub>2</sub>), 1.78 (s, 12H, CH<sub>3</sub>), 1.13 (t, 12H, CH<sub>3</sub>).

#### 4.5.4 2,2'-Bis[(5-(2,3,13,17-tetraethyl-3,7,12,18-tetramethylporphyrinyl))]diphenylether, H<sub>4</sub>(DPP) (38)

A suspension of dipyrromethane dialdehyde **3** (1.14 g, 4 mmol) and **37** (1.25 g, 2 mmol) in 400 mL of dry methanol was purged with nitrogen for 45 min. A solution of *p*-toluenesulfonic acid (0.89 g) in methanol (18 mL) was added dropwise over a period of 1 h. The resulting dark red mixture was stirred in the dark under nitrogen for 2 days. Solid *o*-chloranil (0.89 g) was added in one portion and stirring was continued in air for 1 day. The mixture was taken to dryness and redissolved in 200 mL of chloroform. A saturated methanolic solution of Zn(OAc)<sub>2</sub>•2H<sub>2</sub>O (10 mL) was added and the mixture was refluxed for 3 h. The solvent was removed and the remaining residue was purified by flash column chromatography (silica gel, 1:1 hexanes/dichloromethane). The first band eluted was collected and vigorously stirred with 4 N HCl (10 mL) for 30 min. The organic phase was separated, washed with water (7 × 50 mL), dried over Na<sub>2</sub>SO<sub>4</sub> and taken to dryness. Purification by flash column chromatography (silica gel, dichloromethane to 5% methanol/dichloromethane) followed by recrystallization from

dichloromethane/methanol yielded pure **38** as royal purple microcrystals (420 mg, 19% yield).  $^1\text{H}$  NMR (500 MHz,  $\text{CDCl}_3$ , 25 °C):  $\delta$  = 10.03 (s, 2H, meso), 8.48 (br s, 4H, meso), 8.05 (d, 2H, ArH), 7.74-7.77 (m, 2H, ArH), 7.17-7.24 (m, 4H, ArH), 4.12-4.31 (m, 8H,  $\text{CH}_2$ ), 3.34 (s, 12H,  $\text{CH}_3$ ), 2.00 (t, 12H,  $\text{CH}_3$ ), 1.54-1.60 (m, 20H,  $\text{CH}_2$ ,  $\text{CH}_3$ ), 1.26 (s, 12H,  $\text{CH}_3$ ), -3.49 (s, 2H, NH), -4.37 (s, 2H, NH). Anal. Calcd for  $\text{C}_{76}\text{H}_{82}\text{N}_8\text{O}$ : C, 81.25; H, 7.36; N, 9.97. Found: C, 81.46, H, 7.37; N, 9.82. HRESIMS ( $\text{MH}^+$ ) calcd for  $\text{C}_{76}\text{H}_{83}\text{N}_8\text{O}$   $m/z$  1123.6690, found 1123.6676.

#### 4.5.5 $\text{Zn}_2(\text{DPP})$ (**39**)

A saturated methanolic solution of  $\text{Zn}(\text{OAc})_2 \cdot 2\text{H}_2\text{O}$  (1 mL) and a solution of **38** (100 mg, 0.08 mmol) in 15 mL chloroform were combined and refluxed for 1 h. The solvent was removed by rotary evaporation. The remaining solid was purified by flash column chromatography (silica gel, 2:1 dichloromethane/hexanes) followed by recrystallization from dichloromethane/methanol to yield analytically pure **39** as a cherry red solid in essentially quantitative yield.  $^1\text{H}$  NMR (500 MHz,  $\text{CDCl}_3$ , 25 °C):  $\delta$  = 10.11 (s, 2H, meso), 8.13 (d, 2H, ArH), 8.05 (br s, 4H, meso), 7.76 (t, 2H, ArH), 7.16 (t, 2H, ArH), 7.11 (d, 2H, ArH), 4.39-4.42 (m, 4H,  $\text{CH}_2$ ), 4.14-4.19 (m, 4H,  $\text{CH}_2$ ), 3.23 (br s, 12H,  $\text{CH}_3$ ), 1.95 (t, 12H,  $\text{CH}_3$ ), 1.73 (br, 12 H,  $\text{CH}_2$ ), 1.27 (m, 20H,  $\text{CH}_2$ ,  $\text{CH}_3$ ). Anal. Calcd for  $\text{C}_{76}\text{H}_{78}\text{N}_8\text{OZn}_2$ : C, 73.01; H, 6.29; N, 8.96. Found: C, 72.82, H, 6.15; N, 9.20. HRESIMS ( $\text{MH}^+$ ) calcd for  $\text{C}_{76}\text{H}_{83}\text{N}_8\text{OZn}_2$   $m/z$  1246.4881, found 1246.4830.

#### 4.5.6 $\text{Fe}_2\text{O}(\text{DPP})$ (**40**)

In a dry box, **38** (100 mg, 0.08 mmol), 2,6-lutidine (0.2 mL),  $\text{FeBr}_2$  (250 mg), and THF (15 mL) and benzene (15 mL) were loaded in 50-mL flask equipped with a condenser. The mixture was refluxed under nitrogen for 12 h, opened to air, and brought to dryness under vacuum. The residue was purified using basic alumina (activity I, chloroform) to give **40** as brown solid (93 mg, 84% yield). HRFABMS ( $[\text{M}-\text{O}]^+$ ) calcd for  $\text{C}_{76}\text{H}_{78}\text{Fe}_2\text{N}_8\text{O}_2$   $m/z$  1230.4997, found 1230.5124.

#### 4.5.7 $\text{Fe}_2\text{Cl}_2(\text{DPP})$ (**41**)

In a dry box, a 100-mL flask equipped with a condenser was charged with **38** (100 mg, 0.08 mmol), 2,6-lutidine (0.2 mL),  $\text{FeBr}_2$  (200 mg), THF (12 mL) and benzene (12 mL). The mixture was refluxed under nitrogen for 12 h, opened to air, and brought to dryness under vacuum. The residue was taken up in a 1:1 mixture of dichloromethane/water (50 mL). The organic layer was separated, washed with water ( $3 \times 50$  mL), and stirred with 3 N HCl (25 mL) for 90 min. The organic layer was decanted and solvent was removed under vacuum. The remaining solid was purified by column chromatography (silica gel, dichloromethane to 5% methanol/dichloromethane) and retreated with HCl as described above. The organic phase was

separated, washed with water (3 × 50 mL), dried over Na<sub>2</sub>SO<sub>4</sub>, and taken to dryness. Recrystallization from dichloromethane and ether afforded pure **41** as a brown powder (96 mg, 83% yield). HRFABMS ([M–Cl]<sup>+</sup>) calcd for C<sub>76</sub>H<sub>78</sub>Cl<sub>2</sub>Fe<sub>2</sub>N<sub>8</sub>O *m/z* 1265.4686, found 1265.4702.

#### 4.5.8 Zn<sub>2</sub>(DPD)(2-aminopyrimidine) (**42**)

Chloroform (10 mL) was added to solid mixture of Zn<sub>2</sub>(DPD) (**28**) (50 mg, 0.04 mmol) and 2-aminopyrimidine (3.8 mg, 0.04 mmol). The resulting solution was layered with hexanes (20 mL) and placed in the –20 °C freezer for 2 days. A crop of ruby red crystals was isolated by gravity filtration, washed with cold hexanes (2 × 10 mL) and dried under vacuum to furnish analytically pure **42** (46 mg, 85% yield). <sup>1</sup>H NMR (500 MHz, CD<sub>2</sub>Cl<sub>2</sub>, 25 °C): δ = 9.63 (s, 4H, meso), 9.58 (s, 2H, meso), 8.74 (d, 2H, ArH), 7.94 (t, 2H, ArH), 7.88 (d, 2H, ArH), 3.72–3.87 (m, 20H, CH<sub>2</sub>), 3.30 (s, 12H, CH<sub>3</sub>), 2.43 (br s, 1H, PymH), 2.32 (s, 12H, CH<sub>3</sub>), 1.58 (t, 12H, CH<sub>3</sub>), 1.51 (t, 12H, CH<sub>3</sub>), –0.73 (m, 2H, PymH), –3.70 (br s, 2H, NH<sub>2</sub>). Anal. Calcd for C<sub>80</sub>H<sub>81</sub>N<sub>11</sub>OZn<sub>2</sub>: C, 71.53; H, 6.08; N, 11.47. Found: C, 71.16; H, 6.03; N, 11.53.

#### 4.5.9 General Details of X-Ray Data Collection and Reduction

X-ray diffraction data were collected using a Siemens Circle 3 diffractometer equipped with a CCD detector. Measurements were carried out at –90° C using Mo Kα (λ = 0.71073 Å) radiation, which was wavelength selected with a single-crystal graphite monochromator. Four sets of data were collected using ω scans and a –0.3° scan width. All calculations were performed using a Silicon Graphics Indigo 2 or a PC workstation. The data frames were integrated to hkl/intensity and final unit cells were calculated by using the SAINT v.4.050 program from Siemens. The structures were solved and refined with the SHELXTL v.5.03 suite of programs developed by G. M. Sheldrick and Siemens Industrial Automation, Inc., 1995.

#### 4.5.10 X-ray Structure of Zn<sub>2</sub>(DPP) (**39**)

A single crystal of **39** was obtained by slow diffusion of methanol into a solution of the compound in dichloromethane. Empirical formula: C<sub>76</sub>H<sub>78</sub>N<sub>8</sub>OZn<sub>2</sub>, MW = 1345.31. monoclinic, C2/c, Z = 4, a = 24.9702(18) Å, b = 14.9651(11) Å, c = 20.5660(15) Å, β = 125.3260(10)°, V = 6270.1(8) Å<sup>3</sup>, ρ<sub>calc</sub> = 1.425 g/cm<sup>3</sup>, F(000) = 2832. Crystal dimension: 0.25 mm × 0.23 mm × 0.13 mm. A total of 12425 reflections were collected in the θ range of 2.39° to 23.29°, of which 4513 were unique (R<sub>int</sub> = 0.0686). The structure was solved by direct methods in conjunction with standard difference Fourier techniques. Hydrogen atoms were placed in calculated positions using a standard riding model and were refined isotropically. The largest peak and hole in the

difference map were  $0.368 \text{ e}\text{\AA}^{-3}$  and  $-0.611 \text{ e}\text{\AA}^{-3}$ , respectively. The least squares refinement converged normally giving residuals of  $R = 0.0387$ ,  $wR^2 = 0.1034$ , and  $\text{GOF} = 1.048$ .

#### 4.5.11 X-ray Structure of $\text{Zn}_2(\text{DPD})(2\text{-aminopyrimidine})$ (42)

A  $0.28 \text{ mm} \times 0.42 \text{ mm} \times 0.50 \text{ mm}$  ruby red crystal was obtained by slow diffusion of hexane into a chloroform solution of the complex. The crystal was coated in Paratone N and mounted onto a glass fiber. A total of 25903 reflections were collected in the  $\theta$  range of  $1.54^\circ$  to  $20.0^\circ$ , of which 8209 were unique ( $R_{\text{int}} = 0.0433$ ). The structure was solved by direct methods in conjunction with standard difference Fourier techniques. Hydrogen atoms were placed in calculated positions using a standard riding model and were refined isotropically. Three chloroform molecules were found in the crystal and one of them was found to be disordered. This molecule was assigned half occupancy at two symmetry-equivalent positions. Restraints were applied to one the solvent molecule by using SADI command of SHELXTL. The largest peak and hole in the difference map were  $1.384 \text{ e}\text{\AA}^{-3}$  and  $-0.708 \text{ e}\text{\AA}^{-3}$ , respectively. The crystal data for  $\text{C}_{83}\text{H}_{84}\text{Cl}_9\text{N}_{11}\text{OZn}_2$ : monoclinic,  $P2_1/n$ ,  $Z = 4$ ,  $a = 17.9742(3) \text{ \AA}$ ,  $b = 19.1934(3) \text{ \AA}$ ,  $c = 26.1291(10) \text{ \AA}$ ,  $\alpha = 90^\circ$ ,  $\beta = 102.1760(10)^\circ$ ,  $\gamma = 90^\circ$ ,  $V = 8811.4(2) \text{ \AA}^3$ ,  $\rho_{\text{calc}} = 1.283 \text{ g/cm}^3$ ,  $F(000) = 3520$ .

#### 4.5.12 Physical Measurements

$^1\text{H}$  NMR spectra were collected in  $\text{CDCl}_3$ ,  $\text{CD}_2\text{Cl}_2$ , or  $d_8$ -toluene (Cambridge Isotope Laboratories) at the MIT Department of Chemistry Instrumentation Facility (DCIF) using either a Mercury 300 or an Inova 500 spectrometer. All chemical shifts are reported using the standard  $\delta$  notation in parts-per-million; positive chemical shifts are to higher frequency from the given reference. Mass spectral analyses were carried out at the University of Illinois Mass Spectrometry Laboratory. Elemental analyses were performed at the University of Illinois Microanalytical Laboratory. Absorption spectra were obtained using a Cary-17 spectrophotometer modified by On-Line Instrument Systems (OLIS) to include computer control, a Spectral Instruments 440 spectrophotometer, or a Hewlett Packard 8453 spectrophotometer equipped with a Hewlett Packard 89090A Peltier temperature control accessory.

#### 4.5.13 Binding Assays

UV-visible titrations were carried out by the addition of small amounts of guest aliquots ( $1 \mu\text{L}$ ) into dilute solutions (*ca.*  $10^{-6} \text{ M}$ ,  $2\text{-}3 \text{ mL}$ ) of porphyrin. Titrations were carried out in at least triplicate. Association constants ( $K_A$ ) were obtained from plots of  $[G]$  against  $[G]/\Delta A$  where  $[G]$  = concentration of guest and  $\Delta A$  is the difference in absorbance of the porphyrin host in the



absence and presence of guest, and were determined independently from data at three different wavelengths.<sup>85</sup> Enthalpies and entropies for ligation were determined by standard van't Hoff plots of  $\ln K_A$  vs  $1/T$  for six temperatures ranging from 283 to 333 K.

#### 4.5.14 Computational Methods

Density functional theory (DFT) calculations were carried out in collaboration with Mr. Zhi-Heng Loh. Calculations were performed using the Amsterdam Density Functional program.<sup>89-91</sup> Gradient corrections were introduced using the Becke exchange functional (B)<sup>92</sup> and the Lee-Yang-Parr (LYP) correlation functional.<sup>93</sup> Relativistic corrections were included using the scalar zero-order regular approximation (ZORA).<sup>94-96</sup> C, H, and O were described by a Slater type orbital double- $\zeta$  basis set augmented with one polarization function. N and Zn were described by a triple- $\zeta$  basis set augmented by two and one polarization function, respectively. Non-hydrogen atoms were assigned a relativistic frozen core potential, treating as core the shells up to and including 2p for Zn, and 1s for C, N, and O. Electronic charges were computed by integrating the orthogonalized-fragment density over the Voronoi cell.

## 4.6 References and Notes

1. Lippard, S. J.; Berg, J. M. *Principles of Bioinorganic Chemistry*; University Science Books: Mill Valley, CA, 1994.
2. Jencks, W. P. *Catalysis in Chemistry and Enzymology*; Dover: Mineola, N. Y., 1987.
3. Fersht, A. *Enzyme Structure and Mechanism*; 2nd ed.; W. H. Freeman: New York, 1985.
4. Sanders, J. K. M. *Chem. Eur. J.* **1998**, *4*, 1378-1383.
5. Kirby, A. J. *Angew. Chem. Int. Ed. Engl.* **1996**, *35*, 707-724.
6. Collman, J. P.; Wagenknecht, P. S.; Hutchison, J. E. *Angew. Chem. Int. Ed. Engl.* **1994**, *33*, 1537-1554.
7. Collman, J. P.; Elliot, C. M.; Halbert, T. R.; Tovrog, B. S. *Proc. Natl. Acad. Sci. USA* **1977**, *74*, 18-22.
8. Collman, J. P.; Chong, A. O.; Jameson, G. B.; Oakley, R. T.; Rose, E.; Schmittou, E. R.; Ibers, J. A. *J. Am. Chem. Soc.* **1981**, *103*, 516-533.
9. Collman, J. P.; Anson, F. C.; Barnes, C. E.; Bencosme, C. S.; Geiger, T.; Evitt, E. R.; Kreh, R. P.; Meier, K.; Pettman, R. B. *J. Am. Chem. Soc.* **1983**, *105*, 2694-2699.
10. Collman, J. P.; Bencosme, C. S.; Durand Jr., R. R.; Kreh, R. P.; Anson, F. C. *J. Am. Chem. Soc.* **1983**, *105*, 2699-2703.
11. Collman, J. P.; Bencosme, C. S.; Barnes, C. E.; Miller, B. D. *J. Am. Chem. Soc.* **1983**, *105*, 2704-2710.
12. Collman, J. P.; Kim, K.; Garner, J. M. *J. Chem. Soc. Chem. Commun.* **1986**, 1711-1713.
13. Kim, K.; Collman, J. P.; Ibers, J. A. *J. Am. Chem. Soc.* **1988**, *110*, 4242-4246.
14. Chang, C. K. *J. Heterocycl. Chem.* **1977**, *14*, 1285-1288.
15. Chang, C. K. *J. Am. Chem. Soc.* **1977**, *99*, 2819-2822.
16. Chang, C. K. *J. Chem. Soc. Chem. Commun.* **1977**, 800-801.
17. Chang, C. K.; Kuo, M. S.; Wang, C. B. *J. Heterocycl. Chem.* **1977**, *14*, 943-945.
18. Ichimura, K. *Chem. Lett.* **1977**, 641-644.
19. Kagan, N. E.; Mauzerall, D.; Merrifield, R. B. *J. Am. Chem. Soc.* **1977**, *99*, 5484-5486.
20. Ogoshi, H.; Sugimoto, H.; Yoshida, Z. *Tetrahedron Lett.* **1977**, 169-172.
21. Paine III, J. B.; Dolphin, D.; Gouterman, M. *Can. J. Chem.* **1978**, *56*, 1712-1715.
22. Cowan, J. A.; Sanders, J. K. M. *J. Chem. Soc. Chem. Commun.* **1985**, 1213-1214.
23. Hunter, C. A.; Meah, M. N.; Sanders, J. K. M. *J. Am. Chem. Soc.* **1990**, *112*, 5773-5780.
24. Hunter, C. A.; Sanders, J. K. M. *J. Am. Chem. Soc.* **1990**, *112*, 5525-5534.
25. Anderson, H. L.; Hunter, C. A.; Meah, M. N.; Sanders, J. K. M. *J. Am. Chem. Soc.* **1990**, *112*, 5780-5789.
26. Anderson, S.; Anderson, H. L.; Sanders, J. K. M. *Acc. Chem. Res.* **1993**, *26*, 469-475.

27. Anderson, S.; Anderson, H. L.; Sanders, J. K. M. *J. Chem. Soc. Perkin Trans. 1* **1995**, 2255-2267.
28. Bookser, B. C.; Bruice, T. C. *J. Am. Chem. Soc.* **1991**, *113*, 4208-4218.
29. Karaman, R.; Bruice, T. C. *J. Org. Chem.* **1991**, *56*, 3470-3472.
30. Karaman, R.; Blasko, A.; Almarsson, O.; Arasasingham, R.; Bruice, T. C. *J. Am. Chem. Soc.* **1992**, *114*, 4889-4898.
31. Karaman, R.; Jeon, S. W.; Almarsson, O.; Bruice, T. C. *J. Am. Chem. Soc.* **1992**, *114*, 4899-4905.
32. Karaman, R.; Almarsson, O.; Blasko, A.; Bruice, T. C. *J. Org. Chem.* **1992**, *57*, 2169-2173.
33. Karaman, R.; Almarsson, O.; Bruice, T. C. *J. Org. Chem.* **1992**, *57*, 1555-1559.
34. Chang, C. K.; Abdalmuhdi, I. *J. Org. Chem.* **1983**, *48*, 5388-5390.
35. Chang, C. K.; Liu, H. Y.; Abdalmuhdi, I. *J. Am. Chem. Soc.* **1984**, *106*, 2725-2726.
36. Chang, C. K.; Abdalmuhdi, I. *Angew. Chem. Int. Ed. Engl.* **1984**, *23*, 164-165.
37. Fillers, J. P.; Ravichandran, K. G.; Abdalmuhdi, I.; Tulinsky, A.; Chang, C. K. *J. Am. Chem. Soc.* **1986**, *108*, 417-424.
38. Proniewicz, L. M.; Odo, J.; Goral, J.; Chang, C. K.; Nakamoto, K. *J. Am. Chem. Soc.* **1989**, *111*, 2105-2110.
39. Collman, J. P.; Kim, K.; Leidner, C. R. *Inorg. Chem.* **1987**, *26*, 1152-1157.
40. Collman, J. P.; Hutchison, J. E.; Lopez, M. A.; Tabard, A.; Guillard, R.; Seok, W. K.; Ibers, J. A.; L'Her, M. *J. Am. Chem. Soc.* **1992**, *114*, 9869-9877.
41. Collman, J. P.; Hutchison, J. E.; Lopez, M. A.; Guillard, R. *J. Am. Chem. Soc.* **1992**, *114*, 8066-8073.
42. Collman, J. P.; Hutchison, J. E.; Ennis, M. S.; Lopez, M. A.; Guillard, R. *J. Am. Chem. Soc.* **1992**, *114*, 8074-8080.
43. Collman, J. P.; Ha, Y.; Wagenknecht, P. S.; Lopez, M. A.; Guillard, R. *J. Am. Chem. Soc.* **1993**, *115*, 9080-9088.
44. Collman, J. P.; Ha, Y. Y.; Guillard, R.; Lopez, M. A. *Inorg. Chem.* **1993**, *32*, 1788-1794.
45. Collman, J. P.; Fish, H. T. *Inorg. Chem.* **1996**, *35*, 7922-7923.
46. Guillard, R.; Lopez, M. A.; Tabard, A.; Richard, P.; Lecomte, C.; Brandes, S.; Hutchison, J. E.; Collman, J. P. *J. Am. Chem. Soc.* **1992**, *114*, 9877-9889.
47. Guillard, R.; Brandes, S.; Tabard, A.; Bouhmaid, N.; LeComte, C.; Richard, P.; Latour, J. M. *J. Am. Chem. Soc.* **1994**, *116*, 10202-10211.
48. Guillard, R.; Brandes, S.; Tardieux, C.; Tabard, A.; L'Her, M.; Miry, C.; Gouerec, P.; Knop, Y.; Collman, J. P. *J. Am. Chem. Soc.* **1995**, *117*, 11721-11729.

49. Harvey, P. D.; Proulx, N.; Martin, G.; Drouin, M.; Nurco, D. J.; Smith, K. M.; Bolze, F.; Gros, C. P.; Guillard, R. *Inorg. Chem.* **2001**, *40*, 4134-4142.
50. Lui, H.-Y.; Abdalmuhdi, I.; Chang, C. K.; Anson, F. C. *J. Phys. Chem.* **1985**, *89*, 665-670.
51. Ni, C.-L.; Abdalmuhdi, I.; Chang, C. K.; Anson, F. C. *J. Phys. Chem.* **1987**, *91*, 1158-1166.
52. Naruta, Y.; Sasayama, M.; Ichihara, K. *J. Mol. Cat. A* **1997**, *117*, 115-121.
53. Le Mest, Y.; L'Her, M.; Hendricks, N. H.; Kim, K.; Collman, J. P. *Inorg. Chem.* **1992**, *31*, 835-847.
54. Le Mest, Y.; L'Her, M.; Saillard, J. Y. *Inorg. Chim. Acta* **1996**, *248*, 181-191.
55. Le Mest, Y.; Inisan, C.; Laouenan, A.; L'Her, M.; Talarmain, J.; El Khalifa, M.; Saillard, J. Y. *J. Am. Chem. Soc.* **1997**, *119*, 6905-6106.
56. Chang, C. J.; Brown, J. D. K.; Chang, M. C. Y.; Baker, E. A.; Nocera, D. G. In *Electron Transfer in Chemistry*; Balzani, V., Ed.; Wiley-VCH: Weinheim, Germany, 2001; Vol. 3.2.4, pp 409-461.
57. Cukier, R. I.; Nocera, D. G. *Annu. Rev. Phys. Chem.* **1998**, *49*, 337-369.
58. Chang, C. J.; Deng, Y.; Heyduk, A. F.; Chang, C. K.; Nocera, D. G. *Inorg. Chem.* **2000**, *39*, 959-966.
59. Deng, Y.; Chang, C. J.; Nocera, D. G. *J. Am. Chem. Soc.* **2000**, *122*, 410-411.
60. Chang, C. J.; Baker, E. A.; Pistorio, B. J.; Deng, Y.; Loh, Z.-H.; Miller, S. E.; Carpenter, S. D.; Nocera, D. G. *Inorg. Chem.* **2002**, *41*, 3102-3109.
61. Miller, J. R.; Dorough, G. D. *J. Am. Chem. Soc.* **1952**, *74*, 3977-3981.
62. Hambright, P. *J. Chem. Soc. Chem. Commun.* **1967**, 470-471.
63. Kirksey, C. H.; Hambright, P.; Storm, C. B. *Inorg. Chem.* **1969**, *8*, 2141-2144.
64. Bonar-Law, R. P.; Sanders, J. K. M. *J. Am. Chem. Soc.* **1995**, *117*, 259-271.
65. Borovkov, V. V.; Lintuluoto, J. M.; Inoue, Y. *J. Phys. Chem. A* **2000**, *104*, 9213-9219.
66. Borovkov, V. V.; Lintuluoto, J. M.; Inoue, Y. *Org. Lett.* **2000**, *2*, 1565-1568.
67. Borovkov, V. V.; Lintuluoto, J. M.; Inoue, Y. *J. Am. Chem. Soc.* **2001**, *123*, 2979-2989.
68. Crossley, M. J.; Hambley, T. W.; Mackay, L. G.; Try, A. C.; Walton, R. *J. Chem. Soc., Chem. Commun.* **1995**, 1077-1079.
69. Crossley, M. J.; Mackay, L. G.; Try, A. C. *J. Chem. Soc., Chem. Commun.* **1995**, 1925-1927.
70. Hiom, J.; Paine, J. B.; Zapf, U.; Dolphin, D. *Can. J. Chem.* **1983**, *61*, 2220-2223.
71. Huang, X.; Rickman, B. H.; Borhan, B.; Berova, N.; Nakanishi, K. *J. Am. Chem. Soc.* **1998**, *120*, 6185-6186.

72. Huang, X.; Borhan, B.; Rickman, B. H.; Nakanishi, K.; Berova, N. *Chem. Eur. J.* **2000**, *6*, 216-224.
73. Hunter, C. A.; Meah, M. N.; Sanders, J. K. M. *J. Chem. Soc., Chem. Commun.* **1988**, 692-694.
74. Hunter, C. A.; Meah, M. N.; Sanders, J. K. M. *J. Chem. Soc., Chem. Commun.* **1988**, 694-696.
75. Hunter, C. A.; Leighton, P.; Sanders, J. K. M. *J. Chem. Soc., Perkin Trans. 1* **1989**, 547-552.
76. Uemori, Y.; Nakatsubo, A.; Imai, H.; Nakagawa, S.; Kyuno, E. *Inorg. Chem.* **1992**, *31*, 5164-5171.
77. Wylie, R. S.; Levy, E. G.; Sanders, J. K. M. *Chem. Commun.* **1997**, 1611-1612.
78. Nakash, M.; Clyde-Watson, Z.; Feeder, N.; Davies, J. E.; Teat, S. J.; Sanders, J. K. M. *J. Am. Chem. Soc.* **2000**, *122*, 5286-5293.
79. Nakash, M.; Sanders, J. K. M. *J. Org. Chem.* **2000**, *65*, 7266-7271.
80. Romesberg, F. E.; Spiller, B.; Schultz, P. G.; Stevens, R. C. *Science* **1998**, *279*, 1929-1933.
81. Heine, A.; Stura, E. A.; Yli-Kauhaluoma, J. T.; Gao, C.; Deng, Q.; Beno, B. R.; Houk, K. N.; Janda, K. D.; Wilson, I. A. *Science* **1998**, *279*, 1934-1940.
82. Katz, H. E. *J. Org. Chem.* **1989**, *54*, 2179-2183.
83. Richardson, D. E.; Taube, H. *J. Am. Chem. Soc.* **1983**, *105*, 40-51.
84. Buchler, J. W. In *Porphyrins and Metalloporphyrins*; 2nd ed.; Smith, K. M., Ed.; Elsevier Scientific: Oxford, 1975, pp 157-232.
85. Connors, K. A. *Binding Constants*; Wiley: New York, 1987.
86. Hill, A. V. *J. Physiol. London* **1910**, *40*, IV-VII.
87. Basicities ( $pK_a$ ) of common heterocyclic nitrogen ligands for zinc(II) porphyrins: pyridine = 5.25, DABCO = 8.60, imidazole = 6.95, pyrazine = 0.65.
88. Armarego, W. L. F.; Perrin, D. D. *Purification of Laboratory Chemicals*; 4th ed.; Butterworth-Heinmann: Oxford, 1996.
89. ADF2000.02, Vrije Universiteit Amsterdam: Amsterdam, The Netherlands, 1999.
90. Baerends, E. J.; Ellis, D. E.; Ros, P. *Chem. Phys.* **1973**, *2*, 41-51.
91. Te Velde, G.; Bickelhaupt, F. M.; Baerends, E. J.; Fonseca Guerra, C.; Van Gisbergen, S. J. A.; Snijders, J. G.; Ziegler, T. *Journal of Computational Chemistry* **2001**, *22*, 931-967.
92. Becke, A. D. *Phys. Rev. A* **1988**, *38*, 3098-3100.
93. Lee, C.; Yang, W.; Parr, R. G. *Phys. Rev. B* **1988**, *37*, 785-789.
94. Van Lenthe, E.; Baerends, E. J.; Snijders, J. G. *J. Chem. Phys.* **1993**, *99*, 4597-4610.

95. Van Lenthe, E.; Van Leeuwen, R.; Baerends, E. J.; Snijders, J. G. *Int. J. Quantum Chem.* **1996**, *57*, 281-293.
96. Van Lenthe, E.; Ehlers, A.; Baerends, E. J. *J. Chem. Phys.* **1999**, *110*, 8943-8953.

*Chapter 5*

**Catalytic Four-Electron Reduction of Oxygen to Water by  
Highly Flexible Dicobalt(II) Pacman Porphyrins**

A portion of the work presented in this chapter has been published:

Chang, C. J.; Deng, Y.; Shi, C.; Chang, C. K.; Anson, F. C.; Nocera, D. G. *Chem. Commun.*

**2000**, 1355-1356.

## 5.1 Motivation and Specific Aims

The comprehensive characterization of the Pacman platforms DPX and DPD described in the preceding chapters sets the stage for exploring their catalytic chemistry mediated by proton-coupled electron transfer (PCET). Of particular interest are the O—O bond-making and bond-breaking reactions that attend the chemical interconversion between water and oxygen. Owing to the principle of microscopic reversibility, we sought to commence our reactivity studies with the thermodynamically favorable process of oxygen reduction to water in order to provide a suitable backdrop for attacking the more challenging thermodynamically uphill reaction of water oxidation to oxygen. We now report in this chapter that the dicobalt(II) derivatives of both DPX and DPD are electrocatalysts for the selective four-electron, four-proton reduction of oxygen to water despite their large difference (ca. 4 Å in metal-metal distances) in vertical pocket sizes. This remarkable result suggests that the unique Pacman flexibility of the DPD system allows this platform to structurally accommodate reaction intermediates for efficient catalytic turnover with an unprecedented range of directed motion.

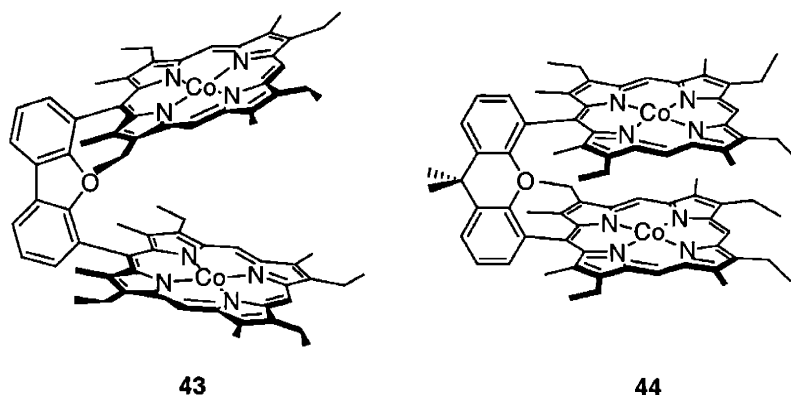
## 5.2 Background

Enzymatic systems are remarkable in their ability to accommodate the large range of motion required for the binding and catalysis of small molecules.<sup>1-3</sup> In many cases, the kinetic steps of the processes involved are ultimately predicated on conformational changes of the active site upon substrate binding, activation, and/or product release. An outstanding example is the binding and biological reduction of dioxygen to water by cytochrome *c* oxidase (CcO).<sup>4-8</sup> The critical O—O bond cleavage chemistry in CcO is mediated by a flexible, dinuclear iron-heme/copper (Fe<sub>a3</sub>/Cu<sub>B</sub>) assembly.<sup>4-8</sup> Nevertheless, the pursuit of structural and functional models for O<sub>2</sub> activation and reduction have emphasized, for the most part, bimetallic reaction centers poised within well-defined, rigid pockets.<sup>9-18</sup> For example, pillared cofacial dicobalt bisporphyrins bridged by anthracene and biphenylene impair ring slippage, and as a result, the corresponding Co<sub>2</sub>(DPA) and Co<sub>2</sub>(DPB) complexes efficiently electrocatalyze the direct four-electron reduction of oxygen to water (as opposed to the two-electron pathway involving peroxide) with little structural reorganization of juxtaposed subunits.<sup>19-32</sup> Can efficient oxygen-activation chemistry be preserved when this cofacial structural motif exhibits a large range of motion? To address this issue, we have developed methods for the facile assembly of new cofacial bisporphyrins incorporating xanthene (DPX) and dibenzofuran (DPD) scaffolds that exhibit variable pocket sizes with minimal lateral displacements.<sup>33-35</sup> Herein, we report that the dicobalt(II) complexes of both DPD and DPX shown in Chart 5.1 efficiently mediate the direct four-electron reduction of oxygen to water despite a ca. 4 Å difference in their metal-metal distances,<sup>36</sup> suggesting that the



substantial Pacman flexibility of these molecular clefts allows the designed binding pocket to structurally accommodate reaction intermediates during multielectron catalysis.

**Chart 5.1**



## 5.3 Results and Discussion

### 5.3.1 Synthesis and Structural Chemistry of Dicobalt(II) Cofacial Bisporphyrins

*Co*<sub>2</sub>(DPD) (**43**). The dicobalt(II) bisporphyrin *Co*<sub>2</sub>(DPD) (**43**) is obtained in excellent yield (91%) from reaction of the corresponding free base bisporphyrin with *CoCl*<sub>2</sub> in the presence of 2,6-lutidine. The paramagnetic complex was characterized using high-resolution mass spectrometry and elemental analyses. Crystals suitable for X-ray diffraction studies were grown from dichloromethane/methanol solutions. Crystallographic data are provided in Table 5.1 and selected metrics are given in Table 5.2. Trends in bond lengths and angles of macrocyclic core structures and side chains agree well with those observed in other DPD cofacial bisporphyrins.<sup>34,35</sup> The structure of **43** represented in Figure 5.1 shows that two methanol solvent molecules are coordinated *inside* the bisporphyrin pocket to the two cobalt(II) centers. In order to accommodate the two exogeneous ligands, the DPD framework opens its “bite” considerably. The interplanar angle between the two macrocycles is 56.5°, resulting in metal-metal (8.624 Å) and center-to-center (8.874 Å) distances that are markedly larger than found in the corresponding dizinc(II) complex *Zn*<sub>2</sub>(DPD) (**28**) (*d*<sub>Zn–Zn</sub> = 7.775 Å, *d*<sub>Ct–Ct</sub> = 7.587 Å).<sup>34</sup>

The *Co*(II) cores adopt an approximate square-pyramidal geometry, as the N—Co—N bond angles are 90 ± 1.3° and the N—Co—O bond angles are 90 ± 5.3°. The *Co* centers are displaced slightly from the porphyrin meanplane (*d*<sub>avg</sub> = 0.1355 Å) toward the axial ligand. The average axial *Co*—O bond length (2.272 Å) is significantly longer than that of the average equatorial *Co*—N bonds (1.982 Å), due to the occupancy of the *d*<sub>z<sup>2</sup></sub> orbital by a single unpaired electron in *Co*(II). A conformational analysis of the two macrocycles indicates inequivalent ring systems.

The porphyrin ring containing Co(1) exhibits an  $S_4$  ruffle with a mean deviation from planarity of 0.1416 Å. In contrast, the ring with Co(2) is essentially flat (avg deviation 0.0307 Å). Lastly, the most important structural feature of **43** in relation to its O<sub>2</sub> reactivity (*vide infra*) is the small torsional twist (9.3°, defined as the torsion angle between the two meso-carbon to spacer bonds) between the porphyrinic subunits, giving a cofacial binding pocket with a directed reaction coordinate along a single longitude for substrate binding and activation.

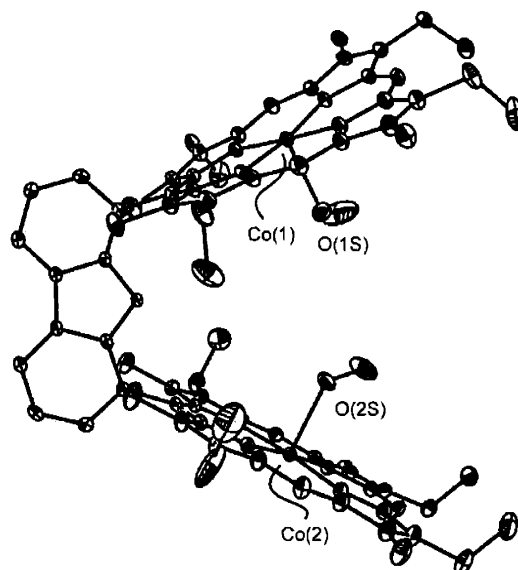


**Figure 5.1.** Crystal structure of Co<sub>2</sub>(DPD)•2MeOH (**43**). Thermal ellipsoids are drawn at the 25% probability level. Hydrogen atoms and solvent molecules within the lattice have been omitted for clarity.

**Co<sub>2</sub>(DPX) (44).** We sought to compare the structure and reactivity of wedge-shaped Co<sub>2</sub>(DPD) (**43**) to a dicobalt(II) cofacial complex where the bite size of the cleft is preorganized for oxygen activation. To this end, the metallobisporphyrin Co<sub>2</sub>(DPX) (**44**) is prepared in excellent yield (95%) by reaction of the corresponding free base bisporphyrin **15** with CoCl<sub>2</sub> and 2,6-lutidine in a THF-benzene solvent system. Complex **44** gave satisfactory high-resolution mass spectral and elemental analyses.

The molecular structure of **44** is depicted in Figure 5.2. Pertinent crystallographic data are contained in Table 5.1, and selected geometric lengths and angles are collected in Table 5.2. Trends in bond lengths and angles of macrocyclic core structures and side chains agree well with those observed in related DPX cofacial bisporphyrins.<sup>33,35</sup> The six-membered center ring of the xanthene spacer of **44** causes the two porphyrin macrocycles to bend slightly in toward each other, giving a mean interplanar distance of 3.519 Å between the two porphyrin rings. This is

quite similar to situation found in  $\text{Co}_2(\text{DPB})$  (3.381 Å).<sup>25</sup> However, the torsional twist (21.1°) between the two rings results in a metal-metal distance of 4.582 Å ( $\text{Co}_2\text{DPB}$ , 3.726 Å). The square geometry for the  $\text{Co}(\text{II})$  cores is confirmed by the  $\text{N}-\text{Co}-\text{N}$  bond angles of  $90 \pm 1.7^\circ$ . As observed for DPD compound **43** and for other structurally characterized DPX metal complexes,<sup>33,35</sup> the two ring systems of **44** are structurally inequivalent in the solid state. The macrocycle with  $\text{Co}(1)$  exhibits a pronounced ruffled conformation with a mean deviation from planarity of 0.2227 Å, while the macrocycle containing  $\text{Co}(2)$  has a less pronounced ruffle with a mean deviation from planarity of 0.1118 Å.

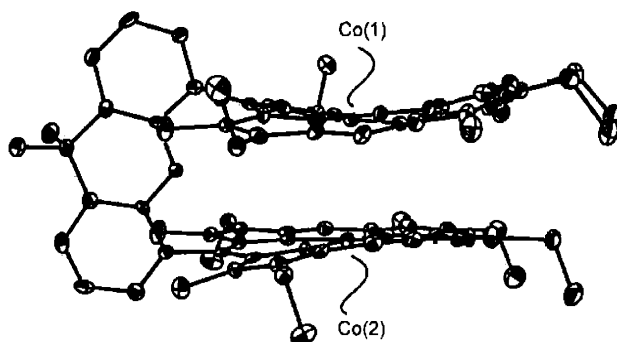


**Figure 5.2.** Crystal structure of  $\text{Co}_2(\text{DPX})$  (**44**). Thermal ellipsoids are drawn at the 25% probability level. Hydrogen atoms and solvent molecules within the lattice have been omitted for clarity.

The collected structural data establish that the dicobalt(II) complexes **43** and **44** exhibit a large disparity in vertical pocket sizes. A particularly important metric in this regard is the large difference in metal-metal distances (8.624 Å for **43**, 4.582 Å for **44**) for the DPD and DPX systems in their natural conformations. Notably, these structural studies have been performed with the actual dicobalt(II) catalysts and not of other related metal derivatives; this has been done in order to test rigorously the structure-function consequences of the Pacman effect for cofacial bisporphyrin systems. Thus, compounds **43** and **44** comprise a unique set of structurally characterized Pacman catalysts for oxygen reduction that exhibit a large range of directed vertical motion.<sup>26</sup>

**Table 5.1.** Crystallographic Data for Co<sub>2</sub>(DPD)•2MeOH (**43**) and Co<sub>2</sub>(DPX) (**44**).

	<b>43</b>	<b>44</b>
Empirical formula	C <sub>80</sub> H <sub>84</sub> Cl <sub>2</sub> N <sub>8</sub> O <sub>4</sub> Co <sub>2</sub>	C <sub>79</sub> H <sub>82</sub> N <sub>8</sub> O <sub>2</sub> Co <sub>2</sub>
Formula weight	1410.31	1277.39
Temperature	183(2) K	183(2) K
Wavelength	0.71073 Å	0.71073 Å
Crystal system	Triclinic	Monoclinic
Space group	<i>P</i> $\bar{1}$	<i>C</i> 2/ <i>c</i>
Unit cell dimensions	<i>a</i> = 10.9872(2) Å <i>b</i> = 13.0824(2) Å <i>c</i> = 27.2127(10) Å $\alpha$ = 84.6800(10)° $\beta$ = 87.2850(10)° $\gamma$ = 71.8840(10)°	<i>a</i> = 24.1310(5) Å <i>b</i> = 10.6260(2) Å <i>c</i> = 50.2717(10) Å $\beta$ = 99.5120(10)°
Volume	3700.93(9) Å <sup>3</sup>	12713.2(4) Å <sup>3</sup>
Z	2	8
Density (calculated)	1.266 Mg/m <sup>3</sup>	1.335 Mg/m <sup>3</sup>
Absorption coefficient	0.572 mm <sup>-1</sup>	0.577 mm <sup>-1</sup>
F(000)	1480	5392
Crystal size	0.50 × 0.50 × 0.20 mm <sup>3</sup>	0.50 × 0.25 × 0.20 mm <sup>3</sup>
$\theta$ range for data collection	1.50 to 23.68°	1.64 to 23.42°
Reflections collected	15393	25472
Independent reflections	10494 (R <sub>int</sub> = 0.0334)	9225 (R <sub>int</sub> = 0.1088)
Data / restraints / params	10494 / 8 / 913	9225 / 0 / 812
Goodness-of-fit on F <sup>2</sup>	1.121	1.149
Final R indices [I > 2 $\sigma$ (I)]	<i>R</i> 1 = 0.0795 <i>w</i> R2 = 0.2186	<i>R</i> 1 = 0.0829 <i>w</i> R2 = 0.1479
R indices (all data)	<i>R</i> 1 = 0.0912 <i>w</i> R2 = 0.2406	<i>R</i> 1 = 0.1545 <i>w</i> R2 = 0.2533
Extinction coefficient	0.0007(10)	0.00010(3)
Largest diff peak	1.651 eÅ <sup>-3</sup>	0.445 eÅ <sup>-3</sup>
Largest diff hole	-0.756 eÅ <sup>-3</sup>	-0.461 eÅ <sup>-3</sup>

**Table 5.2a.** Selected Bond Lengths (Å) and Angles (deg) for Compound 43.

<i>Bond Lengths (Å)</i>		<i>Bond Angles (deg)</i>			
Co(1)–N(1)	1.979(4)	N(1)–Co(1)–N(2)	88.7(2)	N(7)–Co(2)–N(8)	88.4(2)
Co(1)–N(2)	1.980(5)	N(1)–Co(1)–N(3)	172.0(2)	N(7)–Co(2)–N(6)	91.2(2)
Co(1)–N(3)	1.985(4)	N(2)–Co(1)–N(3)	91.0(2)	N(8)–Co(2)–N(6)	175.2(2)
Co(1)–N(4)	1.986(5)	N(1)–Co(1)–N(4)	91.4(2)	N(7)–Co(2)–N(5)	175.4(2)
Co(1)–O(1S)	2.283(5)	N(2)–Co(1)–N(4)	177.5(2)	N(8)–Co(2)–N(5)	91.1(2)
Co(2)–N(5)	1.983(4)	N(3)–Co(1)–N(4)	88.6(2)	N(6)–Co(2)–N(5)	88.9(2)
Co(2)–N(6)	1.981(4)	N(1)–Co(1)–O(1S)	92.7(2)	N(5)–Co(2)–O(2S)	92.0(2)
Co(2)–N(7)	1.982(4)	N(2)–Co(1)–O(1S)	89.5(2)	N(6)–Co(2)–O(2S)	91.3(2)
Co(2)–N(8)	1.982(5)	N(3)–Co(1)–O(1S)	95.3(2)	N(7)–Co(2)–O(2S)	92.6(2)
Co(2)–O(2S)	2.262(4)	N(4)–Co(1)–O(1S)	93.0(2)	N(8)–Co(2)–O(2S)	93.5(2)

**Table 5.2b.** Selected Bond Lengths (Å) and Angles (deg) for Compound 44.

<i>Bond Lengths (Å)</i>		<i>Bond Angles (deg)</i>			
Co(1)–N(1)	1.951(6)	N(1)–Co(1)–N(2)	89.1(2)	N(7)–Co(2)–N(8)	88.6(2)
Co(1)–N(2)	1.954(6)	N(1)–Co(1)–N(3)	177.4(2)	N(7)–Co(2)–N(6)	91.1(2)
Co(1)–N(3)	1.959(6)	N(2)–Co(1)–N(3)	90.9(2)	N(8)–Co(2)–N(6)	176.5(2)
Co(1)–N(4)	1.943(6)	N(1)–Co(1)–N(4)	91.0(2)	N(7)–Co(2)–N(5)	179.6(2)
Co(2)–N(5)	1.963(6)	N(2)–Co(1)–N(4)	178.9(3)	N(8)–Co(2)–N(5)	91.6(2)
Co(2)–N(6)	1.964(5)	N(3)–Co(1)–N(4)	88.9(2)	N(6)–Co(2)–N(5)	88.7(2)
Co(2)–N(7)	1.972(6)				
Co(2)–N(8)	1.979(5)				

### 5.3.2 Redox Properties and Electrocatalytic Reduction of Oxygen to Water

The redox properties of the dicobalt(II) Pacman porphyrins **43** and **44** have been examined using cyclic voltammetry, and the ability of these systems to selectively mediate the direct four-electron reduction of oxygen to water instead of the more commonly observed two-electron reduction to peroxide has been evaluated using rotating ring-disk electrochemistry. Cyclic voltammograms of **43** in nitrobenzene using a thin-layer technique<sup>37</sup> (Figure 5.3a) give a single, reversible oxidative wave at +0.33 V (vs Ag/AgCl), consistent with two non-interacting metal centers.

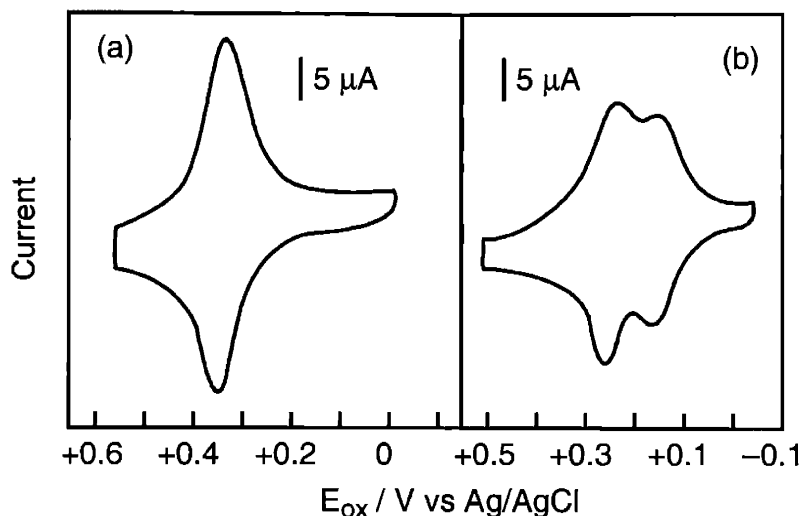


**Figure 5.3.** Cyclic voltammetric responses at an edge-plane graphite (EPG) electrode, covered with a thin layer of nitrobenzene containing (a) 0.17 mM  $Co_2(DPD)$  (**43**) or (b) 0.20 mM  $Co_2(DPX)$  (**44**). The EPG electrode was immersed in an aqueous supporting electrolyte containing 2 M  $HClO_4$ . Scan rate, 10 mV/s.

The complex was then screened as an electrocatalyst for the reduction of dioxygen. Figure 5.4a displays a rotating ring-disk voltammogram for the reduction of  $O_2$  at an edge-plane graphite electrode coated with **43**. Remarkably, **43** catalyzes the reduction of oxygen at the unusually positive potential of +0.37 V (vs Ag/AgCl) with 80% of the  $O_2$  reduction proceeding along the four-electron pathway to produce water, even though the natural conformation of the DPD platform is quite splayed. The vertical Pacman flexibility of this molecular cleft apparently allows it to “bite” down on the  $O_2$  substrate resulting in efficient and selective catalytic activation of the dioxygen substrate.

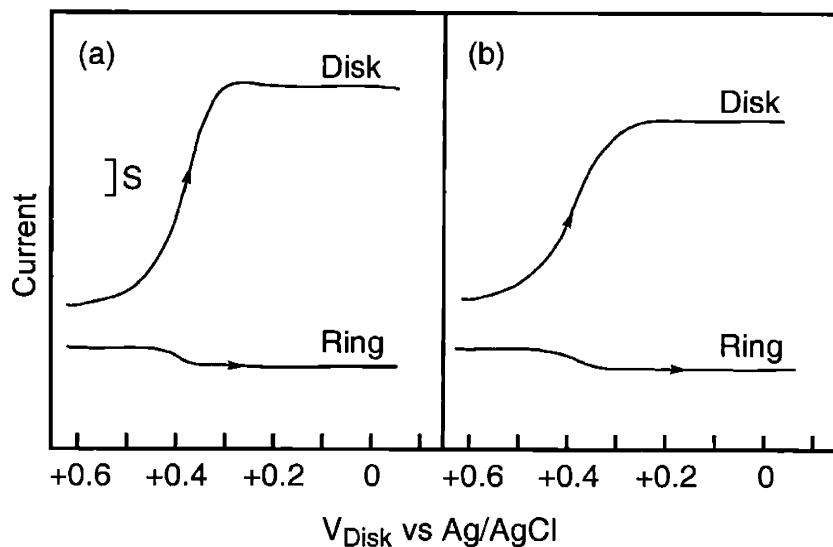
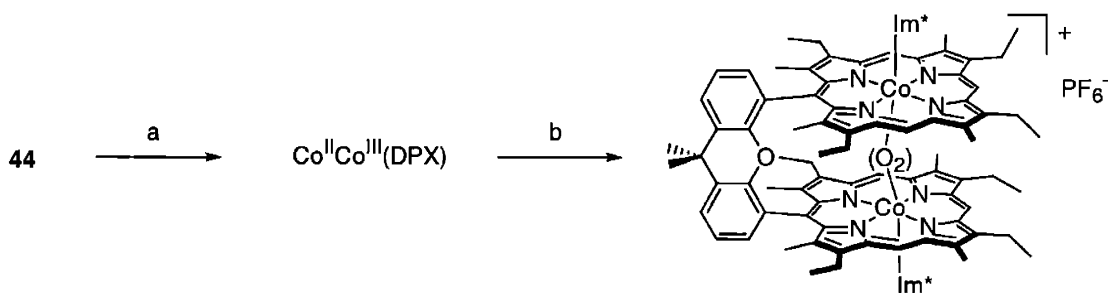


**Figure 5.4.** Rotating Pt ring-disk voltammograms for reduction of O<sub>2</sub> at pyrolytic graphite disks coated with (a) Co<sub>2</sub>(DPD) (**43**) or (b) Co<sub>2</sub>(DPX) (**44**). Rotation rate, 100 rpm; disk current,  $S = 10 \mu\text{A}$ ; ring current,  $S = 5 \mu\text{A}$ ; supporting electrolyte, 0.5 M HClO<sub>4</sub>/1.5 M TFA saturated with air.

The electrochemistry of the analogous DPX complex **44** is examined in a similar manner. The more compressed structure of **44** engenders mixed-valence behavior, as two reversible electrochemical oxidations are observed at +0.28 and +0.17 V vs Ag/AgCl. The Co(II)/Co(III) DPX complex reacts with dioxygen in the presence of 1,5-dicyclohexylimidazole to give a species with an EPR spectrum typical of a symmetrical biscobalt(III) superoxo complex (Scheme 5.1).<sup>25,38</sup>



**Scheme 5.1.** (a) AgPF<sub>6</sub>; (b) i. O<sub>2</sub>; ii. Im\*. Im\* denotes 1,5-dicyclohexylimidazole.

Analysis of the 15-line EPR spectrum depicted in Figure 5.5 yields standard parameters for a superoxo species ( $g = 2.02$ ,  $A_{\text{Co}} = 11.14 \text{ G}$ ). Nevertheless, **44** efficiently catalyzes the reduction of oxygen at a potential (+0.38 V vs Ag/AgCl) and with a selectivity for the four-electron pathway to produce water (72%) commensurate to **43** (Figure 5.4b).

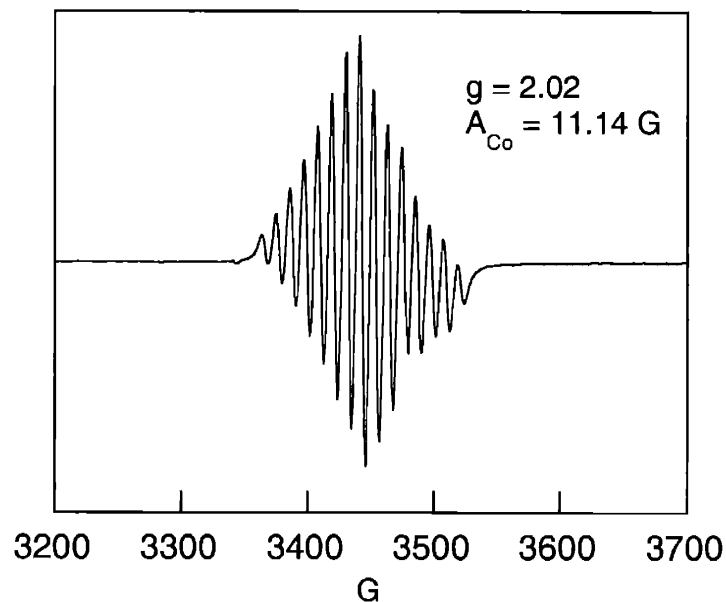


**Figure 5.5.** EPR spectrum of  $[\text{Co}_2(\text{DPX})(\mu\text{-O}_2)(1,5\text{-Dicyclohexylimidazole})_2][\text{PF}_6]$  taken in dichloromethane solution at 298 K.

## 5.4 Concluding Remarks

The observation that both complexes are efficient catalysts for the four-electron reduction of oxygen to water, despite their notable differences in structure and redox behavior, is striking. The results suggest that the vertical open-to-closed conformational change in the presence of oxygen, especially dramatic in the DPD framework, involves only a small change in conformational energy. The structure of the bisiron(III)  $\mu$ -oxo complex of DPD provides further evidence of the Pacman effect, as the framework readily closes its structure to give a complex with a compressed metal-metal distance of 3.504 Å.<sup>34</sup> Accordingly, the conformational flexibility of these Pacman porphyrins provides a directed reaction coordinate for facile substrate activation and product release. Moreover, this unique structure-function relation is not limited to reductive catalytic pathways; for example, we have recently exploited this directed Pacman flexibility to achieve the first photocatalytic oxidation reactions with cofacial bisporphyrins using “spring-loaded” derivatives of our DPX and DPD systems.<sup>39</sup>

With the synthetic availability and tunability of both the DPD and DPX frameworks, we are poised to incisively investigate structural and electronic effects on the small-molecule reactivity of these pillared cofacial bisporphyrins. Current studies are aimed at addressing mechanistic issues concerning the proton-coupled O—O bond cleavage chemistry within the Pacman motif



and expanding the scope of catalytic PCET reactions<sup>40,41</sup> with cofacial bisporphyrins and related architectures.<sup>42,43</sup>

## 5.5 Experimental Section

### 5.5.1 Materials

Aluminum oxide 60 (EM Science) was used for column chromatography. Analytical thin layer chromatography was performed using JT Baker IB-F aluminum oxide (precoated sheets, 0.2 mm thick). Solvents for synthesis were of reagent grade or better, and were dried according to standard methods.<sup>44</sup> Spectroscopic experiments employed dichloromethane (spectroscopic grade, Burdick & Jackson), which was stored over 4 Å molecular sieves under high vacuum or in a glovebox. The Pacman porphyrins H<sub>4</sub>(DPX) (**15**) and H<sub>4</sub>(DPD) (**27**) were available using the procedures outlined in chapter 2. All other reagents were used as received.

### 5.5.2 Co<sub>2</sub>(DPD) (**43**)

In a dry box, a 100-mL flask equipped with a condenser was charged with H<sub>4</sub>(DPD) (**27**) (50 mg, 0.045 mmol), 2,6-lutidine (0.1 mL), CoCl<sub>2</sub> (100 mg), THF (12 mL) and benzene (12 mL). The mixture was refluxed under nitrogen for 12 h. The solvent was removed in vacuo and the residue was purified by flash column chromatography under an inert atmosphere (alumina, THF). Recrystallation from dichloromethane/methanol and drying under high vacuum gave **43** as an analytically pure maroon crystalline powder in 91% yield. Anal. Calcd for C<sub>76</sub>H<sub>76</sub>Co<sub>2</sub>N<sub>8</sub>O: C, 73.89; H, 6.20; N, 9.54. Found: C, 73.82; H, 6.26; N, 8.94. HRFABMS (M<sup>+</sup>) calcd for C<sub>76</sub>H<sub>76</sub>Co<sub>2</sub>N<sub>8</sub>O *m/z* 1234.4806, found 1234.4801.

### 5.5.3 Co<sub>2</sub>(DPX) (**44**)

In a dry box, H<sub>4</sub>(DPX) (**15**) (120 mg, 0.10 mmol), anhydrous cobalt(II) chloride (200 mg), 2,6-lutidine (0.2 mL), and THF (120 mL) were loaded in a 250-mL round-bottom flask. The mixture was refluxed under nitrogen for 12 h. The solvent was removed in vacuo and the residue was purified by flash column chromatography under an inert atmosphere (alumina, THF). Recrystallation from dichloromethane/methanol and drying under high vacuum gave **44** as an analytically pure purple crystalline powder in 95% yield. Anal. Calcd for C<sub>79</sub>H<sub>82</sub>Co<sub>2</sub>N<sub>8</sub>O: C, 74.24; H, 6.47; N, 8.77. Found: C, 73.86; H, 6.42; N, 8.71. HRFABMS (M<sup>+</sup>) calcd for C<sub>79</sub>H<sub>82</sub>Co<sub>2</sub>N<sub>8</sub>O *m/z* 1276.5276, found 1276.5257.

#### 5.5.4 *In-Situ* Preparation of [Co<sub>2</sub>(DPX)(μ-O<sub>2</sub>)(1,5-Dicyclohexylimidazole)<sub>2</sub>][PF<sub>6</sub>] for EPR Measurements

In a dry box, Co<sub>2</sub>(DPX) (**44**) (13 mg, 0.01 mmol) was dissolved in benzene (5 mL). A solution of AgPF<sub>6</sub> in THF (2.5 mg in 0.5 mL) was added dropwise to the stirred porphyrin solution and the resulting mixture was stirred at room temperature for 4 h after the final addition of oxidant. The reaction was filtered through a glass wool plug to remove precipitated silver metal and the oxidized product, and the plug was washed with benzene (3 × 5 mL) to eliminate any unreacted starting material. The plug was then washed with dichloromethane to collect the mixed-valent Co(II)/Co(III) product, which was isolated by subsequent removal of the solvent under reduced pressure. The Co(II)/Co(III) species was redissolved in dichloromethane (3 mL), removed from the dry box, and the solution was saturated with dry oxygen. A solution of 1,5-dicyclohexylimidazole in dichloromethane (4.7 mg in 0.5 mL) was then added to the oxygen-saturated solution and the resulting capped biscobalt(III) superoxo species was diluted to the appropriate concentrations for spectroscopic measurements.

#### 5.5.5 General Details of X-ray Data Collection and Reduction

X-ray diffraction data were collected using a Siemens 3 circle diffractometer equipped with a CCD detector. Measurements were carried out at -90° C using Mo Kα (λ = 0.71073 Å) radiation, which was wavelength selected with a single-crystal graphite monochromator. Four sets of data were collected using ω scans and a -0.3° scan width. All calculations were performed using either a Silicon Graphics Indigo 2 or a PC workstation. The data frames were integrated to *hkl*/intensity, and final unit cells were calculated by using the SAINT v.4.050 program from Siemens. The structures were solved and refined with the SHELXTL v.5.03 suite of programs developed by G. M. Sheldrick and Siemens Industrial Automation, Inc., 1995.

#### 5.5.6 X-ray Structure of Co<sub>2</sub>(DPD) (**43**)

A single crystal was obtained by slowly diffusing methanol into the solution of **43**. Empirical formula: C<sub>80</sub>H<sub>84</sub>Cl<sub>2</sub>Co<sub>2</sub>N<sub>8</sub>O<sub>4</sub>, MW = 1410.31. triclinic,  $P\bar{1}$ , Z = 2, a = 10.9872(2) Å, b = 13.0824(2) Å, c = 27.2127(10) Å, α = 84.68°, β = 87.2850(10)°, γ = 71.8840(10)°, V = 3700.93(9) Å<sup>3</sup>, ρ<sub>calc</sub> = 1.266 g/cm<sup>3</sup>, F(000) = 1480. Crystal dimension: 0.5 mm × 0.5 mm × 0.20 mm. A total of 15393 reflections were collected in the θ range of 1.50° to 23.68°, of which 10494 were unique (R<sub>int</sub> = 0.0334). The structure was solved by direct methods in conjunction with standard difference Fourier techniques. None hydrogen atoms were refined anisotropically. Due to the disorder, the C22A—C22B bond length of one ethyl group was restrained according to the C13A—C13B bond length using SAME instruction. Hydrogen atoms were placed in

calculated positions using a standard riding model and were refined isotropically. One dichloromethane and one methanol molecule co-crystallized with **43**. Both were found disordered in the crystal and were assigned half occupancy at two positions, respectively. The C3S—C11S, C4S—C13S, C4S—C14S bond lengths were restrained according to the C3S—C12S bond length and the O4S—C6S bond length was restrained according to the O3S—C5S bond length. The largest peak and hole in the difference map were  $1.651 \text{ e}\text{\AA}^{-3}$  and  $-0.756 \text{ e}\text{\AA}^{-3}$ , respectively. The least squares refinement converged normally giving residuals of  $R = 0.0795$ ,  $wR^2 = 0.2186$ , and  $GOF = 1.121$ .

### 5.5.7 X-ray Structure of $\text{Co}_2(\text{DPX})$ (**44**)

A single crystal was obtained by slowly diffusing of methanol into the solution of **44** in dichloromethane. Empirical formula:  $\text{C}_{79}\text{H}_{82}\text{Co}_2\text{N}_8\text{O}_2$ ,  $MW = 1277.39$ . monoclinic,  $C2/c$ ,  $Z = 8$ ,  $a = 24.1310(5) \text{ \AA}$ ,  $b = 10.6260(2) \text{ \AA}$ ,  $c = 50.2717(10) \text{ \AA}$ ,  $\alpha = 90^\circ$   $\beta = 99.5120(10)^\circ$ ,  $\gamma = 90^\circ$ ,  $V = 12713.2(4) \text{ \AA}^3$ ,  $\rho_{\text{calc}} = 1.335 \text{ Mg/cm}^3$ ,  $F(000) = 5392$ . Crystal dimension:  $0.5 \text{ mm} \times 0.25 \text{ mm} \times 0.20 \text{ mm}$ . A total of 25472 reflections were collected in the  $\theta$  range of  $1.64^\circ$  to  $23.42^\circ$ , of which 9225 were unique ( $R_{\text{int}} = 0.1088$ ). The structure was solved by direct methods in conjunction with standard difference Fourier techniques. None hydrogen atoms were refined anisotropically. Hydrogen atoms were placed in calculated positions using a standard riding model and were refined isotropically. The largest peak and hole in the difference map were  $0.445 \text{ e}\text{\AA}^{-3}$  and  $-0.461 \text{ e}\text{\AA}^{-3}$ , respectively. The least squares refinement converged normally giving residuals of  $R = 0.0829$ ,  $wR^2 = 0.1479$ , and  $GOF = 1.149$ .

### 5.5.8 Physical Measurements

Mass spectral analyses were carried out by the University of Illinois Mass Spectrometry Laboratory. Elemental analyses were performed at H. Kolbe Mikroanalytisches Laboratorium. X-band EPR spectra were recorded in dichloromethane at 298 K in 4 mm quartz tubes using a Bruker 300 EMX EPR spectrometer. Data manipulation was carried out using the Win-EPR program. Absorption spectra were obtained using a Cary-17 spectrophotometer modified by On-Line Instrument Systems (OLIS) to include computer control or a Spectral Instruments 440 Model spectrophotometer.

### 5.5.9 Electrochemical Apparatus and Procedures

The electrocatalytic studies were carried out in collaboration with Prof. Fred Anson and Dr. Chunnian Shi at the California Institute of Technology. Cylindrical pyrolytic graphite rods with the edges of the graphitic planes exposed (Union Carbide) were mounted to stainless steel shafts with heat-shrinkable polyolefin tubing (Alpha Wire). The exposed graphite disk had an area of

0.32 cm<sup>2</sup>. Electrode pre-treatment and catalyst loading were carried out using standard procedures.<sup>45-47</sup> Briefly, the pyrolytic graphite rods were polished with 600 grit SiC paper (3M), sonicated in purified water (MilliQ Plus), washed with acetone, and dried. Porphyrins were adsorbed on the electrode surface by means of a dip-coating procedure: the freshly polished electrode was dipped for 1 min in a 0.1 mM solution of the porphyrin in chloroform, removed, washed immediately with pure chloroform, and dried in air. The dry, coated electrodes were transferred to the aqueous supporting electrolytes and utilized immediately.

The commercial rotating graphite-disk-platinum ring electrode (Pine Instruments) was polished with 0.3- $\mu$ m alumina on microcloth. The collection efficiency of the rotating ring-disk electrode (RRDE) employed was 0.39 as established by measurements with the Fe(CN)<sub>6</sub><sup>3-/4-</sup> couple. The percentage of oxygen reduction proceeding along the four-electron pathway to produce water was calculated using the formula  $f_{\text{water}} = [N - (i_{\text{R}}/i_{\text{D}})]/[N + (i_{\text{R}}/i_{\text{D}})]$  where  $f_{\text{water}}$  is the fraction of oxygen reduced to water,  $N$  is the collection efficiency of the RRDE, and  $i_{\text{R}}$  and  $i_{\text{D}}$  are the ring and disk currents, respectively.

## 5.6 References and Notes

1. Jencks, W. P. *Catalysis in Chemistry and Enzymology*; Dover: Mineola, N. Y., 1987.
2. Fersht, A. *Enzyme Structure and Mechanism*; 2nd ed.; W. H. Freeman: New York, 1985.
3. Lippard, S. J.; Berg, J. M. *Principles of Bioinorganic Chemistry*; University Science Books: Mill Valley, CA, 1994.
4. Malmström, B. G. In *Electron Transfer in Chemistry*; Balzani, V., Ed.; Wiley-VCH: Weinheim, Germany, 2001; Vol. 3.1.3, pp 39-55.
5. Babcock, G. T.; Wikström, M. *Nature* **1992**, *356*, 301-309.
6. Ferguson-Miller, S.; Babcock, G. T. *Chem. Rev.* **1996**, *96*, 2889-2907.
7. Michel, H.; Behr, J.; Harrenga, A.; Kannt, A. *Annu. Rev. Biophys. Biomol. Struct.* **1998**, *27*, 329-356.
8. Schultz, B. E.; Chan, S. I. *Annu. Rev. Biophys. Biomol. Struct.* **2001**, *30*, 23-65.
9. Collman, J. P.; Sunderland, C. J.; Boulatov, R. *Inorg. Chem.* **2002**, *41*, 2282-2291.
10. Collman, J. P.; Rapta, M.; Bröring, M.; Raptova, L.; Schwenninger, R.; Boitrel, B.; Fu, L.; L'Her, M. *J. Am. Chem. Soc.* **1999**, *121*, 1387-1388.
11. Collman, J. P.; Fu, L.; Herrmann, P. C.; Wang, Z.; Rapta, M.; Bröring, M.; Schwenninger, R.; Boitrel, B. *Angew. Chem. Int. Ed.* **1998**, *37*, 3397-3400.
12. Baeg, J. O.; Holm, R. H. *Chem. Commun.* **1998**, 571-572.
13. Holm, R. H. *Pure Appl. Chem.* **1995**, *67*, 217-224.
14. Ghiladi, R. A.; Hatwell, K. R.; Karlin, K. D.; Huang, H.-w.; Moënne-Lopez, P.; Krebs, C.; Huynh, B. H.; Marzilli, L. A.; Cotter, R. J.; Kaderli, S.; Zuberbühler, A. D. *J. Am. Chem. Soc.* **2001**, *123*, 6183-6184.
15. Liang, H. C.; Dahan, M.; Karlin, K. D. *Curr. Opin. Chem. Biol.* **1999**, *3*, 168-175.
16. Ricard, D.; Didier, A.; L'Her, M.; Boitrel, B. *ChemBioChem* **2001**, *2*, 144-148.
17. Ricard, D.; L'Her, M.; Richard, P.; Boitrel, B. *Chem. Eur. J.* **2001**, *7*, 3291-3297.
18. Ricard, D.; Andrioletti, B.; L'Her, M.; Boitrel, B. *Chem. Commun.* **1999**, 1523-1524.
19. Chang, C. K.; Abdalmuhdi, I. *J. Org. Chem.* **1983**, *48*, 5388-5390.
20. Chang, C. K.; Liu, H. Y.; Abdalmuhdi, I. *J. Am. Chem. Soc.* **1984**, *106*, 2725-2726.
21. Chang, C. K.; Abdalmuhdi, I. *Angew. Chem. Int. Ed. Engl.* **1984**, *23*, 164-165.
22. Lui, H.-Y.; Abdalmuhdi, I.; Chang, C. K.; Anson, F. C. *J. Phys. Chem.* **1985**, *89*, 665-670.
23. Ni, C.-L.; Abdalmuhdi, I.; Chang, C. K.; Anson, F. C. *J. Phys. Chem.* **1987**, *91*, 1158-1166.
24. Proniewicz, L. M.; Odo, J.; Goral, J.; Chang, C. K.; Nakamoto, K. *J. Am. Chem. Soc.* **1989**, *111*, 2105-2110.

25. Collman, J. P.; Hutchison, J. E.; Lopez, M. A.; Tabard, A.; Guillard, R.; Seok, W. K.; Ibers, J. A.; L'Her, M. *J. Am. Chem. Soc.* **1992**, *114*, 9869-9877.
26. Collman, J. P.; Wagenknecht, P. S.; Hutchison, J. E. *Angew. Chem. Int. Ed. Engl.* **1994**, *33*, 1537-1554.
27. Guillard, R.; Lopez, M. A.; Tabard, A.; Richard, P.; Lecomte, C.; Brandes, S.; Hutchison, J. E.; Collman, J. P. *J. Am. Chem. Soc.* **1992**, *114*, 9877-9889.
28. Guillard, R.; Brandes, S.; Tabard, A.; Bouhmaida, N.; LeComte, C.; Richard, P.; Latour, J. M. *J. Am. Chem. Soc.* **1994**, *116*, 10202-10211.
29. Guillard, R.; Brandes, S.; Tardieux, C.; Tabard, A.; L'Her, M.; Miry, C.; Gouerac, P.; Knop, Y.; Collman, J. P. *J. Am. Chem. Soc.* **1995**, *117*, 11721-11729.
30. Le Mest, Y.; L'Her, M.; Hendricks, N. H.; Kim, K.; Collman, J. P. *Inorg. Chem.* **1992**, *31*, 835-847.
31. Le Mest, Y.; L'Her, M.; Saillard, J. Y. *Inorg. Chim. Acta* **1996**, *248*, 181-191.
32. Le Mest, Y.; Inisan, C.; Laouenan, A.; L'Her, M.; Talarmain, J.; El Khalifa, M.; Saillard, J. Y. *J. Am. Chem. Soc.* **1997**, *119*, 6905-6106.
33. Chang, C. J.; Deng, Y.; Heyduk, A. F.; Chang, C. K.; Nocera, D. G. *Inorg. Chem.* **2000**, *39*, 959-966.
34. Deng, Y.; Chang, C. J.; Nocera, D. G. *J. Am. Chem. Soc.* **2000**, *122*, 410-411.
35. Chang, C. J.; Baker, E. A.; Pistorio, B. J.; Deng, Y.; Loh, Z.-H.; Miller, S. E.; Carpenter, S. D.; Nocera, D. G. *Inorg. Chem.* **2002**, *41*, 3102-3109.
36. Chang, C. J.; Deng, Y.; Shi, C.; Chang, C. K.; Anson, F. C.; Nocera, D. G. *Chem. Commun.* **2000**, 1355-1356.
37. Shi, C.; Anson, F. C. *Anal. Chem.* **1998**, *70*, 3114-3118.
38. Chang, C. K. *J. Chem. Soc. Chem. Commun.* **1977**, 800-801.
39. Pistorio, B. J.; Chang, C. J.; Nocera, D. G. *J. Am. Chem. Soc.* **2002**, *124*, 7884-7885.
40. Chang, C. J.; Brown, J. D. K.; Chang, M. C. Y.; Baker, E. A.; Nocera, D. G. In *Electron Transfer in Chemistry*; Balzani, V., Ed.; Wiley-VCH: Weinheim, Germany, 2001; Vol. 3.2.4, pp 409-461.
41. Cukier, R. I.; Nocera, D. G. *Annu. Rev. Phys. Chem.* **1998**, *49*, 337-369.
42. Chang, C. J.; Yeh, C.-Y.; Nocera, D. G. *J. Org. Chem.* **2002**, *67*, 1403-1406.
43. Yeh, C.-Y.; Chang, C. J.; Nocera, D. G. *J. Am. Chem. Soc.* **2001**, *123*, 1513-1514.
44. Armarego, W. L. F.; Perrin, D. D. *Purification of Laboratory Chemicals*; 4th ed.; Butterworth-Heinmann: Oxford, 1996.
45. Yuasa, M.; Steiger, B.; Anson, F. C. *J. Porphyrins Phthalocyanines* **1997**, *1*, 181-187.
46. Steiger, B.; Anson, F. C. *Inorg. Chem.* **1997**, *36*, 4138 - 4140.
47. Anson, F. C.; Shi, C.; Steiger, B. *Acc. Chem. Res.* **1997**, *30*, 437-444.

*Chapter 6*

**Fine Tuning the Pocket Sizes of Cofacial Bisporphyrins:  
Molecular Teeth for the Pacman Jaws**

A portion of the work presented in this chapter has been published:

Chang, C. J.; Deng, Y.; Lee, G.-H.; Peng, S.-M.; Yeh, C.-Y.; Nocera, D. G. *Inorg. Chem.*

**2002**, *41*, 3008-3016.

## 6.1 Motivation and Specific Aims

The combined structure-reactivity studies of the parent Pacman frameworks DPX and DPD highlight the importance of directed flexibility within catalytic microenvironments, and demonstrate that synthetic constructs with the ability to undergo large structural changes can lead to the design of efficient multielectron catalytic cycles. With these results in hand, we became interested in developing methods that would allow for more precise control of the Pacman binding pocket. Since modifications to the cofacial bisporphyrin motif have largely centered on the choice of pillar, we reasoned that altering the porphyrin superstructure itself would provide a versatile synthetic inroad to this type of fine control. Upon inspection of the etio-type porphyrin subunits of the parent DPX and DPD platforms, we decided to introduce sterically-demanding aryl groups *trans* to the spacer. Such ancillary functionalities serve as molecular “teeth” at the edge of the Pacman “bite”, and judicious choice of these substituents offers unprecedented electronic and sterically tunability of the Pacman motif. This chapter describes the synthesis, coordination chemistry, and structural attributes of the second-generation Pacman porphyrins DPXM (diporphyrin xanthene methoxyaryl) and DPDM (diporphyrin dibenzofuran methoxyaryl). The results establish that a single ancillary modification can lead to a marked effect on the pocket size and shape of the Pacman cavity.

## 6.2 Background

The continuing search for synthetic platforms to catalyze the multielectron transformation of small-molecule substrates has prompted significant attention towards the study of cofacial bisporphyrins and their transition-metal complexes.<sup>1,2</sup> At the forefront of this research is the development of cofacial Pacman bisporphyrins anchored by a single rigid pillar.<sup>3-24</sup> Such systems readily provide a face-to-face geometry with little lateral displacement between porphyrin subunits, while the single bridge allows for a range of binding geometries through distortion of the pocket “bite”. For the past 25 years, the cofacial Pacman systems have been limited to two spacers, anthracene (DPA)<sup>3</sup> and biphenylene (DPB).<sup>5</sup> These constructs have been quite prominent as electrocatalysts for the reduction of oxygen and other small molecules,<sup>4-7,11-14,17,19-22</sup> though the arduous synthesis of their prerequisite dialdehyde bridges has hampered extensive investigation.<sup>3,5,11,17</sup> In addition, the vertical pocket sizes of DPA and DPB differ by only ca. 1 Å,<sup>9</sup> offering a restricted window of conformational flexibility for exploring structure/function relationships.

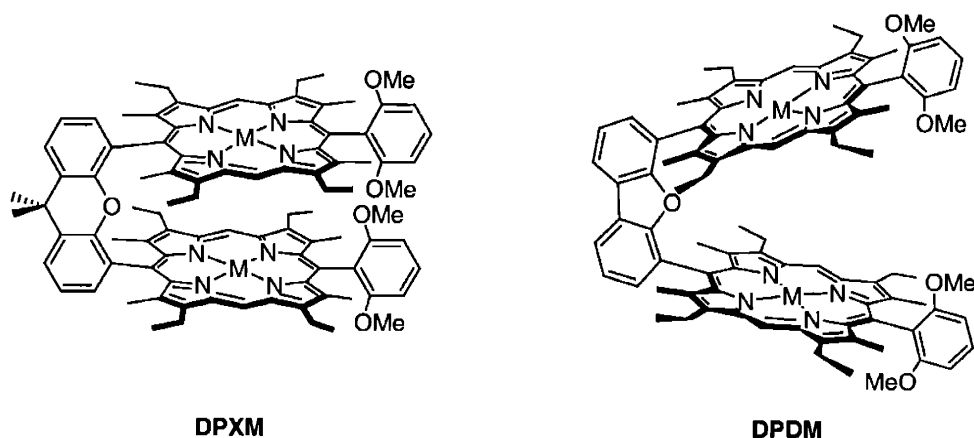
Our interest in the activation of small-molecule substrates within a proton-coupled electron transfer (PCET) framework<sup>25,26</sup> has led us to develop new cofacial bisporphyrins supported by xanthene (DPX) and dibenzofuran (DPD) scaffolds.<sup>27-30</sup> These systems display vertical pocket



sizes spanning over 5 Å in metal-metal distances with little to no lateral displacements. In particular, the DPD platform provided the first direct structural evidence for the Pacman effect within a pillared cofacial bisporphyrin motif through a comparative structural analysis of its bizinc(II) and bisiron(III)  $\mu$ -oxo complexes, which showed that this platform can open and close its binding pocket by a vertical distance of over 4 Å in the presence of appropriate substrates.<sup>30</sup> Subsequent reactivity studies demonstrate that the above-mentioned vertical flexibility of these platforms has important ramifications for the dynamic binding, activation and release of substrates and products. Notably, dicobalt(II) complexes of both DPX and DPD are effective electrocatalysts for the four-electron reduction of oxygen to water despite their ca. 4 Å difference in metal-metal distances,<sup>28</sup> and the bisiron(III)  $\mu$ -oxo complex of DPD shows superior reactivity compared to rigid or unbridged counterparts for the aerobic, photocatalytic oxidation of sulfides under mild conditions.<sup>31</sup>

The success of pillared cofacial bisporphyrins for multielectron small-molecule activation is based on their ability to provide a reaction pocket of suitable size and flexibility. Typically, such structural attributes have been largely controlled by the choice of spacer. In this chapter, we present a complementary approach for tuning the pocket sizes of pillared bisporphyrins by the selective introduction of sterically-demanding aryl groups opposite the cofacial bridge. The synthesis and coordination chemistry of xanthene and dibenzofuran anchored platforms structurally-modified with 2,6-dimethoxyaryl groups (DPXM = diporphyrin xanthene methoxyaryl and DPDM = diporphyrin dibenzofuran methoxyaryl, respectively in Chart 6.1) are described.<sup>32</sup>

**Chart 6.1**



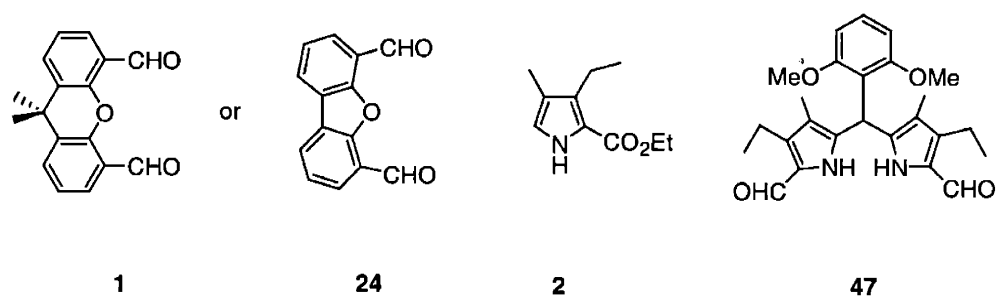
Crystallographic studies reveal that the *trans*-aryl groups serve as molecular “teeth” within the cleft of the cofacial bisporphyrin “bite”, affording a powerful approach for systematically tailoring the steric and electronic properties of the binding pockets through minimal changes along the porphyrin superstructure. The versatility of this synthetic methodology opens new avenues for the development of novel cofacial bisporphyrin systems for proton-coupled small-molecule activation chemistry.

## 6.3 Results and Discussion

### 6.3.1 Cofacial Bisporphyrin Derivatives Containing a Sterically-Demanding Aryl Group Opposite the Spacer

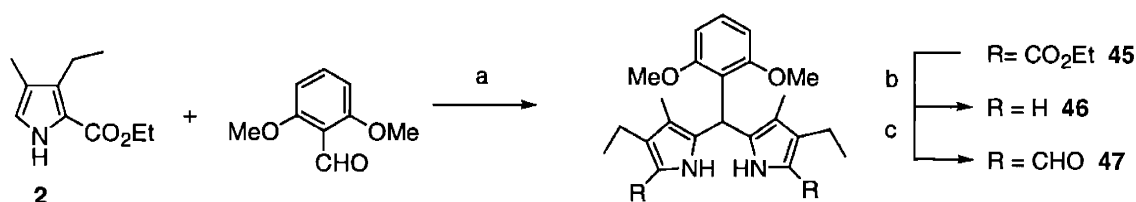
The synthetic strategy for the preparation of pillared cofacial bisporphyrins containing a single aryl group *trans* to the spacer is outlined in Schemes 6.1 to 6.5. We employ the convergent three-branch approach (Chart 6.2) developed by Chang<sup>3</sup> and modified by Collman;<sup>11</sup> the stepwise approach described here allows for the synthesis of meso and/or  $\beta$ -substituted derivatives with more precise control over statistical methods (e.g., Adler-Longo, Lindsey) that have been previously used to prepare  $\beta$ -free cofacial bisporphyrins bearing meso-aryl substituents.<sup>22,33</sup>

Chart 6.2

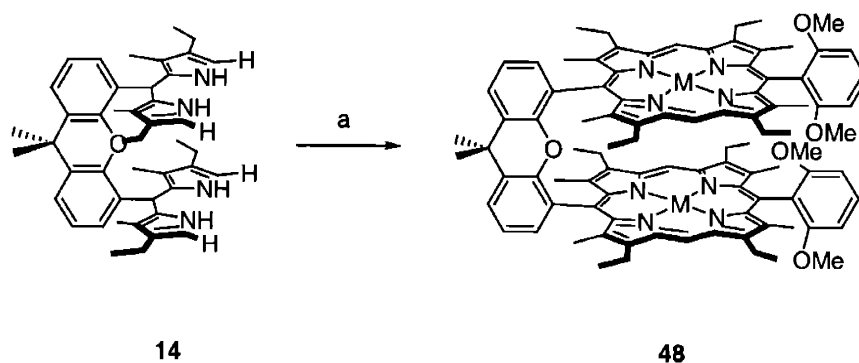


Aryl-substituted dipyrromethane dialdehydes are conveniently supplied in a three-step protocol from a pyrrole and an aldehyde; the 2,6-dimethoxyphenyl derivative is an exemplary system. Ester-protected dipyrromethane **45** is obtained in 89% yield by acid-catalyzed reaction of 2,6-dimethoxybenzaldehyde with  $\alpha$ -free pyrrole **2** in boiling ethanol. Deprotection of the  $\alpha$ -ethyl esters of **45** with sodium hydroxide in ethylene glycol gives  $\alpha$ -free dipyrromethane **46** in almost quantitative yield. Vilsmeier formylation of **46** using POCl<sub>3</sub>/DMF followed by base hydrolysis produces **47** in 98% yield.

Cyclization of xanthene tetrapyrrole **14** with dipyrromethane dialdehyde **47** in the presence of *p*-toluenesulfonic acid (PTSA) followed by oxidation with *o*-chloranil affords bisporphyrin **48** (DPXM = diporphyrin xanthene methoxyaryl) after workup and purification. The yield for the final coupling step (34%) is the highest reported for these types of pillared compounds. The <sup>1</sup>H NMR spectrum of **48** is consistent with a splayed structure in solution, as the internal NH-pyrrolic resonances ( $\delta$  -2.27, -3.68 ppm) are in the same range as an analogous monomeric xanthene porphyrin ( $\delta$  -3.10, -3.29 ppm).<sup>27</sup>



**Scheme 6.1.** (a) ethanol, HCl, reflux; (b) NaOH, ethylene glycol, reflux; (c) i. POCl<sub>3</sub>/DMF; ii. Na<sub>2</sub>CO<sub>3</sub>.

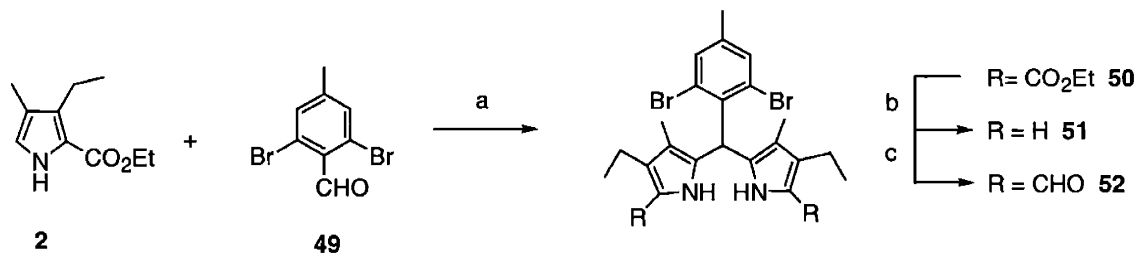


**Scheme 6.2.** (a) i. **47**, PTSA, methanol; ii. *o*-chloranil; M = 2H.

Xanthene-bridged cofacial bisporphyrins with a variety of aryl groups *trans* to the spacer may be envisioned using the strategies outlined in Schemes 6.1 and 6.2. Particularly interesting classes of examples are halogenated dipyrromethanes, owing to the facile applicability of metal-catalyzed cross-coupling reactions to elaborate these types of platforms.<sup>34-39</sup> Schemes 6.3 and 6.4 display the synthetic routes to a 2,6-dibromoaryldipyrromethane precursor and its installation into a xanthene-bridged cofacial bisporphyrin framework.

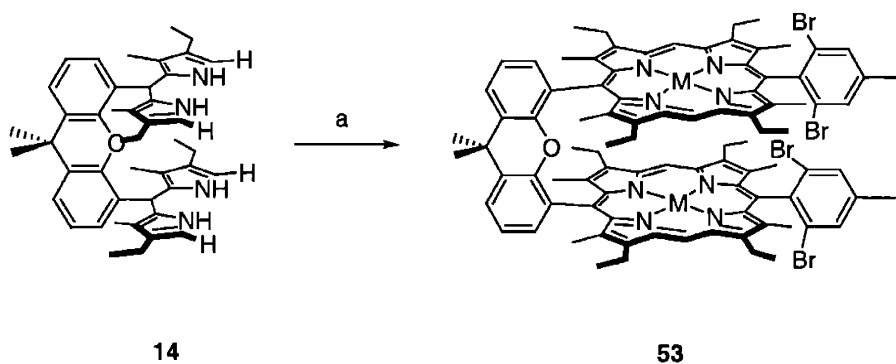
Dipyrromethane dialdehyde **52** is available using the standard three-step protocol. Ester-protected dipyrromethane **50** is obtained by acid-catalyzed reaction of 2,6-dibromo-4-methylbenzaldehyde **49** with  $\alpha$ -free pyrrole **2** in boiling ethanol. Deprotection of the  $\alpha$ -ethyl esters of

**50** with sodium hydroxide in ethylene glycol gives  $\alpha$ -free dipyrromethane **51** (75% yield over two steps). Vilsmeier formylation of **51** using POCl<sub>3</sub>/DMF followed by base hydrolysis produces **52** in 75% yield.



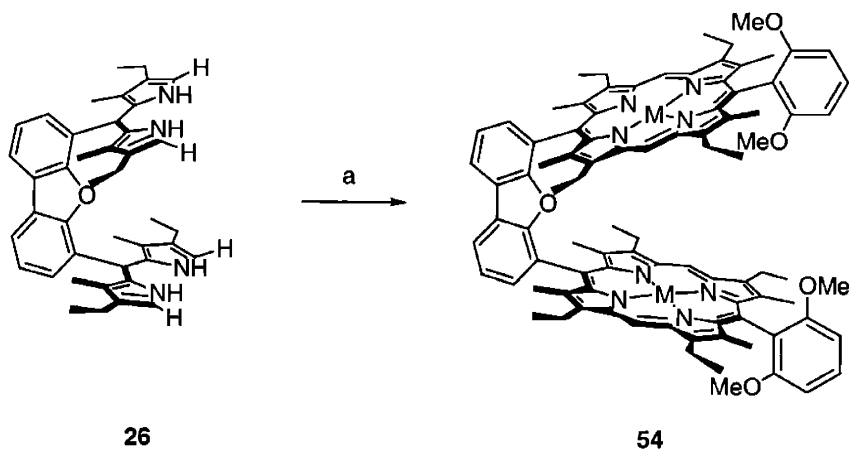
**Scheme 6.3.** (a) ethanol, HCl, reflux; (b) NaOH, ethylene glycol, reflux; (c) i. POCl<sub>3</sub>/DMF; ii. Na<sub>2</sub>CO<sub>3</sub>.

Cyclization of xanthene tetrapyrrole **14** with dipyrromethane dialdehyde **52** in the presence of PTSA followed by oxidation with *o*-chloranil affords bisporphyrin **53** (DPXB = diporphyrin xanthene bromoaryl) after workup and purification. The yield for the final coupling step (22%) is typical for these types of pillared compounds. The <sup>1</sup>H NMR spectrum of **53** is consistent with a splayed structure in solution, as the internal NH-pyrrolic resonances ( $\delta$ –2.46, –3.61 ppm) are in the same range as an analogous monomeric xanthene porphyrin ( $\delta$ –3.10, –3.29 ppm).<sup>27</sup>



**Scheme 6.4.** (a) i. **52**, PTSA, methanol; ii. *o*-chloranil; M = 2H.

The use of aryl dipyrromethanes is not limited to bisporphyrin templates containing a xanthene pillar. For example, the dibenzofuran tetrapyrrole **26** undergoes cyclization with **47** in the presence of PTSA to give the corresponding cofacial bisporphyrin H<sub>4</sub>(DPDM) (**54**) (DPDM = diporphyrin dibenzofuran methoxyaryl) in 11% yield. As observed for **54** and the parent bisporphyrin H<sub>4</sub>(DPD), the chemical shift for the internal NH-pyrrolic resonances ( $\delta$ –2.83 ppm) indicates an open structure in solution.<sup>30</sup>



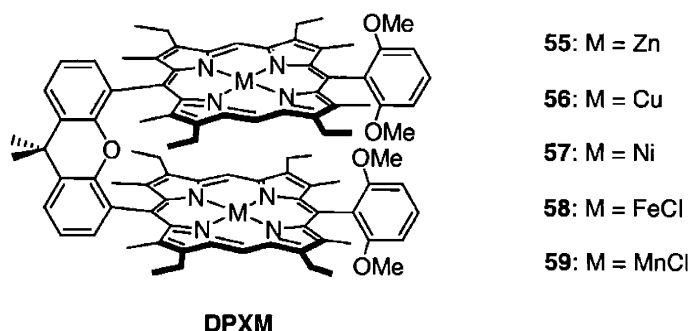
**Scheme 6.5.** (a) i. **47**, PTSA, methanol; ii. *o*-chloranil; M = 2H.

### 6.3.2 Transition-Metal Complexes of DPXM and DPDM

The coordination chemistry of xanthene- and dibenzofuran-bridged cofacial bisporphyrins structurally modified with sterically-demanding aryl groups *trans* to the spacer (DPXM and DPDM, respectively) proceeds as described for the parent DPX and DPD compounds.

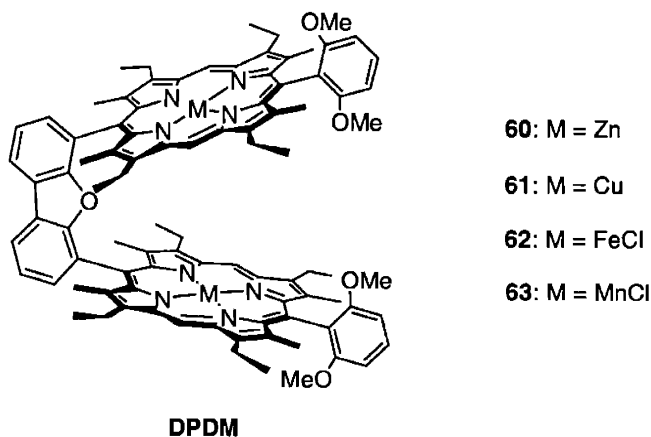
Homobimetallic coordination complexes of H<sub>4</sub>(DPXM) (**48**) are prepared smoothly by direct reaction with metal salts (Chart 6.3). The binuclear zinc(II) complex Zn<sub>2</sub>(DPXM) (**55**) is obtained in quantitative yield by reaction of **48** with Zn(OAc)<sub>2</sub>·2H<sub>2</sub>O in methanol/chloroform mixtures. Complex **55** was characterized by <sup>1</sup>H NMR, high-resolution mass spectrometry and elemental analyses. The biscopper(II) complex Cu<sub>2</sub>(DPXM) (**56**) is prepared in excellent yield (87%) from H<sub>4</sub>(DPXM) (**48**) using Cu(OAc)<sub>2</sub>·2H<sub>2</sub>O and potassium acetate in methanol/chloroform mixtures. Complex **56** gave satisfactory high-resolution mass spectral and elemental analyses. Dinickel complex Ni<sub>2</sub>(DPXM) (**57**) is synthesized in good yield (81%) using Adler's method (NiCl<sub>2</sub>/DMF).<sup>40</sup> The diamagnetic compound was characterized by <sup>1</sup>H NMR, high-resolution mass spectrometry and elemental analyses. Bischloroiron(III) compound **58** is delivered in good yield (83%) from reaction of **48** with FeBr<sub>2</sub> and 2,6-lutidine in a THF/benzene solvent system followed by anion exchange with aq NaCl and HCl. Satisfactory high-resolution mass spectral data and elemental analyses accompanied **58**. Lastly, bischloromanganese(III) complex **59** is afforded in high yield (89%) by an Alder reaction of **48** with Mn(OAc)<sub>2</sub>·4H<sub>2</sub>O in DMF with subsequent anion exchange in the same manner as the bischloroiron(III) derivative (aq NaCl/HCl).

### Chart 6.3



Coordination compounds of the analogous dibenzofuran-bridged DPDM framework are also available by reaction with metal salts (Chart 6.4). Zinc insertion proceeds in quantitative yield using the standard method ( $\text{Zn}(\text{OAc})_2 \cdot 2\text{H}_2\text{O}$ , methanol/dichloromethane) to generate  $\text{Zn}_2(\text{DPDM})$  (**60**). Complex **60** was fully characterized by  $^1\text{H}$  NMR, high-resolution spectrometry and elemental analyses. The biscopper(II) complex  $\text{Cu}_2(\text{DPDM})$  (**61**) is prepared in excellent yield (88%) from  $\text{H}_4(\text{DPDM})$  (**54**) using  $\text{Cu}(\text{OAc})_2 \cdot 2\text{H}_2\text{O}$  and potassium acetate in methanol/chloroform mixtures. Complex **61** gave satisfactory high-resolution mass spectral analysis. Bischloroiron(III) compound **62** is delivered in good yield (86%) from reaction of **54** with  $\text{FeBr}_2$  and 2,6-lutidine in a THF/benzene solvent system followed by anion exchange with HCl. Satisfactory high-resolution mass spectral data accompanied **62**. Lastly, bischloromanganese(III) complex **63** is afforded in high yield (91%) by an Alder reaction of **54** with  $\text{Mn}(\text{OAc})_2 \cdot 4\text{H}_2\text{O}$  in DMF followed by anion exchange using aq NaCl/HCl.

### Chart 6.4



### 6.3.3 Structural Chemistry of DPXM

The structural consequences of a single aryl group *trans* to the spacer have been investigated using single-crystal X-ray analysis. In order to provide a systematic study, three structures of the DPXM framework have been determined for comparison with known DPX and DPD congeners: the free-base bisporphyrin **48**, compound **55** containing the non-redox-active zinc(II) metal, and complex **59** bearing redox-active manganese centers. The molecular structures of **48**, **55** and **59** are shown in Figures 6.1 to 6.3. Crystallographic data and selected geometrical measurements are given in Tables 6.1-6.4. Trends in bond lengths and angles of macrocyclic core structures and side chains agree well with those observed in related systems such as DPX and DPD.<sup>27-30</sup> Structural highlights of the core structures for **48**, **55** and **59** are as follows.

**H<sub>4</sub>(DPXM) (48)**. Both ring systems display a saddle conformation in the solid state. The porphyrin subunit containing N(1) to N(4) (ring 1) has a mean deviation from planarity of 0.23 Å with meso carbons alternately displaced from the porphyrin mean plane, ranging from 0.39 Å above to 0.38 Å below the 24-atom macrocyclic unit. The macrocycle containing N(5) to N(8) (ring 2) exhibits a slightly greater mean deviation from planarity (0.29 Å). Similar to the ring containing N(1) to N(4), the porphyrin with N(5) to N(8) contains meso carbons alternately displaced from the macrocyclic mean plane, ranging from 0.30 Å above to 0.36 Å below the 24-atom ring subunit. The internal pyrrolic hydrogen atoms are in their calculated positions, and are disordered over all the nitrogen atoms. A interesting feature of **48** is the small butterfly fold of the xanthene backbone along its center O(1)—C(47) axis. For **48**, the butterfly angle is 5.5°; in contrast, the parent porphyrin H<sub>4</sub>(DPX) has a large butterfly distortion of 36.1°.<sup>29</sup>

**Zn<sub>2</sub>(DPXM) (55)**. A conformational analysis reveals inequivalent ring systems; however, both macrocycles of **55** display a saddle conformation. The core containing Zn(1) has a more pronounced saddle distortion with a mean deviation from planarity of 0.16 Å. The ring with Zn(2) has a mean deviation from planarity of 0.11 Å. The zinc(II) ions are situated in different coordination environments. Zn(1) is five-coordinate, binding an axial methanol solvate within the bisporphyrin pocket at a distance of 2.175(5) Å. The Zn(II) core adopts an approximate square-pyramidal geometry, as the N—Zn—N bond angles are 90 ± 3.5° and the N—Zn—O bond angles are 90 ± 9.2°. The zinc center is displaced slightly from the porphyrin meanplane toward the axial ligand (0.21 Å). The average equatorial Zn—N bond length of 2.062(4) Å is in good agreement with literature values for five-coordinate zinc(II) porphyrins.<sup>41</sup> In contrast, Zn(2) is six-coordinate, binding an axial methanol solvate outside the bisporphyrin pocket and an axial water molecule inside the cofacial cleft. The Zn—O bond lengths for the axial methanol and water are 2.252(6) Å and 2.459(17) Å, respectively. The Zn(II) center assumes a distorted

octahedral geometry, and is displaced 0.11 Å toward the outer face of the bisporphyrin toward the axial methanol; the N–Zn–N bond angles are  $90 \pm 3.2^\circ$  and the N–Zn–O bond angles are  $90 \pm 5.5^\circ$ . The average equatorial Zn–N bond length is 2.057(5) Å.

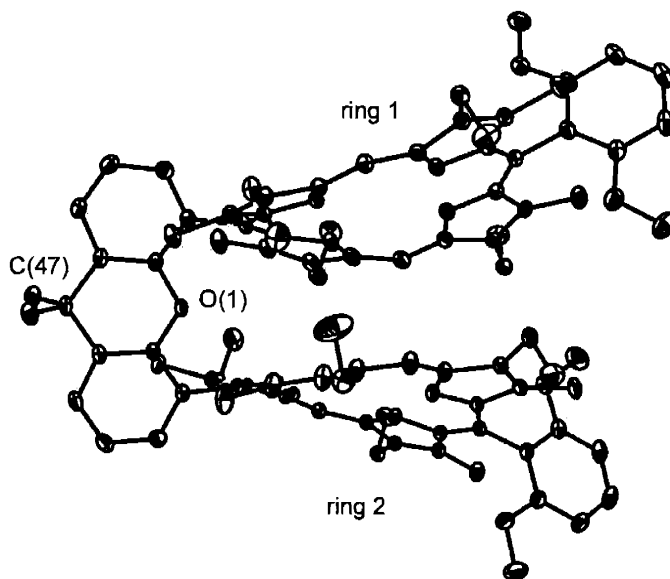


**Figure 6.1.** Crystal structure of  $H_4(DPXM)$  (**48**). Thermal ellipsoids are drawn at the 25% probability level. Hydrogen atoms and solvent molecules within the lattice have been omitted for clarity.

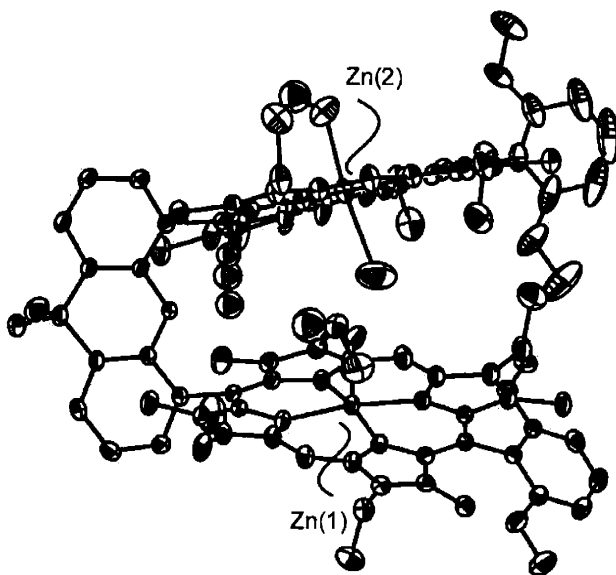


**Figure 6.2.** Crystal structure of  $Zn_2(DPXM)$  (**55**). Thermal ellipsoids are drawn at the 25% probability level. Hydrogen atoms and solvent molecules within the lattice have been omitted for clarity.



*Mn<sub>2</sub>Cl<sub>2</sub>(DPXM)* (**59**). The pentacoordinate Mn centers assume a highly distorted square-pyramidal geometry, as the N—Mn—N bond angles are  $90 \pm 4.7^\circ$  and the N—Mn—Cl bond angles are  $90 \pm 10.3^\circ$ . The axial chlorides are coordinated to the Mn(III) ions outside the cofacial pocket with an average Mn—Cl bond length of 2.405(2) Å. The metal centers Mn(1) and Mn(2) are displaced out of the porphyrin planes toward the axial chloride ligands by 0.25 Å and 0.27 Å, respectively. The average Mn—N bond length is 2.009(5) Å. Both Mn(III) macrocycles exhibit a pronounced nonplanar distortion. The macrocycle containing Mn(1) has mean deviation from planarity of 0.70 Å, while the ring with Mn(2) has a mean deviation from planarity of 0.64 Å.

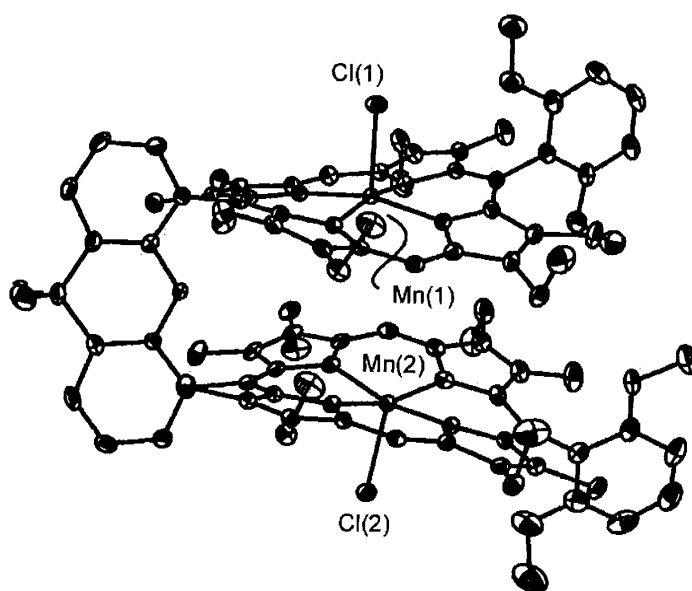


**Figure 6.3.** Crystal structure of *Mn<sub>2</sub>Cl<sub>2</sub>(DPXM)* (**59**). Thermal ellipsoids are drawn at the 25% probability level. Hydrogen atoms and solvent molecules within the lattice have been omitted for clarity.

**Table 6.1.** Crystallographic Data for H<sub>4</sub>(DPXM) (**48**), Zn<sub>2</sub>(DPXM) (**55**), and Mn<sub>2</sub>Cl<sub>2</sub>(DPXM) (**59**).

	<b>48</b>	<b>55</b>	<b>59</b>
Empirical formula	C <sub>97</sub> H <sub>106</sub> Cl <sub>4</sub> N <sub>8</sub> O <sub>5</sub>	C <sub>101</sub> H <sub>123</sub> Cl <sub>2</sub> N <sub>8</sub> O <sub>11.5</sub> Zn <sub>2</sub>	C <sub>99</sub> H <sub>102</sub> Cl <sub>14</sub> N <sub>8</sub> O <sub>5</sub> Mn <sub>2</sub>
Formula weight	1605.72	1834.71	2090.10
Temperature	183(2)	183(2)	183(2)
Wavelength	0.71073 Å	0.71073 Å	0.71073 Å
Crystal system	Monoclinic	Monoclinic	Monoclinic
Space group	P2 <sub>1</sub> /c	P2 <sub>1</sub> /n	P2/c
Unit cell dimensions	$a = 28.8353(12)$ Å $b = 17.1139(7)$ Å $c = 17.5978(7)$ Å  $\beta = 98.826(1)^\circ$	$a = 14.5517(6)$ Å $b = 22.9226(10)$ Å $c = 28.5155(13)$ Å  $\beta = 90.3121(14)^\circ$	$a = 19.5891(3)$ Å $b = 15.0741(2)$ Å $c = 33.2019(6)$ Å  $\beta = 91.947(10)^\circ$
Volume	8581.4(6) Å <sup>3</sup>	9511.6(7) Å <sup>3</sup>	9798.5(3) Å <sup>3</sup>
Z	4	4	4
Density (calculated)	1.243 Mg/m <sup>3</sup>	1.281 Mg/m <sup>3</sup>	1.420 Mg/m <sup>3</sup>
Absorption coefficient	0.196 mm <sup>-1</sup>	0.624 mm <sup>-1</sup>	0.696 mm <sup>-1</sup>
F(000)	3408	3884	4336
Crystal size	0.50 × 0.31 × 0.30 mm <sup>3</sup>	0.10 × 0.26 × 0.40 mm <sup>3</sup>	0.50 × 0.25 × 0.20 mm <sup>3</sup>
θ range for data collect	2.14 to 26.37°	2.32 to 26.38°	1.23 to 23.24°
Reflections collected	43593	48278	38526
Independent reflections	17101 (R <sub>int</sub> = 0.0342)	19020 (R <sub>int</sub> = 0.0394)	14012 (R <sub>int</sub> = 0.0446)
Data / restraints /param	17101 / 0 / 1043	19020 / 4 / 1078	13991 / 0 / 1154
Goodness-of-fit on F <sup>2</sup>	1.051	1.022	1.101
Final R indices	R1 = 0.0683	R1 = 0.0854	R1 = 0.0812
[I>2σ(I)]	wR2 = 0.1850	wR2 = 0.2323	wR2 = 0.2045
R indices (all data)	R1 = 0.0974 wR2 = 0.2095	R1 = 0.1283 wR2 = 0.2737	R1 = 0.1026 wR2 = 0.2286
Largest diff peak	0.934 eÅ <sup>-3</sup>	1.208 eÅ <sup>-3</sup>	1.486 eÅ <sup>-3</sup>
Largest diff hole	-0.502 eÅ <sup>-3</sup>	-0.931 eÅ <sup>-3</sup>	-1.021 eÅ <sup>-3</sup>

**Table 6.2.** Selected Geometric Lengths (Å) for H<sub>4</sub>(DPXM) (**48**), Zn<sub>2</sub>(DPXM) (**55**), and Mn<sub>2</sub>Cl<sub>2</sub>(DPXM) (**59**).

	48	55	59		
Ct(1)–N(1)	2.129	Zn(1)–N(1)	2.063(4)	Mn(1)–N(1)	2.015(5)
Ct(1)–N(2)	2.014	Zn(1)–N(2)	2.062(4)	Mn(1)–N(2)	1.999(5)
Ct(1)–N(3)	2.118	Zn(1)–N(3)	2.066(4)	Mn(1)–N(3)	2.015(5)
Ct(1)–N(4)	2.021	Zn(1)–N(4)	2.057(4)	Mn(1)–N(4)	1.996(5)
Ct(2)–N(5)	2.013	Zn(2)–N(5)	2.047(4)	Mn(2)–N(5)	2.004(7)
Ct(2)–N(6)	2.119	Zn(2)–N(6)	2.049(5)	Mn(2)–N(6)	2.014(5)
Ct(2)–N(7)	2.007	Zn(2)–N(7)	2.065(4)	Mn(2)–N(7)	2.010(4)
Ct(2)–N(8)	2.114	Zn(2)–N(8)	2.068(4)	Mn(2)–N(8)	2.017(5)
O(1)–C(52)	1.375(3)	Zn(1)–O(6)	2.175(5)	Mn(1)–Cl(1)	2.400(2)
O(1)–C(53)	1.376(3)	Zn(2)–O(7)	2.252(6)	Mn(2)–Cl(2)	2.409(2)
		Zn(2)–O(8)	2.459(17)		

Taken together, the crystallographic data reveal that the introduction of a single aryl group *trans* to the spacer can considerably alter the pocket sizes of pillared cofacial bisporphyrins. Metrics are given in Figure 6.4.

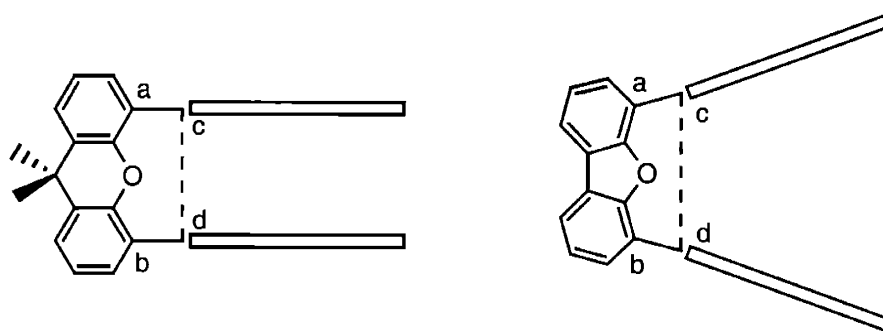


**Figure 6.4.** Illustrated distances a–b and c–d for the cofacial bisporphyrin systems DPXM (left) and DPDM (right). Table 6.4 sub-caption defines the methods by which the crystallographically derived geometric features were measured.

The molecular structures of homologous biszinc(II) complexes of the DPX, DPXM and DPD series shown in Figure 6.5 confirm that this type of substitution for the DPXM framework affords a family of bisporphyrin platforms that exhibit vertical pocket sizes that are intermediate

to those of the parent systems DPX and DPD. This is clearly illustrated by the observed center-to-center distances, which vary from 5.0 to 6.1 Å for the DPXM platforms. For comparison, the DPX and DPD systems have center-to-center distances of 3.8 to 4.7 Å and 7.6 to 8.2 Å, respectively. The pocket size enlargements of the DPXM series compared to their DPX counterparts are predominantly due to vertical changes, revealed by the interplanar angles between the two porphyrinic subunits. The DPXM series has interplanar angles in the range of 16.9° to 32.9°. In contrast, the ring-parallel DPX complexes display interplanar angles of less than 5°. Horizontal changes are modest, as the torsional angles for the structures of **48**, **55**, and **59** are all less than 26°.

**Table 6.3.** Selected Geometric Angles (deg) for H<sub>4</sub>(DPXM) (**48**), Zn<sub>2</sub>(DPXM) (**55**), and Mn<sub>2</sub>Cl<sub>2</sub>(DPXM) (**59**).

	<b>48</b>		<b>55</b>		<b>59</b>
N(1)-Ct(1)-N(2)	83.3	N(1)-Zn(1)-N(2)	86.6(2)	N(1)-Mn(1)-N(2)	91.9(2)
N(1)-Ct(1)-N(3)	179.4	N(1)-Zn(1)-N(3)	166.3(2)	N(1)-Mn(1)-N(3)	163.1(2)
N(2)-Ct(1)-N(3)	96.5	N(2)-Zn(1)-N(3)	92.0(2)	N(2)-Mn(1)-N(3)	86.4(2)
N(1)-Ct(1)-N(4)	97.0	N(1)-Zn(1)-N(4)	92.1(2)	N(1)-Mn(1)-N(4)	86.6(2)
N(2)-Ct(1)-N(4)	179.3	N(2)-Zn(1)-N(4)	169.9(2)	N(2)-Mn(1)-N(4)	168.3(2)
N(3)-Ct(1)-N(4)	83.2	N(3)-Zn(1)-N(4)	86.9(2)	N(3)-Mn(1)-N(4)	91.7(2)
N(7)-Ct(2)-N(8)	83.4	N(7)-Zn(2)-N(8)	86.5(2)	N(7)-Mn(2)-N(8)	92.4(2)
N(7)-Ct(2)-N(6)	96.5	N(7)-Zn(2)-N(6)	92.5(2)	N(7)-Mn(2)-N(6)	85.3(2)
N(8)-Ct(2)-N(6)	177.8	N(8)-Zn(2)-N(6)	172.0(2)	N(8)-Mn(2)-N(6)	162.2(2)
N(7)-Ct(2)-N(5)	177.7	N(7)-Zn(2)-N(5)	176.1(2)	N(7)-Mn(2)-N(5)	166.6(2)
N(8)-Ct(2)-N(5)	96.5	N(8)-Zn(2)-N(5)	92.8(2)	N(8)-Mn(2)-N(5)	86.3(2)
N(6)-Ct(2)-N(5)	83.7	N(6)-Zn(2)-N(5)	87.7(2)	N(6)-Mn(2)-N(5)	91.9(2)
C(53)-O(1)-C(52)	119.6(2)	N(1)-Zn(1)-O(6)	99.2(2)	N(1)-Mn(1)-Cl(1)	98.2(1)
C(52)-C(51)-C(25)	121.3(2)	N(2)-Zn(1)-O(6)	94.6(2)	N(2)-Mn(1)-Cl(1)	94.3(2)
C(53)-C(41)-C(5)	122.3(2)	N(3)-Zn(1)-O(6)	94.5(2)	N(3)-Mn(1)-Cl(1)	98.7(1)
C(50)-C(51)-C(25)	120.0(2)	N(4)-Zn(1)-O(6)	95.5(2)	N(4)-Mn(1)-Cl(1)	97.4(1)
C(42)-C(41)-C(5)	119.3(2)	N(5)-Zn(2)-O(7)	94.2(2)	N(5)-Mn(2)-Cl(2)	97.1(1)
C(51)-C(52)-O(1)	115.0(2)	N(6)-Zn(2)-O(7)	92.5(2)	N(6)-Mn(2)-Cl(2)	102.6(2)
C(41)-C(53)-O(1)	115.0(2)	N(7)-Zn(2)-O(7)	89.7(2)	N(7)-Mn(2)-Cl(2)	96.3(1)
		N(8)-Zn(2)-O(7)	83.6(5)	N(8)-Mn(2)-Cl(2)	95.2(1)

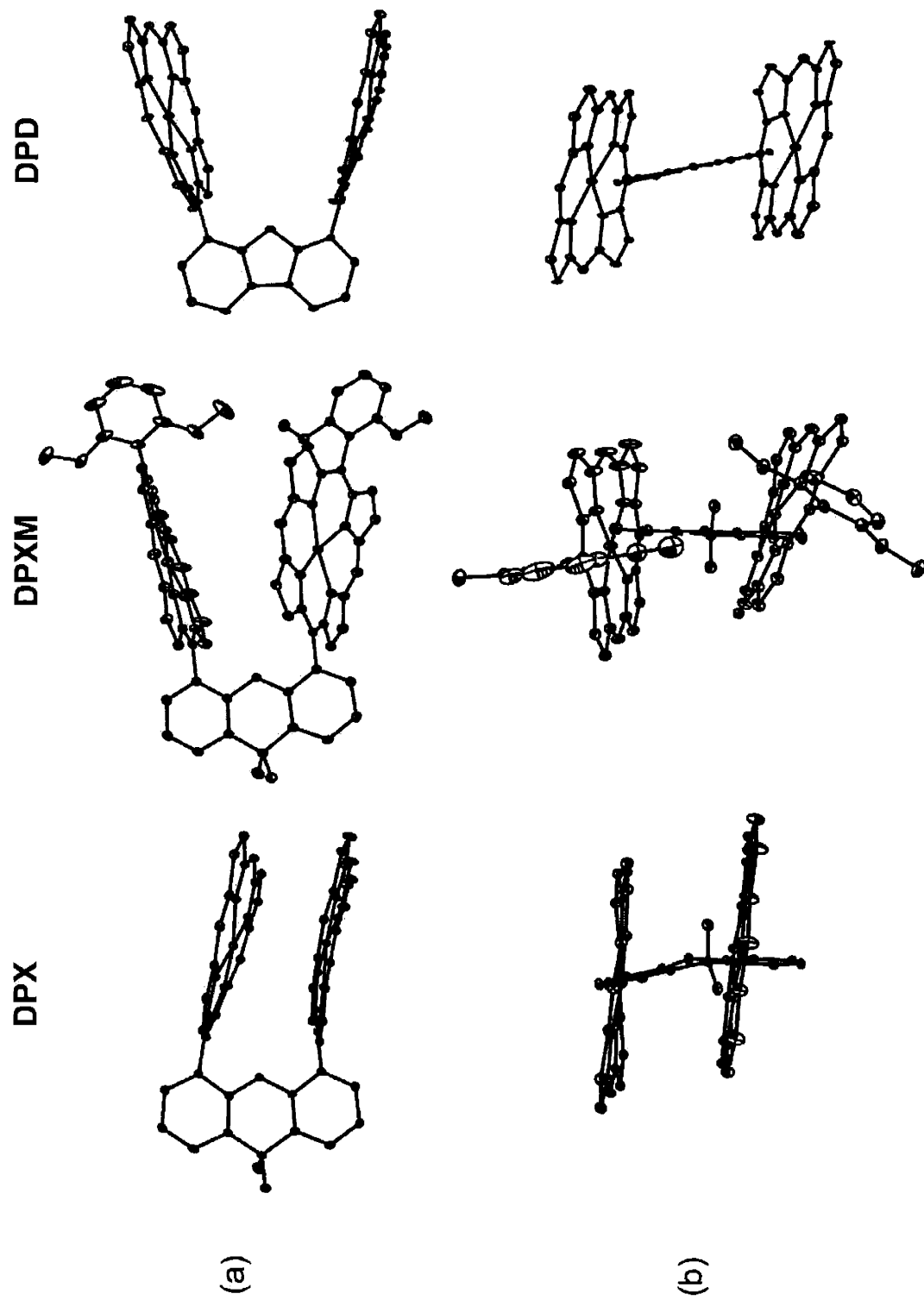


**Figure 6.5.** Comparative views of the crystal structures of  $Zn_2(DPX)$  (16),  $Zn_2(DPXM)$  (55), and  $Zn_2(DPD)$  (28): (a) side view, perpendicular to the bridge plane; (b) side view, parallel to the bridge plane. Alkyl side groups and hydrogen atoms omitted for clarity.

**Table 6.4.** Crystallographically Derived Intradimer Geometrical Features for DPX, DPD, and DPXM Compounds.<sup>a</sup>

	M—M (Å)	Ct—Ct (Å)	interplanar angle (deg)	torsional twist (deg)	a—b dist (Å)	c—d dist (Å)
H <sub>4</sub> (DPX) (15)	NA	4.002	4.7	14.3	3.552	4.324
H <sub>4</sub> (DPD) (27)	NA	8.220	23.0	1.9	4.853	5.654
H <sub>4</sub> (DPXM) (48)	NA	6.104	16.9	26.0	4.675	4.602
Zn <sub>2</sub> (DPX) (16)	3.708	3.863	4.4	7.9	4.619	4.272
Zn <sub>2</sub> (DPD) (28)	7.775	7.587	24.6	1.2	4.800	5.577
Zn <sub>2</sub> (DPXM) (55)	5.913	5.987	32.9	13.1	4.676	4.677
Mn <sub>2</sub> (DPXM) (59)	5.378	4.982	20.8	19.2	4.656	4.485

<sup>a</sup> Metrics were derived as follows. Macrocyclic centers (Ct) were calculated as the centers of the four nitrogen planes (4-N plane) for each macrocycle. Interplanar angles were measured as the angle between the 4-N least squares planes. Torsional twists were measured as the angle between the two meso-carbon to spacer bonds. The a-b and c-d separations represent the distances between the bridge carbons attached to the porphyrin meso positions and those porphyrin meso carbons, respectively (Figure 6.4).

## 6.4 Concluding Remarks

The success of cofacial bisporphyrins for efficient multielectron catalysis has traditionally relied on the choice of spacer to provide a suitable cavity for substrate activation. In contrast, our results reveal that strategic modification of the porphyrin superstructure by substitution *trans* to the spacer can also dramatically tune the vertical pocket sizes of cofacial bisporphyrins. To this end, the synthesis and coordination chemistry of methoxyaryl-modified xanthene (DPXM) and dibenzofuran (DPDM) systems has been achieved. In particular, crystallographic analysis confirms the ability of the DPXM platform to provide cofacial pockets with vertical pocket sizes that span the parent DPX and DPD platforms. The modular nature of this synthetic methodology should provide ready access to more intricate structural modifications, as the prerequisite aryl dipyrromethanes are readily obtained in large gram-scale quantities. The application of these and related systems for the study of proton-coupled small-molecule activation is underway.

## 6.5 Experimental Section

### 6.5.1 Materials

Silica gel 60 (70-230 and 230-400 mesh, Fisher) was used for column chromatography. Analytical thin layer chromatography was performed using silica gel (precoated sheets, 0.2 mm thick). Solvents for synthesis were of reagent grade or better, and were dried according to standard methods.<sup>42</sup> Spectroscopic experiments employed dichloromethane (spectroscopic grade, Burdick & Jackson), which was stored over 4 Å molecular sieves under high vacuum or in a glovebox. Starting materials for syntheses were obtained as follows: 2-(Ethoxycarbonyl)-3-ethyl-4-methylpyrrole (**2**), 4,5-bis[4,4'-diethyl-3,3'-dimethyl-2,2'-dipyrromethyl]-9,9-dimethylxanthene (**14**), and 4,6-bis[4,4'-diethyl-3,3'-dimethyl-2,2'-dipyrromethyl]dibenzofuran (**26**) were prepared as described in chapter 2. 2,6-Dibromo-4-methylbenzaldehyde (**49**) was synthesized by reduction of the corresponding cyano compound with DIBAL-H.<sup>43</sup> All other reagents were used as received.

### 6.5.2 (2,6-Dimethoxyphenyl)-bis(5-ethoxycarbonyl-4-ethyl-3-methyl-2-pyrrolyl)methane (**45**)

A mixture of 2,6-dimethoxybenzaldehyde (5.0 g, 30.1 mmol) and pyrrole **2** (10.9 g, 60.2 mmol, 2 equiv) in absolute ethanol (150 mL) containing concentrated HCl (2.5 mL) was refluxed under nitrogen for 18 h and cooled in an ice bath. The precipitate was filtered and washed with cold methanol to give **45** as a pale-pink powder (13.8 g, 89% yield). <sup>1</sup>H NMR (300 MHz, CDCl<sub>3</sub>, 25 °C): δ = 9.07 (br s, 2H, NH), 7.18 (t, *J* = 8.4 Hz, 1H, ArH), 6.60 (d, *J* = 8.4 Hz, 2H, ArH), 6.19 (s, 1H, CH), 4.23 (q, *J*<sub>1</sub> = 7.2 Hz, *J*<sub>2</sub> = 7.2 Hz, 4H, CH<sub>2</sub>), 3.78 (s, 6H, CH<sub>3</sub>), 2.69 (q, *J*<sub>1</sub> = 7.2 Hz,

$J_2 = 7.5$  Hz, 4H, CH<sub>2</sub>), 1.81 (s, 6H, CH<sub>3</sub>), 1.31 (t,  $J = 7.2$  Hz, 6H, CH<sub>3</sub>), 1.06 (t,  $J = 7.5$  Hz, 6H, CH<sub>3</sub>).

### 6.5.3 (2,6-Dimethoxyphenyl)-bis(4-ethyl-3-methyl-2-pyrrolyl)methane (46)

Powdered NaOH (12 g) in water (15 mL) was combined with **45** (12.0 g, 23.5 mmol) suspended in ethylene glycol (120 mL). The mixture was refluxed under nitrogen for 16 h and cooled to room temperature. The precipitate was collected by suction filtration, washed with water until the washings became neutral, and dried under vacuum over P<sub>2</sub>O<sub>5</sub>. Product **46**, which was obtained as a goldenrod solid (8.5 g, 99% yield), was stored under nitrogen at -20 °C. <sup>1</sup>H NMR (300 MHz, CDCl<sub>3</sub>, 25 °C):  $\delta = 8.15$  (br s, 2H, NH), 7.00 (t,  $J = 8.4$  Hz, 1H, ArH), 6.47 (d,  $J = 8.4$  Hz, 2H, ArH), 6.24 (d,  $J = 2.4$  Hz, 2H, CH), 6.07 (s, 1H, CH), 3.63 (s, 6H, CH<sub>3</sub>), 2.29 (q,  $J_1 = 7.5$  Hz,  $J_2 = 7.8$  Hz, 4H, CH<sub>2</sub>), 1.70 (s, 6H, CH<sub>3</sub>), 1.31 (t,  $J = 7.2$  Hz, 6H, CH<sub>3</sub>).

### 6.5.4 (2,6-Dimethoxyphenyl)-bis(5-formyl-4-ethyl-3-methyl-2-pyrrolyl)methane (47)

Under a nitrogen atmosphere, phosphorus oxychloride (14 mL) was added dropwise to a solution of **46** in anhydrous DMF (50 mL) at -10 °C. After stirring at -10 °C for 30 min, the resulting mixture was allowed to warm to room temperature and stirred for an additional 2 h. The reaction was concentrated to half its original volume and methanol (200 mL) and Na<sub>2</sub>CO<sub>3</sub> (20 g) were added. The mixture was heated at 60 °C for 30 min and cooled to room temperature. The precipitate was filtered and washed with water until the washings became neutral. Recrystallization from methanol afforded **47** as an ochre solid (7.2 g, 98% yield). <sup>1</sup>H NMR (300 MHz, CDCl<sub>3</sub>, 25 °C):  $\delta = 9.48$  (s, 2H, CHO), 9.14 (br s, 2H, NH), 7.21 (t,  $J = 8.4$  Hz, 1H, ArH), 6.60 (d,  $J = 8.4$  Hz, 2H, ArH), 6.17 (br s, 1H, CH), 3.76 (s, 6H, CH<sub>3</sub>), 2.65 (q,  $J_1 = 7.5$  Hz,  $J_2 = 7.8$  Hz, 4H, CH<sub>2</sub>), 1.78 (s, 6H, CH<sub>3</sub>), 1.15 (t,  $J = 7.2$  Hz, 6H, CH<sub>3</sub>).

### 6.5.5 4,5-Bis[(2,3,13,17-tetraethyl-3,7,12,18-tetramethyl-15-(2,6-dimethoxyphenyl)-5-porphyrinyl)]-9,9-dimethylxanthene, H<sub>4</sub>(DPXM) (48)

A suspension of xanthene tetrapyrrole **14** (2.19 g, 3.28 mmol) and **47** (2.80 g, 6.63 mmol) in freshly distilled methanol (400 mL) was purged with nitrogen for 20 min. A solution of *p*-toluenesulfonic acid (1.2 g) in methanol (20 mL) was added dropwise over a period of 1 h. The resulting red mixture was stirred in the dark under nitrogen for 2 d. Solid *o*-chloranil (0.9 g) was added in one portion and stirring was continued in air for 24 h. The mixture was concentrated to half its original volume and the precipitate was suction-filtered and washed with cold methanol and water. The solid was redissolved in chloroform (100 mL), a saturated methanolic solution of Zn(OAc)<sub>2</sub>·2H<sub>2</sub>O (10 mL) was added, and the solution was refluxed for 30 min. The solvent was removed and the remaining residue was purified by flash column chromatography (silica gel, 1:1



dichloromethane/hexanes). The bright red band eluted was collected, taken to dryness, and redissolved in dichloromethane (150 mL). The solution was vigorously stirred with 6 N HCl (16 mL) for 15 min, neutralized with a 10% aqueous sodium carbonate solution and the mixture was stirred for an additional 15 min. The organic phase was separated, washed with water (3 × 50 mL), dried over Na<sub>2</sub>SO<sub>4</sub> and taken to dryness. Recrystallization from dichloromethane/methanol afforded pure **48** as a royal purple microcrystalline powder (1.57 g, 34% yield). <sup>1</sup>H NMR (500 MHz, CDCl<sub>3</sub>, 25 °C): δ = 8.01 (s, 4H, meso), 7.95 (d, *J* = 9.9 Hz, 2H, ArH), 7.76 (t, *J* = 8.4 Hz, 2H, ArH), 7.28 (t, *J* = 7.5 Hz, 2H, ArH), 7.19 (d, *J* = 8.7 Hz, 2H, ArH), 6.98 (d, *J* = 7.2 Hz, 2H, ArH), 6.80 (d, *J* = 8.7 Hz, 2H, ArH), 4.17 (s, 6H, OCH<sub>3</sub>), 3.33 (m, 4H, CH<sub>2</sub>), 3.02 (s, 6H, OCH<sub>3</sub>), 2.70 (m, 4H, CH<sub>2</sub>), 2.53 (s, 12H, CH<sub>3</sub>), 2.33 (s, 6H, CH<sub>3</sub>), 2.25 (s, 12H, CH<sub>3</sub>), 1.70 (m, 4H, CH<sub>2</sub>), 1.28 (t, *J* = 7.2 Hz, 6H, CH<sub>3</sub>), 0.729 (t, *J* = 7.2 Hz, 6H, CH<sub>3</sub>), -2.27 (br s, 2H, NH), -3.68 (br s, 2H, NH). HRFABMS (MH<sup>+</sup>) calcd for C<sub>95</sub>H<sub>102</sub>N<sub>8</sub>O<sub>5</sub> *m/z* 1435.798, found 1435.804.

#### **6.5.6 (2,6-Dibromo-4-methylphenyl)-bis(5-ethoxycarbonyl-4-ethyl-3-methyl-2-pyrryl)methane (50)**

A mixture of 2,6-dibromo-4-methylbenzaldehyde (**49**) (1.4 g, 5.03 mmol) and pyrrole **2** (1.81 g, 10 mmol, 2 equiv) in absolute methanol (25 mL) containing concentrated HCl (0.5 mL) was refluxed under nitrogen for 18 h and cooled in an ice bath. The precipitate was filtered and washed with cold methanol to give **50** as a pale-pink powder. The isolated product was used directly in the next step without further purification.

#### **6.5.7 (2,6-Dibromo-4-methylphenyl)-bis(4-ethyl-3-methyl-2-pyrryl)methane (51)**

Powdered NaOH (1.5 g) was combined with **50** suspended in ethylene glycol (10 mL). The mixture was refluxed under nitrogen for 24 h and cooled to room temperature. Water (50 mL) was added, the precipitate was collected by suction filtration, washed with water until the washings became neutral, and dried under vacuum over P<sub>2</sub>O<sub>5</sub>. Product **51**, which was obtained as a goldenrod solid (1.8 g, 75% yield over two steps), was stored under nitrogen at -20 °C. <sup>1</sup>H NMR (300 MHz, CDCl<sub>3</sub>, 25 °C): δ = 7.62 (br s, 2H, NH), 7.12 (s, 2H, ArH), 6.69 (s, 1H, CH), 6.26 (s, 2H, CH), 2.55 (q, *J*<sub>1</sub> = 8 Hz, *J*<sub>2</sub> = 8 Hz, 4H, CH<sub>2</sub>), 2.03 (s, 6H, CH<sub>3</sub>), 1.73 (s, 3H, CH<sub>3</sub>), 1.28 (t, *J* = 8 Hz, 6H, CH<sub>3</sub>).

#### **6.5.8 (2,6-Dibromo-4-methylphenyl)-bis(5-formyl-4-ethyl-3-methyl-2-pyrryl)methane (52)**

Under a nitrogen atmosphere, phosphorus oxychloride (2 mL) was added dropwise to a solution of **51** in anhydrous DMF (10 mL) at -10 °C. After stirring at -10 °C for 30 min, the resulting mixture was allowed to warm to room temperature and stirred for an additional 2 h. The reaction was concentrated to half its original volume and methanol (20 mL) and Na<sub>2</sub>CO<sub>3</sub> (2 g) were

added. The mixture was heated at 60 °C for 30 min and cooled to room temperature. The precipitate was filtered and washed with water until the washings became neutral. Recrystallization from methanol afforded **52** as an ochre solid (1.5 g, 75% yield). <sup>1</sup>H NMR (300 MHz, CDCl<sub>3</sub>, 25 °C): δ = 9.51 (s, 2H, CHO), 8.59 (br s, 2H, NH), 7.42 (s, 2H, ArH), 6.33 (br s, 1H, CH), 2.70 (q, *J*<sub>1</sub> = 8 Hz, *J*<sub>2</sub> = 8 Hz, 4H, CH<sub>2</sub>), 2.31 (s, 3H, CH<sub>3</sub>), 1.76 (s, 6H, CH<sub>3</sub>), 1.20 (t, *J* = 8 Hz, 6H, CH<sub>3</sub>).

#### 6.5.9 4,5-Bis[(2,3,13,17-tetraethyl-3,7,12,18-tetramethyl-15-(2,6-dibromo-4methylphenyl)-5-porphyrinyl)]-9,9-dimethylxanthene, H<sub>4</sub>(DPXB) (**53**)

A suspension of xanthene tetrapyrrole **14** (1 g, 1.51 mmol) and **52** (1.6 g, 3.02 mmol) in freshly distilled methanol (180 mL) was purged with nitrogen for 20 min. A solution of *p*-toluenesulfonic acid (0.55 g) in methanol (10 mL) was added dropwise over a period of 1 h. The resulting red mixture was stirred in the dark under nitrogen for 2 d. Solid *o*-chloranil (0.5 g) was added in one portion and stirring was continued in air for 24 h. The mixture was concentrated to half its original volume and the precipitate was suction-filtered and washed with cold methanol and water. The solid was redissolved in chloroform (50 mL), a saturated methanolic solution of Zn(OAc)<sub>2</sub>·2H<sub>2</sub>O (10 mL) was added, and the solution was refluxed for 30 min. The solvent was removed and the remaining residue was purified by flash column chromatography (silica gel, 1:1 dichloromethane/hexanes). The bright red band eluted was collected, taken to dryness, and redissolved in dichloromethane (100 mL). The solution was vigorously stirred with 6 N HCl (16 mL) for 15 min, neutralized with a 10% aqueous sodium carbonate solution and the mixture was stirred for an additional 15 min. The organic phase was separated, washed with water (3 × 50 mL), dried over Na<sub>2</sub>SO<sub>4</sub> and taken to dryness. Recrystallization from dichloromethane/methanol afforded pure **53** as a royal purple microcrystalline powder (600 mg, 22% yield). <sup>1</sup>H NMR (500 MHz, CDCl<sub>3</sub>, 25 °C): δ = 8.31 (s, 4H, meso), 8.02 (s, 2H, ArH), 7.94 (d, *J* = 7 Hz, 2H, ArH), 7.70 (s, 2H, ArH), 7.29 (m, 2H, ArH), 6.91 (d, *J* = 7 Hz, 2H, ArH), 3.47 (m, 4H, CH<sub>2</sub>), 3.03 (m, 4H, CH<sub>2</sub>), 2.70 (s, 6H, CH<sub>3</sub>), 2.50 (s, 12H, CH<sub>3</sub>), 2.35 (s, 9H, CH<sub>3</sub>), 2.24 (s, 9H, CH<sub>3</sub>), 1.35 (t, *J* = 7 Hz, 6H, CH<sub>3</sub>), 0.613 (t, *J* = 7 Hz, 6H, CH<sub>3</sub>), -2.46 (br s, 2H, NH), -3.61 (br s, 2H, NH). HRFABMS (MH<sup>+</sup>) calcd for C<sub>93</sub>H<sub>94</sub>Br<sub>4</sub>N<sub>8</sub>O *m/z* 1654.428, found 1654.495.

#### 6.5.10 4,6-Bis[(2,3,13,17-tetraethyl-3,7,12,18-tetramethyl-15-(2,6-dimethoxyphenyl)-5-porphyrinyl)]-dibenzofuran, H<sub>4</sub>(DPDM) (**54**)

A suspension of **26** (1 g, 1.60 mmol) and **47** (2.8 g, 3.20 mmol) in freshly distilled methanol (300 mL) was purged with nitrogen for 15 min. A solution of *p*-toluenesulfonic acid (0.67 g) in methanol (15 mL) was added dropwise over a period of 90 min. The resulting red mixture was stirred in the dark under nitrogen for 2 d. Solid *o*-chloranil (533 mg) was added in one portion

and stirring was continued in air for 24 h. The mixture was taken to dryness and the solid was redissolved in chloroform (50 mL). A saturated methanolic solution of  $\text{Zn}(\text{OAc})_2 \cdot 2\text{H}_2\text{O}$  (5 mL) was added, and the solution was refluxed for 1 h. The solvent was removed and the remaining residue was purified by repeated flash column chromatography (silica gel, 1:1 dichloromethane/hexanes). The bright red band that eluted was collected, taken to dryness, and redissolved in dichloromethane (60 mL). The solution was vigorously stirred with 6 N HCl (6 mL) for 25 min. The solution was neutralized with a 10% aqueous sodium carbonate solution and the mixture was stirred for an additional 15 min. The organic phase was separated, washed with water ( $3 \times 25$  mL), dried over  $\text{Na}_2\text{SO}_4$ , and taken to dryness. Recrystallization from dichloromethane/methanol afforded pure **54** as a plum solid (250 mg, 11% yield).  $^1\text{H}$  NMR (500 MHz,  $\text{CDCl}_3$ , 25 °C):  $\delta$  = 9.78 (s, 4H, meso), 8.66 (d,  $J$  = 7.5 Hz, 2H, ArH), 7.76 (t,  $J$  = 6.9 Hz, 2H, ArH), 7.70 (d,  $J$  = 7.2 Hz, 2H, ArH), 7.58 (t,  $J$  = 7.8 Hz, 2H, ArH), 6.83 (d,  $J$  = 8.2 Hz, 2H, ArH), 6.80 (d,  $J$  = 8.2 Hz, 2H, ArH), 3.80 (m, 16H,  $\text{CH}_2$ ), 3.37 (s, 6H,  $\text{OCH}_3$ ), 3.17 (s, 6H,  $\text{OCH}_3$ ), 2.43 (s, 12H,  $\text{CH}_3$ ), 2.36 (s, 12H,  $\text{CH}_3$ ), 1.58 (m, 24H,  $\text{CH}_3$ ), -2.83 (br s, 4H, NH). HRFABMS ( $\text{M}^+$ ) calcd for  $\text{C}_{92}\text{H}_{96}\text{N}_8\text{O}_5$   $m/z$  1393.798, found 1393.758.

#### 6.5.11 $\text{Zn}_2(\text{DPXM})$ (**55**)

A saturated methanolic solution of  $\text{Zn}(\text{OAc})_2 \cdot 2\text{H}_2\text{O}$  (1 mL) was added to a solution of **48** (20 mg, 0.014 mmol) in chloroform (5 mL). The reaction was refluxed for 30 min and taken to dryness. The solid residue was purified by flash column chromatography (silica gel, 1:1 to 3:1 dichloromethane/hexanes) followed by recrystallization from dichloromethane/ methanol to deliver analytically pure **55** as a scarlet microcrystalline powder in essentially quantitative yield.  $^1\text{H}$  NMR (500 MHz,  $\text{CDCl}_3$ , 25 °C):  $\delta$  = 8.40 (s, 4H, meso), 7.83 (d,  $J$  = 7.8 Hz, 2H, ArH), 7.50 (t,  $J$  = 8.4 Hz, 2H, ArH), 7.12 (t,  $J$  = 6.9 Hz, 2H, ArH), 6.88 (d,  $J$  = 8.4 Hz, 2H, ArH), 6.73 (d,  $J$  = 6.9 Hz, 2H, ArH), 6.63 (d,  $J$  = 8.4 Hz, 2H, ArH), 3.63 (s, 6H,  $\text{OCH}_3$ ), 3.35 (m, 4H,  $\text{CH}_2$ ), 3.07 (m, 8H,  $\text{CH}_2$ ), 2.88 (s, 6H,  $\text{OCH}_3$ ), 2.71 (m, 4H,  $\text{CH}_2$ ), 2.33 (s, 6H,  $\text{CH}_3$ ), 2.23 (s, 24H,  $\text{CH}_3$ ), 1.24 (t,  $J$  = 7.2 Hz, 6H,  $\text{CH}_3$ ), 1.06 (t,  $J$  = 7.2 Hz, 6H,  $\text{CH}_3$ ). Anal. Calcd for  $\text{C}_{95}\text{H}_{98}\text{N}_8\text{O}_5\text{Zn}_2$ : C, 73.02; H, 6.32; N, 7.17. Found: C, 73.06; H, 6.56; N, 7.17. HRFABMS ( $\text{M}^+$ ) calcd for  $\text{C}_{95}\text{H}_{98}\text{N}_8\text{O}_5\text{Zn}_2$   $m/z$  1558.624, found 1558.630.

#### 6.5.12 $\text{Cu}_2(\text{DPXM})$ (**56**)

To a 12-mL chloroform solution of **48** (56 mg, 0.039 mmol) was added a solution of  $\text{Cu}(\text{OAc})_2 \cdot 2\text{H}_2\text{O}$  (130 mg) and potassium acetate (145 mg) in 12 mL of methanol. The resulting solution was refluxed for 5 h and the solvent was removed by rotary evaporation. The remaining solid was taken up in a 1:1 mixture of dichloromethane/water (150 mL). The organic layer was decanted and taken to dryness. The crude material was purified by flash column chromatography

(silica gel, 1:1 dichloromethane/hexanes) followed by recrystallization from dichloromethane/methanol to afford analytically pure **56** as a brick red solid (53 mg, 87% yield). Anal. Calcd for  $C_{95}H_{98}N_8O_5Cu_2$ : C, 73.19; H, 6.34; N, 7.19. Found: C, 73.05; H, 6.24; N, 7.14. HRFABMS (M+) calcd for  $C_{95}H_{98}N_8O_5Cu_2$   $m/z$  1556.645, found 1556.644.

#### 6.5.13 $Ni_2(DPXM)$ (**57**)

A mixture of **48** (53 mg, 0.037 mmol) and  $NiCl_2$  (102 mg, mmol) in 6 mL of DMF was refluxed under nitrogen for 4 h. The solvent was removed under vacuum and the remaining solid was taken up in a 1:1 mixture of dichloromethane/water (150 mL). The organic layer was decanted and taken to dryness. Purification by flash column chromatography (silica gel, 1:1 dichloromethane/hexanes) followed by recrystallization from dichloromethane/ methanol gave analytically pure **57** as a ruby red microcrystalline powder (46 mg, 81% yield).  $^1H$  NMR (500 MHz,  $CDCl_3$ , 25 °C):  $\delta$  = 7.83 (d, 2H, ArH), 7.76 (s, 4H, meso), 7.58 (t,  $J$  = 7.5 Hz, 2H, ArH), 7.16 (t,  $J$  = 7.8 Hz, 2H, ArH), 7.04 (d,  $J$  = 8.7 Hz, 2H, ArH), 6.82 (d,  $J$  = 7.2 Hz, 2H, ArH), 6.68 (d,  $J$  = 8.4 Hz, 2H, ArH), 4.11 (s, 6H,  $OCH_3$ ), 3.03 (s, 6H,  $OCH_3$ ), 2.72 (m, 4H,  $CH_2$ ), 2.50 (m, 4H,  $CH_2$ ), 2.24 (m, 8H,  $CH_2$ ), 2.21 (s, 6H,  $CH_3$ ), 2.17 (s, 12H,  $CH_3$ ), 2.12 (s, 12H,  $CH_3$ ), 1.15 (t,  $J$  = 7.2 Hz, 6H,  $CH_3$ ), 1.03 (t,  $J$  = 7.2 Hz, 6H,  $CH_3$ ). Anal. Calcd for  $C_{95}H_{98}N_8O_5Ni_2$ : C, 73.65; H, 6.38; N, 7.23. Found: C, 73.53; H, 6.22; N, 7.42. HRFABMS (M+) calcd for  $C_{95}H_{98}N_8O_5Ni_2$   $m/z$  1546.637, found 1546.636.

#### 6.5.14 $Fe_2Cl_2(DPXM)$ (**58**)

In a dry box, a 100-mL flask equipped with a condenser was charged with **48** (202 mg, 0.141 mmol), 2,6-lutidine (0.4 mL),  $FeBr_2$  (495 mg), THF (25 mL) and benzene (12 mL). The mixture was refluxed under nitrogen for 12 h, opened to air, and brought to dryness under vacuum. The residue was taken up in a 1:1 mixture of dichloromethane/water (50 mL). The organic layer was separated, washed with water (3  $\times$  75 mL), and stirred with 3N HCl (35 mL) for 90 min. The organic layer was decanted and solvent was removed under vacuum. The remaining solid was purified by column chromatography (silica gel, dichloromethane to 5% methanol/dichlormethane) and retreated with HCl as described above. The organic phase was separated, washed with water (3  $\times$  75 mL), dried over  $Na_2SO_4$ , and taken to dryness. Recrystallization from dichloromethane and ether afforded pure **58** as a brown powder (189 mg, 83% yield). Anal. Calcd for  $C_{95}H_{98}N_8O_5Cl_2Fe_2$ : C, 70.68; H, 6.12; N, 6.94. Found: C, 70.72; H, 6.15; N, 7.00. HRFABMS ( $[M-Cl]^+$ ) calcd for  $C_{95}H_{98}N_8O_5Cl_2Fe_2$   $m/z$  1577.605, found 1577.599.

### 6.5.15 Mn<sub>2</sub>Cl<sub>2</sub>(DPXM) (59)

A solution of **48** (202 mg, 0.141 mmol) and Mn(OAc)<sub>2</sub>•4H<sub>2</sub>O (495 mg) in DMF (15 mL) was refluxed in air for 3 h. The reaction was cooled to room temperature and taken to dryness. The remaining was taken up in a 1:1 mixture of dichloromethane/water (50 mL). The organic layer was separated, washed with water (3 × 75 mL), and stirred with a 5:1 mixture of saturated aq NaCl and HCl (72 mL) for 90 min. The organic layer was decanted and solvent was removed under vacuum. The remaining solid was purified by column chromatography (silica gel, dichloromethane to 5% methanol/dichloromethane) and retreated with aq NaCl and HCl as described above. The organic phase was separated, washed with water (3 × 75 mL), dried over Na<sub>2</sub>SO<sub>4</sub>, and taken to dryness. Recrystallization from dichloromethane and ether afforded pure **59** as a brown solid (202 mg, 89% yield). Anal. Calcd for C<sub>95</sub>H<sub>98</sub>N<sub>8</sub>O<sub>5</sub>Cl<sub>2</sub>Mn<sub>2</sub>: C, 70.76; H, 6.13; N, 6.95; Cl, 4.40. Found: C, 70.35; H, 6.56; N, 6.84; Cl, 4.40. HRFABMS ([M-Cl]<sup>+</sup>) calcd for C<sub>95</sub>H<sub>98</sub>N<sub>8</sub>O<sub>5</sub>Cl<sub>2</sub>Mn<sub>2</sub> *m/z* 1575.611, found 1575.611.

### 6.5.16 Zn<sub>2</sub>(DPDM) (60)

A saturated methanolic solution of Zn(OAc)<sub>2</sub>•2H<sub>2</sub>O (1 mL) was added to a solution of **54** (50 mg, 0.0359 mmol) in chloroform (5 mL). The reaction was refluxed for 30 min and taken to dryness. The solid residue was purified by flash column chromatography (silica gel, 3:1 dichloromethane/hexanes) followed by recrystallization from dichloromethane/methanol to deliver analytically pure **60** as a bright red powder in essentially quantitative yield. <sup>1</sup>H NMR (500 MHz, CDCl<sub>3</sub>, 25 °C): δ = 9.72 (s, 4H, meso), 8.65 (d, *J* = 7.5 Hz, 2H, ArH), 7.74 (m, 4H, ArH), 7.58 (t, *J* = 8.1 Hz, 2H, ArH), 6.85 (d, *J* = 7.8 Hz, 2H, ArH), 6.79 (d, *J* = 8.4 Hz, 2H, ArH), 3.77 (m, 16H, CH<sub>2</sub>), 3.41 (s, 6H, OCH<sub>3</sub>), 3.09 (s, 6H, OCH<sub>3</sub>), 2.43 (s, 12H, CH<sub>3</sub>), 2.34 (s, 12H, CH<sub>3</sub>), 1.59 (m, 24H, CH<sub>3</sub>). Anal. Calcd for C<sub>92</sub>H<sub>92</sub>N<sub>8</sub>O<sub>5</sub>Zn<sub>2</sub>: C, 72.67; H, 6.10; N, 7.37. Found: C, 72.44; H, 5.84; N, 7.49. HRFABMS (M<sup>+</sup>) calcd for C<sub>95</sub>H<sub>98</sub>N<sub>8</sub>O<sub>5</sub>Zn<sub>2</sub> *m/z* 1516.577, found 1516.567.

### 6.5.17 Cu<sub>2</sub>(DPDM) (61)

To a 12-mL chloroform solution of **54** (50 mg, 0.0359 mmol) was added a solution of Cu(OAc)<sub>2</sub>•2H<sub>2</sub>O (100 mg) and potassium acetate (150 mg) in 12 mL of methanol. The resulting solution was refluxed for 5 h and the solvent was removed by rotary evaporation. The remaining solid was taken up in a 1:1 mixture of dichloromethane/water (150 mL). The organic layer was decanted and taken to dryness. The crude material was purified by flash column chromatography (silica gel, 1:1 dichloromethane/hexanes) followed by recrystallization from

dichloromethane/methanol to afford analytically pure **61** as a brick red solid (48 mg, 88% yield). HRFABMS (M+) calcd for C<sub>95</sub>H<sub>98</sub>N<sub>8</sub>O<sub>5</sub>Cu<sub>2</sub> *m/z* 1514.598, found 1514.573.

#### 6.5.18 Fe<sub>2</sub>Cl<sub>2</sub>(DPDM) (**62**)

In a dry box, a 100-mL flask equipped with a condenser was charged with **54** (100 mg, 0.0718 mmol), 2,6-lutidine (0.2 mL), FeBr<sub>2</sub> (200 mg), THF (12 mL) and benzene (8 mL). The mixture was refluxed under nitrogen for 12 h, opened to air, and brought to dryness under vacuum. The residue was taken up in a 1:1 mixture of dichloromethane/water (50 mL). The organic layer was separated, washed with water (3 × 75 mL), and stirred with 3 N HCl (30 mL) for 90 min. The organic layer was decanted and solvent was removed under vacuum. The remaining solid was purified by column chromatography (silica gel, dichloromethane to 5% methanol/dichloromethane) and retreated with HCl as described above. The organic phase was separated, washed with water (3 × 25 mL), dried over Na<sub>2</sub>SO<sub>4</sub>, and taken to dryness. Recrystallization from dichloromethane and ether afforded pure **62** as a brown powder (97 mg, 86% yield). HRFABMS ([M-Cl]<sup>+</sup>) calcd for C<sub>92</sub>H<sub>92</sub>N<sub>8</sub>O<sub>5</sub>Cl<sub>2</sub>Fe<sub>2</sub> *m/z* 1535.558, found 1535.560.

#### 6.5.19 Mn<sub>2</sub>Cl<sub>2</sub>(DPDM) (**63**)

A solution of **54** (100 mg, 0.0718 mmol) and Mn(OAc)<sub>2</sub>·4H<sub>2</sub>O (250 mg) in DMF (15 mL) was refluxed in air for 3 h. The reaction was cooled to room temperature and taken to dryness. The remaining was taken up in a 1:1 mixture of dichloromethane/water (50 mL). The organic layer was separated, washed with water (3 × 50 mL), and stirred with a 5:1 mixture of saturated aq NaCl and HCl (60 mL) for 90 min. The organic layer was decanted and solvent was removed under vacuum. The remaining solid was purified by column chromatography (silica gel, dichloromethane to 5% methanol/dichloromethane) and retreated with aq NaCl and HCl as described above. The organic phase was separated, washed with water (3 × 50 mL), dried over Na<sub>2</sub>SO<sub>4</sub>, and taken to dryness. Recrystallization from dichloromethane and ether afforded pure **63** as a brown solid (103 mg, 91% yield). HRFABMS ([M-Cl]<sup>+</sup>) calcd for C<sub>92</sub>H<sub>92</sub>N<sub>8</sub>O<sub>5</sub>Cl<sub>2</sub>Mn<sub>2</sub> *m/z* 1533.564, found 1533.555.

#### 6.5.20 General Details of X-ray Data Collection and Reduction

X-ray diffraction data were collected using a Siemens 3 circle diffractometer equipped with a CCD detector. Measurements were carried out at -90° C using Mo Kα (λ = 0.71073 Å) radiation, which was wavelength selected with a single-crystal graphite monochromator. Four sets of data were collected using ω scans and a -0.3° scan width. All calculations were performed using a Silicon Graphics Indigo 2 or PC workstation. The data frames were integrated to *hkl*/intensity, and final unit cells were calculated by using the SAINT v.4.050 program from

Siemens. The structures were solved and refined with the SHELXTL v.5.03 suite of programs developed by G. M. Sheldrick and Siemens Industrial Automation, Inc., 1995.

#### 6.5.21 X-ray Structure of $\text{H}_4(\text{DPXM})\cdot 2\text{CH}_2\text{Cl}_2$ (48)

A 0.50 mm  $\times$  0.31 mm  $\times$  0.30 mm royal purple crystal of plate morphology was obtained from slow diffusion of methanol into a dichloromethane solution of the compound. The crystal was coated in STP and mounted onto a glass fiber. A total of 43593 reflections were collected in the  $\theta$  range 2.14 to 26.37°, of which 17101 were unique ( $R_{\text{int}} = 0.0342$ ). Hydrogen atoms were placed in calculated positions using a standard riding model and were refined isotropically. The largest peak and hole in the difference map were 0.934 eÅ<sup>-3</sup> and -0.502 eÅ<sup>-3</sup>, respectively. The least squares refinement converged normally giving residuals of  $R1 = 0.0683$  and  $wR2 = 0.1850$ , with  $\text{GOF} = 1.051$ .

#### 6.5.22 X-ray Structure of $\text{Zn}_2(\text{DPXM})\cdot 5\text{CH}_3\text{OH}\cdot 1.5\text{H}_2\text{O}\cdot \text{CH}_2\text{Cl}_2$ (55)

A 0.10 mm  $\times$  0.26 mm  $\times$  0.40 mm brick red crystal of needle morphology was obtained from slow diffusion of methanol into a dichloromethane solution of the compound. The crystal was coated in STP and mounted onto a glass fiber. A total of 48278 reflections were collected in the  $\theta$  range 2.32 to 26.38°, of which 19020 were unique ( $R_{\text{int}} = 0.0394$ ). The Patterson method was used to locate the zinc atoms, all remaining atoms were placed using the difference Fourier map. Hydrogen atoms were placed in calculated positions using a standard riding model and were refined isotropically. A disordered ethyl group attached to C(28) was assigned half occupancy in two different conformations. Oxygen atoms O(8) and O(11) from two disordered methanol solvent molecules were assigned half occupancy in two different conformations. The largest peak and hole in the difference map were 1.208 eÅ<sup>-3</sup> and -0.931 eÅ<sup>-3</sup>, respectively. The least squares refinement converged normally giving residuals of  $R1 = 0.0854$  and  $wR2 = 0.2323$ , with  $\text{GOF} = 1.022$ .

#### 6.5.23 X-ray Structure of $\text{Mn}_2\text{Cl}_2(\text{DPXM})\cdot 4\text{CHCl}_3$ (59)

A 0.50 mm  $\times$  0.25 mm  $\times$  0.20 mm dark brown crystal of needle morphology was obtained from slow diffusion of hexane into a chloroform solution of the compound. The crystal was coated in STP and mounted onto a glass fiber. A total of 38526 reflections were collected in the  $\theta$  range 1.23 to 23.24°, of which 14012 were unique ( $R_{\text{int}} = 0.0446$ ). The Patterson method was used to locate the manganese atoms, all remaining atoms were placed using the difference Fourier map. Hydrogen atoms were placed in calculated positions using a standard riding model and were refined isotropically. The largest peak and hole in the difference map were 1.486 eÅ<sup>-3</sup> and -

1.021 eÅ<sup>-3</sup>, respectively. The least squares refinement converged normally giving residuals of R1 = 0.0812 and wR2 = 0.2045, with GOF = 1.101.

#### **6.5.24 Physical Measurements**

<sup>1</sup>H NMR spectra were collected in CDCl<sub>3</sub> (Cambridge Isotope Laboratories) at the MIT Department of Chemistry Instrumentation Facility (DCIF) using either a Unity 300, Mercury 300 or Inova 500 spectrometer at 25 °C. All chemical shifts are reported using the standard  $\delta$  notation in parts-per-million; positive chemical shifts are to higher frequency from the given reference. Absorption spectra were obtained using a Cary-17 spectrophotometer modified by On-Line Instrument Systems (OLIS) to include computer control or a Spectral Instruments 440 spectrophotometer. Mass spectral analyses were carried out by the University of Illinois Mass Spectrometry Laboratory and the MIT Department of Chemistry Instrument Facility. Elemental analyses were performed at Michigan State University and Quantitative Technologies, Inc. (New Jersey).



## 6.6 References and Notes

1. Collman, J. P.; Wagenknecht, P. S.; Hutchison, J. E. *Angew. Chem. Int. Ed. Engl.* **1994**, *33*, 1537-1554.
2. Sanders, J. K. M. *Chem. Eur. J.* **1998**, *4*, 1378-1383.
3. Chang, C. K.; Abdalmuhdi, I. *J. Org. Chem.* **1983**, *48*, 5388-5390.
4. Chang, C. K.; Liu, H. Y.; Abdalmuhdi, I. *J. Am. Chem. Soc.* **1984**, *106*, 2725-2726.
5. Chang, C. K.; Abdalmuhdi, I. *Angew. Chem. Int. Ed. Engl.* **1984**, *23*, 164-165.
6. Lui, H.-Y.; Abdalmuhdi, I.; Chang, C. K.; Anson, F. C. *J. Phys. Chem.* **1985**, *89*, 665-670.
7. Ni, C.-L.; Abdalmuhdi, I.; Chang, C. K.; Anson, F. C. *J. Phys. Chem.* **1987**, *91*, 1158-1166.
8. Proniewicz, L. M.; Odo, J.; Goral, J.; Chang, C. K.; Nakamoto, K. *J. Am. Chem. Soc.* **1989**, *111*, 2105-2110.
9. Fillers, J. P.; Ravichandran, K. G.; Abdalmuhdi, I.; Tulinsky, A.; Chang, C. K. *J. Am. Chem. Soc.* **1986**, *108*, 417-424.
10. Collman, J. P.; Kim, K.; Leidner, C. R. *Inorg. Chem.* **1987**, *26*, 1152-1157.
11. Collman, J. P.; Hutchison, J. E.; Lopez, M. A.; Tabard, A.; Guilard, R.; Seok, W. K.; Ibers, J. A.; L'Her, M. *J. Am. Chem. Soc.* **1992**, *114*, 9869-9877.
12. Collman, J. P.; Hutchison, J. E.; Lopez, M. A.; Guilard, R. *J. Am. Chem. Soc.* **1992**, *114*, 8066-8073.
13. Collman, J. P.; Hutchison, J. E.; Ennis, M. S.; Lopez, M. A.; Guilard, R. *J. Am. Chem. Soc.* **1992**, *114*, 8074-8080.
14. Collman, J. P.; Ha, Y.; Wagenknecht, P. S.; Lopez, M. A.; Guilard, R. *J. Am. Chem. Soc.* **1993**, *115*, 9080-9088.
15. Collman, J. P.; Ha, Y. Y.; Guilard, R.; Lopez, M. A. *Inorg. Chem.* **1993**, *32*, 1788-1794.
16. Collman, J. P.; Fish, H. T. *Inorg. Chem.* **1996**, *35*, 7922-7923.
17. Guilard, R.; Lopez, M. A.; Tabard, A.; Richard, P.; Lecomte, C.; Brandes, S.; Hutchison, J. E.; Collman, J. P. *J. Am. Chem. Soc.* **1992**, *114*, 9877-9889.
18. Guilard, R.; Brandes, S.; Tabard, A.; Bouhmaid, N.; LeComte, C.; Richard, P.; Latour, J. M. *J. Am. Chem. Soc.* **1994**, *116*, 10202-10211.
19. Guilard, R.; Brandes, S.; Tardieux, C.; Tabard, A.; L'Her, M.; Miry, C.; Guerac, P.; Knop, Y.; Collman, J. P. *J. Am. Chem. Soc.* **1995**, *117*, 11721-11729.
20. Le Mest, Y.; L'Her, M.; Saillard, J. Y. *Inorg. Chim. Acta* **1996**, *248*, 181-191.
21. Le Mest, Y.; Inisan, C.; Laouenan, A.; L'Her, M.; Talarmain, J.; El Khalifa, M.; Saillard, J. Y. *J. Am. Chem. Soc.* **1997**, *119*, 6905-6106.

22. Naruta, Y.; Sasayama, M.; Ichihara, K. *J. Mol. Cat. A* **1997**, *117*, 115-121.
23. Harvey, P. D.; Proulx, N.; Martin, G.; Drouin, M.; Nurco, D. J.; Smith, K. M.; Bolze, F.; Gros, C. P.; Guillard, R. *Inorg. Chem.* **2001**, *40*, 4134-4142.
24. Bolze, F. G., Claude P.; Drouin, M.; Espinosa, E.; Harvey, P. D.; Guillard, R. *J. Organomet. Chem.* **2002**, *643-644*, 89-97.
25. Chang, C. J.; Brown, J. D. K.; Chang, M. C. Y.; Baker, E. A.; Nocera, D. G. In *Electron Transfer in Chemistry*; Balzani, V., Ed.; Wiley-VCH: Weinheim, Germany, 2001; Vol. 3.2.4, pp 409-461.
26. Cukier, R. I.; Nocera, D. G. *Annu. Rev. Phys. Chem.* **1998**, *49*, 337-369.
27. Chang, C. J.; Deng, Y.; Heyduk, A. F.; Chang, C. K.; Nocera, D. G. *Inorg. Chem.* **2000**, *39*, 959-966.
28. Chang, C. J.; Deng, Y.; Shi, C.; Chang, C. K.; Anson, F. C.; Nocera, D. G. *Chem. Commun.* **2000**, 1355-1356.
29. Chang, C. J.; Baker, E. A.; Pistorio, B. J.; Deng, Y.; Loh, Z.-H.; Miller, S. E.; Carpenter, S. D.; Nocera, D. G. *Inorg. Chem.* **2002**, *41*, 3102-3109.
30. Deng, Y.; Chang, C. J.; Nocera, D. G. *J. Am. Chem. Soc.* **2000**, *122*, 410-411.
31. Pistorio, B. J.; Chang, C. J.; Nocera, D. G. *J. Am. Chem. Soc.* **2002**, *124*, 7884-7885.
32. Chang, C. J.; Deng, Y.; Lee, G.-H.; Peng, S.-M.; Yeh, C.-Y.; Nocera, D. G. *Inorg. Chem.* **2002**, *41*, 3008-3016.
33. Collman, J. P.; Tyvoll, D. A.; Chng, L. L.; Fish, H. T. *J. Org. Chem.* **1995**, *60*, 1926-1931.
34. Chang, C. K.; Bag, N. *J. Org. Chem.* **1995**, *60*, 7030-7032.
35. Sharman, W. M.; Van Lier, J. E. *J. Porphyrins Phthalocyanines* **2000**, *4*, 441-453.
36. Deng, Y.; Chang, C. K.; Nocera, D. G. *Angew. Chem. Int. Ed.* **2000**, *39*, 1066-1068.
37. Boyle, R. W.; Johnson, C. K.; Dolphin, D. *J. Chem. Soc. Chem. Commun.* **1995**, 527-528.
38. Hyslop, A. G.; Kellett, M. A.; Iovine, P. M.; Therien, M. J. *J. Am. Chem. Soc.* **1998**, *120*, 12676-12677.
39. Zhou, X.; Tse, M. K.; Wan, T. S. M.; Chan, K. S. *J. Org. Chem.* **1996**, *61*, 3590-3593.
40. Adler, A. D.; Longo, F. R.; Kampas, F.; Kim, J. *J. Inorg. Nucl. Chem.* **1970**, *32*, 2443-2445.
41. Kadish, K. M.; Smith, K. M.; Guillard, R. *The Porphyrin Handbook*; Academic Press: San Diego, 2000.
42. Armarego, W. L. F.; Perrin, D. D. *Purification of Laboratory Chemicals*; 4th ed.; Butterworth-Heinmann: Oxford, 1996.
43. Yeh, C.-Y., Ph.D. Thesis, Michigan State University: East Lansing, MI, 1999.

*Chapter 7*

**Catalytic Oxygen Reduction by Dicobalt(II) Cofacial  
Bisporphyrins: The Proton Issue**

## 7.1 Motivation and Specific Aims

The combination of cyclic ether pillars and *trans*-aryl substitution patterns affords an unprecedented set of synthetic tools for tuning the pocket sizes of Pacman architectures. These cofacial systems thus offer a unique opportunity to develop a structure-function relationship for PCET-mediated reductive catalysis, with particular emphasis on oxygen activation and reduction chemistry. Our specific interest is the contribution of protons to selecting oxygen-reaction pathways. In this chapter, a comprehensive study of dicobalt(II) Pacman porphyrins affixed to xanthene (DPX/DPXM) and dibenzofuran (DPD/DPDM) scaffolds is presented. Structural chemistry, electrochemistry, and density functional calculations reveal the essential catalyst features for achieving the selective four-electron, four-proton reduction of oxygen to water. Remarkably, we find that the electronic structures of the Pacman porphyrins track their experimental catalytic oxygen-reduction pathway selectivities by modulation of proton affinities for the [Co<sub>2</sub>O<sub>2</sub>] core. The results are significant in regard to the design of catalysts for effective oxygen-activation chemistry, and underscore the emerging importance of protons in guiding catalytic bond-making and bond-breaking processes in the chemical and biological arenas.

## 7.2 Background

The proton-coupled reduction of oxygen to water by cytochrome *c* oxidase (CcO) forms the molecular basis for biological energy production during aerobic respiration.<sup>1-6</sup> The terminal enzyme of the respiratory chain, CcO catalyzes the conversion of oxygen to water and couples this exergonic reaction to intramembrane proton translocation.<sup>6-9</sup> The free energy resulting from this proton-driven electrochemical gradient is used to generate the cellular energy source ATP via the phosphorylation of ADP. Production of ATP is maximized by ability of CcO to mediate the complete reduction of oxygen to water, avoiding toxic reactive oxygen species such as peroxide and superoxide. Accordingly, the conception of molecular catalysts for selective reduction of O<sub>2</sub> to H<sub>2</sub>O is of fundamental importance in the design of credible functional models for these enzymatic machines as well as electrode materials for clean fuel cells and batteries that utilize oxygen as the reducible reductant.<sup>10</sup>

The direct conversion of oxygen to water is a challenging chemical transformation, requiring the successful navigation of four electron *and* four proton equivalents. Such proton-coupled electron transfer (PCET) events continue to emerge in small-molecule activation chemistry catalyzed by CcO and a wide range of other oxygen-metabolizing enzymes.<sup>11-20</sup> Nevertheless, the pursuit of synthetic catalysts for the reduction of oxygen to water have emphasized for the most part the design of preorganized structural architectures for O<sub>2</sub> binding and activation.<sup>21-37</sup> For example, a number of dicobalt(II) cofacial bisporphyrins connected by a single rigid Pacman pillar are

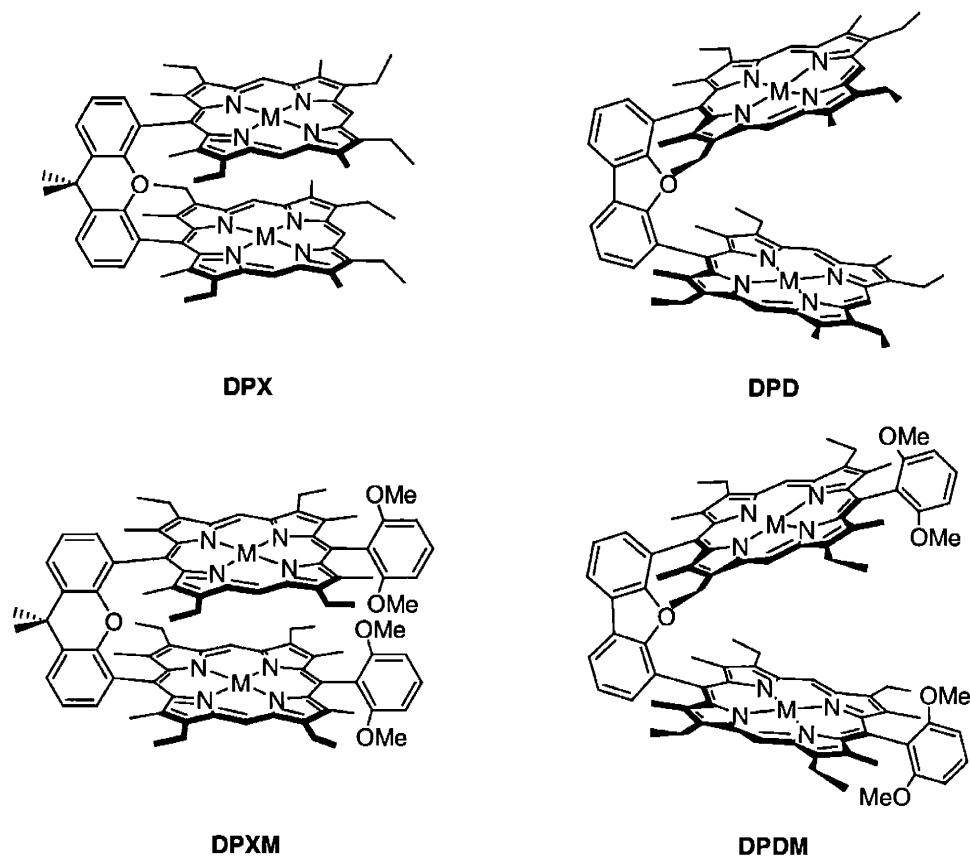
effective electrocatalysts for mediating the direct four-electron, four-proton pathway for oxygen reduction to produce water in strongly acidic media.<sup>38-51</sup> The success of these pillared compounds is attributed to their ability to maintain a face-to-face arrangement of porphyrin subunits while exhibiting vertical flexibility via the Pacman effect.<sup>45,52</sup> Studies of cofacial bisporphyrins for catalytic O<sub>2</sub> activation chemistry have largely centered on structural attributes presented by the size and flexibility of these supramolecular clefts, particularly with regard to the binding modes of their O<sub>2</sub> adducts. In particular, we recently demonstrated that efficient oxygen-activation chemistry could be achieved with Pacman motifs displaying large changes in vertical motion. Dicobalt(II) bisporphyrins affixed to xanthene (DPX = diporphyrin xanthene)<sup>53,54</sup> and dibenzofuran (DPD = diporphyrin dibenzofuran)<sup>52,54</sup> selectively mediate the direct reduction of O<sub>2</sub> to H<sub>2</sub>O despite a ca. 4 Å difference in their metal-metal distances, suggesting that the substantial Pacman flexibility of these molecular clefts allows the designed binding pocket to structurally accommodate reaction intermediates during multielectron catalysis.<sup>51,52,55</sup>

However, an equally intriguing but heretofore overlooked issue is the role of electronic factors, and in particular, proton coupling, in selecting O<sub>2</sub> reduction pathways. In an effort to evaluate the electronic influence of protons in catalytic oxygen reduction cycles mediated by Pacman constructs, we recently developed a convergent synthetic approach using sterically-demanding aryl dipyrromethanes to fine tune the vertical pocket sizes of xanthene- and dibenzofuran-pillared cofacial bisporphyrins (DPXM = diporphyrin xanthene methoxyaryl, DPDM = diporphyrin dibenzofuran methoxyaryl).<sup>56</sup> The introduction of aryl groups *trans* to the spacer provides molecular “teeth” within the cleft of the Pacman “bite”, delivering a library of Pacman systems based on xanthene and dibenzofuran spacers that afford precise control over the vertical cleft dimension.

We report in this chapter a comprehensive structure-function study of dicobalt(II) Pacman porphyrin constructs that exhibit broad tunability in the vertical dimension (Chart 7.1). The results obtained from single-crystal X-ray structural analysis, electrochemistry, and comparative reactivity studies together with those of density functional theory calculations identify the essential catalyst features that govern the pathway selectivities for O<sub>2</sub> reduction mediated by dicobalt(II) cofacial bisporphyrins. Remarkably, we find that the proton affinity of Pacman-O<sub>2</sub> adducts derived from the electronic structure of the macrocyclic superstructure is crucial for controlling the selectivity for four-electron, four-proton versus two-electron, two-proton reduction pathways. These observations reveal that electronic tuning of the Pacman motif plays a significant role in the reactivity of such cofacial architectures, and highlight the emerging

importance of proton participation in the catalytic activation of oxygen and other small-molecule substrates in chemical and biological systems.

Chart 7.1



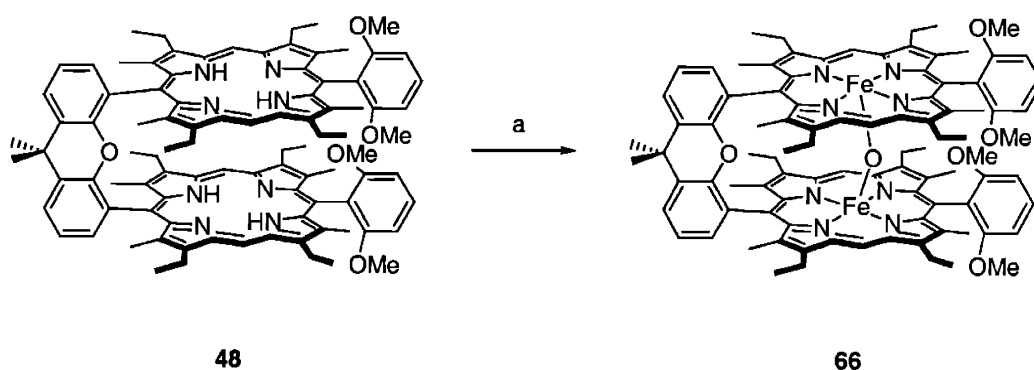
## 7.3 Results and Discussion

### 7.3.1 Synthesis and Structural Chemistry

Dicobalt(II) coordination complexes of the four Pacman systems DPX, DPXM, DPD, and DPDM are obtained in a similar fashion by reaction of their corresponding free base bisporphyrins with  $\text{CoCl}_2$  and 2,6-lutidine in a benzene/tetrahydrofuran solvent mixture. Purification by column chromatography in an inert atmosphere over neutral alumina followed by recrystallization furnishes the  $\text{Co}_2(\text{DPX})$  (**44**) and  $\text{Co}_2(\text{DPD})$  (**43**) complexes and their newly prepared  $\text{Co}_2(\text{DPXM})$  (**64**) and  $\text{Co}_2(\text{DPDM})$  (**65**) counterparts in excellent yields (> 90%). All four complexes were fully characterized by high-resolution mass spectrometry and elemental analyses. The successful preparation of **64** and **65** completes a homologous series of dicobalt(II) Pacman porphyrins spanning a wide range of tunable vertical pocket sizes for further study.

Installation of a single rigid pillar into the cofacial bisporphyrin motif affords face-to-face systems where the motion of macrocyclic subunits within the molecular cleft is constrained to the vertical dimension (e.g., the Pacman effect); this vertical Pacman flexibility is crucial for accommodating reaction intermediates during catalysis. The DPD system provided the first direct evidence for the Pacman effect. Comparative structural analysis of biszinc(II) and bisiron(III)  $\mu$ -oxo complexes of DPD demonstrate that this platform can open and close its binding pocket by over 4 Å in metal-metal distances in the presence of suitable ligands.<sup>52</sup> An analogous intramolecular bisiron(III)  $\mu$ -oxo complex is also obtained for the DPX template.<sup>54</sup>

We thus sought to test whether the Pacman effect would occur for cofacial platforms that contain a single aryl group *trans* to the spacer. To this end, the methoxyaryl derivative Fe<sub>2</sub>O(DPXM) (**66**) is readily prepared in excellent yield (92%) by iron insertion into H<sub>4</sub>(DPXM) (**48**) followed by basic workup (Scheme 7.1). Compound **66** gives satisfactory high-resolution mass spectral and elemental analyses.



**Scheme 7.1.** (a) i. FeBr<sub>2</sub>, THF/benzene, 2,6-lutidine; ii. O<sub>2</sub>, NaOH.

Material suitable for single-crystal X-ray analysis is obtained from dichloromethane/hexanes solutions. The structure of **66** depicted in Figure 7.1 confirms the ability of the DPXM scaffold to clamp its porphyrin jaws down on an exogenous ligand. Figure 7.2 displays comparative views of the methoxyaryl-substituted framework in its open and closed forms. Crystallographic data are provided in Table 7.1 and selected geometrical measurements are collected in Tables 7.2 and 7.3.

The clamping action of the porphyrin subunits in  $\mu$ -oxo complex **66** is revealed by its reduced interplanar angle of 25.4° and shortened metal-metal distance of 3.489 Å compared to the relaxed Zn<sub>2</sub>(DPXM) (**55**) compound (IPA = 32.9°, Zn—Zn = 5.913 Å).<sup>56</sup> Notably, the small torsional twist between porphyrin subunits in complex **66** (9.5°, defined as the torsion angle

between the two meso-carbon to spacer bonds) confirms that the Pacman flexibility of the DPXM system is confined to the vertical direction. A striking intraporphyrin angle of  $150.6^\circ$  is measured between 12-atom planes calculated for each half of the macrocycle closest and farthest from the bridge, and the bent Fe—O—Fe angle of  $155.2^\circ$  is the smallest on record for bisiron(III)  $\mu$ -oxo bisporphyrins.<sup>52,57</sup> The five-coordinate iron atoms are raised  $0.56 \text{ \AA}$  out of their respective 24-atom macrocyclic planes. Normal Fe—N ( $d_{\text{avg}} = 2.088 \text{ \AA}$ ) and Fe—O ( $d_{\text{avg}} = 1.788 \text{ \AA}$ ) distances are observed.<sup>58,59</sup> Taken together, the structural data suggest that introduction of an aryl group *trans* to the cyclic ether pillar does not greatly diminish the Pacman flexibility of the DPXM and DPDM platforms relative to their parent DPX and DPD counterparts.

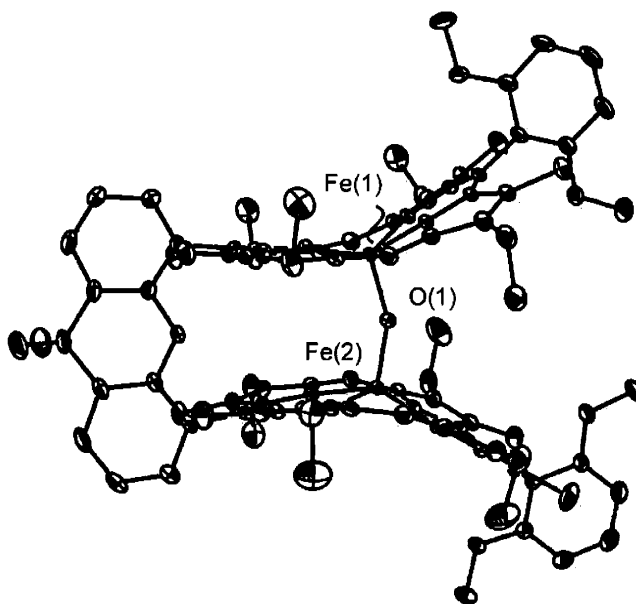


**Figure 7.1.** Crystal structure of  $\text{Fe}_2\text{O}(\text{DPXM})$  (**66**). Thermal ellipsoids are drawn at the 25% probability level. Hydrogen atoms and solvent molecules within the lattice have been omitted for clarity.



**Table 7.1.** Crystallographic Data for Fe<sub>2</sub>O(DPXM) (66).

66	
Empirical formula	C <sub>105</sub> H <sub>122</sub> Cl <sub>8</sub> Fe <sub>2</sub> N <sub>8</sub> O <sub>6</sub>
Formula weight	1987.41
Temperature	183(2) K
Wavelength	0.71073 Å
Crystal system	Triclinic
Space group	$P\bar{1}$
Unit cell dimensions	$a = 15.1206(6)$ Å $b = 16.0783(7)$ Å $c = 24.5229(11)$ Å $\alpha = 72.500(1)^\circ$ $\beta = 79.253(1)^\circ$ $\gamma = 66.396(1)^\circ$
Volume	5195.3(4) Å <sup>3</sup>
Z	2
Density (calculated)	1.270 Mg/m <sup>3</sup>
Absorption coefficient	0.540 mm <sup>-1</sup>
F(000)	2088
Crystal size	0.36 mm × 0.11 mm × 0.10 mm
$\theta$ range for data collection	2.37 to 25.00°
Reflections collected	23352
Independent reflections	17671 [R(int) = 0.0387]
Data/restraints/parameters	17671 / 14 / 1144
Goodness-of-fit on F <sup>2</sup>	1.051
Final R indices [I > 2σ(I)]	R1 = 0.0858 wR2 = 0.2103
R indices (all data)	R1 = 0.1311 wR2 = 0.2496
Largest diff peak	1.554 eÅ <sup>-3</sup>
Largest diff hole	-0.787 eÅ <sup>-3</sup>

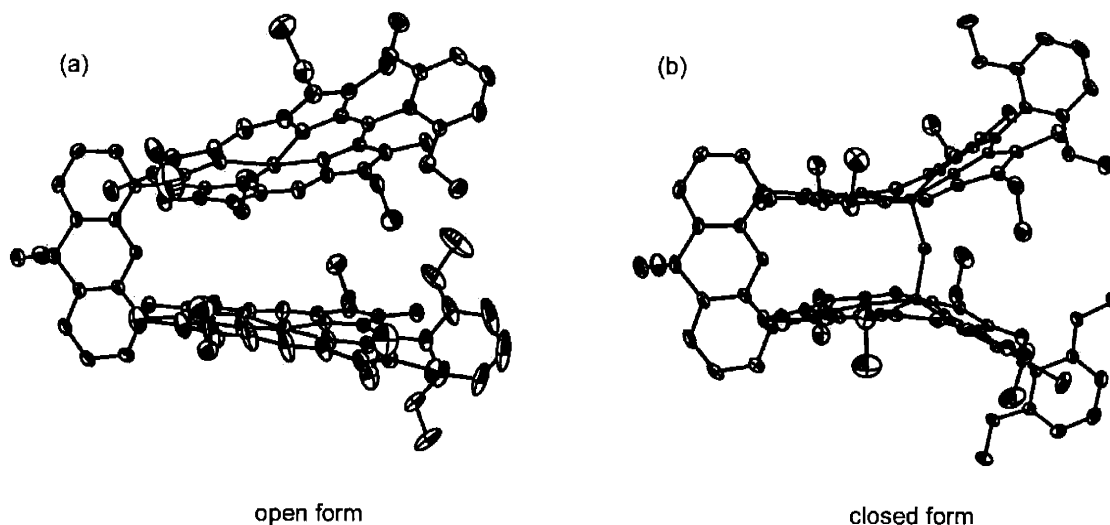


**Figure 7.2.** Structural observation of the Pacman effect for the DPXM framework, depicting (a) open and (b) closed forms of the platform. Thermal ellipsoids are drawn at the 25% probability level. Hydrogen atoms and solvent molecules within the lattice have been omitted for clarity.

**Table 7.2.** Selected Bond Lengths (Å) and Angles (deg) for Fe<sub>2</sub>O(DPXM) (**66**).

<i>Bond Lengths (Å)</i>		<i>Bond Angles (deg)</i>			
Fe(1)-N(1)	2.081(5)	O(1)-Fe(1)-N(3)	104.77(17)	O(1)-Fe(2)-N(5)	103.88(16)
Fe(1)-N(2)	2.084(4)	O(1)-Fe(1)-N(4)	107.40(17)	O(1)-Fe(2)-N(7)	108.29(17)
Fe(1)-N(3)	2.085(5)	N(3)-Fe(1)-N(4)	83.92(19)	N(5)-Fe(2)-N(7)	147.80(17)
Fe(1)-N(4)	2.099(4)	O(1)-Fe(1)-N(2)	105.79(16)	O(1)-Fe(2)-N(6)	106.56(17)
Fe(1)-O(1)	1.786(3)	N(3)-Fe(1)-N(2)	87.52(17)	N(5)-Fe(2)-N(6)	84.51(17)
Fe(2)-N(5)	2.091(4)	N(4)-Fe(1)-N(2)	146.82(17)	N(7)-Fe(2)-N(6)	87.67(17)
Fe(2)-N(6)	2.082(4)	O(1)-Fe(1)-N(1)	105.12(17)	O(1)-Fe(2)-N(8)	103.86(16)
Fe(2)-N(7)	2.091(4)	N(3)-Fe(1)-N(1)	150.11(17)	N(5)-Fe(2)-N(8)	87.57(17)
Fe(2)-N(8)	2.085(4)	N(4)-Fe(1)-N(1)	87.21(19)	N(7)-Fe(2)-N(8)	83.54(17)
Fe(2)-O(1)	1.791(3)	N(2)-Fe(1)-N(1)	84.46(17)	N(6)-Fe(2)-N(8)	149.56(17)

**Table 7.3.** Crystallographically Derived Intradimer Geometrical Features for DPXM Compounds.<sup>a</sup>

	<b>48</b>	<b>55</b>	<b>59</b>	<b>66</b>
M—M distance (Å)	NA	5.913	5.378	3.493
Ct—Ct distance (Å)	6.104	5.987	4.982	4.599
Interplanar angle (deg)	16.9	32.9	20.8	25.4
Torsional twist (deg)	26.0	13.1	19.2	9.5
a–b dist (Å)	4.675	4.676	4.656	4.623
c–d dist (Å)	4.602	4.677	4.485	4.247

<sup>a</sup> Metrics were derived as follows. Macrocyclic centers (Ct) were calculated as the centers of the four nitrogen planes (4–N plane) for each macrocycle. Interplanar angles were measured as the angle between the 4–N least squares planes. Torsional twists were measured as the angle between the two meso-carbon to spacer bonds. The a–b and c–d separations represent the distances between the bridge carbons attached to the porphyrin meso positions and those porphyrin meso carbons, respectively.

### 7.3.2 Electrochemistry

Electrochemical measurements concur with the results obtained from structural studies. The data establish that the redox properties of the parent DPX and DPD systems are not significantly perturbed by introduction of a sterically-demanding aryl group *trans* to the spacer. Table 7.4 lists the oxidative redox potentials of the dicobalt(II) bisporphyrin systems. Cyclic voltammograms of Co<sub>2</sub>(DPXM) (**64**) in toluenitrile using a thin-layer technique<sup>60</sup> (Figure 7.3a) exhibit two reversible one-electron oxidation waves at +0.31 and +0.14 V (vs Ag/AgCl). The splitting of the oxidation processes arises from strong interactions between two proximate porphyrin  $\pi$  systems.<sup>48,49,54</sup> The mixed-valence behavior displayed by **64** is similar to what is observed for the compressed parent complex Co<sub>2</sub>(DPX) (**44**) at comparable potentials ( $E^0 = +0.28$  and +0.17 V vs Ag/AgCl).<sup>51</sup> Conversely, cyclic voltammograms of Co<sub>2</sub>(DPDM) (**65**) in nitrobenzene (Figure 7.3b) give a single, reversible two-electron oxidative wave at an identical potential to the splayed derivative Co<sub>2</sub>(DPD) (**43**) ( $E^0 = +0.33$  V vs Ag/AgCl),<sup>51</sup> suggesting that the porphyrinic subunits in these platforms are too far apart to perturb each other electronically. The electrochemical results thus confirm that the redox behavior of the DPXM and DPDM platforms mirror their respective DPX and DPD congeners.

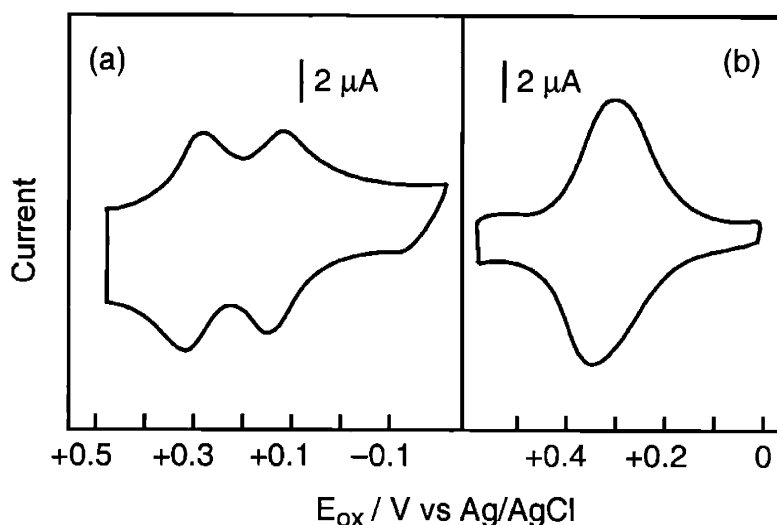


**Figure 7.3.** Cyclic voltammetric responses at an edge-plane graphite (EPG) electrode, covered with a thin layer containing (a) 0.07 mM  $\text{Co}_2(\text{DPXM})$  (**64**) in toluenitrile or (b) 0.20 mM  $\text{Co}_2(\text{DPDM})$  (**65**) in nitrobenzene. The EPG electrode was immersed in an aqueous supporting electrolyte containing 2 M  $\text{HClO}_4$ . Scan rate, 10 mV/s.

**Table 7.4.** Cyclic Voltammetric and Electrocatalytic Data for Dicobalt(II) Pacman Porphyrins at 298 K.

	$E_{\text{ox}} / \text{V vs Ag/AgCl}$	<i>electrocatalytic <math>\text{O}_2</math> reduction</i>	
		$E_{\text{disk}} \text{ vs Ag/AgCl}$	% $\text{H}_2\text{O}$ product
<b>44</b>	+0.28, +0.17	+0.38	72
<b>43</b>	+0.33	+0.37	80
<b>64</b>	+0.31, +0.14	+0.24	52
<b>65</b>	+0.33	+0.25	46

### 7.3.3 Electrocatalytic Reduction of Oxygen

With a solid understanding of the structural and redox properties of dicobalt(II) derivatives of the xanthene- and dibenzofuran-bridged cofacial systems, we turned our attention to their proton-coupled oxygen-activation reactivity. The dicobalt(II) bisporphyrin complexes were screened as electrocatalysts for the reduction of  $\text{O}_2$  in acidic media. Current-potential responses for catalytic oxygen reduction at a rotating graphite disk/platinum ring electrode coated with **43**, **44**, **64**, and **65** are shown in Figure 7.4 and data are collected in Table 7.4.

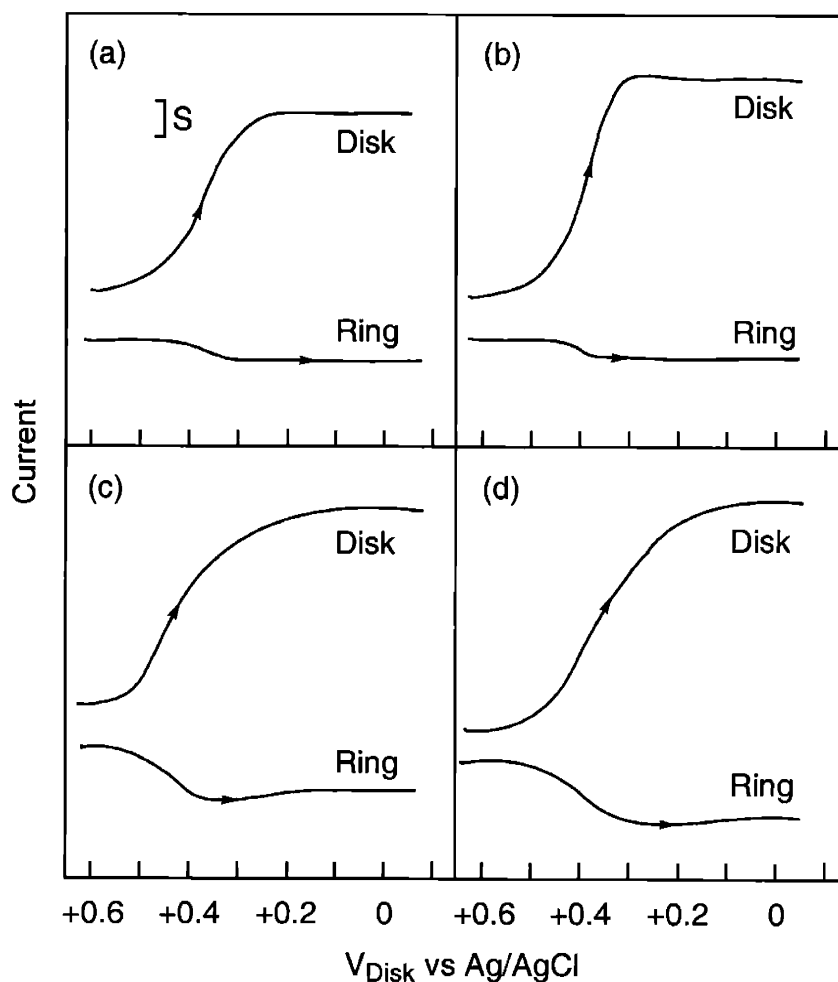


**Figure 7.4.** Rotating Pt ring-disk voltammograms for reduction of  $O_2$  at pyrolytic graphite disks coated with (a)  $Co_2(DPX)$  (**44**), (b)  $Co_2(DPD)$  (**43**), (c)  $Co_2(DPXM)$  (**64**), or (d)  $Co_2(DPDM)$  (**65**). Rotation rate, 100 rpm; disk current,  $S = 10 \mu A$ ; ring current,  $S = 5 \mu A$ ; supporting electrolyte for **43** and **44**, 0.5 M  $HClO_4/1.5$  M TFA saturated with air; supporting electrolyte for **64** and **65**, 2 M  $HClO_4$  saturated with air.

Dicobalt(II) coordination compounds of both DPX and DPD are selective catalysts for the direct reduction of  $O_2$  to  $H_2O$  over  $H_2O_2$  at unusually positive potentials with commensurate selectivities. DPX complex **44** reduces oxygen at +0.38 V (vs Ag/AgCl) with 72% selectivity for the four-electron, four-proton pathway to produce water, and DPD **43** catalyzes  $O_2$  reduction at 0.37 V (vs Ag/AgCl) with direct production of water from oxygen at 80% selectivity.<sup>51</sup> In contrast, the dicobalt(II) complexes of the methoxyaryl frameworks display markedly lower  $H_2O/H_2O_2$  product ratios than their DPX and DPD counterparts, while exhibiting similar

selectivities compared to each other. DPXM **64** catalyzes the reduction of oxygen at a positive potential of +0.24 V (vs Ag/AgCl) with 52% proceeding along the four-electron pathway to produce water, while DPDM **65** catalyzes oxygen reduction at a potential of +0.25 V (vs Ag/AgCl) with 46% going directly to water. The electrocatalytic data reveal the general trend that installation of a methoxyaryl group into the Pacman motif leads to a decreased selectivity for the four-electron, four-proton pathway for O<sub>2</sub> reduction, and that this substitution has an effect of comparable magnitude for both the DPX and DPD scaffolds. As the structural properties of the DPXM/DPDM platforms largely track their DPX/DPD complements, the results intimate that electronic factors contribute to directing oxygen reduction pathways. Accordingly, we sought to examine the electronic structures of the Pacman constructs.

### 7.3.4 Electronic Structure Calculations

Previous considerations of dioxygen binding to dicobalt(II) cofacial bisporphyrins have focused on the mode of O<sub>2</sub> binding between two metal centers.<sup>61</sup> The major binding modes of metal-O<sub>2</sub> adducts can be restricted to end-on<sup>62</sup> ( $\eta^1$ , Pauling) or side-on<sup>63</sup> ( $\eta^2$ , Griffith) models. Tatsumi and Hoffmann calculated the relative energies of possible structural isomers for O<sub>2</sub>-bridged d<sup>n</sup>-d<sup>n</sup> metalloporphyrin dimers using the extended Hückel method.<sup>64</sup> For a dicobalt(III) peroxide bisporphyrin, which corresponds to a d<sup>6</sup>-d<sup>6</sup> configuration, oxygen binding in an end-on geometry is 1.8 eV more favorable than binding in a side-on geometry. In addition, the end-on geometry can exist as a mixture of isomers in which the two Co(porphyrin) fragments are either *cis* or *trans* to each other about the O—O axis. Along these lines of investigation, Le Mest, Saillard, and co-workers examined the bonding interactions in a simplified [Co<sub>2</sub>(FTF4)(O<sub>2</sub>)]<sup>2+</sup> model to rationalize the high selectivity demonstrated by this catalyst for oxygen reduction by a four-electron, four-proton pathway.<sup>50</sup> Constraining the O<sub>2</sub> fragment to a side-on binding geometry, they proposed that the ability of Co<sub>2</sub>(FTF4) to give a high H<sub>2</sub>O/H<sub>2</sub>O<sub>2</sub> product ratio is a result of substantial Co<sub>2</sub>—O<sub>2</sub> overlap that gives rise to efficient transfer of electron density from the cobalt bisporphyrin fragment to the O<sub>2</sub> substrate.

These structure-based bonding arguments are plausibly applicable to addressing the bifurcated oxygen reduction pathways exhibited by the DPX/DPD and DPXM/DPDM scaffolds. However, the combined structural and electrochemical results demonstrate that the introduction of a methoxyaryl substituent onto the ancillary porphyrin skeleton does not significantly alter the structural Pacman flexibility or redox properties of DPX- and DPD-type frameworks. We thus became interested in characterizing electronic distinctions between the DPX/DPD and DPXM/DPDM Pacman systems that lead to selection of oxygen-activation pathways. Of interest is direct evaluation of the electronic structures of O<sub>2</sub> adducts which are critical in directing the

formation of H<sub>2</sub>O or H<sub>2</sub>O<sub>2</sub> products, particularly in regard to proton contributions. Specifically, the nature of the HOMOs of such metal-O<sub>2</sub> species is directly correlated to their proton affinity.

To this end, density functional theory (DFT) calculations were undertaken to assess the electronic structural contributions of methoxyaryl substitution and the role of proton coupling in catalytic oxygen-reduction processes. Owing to the parallel properties of the xanthene- and dibenzofuran-based systems, we chose to evaluate the effect of methoxyaryl substitution by examining analogous O<sub>2</sub> adducts of the DPX and DPXM platforms. As the key intermediates that influence the selectivities of dicobalt(II) bisporphyrins for H<sub>2</sub>O<sub>2</sub> versus H<sub>2</sub>O products are likely to be adducts where O<sub>2</sub> units reversibly bind, we examined [Co<sub>2</sub>(bisporphyrin)(O<sub>2</sub>)]<sup>+</sup> and [Co<sub>2</sub>(bisporphyrin)(O<sub>2</sub>)]<sup>2+</sup> complexes in our DFT study. In order to avoid complications arising from predisposed structural models, we placed no constraints of oxygen binding to an end-on or side-on arrangement. Two minor structural simplifications were made; methyl groups replaced the ancillary ethyl substituents along the porphyrin superstructure, and hydrogen atoms replaced the methyl groups on the xanthene backbone. Figure 7.5 displays the calculated structures for the monocation [Co<sub>2</sub>(DPX)(O<sub>2</sub>)]<sup>+</sup> and dication [Co<sub>2</sub>(DPX)(O<sub>2</sub>)]<sup>2+</sup>. Figure 7.6 presents the optimized structures for monocations [Co<sub>2</sub>(DPX)(O<sub>2</sub>)]<sup>+</sup> and [Co<sub>2</sub>(DPXM)(O<sub>2</sub>)]<sup>+</sup>, while Figure 7.7 depicts their HOMOs. Figure 7.8 compares the HOMOs of the analogous [Co<sub>2</sub>(DPX)(O<sub>2</sub>)]<sup>2+</sup> and [Co<sub>2</sub>(DPXM)(O<sub>2</sub>)]<sup>2+</sup> complexes. The key geometric parameters of optimized structures are summarized in Table 7.5, and the calculated Mulliken charges, atomic spin densities, and overlap populations for the [Co<sub>2</sub>O<sub>2</sub>] cores are collected in Table 7.6. Highlights for the DPX/DPXM set of dicobalt-O<sub>2</sub> monocation and dication species are summarized as follows.

Geometry optimization of [Co<sub>2</sub>(DPX)(O<sub>2</sub>)]<sup>+</sup> with a doublet spin state affords a structure in which the O<sub>2</sub> adduct adopts an end-on binding geometry. Notably, this end-on structure is obtained from an initial input geometry using an idealized side-on [Co<sub>2</sub>O<sub>2</sub>] core. The Co fragments are slightly displaced out of the N<sub>4</sub> porphyrin mean plane ( $d_{\text{avg}} = 0.07 \text{ \AA}$ ), giving a Co—Co distance of 4.35 Å. The calculated O—O bond length (1.35 Å) falls within a range consistent with a superoxo-bridged bimetallic core (1.26 – 1.36 Å), suggesting that the [Co<sub>2</sub>O<sub>2</sub>] core can be described by a [Co<sup>III</sup><sub>2</sub>—(O<sub>2</sub><sup>-</sup>)] configuration. Mulliken population analysis reveals that the total spin density on the [Co<sub>2</sub>O<sub>2</sub>] core is 1.068 e, suggesting that the majority of the unpaired spin density is localized on the [Co<sub>2</sub>O<sub>2</sub>] core. These results are in accord with the experimental observation of a 15-line EPR spectrum for the [Co<sub>2</sub>(DPX)(O<sub>2</sub>)(1,5-dicyclohexylimidazole)<sub>2</sub>]<sup>+</sup> adduct<sup>51</sup> and similar FTF<sup>65,66</sup> and DPB<sup>40,44</sup> complexes, ascribed to  $\mu$ -superoxodicobalt species in which the unpaired electron is partially delocalized on the two Co fragments. The electronic structure of [Co<sub>2</sub>(DPX)(O<sub>2</sub>)]<sup>+</sup> shows that the singly-occupied HOMO consists of localized

molecular orbitals with  $\pi^*(\text{Co—O})$  and  $\pi^*(\text{O—O})$  character on the  $[\text{Co}_2\text{O}_2]$  core, in addition to a  $\pi$ -delocalized system of  $a_{1u}$  symmetry on one of the porphyrin macrocycles.

Geometry optimization of  $[\text{Co}_2(\text{DPX})(\text{O}_2)]^{2+}$  on the singlet potential energy surface results in a structure that is almost identical to that of the monocation analogue. The O—O bond length remains virtually unchanged (1.35 Å for the monocation, 1.34 Å for the dication). The HOMO–LUMO energy gap decreases from 0.48 eV in the monocation to 0.10 eV in the dication. Notably, the 0.10 eV HOMO–LUMO gap of  $[\text{Co}_2(\text{DPX})(\text{O}_2)]^{2+}$  is markedly smaller than that calculated for the FTF4 dication analogue (0.63 eV). Despite removal of an electron on going from the monocation to the dication, the total charge on the  $[\text{Co}_2\text{O}_2]$  core for the two species are commensurate (+1.588 e for the monocation, +1.620 e for the dication). This suggests that most of the additional positive charge in the dication species is delocalized over the organic framework of the metalloporphyrin. Comparison of the Mulliken overlap populations for the Co—O and O—O bonds between the dication and monocation shows that these bonds are strengthened upon one-electron oxidation of the latter. In particular, the HOMO of  $[\text{Co}_2(\text{DPX})(\text{O}_2)]^{2+}$  has porphyrin  $\pi$  character of  $a_{1u}$  symmetry, whereas the LUMO exhibits features that are coincident with the singly-occupied HOMO of the monocation species.

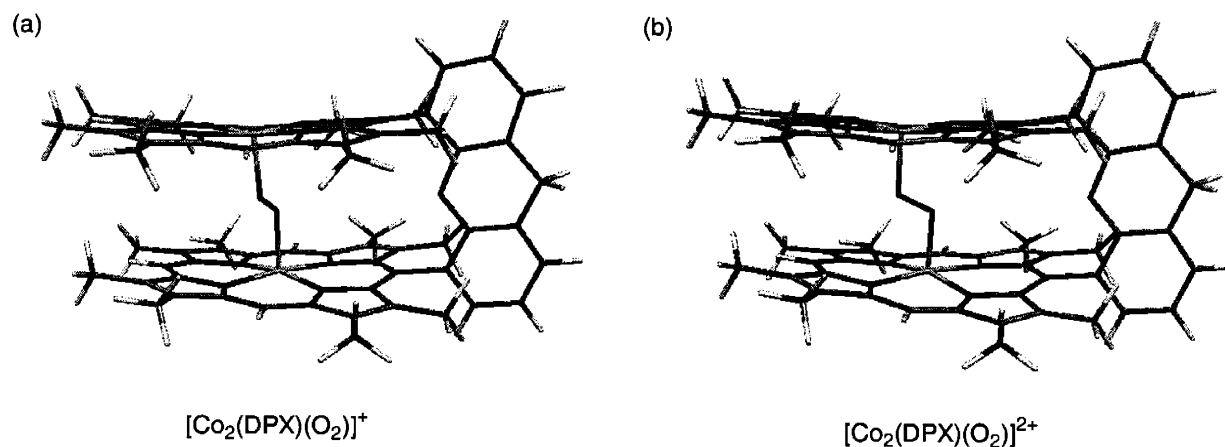


**Figure 7.5.** Optimized structures of the DPX- $\text{O}_2$  adducts (a)  $[\text{Co}_2(\text{DPX})(\text{O}_2)]^+$  and (b)  $[\text{Co}_2(\text{DPX})(\text{O}_2)]^{2+}$ .

In contrast to its DPX counterpart, the optimized geometry of the  $[\text{Co}_2(\text{DPXM})(\text{O}_2)]^+$  monocation with a doublet spin state displays large non-planar distortions of the porphyrin macrocycles. One porphyrin exhibits a ruffled-type conformation, whereas distortion of the other macrocycle is dominated by saddling. The average mean plane deviations for these macrocycles are 0.31 Å and 0.20 Å, respectively. Another notable structural departure from the DPX analogue is the Co—O—O—Co dihedral angle, which decreases from 175.2° in  $[\text{Co}_2(\text{DPX})(\text{O}_2)]^+$  to



153.3° in  $[\text{Co}_2(\text{DPXM})(\text{O}_2)]^+$ . Defining the four pyrrolic nitrogens as the  $xy$ -plane, the non-planar distortion of the porphyrin causes the local  $z$ -axes of the two Co atoms (corresponding to the Co—O bond vectors) to point away from each other, resulting in a Co—O—O—Co dihedral angle that deviates significantly from 180°. Nevertheless, the average Co—O (1.88 Å) and O—O (1.32 Å) bond lengths for  $[\text{Co}_2(\text{DPXM})(\text{O}_2)]^+$  are virtually identical to those of the DPX analogue (Co—O = 1.83 Å, Co—O = 1.35 Å), and the Co—Co distance for the DPXM complex (4.50 Å) compares favorably to the DPX congener (4.35 Å). Like its DPX analogue, the O—O bond length for the DPXM monocation complex is suggestive of a  $\mu$ -superoxodicobalt species. The shorter O—O bond length in  $[\text{Co}_2(\text{DPXM})(\text{O}_2)]^+$  compared to  $[\text{Co}_2(\text{DPX})(\text{O}_2)]^+$  is indicative of a stronger O—O bond in the former; indeed, the Mulliken overlap population for the O—O bond in  $[\text{Co}_2(\text{DPXM})(\text{O}_2)]^+$  is +0.175 e, which is significantly larger than the value of +0.159 e found for  $[\text{Co}_2(\text{DPX})(\text{O}_2)]^+$ . In addition, the average Co—O Mulliken overlap population of the DPXM metalloporphyrin (+0.202 e) is substantially larger than that of its DPX congener (+0.146 e). The charge on the dioxygen substrate is more negative in  $[\text{Co}_2(\text{DPX})(\text{O}_2)]^+$  (−0.284 e) than in the DPXM analogue (−0.237 e), suggesting that non-planar distortion in the latter results in less effective charge transfer from the cobalt bisporphyrin fragment to the O<sub>2</sub> substrate. Similar to the DPX porphyrin, Mulliken population analysis confirms that the unpaired spin density is localized on the  $[\text{Co}_2\text{O}_2]$  fragment (1.082 e total). The singly-occupied HOMO of  $[\text{Co}_2(\text{DPXM})(\text{O}_2)]^+$  consists solely of a porphyrin  $\pi$  system of  $a_{1u}$  symmetry. Conversely, the singly-occupied HOMO of  $[\text{Co}_2(\text{DPX})(\text{O}_2)]^+$  bears both porphyrin- $\pi$  and  $\text{Co}_2\text{O}_2$ - $\pi$  character.

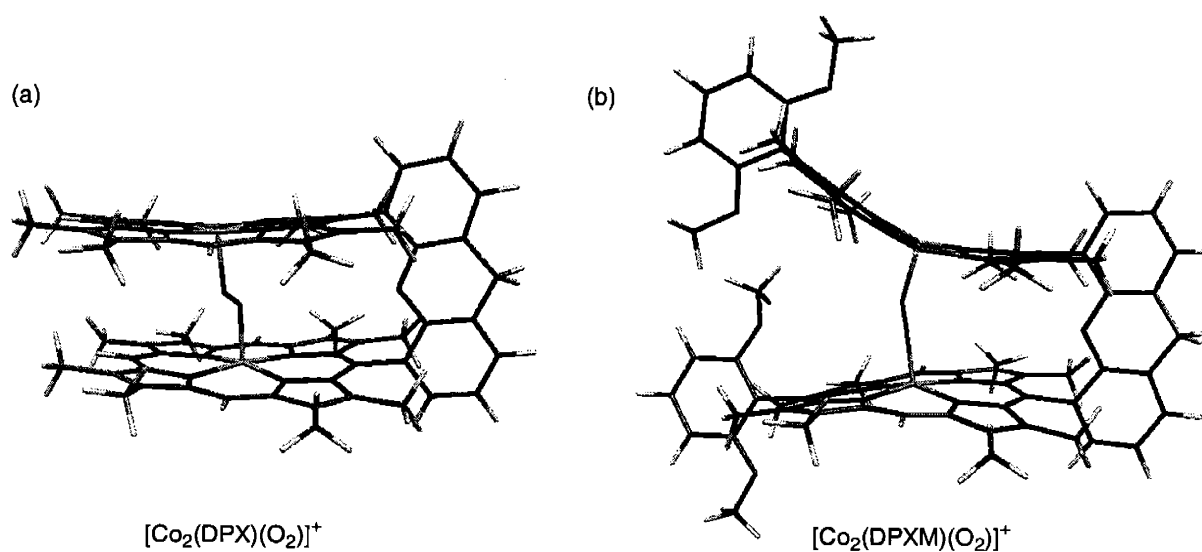


**Figure 7.6.** Optimized structures of the monocations (a)  $[\text{Co}_2(\text{DPX})(\text{O}_2)]^+$  and (b)  $[\text{Co}_2(\text{DPXM})(\text{O}_2)]^{2+}$ .

Geometry optimizations for the DPX systems establish that the molecular structures of the monocation and dication species are virtually identical. Accordingly, the  $[\text{Co}_2(\text{DPXM})(\text{O}_2)]^{2+}$  dication was examined by carrying out a single-point energy calculation using the optimized geometry of the monocation species; this calculation was performed on the singlet potential energy surface. The HOMO–LUMO gap decreases from 0.38 eV in the monocation species to 0.07 eV in the dication. The total charges centered on the  $[\text{Co}_2\text{O}_2]$  core are similar for both the monocation (+1.600 e) and dication (+1.609 e) species despite differences in their overall charges. As observed for  $[\text{Co}_2(\text{DPXM})(\text{O}_2)]^+$ , non-planar distortion of the macrocyclic subunits in  $[\text{Co}_2(\text{DPXM})(\text{O}_2)]^{2+}$  results in strengthening of the Co—O and O—O bonds. In addition, less effective charge transfer from the cobalt bisporphyrin fragment to the  $\text{O}_2$  substrate occurs in DPXM compared to DPX. The Mulliken overlap populations of Co—O (+0.211 e) and O—O (+0.178 e) for  $[\text{Co}_2(\text{DPXM})(\text{O}_2)]^{2+}$  are comparable to those for  $[\text{Co}_2(\text{DPXM})(\text{O}_2)]^+$ . Finally, the HOMO of  $[\text{Co}_2(\text{DPXM})(\text{O}_2)]^{2+}$  is localized on the Co—O—O—Co backbone, with  $\pi^*$  character within the Co—O and O—O bonds. This frontier orbital picture contrasts with the porphyrin  $\pi$  orbital character found for the HOMO of  $[\text{Co}_2(\text{DPX})(\text{O}_2)]^{2+}$ .

From the above results, several conclusions can be drawn between similarly-charged  $\text{Co}_2(\text{DPX})$  and  $\text{Co}_2(\text{DPXM})$  porphyrins with respect to the bonding interactions in the  $[\text{Co}_2\text{O}_2]$  core and the overall electronic structures of the molecules: (i) the Co—O and O—O bonds in the DPXM series are stronger than those in the corresponding DPX series; (ii) the  $\text{O}_2$  fragments in the DPX complexes are more negatively charged compared to those in the DPXM congeners; (iii) the nature of the HOMOs in the monocation and dication species are reversed for the DPX and DPXM cases. Points (i) and (ii) are a simple consequence of non-planar distortions of the porphyrin macrocycles in the DPXM series relative to their DPX congeners. Non-planar distortions decrease  $d_{\pi}\text{--}p_{\pi}$  interactions between the metal  $d_{xz}$  and  $d_{yz}$  orbitals and the porphyrin  $\pi$  orbitals,<sup>58</sup> thereby allowing the metal d orbitals to participate in more extensive  $\pi$  bond formation with the  $\text{O}_2$  substrate. Similarly, the stronger O—O bonds in the DPXM series compared to those in the respective DPX analogues are attributable to the stronger Co—O  $\pi$  bonds in the former, which result in depopulation of the O—O  $\pi^*$  orbitals. The less negatively charged dioxygen fragments in the DPXM compounds compared to the DPX complexes are consistent with the greater utilization of electron density on the dioxygen substrate for bond formation with the cobalt bisporphyrin to give a stronger Co—O bond. Since charge transfer from the Co fragments to the  $\text{O}_2$  substrate is accompanied by population of the O—O  $\pi^*$  orbitals, the less negatively charged dioxygen fragment in  $[\text{Co}_2(\text{DPXM})(\text{O}_2)]^{n+}$  ( $n = 1, 2$ ) is also consistent with a stronger O—O bond. The most intriguing result in regard to oxygen-reduction selectivity is conclusion (iii), which directly assesses the relative proton affinities of the monocation and dication adducts

of the dicobalt Pacman porphyrins upon methoxyaryl substitution. These electronic structure contributions to proton coupling, and hence selectivity in oxygen-reduction pathways, are discussed in further detail in the next section.

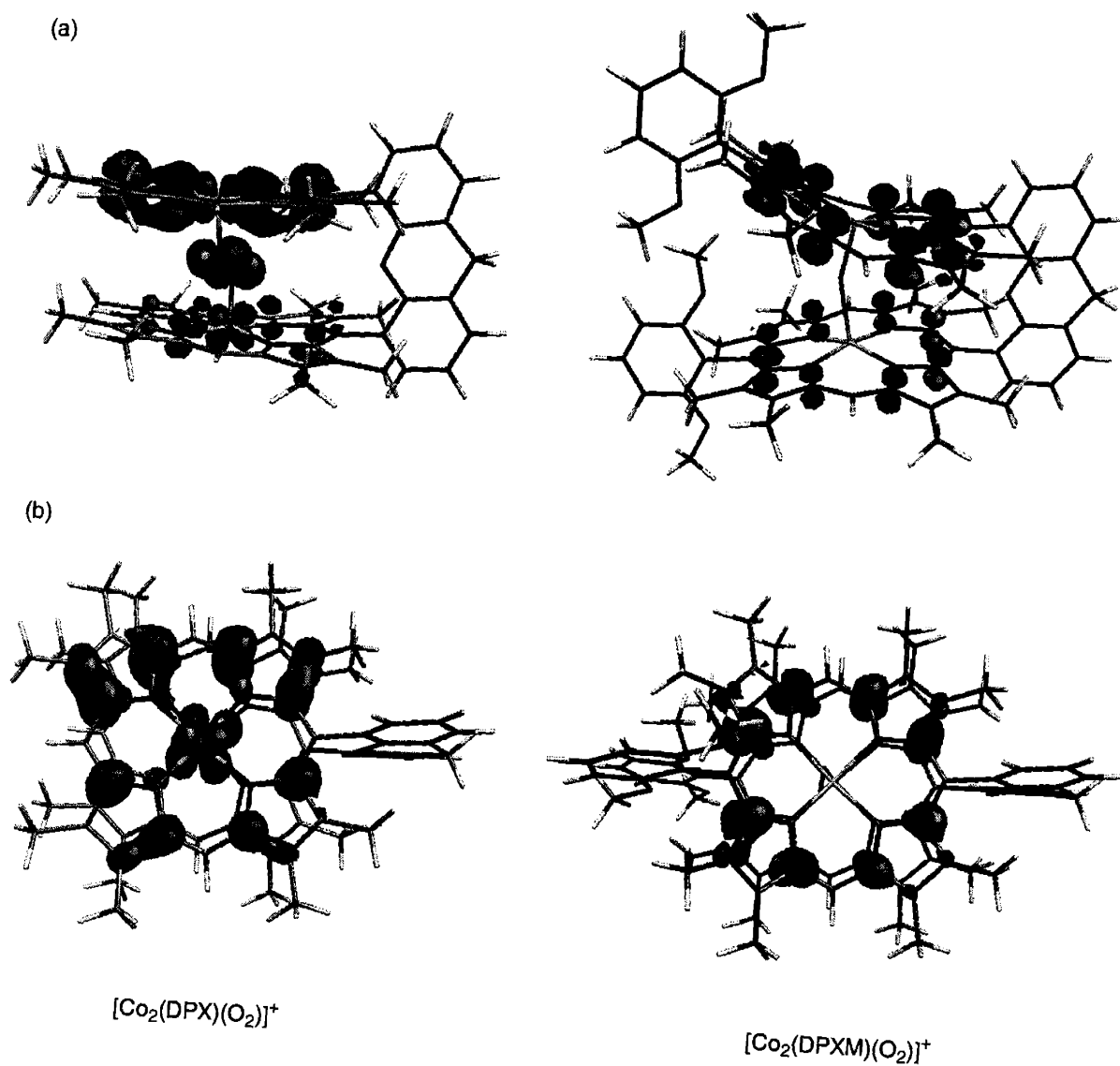


**Figure 7.7.** Singly-occupied HOMOs of  $[\text{Co}_2(\text{DPX})(\text{O}_2)]^+$  (left) and  $[\text{Co}_2(\text{DPXM})(\text{O}_2)]^+$  (right). (a) Side view, perpendicular to the bridge plane, (b) top view, perpendicular to the porphyrin planes.

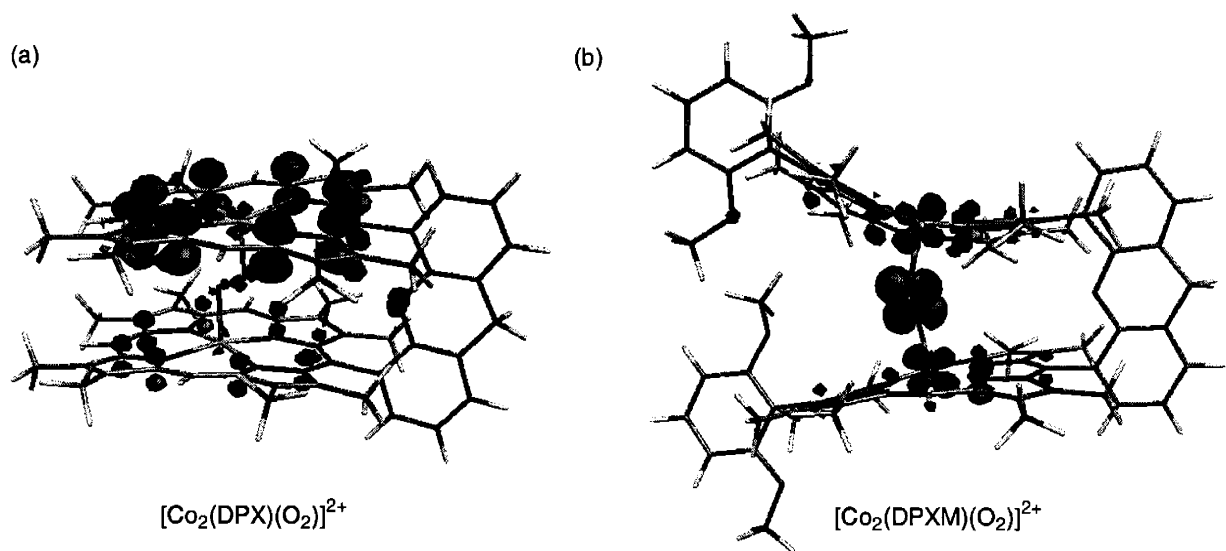


**Figure 7.8.** HOMOs of (a)  $[\text{Co}_2(\text{DPX})(\text{O}_2)]^{2+}$  and (b)  $[\text{Co}_2(\text{DPXM})(\text{O}_2)]^{2+}$ .

**Table 7.5.** Geometric Parameters for the Optimized Structures of the  $\text{O}_2$  Adducts of Dicobalt Pacman Porphyrins.

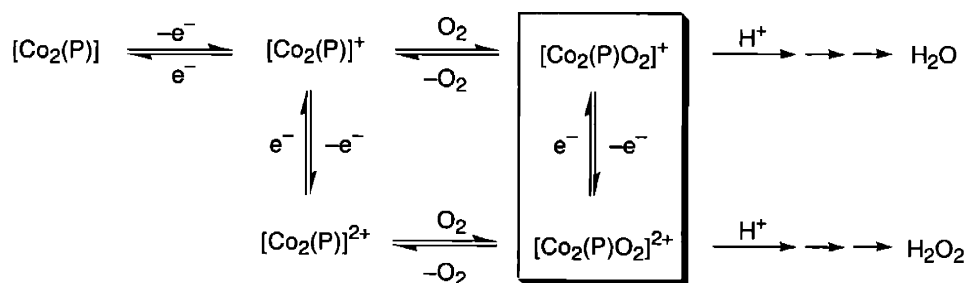
	$[\text{Co}_2(\text{DPX})(\text{O}_2)]^+$	$[\text{Co}_2(\text{DPX})(\text{O}_2)]^{2+}$	$[\text{Co}_2(\text{DPXM})(\text{O}_2)]^+$
Co—O (Å)	1.83, 1.82	1.80, 1.81	1.88, 1.88
O—O (Å)	1.35	1.34	1.32
Co—Co (Å)	4.35	4.35	4.50
Co—O—O (deg)	111.8, 114.6	114.1, 116.1	118.6, 121.4
Co—O—O—Co (deg)	175.2	174.8	153.3
torsional twist (deg)	6.9	7.4	4.3
Co dist from $\text{N}_4$ plane (Å)	0.07, 0.07	0.08, 0.10	0.11, 0.13
24-atom mean plane dev (Å)	0.13, 0.14	0.13, 0.17	0.31, 0.20

**Table 7.6.** Atomic Charges and Overlap Populations Obtained from Mulliken Population Analysis with Atomic Spin Densities for the Monocation Species Given in Parentheses.

	$[\text{Co}_2(\text{DPX})(\text{O}_2)]^+$	$[\text{Co}_2(\text{DPX})(\text{O}_2)]^{2+}$	$[\text{Co}_2(\text{DPXM})(\text{O}_2)]^+$	$[\text{Co}_2(\text{DPXM})(\text{O}_2)]^{2+}$
<i>Atomic charge</i>				
Co1	+0.935 (0.196)	+0.939	+0.904 (0.279)	+0.901
Co2	+0.937 (0.166)	+0.944	+0.932 (0.345)	+0.931
O1	-0.140 (0.350)	-0.128	-0.119 (0.229)	-0.114
O2	-0.144 (0.357)	-0.135	-0.117 (0.229)	-0.110
<i>Overlap population</i>				
Co1—O1	+0.144	+0.161	+0.203	+0.214
Co2—O2	+0.148	+0.160	+0.200	+0.209
O1—O2	+0.159	+0.171	+0.175	+0.178

### 7.3.5 Electronic Structure Contribution of Proton Coupling to the Selectivity for Four- or Two-Electron Oxygen Reduction Pathways

The mechanism proposed by Le Mest, Saillard and co-workers for the catalytic reduction of oxygen by dicobalt(II) cofacial bisporphyrins provides a useful starting point for analyzing the influence of proton coupling on selecting  $\text{O}_2$ -reduction pathways.<sup>50</sup> Scheme 7.1 depicts the key cobalt bisporphyrin monocation and dication intermediates along the pathways to water and peroxide products.



**Scheme 7.1.** Oxygen reduction pathways leading to water and peroxide products.

Protonation of the  $[\text{Co}_2(\text{bisporphyrin})(\text{O}_2)]^+$  monocation species for a dicobalt cofacial bisporphyrin funnels the reduction pathway through four-electron, four-proton route to produce water, whereas protonation of the corresponding  $[\text{Co}_2(\text{bisporphyrin})(\text{O}_2)]^{2+}$  dication species

channels the reduction towards the two-electron, two-proton pathway to generate peroxide. Within this mechanistic framework, weakening of the O—O bond in the monocation pre-disposes the O—O bond to cleave upon protonation, thereby enabling the facile formation of two H<sub>2</sub>O molecules from the O<sub>2</sub> substrate.

Electronic structure calculations on etio-type cofacial bisporphyrins with (DPXM) and without (DPX) methoxyaryl substitution provide an underpinning for interpreting the catalytic selectivities of the DPX/DPD and DPXM/DPDM platforms. The experimental data compiled for the dicobalt(II) derivatives establish the applicability of these results for both xanthene- and dibenzofuran-bridged systems. For the [Co<sub>2</sub>(DPX)(O<sub>2</sub>)]<sup>+</sup> monocation, the singly-occupied HOMO consists of partial contribution from the Co—O—O—Co  $\pi$  system with Co—O and O—O  $\pi^*$  character, whereas the HOMO of the [Co<sub>2</sub>(DPX)(O<sub>2</sub>)]<sup>2+</sup> dication is located solely on the porphyrin  $\pi$  system. On the other hand, the HOMO of the corresponding [Co<sub>2</sub>(DPXM)(O<sub>2</sub>)]<sup>+</sup> monocation is found on the porphyrin  $\pi$  system, with the HOMO of the [Co<sub>2</sub>(DPXM)(O<sub>2</sub>)]<sup>2+</sup> dication residing along the Co—O—O—Co fragment. The simple reversal in the character of the HOMOs for O<sub>2</sub>-bound Co<sub>2</sub>(DPX) and Co<sub>2</sub>(DPXM) bisporphyrins is consistent with the observed differences in their selectivities for the four-electron, four-proton reduction pathway. As protonation is expected to occur at the site where the HOMO resides, the DPX molecule is expected to exhibit a higher selectivity for the four-electron, four-proton reduction pathway since the HOMO of the monocation species resides on the [Co<sub>2</sub>O<sub>2</sub>] core. Conversely, the HOMO of the dication species resides on the porphyrin macrocycle, which should resist both [Co<sub>2</sub>O<sub>2</sub>] core protonation and the pathway to yield two-electron, two-proton reduced product (H<sub>2</sub>O<sub>2</sub>). It follows that the methoxyaryl analogue is not expected to demonstrate as high selectivity for the four-electron, four-proton reduction pathway since the HOMO of the monocation resides on the porphyrin  $\pi$  system, whereas the HOMO of the dication resides on the [Co<sub>2</sub>O<sub>2</sub>] core. Finally, we note that although the geometry optimizations yield O<sub>2</sub> adducts with end-on binding modes, these electronic structure arguments are not restrictive to an end-on or side-on binding mode for bisporphyrin-O<sub>2</sub> adducts. In fact, the extended Hückel calculations by Le Mest, Saillard, and co-workers on a confined side-on O<sub>2</sub> species for the selective four-electron, four-proton catalyst Co<sub>2</sub>(FTF4) concur with our results; the HOMO of the [Co<sub>2</sub>(FTF4)(O<sub>2</sub>)]<sup>2+</sup> complex is porphyrin-localized.<sup>50</sup>

## 7.4 Concluding Remarks

The effective utilization of the dioxygen molecule in biological and chemical catalysis is predicated on the dual control of electron and proton inventories. With regard to O<sub>2</sub> reduction, the coupled management of proton and electron equivalents is critical for selecting the four-

electron, four-proton pathway to produce water over the more common two-electron, two-proton pathway to produce peroxide. Dicobalt(II) cofacial bisporphyrins are among the few molecular catalysts capable of mediating the selective four-electron, four-proton reduction of oxygen to water. As discussed by Collman<sup>45,67</sup> and Taube,<sup>68</sup> these systems fulfill the two general requirements for an effective four-electron, four-proton oxygen-reduction catalyst: (i) the bypass of kinetically available one-electron and two-electron routes through cooperative bimetallic reactivity, and (ii) the stability of reducible peroxo-type intermediates to protonation and release.

The substantial body of work on cofacial bisporphyrins as O<sub>2</sub>-reduction catalysts has clarified the structural attributes of an effective architecture, including the restriction of macrocyclic subunits to a face-to-face arrangement with minimal lateral displacements, while allowing sufficient vertical flexibility to bind and activate the O<sub>2</sub> substrate. Against this backdrop of expertise, we have sought to define electronic features, particularly with regard to proton coupling, that guide the O<sub>2</sub>-reduction pathways of these molecular clefts. Towards this goal, we prepared a library of dicobalt(II) cofacial bisporphyrins based on xanthene (DPX/DPXM) and dibenzofuran (DPD/DPDM) pillars that span a range of vertical pocket sizes. The collected experimental data support the contention that the structural and redox properties of the methoxyaryl Pacman derivatives DPXM and DPDM mirror their corresponding DPX and DPD parent systems, while the reactivity patterns place the Pacman porphyrins in two groups, DPX/DPD and DPXM/DPDM. In particular, the introduction of a single methoxyaryl substituent onto the porphyrin platform leads to catalysts with markedly reduced selectivity for oxygen reduction via the four-electron, four-proton pathway compared to etio-type derivatives. The compilation of structural and electrochemical data suggest that the observed differences in pathway selectivity result from electronic contributions. Electronic structure calculations of Pacman-O<sub>2</sub> adducts ([Co<sub>2</sub>(bisporphyrin)O<sub>2</sub>]<sup>+</sup>) and ([Co<sub>2</sub>(bisporphyrin)O<sub>2</sub>]<sup>+</sup>) reveal that the nature of the HOMOs in the monocation and dication species are reversed for Pacman templates with and without a methoxyaryl group. As a result of HOMO character switch for the monocation and dication species, the DPX/DPD-type systems exhibit higher H<sub>2</sub>O/H<sub>2</sub>O<sub>2</sub> product ratios than their DPXM/DPDM counterparts.

To close, the combined experimental and theoretical findings provide important insights for effecting selective oxygen activation and reduction chemistry. Our results highlight the importance of proton affinity and electronic structure in directing catalytic O<sub>2</sub>-reduction pathways. The incorporation of such attributes in the design of efficient catalysts for the proton-coupled activation of oxygen and other small-molecule substrates is underway.

## 7.5 Experimental Section

### 7.5.1 Materials

Aluminum oxide 60 (EM Science) was used for column chromatography. Analytical thin layer chromatography was performed using JT Baker IB-F aluminum oxide (precoated sheets, 0.2 mm thick). Solvents for synthesis were of reagent grade or better, and were dried according to standard methods.<sup>69</sup> Spectroscopic experiments employed dichloromethane (spectroscopic grade, Burdick & Jackson), which was stored over 4 Å molecular sieves under high vacuum or in a glovebox. The Pacman porphyrins H<sub>4</sub>(DPXM) (**48**) and H<sub>4</sub>(DPDM) (**54**) were available using the procedures outlined in chapter 6. All other reagents were used as received.

### 7.5.2 Co<sub>2</sub>(DPXM) (**64**)

To a solution of H<sub>4</sub>(DPXM) (**48**) (105 mg, 0.073 mmol) in THF (15 mL) and benzene (10 mL) containing 2,6-lutidine (0.2 mL) was added CoCl<sub>2</sub> (200 mg). The resulting mixture was refluxed for 10 h under nitrogen and taken to dryness. The solvent was removed in vacuo and the residue was purified by flash column chromatography in an inert atmosphere (neutral alumina, THF). Recrystallation from dichloromethane/methanol gave **64** as an analytically pure brick red powder (110 mg, 97% yield). Anal. Calcd for C<sub>95</sub>H<sub>102</sub>N<sub>8</sub>O<sub>5</sub>Co<sub>2</sub>: C, 73.63; H, 6.37; N, 7.23. Found: C, 73.77; H, 6.53; N, 6.84. HRFABMS (M<sup>+</sup>) calcd for C<sub>95</sub>H<sub>102</sub>N<sub>8</sub>O<sub>5</sub>Co<sub>2</sub> *m/z* 1548.632, found 1548.633.

### 7.5.3 Co<sub>2</sub>(DPDM) (**65**)

To a solution of H<sub>4</sub>(DPDM) (**54**) (52 mg, 0.037 mmol) in THF (8 mL) and benzene (8 mL) containing 2,6-lutidine (0.1 mL) was added CoCl<sub>2</sub> (120 mg). The resulting mixture was refluxed for 15 h under nitrogen and taken to dryness. The solvent was removed in vacuo and the residue was purified by flash column chromatography in an inert atmosphere (neutral alumina, THF). Recrystallation from dichloromethane/methanol gave **65** as an analytically pure blood red powder (51 mg, 91% yield). Anal. Calcd for C<sub>92</sub>H<sub>92</sub>N<sub>8</sub>O<sub>5</sub>Co<sub>2</sub>: C, 73.29; H, 6.15; N, 7.43. Found: C, 73.60; H, 6.49; N, 6.90. HRFABMS (M<sup>+</sup>) calcd for C<sub>92</sub>H<sub>92</sub>N<sub>8</sub>O<sub>5</sub>Co<sub>2</sub> *m/z* 1506.586, found 1506.590.

### 7.5.4 Fe<sub>2</sub>O(DPXM) (**66**)

A mixture of H<sub>4</sub>(DPXM) (**48**) (45 mg, 0.031 mmol) and FeBr<sub>2</sub> (100 mg) in THF (7 mL) and benzene (5 mL) containing 2,6-lutidine (0.1 mL) was refluxed under nitrogen for 5 h. The reaction was opened to air and the solvent was removed by rotary evaporation. The remaining residue was taken up in dichloromethane and vigorously stirred with a 0.5 N NaOH solution (20



mL) for 30 min. The organic phase was separated, washed with water (3 × 25 mL), dried over Na<sub>2</sub>SO<sub>4</sub>, and taken to dryness. Purification by column chromatography (basic alumina, 85/15 chloroform/ethyl acetate) followed by recrystallization from dichloromethane/hexanes afforded analytically pure **66** (45 mg, 92% yield) as a brown crystalline solid. Anal. Calcd for C<sub>95</sub>H<sub>102</sub>N<sub>8</sub>O<sub>6</sub>Fe<sub>2</sub>: C, 73.16; H, 6.33; N, 7.19. Found: C, 73.01; H, 6.20; N, 7.06. HRFABMS ([M–O]<sup>+</sup>) calcd for C<sub>95</sub>H<sub>102</sub>N<sub>8</sub>O<sub>5</sub>Fe<sub>2</sub> *m/z* 1542.636, found 1542.633.

### 7.5.5 General Details of X-ray Data Collection and Reduction

X-ray diffraction data were collected using a Siemens 3 circle diffractometer equipped with a CCD detector. Measurements were carried out at –90° C using Mo K $\alpha$  ( $\lambda = 0.71073 \text{ \AA}$ ) radiation, which was wavelength selected with a single-crystal graphite monochromator. Four sets of data were collected using  $\omega$  scans and a –0.3° scan width. All calculations were performed using a PC workstation. The data frames were integrated to *hkl*/intensity, and final unit cells were calculated by using the SAINT v.4.050 program from Siemens. The structures were solved and refined with the SHELXTL v.5.03 suite of programs developed by G. M. Sheldrick and Siemens Industrial Automation, Inc., 1995.

### 7.5.6 X-ray Structure of Fe<sub>2</sub>O(DPXM)•4CH<sub>2</sub>Cl<sub>2</sub>•C<sub>6</sub>H<sub>14</sub> (**66**)

A 0.36 mm × 0.11 mm × 0.10 mm chocolate crystal of plate morphology was obtained from slow diffusion of hexane into a dichloromethane solution of the compound. The crystal was coated in STP and mounted onto a glass fiber. A total of 23352 reflections were collected in the  $\theta$  range 2.37 to 25.00°, of which 17671 were unique ( $R_{\text{int}} = 0.0387$ ). The Patterson method was used to locate the iron atoms, all remaining atoms were placed using the difference Fourier map. Hydrogen atoms were placed in calculated positions using a standard riding model and were refined isotropically. The largest peak and hole in the difference map were 1.554 e $\text{\AA}^{-3}$  and –0.787 e $\text{\AA}^{-3}$ , respectively. The least squares refinement converged normally giving residuals of  $R1 = 0.0858$  and  $wR2 = 0.2103$ , with  $\text{GOF} = 1.051$ .

### 7.5.7 Physical Measurements

Mass spectral analyses were carried out by the University of Illinois Mass Spectrometry Laboratory. Elemental analyses were performed at Michigan State University. Absorption spectra were obtained using a Cary-17 spectrophotometer modified by On-Line Instrument Systems (OLIS) to include computer control or a Spectral Instruments 440 Model spectrophotometer.

### 7.5.8 Electrochemical Apparatus and Procedures

The electrocatalytic studies were carried out in collaboration with Prof. Fred Anson and Dr. Chunnian Shi at the California Institute of Technology. Cylindrical pyrolytic graphite rods with the edges of the graphitic planes exposed (Union Carbide) were mounted to stainless steel shafts with heat-shrinkable polyolefin tubing (Alpha Wire). The exposed graphite disk had an area of 0.32 cm<sup>2</sup>. Electrode pre-treatment and catalyst loading were carried out using standard procedures.<sup>70</sup> Briefly, the pyrolytic graphite rods were polished with 600 grit SiC paper (3M), sonicated in purified water (MilliQ Plus), washed with acetone, and dried. Porphyrins were adsorbed on the electrode surface by means of a dip-coating procedure: the freshly polished electrode was dipped for 1 min in a 0.1 mM solution of the porphyrin in chloroform, removed, washed immediately with pure chloroform, and dried in air. The dry, coated electrodes were transferred to the aqueous supporting electrolytes and utilized immediately.

The commercial rotating graphite-disk-platinum ring electrode (Pine Instruments) was polished with 0.3- $\mu$ m alumina on microcloth. The collection efficiency of the rotating ring-disk electrode (RRDE) employed was 0.39 as established by measurements with the Fe(CN)<sub>6</sub><sup>3-/4-</sup> couple. The percentage of oxygen reduction proceeding along the four-electron pathway to produce water was calculated using the formula  $f_{\text{water}} = [N - (i_{\text{R}}/i_{\text{D}})]/[N + (i_{\text{R}}/i_{\text{D}})]$  where  $f_{\text{water}}$  is the fraction of oxygen reduced to water,  $N$  is the collection efficiency of the RRDE, and  $i_{\text{R}}$  and  $i_{\text{D}}$  are the ring and disk currents, respectively.

### 7.5.9 Computational Methods

Density functional theory (DFT) calculations were carried out in collaboration with Mr. Zhi-Heng Loh. Calculations were performed at the local density approximation (LDA) level of theory using the Amsterdam Density Functional program.<sup>71-74</sup> Part of the calculations were performed on a home-built Linux cluster consisting of 12 processors running in parallel. Gradient corrections were introduced by using the Becke exchange functional (B)<sup>75</sup> and the Perdew-Wang (PW91) correlation functional.<sup>76</sup> C and H were described by a Slater-type orbital double- $\xi$  basis set augmented by one set of polarization functions. Co, N, and O atoms were described by a Slater-type orbital triple- $\xi$  basis set augmented by one set of polarization functions. Non-hydrogen atoms were assigned a frozen core potential, treating as core the shells up to and including 2p for Co, and 1s for C, N, and O. Calculations on the doublet spin state were performed within the unrestricted formalism. Population analyses were carried out using the Mulliken method. The cobalt bisporphyrin models employed in the calculations were structurally simplified as follows: (i) ethyl groups on the porphyrin macrocycles were replaced with methyl groups, and (ii) methyl groups on the xanthene pillar were replaced with hydrogens.

## 7.6 References and Notes

1. Ferguson-Miller, S.; Babcock, G. T. *Chem. Rev.* **1996**, *96*, 2889-2907.
2. Michel, H.; Behr, J.; Harrenga, A.; Kannt, A. *Annu. Rev. Biophys. Biomol. Struct.* **1998**, *27*, 329-356.
3. Malmström, B. G. In *Electron Transfer in Chemistry*; Balzani, V., Ed.; Wiley-VCH: Weinheim, Germany, 2001; Vol. 3.1.3, pp 39-55.
4. Schultz, B. E.; Chan, S. I. *Annu. Rev. Biophys. Biomol. Struct.* **2001**, *30*, 23-65.
5. Brzezinski, P. *Biochim. Biophys. Acta* **2000**, *1458*, 1-5.
6. Babcock, G. T.; Wikström, M. *Nature* **1992**, *356*, 301-309.
7. Wikström, M. *Biochim. Biophys. Acta* **2000**, *1458*, 188-198.
8. Gennis, R. B. *Proc. Natl. Acad. Sci. USA* **1998**, *95*, 12747-12749.
9. Ruitenbergh, M.; Kannt, A.; Bamberg, E.; Fendler, K.; Michel, H. *Nature* **2002**, *417*, 99-102.
10. Anson, F. C.; Shi, C.; Steiger, B. *Acc. Chem. Res.* **1997**, *30*, 437-444.
11. Klinman, J. P. *J. Biol. Inorg. Chem.* **2001**, *6*, 1-13.
12. Whittaker, M. M.; Whittaker, J. W. *Biochemistry* **2001**, *40*, 7140-7148.
13. Solomon, E. I.; Chen, P.; Metz, M.; Lee, S.-K.; Palmer, A. E. *Angew. Chem. Int. Ed.* **2001**, *40*, 4570-4590.
14. Guallar, V.; Gherman, B. F.; Lippard, S. J.; Friesner, R. A. *Curr. Opin. Chem. Biol.* **2002**, *6*, 236-242.
15. Que Jr., L.; Ho, R. Y. N. *Chem. Rev.* **1996**, *96*, 2607-2624.
16. Lee, S.-K.; Lipscomb, J. D. *Biochemistry* **1999**, *38*, 4423-4432.
17. Ortiz de Montellano, P. R. *Cytochrome P450: Structure, Mechanism, and Biochemistry*; 2nd ed.; Plenum: New York, 1995.
18. Poulos, T. L. *Curr. Opin. Struct. Biol.* **1995**, *5*, 767-774.
19. Sono, M.; Roach, M. P.; Coulter, E. D.; Dawson, J. H. *Chem. Rev.* **1996**, *96*, 2841-2887.
20. Pond, A. E.; Ledbetter, A. P.; Sono, M.; Goodin, D. B.; Dawson, J. H. In *Electron Transfer in Chemistry*; Balzani, V., Ed.; Wiley-VCH: Weinheim, Germany, 2001; Vol. 3.1.4, pp 56-104.
21. Collman, J. P.; Sunderland, C. J.; Boulatov, R. *Inorg. Chem.* **2002**, *41*, 2282-2291.
22. Collman, J. P.; Rapta, M.; Bröring, M.; Raptova, L.; Schwenninger, R.; Boitrel, B.; Fu, L.; L'Her, M. *J. Am. Chem. Soc.* **1999**, *121*, 1387-1388.
23. Collman, J. P.; Fu, L.; Herrmann, P. C.; Wang, Z.; Rapta, M.; Bröring, M.; Schwenninger, R.; Boitrel, B. *Angew. Chem. Int. Ed.* **1998**, *37*, 3397-3400.
24. Collman, J. P.; Fu, L.; Herrmann, P. C.; Zhang, X. *Science* **1997**, *275*, 949-951.

25. Ricard, D.; L'Her, M.; Richard, P.; Boitrel, B. *Chem. Eur. J.* **2001**, *7*, 3291-3297.
26. Ricard, D.; Didier, A.; L'Her, M.; Boitrel, B. *ChemBioChem* **2001**, *2*, 144-148.
27. Ricard, D.; Andrioletti, B.; L'Her, M.; Boitrel, B. *Chem. Commun.* **1999**, 1523-1524.
28. Baeg, J. O.; Holm, R. H. *Chem. Commun.* **1998**, 571-572.
29. Holm, R. H. *Pure Appl. Chem.* **1995**, *67*, 217-224.
30. Oyaizu, K.; Haryono, A.; Natori, J.; Shinoda, H.; Tsuchida, E. *Bull. Chem. Soc. Jpn.* **2001**, *73*, 1153-1160.
31. Liang, H. C.; Dahan, M.; Karlin, K. D. *Curr. Opin. Chem. Biol.* **1999**, *3*, 168-175.
32. Karlin, K. D.; Lee, D.-H.; Obias, H. V.; Humphreys, K. J. *Pure Appl. Chem.* **1998**, *70*, 855-862.
33. Ghiladi, R. A.; Ju, T. D.; Lee, D.-H.; Moeenne-Loccoz, P.; Kaderli, S.; Neuhold, Y.-M.; Zuberbuehler, A. D.; Woods, A. S.; Cotter, R. J.; Karlin, K. D. *J. Am. Chem. Soc.* **1999**, *121*, 9885-9886.
34. Kopf, M.-A.; Karlin, K. D. *Inorg. Chem.* **1999**, *38*, 4922-4923.
35. Ghiladi, R. A.; Hatwell, K. R.; Karlin, K. D.; Huang, H.-w.; Moeenne-Loccoz, P.; Krebs, C.; Huynh, B. H.; Marzilli, L. A.; Cotter, R. J.; Kaderli, S.; Zuberbuehler, A. D. *J. Am. Chem. Soc.* **2001**, *123*, 6183-6184.
36. Gavrilova, A. L.; Qin, C. J.; Sommer, R. D.; Rheingold, A. L.; Bosnich, B. *J. Am. Chem. Soc.* **2002**, *124*, 1714-1722.
37. Bosnich, B. *Inorg. Chem.* **1999**, *38*, 2554-2562.
38. Chang, C. K.; Abdalmuhdi, I. *J. Org. Chem.* **1983**, *48*, 5388-5390.
39. Chang, C. K.; Liu, H. Y.; Abdalmuhdi, I. *J. Am. Chem. Soc.* **1984**, *106*, 2725-2726.
40. Chang, C. K.; Abdalmuhdi, I. *Angew. Chem. Int. Ed. Engl.* **1984**, *23*, 164-165.
41. Lui, H.-Y.; Abdalmuhdi, I.; Chang, C. K.; Anson, F. C. *J. Phys. Chem.* **1985**, *89*, 665-670.
42. Ni, C.-L.; Abdalmuhdi, I.; Chang, C. K.; Anson, F. C. *J. Phys. Chem.* **1987**, *91*, 1158-1166.
43. Proniewicz, L. M.; Odo, J.; Goral, J.; Chang, C. K.; Nakamoto, K. *J. Am. Chem. Soc.* **1989**, *111*, 2105-2110.
44. Collman, J. P.; Hutchison, J. E.; Lopez, M. A.; Tabard, A.; Guillard, R.; Seok, W. K.; Ibers, J. A.; L'Her, M. *J. Am. Chem. Soc.* **1992**, *114*, 9869-9877.
45. Collman, J. P.; Wagenknecht, P. S.; Hutchison, J. E. *Angew. Chem. Int. Ed. Engl.* **1994**, *33*, 1537-1554.
46. Guillard, R.; Lopez, M. A.; Tabard, A.; Richard, P.; Lecomte, C.; Brandes, S.; Hutchison, J. E.; Collman, J. P. *J. Am. Chem. Soc.* **1992**, *114*, 9877-9889.

47. Guillard, R.; Brandes, S.; Tardieux, C.; Tabard, A.; L'Her, M.; Miry, C.; Guerac, P.; Knop, Y.; Collman, J. P. *J. Am. Chem. Soc.* **1995**, *117*, 11721-11729.
48. Le Mest, Y.; L'Her, M.; Hendricks, N. H.; Kim, K.; Collman, J. P. *Inorg. Chem.* **1992**, *31*, 835-847.
49. Le Mest, Y.; L'Her, M.; Saillard, J. Y. *Inorg. Chim. Acta* **1996**, *248*, 181-191.
50. Le Mest, Y.; Inisan, C.; Laouenan, A.; L'Her, M.; Talarmain, J.; El Khalifa, M.; Saillard, J. Y. *J. Am. Chem. Soc.* **1997**, *119*, 6905-6106.
51. Chang, C. J.; Deng, Y.; Shi, C.; Chang, C. K.; Anson, F. C.; Nocera, D. G. *Chem. Commun.* **2000**, 1355-1356.
52. Deng, Y.; Chang, C. J.; Nocera, D. G. *J. Am. Chem. Soc.* **2000**, *122*, 410-411.
53. Chang, C. J.; Deng, Y.; Heyduk, A. F.; Chang, C. K.; Nocera, D. G. *Inorg. Chem.* **2000**, *39*, 959-966.
54. Chang, C. J.; Baker, E. A.; Pistorio, B. J.; Deng, Y.; Loh, Z.-H.; Miller, S. E.; Carpenter, S. D.; Nocera, D. G. *Inorg. Chem.* **2002**, *41*, 3102-3109.
55. Pistorio, B. J.; Chang, C. J.; Nocera, D. G. *J. Am. Chem. Soc.* **2002**, *124*, 7884-7885.
56. Chang, C. J.; Deng, Y.; Lee, G.-H.; Peng, S.-M.; Yeh, C.-Y.; Nocera, D. G. *Inorg. Chem.* **2002**, *41*, 3008-3016.
57. Landrum, J. T.; Grimmett, D.; Haller, K. J.; Scheidt, W. R.; Reed, C. A. *J. Am. Chem. Soc.* **1981**, *103*, 2640-2650.
58. Kadish, K. M.; Smith, K. M.; Guillard, R. *The Porphyrin Handbook*; Academic Press: San Diego, 2000.
59. Scheidt, W. R.; Reed, C. A. *Chem. Rev.* **1981**, *81*, 543-555.
60. Shi, C.; Anson, F. C. *Anal. Chem.* **1998**, *70*, 3114-3118.
61. Yeager, E. J. *Electrochem. Soc.* **1981**, *128*, 160C-170C.
62. Pauling, L. *Nature* **1964**, *203*, 182-183.
63. Griffith, J. S. *Proc. Roy. Soc. (London)* **1956**, *235A*, 23-36.
64. Tatsumi, K.; Hoffmann, R. *J. Am. Chem. Soc.* **1981**, *103*, 3328-3341.
65. Chang, C. K. *J. Chem. Soc. Chem. Commun.* **1977**, 800-801.
66. Le Mest, Y.; L'Her, M.; Courtot-Coupez, J.; Collman, J. P.; Evitt, E. R.; Bencosme, C. S. *J. Chem. Soc. Chem. Commun.* **1983**, 1286-1287.
67. Collman, J. P.; Elliot, C. M.; Halbert, T. R.; Tovrog, B. S. *Proc. Natl. Acad. Sci. USA* **1977**, *74*, 18-22.
68. Taube, H. *Prog. Inorg. Chem.* **1986**, *34*, 607-625.
69. Armarego, W. L. F.; Perrin, D. D. *Purification of Laboratory Chemicals*; 4th ed.; Butterworth-Heinmann: Oxford, 1996.
70. Yuasa, M.; Steiger, B.; Anson, F. C. *J. Porphyrins Phthalocyanines* **1997**, *1*, 181-187.

71. ADF2000.02, Vrije Universiteit Amsterdam: Amsterdam, The Netherlands, 1999.
72. Baerends, E. J.; Ellis, D. E.; Ros, P. *Chem. Phys.* **1973**, *2*, 41-51.
73. Te Velde, G.; Bickelhaupt, F. M.; Baerends, E. J.; Fonseca Guerra, C.; Van Gisbergen, S. J. A.; Snijders, J. G.; Ziegler, T. *J. Comput. Chem.* **2001**, *22*, 931-967.
74. van Gisbergen, S. J. A.; Snijders, J. G.; Baerends, E. J. *Comput. Phys. Commun.* **1999**, *118*, 119-138.
75. Becke, A. D. *Phys. Rev. A* **1988**, *38*, 3098-3100.
76. Perdew, J. P.; Wang, Y. *Phys. Rev. B* **1992**, *46*, 12947-12954.

*Chapter 8*

**Pacman Porphyrins for Catalytic  
PCET Oxidation Chemistry**

## 8.1 Motivation and Specific Aims

With a firm understanding of the structure-activity relationships that govern Pacman systems and their catalytic oxygen reduction chemistry mediated by proton-coupled electron transfer (PCET), we refocused our efforts toward applying Pacman constructs to catalyze water oxidation and other multielectron oxidation reactions within a PCET framework. Upon inspection of our DPX and DPD systems, we reasoned that the etioporphyrin-type subunits of these ligand architectures were unsuitable for achieving these goals for the following reasons: (i) the modest steric functionalities lead to the facile formation of thermodynamic  $\mu$ -oxo sinks, and (ii) the unsubstituted meso positions along the porphyrin superstructure are highly susceptible to nucleophilic attack and oxidative degradation. Because the only existing methods for preparing sterically-demanding cofacial bisporphyrins employed statistical methods with arduous amounts of chromatography, we sought rational synthetic routes to access Pacman systems with steric and electronic tunability, as well as oxidative stability. This chapter describes two novel approaches toward this end. The first uses a three-branch scheme with aryl-substituted pyrrole and dipyrromethane precursors, and the second employs metal-catalyzed Suzuki cross-coupling chemistry. In particular, the latter strategy provides a convenient and modular entry into sterically-demanding meso-tetraaryl Pacman porphyrins anchored by xanthene (DTMPX = di-trimesitylporphyrin xanthene) and dibenzofuran (DTMPD = di-trimesitylporphyrin dibenzofuran). Moreover, we have applied these systems for multielectron oxidation chemistry with reactive oxygen species; manganese derivatives of DTMPX and DTMPD catalyze oxygen evolution via the catalase-like disproportionation of hydrogen peroxide.

## 8.2 Background

Porphyrins presented in a face-to-face manner have been a prominent structural motif for the development of multielectron catalytic cycles.<sup>1,2</sup> Most successful in this regard are the Pacman systems consisting of two etio-type porphyrins linked by a single rigid bridge; these platforms have been utilized extensively in the catalytic reduction of small-molecule substrates (e.g. O<sub>2</sub>, H<sub>2</sub>, N<sub>2</sub>).<sup>3-17</sup> The exceptional activity of Pacman complexes is based on the cofacial presentation of macrocyclic subunits with minimal lateral perturbations, allowing two metal centers in close proximity to act in a cooperative manner for multielectron reduction chemistry.

The ability to tune the spatial orientation between catenated porphyrins is central to controlling their multielectron reactivity. For example, we have explored the limits of pocket size and flexibility within the Pacman motif by creating new systems with two etio-type porphyrins anchored by xanthene (DPX) and dibenzofuran (DPD) scaffolds.<sup>18-20</sup> In particular, the DPD framework provided the first direct observation of the Pacman effect for a single cofacial



bisporphyrin platform. A comparative structural study of its biszinc(II) and bisiron(III)  $\mu$ -oxo complexes shows that this cofacial cleft can open and close its binding pocket by a vertical distance of over 4 Å in the presence of the appropriate exogenous ligands.<sup>19</sup> In addition, subsequent reactivity studies reveal that biscobalt(II) complexes of both DPX and DPD are efficient electrocatalysts for the selective four-electron, four-proton reduction of oxygen to water despite their ca. 4 Å difference in metal-metal distances, demonstrating that effective multielectron reduction chemistry can be mediated within Pacman platforms that undergo large changes in vertical pocket sizes.<sup>21</sup>

Encouraged by these results, we sought to expand the reactivity of the DPX and DPD constructs to pursue multielectron oxidation reactions mediated by proton-coupled electron transfer (PCET);<sup>22-25</sup> however, the etioporphyrin-type substitution patterns of the parent DPX and DPD systems are generally unstable to oxidizing conditions owing to their unprotected meso positions. Additionally, the sterically modest alkyl functionalities of DPX and DPD lead to the facile formation of  $\mu$ -oxo complexes, which represent a thermodynamic sink for oxidative catalysis.

To address these issues, we targeted cofacial bisporphyrins with that would avoid the formation of bridging oxo species and display enhanced stability to oxidizing media. In this chapter, we present the synthesis and application of novel Pacman porphyrins for catalytic oxidation chemistry. Two distinct synthetic approaches are elaborated here. The first relies on the versatile three-branch coupling method to furnish a sterically-demanding, dibenzofuran-bridged Pacman porphyrin (DPD-Mes<sub>6</sub>) with synthetic tunability at the meso and  $\beta$  positions. The second describes a modular and general synthetic method for the facile preparation of meso-tetraaryl cofacial bisporphyrins affixed to a xanthene (DTMPX = di-trimesitylporphyrin xanthene) or dibenzofuran (DTMPD = di-trimesitylporphyrin dibenzofuran) scaffold using Suzuki cross-coupling methods. In addition, we demonstrate the suitability of these platforms for multielectron oxidation reactions; bismanganese(III) derivatives of mesityl-derived DTMPX and DTMPD systems catalyze oxygen evolution via the catalase-like disproportionation of hydrogen peroxide. Our results establish that appropriate ancillary modification of the porphyrin subunits can enhance oxidative stability and reactivity, and provide a synthetic underpinning for the design of additional Pacman systems to catalyze PCET-mediated oxidation reactions.

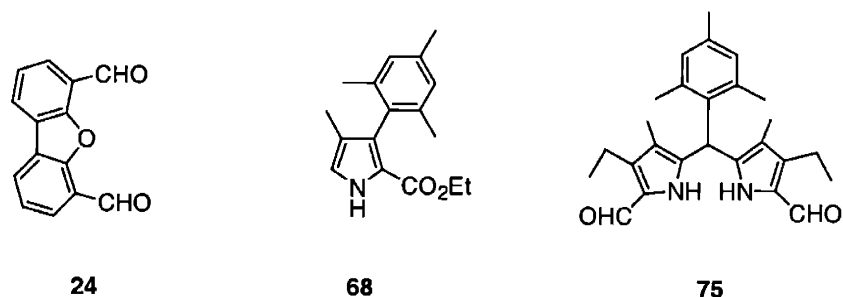
## 8.3 Results and Discussion

### 8.3.1 Three-Branch Strategy for Sterically-Demanding Pacman Porphyrins

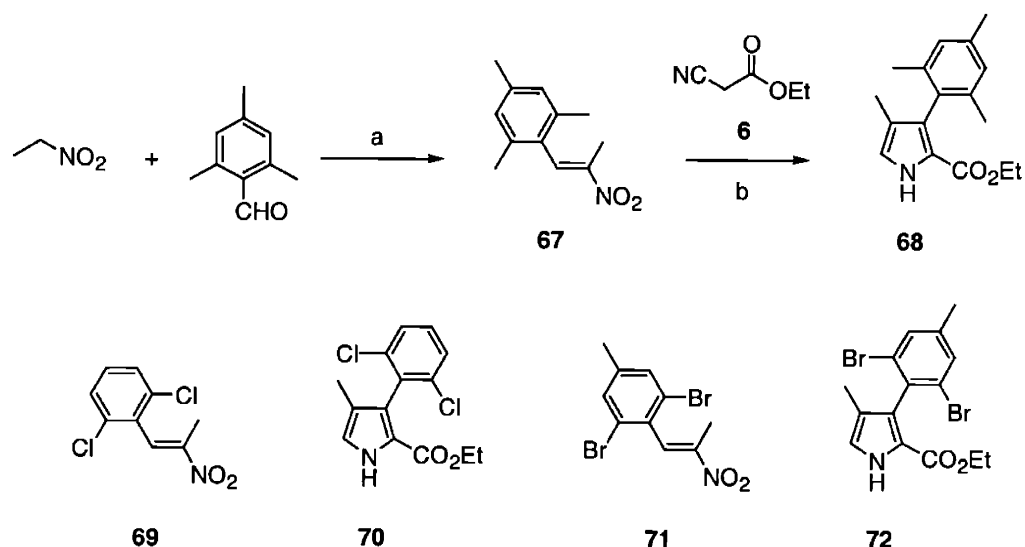
The traditional three-branch strategy<sup>3,9</sup> is utilized to construct sterically-demanding Pacman porphyrins with an etio-II-type substitution pattern; Chart 8.1 depicts the component branches.

As outlined in Schemes 8.1 to 8.3, this synthetic approach affords precise control over porphyrin substitution patterns at both the meso and  $\beta$  positions.

**Chart 8.1**

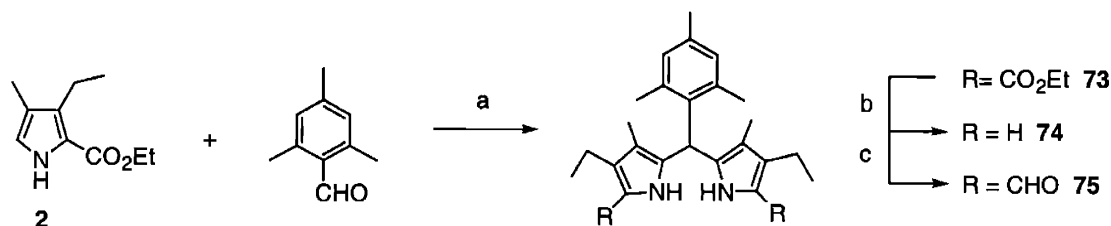


Aryl-substituted pyrroles are obtained as described in Scheme 8.1 using Barton-Zard conditions<sup>26</sup> modified by Ono.<sup>27</sup> Condensation of mesitaldehyde and nitroethane catalyzed by ammonium acetate affords nitroalkene **67** in 90% yield. Nitroalkene **67** is converted to mesityl pyrrole **68** in excellent yield (98%) from reaction with ethyl isocyanoacetate **6** in the presence of 1,8-diazabicyclo[5.4.0]undec-7-ene (DBU) in THF. The Ono conditions are successful for the synthesis of aryl pyrroles with varying steric and electronic properties. For example, halogenated pyrroles **70** and **72** are available from the appropriate nitroalkene precursors in 92% and 89% yield, respectively.



**Scheme 8.1.** (a)  $\text{NH}_4\text{OAc}$ , reflux; (b) DBU, THF,  $< 30^\circ\text{C}$ .

Aryl-substituted dipyrromethane dialdehydes are conveniently supplied from a pyrrole and an aryl aldehyde using the three-step protocol (Scheme 8.2) described previously in chapter 6.<sup>23</sup> For example, reaction of mesitaldehyde with two equivalents of 2-(ethoxycarbonyl)-3-ethyl-4-methylpyrrole (**2**) delivers dipyrromethane **73** in 78% yield. Deprotection of **73** with powdered sodium hydroxide suspended in ethylene glycol provides **74** in 84% yield. Subsequent treatment of **74** with a POCl<sub>3</sub>/DMF Vilsmeier reagent gives **75** in 89% yield after basic hydrolysis.

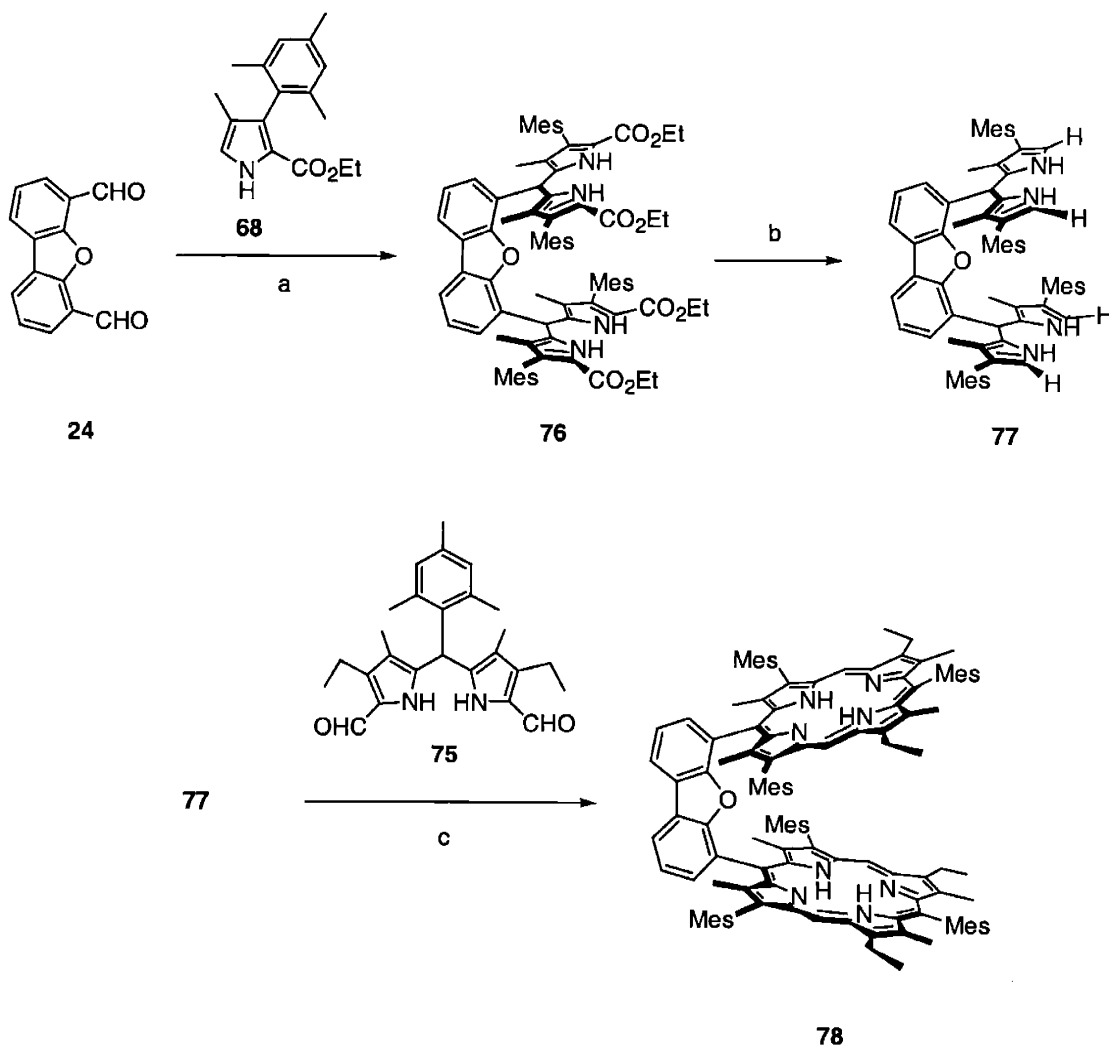


**Scheme 8.2.** (a) ethanol, HCl, reflux; (b) NaOH, ethylene glycol, reflux; (c) i. POCl<sub>3</sub>/DMF; ii. Na<sub>2</sub>CO<sub>3</sub>.

The convergent coupling of the three branches follows Scheme 8.3. Acid-catalyzed coupling of four equivalents of mesityl pyrrole **68** with dibenzofuran dialdehyde **24** in absolute ethanol affords tetrapyrrole **76** in 60% yield. The relatively low yield of this condensation reaction is due to steric hinderance from the mesityl substituents. In fact, the bulk of this aryl pyrrole precludes reaction with the analogous xanthene dialdehyde **1**. Hydrolysis and decarboxylation of the  $\alpha$ -ethyl esters of **76** with sodium hydroxide in ethylene glycol proceeds almost quantitatively (99% yield) to give  $\alpha$ -free tetrapyrrole **77**. Cyclization of dipyrromethane **75** and tetrapyrrole **77** in methanol with a catalytic amount of *p*-toluenesulfonic acid (PTSA) followed by oxidation with *o*-chloranil supplies analytically pure H<sub>4</sub>(DPD-Mes<sub>6</sub>) (**78**) in 3% yield after workup and exhaustive purification using column chromatography. The splayed structure of porphyrin **78** is revealed by <sup>1</sup>H NMR spectroscopy, as the internal NH-pyrrolic resonances are only slightly shifted (−2.29 ppm, −2.56 ppm) compared to those found in monomeric porphyrins.<sup>19</sup>

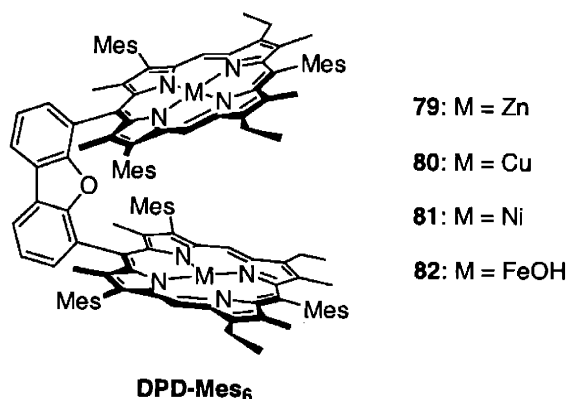
Homobimetallic complexes of H<sub>4</sub>(DPD-Mes<sub>6</sub>) (**78**) are secured by direct reaction with metal salts (Chart 8.2).<sup>28,29</sup> For example, Zn<sub>2</sub>(DPD-Mes<sub>6</sub>) (**79**) is obtained in quantitative yield from direct reaction of **78** with Zn(OAc)<sub>2</sub>•2H<sub>2</sub>O. Complex **79** was fully characterized by <sup>1</sup>H NMR spectroscopy and high-resolution mass spectral and elemental analyses. Treatment of H<sub>4</sub>(DPD-Mes<sub>6</sub>) (**78**) with Cu(OAc)<sub>2</sub>•2H<sub>2</sub>O in methanol/chloroform mixtures affords the corresponding binuclear copper(II) complex Cu<sub>2</sub>(DPD-Mes<sub>6</sub>) (**80**) in good yield (84%). Complex **80** gave satisfactory high-resolution mass spectral analyses. Also, Ni<sub>2</sub>(DPD-Mes<sub>6</sub>) (**81**) was prepared according to Adler's method (NiCl<sub>2</sub>/refluxing DMF)<sup>28</sup> in 75% yield. The diamagnetic complex was characterized using <sup>1</sup>H NMR spectroscopy and high-resolution mass spectrometry.

Likewise, the corresponding diiron(II) complex is generated by treatment of **78** with FeBr<sub>2</sub> in THF containing 2,6-lutidine. Exposure of this diiron(II) to air followed by standard workup and column chromatography on basic alumina affords a product assigned to the corresponding bisiron(III) hydroxide complex Fe<sub>2</sub>(OH)<sub>2</sub>(DPD-Mes<sub>6</sub>) (**82**), as no bands indicative of a bisiron(III) μ-oxo complex are seen in the 800 to 900 cm<sup>-1</sup> region. Magnetic studies are underway to further characterize this ferric porphyrin species.



**Scheme 8.3.** (a) **68**, ethanol, HCl, reflux; (b) NaOH, ethylene glycol, reflux; (c) i. **75**, PTSA, methanol; ii. *o*-chloranil.

Chart 8.2



### 8.3.2 Suzuki Cross-Coupling Strategy for Meso-Tetraaryl Pacman Porphyrins

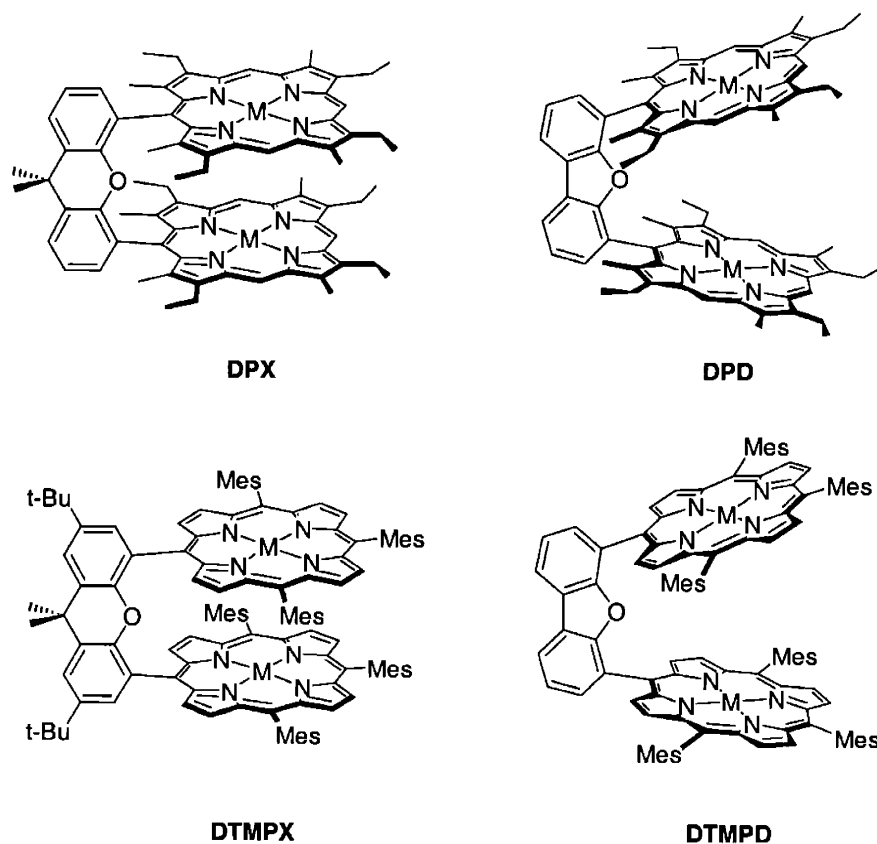
Although we were successful in using the three-branch strategy to prepare a sterically-demanding Pacman architecture on a dibenzofuran scaffold, this synthetic method proved to be time consuming and technically challenging. Significant drawbacks include the low-yielding final coupling step (3%), arduous chromatography, and the need to synthesize multiple pyrrole and dipyrromethane precursors. Moreover, the analogous xanthene framework was unavailable using this method. Thus, we desired a more expedient route to deliver Pacman systems with oxidative stability, steric and electronic tunability, and directed pocket size flexibility.

Owing to the emergence of metal-catalyzed cross-coupling reactions as powerful tools in porphyrin synthesis,<sup>30-34</sup> we sought to utilize this chemistry for our purposes. Accordingly, meso-tetraaryl cofacial bisporphyrins anchored by xanthene and dibenzofuran are accessible using the synthetic procedures outlined in Schemes 8.4 to 8.8. The derivatives H<sub>4</sub>(DTMPX) (**95**) and H<sub>4</sub>(DTMPD) (**96**) are exemplary of this synthetic strategy (Chart 8.3). The mesityl substituents provide steric bulk as well as oxidative stability for high-valent transition-metal species.<sup>35,36</sup> It is noteworthy that the modular cross-coupling approach employed here allows for more precise control of architecture over the statistical methods that have been previously used to prepare related DPA and DPB systems with meso-tetraaryl substitution patterns.<sup>37,38</sup>

The key synthon for the cross-coupling approach is the meso-triarylporphyrin, 5,10,15-trimesitylporphyrin **91**,<sup>39</sup> which is prepared using a combination of Lindsey<sup>40</sup> and zinc-mediated coupling methods.<sup>41</sup> This stepwise route allows for the selective introduction of different meso-aryl substituents during the synthesis with minimal chromatography. The  $\beta$ -unsubstituted dipyrromethane **87** building block is prepared in three steps from pyrrole (Scheme 8.4);<sup>42,43</sup> this synthetic route is more amenable to reaction scale-up compared to alternative one-pot methods.<sup>44</sup>

Condensation of thiophosgene with pyrrole in a benzene/ether mixture affords thione **85** in large quantities (up to 20 g). Treatment of **85** with potassium hydroxide to generate the thiolate *in situ* followed by reaction with hydrogen peroxide delivers 2,2'-dipyrrylketone **86** in 84% yield. Reduction of ketone **86** using sodium borohydride furnishes dipyrromethane **87** in 88% yield.

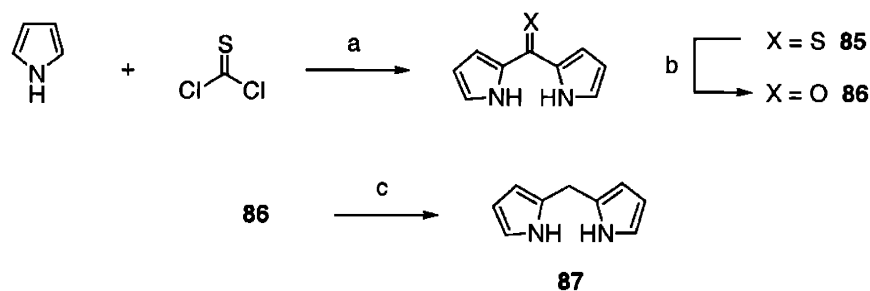
**Chart 8.3**



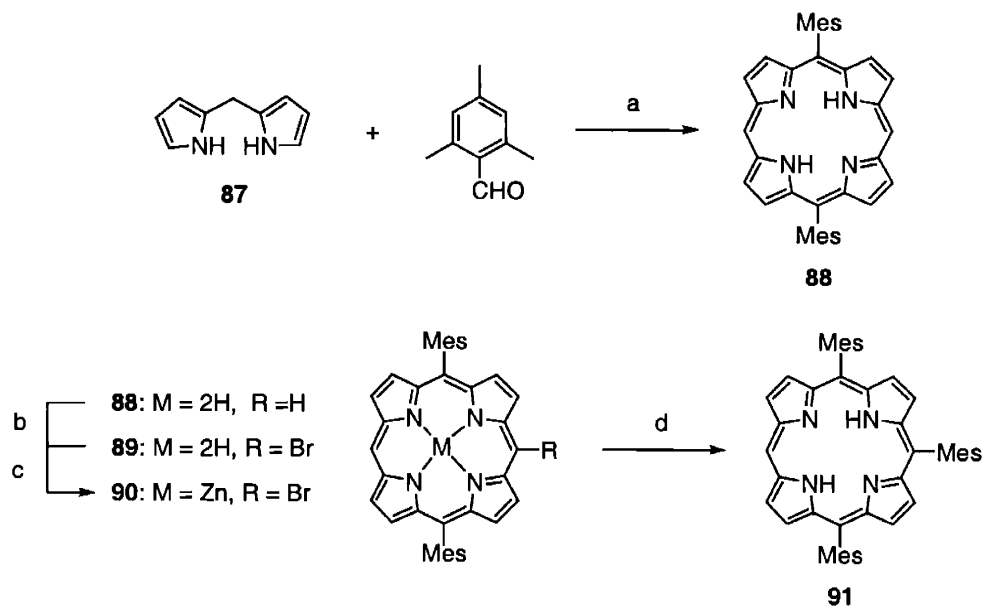
The triarylporphyrin is assembled as described in Scheme 8.5. The acid-catalyzed cyclization of **87** with mesitaldehyde generates meso-diarylporphyrin **88** in 24% yield. Selective mono-bromination gives porphyrin **89** in 61% yield after workup and purification. Zinc insertion is achieved using  $Zn(OAc)_2 \cdot 2H_2O$  in a chloroform/methanol solvent mixture to provide **90** in quantitative yield. The palladium-catalyzed cross coupling of a mesityl zinc reagent with **90** supplies the triarylporphyrin **91** in 65% yield.

The meso-boronate zinc(II) porphyrin **94** is readily obtained in three steps from 5,10,15-trimesitylporphyrin **91** (Scheme 8.6). Regioselective meso-bromination of **94** with *N*-bromosuccinimide in chloroform at room temperature affords bromoporphyrin **92** in 90% yield. Zinc insertion with  $Zn(OAc)_2 \cdot 2H_2O$  in a chloroform/methanol solvent mixture proceeds to

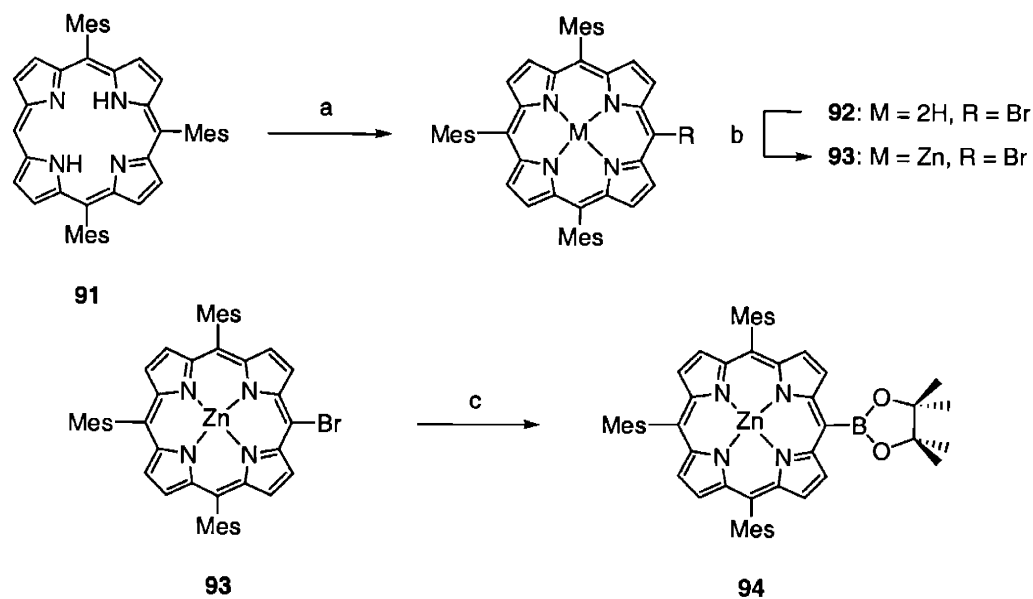
deliver **93** in quantitative yield. The zinc(II) haloporphyrin **93** is then smoothly converted to boronate **94** in excellent yield (96%) using pinacol borane under Masuda conditions.<sup>32,33,45</sup>



**Scheme 8.4.** (a) benzene/ether, 0°C; (b) i. KOH; ii. H<sub>2</sub>O<sub>2</sub>; (c) NaBH<sub>4</sub>, water.

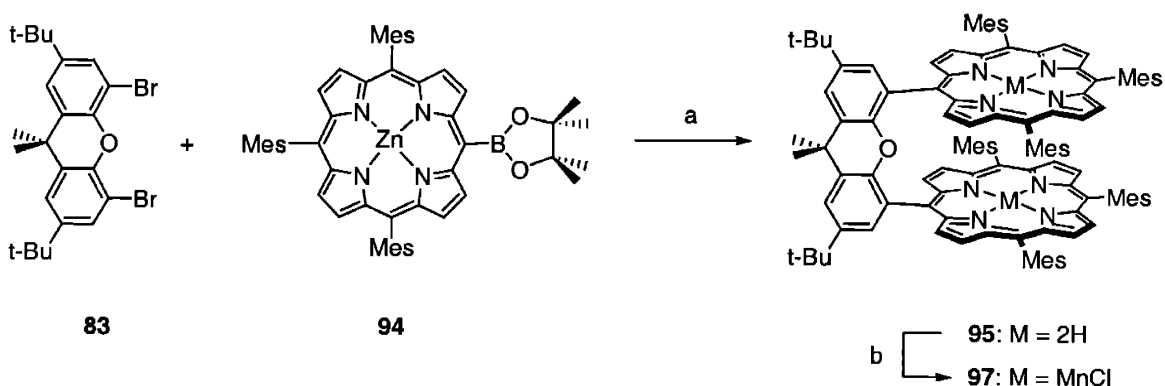


**Scheme 8.5.** (a) i. BF<sub>3</sub>•OEt<sub>2</sub>, chloroform; ii. 2,3-dichloro-5,6-dicyano-1,4-benzoquinone (DDQ); (b) *N*-bromosuccinimide (NBS), chloroform; (c) Zn(OAc)<sub>2</sub>•2H<sub>2</sub>O, chloroform/methanol; (d) i. mesitylmagnesium bromide, ZnCl<sub>2</sub>; ii. 1-methyl-2-pyrrolidone, **90**, Pd(P(*t*-Bu)<sub>3</sub>)<sub>2</sub>, 100 °C; iii. HCl.



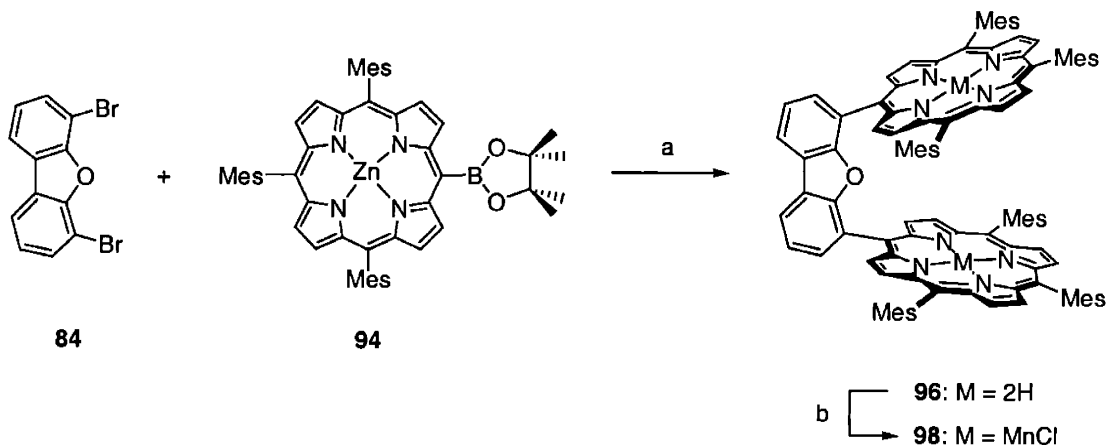
**Scheme 8.6.** (a) *N*-bromosuccinimide (NBS), chloroform; (b)  $\text{Zn}(\text{OAc})_2 \cdot 2\text{H}_2\text{O}$ , chloroform/methanol; (c) pinacol borane,  $\text{Pd}(\text{PPh})_3\text{Cl}_2$ , 1,2-dichloroethane, 90 °C.

The resulting boronate porphyrin **94** serves as a versatile transmetalating agent for the preparation of pillared cofacial bisporphyrins using metal-catalyzed cross-coupling chemistry (Schemes 8.7 and 8.8). For example, reactions of **94** with xanthene **83** or dibenzofuran **84** dibromides under standard Suzuki conditions<sup>32,33,46</sup> furnish the Pacman porphyrins  $\text{H}_4(\text{DTMPX})$  (**95**) and  $\text{H}_4(\text{DTMPD})$  (**96**) in modest to good yields (21% and 67%, respectively). The lower yield obtained for the xanthene derivative versus its dibenzofuran counterpart is likely due to steric constraints for the former during double transmetalation reactions.



**Scheme 8.7.** (a)  $\text{Pd}(\text{PPh}_3)_4$ ,  $\text{Ba}(\text{OH})_2 \cdot 8\text{H}_2\text{O}$ , 1,2-dimethoxyethane/water, 95 °C; (b) i.  $\text{Mn}(\text{OAc})_2 \cdot 4\text{H}_2\text{O}$ , DMF; ii. aq NaCl, HCl.





**Scheme 8.8.** (a) Pd(PPh<sub>3</sub>)<sub>4</sub>, K<sub>3</sub>PO<sub>4</sub>, DMF, 100 °C; b) i. Mn(OAc)<sub>2</sub>•4H<sub>2</sub>O, DMF; ii. aq NaCl, HCl.

### 8.3.3 Peroxide Disproportionation Reactions with Meso-Tetraaryl Pacman Porphyrins

With the preparation of meso-tetraaryl Pacman porphyrins in hand, we sought to establish their suitability for catalyzing multielectron oxidation reactions. We became interested in a biological oxygen evolution process related to water oxidation – the catalase-like disproportionation of hydrogen peroxide to oxygen and water.<sup>47</sup> To this end, the homobimetallic bischloromanganese(III) complexes Mn<sub>2</sub>Cl<sub>2</sub>(DTMPX) (**97**) and Mn<sub>2</sub>Cl<sub>2</sub>(DTMPD) (**98**) are prepared in excellent yields (86% and 89%, respectively) by reaction of the corresponding free-base porphyrins with Mn(OAc)<sub>2</sub>•4H<sub>2</sub>O followed by treatment with NaCl and HCl. Compounds **97** and **98** gave satisfactory high-resolution mass spectral analyses. For comparative purposes, we employ the analogous etio-type bisporphyrins Mn<sub>2</sub>Cl<sub>2</sub>(DPX) (**21**) and Mn<sub>2</sub>Cl<sub>2</sub>(DPD) (**33**) along with the tetraarylporphyrin monomer MnCl(TMP).

The manganese complexes were screened for their H<sub>2</sub>O<sub>2</sub> disproportionation reactivity. Oxygen evolution was monitored volumetrically and detected using a standard pyrogallol assay. The comparative catalytic activities in turnover numbers (TON) for binuclear complexes **97** and **98** along with Mn<sub>2</sub>Cl<sub>2</sub>(DPX) (**21**), Mn<sub>2</sub>Cl<sub>2</sub>(DPD) (**33**), and the monomer MnCl(TMP) are summarized in Figure 8.1. Complex **97**, containing the xanthene bridge with meso-tetraarylporphyrin subunits, is the most active (579 ± 30 TON), catalyzing the oxygen evolution process by 10-fold over all the other compounds examined. Notably, the analogous platforms with an etio-type substitution pattern (DPX **21**, 37 ± 4 TON) and/or a dibenzofuran bridge (DPD **33**, 27 ± 3 TON; DTMPD **98**, 54 ± 5 TON) show no reactivity over the baseline monomer MnCl(TMP) (58 ± 5 TON).

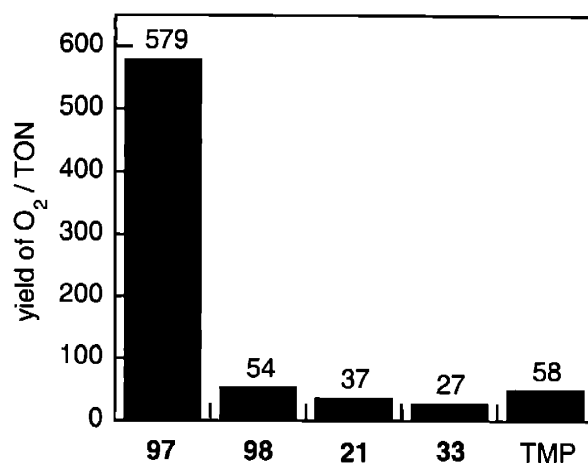


**Figure 8.1** Turnover numbers (TON) for oxygen release from  $\text{H}_2\text{O}_2$  dismutation catalyzed by  $\text{Mn}_2\text{Cl}_2(\text{DTMPX})$  (**97**) and  $\text{Mn}_2\text{Cl}_2(\text{DTMPD})$  (**98**), their parent etio-type systems  $\text{Mn}_2\text{Cl}_2(\text{DPX})$  (**21**) and  $\text{Mn}_2\text{Cl}_2(\text{DPD})$  (**33**), and the monomer  $\text{MnCl}(\text{TMP})$  (denoted as TMP). Error bars for the TON (not shown) are approximately  $\pm 10\%$ .

## 8.4 Concluding Remarks

We have developed two general approaches for preparing Pacman porphyrins to catalyze the multielectron oxidation of small-molecule substrates via PCET. Both methods furnish cofacial bisporphyrin templates with enhanced steric and electronic protection from  $\mu$ -oxo formation and oxidative degradation. The versatile three-branch method has been applied to construct a dibenzofuran-bridged system DPD-Mes<sub>6</sub> that includes steric bulk at both meso and  $\beta$  positions along the porphyrin superstructure, and a wide synthetic range of tunability should be derived from varying aryl pyrrole and dipyrromethane precursors. Modular Suzuki cross-coupling methods have been exploited to prepare meso-tetraaryl Pacman porphyrins anchored by either xanthene or dibenzofuran. The facile synthesis of the mesityl derivatives DTMPX and DTMPD attests to the efficacy of this approach. In addition, we have demonstrated the suitability of the meso-tetraaryl Pacman porphyrins for catalyzing multielectron transformations under oxidizing conditions. Specifically, manganese derivatives of DTMPX and DTMPD have been employed to effect catalytic oxygen evolution from the disproportionation of hydrogen peroxide. Comparative reactivity studies with the parent etioporphyrin-type DPX and DPD frameworks reveal that both the choice of pillar and ancillary porphyrin substitution are critical for achieving cooperative bimetallic reactivity. With the modular Suzuki cross-coupling method for Pacman synthesis at our disposal, we are poised to synthetically tailor the electronic and steric properties of the

ancillary porphyrin subunits at will. Current studies are aimed at exploring the opportunities for these and related architectures in catalytic multielectron oxidation chemistry.

## 8.5 Experimental Section

### 8.5.1 Materials

Silica gel 60 (70-230 and 230-400 mesh, Merck) and aluminum oxide 60 (EM Science) were used for column chromatography. Analytical thin layer chromatography was performed using Merck 60 F254 silica gel (precoated sheets, 0.2 mm thick) or JT Baker IB-F aluminum oxide (precoated sheets, 0.2 mm thick). Solvents for synthesis were of reagent grade or better, and were dried according to standard methods.<sup>48</sup> Ethyl isocyanoacetate **6** and 2,6-dibromo-4-methylbenzaldehyde **49** were available according to the methods described in chapters 2 and 6, respectively. The compounds 4,5-dibromo-2,7-di-*tert*-butyl-9,9-dimethylxanthene **83**<sup>49</sup> and 4,6-dibromodibenzofuran **84**<sup>50</sup> were prepared according to literature procedures. MnCl(TMP) was available according to standard methods.<sup>28,29</sup> Pyrrole was distilled from CaH<sub>2</sub> and stored at -20 °C under nitrogen in the dark. Chloroform containing 0.75% ethanol was distilled from K<sub>2</sub>CO<sub>3</sub>. Ammonium acetate was dried by heating at 50 °C under vacuum overnight and stored in a desiccator. All other reagents were used as received.

### 8.5.2 1-(2,4,6-Trimethylphenyl)-2-nitropropene (**67**)

Mesitaldehyde (10 g) and ammonium acetate (7.8 g) were combined in nitroethane (125 mL) and the resulting solution was refluxed under a nitrogen atmosphere for 17 h. The solvent was removed by rotary evaporation and the remaining residue was taken up a 1:1 mixture of dichloromethane (100 mL) and water (100 mL). The organic layer was decanted, washed with water (3 × 50 mL), dried over Na<sub>2</sub>SO<sub>4</sub>, and the solvent was removed under reduced pressure to afford **67** as a pale yellow powder (12.5 g, 90% yield). <sup>1</sup>H NMR (500 MHz, CDCl<sub>3</sub>, 25 °C): δ = 8.02 (s, 1H), 6.93 (s, 2H), 2.32 (s, 3H), 2.17 (s, 6H), 2.04 (s, 3H).

### 8.5.3 2-(Ethylloxycarbonyl)-3-(2,4,6-trimethylphenyl)-4-methylpyrrole (**68**)

Ethyl isocyanoacetate (**6**) (7.59 g, 0.067 mol) and 1-(2,4,6-trimethylphenyl)-2-nitropropene (**67**) (12.52 g, 0.061 mol) were dissolved in freshly distilled tetrahydrofuran (75 mL) and the contents were added to a dry round bottom flask equipped with an addition funnel. The solution was cooled in an ice-acetone bath under nitrogen. A solution of 1,8-diazabicyclo[5.4.0]undec-7-ene (DBU) (11.0 g, 0.072 mol) in tetrahydrofuran (20 mL) was added dropwise to the solution, keeping the temperature below 30 °C. The reaction color changed from light yellow to orange, and a white precipitate formed. Stirring was continued at room temperature under nitrogen for an

additional 14 h. The solvent was removed by rotary evaporation and warm water (100 mL) was added to the resulting orange oil. The biphasic mixture was allowed to cool to room temperature and extracted with dichloromethane (2 × 50 mL). The ether extracts were washed with water (2 × 50 mL), dried over Na<sub>2</sub>SO<sub>4</sub>, and the solvent was removed by rotary evaporation. Recrystallization from ethanol/water mixtures delivered  $\alpha$ -free pyrrole **68** as a tan solid (15.71 g, 95% yield). <sup>1</sup>H NMR (500 MHz, CDCl<sub>3</sub>, 25 °C):  $\delta$  = 8.97 (br s, 1H, NH), 6.89 (s, 2H, ArH), 6.82 (d, *J* = 3 Hz, 1H, CH), 4.06 (q, *J* = 8 Hz, 2H, CH<sub>2</sub>), 2.31 (s, 3H, CH<sub>3</sub>), 1.96 (s, 6H, CH<sub>3</sub>), 1.79 (s, 3H, CH<sub>3</sub>), 1.03 (t, *J* = 12 Hz, 3H, CH<sub>3</sub>).

#### 8.5.4 1-(2,6-Dichlorophenyl)-2-nitropropene (**69**)

2,6-Dichlorobenzaldehyde (12 g) and ammonium acetate (12 g) were combined in nitroethane (120 mL) and the resulting solution was refluxed under a nitrogen atmosphere for 14 h. The solvent was removed by rotary evaporation and the remaining residue was taken up a 1:1 mixture of dichloromethane (100 mL) and water (100 mL). The organic layer was decanted, washed with water (3 × 50 mL), dried over Na<sub>2</sub>SO<sub>4</sub>, and the solvent was removed under reduced pressure to afford **69** as a pale yellow powder (14 g, 88% yield). <sup>1</sup>H NMR (500 MHz, CDCl<sub>3</sub>, 25 °C):  $\delta$  = 7.79 (s, 1H), 7.42 (m, 2H), 7.30 (m, 1H), 2.12 (s, 3H).

#### 8.5.5 2-(Ethyloxycarbonyl)-3-(2,6-dichlorophenyl)-4-methylpyrrole (**70**)

Ethyl isocyanoacetate (**6**) (6.44 g, 0.057 mol) and 1-(2,6-dichlorophenyl)-2-nitropropene (**69**) (12.0 g, 0.052 mol) were dissolved in freshly distilled tetrahydrofuran (75 mL) and the contents were added to a dry round bottom flask equipped with an addition funnel. The solution was cooled in an ice-acetone bath under nitrogen. A solution of 1,8-diazabicyclo[5.4.0]undec-7-ene (DBU) (9.0 g, 0.059 mol) in tetrahydrofuran (20 mL) was added dropwise to the solution, keeping the temperature below 30 °C. The reaction color changed from light yellow to orange, and a white precipitate formed. Stirring was continued at room temperature under nitrogen for an additional 14 h. The solvent was removed by rotary evaporation and warm water (100 mL) was added to the resulting orange oil. The biphasic mixture was allowed to cool to room temperature and extracted with dichloromethane (2 × 50 mL). The ether extracts were washed with water (2 × 50 mL), dried over Na<sub>2</sub>SO<sub>4</sub>, and the solvent was removed by rotary evaporation. Recrystallization from ethanol/water mixtures delivered  $\alpha$ -free pyrrole **70** as a yellow powder (14.2 g, 92% yield). <sup>1</sup>H NMR (500 MHz, CDCl<sub>3</sub>, 25 °C):  $\delta$  = 9.10 (br s, 1H, NH), 7.38 (m, 2H, ArH), 7.19 (m, 1H, ArH), 6.88 (m, 1H, CH), 4.10 (q, *J* = 7.2 Hz, 2H, CH<sub>2</sub>), 1.91 (s, 3H, CH<sub>3</sub>), 1.03 (t, *J* = 7.2 Hz, 3H, CH<sub>3</sub>).

### 8.5.6 1-(2,6-Dibromo-4-methylphenyl)-2-nitropropene (71)

2,6-Dibromo-4-methylbenzaldehyde (**49**) (2.78 g, 10 mmol) and ammonium acetate (1.1 g, 14 mmol) were combined in nitroethane (12 mL) and the resulting solution was refluxed under a nitrogen atmosphere for 17 h. The solvent was removed by rotary evaporation and the remaining residue was taken up a 1:1 mixture of dichloromethane (50 mL) and water (50 mL). The organic layer was decanted, washed with water (3 × 50 mL), dried over Na<sub>2</sub>SO<sub>4</sub>, and the solvent was removed under reduced pressure to afford **71** as a yellow powder (3.2 g, 96% yield). <sup>1</sup>H NMR (300 MHz, CDCl<sub>3</sub>, 25 °C): δ = 7.77 (s, 1H), 7.40 (s, 2H), 2.33 (s, 3H), 2.07 (s, 3H).

### 8.5.7 2-(Ethylloxycarbonyl)-3-(2,6-dibromo-4-methylphenyl)-4-methylpyrrole (72)

Ethyl isocyanoacetate (**6**) (1.25 g, 11 mmol) and 1-(2,6-dibromo-4-methylphenyl)-2-nitropropene (**71**) (3.35 g, 10 mmol) were dissolved in freshly distilled tetrahydrofuran (50 mL) and the contents were added to a dry round bottom flask equipped with an addition funnel. The solution was cooled in an ice-acetone bath under nitrogen. A solution of 1,8-diazabicyclo[5.4.0]undec-7-ene (DBU) (3.05 g, 20 mmol) in tetrahydrofuran (10 mL) was added dropwise to the solution, keeping the temperature below 30 °C. The reaction color changed from light yellow to orange, and a white precipitate formed. Stirring was continued at room temperature under nitrogen for an additional 14 h. The solvent was removed by rotary evaporation and warm water (100 mL) was added to the resulting orange oil. The biphasic mixture was allowed to cool to room temperature and extracted with dichloromethane (2 × 50 mL). The ether extracts were washed with water (2 × 50 mL), dried over Na<sub>2</sub>SO<sub>4</sub>, and the solvent was removed by rotary evaporation. Recrystallization from ethanol/water mixtures delivered α-free pyrrole **72** as a bright yellow-orange solid (3.57 g, 89% yield). <sup>1</sup>H NMR (500 MHz, CDCl<sub>3</sub>, 25 °C): δ = 9.05 (br s, 1H, NH), 7.44 (s, 2H, ArH), 6.84 (m, 1H, CH), 4.12 (q, *J* = 7.5 Hz, 2H, CH<sub>2</sub>), 2.35 (s, 3H, CH<sub>3</sub>), 1.89 (s, 3H, CH<sub>3</sub>), 1.06 (t, *J* = 7.5 Hz, 3H, CH<sub>3</sub>).

### 8.5.8 (2,4,6-Trimethylphenyl)-bis(5-ethoxycarbonyl-4-ethyl-3-methyl-2-pyrrolyl)methane (73)

A solution of mesitaldehyde (1.48 g, 10 mmol) and pyrrole **2** (1.81 g, 10 mmol) in chloroform (30 mL) was degassed with nitrogen for 15 min. A portion of *p*-toluenesulfonic acid (0.3 g) was added and the reaction was refluxed under nitrogen for 2.5 h and cooled to room temperature. The solution was washed with saturated aq NaHCO<sub>3</sub> solution (25 mL) and water (2 × 25 mL), dried over Na<sub>2</sub>SO<sub>4</sub>, and the solvent was removed by rotary evaporation. Purification by column chromatography (silica gel, 3:2 hexanes/dichloromethane to dichloromethane) furnished dipyrrolylmethane **73** as a foamy orange solid (1.91 g, 78% yield). <sup>1</sup>H NMR (300 MHz, CDCl<sub>3</sub>, 25

°C):  $\delta$  = 8.17 (br s, 2H, NH), 6.86 (s, 2H, ArH), 5.75 (s, 1H, CH), 4.25 (m, 4H, CH<sub>2</sub>), 2.75 (q,  $J$  = 8 Hz, 4H, CH<sub>2</sub>), 2.29 (s, 3H, CH<sub>3</sub>), 1.99 (s, 6H, CH<sub>3</sub>), 1.74 (s, 6H, CH<sub>3</sub>), 1.33 (t,  $J$  = 7.5 Hz, 6H, CH<sub>3</sub>), 1.12 (t,  $J$  = 7.5 Hz, 6H, CH<sub>3</sub>).

#### 8.5.9 (2,4,6-Trimethylphenyl)-bis(4-ethyl-3-methyl-2-pyrrolyl)methane (74)

Powdered NaOH (1.5 g) was combined with **73** (1.91 g, 3.88 mmol) suspended in ethylene glycol (10 mL). The mixture was refluxed under nitrogen for 24 h and cooled to room temperature. The reaction was extracted with ether (3 × 30 mL), and the combined organic extracts were washed with saturated aq NaCl (50 mL), water (3 × 50 mL). The solvent was removed by rotary evaporation and the resulting solid was dried under vacuum over P<sub>2</sub>O<sub>5</sub>. Product **74**, which was obtained as a foamy ochre solid (1.14 g, 84% yield), was stored under nitrogen at -20 °C. <sup>1</sup>H NMR (300 MHz, CDCl<sub>3</sub>, 25 °C):  $\delta$  = 7.35 (br s, 2H, NH), 6.82 (s, 2H, ArH), 6.32 (d,  $J$  = 2.4 Hz, 2H, CH), 5.78 (s, 1H, CH), 2.42 (q,  $J_1$  = 7.2 Hz, 4H, CH<sub>2</sub>), 1.98 (s, 6H, CH<sub>3</sub>), 1.74 (s, 6H, CH<sub>3</sub>), 1.17 (t,  $J$  = 7.5 Hz, 6H, CH<sub>3</sub>).

#### 8.5.10 (2,4,6-Trimethylphenyl)-bis(5-formyl-4-ethyl-3-methyl-2-pyrrolyl)methane (75)

Under a nitrogen atmosphere, phosphorus oxychloride (4 mL) was added dropwise to a solution of **74** (1.69 g, 4.85 mmol) in anhydrous DMF (14 mL) at -10 °C. After stirring at -10 °C for 30 min, the resulting mixture was allowed to warm to room temperature and stirred for an additional 2.5 h. The reaction was concentrated to half its original volume and methanol (60 mL), water (10 mL) and Na<sub>2</sub>CO<sub>3</sub> (5 g) were added. The mixture was heated at 60 °C for 30 min and cooled to room temperature. The precipitate was filtered and washed with water until the washings became neutral. Recrystallization from methanol afforded **75** as an ochre solid (1.75 g, 89% yield). <sup>1</sup>H NMR (300 MHz, CDCl<sub>3</sub>, 25 °C):  $\delta$  = 9.50 (s, 2H, CHO), 8.37 (br s, 2H, NH), 6.88 (s, 2H, ArH), 5.77 (br s, 1H, CH), 2.72 (m, 4H, CH<sub>2</sub>), 2.30 (s, 3H, CH<sub>3</sub>), 1.97 (s, 6H, CH<sub>3</sub>), 1.75 (s, 6H, CH<sub>3</sub>), 1.61 (s, 3H, CH<sub>3</sub>), 1.23 (t,  $J$  = 7.5 Hz, 6H, CH<sub>3</sub>).

#### 8.5.11 4,6-Bis[5,5'-bis(ethyloxycarbonyl)-4,4'-di-(2,4,6-trimethylphenyl)-3,3'-dimethyl-2,2'-dipyrrolylmethyl] dibenzofuran (76)

2-(Ethyloxycarbonyl)-3-(2,4,6-trimethylphenyl)-4-methylpyrrole (**68**) (2.71 g, 10 mmol, 4 equiv) and **24** (0.559 g, 2.5 mmol) and were added to absolute ethanol (30 mL) containing conc HCl (0.6 mL). The resultant mixture was refluxed under nitrogen for 16 h and cooled in an ice-water bath. The precipitate was filtered by suction and washed with cold methanol to afford **76** as a goldenrod powder (1.9 g, 60% yield). <sup>1</sup>H NMR (300 MHz, CDCl<sub>3</sub>, 25 °C):  $\delta$  = 8.62 (br s, 4H, NH), 7.93 (d,  $J$  = 7.5 Hz, 2H, ArH), 7.29 (t,  $J$  = 7.8 Hz, 2H, ArH), 7.11 (d,  $J$  = 7.5 Hz, 2H, ArH), 6.85 (d,  $J$  = 11 Hz, 8H, ArH), 5.96 (s, 2H, CH), 4.03 (q,  $J$  = 7.2 Hz, 8H, CH<sub>2</sub>), 2.29 (s, 12H,

CH<sub>3</sub>), 2.03 (s, 12H, CH<sub>3</sub>), 1.88 (s, 12H, CH<sub>3</sub>), 1.59 (s, 12H, CH<sub>3</sub>), 1.49 (s, 12H, CH<sub>3</sub>), 1.07 (t, *J* = 7.2 Hz, 12H, CH<sub>3</sub>).

#### 8.5.12 4,6-Bis[4,4'-di-(2,4,6-trimethylphenyl)-3,3'-dimethyl-2,2'-dipyrrylmethyl] dibenzofuran (77)

Powdered NaOH (1.5 g) and **76** (1.9 g, 5.7 mmol) were suspended in 15 mL of ethylene glycol, and the mixture was refluxed under nitrogen for 24 h. After cooling, the precipitate was collected by suction filtration, washed with water until the washings became neutral, and dried under vacuum over P<sub>2</sub>O<sub>5</sub>. The product **77** was obtained as a manila solid (1.45 g, 99% yield). It was stored under nitrogen at -20 °C. <sup>1</sup>H NMR (300 MHz, CDCl<sub>3</sub>, 25 °C): δ = 7.90 (d, *J* = 7.5 Hz, 2H, ArH), 7.72 (br s, 4H, NH), 7.36 (t, *J* = 7.8 Hz, 2H, ArH), 7.21 (d, *J* = 7.5 Hz, 2H, ArH), 6.89 (d, *J* = 11 Hz, 8H, ArH), 6.40 (d, *J* = 2.4 Hz, 2H, CH), 6.05 (s, 2H, CH), 2.31 (s, 12H, CH<sub>3</sub>), 2.09 (s, 12H, CH<sub>3</sub>), 2.03 (s, 12H, CH<sub>3</sub>), 1.61 (s, 24H, CH<sub>3</sub>).

#### 8.5.13 4,6-Bis[(5-(2,3,13,17-tetra-(2,4,6-trimethylphenyl)-3,7,12,18-tetramethyl porphyrinyl)] dibenzofuran, H<sub>4</sub>(DPD-Mes<sub>6</sub>) (78)

A suspension of **77** (1.65 g, 1.67 mmol) and **75** (1.35 g, 3.34 mmol) in freshly distilled methanol (200 mL) was purged with nitrogen for 20 min. A solution of *p*-toluenesulfonic acid (0.60 g) in methanol (10 mL) was added dropwise over a period of 1 h. The resulting red mixture was stirred in the dark under nitrogen for 2 d. Solid *o*-chloranil (500 mg) was added in one portion and stirring was continued in air for 24 h. The mixture was taken to dryness and the solid was redissolved in chloroform (100 mL). A saturated methanolic solution of Zn(OAc)<sub>2</sub>·2H<sub>2</sub>O (10 mL) was added, and the solution was refluxed for 1 h. The solvent was removed and the remaining residue was purified by repeated flash column chromatography (silica gel, 1:1 dichloromethane/hexanes to dichloromethane). The isolated crude product was redissolved in dichloromethane (50 mL) and vigorously stirred with 6 N HCl (6 mL) for 25 min. The solution was neutralized with a 10% aqueous sodium carbonate solution and the mixture was stirred for an additional 15 min. The organic phase was separated, washed with water (3 × 25 mL), dried over Na<sub>2</sub>SO<sub>4</sub>, and taken to dryness. Purification by preparative thin-layer chromatography (silica gel, 2% methanol in dichloromethane) followed by recrystallization from dichloromethane/methanol afforded pure **78** as a purple powder (86 mg, 3% yield). <sup>1</sup>H NMR (500 MHz, CDCl<sub>3</sub>, 25 °C): δ = 9.34 (s, 4H, meso), 8.66 (d, *J* = 7.5 Hz, 2H, ArH), 7.72 (t, *J* = 7.8 Hz, 2H, ArH), 7.68 (d, *J* = 7.2 Hz, 2H, ArH), 7.58 (t, *J* = 7.8 Hz, 2H, ArH), 7.17 (m, 4H, ArH), 7.00 (s, 4H, ArH), 3.48 (m, 8H, CH<sub>2</sub>), 2.57 (s, 12H, CH<sub>3</sub>), 2.53 (s, 6H, CH<sub>3</sub>), 2.24 (s, 24H, CH<sub>3</sub>), 1.92 (s, 12H, CH<sub>3</sub>), 1.58 (s, 12H, CH<sub>3</sub>), 1.32 (t, *J* = 7.5 Hz, 12H, CH<sub>3</sub>), 1.24 (s, 12H, CH<sub>3</sub>), -2.29 (br s, 2H, NH), -2.56 (br s, 4H, NH). Anal. Calcd for C<sub>122</sub>H<sub>125</sub>N<sub>8</sub>O: C, 85.27; H, 7.27; N, 6.52.

Found: C, 85.49; H, 7.44; N, 6.32. HRESIMS (M<sup>+</sup>) calcd for C<sub>122</sub>H<sub>124</sub>N<sub>8</sub>O *m/z* 1716.990, found 1716.993.

#### 8.5.14 Zn<sub>2</sub>(DPD-Mes<sub>6</sub>) (79)

A saturated methanolic solution of Zn(OAc)<sub>2</sub>•2H<sub>2</sub>O (1 mL) and a solution of **78** (20 mg, 0.012 mmol) in 5 mL chloroform were combined and refluxed for 30 min. The solvent was removed by rotary evaporation. The remaining solid was purified by flash column chromatography (silica gel, dichloromethane) followed by recrystallization from dichloromethane/methanol to yield analytically pure **79** as a ruby red solid in essentially quantitative yield. <sup>1</sup>H NMR (500 MHz, CDCl<sub>3</sub>, 25 °C): δ = 9.26 (s, 4H, meso), 8.57 (d, *J* = 6 Hz, 2H, ArH), 7.75 (m, 4H, ArH), 7.09 (m, 12H, ArH), 3.49 (m, 8H, CH<sub>2</sub>), 2.56 (s, 12H, CH<sub>3</sub>), 2.53 (s, 6H, CH<sub>3</sub>), 2.19 (s, 12H, CH<sub>3</sub>), 2.15 (s, 12H, CH<sub>3</sub>), 1.61 (s, 12H, CH<sub>3</sub>), 1.32 (m, 12H, CH<sub>3</sub>), 1.27 (s, 12H, CH<sub>3</sub>), 1.15 (s, 12H, CH<sub>3</sub>). Anal. Calcd for C<sub>122</sub>H<sub>120</sub>N<sub>8</sub>OZn<sub>2</sub>: C, 79.42; H, 6.56; N, 6.07. Found: C, 79.37; H, 6.45; N, 6.24. HRESIMS (M<sup>+</sup>) calcd for C<sub>122</sub>H<sub>120</sub>N<sub>8</sub>OZn<sub>2</sub> *m/z* 1840.817, found 1840.821.

#### 8.5.15 Cu<sub>2</sub>(DPD-Mes<sub>6</sub>) (80)

To a 20-mL chloroform solution of **78** (20 mg, 0.012 mmol) was added a solution of Cu(OAc)<sub>2</sub>•2H<sub>2</sub>O (50 mg) and potassium acetate (50 mg) in 7 mL of methanol. The resulting solution was refluxed for 4 h and solvent was removed by rotary evaporation. The solid was taken up in a 1:1 mixture of dichloromethane/water (25 mL). The organic layer was decanted, washed with water (3 × 15 mL), dried over Na<sub>2</sub>SO<sub>4</sub>, and taken to dryness. The crude material was purified by flash column chromatography (silica gel, 3:1 dichloromethane/hexanes) followed by recrystallization from dichloromethane/methanol to afford **80** as a red solid (18 mg, 84% yield). HRFABMS (M<sup>+</sup>) calcd for C<sub>122</sub>H<sub>120</sub>N<sub>8</sub>OCu<sub>2</sub> *m/z* 1838.838, found 1838.834.

#### 8.5.16 Ni<sub>2</sub>(DPD-Mes<sub>6</sub>) (81)

A mixture of **78** (20 mg, 0.012 mmol) and NiCl<sub>2</sub> (50 mg) in 5 mL DMF was refluxed for 3 h. The solvent was removed under vacuum and the remaining solid was taken up in a 1:1 mixture of dichloromethane/water (50 mL). The organic layer was decanted, washed with water (3 × 25 mL), dried over Na<sub>2</sub>SO<sub>4</sub> and taken to dryness. Purification by flash column chromatography (silica gel, 3:1 dichloromethane/hexanes) followed by recrystallization from dichloromethane/methanol gave **81** as a plum red solid (16 mg, 75% yield). <sup>1</sup>H NMR (500 MHz, CDCl<sub>3</sub>, 25 °C): δ = 8.57 (s, 4H, meso), 8.38 (m, 2H, ArH), 7.62 (m, 4H, ArH), 7.06 (m, 6H, ArH), 6.97 (br s, 3H, ArH), 6.81 (br s, 6H, ArH), 3.29 (m, 8H, CH<sub>2</sub>), 2.47 (br s, 18H, CH<sub>3</sub>), 2.03 (br s, 12H, CH<sub>3</sub>), 1.91 (s, 12H, CH<sub>3</sub>), 1.73 (s, 6H, CH<sub>3</sub>), 1.56 (s, 12H, CH<sub>3</sub>), 1.28 (m, 18H, CH<sub>3</sub>), 1.01 (s, 12H, CH<sub>3</sub>). HRFABMS (M<sup>+</sup>) calcd for C<sub>122</sub>H<sub>120</sub>N<sub>8</sub>ONi<sub>2</sub> *m/z* 1828.830, found 1828.830.



### 8.5.17 Fe<sub>2</sub>(OH)<sub>2</sub>(DPD-Mes<sub>6</sub>) (**82**)

In a dry box, **78** (40 mg, 0.024 mmol), pyridine (0.1 mL), FeBr<sub>2</sub> (100 mg), and THF (15 mL) were loaded in 100-mL flask equipped with a condenser. The mixture was refluxed under nitrogen for 5 h, opened to air, and brought to dryness under vacuum. The residue was purified using basic alumina (activity I, chloroform) to give **82** as brown solid (39 mg, 87% yield). HRFABMS ([M-OH]<sup>+</sup>) calcd for C<sub>122</sub>H<sub>121</sub>Fe<sub>2</sub>N<sub>8</sub>O<sub>2</sub> *m/z* 1841.831, found 1841.827.

### 8.5.18 2,2'-Dipyrrylthione (**85**)

Compound **85** was synthesized by modification of a literature procedure.<sup>42,43</sup> A solution of pyrrole (25 g) in dry ether (250 mL) was added dropwise to a stirred solution of thiophosgene (21 g) in dry benzene (500 mL) at 0 °C. The reaction was stirred at 0 °C for 15 min, a mixture of methanol (480 mL) and water (120 mL) was added, and then stirring continued at room temperature for an additional 30 min. The solvents were removed under reduced pressure and the residue was purified by column chromatography (alumina, 9:1 benzene/chloroform). The first band eluted was collected and recrystallization from ethanol and water afforded thione **85** as lustrous ruby red crystals (20 g). The compound was used without further purification. GCMS (M<sup>+</sup>) calcd for C<sub>9</sub>H<sub>8</sub>N<sub>2</sub>S *m/z* 176, found 176.

### 8.5.19 2,2'-Dipyrrylketone (**86**)

Compound **86** was synthesized by modification of a literature procedure.<sup>42,43</sup> 2,2'-dipyrrylthione **85** (15 g) was dissolved in 95% ethanol (1L) to afford a clear red solution. The thiolate was generated by the addition of crushed KOH (10 g), and the color of the reaction mixture became wine red. A solution of 5% aq H<sub>2</sub>O<sub>2</sub> (100 mL) was added dropwise to the thiolate solution over 15 min. The resulting goldenrod-colored reaction was stirred at room temperature for an additional 15 min, and then heated to 100 °C for 15 min to provide a lemon-yellow mixture. The reaction was concentrated to ca. 200 mL by rotary evaporation, and water (200 mL) was added. The precipitate was isolated by filtration and washed with water. The ketone **86** was obtained as an off-white solid (11.4 g, 84% yield) that was used without further purification. GCMS (M<sup>+</sup>) calcd for C<sub>9</sub>H<sub>8</sub>N<sub>2</sub>O *m/z* 160, found 160.

### 8.5.20 2,2'-Dipyrrylmethane (**87**)

Compound **87** was synthesized by modification of a literature procedure.<sup>42,43</sup> 2,2'-dipyrrylketone **86** (10 g) was dissolved in 95% ethanol (250 mL) containing morpholine (10 mL) and the solution was brought to reflux under a nitrogen atmosphere. Sodium borohydride was added to the reaction in portions (6 × 5 g) over 3 h, and water (15 mL) was added 15 min after the

addition of each portion of borohydride. After the last addition of borohydride and water, the mixture was refluxed for an additional 2 h, cooled to room temperature, and poured into water (500 mL). The reaction was extracted with ether (5 × 200 mL). The organic extracts were combined, washed with water (5 × 200 mL), dried over Na<sub>2</sub>SO<sub>4</sub>, and the solvent was removed under reduced pressure to leave a viscous oil. Petroleum ether (50 mL) was added and removed by rotary evaporation, and the residue solidified. Drying under vacuum overnight afforded dipyrromethane **87** as a tan powder (8 g, 88% yield) which was used without further purification. GCMS (M+) calcd for C<sub>9</sub>H<sub>10</sub>N<sub>2</sub> *m/z* 146, found 146.

Compound **87** was alternatively prepared in a one-pot procedure from pyrrole and paraformaldehyde on small scales. Under a nitrogen atmosphere, acetic acid (30 mL) and methanol (10 mL) were added to a stirred solution of pyrrole (20 mL) and paraformaldehyde (216 mg, 7.2 mmol). The resulting solution was stirred at room temperature under nitrogen overnight. Dichloromethane (100 mL) was added, and the organic layer was washed with water (3 × 50 mL), 0.1 M KOH (2 × 50 mL), and water again (2 × 50 mL). The organic phase was decanted, dried over Na<sub>2</sub>SO<sub>4</sub>, and dichloromethane was removed by rotary evaporation with mild heating. Vacuum distillation at room temperature removed excess pyrrole and recrystallization from petroleum ether delivered **87** as a tan solid (400 mg, 38% yield).

#### 8.5.21 5,15-Dimesitylporphyrin (**88**)

A solution of mesitaldehyde (2.84 g, 19.2 mmol) and 2,2'-dipyrromethane **87** (2.80 g, 19.2 mmol) in dry chloroform (1.9 L) was purged with nitrogen for 30 min after which BF<sub>3</sub>•OEt<sub>2</sub> (0.80 mL, 6.32 mmol) was added via syringe. The solution was stirred at room temperature under nitrogen in the dark for 45 min and 2,3-dichloro-5,6-dicyano-1,4-benzoquinone (6.52 g, 28.7 mmol) was added to the reaction. After stirring for an additional hour under nitrogen, triethylamine (1 mL) was added and the solvent was removed by rotary evaporation. Purification by column chromatography (silica gel, 2:1 dichloromethane/hexanes) delivered porphyrin **88** as a purple solid (1.25 g, 24% yield). <sup>1</sup>H NMR (300 MHz, CDCl<sub>3</sub>, 25 °C): δ = 10.23 (s, 2H), 9.34 (d, *J* = 4.7 Hz, 4H), 8.89 (d, *J* = 4.7 Hz, 4H), 7.33 (s, 4H), 2.67 (s, 6H), 1.86 (s, 12H), -3.06 (s, 2H). HRESIMS (MH<sup>+</sup>) calcd for C<sub>38</sub>H<sub>35</sub>N<sub>4</sub> *m/z* 547.2856, found 547.2873.

#### 8.5.22 5-Bromo-10,20-dimesitylporphyrin (**89**)

A single portion of *N*-bromosuccinimide (182 mg, 1.02 mmol) was added to a solution of **88** (700 mg, 1.28 mmol) in chloroform (670 mL) and the reaction mixture was stirred in air at room temperature for 30 min. The solvent was removed by rotary evaporation and the residue was purified by column chromatography (silica gel, 2:1 hexanes/dichloromethane). The second eluted

band was collected to furnish bromoporphyrin **89** as a purple powder (489 mg, 61% yield). The 5,15-dibromoporphyrin and starting material were isolated from the first and third eluted bands, respectively. <sup>1</sup>H NMR (300 MHz, CDCl<sub>3</sub>, 25 °C): δ = 10.10 (s, 1H), 9.67 (d, *J* = 4.6 Hz, 2H), 9.24 (d, *J* = 4.6 Hz, 2H), 8.80 (d, *J* = 4.6 Hz, 4H), 7.31 (s, 4H), 2.66 (s, 6H), 1.84 (s, 12H), -2.87 (s, 2H). HRESIMS (MH<sup>+</sup>) calcd for C<sub>38</sub>H<sub>34</sub>BrN<sub>4</sub> *m/z* 625.1962, found 625.1968.

#### 8.5.23 Zinc(II) 5-bromo-10,20-dimesitylporphyrin (**90**)

A solution of Zn(OAc)<sub>2</sub>•2H<sub>2</sub>O (686 mg, 3.13 mmol) in methanol (10 mL) was added to a solution of porphyrin **89** (489 mg, 0.782 mmol) in chloroform (100 mL), and the reaction mixture was stirred for 18 h in air at room temperature. The solvent was removed by rotary evaporation. Purification by column chromatography (silica gel, 1:1 hexanes/dichloromethane) afforded **90** as a red solid in quantitative yield. <sup>1</sup>H NMR (300 MHz, CDCl<sub>3</sub>, 25 °C): δ = 10.16 (s, 1H), 9.76 (d, *J* = 4.7 Hz, 2H), 9.32 (d, *J* = 4.7 Hz, 2H), 8.89 (d, *J* = 4.4 Hz, 4H), 7.32 (s, 4H), 2.67 (s, 6H), 1.83 (s, 12H). HRESIMS (MH<sup>+</sup>) calcd for C<sub>38</sub>H<sub>32</sub>BrN<sub>4</sub>Zn *m/z* 687.1097, found 687.1112.

#### 8.5.24 5,10,15-Trimesitylporphyrin (**91**)

Under a nitrogen atmosphere, mesitylmagnesium bromide (1.0 M solution in THF, 17.4 mL, 17.4 mmol) was slowly added via syringe to a Schlenk tube containing ZnCl<sub>2</sub> (0.5 M solution in THF, 38.3 mL, 19.2 mmol), and the resulting solution was stirred at room temperature for 20 min. 1-Methyl-2-pyrrolidinone (25.9 mL, 269 mmol) was then added and the mixture was stirred for an additional 5 min. In a separate Schlenk tube, zinc(II) bromoporphyrin **90** (400 mg, 0.58 mmol) and bis(tri-*t*-butylphosphine)palladium(0) (44.5 mg, 0.087 mmol) were dissolved in dry THF (20 mL). The porphyrin/palladium catalyst solution was added via syringe to the grignard/zinc catalyst solution and the reaction mixture was heated at 100 °C for 21 h. The reaction was allowed to cool to room temperature and the solvent was removed under reduced pressure. The remaining residue was redissolved in dichloromethane (80 mL) and stirred with 6 N HCl (80 mL) for 30 min. The organic layer was decanted, washed with 20% aq Na<sub>2</sub>CO<sub>3</sub> (50 mL) and water (2 × 50 mL), and the solvent was removed under reduced pressure. Purification by column chromatography (silica gel, 3:1 hexanes/dichloromethane) furnished the product **91** as a royal purple solid (252 mg, 65% yield). <sup>1</sup>H NMR (300 MHz, CDCl<sub>3</sub>, 25 °C): δ = 10.11 (s, 1H), 9.27 (d, *J* = 4.5 Hz, 2H), 8.82 (d, *J* = 4.5 Hz, 2H), 8.68 (s, 4H), 7.30 (s, 6H), 2.65 (s, 6H), 2.63 (s, 3H), 1.86 (s, 12H), 1.85 (s, 6H), -2.81 (s, 2H).

### 8.5.25 5-Bromo-10,15,20-trimesitylporphyrin (**92**)

*N*-Bromosuccinimide (164 mg, 0.920 mmol) was added in one portion to a solution of **91** (612 mg, 0.920 mmol) in chloroform (450 mL) and the reaction was stirred at room temperature under air for 20 min. The solvent was removed and the residue was purified by column chromatography (silica gel, 1:1 hexanes/dichloromethane) to yield the product as a reddish-brown solid (616 mg, 90% yield). <sup>1</sup>H NMR (300 MHz, CDCl<sub>3</sub>, 25 °C): δ = 9.60 (d, *J* = 4.7 Hz, 2H), 8.74 (d, *J* = 4.7 Hz, 2H), 8.61 (s, 4H), 7.29 (s, 6H), 2.64 (s, 6H), 2.62 (s, 3H), 1.86 (s, 6H), 1.85 (s, 12H), -2.54 (s, 2H). HRESIMS (MH<sup>+</sup>) calcd for C<sub>47</sub>H<sub>44</sub>BrN<sub>4</sub> *m/z* 743.2744, found 743.2753.

### 8.5.26 Zinc (II) 5-bromo-10,15,20-trimesitylporphyrin (**93**)

To a solution of **92** (600 mg, 0.807 mmol) in dichloromethane (200 mL) was added a solution of Zn(OAc)<sub>2</sub>•2H<sub>2</sub>O (354 mg, 1.61 mmol) in methanol (10 mL). The reaction mixture was stirred at room temperature under air overnight. Purification by column chromatography (silica gel, 1:1 hexanes/dichloromethane) furnished the product **93** as a bright red solid in quantitative yield. <sup>1</sup>H NMR (300 MHz, CDCl<sub>3</sub>, 25 °C): δ = 9.69 (m, 2H), 8.81 (m, 2H), 8.68 (m, 4H), 7.29 (s, 6H), 2.64 (m, 9H), 1.83 (m, 18 H). HRESIMS (MH<sup>+</sup>) calcd for C<sub>47</sub>H<sub>42</sub>BrN<sub>4</sub>Zn *m/z* 805.1879, found 805.1864.

### 8.5.27 Zinc(II) 5,10,15-trimesityl-20-(4',4',5',5'-tetramethyl[1',3',2']dioxaborolan-2'-yl)-porphyrin (**94**)

Under nitrogen a nitrogen atmosphere, triethylamine (1.4 mL, 10 mmol), *trans*-dichlorobis(triphenylphosphine)palladium (II) (16.2 mg, 0.023 mmol) and pinacolborane (0.94 mL, 6.47 mmol) were added to a solution of **93** (622 mg, 0.771 mmol) in anhydrous 1,2-dichloroethane (90 mL). The resulting mixture was stirred at 90 °C for 45 min under nitrogen. The reaction was cooled to room temperature, quenched with 30% aq KCl (30 mL), washed with water (100 mL) and the solvent was removed by rotary evaporation. The residue was then purified by column chromatography (silica gel, 1:1 hexanes/dichloromethane) to deliver **94** as a ruby red powder (635 mg, 96% yield). <sup>1</sup>H NMR (300 MHz, CDCl<sub>3</sub>, 25 °C): δ = 9.82 (d, *J* = 4.5 Hz, 2H), 8.90 (d, *J* = 4.5 Hz, 2H), 8.73 (d, *J* = 4.5 Hz, 2H), 8.69 (d, *J* = 4.5 Hz, H), 7.28 (s, 6H), 2.65 (s, 6H), 2.63 (s, 3H), 1.86 (s, 18H), 1.82 (s, 12H). HRESIMS (MH<sup>+</sup>) calcd for C<sub>53</sub>H<sub>54</sub>BN<sub>4</sub>O<sub>2</sub>Zn *m/z* 853.3626, found 853.3608.

#### 8.5.28 4,5-Bis[5-(10,15,20-trimesitylporphyrinyl)]-2,7-di-*tert*-butyl-9,9-dimethylxanthene, H<sub>4</sub>(DTMPX) (95)

Under a nitrogen atmosphere, a Schlenk tube was charged with dibromide **83** (46 mg, 0.0958 mmol), **94** (245 mg, 0.287 mmol), Ba(OH)<sub>2</sub>·8H<sub>2</sub>O (90.6 mg, 0.287 mmol), and Pd(PPh<sub>3</sub>)<sub>4</sub> (55 mg, 0.0479 mmol). 1,2-Dimethoxyethane (31 mL) and deionized water (3.1 mL) were added and the resulting solution was heated at 95 °C for 22 h under nitrogen. The solvent was removed and the residue was redissolved in dichloromethane (50 mL) and stirred with 6 N HCl (25 mL) for 30 min. The organic layer was separated and washed with 20% aq Na<sub>2</sub>CO<sub>3</sub> (40 mL) followed by water (2 × 60 mL). The solvent was evaporated and the residue was purified by column chromatography (silica gel, 2:1 hexanes/dichloromethane) to afford the product **95** as a purple powder (33 mg, 21% yield). <sup>1</sup>H NMR (300 MHz, CDCl<sub>3</sub>, 25 °C): δ = 8.36 (d, *J* = 4.8 Hz, 4H), 8.33 (d, *J* = 4.4 Hz, 4H), 8.15 (d, *J* = 4.4 Hz, 4H), 7.92 (d, *J* = 2.5 Hz, 2H), 7.65 (d, *J* = 4.8 Hz, 4H), 7.24 (s, 2H), 7.09 (s, 2H), 7.00 (s, 4H), 6.87 (d, *J* = 2.5 Hz, 2H), 6.38 (s, 4H), 2.56 (s, 6H), 2.45 (s, 12H), 2.34 (s, 6H), 1.93 (s, 6H), 1.57 (s, 12H), 1.40 (s, 6H), 1.23 (s, 18H), -0.31 (s, 12H), -3.30 (s, 4H). HRESIMS (MH<sup>+</sup>) calcd for C<sub>117</sub>H<sub>115</sub>N<sub>8</sub>O *m/z* 1647.9188, found 1647.9192.

#### 8.5.29 4,6-Bis[(5-(10,15,20-trimesitylporphyrinyl)]dibenzofuran, H<sub>4</sub>(DTMPD) (96)

Under a nitrogen atmosphere, a mixture of **84** (50.8 mg, 0.156 mmol), **94** (400 mg, 0.468 mmol), potassium phosphate (397 mg, 1.87 mmol), Pd(PPh<sub>3</sub>)<sub>4</sub> (54 mg, 0.0467 mmol), and anhydrous DMF (71 mL) was heated at 100 °C for 20 h. The solvent was removed and the residue was redissolved in dichloromethane (90 mL) and stirred with 6 N HCl (40 mL) for 30 min. The organic layer was separated and washed with 20% aq Na<sub>2</sub>CO<sub>3</sub> (40 mL) followed by water (2 × 60 mL). The solvent was evaporated and the residue was purified by column chromatography (silica gel, 2:1 hexanes/dichloromethane) to deliver the product **96** as a plum purple solid (180 mg, 77%). <sup>1</sup>H NMR (300 MHz, CDCl<sub>3</sub>, 25 °C): δ = 8.62 (dd, *J* = 7.7, 1.1 Hz, 2H), 8.46 (d, *J* = 4.9 Hz, 4H), 8.35 (d, *J* = 4.7 Hz, 4H), 8.26 (d, *J* = 4.7 Hz, 4H), 8.16 (d, *J* = 4.7 Hz, 4H), 8.04 (dd, *J* = 7.5, 1.1 Hz, 2H), 7.79 (t, *J* = 7.5 Hz, 2H), 7.16 (s, 2H), 7.13 (s, 2H), 7.10 (s, 4H), 6.76 (s, 4H), 2.55 (s, 6H), 2.53 (s, 12H), 1.71 (s, 6H), 1.59 (s, 12H), 1.45 (s, 6H), 0.73 (s, 12H), -3.07 (s, 4H). HRESIMS (MH<sup>+</sup>) calcd for C<sub>106</sub>H<sub>93</sub>N<sub>8</sub>O *m/z* 1493.7467, found 1493.7474.

#### 8.5.30 Mn<sub>2</sub>Cl<sub>2</sub>(DTMPX) (97)

Mn(OAc)<sub>2</sub>·4H<sub>2</sub>O (16 mg, 0.0653 mmol) was added to a refluxing solution of **95** (20 mg, 0.012 mmol) in DMF (9 mL) and the reaction was refluxed in air for 30 min. Two more portions of Mn(OAc)<sub>2</sub>·4H<sub>2</sub>O (16 mg each) were added at intervals of 30 min and heating was continued for 30 min after the last addition of metal salt. The reaction was cooled to room temperature and

poured into ice-cold brine (12 mL). The green precipitate was collected by filtration and washed with deionized water (120 mL). The solid was then redissolved in methanol (12 mL) and the solution was poured into ice-cold 6 N HCl (12 mL). The brownish precipitate was redissolved in dichloromethane (20 mL), the organic phase was washed with water (2 × 50 mL), and the solvent was removed. The residue was purified by column chromatography (silica gel, dichloromethane to 10% methanol/dichloromethane), redissolved in dichloromethane (10 mL) and stirred with 4 N HCl (2 mL) for 30 min. The organic layer was separated, washed with water (3 × 40 mL), dried over Na<sub>2</sub>SO<sub>4</sub>, and the solvent was removed by rotary evaporation to give **97** as a green powder (18 mg, 86% yield). HRFABMS ([M-Cl]<sup>+</sup>) calcd for C<sub>117</sub>H<sub>110</sub>ClMn<sub>2</sub>N<sub>8</sub>O *m/z* 1787.7252, found 1787.7252.

#### 8.5.31 Mn<sub>2</sub>Cl<sub>2</sub>(DTMPD) (**98**)

Mn(OAc)<sub>2</sub>•4H<sub>2</sub>O (16 mg, 0.0653 mmol) was added to a refluxing solution of **96** (10 mg, 0.00669 mmol) in DMF (9 mL) and the reaction was refluxed in air for 30 min. Two more portions of Mn(OAc)<sub>2</sub>•4H<sub>2</sub>O (16 mg each) were added at intervals of 30 min and heating was continued for 30 min after the last addition of metal salt. The reaction was cooled to room temperature and poured into ice-cold brine (12 mL). The green precipitate was collected by filtration and washed with deionized water (120 mL). The solid was then redissolved in methanol (12 mL) and the solution was poured into ice-cold 6 N HCl (12 mL). The brownish precipitate was redissolved in dichloromethane (20 mL), the organic phase was washed with water (2 × 50 mL), and the solvent was removed. The residue was purified by column chromatography (silica gel, dichloromethane to 10% methanol/dichloromethane), redissolved in dichloromethane (10 mL) and stirred with 4 N HCl (2 mL) for 30 min. The organic layer was separated, washed with water (3 × 40 mL), dried over Na<sub>2</sub>SO<sub>4</sub>, and the solvent was removed by rotary evaporation to deliver **98** as a green powder (10 mg, 89% yield). HRFABMS (M<sup>+</sup>) calcd for C<sub>106</sub>H<sub>88</sub>Cl<sub>2</sub>Mn<sub>2</sub>N<sub>8</sub>O *m/z* 1668.5219, found 1668.5212.

#### 8.5.32 Physical Measurements

<sup>1</sup>H NMR spectra were collected at 25 °C in CDCl<sub>3</sub> (Cambridge Isotope Laboratories) at the MIT Department of Chemistry Instrumentation Facility (DCIF) using either a Mercury 300 or an Inova 500 spectrometer. All chemical shifts are reported using the standard δ notation in parts-per-million; positive chemical shifts are to higher frequency from the given reference. High-resolution mass spectral analyses were carried out at the University of Illinois Mass Spectrometry Laboratory or the MIT Department of Chemistry Instrumentation Facility (DCIF). Elemental analyses were performed at Michigan State University.

### 8.5.33 Peroxide Disproportionation Reactions

Dismutation reactions were performed at room temperature in a 5 mL conical reaction vial with a side port, equipped with a magnetic spinvane stirbar and a capillary gas delivery tube linked to a graduated buret filled with water. The reaction vial was charged with 1  $\mu\text{mol}$  of the manganese Pacman porphyrin, 25  $\mu\text{mol}$  of 1,5-dicyclohexylimidazole, 4  $\mu\text{mol}$  of benzyldimethyltetradecylammonium chloride, 2 mL of dichloromethane and 1 mL of phosphate buffer, pH 7. The solution was stirred to ensure gas pressure equilibration. An aliquot of 30%  $\text{H}_2\text{O}_2$  (0.11 mL) was added to the reaction mixture via syringe through the side port. The oxygen evolution was measured using a buret. The identity of the oxygen gas was confirmed independently using the alkaline pyrogallol test.<sup>51</sup>

## 8.6 References and Notes

1. Collman, J. P.; Wagenknecht, P. S.; Hutchison, J. E. *Angew. Chem. Int. Ed. Engl.* **1994**, *33*, 1537-1554.
2. Anderson, S.; Anderson, H. L.; Sanders, J. K. M. *Acc. Chem. Res.* **1993**, *26*, 469-475.
3. Chang, C. K.; Abdalmuhdi, I. *J. Org. Chem.* **1983**, *48*, 5388-5390.
4. Chang, C. K.; Liu, H. Y.; Abdalmuhdi, I. *J. Am. Chem. Soc.* **1984**, *106*, 2725-2726.
5. Chang, C. K.; Abdalmuhdi, I. *Angew. Chem. Int. Ed. Engl.* **1984**, *23*, 164-165.
6. Lui, H.-Y.; Abdalmuhdi, I.; Chang, C. K.; Anson, F. C. *J. Phys. Chem.* **1985**, *89*, 665-670.
7. Ni, C.-L.; Abdalmuhdi, I.; Chang, C. K.; Anson, F. C. *J. Phys. Chem.* **1987**, *91*, 1158-1166.
8. Proniewicz, L. M.; Odo, J.; Goral, J.; Chang, C. K.; Nakamoto, K. *J. Am. Chem. Soc.* **1989**, *111*, 2105-2110.
9. Collman, J. P.; Hutchison, J. E.; Lopez, M. A.; Tabard, A.; Guilard, R.; Seok, W. K.; Ibers, J. A.; L'Her, M. *J. Am. Chem. Soc.* **1992**, *114*, 9869-9877.
10. Collman, J. P.; Hutchison, J. E.; Lopez, M. A.; Guilard, R. *J. Am. Chem. Soc.* **1992**, *114*, 8066-8073.
11. Collman, J. P.; Hutchison, J. E.; Ennis, M. S.; Lopez, M. A.; Guilard, R. *J. Am. Chem. Soc.* **1992**, *114*, 8074-8080.
12. Collman, J. P.; Ha, Y.; Wagenknecht, P. S.; Lopez, M. A.; Guilard, R. *J. Am. Chem. Soc.* **1993**, *115*, 9080-9088.
13. Guilard, R.; Lopez, M. A.; Tabard, A.; Richard, P.; Lecomte, C.; Brandes, S.; Hutchison, J. E.; Collman, J. P. *J. Am. Chem. Soc.* **1992**, *114*, 9877-9889.
14. Guilard, R.; Brandes, S.; Tardieux, C.; Tabard, A.; L'Her, M.; Miry, C.; Gouerac, P.; Knop, Y.; Collman, J. P. *J. Am. Chem. Soc.* **1995**, *117*, 11721-11729.
15. Le Mest, Y.; L'Her, M.; Hendricks, N. H.; Kim, K.; Collman, J. P. *Inorg. Chem.* **1992**, *31*, 835-847.
16. Le Mest, Y.; L'Her, M.; Saillard, J. Y. *Inorg. Chim. Acta* **1996**, *248*, 181-191.
17. Le Mest, Y.; Inisan, C.; Laouenan, A.; L'Her, M.; Talarmain, J.; El Khalifa, M.; Saillard, J. Y. *J. Am. Chem. Soc.* **1997**, *119*, 6905-6106.
18. Chang, C. J.; Deng, Y.; Heyduk, A. F.; Chang, C. K.; Nocera, D. G. *Inorg. Chem.* **2000**, *39*, 959-966.
19. Deng, Y.; Chang, C. J.; Nocera, D. G. *J. Am. Chem. Soc.* **2000**, *122*, 410-411.
20. Chang, C. J.; Baker, E. A.; Pistorio, B. J.; Deng, Y.; Loh, Z.-H.; Miller, S. E.; Carpenter, S. D.; Nocera, D. G. *Inorg. Chem.* **2002**, *41*, 3102-3109.



21. Chang, C. J.; Deng, Y.; Shi, C.; Chang, C. K.; Anson, F. C.; Nocera, D. G. *Chem. Commun.* **2000**, 1355-1356.
22. Pistorio, B. J.; Chang, C. J.; Nocera, D. G. *J. Am. Chem. Soc.* **2002**, *124*, 7884-7885.
23. Chang, C. J.; Deng, Y.; Lee, G.-H.; Peng, S.-M.; Yeh, C.-Y.; Nocera, D. G. *Inorg. Chem.* **2002**, *41*, 3008-3016.
24. Chang, C. J.; Brown, J. D. K.; Chang, M. C. Y.; Baker, E. A.; Nocera, D. G. In *Electron Transfer in Chemistry*; Balzani, V., Ed.; Wiley-VCH: Weinheim, Germany, 2001; Vol. 3.2.4, pp 409-461.
25. Cukier, R. I.; Nocera, D. G. *Annu. Rev. Phys. Chem.* **1998**, *49*, 337-369.
26. Barton, D. H. R.; Zard, S. Z. *J. Chem. Soc. Chem. Commun.* **1985**, 1098-1100.
27. Ono, N.; Kawamura, H.; Bougauchi, M.; Maruyama, K. *Tetrahedron* **1990**, *46*, 7483-7496.
28. Adler, A. D.; Longo, F. R.; Kampas, F.; Kim, J. *J. Inorg. Nucl. Chem.* **1970**, *32*, 2443-2445.
29. Buchler, J. W. In *Porphyrins and Metalloporphyrins*; 2nd ed.; Smith, K. M., Ed.; Elsevier Scientific: Oxford, 1975, pp 157-232.
30. Sharman, W. M.; Van Lier, J. E. *J. Porphyrins Phthalocyanines* **2000**, *4*, 441-453.
31. Chang, C. K.; Bag, N. *J. Org. Chem.* **1995**, *60*, 7030-7032.
32. Hyslop, A. G.; Kellett, M. A.; Iovine, P. M.; Therien, M. J. *J. Am. Chem. Soc.* **1998**, *120*, 12676-12677.
33. Deng, Y.; Chang, C. K.; Nocera, D. G. *Angew. Chem. Int. Ed.* **2000**, *39*, 1066-1068.
34. Zhou, X.; Tse, M. K.; Wan, T. S. M.; Chan, K. S. *J. Org. Chem.* **1996**, *61*, 3590-3593.
35. Groves, J. T.; Haushalter, R. C.; Nakamura, M.; Nemo, T. E.; Evans, B. J. *J. Am. Chem. Soc.* **1981**, *103*, 2884-2886.
36. Cheng, R.-J.; Latos-Grazynski, L.; Balch, A. L. *Inorg. Chem.* **1982**, *21*, 2412-2418.
37. Collman, J. P.; Tyvoll, D. A.; Chng, L. L.; Fish, H. T. *J. Org. Chem.* **1995**, *60*, 1926-1931.
38. Naruta, Y.; Sasayama, M.; Ichihara, K. *J. Mol. Cat. A* **1997**, *117*, 115-121.
39. Shultz, D. A.; Gwaltney, K. P.; Lee, H. *J. Org. Chem.* **1998**, *63*.
40. Lindsey, J. S.; Wagner, R. W. *J. Org. Chem.* **1989**, *54*, 828-836.
41. DiMugno, S. G.; Lin, V. S. Y.; Therien, M. J. *J. Org. Chem.* **1993**, *58*.
42. Clezy, P. S.; Smythe, G. A. *Aust. J. Chem.* **1969**, *22*, 239-249.
43. Chong, R.; Clezy, P. S.; Liepa, A. J.; Nichol, A. W. *Aust. J. Chem.* **1969**, *22*, 229-238.
44. Bruce, D. W.; Wang, Q. M. *Synlett* **1995**, 1267-1268.
45. Murata, M.; Watanabe, S.; Masuda, Y. *J. Org. Chem.* **1997**, *62*, 6458-6459.
46. Miyaura, N.; Suzuki, A. *Chem. Rev.* **1995**, *95*, 2457-2483.

47. Nicholls, P.; Fita, I.; Loewen, P. C. *Adv. Inorg. Chem.* **2001**, *51*, 51-106.
48. Armarego, W. L. F.; Perrin, D. D. *Purification of Laboratory Chemicals*; 4th ed.; Butterworth-Heinmann: Oxford, 1996.
49. Nowick, J. S.; Ballester, P.; Ebmeyer, F.; Rebek Jr., J. *J. Am. Chem. Soc.* **1990**, *112*, 8902-8906.
50. Schwartz, E. B.; Knobler, C. B.; Cram, D. J. *J. Am. Chem. Soc.* **1992**, *114*, 10775-10784.
51. Duncan, I. A.; Harriman, A.; Porter, G. *Anal. Chem.* **1979**, *51*, 2206-2208.

*Chapter 9*

**Hangman Porphyrins Based on Naphthalene,  
Xanthene, and Dibenzofuran Scaffolds**

A portion of the work presented in this chapter has been published:

Chang, C. J.; Yeh, C.-Y.; Nocera, D. G. *J. Org. Chem.* **2002**, *67*, 1403-1406.

## 9.1 Motivation and Specific Aims

Our initial explorations of small-molecule activation chemistry catalyzed by proton-coupled electron transfer (PCET) focused on the study of Pacman porphyrins. These symmetric cofacial architectures provide proficient catalysts for the direct reduction of oxygen to water and the photoinduced oxidation of organic substrates, as well as establishing the importance of directed ligand flexibility and proton inventory for carrying out these catalytic cycles. In pursuit of our next generation of catalysts, we sought to develop systems where the PCET functionalities are more intimately crafted into the metal-ligand framework. The success of the Pacman motif led us to design analogous asymmetric cofacial architectures composed of porphyrins and hydrogen-bonding groups anchored to a rigid naphthalene (HPN = hanging porphyrin naphthalene), xanthene (HPX = hanging porphyrin xanthene), and dibenzofuran (HPD = hanging porphyrin dibenzofuran) pillar; this chapter presents three distinct synthetic strategies for preparing a library of such compounds. The convenience and versatility of these synthetic methods provide a solid foundation for examining PCET-mediated catalytic chemistry, as the combination of redox and acid-base sites in the Hangman motif presents a pathway for direct delivery of proton and electron equivalents. Moreover, the Hangman construct allows us to tune the functional nature of the hydrogen-bonding group in terms of proton-donating ability ( $pK_a$ ) and arrangement in relation to the metalloporphyrin redox site, presenting a unique opportunity to rigorously test the influence of proton motion on catalytic bond-making and bond-breaking processes.

## 9.2 Background

Porphyrins functionalized with hydrogen-bond synthons offer attractive building blocks for the efficient construction of supramolecular assemblies with appealing structural and electronic properties.<sup>1</sup> Such systems underlie efforts directed at unraveling the effect of hydrogen bonding on energy and electron transfer reactions.<sup>2-4</sup> We have exploited this approach in the development of hydrogen-bond networks for the study of proton-coupled electron transfer (PCET) reactions.<sup>2,5-12</sup> In particular, our work has focused on porphyrins modified with an amidinium group;<sup>6,7,11</sup> these porphyrins associate with carboxylates to form stable, directional salt bridge complexes where the porphyrin macrocycle and hydrogen-bond functionality are juxtaposed in a *side-to-side* arrangement.

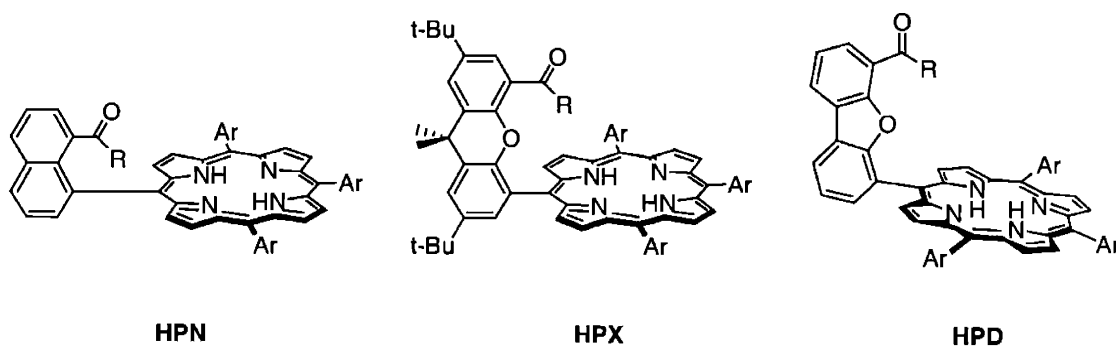
We sought to extend our PCET studies to the multielectron activation chemistry of oxygen, water, and other small molecules.<sup>2,13,14</sup> To this end, we have developed methods for the facile assembly of symmetric cofacial bisporphyrins based on xanthene (DPX)<sup>15-17</sup> and dibenzofuran (DPD)<sup>16-18</sup> scaffolds that exhibit variable pocket sizes with minimal lateral displacements. In these systems, the *face-to-face* arrangement of porphyrin subunits allows for the efficient

delivery of the oxidizing or reducing equivalents necessary to effect the overall multielectron activation of small molecule substrates.<sup>13,14</sup>

A complement to both these approaches is the construction of chemical architectures containing porphyrins *and* hydrogen-bond synthons in a face-to-face arrangement.<sup>4,19-33</sup> Towards this end, we now introduce asymmetric cofacial platforms in which a rigid spacer is used to “hang” a hydrogen-bond functionality over the porphyrin macrocycle.<sup>34,35</sup> These asymmetric platforms combine both redox (metalloporphyrin) and acid-base (hydrogen-bonding group) sites into a single molecular system, providing a versatile framework for exploring small-molecule activation chemistry catalyzed by PCET.

In this chapter, we describe the design and synthetic details for preparing Hangman porphyrins anchored by a functionalized naphthalene, xanthene, or dibenzofuran spacer. The HPN (hanging porphyrin naphthalene), HPX (hanging porphyrin xanthene), and HPD (hanging porphyrin dibenzofuran) systems of Chart 9.1 afford the ability to modify both the identity of the hydrogen-bonding functionality and its orientation with respect to the metalloporphyrin redox cofactor. Three distinct synthetic methodologies have been elaborated. First, naphthalene-bridged constructs are furnished via base-catalyzed ring-opening reactions of porphotrimethene synthons. Porphyrins with functionalized xanthene spacers are obtained using mild Lindsey-type cyclizations. Finally, the Suzuki cross-coupling reaction provides a modular synthetic strategy for the facile preparation of Hangman porphyrins bridged by either dibenzofuran or xanthene. The convenience and versatility of the combined synthetic methods presents enticing possibilities for the use of these and related porphyrinic structures for the study of PCET-mediated small-molecule activation chemistry.

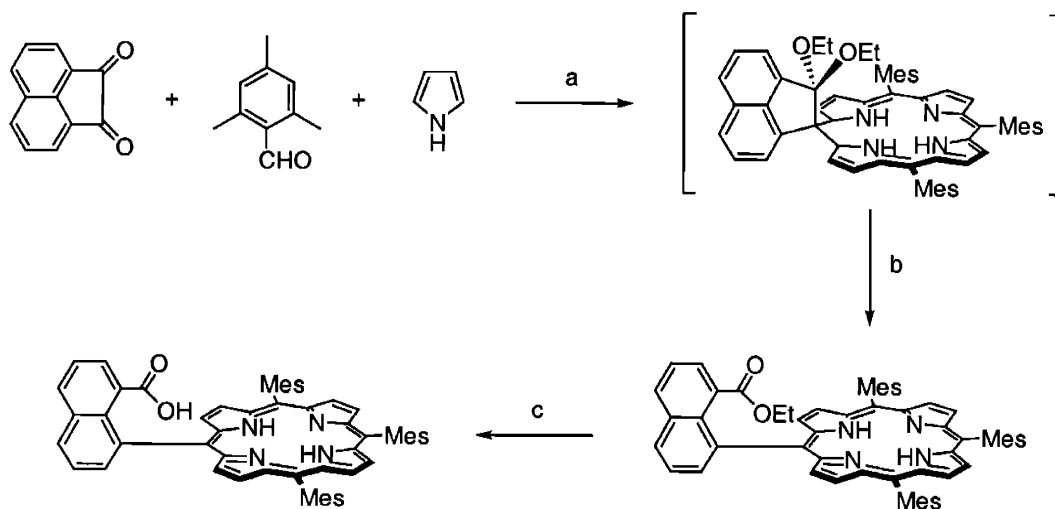
**Chart 9.1**



## 9.3 Results and Discussion

### 9.3.1 Synthesis of Hanging Porphyrin Naphthalene (HPN) Architectures via Porphotrimethenes

The installation of a functionalized naphthalene spacer onto an asymmetric cofacial porphyrin platform affords ditopic systems with proximate redox and acid-base sites. The resulting naphthalene-bridged Hangman porphyrins (HPN = hanging porphyrin naphthalene) are synthesized as outlined in Scheme 9.1. We utilize an approach recently developed by Scott and co-workers, who prepared symmetric *trans*-5,15-arylporphyrins bearing two functionalized naphthalene spacers from base-activated ring-opening reactions of porphodimethene intermediates.<sup>19,27-31</sup> For porphyrins with one such substituent, we employ a porphotrimethene synthon. Reaction of acenaphthalenequinone with pyrrole and mesitylaldehyde in the presence of  $\text{BF}_3 \cdot \text{OEt}_2$  gives, after oxidation with 2,3-dichloro-5,6-dicyano-1,4-benzoquinone (DDQ), the corresponding porphotrimethene diethyl acetal. The acetal is identified using mass spectrometry; the generation of the ethyl-protected acetal most likely arises from the ethanol contained in the chloroform reaction solvent. Treatment of the crude porphotrimethene acetal with potassium hydroxide in THF affords the ethyl ester porphyrin  $\text{H}_2(\text{HPN-CO}_2\text{Et})$  (**99**) in 5% overall yield based on the diketone starting material. Hydrolysis of **99** with a mixture of acetic and sulfuric acids under harsh conditions (reflux for 7 days) delivers acid porphyrin  $\text{H}_2(\text{HPN-CO}_2\text{H})$  (**100**) in 90% yield. Porphyrins **99** and **100** yield a set of HPN derivatives for examining the reactivity consequences of protic and aprotic hydrogen-bond functionalities appended to a redox-active platform.

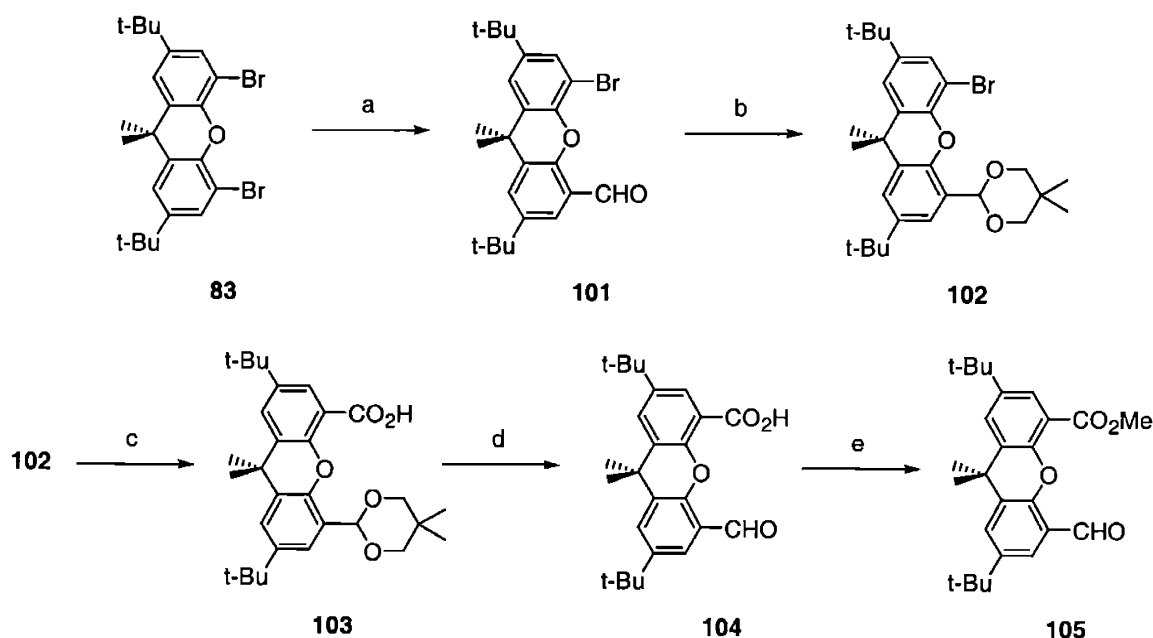


**Scheme 9.1.** (a) i.  $\text{BF}_3 \cdot \text{OEt}_2$ , chloroform; ii. 2,3-dichloro-5,6-dicyano-1,4-benzoquinone (DDQ); (b) KOH; THF, reflux; (c)  $\text{H}_2\text{SO}_4$ , acetic acid, reflux.

### 9.3.2 Synthesis of Hanging Porphyrin Xanthene (HPX) Architectures using Lindsey Cyclizations

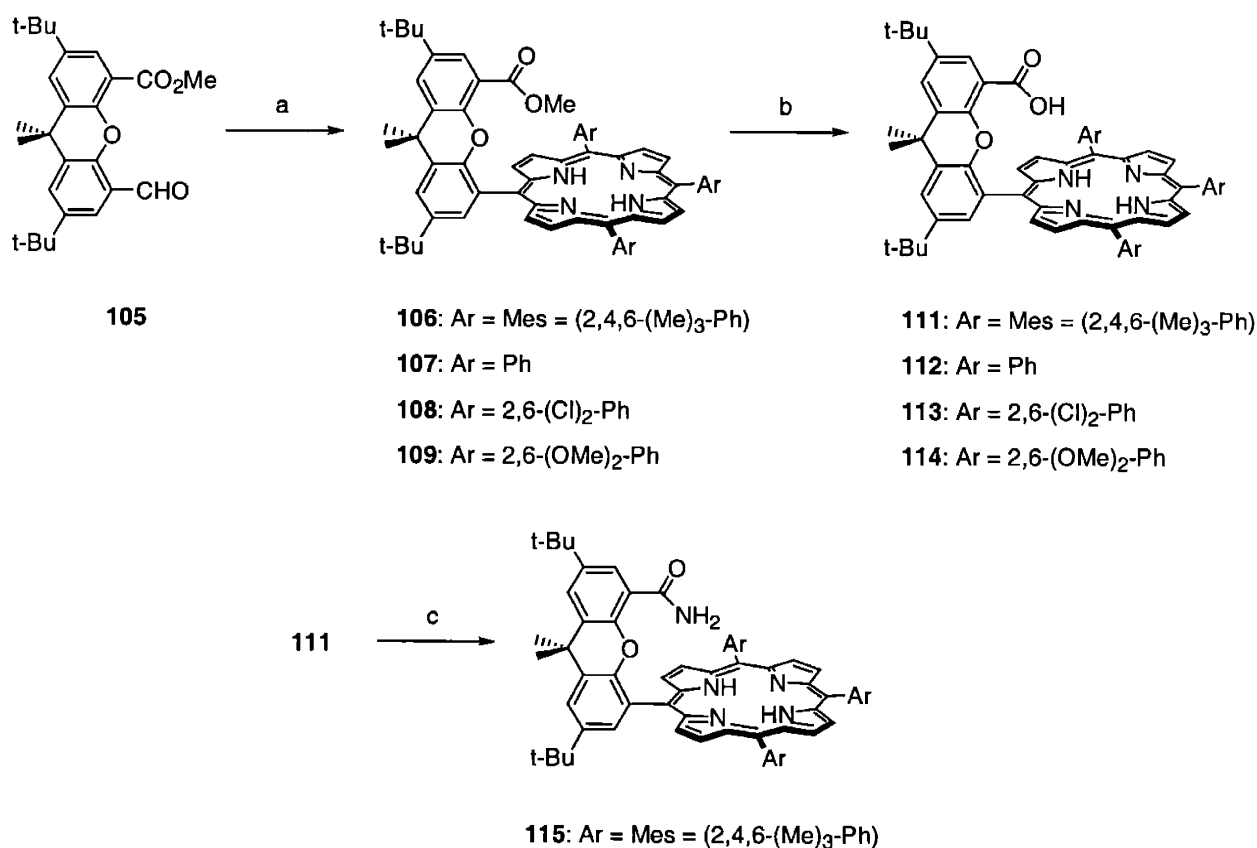
Substitution of naphthalene with xanthene results in ditopic cofacial architectures with extended vertical pocket sizes. The synthetic strategy for the preparation of xanthene-bridged Hangman porphyrins (HPX = hanging porphyrin xanthene) is summarized in Schemes 9.2 to 9.4. Porphyrin cyclizations are carried out using mild, high-dilution Lindsey conditions.<sup>36</sup> We employ a stepwise protection-deprotection route for the xanthene pillar; this modular approach provides a number of synthetically useful intermediates that are isolated and purified on a multigram scale.<sup>37</sup>

Selective monolithiation of Rebek's xanthene dibromide **83** with phenyllithium in the presence of dry DMF followed by hydrolysis of the intermediate imidate salt provides aldehyde **101** in 81% yield. Protection of the aldehyde group using neopentyl glycol with a catalytic amount of benzenesulfonic acid affords acetal **102** in 93% yield. Lithiation of the remaining bromide on **102** and subsequent quenching with CO<sub>2</sub> gas delivers acid **103** in 86% yield. Deprotection of the acetal of **103** with trifluoroacetic acid (TFA) proceeds smoothly to furnish aldehyde **104** in 89% yield. Reaction of **104** with H<sub>2</sub>SO<sub>4</sub> in methanol supplies ester **105** in 93% yield.



**Scheme 9.2.** (a) i. phenyllithium, cyclohexane/THF, ii. DMF, H<sub>2</sub>O; (b) neopentyl glycol, benzenesulfonic acid, toluene, N<sub>2</sub>, reflux; (c) i. phenyllithium, cyclohexane/THF, ii. CO<sub>2</sub> gas; (d) trifluoroacetic acid, water; (e) methanol, H<sub>2</sub>SO<sub>4</sub>, reflux.

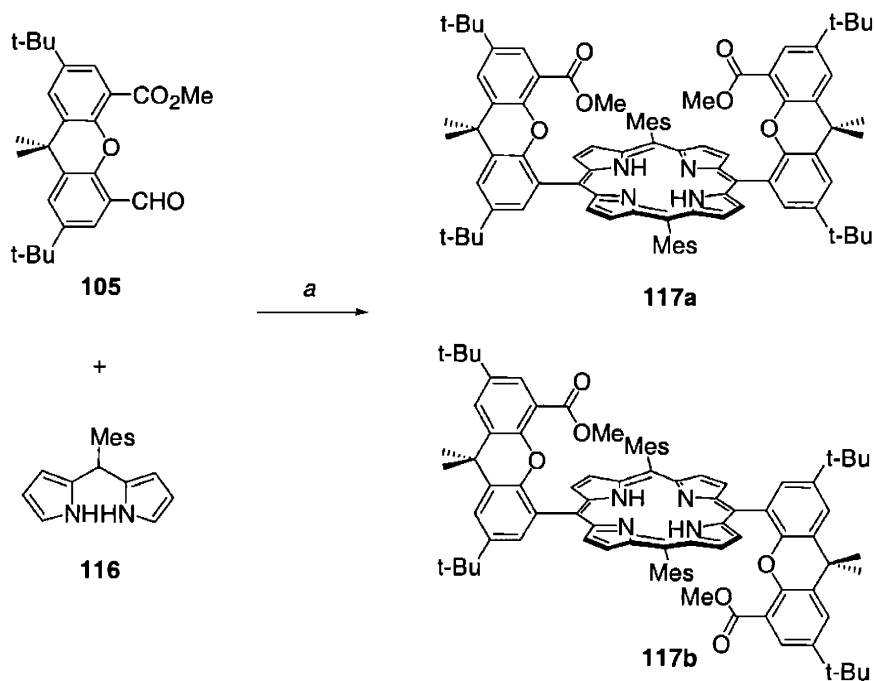
Compound **105** serves as a common synthon for construction of a variety of porphyrins containing hydrogen-bond functionalities anchored to xanthene spacers. In all cases, standard high-dilution Lindsey conditions are employed for macrocyclization,<sup>36</sup> as exemplified by the acid-catalyzed condensation of **105** with mesitylaldehyde and pyrrole to produce H<sub>2</sub>(HPX-CO<sub>2</sub>Me) (**106**) in 26% yield. As illustrated in Scheme 9.3, the Lindsey reaction proves to be quite versatile. Through simple substitutions of the aryl groups, this general pathway allows for the isolation of singly-bridged, xanthene-functionalized ester porphyrins **106-109** with varying steric and electronic properties. Yields for cyclization range from 20-30%. Especially noteworthy are the mild reaction conditions used for porphyrin formation, in contrast to the harsh Alder-Longo methods employed by Rebek in the synthesis of related dixanthene cleft porphyrins.<sup>24</sup>



**Scheme 9.3.** (a) i. pyrrole, arylaldehyde, BF<sub>3</sub>•OEt<sub>2</sub>, chloroform/ethanol, ii. DDQ; (b) i. Zn(OAc)<sub>2</sub>•2H<sub>2</sub>O, chloroform/methanol, reflux, ii. NaOH, THF/H<sub>2</sub>O, N<sub>2</sub>, reflux, iii. HCl; (c) i. SOCl<sub>2</sub>, N<sub>2</sub>, reflux, ii. NH<sub>3</sub>.



The HPX ester groups of **106-109** are easily converted to their corresponding acid derivatives in the following way. Zinc(II) derivatives of **106-109** are prepared in quantitative yields upon reaction of the free base porphyrin with  $\text{Zn}(\text{OAc})_2 \cdot 2\text{H}_2\text{O}$ ; the trimesityl complex  $\text{Zn}(\text{HPX-CO}_2\text{Me})$  (**110**) has been isolated and fully characterized. Treatment of the zinc(II)-protected porphyrins with aqueous sodium hydroxide in THF under harsh conditions (reflux, 3 days) followed by zinc(II) removal with HCl affords the HPX acid derivatives **111-114** in excellent yields (> 90%). In addition, the carboxylic acid group also provides access to other functional groups; as an example, the HPX amide derivative  $\text{H}_2(\text{HPX-CONH}_2)$  (**115**) is obtained in 90% yield by reaction of **111** with  $\text{SOCl}_2$  (to generate the acid chloride) followed by quenching with  $\text{NH}_3$  gas. It is noteworthy that the mesityl HPX derivatives **106**, **111**, and **115** comprise a structurally homologous series of singly-bridged xantheno Hangman porphyrins bearing hydrogen-bond functionalities.



**Scheme 9.4.** (a) i.  $\text{BF}_3 \cdot \text{OEt}_2$ , chloroform/ethanol, ii. DDQ.

The use of compound **105** is not limited to porphyrin architectures containing a single xantheno pillar. For example, the MacDonald [2 + 2] condensation of **105** with aryl dipyrromethanes such as 5-mesityldipyrromethane **116**<sup>38</sup> generates the corresponding *trans*-porphyrins bearing a pair of xantheno pillars in overall 16% yield (Scheme 9.4). Equimolar amounts of the  $\alpha,\alpha$ - and  $\alpha,\beta$ -atropisomers (**117a** and **117b**, respectively) are secured from the reaction in pure form after column chromatography. As expected by literature precedence,<sup>39</sup> the  $\alpha,\alpha$  isomer has a lower  $R_f$

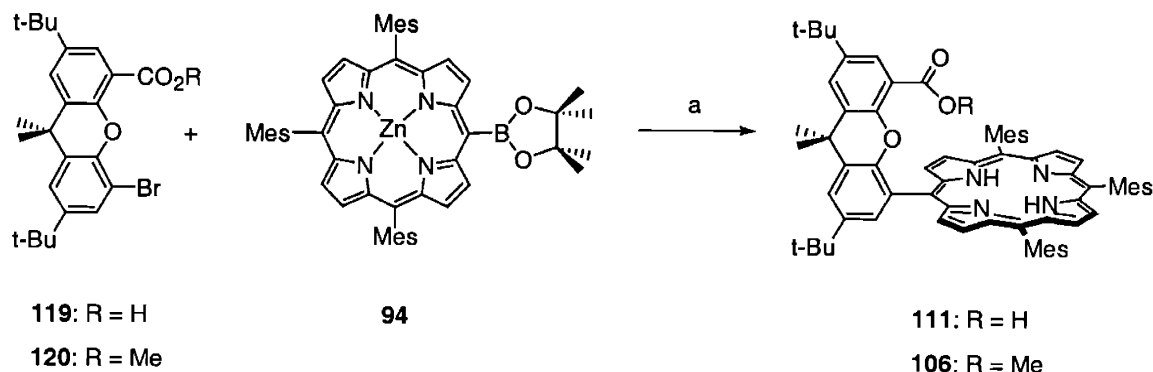
on silica gel. Unambiguous identification of the atropisomers of **117** is revealed by  $^1\text{H}$  NMR spectroscopy. The  $C_5$ -symmetric  $\alpha,\alpha$ -atropisomer (**117a**) displays two distinct resonances at  $\delta = 1.82$  and  $2.01$  ppm for the *ortho* methyl groups on the flanking mesityl rings while the  $C_2$ -symmetric  $\alpha,\beta$ -atropisomer (**117b**) exhibits a single resonance for these groups at  $\delta = 1.90$  ppm. The atropisomers are quite thermally stable; no interconversion between atropisomers is observed by  $^1\text{H}$  NMR up to  $100^\circ\text{C}$ . However, refluxing a solution of pure **117a** or **117b** in toluene for several hours leads to detectable amounts of the other atropisomer.

### 9.3.3 Synthesis of Hanging Porphyrin Dibenzofuran (HPD) and Xanthene (HPX) Architectures using Metal-Catalyzed Cross-Coupling Chemistry

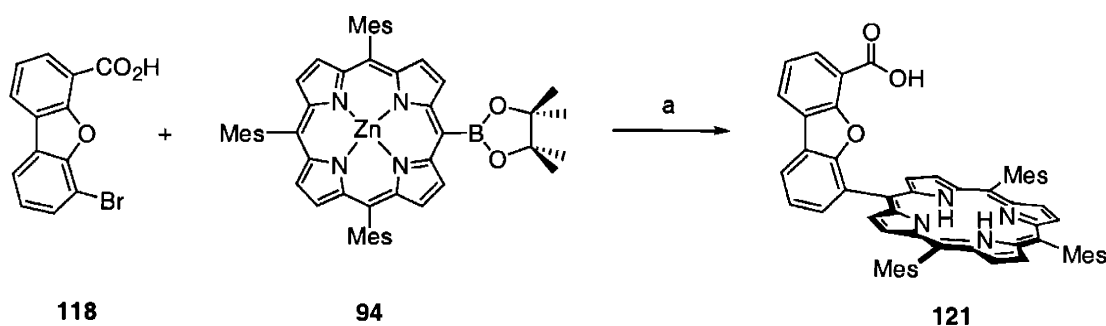
The incorporation of dibenzofuran into the Hangman motif creates a cofacial derivative with a large vertical distance between redox and acid-base functionalities. Building upon our previous experience in the synthesis of meso-tetraaryl Pacman porphyrins, we have exploited the finesse of metal-catalyzed Suzuki cross coupling reactions<sup>40-47</sup> to afford a facile and modular synthetic entry towards the preparation of Hangman porphyrins anchored by either dibenzofuran (HPD = hanging dibenzofuran porphyrin) and xanthene (HPX = hanging xanthene porphyrin). The HPX and HPD complexes are delivered according to the methods outlined in Schemes 9.5 and 9.6. Notably, these Suzuki-based routes augment the Lindsey-type syntheses that have been previously used to produce a library of porphyrin architectures bearing functionalized xanthene spacers.<sup>34</sup>

The appropriate xanthene and dibenzofuran bridge precursors are readily available from dihalide starting materials. 6-Bromo-4-dibenzofurancarboxylic acid **118** is available from 4,6-dibromobenzofuran using literature methods.<sup>48</sup> Regioselective monolithiation of Rebek's xanthene dibromide **83** with phenyllithium followed by quenching with  $\text{CO}_2$  and acid workup furnishes carboxylic acid **119** in 75% yield. Reaction of **119** with  $\text{H}_2\text{SO}_4$  in methanol affords methyl ester **120** in high yield (93%).

The trimesitylporphyrin boronate **94** is a versatile transmetalating agent for the preparation of HPX and HPD porphyrins. Metal-catalyzed cross couplings of **94** with halide compounds **118**, **119**, or **120** proceed smoothly under typical Suzuki reaction conditions using a  $\text{Pd}(\text{PPh}_3)_4/\text{NaCO}_3$  catalyst system. Previously synthesized xanthene-bridged porphyrins bearing a pendant carboxylic acid  $\text{H}_2(\text{HPX-CO}_2\text{H})$  (**111**) or methyl ester  $\text{H}_2(\text{HPX-CO}_2\text{Me})$  (**106**) group are prepared in 72% and 69%, respectively.<sup>34</sup> For comparison, macrocycle **106** is prepared in 22% yield using standard Lindsey conditions. Dibenzofuran-bridged porphyrin  $\text{H}_2(\text{HPD-CO}_2\text{H})$  (**121**) is synthesized in 67% yield from **94** and **118**.



**Scheme 9.5.** (a) i. Pd(PPh<sub>3</sub>)<sub>4</sub>, Na<sub>2</sub>CO<sub>3</sub>, DMF, water, reflux, ii. HCl.



**Scheme 9.6.** (a) i. Pd(PPh<sub>3</sub>)<sub>4</sub>, Na<sub>2</sub>CO<sub>3</sub>, DMF, water, reflux, ii. HCl.

## 9.4 Concluding Remarks

To summarize, we have presented the design and synthetic details for the construction of asymmetric, cofacial architectures composed of porphyrins and hydrogen-bond functionalities anchored to a naphthalene, xanthene, or dibenzofuran spacer. These HPN, HPX, and HPD Hangman porphyrins complement our ongoing work with the amidinium porphyrins bearing side-to-side hydrogen-bond synthons for PCET model studies and the face-to-face bisporphyrin structures for PCET small-molecule activation.

Three synthetic approaches have been established: (i) the ring-opening of porphortrimethene synthons, (ii) macrocyclizations employing high-dilution Lindsey conditions, and (iii) the metal-catalyzed cross-coupling of functionalized halospacers and boronate porphyrins using Suzuki methods. These strategies offer a powerful array of synthetic tools for combining redox and acid-base functionalities onto a convergent platform. The porphortrimethene skeleton is conveniently unmasked under basic conditions to yield naphthalene-bridged porphyrins with hanging hydrogen-bonding groups. The mild Lindsey conditions employed for cyclization are tolerant of

a wide range of substituent patterns and should allow for the synthesis of more elaborate structures. Notably, the key xanthene aldehyde-ester building block **105** is readily obtained on a gram scale with minimal purification and serves as a useful synthon for the preparation of a host of porphyrins bearing one or two functionalized xanthene spacers. The Suzuki reaction provides a modular entry for the facile synthesis of both dibenzofuran- and xanthene-bridged Hangman porphyrins. Finally, the HPN, HPX, and HPD platforms allow for direct modification of the hydrogen-bond synthon after cyclization to readily afford a systematic, homologous series of functional groups for study. With the ability to control both the protic capability (carboxylic acid, ester, amide) and orientation (naphthalene, xanthene, dibenzofuran) of the distal hydrogen-bonding functionality, the HPN, HPX, and HPD platforms provide a set of well-defined molecular scaffolds for systematic examination of proton-coupled effects on catalytic bond-forming and bond-cleaving chemistry. These possibilities are being enthusiastically pursued.

## 9.5 Experimental Section

### 9.5.1 Materials

Silica gel 60 (70-230 and 230-400 mesh, Merck) and aluminum oxide 60 (EM Science) were used for column chromatography. Analytical thin layer chromatography was performed using Merck 60 F254 silica gel (precoated sheets, 0.2 mm thick) or JT Baker IB-F aluminum oxide (precoated sheets, 0.2 mm thick). Solvents for synthesis were of reagent grade or better, and were dried according to standard methods.<sup>49</sup> Pyrrole was distilled from CaH<sub>2</sub> and stored at -20 °C under nitrogen in the dark. Chloroform containing 0.75% ethanol was distilled from K<sub>2</sub>CO<sub>3</sub>. The compounds 4,5-dibromo-2,7-di-*tert*-butyl-9,9-dimethylxanthene **83**, 4,6-dibromodibenzofuran **84**, and 6-bromo-4-dibenzofurancarboxylic acid **118** were prepared according to literature procedures.<sup>37,48</sup> Zinc(II) 5,10,15-trimesityl-20-(4',4',5',5'-tetramethyl[1',3',2']dioxaborolan-2'-yl)-porphyrin (**94**) was available using methods described in chapter 8. 5-Mesityldipyrromethane **116** was obtained from the acid-catalyzed condensation of pyrrole and mesitylaldehyde using the general method described by Lindsey.<sup>38</sup> All other reagents were used as received.

### 9.5.2 5-(1-(8-Ethoxycarbonylnaphthalene))-10,15,20-trimesitylporphyrin, H<sub>2</sub>(HPN-CO<sub>2</sub>Et) (**99**)

A solution of acenaphthenequinone (0.182 g, 1 mmol), mesitaldehyde (2.22 g, 15 mmol) and pyrrole (1.11 mL, 16 mmol) in chloroform containing 0.75% ethanol (1.6 L) was purged with nitrogen for 20 min after which a portion of BF<sub>3</sub>•OEt<sub>2</sub> (0.67 mL, 5.28 mmol) was added via syringe. The resulting solution was stirred at room temperature under nitrogen in the dark for 90

min and 2,3-dichloro-5,6-dicyano-1,4-benzoquinone (2.72 g, 12 mmol) was added to the reaction. The resulting mixture was stirred for an additional hour and the solvent was removed by rotary evaporation. The dark residue was dissolved in dichloromethane (300 mL) and filtered. The filtrate was loaded directly onto a silica gel column packed with dichloromethane and eluted with dichloromethane until no more porphorotrimethene was detected. Without further purification, the crude reaction was dissolved in THF (50 mL) and 20% aq KOH (25 mL) was added. The mixture was refluxed in air overnight. The organic solvent was removed and the solid was filtered and washed with water until the washings were at neutral pH. Purification by repeated column chromatography (silica gel, 1:1 hexanes/dichloromethane) afforded **99** as a violet powder (46 mg, 5% yield based on the diketone bridge).  $^1\text{H NMR}$  (500 MHz,  $\text{CDCl}_3$ , 25 °C):  $\delta$  = 8.54-8.70 (m, 8H), 8.31 (dd,  $J_1$  = 8.4 Hz;  $J_2$  = 1.2 Hz, 1H), 8.28 (dd,  $J_1$  = 8.4 Hz;  $J_2$  = 1.2 Hz, 1H), 8.11 (dd,  $J_1$  = 6.9 Hz;  $J_2$  = 1.2 Hz, 1H), 7.83 (t,  $J$  = 7.2 Hz, 1H), 7.63 (t,  $J$  = 7.2 Hz, 1H), 7.48 (dd,  $J_1$  = 6.9 Hz;  $J_2$  = 1.2 Hz, 1H), 7.35 (s, 1H), 7.23-7.33 (m, 5H), 2.65 (s, 3H), 2.63 (s, 6H), 2.16 (s, 3H), 1.96 (s, 6H), 1.83 (s, 6H), 1.70 (s, 3H), 0.85 (b, 2H), -0.51 (t,  $J$  = 7.2 Hz, 3H), -2.38 (s, 2H). HRFABMS (M+) calcd for  $\text{C}_{60}\text{H}_{54}\text{N}_4\text{O}_2$   $m/z$  862.4247, found 862.4279.

### 9.5.3 5-(1-(8-Hydroxycarbonylnaphthalene))-10,15,20-trimesitylporphyrin, $\text{H}_2(\text{HPN-CO}_2\text{H})$ (**100**)

Porphyrin **99** (120 mg, 0.139 mmol) was dissolved in a mixture of acetic acid (30 mL) and sulfuric acid (5 mL). Water (10 mL) was added to the green solution and the reaction was refluxed under  $\text{N}_2$  in the dark for 7 days. The reaction was cooled to room temperature and extracted with dichloromethane (50 mL). The organic layer was washed with water, dried over  $\text{Na}_2\text{SO}_4$ , and the solvent was removed by rotary evaporation. Purification by column chromatography (silica gel, dichloromethane to 30:1 dichloromethane/methanol) provided porphyrin **100** as a purple solid (104 mg, 90 %).  $^1\text{H NMR}$  (500 MHz,  $\text{CDCl}_3$ , 25 °C):  $\delta$  = 8.64 (d,  $J$  = 4.8 Hz, 2H), 8.60 (d,  $J$  = 4.8 Hz, 2H), 8.49 (d,  $J$  = 4.8 Hz, 2H), 8.44 (d,  $J$  = 4.8 Hz, 2H), 8.42 (dd,  $J_1$  = 8.4 Hz;  $J_2$  = 1.2 Hz, 1H), 8.32 (dd,  $J_1$  = 8.4 Hz;  $J_2$  = 1.2 Hz, 1H), 8.22 (dd,  $J_1$  = 8.4 Hz;  $J_2$  = 1.2 Hz, 1H), 7.92 (dd,  $J_1$  = 6.9;  $J_2$  = 6.9 Hz, 1H), 7.40 (dd,  $J_1$  = 6.9;  $J_2$  = 6.9 Hz, 1H), 7.31 (s, 2H), 7.26 (s, 4H), 6.79 (br, 1H), 2.63 (s, 3H), 2.59 (s, 6H), 1.90 (s, 3H), 1.89 (s, 3H), 1.82 (s, 6H), 1.78 (s, 6H), -2.55 (s, 2H). HRFABMS (M+) calcd for  $\text{C}_{58}\text{H}_{50}\text{N}_4\text{O}_2$   $m/z$  834.3934, found 834.4000.

### 9.5.4 4-Formyl-5-bromo-2,7-di-*tert*-butyl-9,9-dimethylxanthene (**101**)

Phenyllithium (1.2 mL, 1.8 M solution in cyclohexane) was added over a period of 10 min to a solution of xanthene dibromide **82** (1.00 g, 2.08 mmol) in dry THF (40 mL) cooled to -78 °C under an  $\text{N}_2$  atmosphere. After stirring at -78 °C under nitrogen for 1 h, dry DMF (1 mL) was

added and the mixture was warmed to room temperature and stirred for an additional hour. The reaction was quenched with water (30 mL) and the organic solvent was removed by rotary evaporation. The resulting white precipitate was filtered and washed with water. Purification by column chromatography (silica gel, 7:3 hexanes/dichloromethane) supplied **101** as a fluffy white powder (0.73 g, 81% yield).  $^1\text{H NMR}$  (300 MHz,  $\text{CDCl}_3$ , 25 °C):  $\delta$  = 10.85 (s, 1H), 7.82 (d,  $J$  = 2.4 Hz, 1H), 7.68 (d,  $J$  = 2.4 Hz, 1H), 7.50 (d,  $J$  = 2.4 Hz, 1H), 7.38 (d,  $J$  = 2.4 Hz, 1H), 1.67 (s, 6H), 1.36 (s, 9H), 1.34 (s, 9H).

#### 9.5.5 4-(5,5'-Dimethyl-1,3-dioxane)-5-bromo-2,7-di-*tert*-butyl-9,9-dimethylxanthene (**102**)

A 100 mL round-bottom flask fitted with a Dean-Stark trap and reflux condenser was charged with a solution of aldehyde **101** (1.07 g, 2.50 mmol), neopentyl glycol (0.27 g, 2.62 mmol) and benzenesulfonic acid (5 mg) in toluene (50 mL) under an  $\text{N}_2$  atmosphere. The reaction was refluxed under nitrogen for 2 h, cooled to room temperature, and washed with a saturated aq  $\text{NaHCO}_3$  solution and then  $\text{H}_2\text{O}$ . After drying with  $\text{Na}_2\text{SO}_4$  and evaporation to dryness, purification by column chromatography (silica gel, dichloromethane) gave bromide **102** as a white solid (1.2 g, 93% yield).  $^1\text{H NMR}$  (300 MHz,  $\text{CDCl}_3$ , 25 °C):  $\delta$  = 7.61 (d,  $J$  = 2.4 Hz, 1H), 7.44 (d,  $J$  = 2.4 Hz, 1H), 7.39 (d,  $J$  = 2.4 Hz, 1H), 7.34 (d,  $J$  = 2.4 Hz, 1H), 6.08 (s, 1H), 3.82 (s, 4H), 1.63 (s, 6H), 1.37 (s, 3H), 1.36 (s, 9H), 1.34 (s, 9H), 0.85 (s, 3H).

#### 9.5.6 4-(5,5'-Dimethyl-1,3-dioxane)-5-hydroxycarbonyl-2,7-di-*tert*-butyl-9,9-dimethylxanthene (**103**)

Phenyllithium (1.2 mL, 1.8 M solution in cyclohexane) was added over a period of 10 min to a solution of bromide **102** (1.03 g, 2.0 mmol) in THF (40 mL) cooled to  $-78$  °C under an  $\text{N}_2$  atmosphere. After stirring at  $-78$  °C under nitrogen for 1 h,  $\text{CO}_2$  gas was bubbled into the lithiate at a rapid rate until the yellow color of the solution had faded. The mixture was then allowed to warm to room temperature and stirred overnight. The reaction was quenched with 2 N HCl (15 mL) and the organic solvent was removed by rotary evaporation. The resulting white precipitate was filtered and washed with water. Purification by column chromatography (silica gel, dichloromethane) delivered **103** as a white powder (0.83 g, 86% yield).  $^1\text{H NMR}$  (300 MHz,  $\text{CDCl}_3$ , 25 °C):  $\delta$  = 8.10 (d,  $J$  = 2.4 Hz, 1H), 7.67 (d,  $J$  = 2.4 Hz, 1H), 7.66 (d,  $J$  = 2.4 Hz, 1H), 7.46 (d,  $J$  = 2.4 Hz, 1H), 5.75 (s, 1H), 3.83 (s, 4H), 1.67 (s, 6H), 1.36 (s, 18H), 1.30 (s, 3H), 0.85 (s, 3H).

#### 9.5.7 4-Formyl-5-hydroxycarbonyl-2,7-di-*tert*-butyl-9,9-dimethylxanthene (**104**)

Acetal **103** (1.5 g, 3.12 mmol) was dissolved in trifluoroacetic acid (10 mL) and water (3 mL) was added. The solution was stirred at room temperature for 24 h and concentrated under

vacuum to give an orange oil. Water (20 mL) was added and the resulting precipitate was filtered. Purification by column chromatography (silica gel, dichloromethane) afforded **104** as a white compound (1.10 g, 89% yield).  $^1\text{H NMR}$  (300 MHz,  $\text{CDCl}_3$ , 25 °C):  $\delta$  = 10.16 (s, 1H), 8.24 (d,  $J$  = 2.4 Hz, 1H), 7.76 (d,  $J$  = 2.4 Hz, 1H), 7.72 (d,  $J$  = 2.4 Hz, 1H), 7.68 (d,  $J$  = 2.4 Hz, 1H), 1.71 (s, 6H), 1.41 (s, 9H), 1.38 (s, 9H).

#### 9.5.8 4-Formyl-5-methoxycarbonyl-2,7-di-*tert*-butyl-9,9-dimethylxanthene (105)

A solution of acid **104** (1.0 g, 2.53 mmol) in methanol (50 mL) and  $\text{H}_2\text{SO}_4$  (2 mL) was refluxed for 4 h. The solvent was removed in vacuo, water (20 mL) was added to the residue and resulting precipitate was filtered. The solid was redissolved in dichloromethane (50 mL), washed with 15% HCl and water, dried over  $\text{Na}_2\text{SO}_4$ , and taken to dryness by rotary evaporation. Purification by column chromatography (silica gel, dichloromethane) provided ester **105** as a white powder (0.96 g, 93% yield).  $^1\text{H NMR}$  (300 MHz,  $\text{CDCl}_3$ , 25 °C):  $\delta$  = 10.79 (s, 1H), 7.82 (d,  $J$  = 2.4 Hz, 1H), 7.81 (d,  $J$  = 2.4 Hz, 1H), 7.68 (d,  $J$  = 2.4 Hz, 1H), 7.63 (d,  $J$  = 2.4 Hz, 1H), 3.99 (s, 3H), 1.69 (s, 6H), 1.38 (s, 9H), 1.37 (s, 9H).

#### 9.5.9a 5-(4-(5-Methoxycarbonyl-2,7-di-*tert*-butyl-9,9-dimethylxanthene))-10,15,20-trimesitylporphyrin, $\text{H}_2(\text{HPX-CO}_2\text{Me})$ (106)

A solution of aldehyde **105** (0.41 g, 1 mmol), mesitaldehyde (2.22 g, 15 mmol) and pyrrole (1.11 mL, 16 mmol) in chloroform (1.6 L) was purged with nitrogen for 20 min after which a portion of  $\text{BF}_3 \cdot \text{OEt}_2$  (0.67 mL, 5.28 mmol) was added via syringe. The solution was stirred at room temperature under nitrogen in the dark for 90 min and 2,3-dichloro-5,6-dicyano-1,4-benzoquinone (2.72 g, 12 mmol) was added to the reaction. After stirring for an additional hour under nitrogen, the solvent was removed by rotary evaporation. The dark residue was redissolved in dichloromethane (300 mL) and filtered. The filtrate was loaded directly onto a silica gel column packed with dichloromethane and eluted with dichloromethane until no more porphyrinic product was detected. Several subsequent recrystallizations from dichloromethane and methanol removed a significant portion of the symmetric tetramesitylporphyrin ( $\text{H}_2\text{TMP}$ ) by-product. Final purification by column chromatography (silica gel, 4:1 hexanes/dichloromethane to 2:1 hexanes/dichloromethane) afforded porphyrin **106** as a plum purple microcrystalline solid (270 mg, 26% yield based on bridge **105**).  $^1\text{H NMR}$  (500 MHz,  $\text{CDCl}_3$ , 25 °C):  $\delta$  = 8.79 (d,  $J$  = 4.8 Hz, 2H), 8.62-8.72 (br, 6H), 7.90 (d,  $J$  = 2.4 Hz, 1H), 7.88 (d,  $J$  = 2.4 Hz, 1H), 7.69 (d,  $J$  = 2.4 Hz, 1H), 7.27-7.38 (m, 6H), 2.67 (s, 3H), 2.66 (s, 6H), 2.13 (s, 3H), 1.99 (s, 6H), 1.98 (s, 6H), 1.88 (s, 6H), 1.76 (s, 3H), 1.52 (s, 9H), 1.31 (s, 9H), -0.08 (s, 3H), -2.37 (s, 2H). Anal. Calcd for  $\text{C}_{72}\text{H}_{74}\text{N}_4\text{O}_3$ : C, 82.88; H, 7.15; N, 5.37. Found: C, 82.49; H, 7.10; N, 5.58. HRFABMS ( $\text{M}^+$ ) calcd for  $\text{C}_{72}\text{H}_{74}\text{N}_4\text{O}_3$   $m/z$  1042.5761, found 1042.5759.

**9.5.9b 5-(4-(5-Methoxycarbonyl-2,7-di-*tert*-butyl-9,9-dimethylxanthene))-10,15,20-trimesitylporphyrin, H<sub>2</sub>(HPX-CO<sub>2</sub>Me) (106), Suzuki Method**

Under a nitrogen atmosphere, the solids **120** (30 mg, 0.065 mmol), **94** (68 mg, 0.080 mmol), Na<sub>2</sub>CO<sub>3</sub> (25 mg), and Pd(PPh<sub>3</sub>)<sub>4</sub> (15 mg, 0.0130 mmol) were combined in a 50-mL Schlenk flask. DMF (10 mL) and deionized water (1 mL) were added and the mixture was heated at reflux overnight under nitrogen. The reaction was taken to dryness and the residue was redissolved in dichloromethane (25 mL), stirred with 6 N HCl (25 mL) for 30 min, and washed with water (7 × 25 mL). The organic layer was separated, dried over Na<sub>2</sub>SO<sub>4</sub>, and the solvent was removed by rotary evaporation. Purification by column chromatography (silica gel, 2:1 hexanes/dichloromethane) delivered **106** as a royal purple powder (47 mg, 69% yield). Complex **106** obtained by this synthetic method gave comparable high-resolution mass spectral and elemental analyses to batches prepared by Lindsey cyclizations.

**9.5.9 5-(4-(5-Methoxycarbonyl-2,7-di-*tert*-butyl-9,9-dimethylxanthene))-10,15,20-triphenylporphyrin, H<sub>2</sub>(HTPPX-CO<sub>2</sub>Me) (107)**

A solution of aldehyde **105** (0.41 g, 1 mmol), benzaldehyde (1.60 g, 15 mmol) and pyrrole (1.11 mL, 16 mmol) in chloroform (1.6 L) was purged with nitrogen for 45 min after which a portion of BF<sub>3</sub>•OEt<sub>2</sub> (0.67 mL, 5.28 mmol) was added via syringe. The solution was stirred at room temperature under nitrogen in the dark for 1 h and 2,3-dichloro-5,6-dicyano-1,4-benzoquinone (2.72 g, 12 mmol) was added to the reaction. After stirring for an additional hour under nitrogen, the solvent was removed by rotary evaporation. The dark residue was redissolved in dichloromethane (250 mL) containing 2% triethylamine and filtered. The filtrate was loaded directly onto a silica gel column packed with dichloromethane and eluted with dichloromethane until no more porphyrinic product was detected. Several subsequent recrystallizations from dichloromethane and methanol removed a significant portion of the symmetric tetraphenylporphyrin (H<sub>2</sub>TPP) by-product. Final purification by column chromatography (silica gel, 2:1 hexanes/dichloromethane) gave porphyrin **107** as a royal purple microcrystalline solid (200 mg, 22% yield based on bridge **105**). <sup>1</sup>H NMR (500 MHz, CDCl<sub>3</sub>, 25 °C): δ = 8.84 (d, *J* = 19 Hz, 9H), 8.21-8.30 (m, 6H), 8.01 (d, *J* = 2.5 Hz, 1H), 7.87 (d, *J* = 2.5 Hz, 1H), 7.74-7.79 (m, 9H), 7.64 (d, *J* = 2.5 Hz, 1H), 7.30 (d, *J* = 2.5 Hz, 1H), 1.92 (s, 6H), 1.52 (s, 9H), 1.25 (s, 9H), -0.34 (s, 3H), -2.66 (s, 2H). Anal. Calcd for C<sub>63</sub>H<sub>56</sub>N<sub>4</sub>O<sub>3</sub>: C, 82.50; H, 6.15; N, 6.11. Found: C, 82.28; H, 6.52; N, 5.94. HRFABMS (M<sup>+</sup>) calcd for C<sub>63</sub>H<sub>56</sub>N<sub>4</sub>O<sub>3</sub> *m/z* 916.4352, found 916.4355.



**9.5.10 5-(4-(5-Methoxycarbonyl-2,7-di-*tert*-butyl-9,9-dimethylxanthene))-10,15,20-tri(2,6-dichlorophenyl)porphyrin, H<sub>2</sub>(HTDCPPX-CO<sub>2</sub>Me) (108)**

A solution of aldehyde **105** (0.41 g, 1 mmol), 2,6-dichlorobenzaldehyde (2.63 g, 15 mmol) and pyrrole (1.11 mL, 16 mmol) in chloroform (1.6 L) was purged with nitrogen for 45 min after which a portion of BF<sub>3</sub>·OEt<sub>2</sub> (0.67 mL, 5.28 mmol) was added via syringe. The solution was stirred at room temperature under nitrogen in the dark for 90 min and 2,3-dichloro-5,6-dicyano-1,4-benzoquinone (2.72 g, 12 mmol) was added to the reaction. After stirring for an additional hour under nitrogen, the solvent was removed by rotary evaporation. The dark residue was redissolved in dichloromethane (500 mL) and filtered. The filtrate was loaded directly onto a silica gel column packed with dichloromethane and eluted with dichloromethane until no more porphyrinic product was detected. Purification by repeated column chromatography (silica gel, 1:1 hexanes/dichloromethane) furnished porphyrin **108** as a purple powder (210 mg, 20% yield based on bridge **105**). <sup>1</sup>H NMR (500 MHz, CDCl<sub>3</sub>, 25 °C): δ = 8.83 (d, *J* = 4.5 Hz, 2H), 8.68 (br, 4H), 8.63 (d, *J* = 4.5 Hz, 2H), 7.69-7.85 (m, 11H), 7.63 (d, *J* = 2.5 Hz, 1H), 7.34 (d, *J* = 2.5 Hz, 1H), 1.92 (s, 6H), 1.47 (s, 9H), 1.25 (s, 9H), -0.02 (s, 3H), -2.46 (s, 2H). Anal. Calcd for C<sub>63</sub>H<sub>50</sub>N<sub>4</sub>O<sub>3</sub>Cl<sub>6</sub>: C, 67.33; H, 4.48; N, 4.99. Found: C, 67.50; H, 4.58; N, 5.11. HRFABMS (M<sup>+</sup>) calcd for C<sub>63</sub>H<sub>50</sub>Cl<sub>6</sub>N<sub>4</sub>O<sub>3</sub> *m/z* 1120.2014, found 1120.2014.

**9.5.11 5-(4-(5-Methoxycarbonyl-2,7-di-*tert*-butyl-9,9-dimethylxanthene))-10,15,20-tri(2,6-dimethoxyphenyl)porphyrin, H<sub>2</sub>(HTDMPPX-CO<sub>2</sub>Me) (109)**

A solution of aldehyde **105** (0.41 g, 1 mmol), 2,6-dimethoxybenzaldehyde (2.49 g, 15 mmol) and pyrrole (1.11 mL, 16 mmol) in chloroform (1.6 L) was purged with nitrogen for 1 h after which a portion of BF<sub>3</sub>·OEt<sub>2</sub> (0.67 mL, 5.28 mmol) was added via syringe. The solution was stirred at room temperature under nitrogen in the dark for 1 h and 2,3-dichloro-5,6-dicyano-1,4-benzoquinone (4.08 g, 18 mmol) was added to the reaction. After stirring for an additional hour under nitrogen, the solvent was removed by rotary evaporation. The dark residue was redissolved in dichloromethane (250 mL) and filtered. The filtrate was loaded directly onto a silica gel column packed with dichloromethane and eluted with dichloromethane until no more porphyrinic product was detected. Purification by repeated column chromatography (silica gel, dichloromethane) delivered porphyrin **109** as a reddish purple powder (220 mg, 20% yield based on bridge **105**). <sup>1</sup>H NMR (500 MHz, CDCl<sub>3</sub>, 25 °C): δ = 8.68-8.71 (m, 6H), 7.86 (d, *J* = 2.5 Hz, 1H), 7.81 (d, *J* = 2.5 Hz, 1H), 7.68-7.73 (m, 4H), 7.62 (d, *J* = 2.5 Hz, 1H), 7.37 (d, *J* = 2.5 Hz, 1H), 7.04 (d, *J* = 9.5 Hz, 1H), 6.97-7.00 (m, 6H), 3.68 (s, 3H), 3.55 (s, 6H), 3.51 (s, 6H), 3.47 (s, 3H), 1.92 (s, 6H), 1.46 (s, 9H), 1.25 (s, 9H), 0.05 (s, 3H), -2.46 (s, 2H). Anal. Calcd for

C<sub>69</sub>H<sub>68</sub>N<sub>4</sub>O<sub>9</sub>: C, 75.53; H, 6.25; N, 5.11. Found: C, 75.28; H, 6.52; N, 4.94. HRFABMS (M+) calcd for C<sub>69</sub>H<sub>68</sub>N<sub>4</sub>O<sub>9</sub> *m/z* 1096.4986, found 1096.4929.

**9.5.12 Zinc(II) 5-(4-(5-methoxycarbonyl-2,7-di-*tert*-butyl-9,9-dimethylxanthene))-10,15,20-trimesitylporphyrin, Zn(HPX-CO<sub>2</sub>Me) (110)**

A saturated methanolic solution of Zn(OAc)<sub>2</sub>·2H<sub>2</sub>O (5 mL) and a solution of **109** (250 mg, 0.040 mmol) in 15 mL chloroform were combined and refluxed for 20 min. The solvent was removed by rotary evaporation. The remaining solid was purified by flash column chromatography (silica gel, 3:1 dichloromethane) followed by recrystallization from dichloromethane/methanol to yield **110** as a ruby red solid in quantitative yield. <sup>1</sup>H NMR (500 MHz, CDCl<sub>3</sub>, 25 °C): δ = 8.83 (d, *J* = 4.8 Hz, 2H), 8.68-8.74 (m, 6H), 7.85 (d, *J* = 2.4 Hz, 1H), 7.83 (d, *J* = 2.4 Hz, 1H), 7.65 (d, *J* = 2.4 Hz, 1H), 7.31 (br, 1H), 7.22-7.30 (m, 6H), 2.64 (s, 3H), 2.62 (s, 6H), 2.05 (s, 3H), 1.97 (s, 6H), 1.94 (s, 6H), 1.77 (s, 6H), 1.72 (s, 3H), 1.47 (s, 9H), 1.26 (s, 9H), 0.30 (s, 3H). Anal. Calcd for C<sub>72</sub>H<sub>74</sub>N<sub>4</sub>O<sub>3</sub>Zn: C, 78.14; H, 6.56; N, 5.06. Found: C, 78.53; H, 7.47; N, 4.81. HRFABMS (M+) calcd for C<sub>72</sub>H<sub>72</sub>N<sub>4</sub>O<sub>3</sub>Zn *m/z* 1104.4896, found 1104.4900.

**9.5.14a 5-(4-(5-Hydroxycarbonyl-2,7-di-*tert*-butyl-9,9-dimethylxanthene))-10,15,20-trimesitylporphyrin, H<sub>2</sub>(HPX-CO<sub>2</sub>H) (111)**

Zinc(II) complex **110** (100 mg, 0.09 mmol) was dissolved in THF (20 mL) and 20% aq NaOH (10 mL) was added. The resulting mixture was refluxed for 3 days under an N<sub>2</sub> atmosphere. The organic solvent was removed by rotary evaporation and the precipitate was filtered and washed with water until the washings were at neutral pH. The solid was redissolved in dichloromethane (50 mL), washed with 10% HCl (2 × 25 mL) and water (5 × 25 mL) and dried over Na<sub>2</sub>SO<sub>4</sub>. Removal of the solvent and purification by column chromatography (silica gel, 2:1 hexanes/dichloromethane to dichloromethane) provided porphyrin **111** as a royal purple powder (83 mg, 90% yield). <sup>1</sup>H NMR (500 MHz, CDCl<sub>3</sub>, 25 °C): δ = 8.69 (d, *J* = 4.8 Hz, 2H), 8.60-8.67 (br, 6H), 8.04 (d, *J* = 2.4 Hz, 1H), 7.91 (d, *J* = 2.4 Hz, 1H), 7.73 (d, *J* = 2.4 Hz, 1H), 7.69 (d, *J* = 2.4 Hz, 1H), 7.24-7.34 (m, 6H), 2.65 (s, 3H), 2.62 (s, 6H), 2.00 (s, 3H), 1.97 (s, 6H), 1.92 (s, 6H), 1.89 (s, 3H), 1.85 (s, 6H), 1.54 (s, 9H), 1.27 (s, 9H), -2.44 (s, 2H). Anal. Calcd for C<sub>71</sub>H<sub>72</sub>N<sub>4</sub>O<sub>3</sub>: C, 82.84; H, 7.05; N, 5.44. Found: C, 82.47; H, 7.19; N, 5.71. HRFABMS (M+) calcd for C<sub>71</sub>H<sub>72</sub>N<sub>4</sub>O<sub>3</sub> *m/z* 1028.5604, found 1028.5579.

**9.5.14b 5-(4-(5-Hydroxycarbonyl-2,7-di-*tert*-butyl-9,9-dimethylxanthene))-10,15,20-trimesitylporphyrin, H<sub>2</sub>(HPX-CO<sub>2</sub>H) (111), Suzuki Method**

Under a nitrogen atmosphere, the solids **119** (30 mg, 0.067 mmol), **94** (68 mg, 0.080 mmol), Na<sub>2</sub>CO<sub>3</sub> (25 mg), and Pd(PPh<sub>3</sub>)<sub>4</sub> (15 mg, 0.0130 mmol) were combined in a 50-mL Schlenk

flask. DMF (10 mL) and deionized water (1 mL) were added and the mixture was heated at reflux overnight under nitrogen. The reaction was taken to dryness and the residue was redissolved in dichloromethane (25 mL), stirred with 6 N HCl (25 mL) for 30 min, and washed with water (7 × 25 mL). The organic layer was separated, dried over Na<sub>2</sub>SO<sub>4</sub>, and the solvent was removed by rotary evaporation. Purification by column chromatography (silica gel, 2:1 hexanes/dichloromethane to dichloromethane) followed by recrystallization from dichloromethane/methanol solutions delivered **111** as a royal purple powder (50 mg, 72% yield). Complex **111** obtained by this synthetic method gave comparable high-resolution mass spectral and elemental analyses to batches prepared by Lindsey cyclizations.

#### **9.5.15 -4-(5-Hydroxycarbonyl-2,7-di-*tert*-butyl-9,9-dimethylxanthene))-10,15,20-triphenylporphyrin, H<sub>2</sub>(HTPPX-CO<sub>2</sub>H) (112)**

The zinc(II) complex of **107** (60 mg) was prepared as described for **110** and dissolved in THF (20 mL). A portion of 20% aq NaOH (10 mL) was added and the resulting mixture was refluxed for 3 days under an N<sub>2</sub> atmosphere. The organic solvent was removed by rotary evaporation and the precipitate was filtered and washed with water until the washings were at neutral pH. The solid was redissolved in dichloromethane (25 mL), washed with 6 M HCl (1 × 10 mL) and water (7 × 25 mL) and dried over Na<sub>2</sub>SO<sub>4</sub>. Removal of the solvent and purification by column chromatography (silica gel, 1:1 hexanes/dichloromethane to dichloromethane) gave porphyrin **112** as purple flakes (56 mg, 95% yield based on **107**). <sup>1</sup>H NMR (500 MHz, CDCl<sub>3</sub>, 25 °C): δ = 8.77-8.85 (m, 9H), 8.19-8.31 (m, 6H), 8.08 (d, *J* = 2.5 Hz, 1H), 7.93 (d, *J* = 2.5 Hz, 1H), 7.72-7.80 (m, 9H), 7.66 (d, *J* = 2.5 Hz, 1H), 1.97 (s, 6H), 1.27 (s, 9H), 1.25 (s, 9H), -2.69 (s, 2H). Anal. Calcd for C<sub>62</sub>H<sub>54</sub>N<sub>4</sub>O<sub>3</sub>: C, 82.45; H, 6.03; N, 6.20. Found: C, 82.44; H, 6.13; N, 6.07. HRESIMS (MH<sup>+</sup>) calcd for C<sub>62</sub>H<sub>55</sub>N<sub>4</sub>O<sub>3</sub> *m/z* 903.4269, found 903.4286.

#### **9.5.16 5-(4-(5-Hydroxycarbonyl-2,7-di-*tert*-butyl-9,9-dimethylxanthene))-10,15,20-tri(2,6-dichlorophenyl)porphyrin, H<sub>2</sub>(HTDCPPX-CO<sub>2</sub>H) (113)**

The zinc(II) complex of **108** (50 mg) was prepared as described for **110** and dissolved in THF (16 mL). A portion of 20% aq NaOH (8 mL) was added and the resulting mixture was refluxed for 3 days under an N<sub>2</sub> atmosphere. The organic solvent was removed by rotary evaporation and the precipitate was filtered and washed with water until the washings were at neutral pH. The solid was redissolved in dichloromethane (20 mL), washed with 6 M HCl (1 × 7 mL) and water (7 × 25 mL) and dried over Na<sub>2</sub>SO<sub>4</sub>. Removal of the solvent and purification by column chromatography (silica gel, 1:1 hexanes/dichloromethane to dichloromethane) delivered porphyrin **113** as a purple powder (47 mg, 95% yield based on **108**). <sup>1</sup>H NMR (500 MHz, CDCl<sub>3</sub>, 25 °C): δ = 8.78 (d, *J* = 4.5 Hz, 2H), 8.63-8.68 (m, 5H), 8.04 (d, *J* = 2.5 Hz, 1H), 7.91 (d, *J* = 2.5

Hz, 1H), 7.77-7.83 (m, 6H), 7.65-7.72 (m, 6H), 1.95 (s, 6H), 1.53 (s, 9H), 1.25 (s, 9H), -2.46 (s, 2H). Anal. Calcd for  $C_{62}H_{48}N_4O_3Cl_6$ : C, 67.10; H, 4.36; N, 5.05. Found: C, 67.28; H, 4.12; N, 5.25. HRESIMS (MH<sup>+</sup>) calcd for  $C_{62}H_{49}Cl_6N_4O_3$   $m/z$  1107.1930, found 1107.1922.

**9.5.17 5-(4-(5-Hydroxycarbonyl-2,7-di-*tert*-butyl-9,9-dimethylxanthene))-10,15,20-tri(2,6-dimethoxyphenyl)porphyrin, H<sub>2</sub>(HTDMPPX-CO<sub>2</sub>H) (114)**

The zinc(II) complex of **109** (145 mg) was prepared as described for **110** and dissolved in THF (45 mL). A portion of 20% aq NaOH (20 mL) was added and the resulting mixture was refluxed for 3 days under an N<sub>2</sub> atmosphere. The organic solvent was removed by rotary evaporation and the precipitate was filtered and washed with water until the washings were at neutral pH. The solid was redissolved in dichloromethane (100 mL), washed with 10% HCl (1 × 100 mL) and water (5 × 50 mL) and dried over Na<sub>2</sub>SO<sub>4</sub>. Removal of the solvent and purification by column chromatography (silica gel, 30:1 dichloromethane/methanol) provided porphyrin **114** as a purple powder (143 mg, quantitative yield based on **109**). <sup>1</sup>H NMR (500 MHz, CDCl<sub>3</sub>, 25 °C):  $\delta$  = 8.71-8.74 (m, 6H), 8.08 (d,  $J$  = 2.5 Hz, 1H), 7.85 (d,  $J$  = 2.5 Hz, 1H), 7.67-7.74 (m, 4H), 7.65 (d,  $J$  = 2.5 Hz, 1H), 7.51 (d,  $J$  = 2.5 Hz, 1H), 6.98-7.01 (m, 6H), 3.56 (s, 6H), 3.53 (s, 6H), 3.52 (s, 6H), 1.92 (s, 6H), 1.52 (s, 9H), 1.24 (s, 9H), -2.46 (s, 2H). Anal. Calcd for  $C_{68}H_{66}N_4O_9$ : C, 75.39; H, 6.14; N, 5.17. Found: C, 75.40; H, 4.12; N, 5.07. HRESIMS (MH<sup>+</sup>) calcd for  $C_{68}H_{67}N_4O_9$   $m/z$  1083.4903, found 1083.4899.

**9.5.18 5-(4-(5-Aminocarbonyl-2,7-di-*tert*-butyl-9,9-dimethylxanthene))-10,15,20-trimesitylporphyrin, H<sub>2</sub>(HPX-CONH<sub>2</sub>) (115)**

Thionyl chloride (2 mL) was added to a solution of porphyrin **111** (103 mg, 0.1 mmol) in dry CH<sub>2</sub>Cl<sub>2</sub> (20 mL) and the resulting solution was refluxed for 90 min under an N<sub>2</sub> atmosphere. The solvent and excess thionyl chloride were removed by rotary evaporation. The residue was further dried under high vacuum, redissolved in dry CH<sub>2</sub>Cl<sub>2</sub> (35 mL), and NH<sub>3</sub> gas was bubbled through the solution at a rapid rate for 2 min. The reaction was washed with water (3 × 25 mL) and dried over Na<sub>2</sub>SO<sub>4</sub>. Purification by column chromatography (silica gel, 100:1 dichloromethane/methanol) followed by recrystallization from dichloromethane/methanol afforded porphyrin **115** as a purple solid (92 mg, 90% yield). <sup>1</sup>H NMR (300 MHz, CDCl<sub>3</sub>, 25 °C):  $\delta$  = 8.78 (d,  $J$  = 4.8 Hz, 2H), 8.70-8.63 (m, 6H), 8.12 (d,  $J$  = 2.4 Hz, 1H), 7.90 (d,  $J$  = 2.4 Hz, 1H), 7.60 (d,  $J$  = 2.4 Hz, 1H), 7.58 (d,  $J$  = 2.4 Hz, 1H), 7.34-7.25 (m, 6H), 2.65 (s, 3H), 2.62 (s, 6H), 2.05 (s, 3H), 1.94 (s, 6H), 1.87 (s, 15H), 1.56 (s, 9H), 1.22 (s, 9H), -2.53 (s, 2H); Anal. Calcd for  $C_{71}H_{73}N_5O_2$ : C, 82.92; H, 7.15; N, 6.81. Found: C, 82.69; H, 6.96; N, 7.08. HRFABMS (MH<sup>+</sup>) calcd for  $C_{71}H_{74}N_5O_2$   $m/z$  1028.5843, found 1028.5810.

### 9.5.19 5,15-Bis-(4-(5-methoxycarbonyl-2,7-di-*tert*-butyl-9,9-dimethylxanthene))-10,20-dimesitylporphyrin, H<sub>2</sub>(HPBX-CO<sub>2</sub>Me) (117a and 117b)

A solution of **105** (204 mg, 0.5 mmol) and 5-mesityldipyrromethane (**116**) (132 mg, 0.5 mmol) in dichloromethane (100 mL) was purged with nitrogen for 30 min after which a portion of BF<sub>3</sub>·OEt<sub>2</sub> (13  $\mu$ L) was added via syringe. The solution was stirred at room temperature under nitrogen in the dark for 90 min and 2,3-dichloro-5,6-dicyano-1,4-benzoquinone (227 mg, 1 mmol) was added to the reaction. After stirring for an additional 30 min under nitrogen, the reaction was loaded directly onto a silica gel column packed with dichloromethane and eluted with dichloromethane until no more porphyrinic product was detected. Purification by column chromatography (silica gel, 1:1 hexanes/dichloromethane) separated the  $\alpha,\alpha$ - and  $\alpha,\beta$ -atropisomers (**117a** and **117b**, respectively) from the crude reaction mixture in 8% yield each.

**117a**: <sup>1</sup>H NMR (500 MHz, CDCl<sub>3</sub>, 25 °C):  $\delta$  = 8.77 (d, *J* = 4.5 Hz, 4H), 8.66 (d, *J* = 4.5 Hz, 4H), 7.94 (d, *J* = 2.5 Hz, 2H), 7.86 (d, *J* = 2.5 Hz, 2H), 7.65 (d, *J* = 2.5 Hz, 2H), 7.34 (d, *J* = 2.5 Hz, 2H), 7.65 (d, *J* = 22 Hz, 4H), 2.61 (s, 6H), 2.01 (s, 6H), 1.94 (s, 12H), 1.82 (d, *J* = 4 Hz, 6H), 1.49 (s, 18H), 1.26 (s, 18H), -0.202 (s, 6H), -2.41 (s, 2H). Anal. Calcd for C<sub>88</sub>H<sub>94</sub>N<sub>4</sub>O<sub>6</sub>: C, 81.07; H, 7.27; N, 4.30. Found: C, 80.80; H, 6.87; N, 4.22. HRFABMS (M<sup>+</sup>) calcd for C<sub>88</sub>H<sub>94</sub>N<sub>4</sub>O<sub>6</sub> *m/z*, 1302.7173, found 1302.7169. The  $\alpha,\beta$ -atropisomer eluted first on the column.

**117b**: <sup>1</sup>H NMR (500 MHz, CDCl<sub>3</sub>, 25 °C):  $\delta$  = 8.77 (d, *J* = 4.5 Hz, 4H), 8.64 (d, *J* = 4.5 Hz, 4H), 8.10 (d, *J* = 2.5 Hz, 2H), 7.85 (d, *J* = 2.5 Hz, 2H), 7.61 (d, *J* = 2.5 Hz, 2H), 7.26 (d, *J* = 2.5 Hz, 6H), 2.60 (s, 6H), 1.92 (s, 12H), 1.90 (s, 12H), 1.53 (s, 18H), 1.23 (s, 18H), -0.492 (s, 6H), -2.39 (s, 2H). Anal. Calcd for C<sub>88</sub>H<sub>94</sub>N<sub>4</sub>O<sub>6</sub>: C, 81.07; H, 7.27; N, 4.30. Found: C, 80.93; H, 7.00; N, 4.53. HRFABMS (M<sup>+</sup>) calcd for C<sub>88</sub>H<sub>94</sub>N<sub>4</sub>O<sub>6</sub> *m/z* 1302.7173, found 1302.7168.

### 9.5.20 4-Hydroxycarbonyl-5-bromo-2,7-di-*tert*-butyl-9,9-dimethylxanthene (119)

Phenyllithium (1.2 mL, 1.8 M solution in cyclohexane) was added over a period of 10 min to a solution of xanthene dibromide **83** (1.00 g, 2.08 mmol) in dry THF (40 mL) cooled to -78 °C under an nitrogen atmosphere. After stirring at -78 °C under nitrogen for 1 h, CO<sub>2</sub> gas was bubbled into the lithiate at a rapid rate until the yellow color of the solution had faded. The mixture was then allowed to warm to room temperature and stirred overnight. The reaction was quenched with 2N HCl (15 mL) and the organic solvent was removed by rotary evaporation. The resulting white precipitate was filtered and washed with water. Purification by column chromatography (silica gel, dichloromethane) delivered **119** as a white powder (0.7 g, 75% yield). <sup>1</sup>H NMR (500 MHz, CDCl<sub>3</sub>, 25 °C):  $\delta$  = 8.18 (d, *J* = 4 Hz, 1H, ArH), 7.66 (d, *J* = 4 Hz, 1H, ArH), 7.50 (d, *J* = 4 Hz, 1H, ArH), 7.40 (d, *J* = 4 Hz, 1H, ArH), 1.68 (s, 6H, CH<sub>3</sub>), 1.37 (s, 9H, CH<sub>3</sub>), 1.35 (s, 9H, CH<sub>3</sub>).

### 9.5.21 4-Methoxycarbonyl-5-bromo-2,7-di-*tert*-butyl-9,9-dimethylxanthene (120)

A solution of acid **119** (1.0 g, 2.53 mmol) in methanol (50 mL) and H<sub>2</sub>SO<sub>4</sub> (2 mL) was refluxed for 4 h. The solvent was removed in vacuo, water (20 mL) was added to the residue and resulting precipitate was filtered. The solid was redissolved in dichloromethane (50 mL), washed with 15% HCl and water, dried over Na<sub>2</sub>SO<sub>4</sub>, and taken to dryness by rotary evaporation. Purification by column chromatography (silica gel, dichloromethane) provided ester **120** as a white powder (0.96 g, 93% yield). <sup>1</sup>H NMR (500 MHz, CDCl<sub>3</sub>, 25 °C):  $\delta$  = 7.72 (d, *J* = 4 Hz, 1H, ArH), 7.55 (d, *J* = 4 Hz, 1H, ArH), 7.46 (d, *J* = 4 Hz, 1H, ArH), 7.32 (d, *J* = 4 Hz, 1H, ArH), 4.02 (s, 3H, CH<sub>3</sub>), 1.64 (s, 6H, CH<sub>3</sub>), 1.35 (s, 9H, CH<sub>3</sub>), 1.33 (s, 9H, CH<sub>3</sub>).

### 9.5.22 5-(4-(6-Hydroxycarbonyldibenzofuran))-10,15,20-trimesitylporphyrin, H<sub>2</sub>(HPD-CO<sub>2</sub>H) (121)

Under a nitrogen atmosphere, a mixture of 6-bromo-4-dibenzofurancarboxylic acid **118** (42 mg, 0.144 mmol), **94** (135 mg, 0.159 mmol), Na<sub>2</sub>CO<sub>3</sub> (49 mg, 0.462 mmol), and Pd(PPh<sub>3</sub>)<sub>4</sub> (25 mg, 0.0216 mmol) were combined in a Schlenk flask. DMF (20 mL) and deionized water (2 mL) were added and the mixture was refluxed for 19 h under nitrogen. The solvent was removed and the residue was redissolved in dichloromethane (30 mL) and stirred with 6 N HCl (20 mL) for 30 min. The organic layer was separated and washed with 20% aq Na<sub>2</sub>CO<sub>3</sub> (20 mL) followed by water (2 × 50 mL). The solvent was evaporated and the residue was purified by column chromatography (silica gel, 2:1 hexanes/dichloromethane to 1:1 ethyl acetate/dichloromethane) to afford **121** as a purple solid (85 mg, 67% yield). <sup>1</sup>H NMR (300 MHz, CDCl<sub>3</sub>, 25 °C):  $\delta$  = 8.66 (m, 8H), 8.41 (m, 2H), 8.30 (dd, *J*<sub>1</sub> = 7.6, *J*<sub>2</sub> = 1.3 Hz, 1H), 8.06 (dd, *J*<sub>1</sub> = 7.8, *J*<sub>2</sub> = 1.3 Hz, 1H), 7.85 (t, *J* = 7.6 Hz, 1H), 7.52 (t, *J* = 7.8 Hz, 1H), 7.30 (s, 1H), 7.29 (s, 1H), 7.26 (s, 4H), 2.65 (s, 3H), 2.62 (s, 6H), 1.91 (s, 3H), 1.88 (s, 9H), 1.87 (s, 6H), -2.46 (s, 2H). HRESIMS (MH<sup>+</sup>) calcd for C<sub>60</sub>H<sub>51</sub>N<sub>4</sub>O<sub>3</sub> *m/z* 875.3956, found 875.3969.

### 9.5.23 Physical Measurements

<sup>1</sup>H NMR spectra were collected at 25 °C in CDCl<sub>3</sub> (Cambridge Isotope Laboratories) at the MIT Department of Chemistry Instrumentation Facility (DCIF) using either a Mercury 300 or an Inova 500 spectrometer. All chemical shifts are reported using the standard  $\delta$  notation in parts-per-million; positive chemical shifts are to higher frequency from the given reference. High-resolution mass spectral analyses were carried out at the University of Illinois Mass Spectrometry Laboratory or the MIT Department of Chemistry Instrumentation Facility (DCIF). Elemental analyses were performed at Michigan State University.

## 9.6 References and Notes

1. Kadish, K. M.; Smith, K. M.; Guillard, R. *The Porphyrin Handbook*; Academic Press: San Diego, 2000.
2. Chang, C. J.; Brown, J. D. K.; Chang, M. C. Y.; Baker, E. A.; Nocera, D. G. In *Electron Transfer in Chemistry*; Balzani, V., Ed.; Wiley-VCH: Weinheim, Germany, 2001; Vol. 3.2.4, pp 409-461.
3. Sessler, J. L.; Wang, B.; Springs, S. L.; Brown, C. T. In *Comprehensive Supramolecular Chemistry*; Murakami, Y., Ed.; Pergamon: Oxford, 1997; Vol. 4, pp 311-336.
4. Hayashi, T.; Ogoshi, H. *Chem. Soc. Rev.* **1997**, *26*, 355-364.
5. Cukier, R. I.; Nocera, D. G. *Annu. Rev. Phys. Chem.* **1998**, *49*, 337-369.
6. Yeh, C.-Y.; Miller, S. E.; Carpenter, S. D.; Nocera, D. G. *Inorg. Chem.* **2001**, *40*, 3643-3646.
7. Deng, Y.; Roberts, J. A.; Peng, S.-M.; Chang, C. K.; Nocera, D. G. *Angew. Chem. Int. Ed.* **1997**, *36*, 2124-2127.
8. Kirby, J. P.; Roberts, J. A.; Nocera, D. G. *J. Am. Chem. Soc.* **1997**, *119*, 9230-9236.
9. Roberts, J. A.; Kirby, J. P.; Wall, S. T.; Nocera, D. G. *Inorg. Chim. Acta* **1997**, *263*, 395-405.
10. Roberts, J. A.; Kirby, J. P.; Nocera, D. G. *J. Am. Chem. Soc.* **1995**, *117*, 8051-8052.
11. Kirby, J. P.; van Dantzig, N. A.; Chang, C. K.; Nocera, D. G. *Tetrahedron Lett.* **1995**, *36*, 3477-3480.
12. Turró, C.; Chang, C. K.; Leroi, G. E.; Cukier, R. I.; Nocera, D. G. *J. Am. Chem. Soc.* **1992**, *114*, 4013-4015.
13. Chang, C. J.; Deng, Y.; Shi, C.; Chang, C. K.; Anson, F. C.; Nocera, D. G. *Chem. Commun.* **2000**, 1355-1356.
14. Pistorio, B. J.; Chang, C. J.; Nocera, D. G. *J. Am. Chem. Soc.* **2002**, *124*, 7884-7885.
15. Chang, C. J.; Deng, Y.; Heyduk, A. F.; Chang, C. K.; Nocera, D. G. *Inorg. Chem.* **2000**, *39*, 959-966.
16. Chang, C. J.; Baker, E. A.; Pistorio, B. J.; Deng, Y.; Loh, Z.-H.; Miller, S. E.; Carpenter, S. D.; Nocera, D. G. *Inorg. Chem.* **2002**, *41*, 3102-3109.
17. Chang, C. J.; Deng, Y.; Lee, G.-H.; Peng, S.-M.; Yeh, C.-Y.; Nocera, D. G. *Inorg. Chem.* **2002**, *41*, 3008-3016.
18. Deng, Y.; Chang, C. J.; Nocera, D. G. *J. Am. Chem. Soc.* **2000**, *122*, 410-411.
19. Chang, C. K.; Kondylis, M. P. *J. Chem. Soc. Chem. Commun.* **1986**, 316-318.
20. Chang, C. K.; Liang, Y.; Aviles, G.; Peng, S.-M. *J. Am. Chem. Soc.* **1995**, *117*, 4191-4192.

21. Momenteau, M.; Reed, C. A. *Chem. Rev.* **1994**, *94*, 659-698.
22. Matsui, M.; Higashi, M.; Takeuchi, T. *J. Am. Chem. Soc.* **2000**, *122*, 5218-5219.
23. Matsu-ura, M.; Tani, F.; Nakayama, S.; Nakamura, N.; Naruta, Y. *Angew. Chem. Int. Ed.* **2000**, *39*, 1989-1991.
24. Shipps Jr., G.; Rebek Jr., J. *Tetrahedron Lett.* **1994**, *35*, 6823-6825.
25. Zhang, X.-X.; Fuhrmann, P.; Lippard, S. J. *J. Am. Chem. Soc.* **1998**, *120*, 10260-10261.
26. Zhang, X.-X.; Lippard, S. J. *J. Org. Chem.* **2000**, *65*, 5298-5305.
27. Harmjanz, M.; Scott, M. J. *Inorg. Chem.* **2000**, *39*, 5428-5429.
28. Harmjanz, M.; Gill, H. S.; Scott, M. J. *J. Am. Chem. Soc.* **2000**, *122*, 10476-10477.
29. Harmjanz, M.; Scott, M. J. *Chem. Commun.* **2000**, 397-398.
30. Harmjanz, M.; Gill, H. S.; Scott, M. J. *J. Org. Chem.* **2001**, *66*, 5374-5383.
31. Harmjanz, M.; Bozidarevic, I.; Scott, M. J. *Org. Lett.* **2001**, *3*, 2281-2284.
32. Walker, F. A.; Bowen, J. *J. Am. Chem. Soc.* **1985**, *107*, 7632-7635.
33. MacBeth, C. E.; Golombek, A. P.; Young Jr., V. G.; Tang, C.; Kuczera, K.; Hendrich, M. P.; Borovik, A. S. *Science* **2000**, *289*, 938-941.
34. Chang, C. J.; Yeh, C.-Y.; Nocera, D. G. *J. Org. Chem.* **2002**, *67*, 1403-1406.
35. Yeh, C.-Y.; Chang, C. J.; Nocera, D. G. *J. Am. Chem. Soc.* **2001**, *123*, 1513-1514.
36. Lindsey, J. S.; Wagner, R. W. *J. Org. Chem.* **1989**, *54*, 828-836.
37. Nowick, J. S.; Ballester, P.; Ebmeyer, F.; Rebek Jr., J. *J. Am. Chem. Soc.* **1990**, *112*, 8902-8906.
38. Littler, B. J.; Miller, M. A.; Hung, C.-H.; Wagner, R. W.; O'Shea, D. F.; Boyle, P. D.; Lindsey, J. S. *J. Org. Chem.* **1999**, *64*, 1391-1396.
39. Sanders, G. M.; Van Dijk, M.; Machiels, B. M.; Van Veldhuizen, A. *J. Org. Chem.* **1991**, *56*, 1301-1305.
40. Sharman, W. M.; Van Lier, J. E. *J. Porphyrins Phthalocyanines* **2000**, *4*, 441-453.
41. Deng, Y.; Chang, C. K.; Nocera, D. G. *Angew. Chem. Int. Ed.* **2000**, *39*, 1066-1068.
42. Hyslop, A. G.; Kellett, M. A.; Iovine, P. M.; Therien, M. J. *J. Am. Chem. Soc.* **1998**, *120*, 12676-12677.
43. Zhou, X.; Tse, M. K.; Wan, T. S. M.; Chan, K. S. *J. Org. Chem.* **1996**, *61*, 3590-3593.
44. Shultz, D. A.; Gwaltney, K. P.; Lee, H. *J. Org. Chem.* **1998**, *63*.
45. Chang, C. K.; Bag, N. *J. Org. Chem.* **1995**, *60*, 7030-7032.
46. Boyle, R. W.; Johnson, C. K.; Dolphin, D. *J. Chem. Soc. Chem. Commun.* **1995**, 527-528.
47. DiMaggio, S. G.; Lin, V. S. Y.; Therien, M. J. *J. Org. Chem.* **1993**, *58*.
48. Schwartz, E. B.; Knobler, C. B.; Cram, D. J. *J. Am. Chem. Soc.* **1992**, *114*, 10775-10784.
49. Armarego, W. L. F.; Perrin, D. D. *Purification of Laboratory Chemicals*; 4th ed.; Butterworth-Heinmann: Oxford, 1996.



*Chapter 10*

**Hydrogen-Bond Mediated Redox Chemistry of  
Naphthalene Hangman Porphyrins**

## 10.1 Motivation and Specific Aims

With the ultimate goal of employing Hangman porphyrin constructs to investigate the catalytic activation of reactive oxygen species (ROS) and other small molecules using proton-coupled electron transfer (PCET), we decided to initiate our studies by characterizing the effects of proton coupling on simple heme redox chemistry. The proximate redox and acid-base sites in the naphthalene-bridged Hangman porphyrins present an attractive scaffold for characterizing these PCET processes on a redox-active platform. In this chapter, we examine proton-coupling effects on both the reduction and oxidation chemistry of the heme unit. Comparative studies with dicyanoiron(III) derivatives demonstrate that the coupling of a single proton to a redox event can lead to significant changes in biologically critical Fe(III)/Fe(II) reduction potentials, and the chemical oxidation pathways of zinc(II) complexes can be selected by tuning proton activation. The results provide a fundamental basis for the application of these and structurally expanded Hangman derivatives for catalytic PCET chemistry.

## 10.2 Background

The heme unit is an indispensable cofactor for oxidation-reduction chemistry in Nature.<sup>1-3</sup> From this single starting point, heme-dependent proteins have evolved to display an amazingly diverse set of chemical reactivities that are precisely dictated by the surrounding polypeptide tertiary structure.<sup>1,4-18</sup> The function of the heme center within a given protein fold is critically dependent on its chemical reduction potential, a parameter that defines not only the thermodynamics for a particular cellular redox reaction, but is also connected with the rate at which such reactions proceed. Nature has elegantly utilized the chemical tunability of the porphyrin cofactor to generate hemoproteins exhibiting a wide range of reduction potentials. A number of well-studied factors influence this equilibrium midpoint potential, including axial ligation,<sup>19-27</sup> nonplanar distortions of the heme,<sup>28,29</sup> local polarity,<sup>30-33</sup> and heme solvent exposure,<sup>34-38</sup> the last of which can make a particularly large contribution (> 400 mV) to reduction potential. Specifically, in line with the original model of Stellwagen,<sup>34</sup> decreasing solvent exposure correlates with increasing Fe(III)/Fe(II) reduction potential owing to the energetic penalty of burying a formally charged ferric heme in a low dielectric environment.

Another factor that can influence heme reduction potentials is the coupling of proton motion to the redox event. Many redox reactions of hemoproteins can be modulated by proton exchange with the aqueous medium or amino acid side chains, as proton binding or release provides a facile means for the protein to internally compensate for changes in electrostatic potential upon charge transport.<sup>39-47</sup> Essential proton-coupled electron transfer (PCET) processes<sup>48,49</sup> continue to emerge in heme-dependent enzymes and many other protein oxidation-reduction sequences.<sup>50-63</sup>

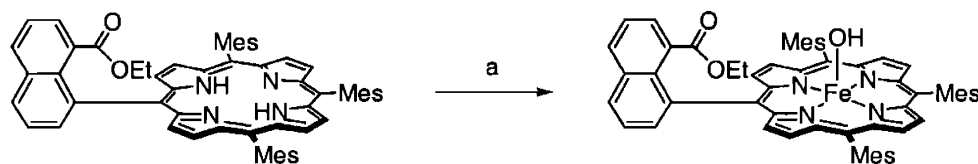
However, despite the importance of PCET in mediating the redox properties of heme proteins, the magnitude and mechanism of proton coupling effects remain largely undefined owing to the difficulty of their extraction from complex biochemical machinery.

Synthetic model systems offer the attractive opportunity to provide intimate and quantitative details into PCET-induced effects on heme redox chemistry without complications involving the surrounding protein milieu.<sup>64-72</sup> Notable in this regard is early work by Sweigart which demonstrated that complete deprotonation of coordinated imidazoles with exogenous bases leads to a Nernst-type shift (ca. 60 mV) in Fe(III)/Fe(II) potential.<sup>73,74</sup> In an effort to investigate heme redox chemistry mediated by PCET,<sup>75,76</sup> we have developed simple constructs consisting of a solvent-exposed porphyrin with a proton-relay functionality appended to a naphthalene scaffold (HPN = hanging porphyrin naphthalene).<sup>64,77-82</sup> These synthetic Hangman architectures allow for systematic examination of proton coupling on heme reduction potentials within a conserved structural motif. In this chapter, we present the redox chemistry and spectral properties of iron and zinc coordination complexes of the HPN framework. Electrochemical measurements of these Hangman systems reveal that the coupling of proton motion to electron transfer can markedly influence the Fe(III)/Fe(II) reduction potential of the heme cofactor, as well as mediating oxidative transformations of the ancillary porphyrin superstructure itself.

## 10.3 Results and Discussion

### 10.3.1 Synthesis and Reduction Chemistry of an Unusual Bisiron(III) Carboxylate-Bridged HPN Dimer

Our initial targets for examining proton coupling effects on heme redox chemistry were monomeric iron(III) hydroxide porphyrins, since such complexes are a single PCET reaction removed from the biologically-important iron(II) aqua and iron(IV) oxo (ferryl) heme species. Towards this end, ancillary mesityl substituents were designed into the HPN framework to provide steric bulk sufficient for the selective formation of iron(III) hydroxide monomers over iron(III)  $\mu$ -oxo dimers.<sup>83,84</sup> For example, treatment of the ester derivative H<sub>2</sub>(HPN-CO<sub>2</sub>Et) (**99**) with FeBr<sub>2</sub> in DMF followed by basic workup furnishes the monomeric iron(III) hydroxide complex FeOH(HPN-CO<sub>2</sub>Et) (**122**) in good yield (87%, Scheme 10.1). Compound **122** gave satisfactory high-resolution mass spectrometry and elemental analyses, and the <sup>1</sup>H NMR spectrum displays a broadened manifold of pyrrole resonances at ca. 80 ppm, indicating a high-spin iron(III) porphyrin species.<sup>76,84</sup> No signals corresponding to a bisiron(III)  $\mu$ -oxo complex are observed. In addition, **122** exhibits an identical electronic absorption profile to the symmetric control compound FeOH(TMP) (TMP = 5,10,15,20-tetramesitylporphyrin), with a Soret band at 419 nm and a well-defined Q-band doublet at 576 and 622 nm (Figure 10.1).



**Scheme 10.1.** (a) i. FeBr<sub>2</sub>, DMF; ii. NaOH.

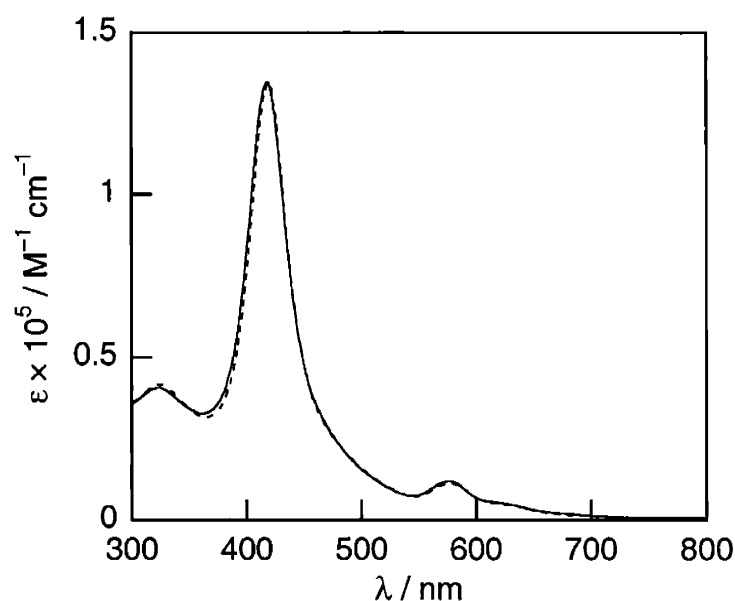


**Figure 10.1.** Absorption spectra of ester **122** (solid line) and FeOH(TMP) (dotted line) in toluene.

Reaction of the acid congener H<sub>2</sub>(HPN-CO<sub>2</sub>H) (**100**) with FeBr<sub>2</sub> under similar metalation conditions affords a single, high-spin iron(III) species **123** with pyrrole resonances at ca. 80 ppm in the <sup>1</sup>H NMR spectrum. However, in contrast to complex **122** and FeOH(TMP), the electronic absorption spectrum of **123** displays a Soret absorption at 422 nm with tailing, low-intensity Q-band shoulders at 490, 565, and 645 nm; this profile is similar to iron(III) porphyrin benzoate complexes (Figure 10.2). Moreover, independent preparation of Fe(1-naphthylcarboxylate)(TMP) from FeOH(TMP) and 1-naphthoic acid generates a species with an electronic absorption spectrum comparable to **123**.

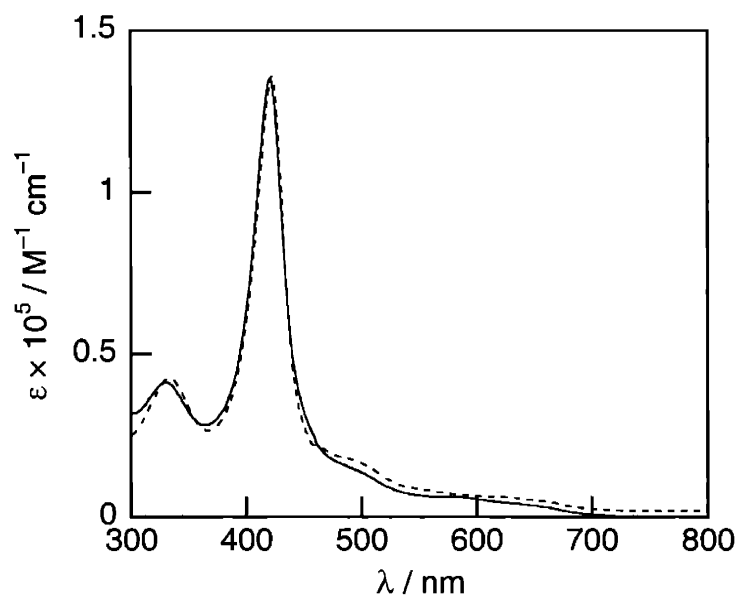


**Figure 10.2.** Absorption spectra of **123** (solid line) and Fe(1-naphthoate)(TMP) (dotted line) in toluene. The spectrum of the latter compound is multiplied by a factor of two.

The data suggest that **123** is an iron(III) carboxylate compound, and this assignment is confirmed by single-crystal X-ray analysis (Figure 10.3). The complex forms an unusual head-to-tail cofacial dimer with the naphthalene carboxylate of one porphyrin ligated to the iron(III) center of the other; the only other structure of this type is a phenolate-bridged (tetraphenylporphyrin)iron(III) dimer obtained by Goff and co-workers.<sup>85</sup> Crystallographic data for **123** are given in Table 10.1, and selected bond lengths and angles are collected in Table 10.2. Specific structural highlights are given as follows. The interplanar distance between porphyrin subunits is 7.06 Å, with an Fe—Fe distance of 6.35 Å. The iron atoms are five-coordinate, with an axial Fe—O carboxylate bond length of 1.883(3) Å and an average Fe—N bond length of 2.05 Å. The metal centers are raised 0.568 Å out of the 24-atom macrocyclic planes, in accord with other five-coordinate, high-spin Fe(III) porphyrin species.<sup>2</sup> The porphyrin cores exhibit a pronounced ruffled structure, with a mean deviation of 0.168 Å from the macrocyclic mean plane. The meso carbons are displaced from 0.352 Å below to 0.358 Å above the porphyrin mean plane.

Scheme 10.2 depicts a proposed mechanism for the production of **123**. Formation of the carboxylate-bridged complex likely involves initial generation of an iron(III) hydroxide species, followed by ligand protonation from the dangling carboxylic acid group and elimination of the axial water. The marked  $pK_a$  differences between the acid and iron(III) hydroxide porphyrin (ca. 5 and 9, respectively) should facilitate this proton-transfer process.<sup>86,87</sup> Subsequent dimerization

by carboxylate coordination to iron(III) affords complex **123**. Future efforts directed toward the synthesis of iron(III) hydroxide porphyrins with pendant hydrogen-bonding functionalities will focus on the use of organic groups that are more basic than the iron(III) hydroxide unit.

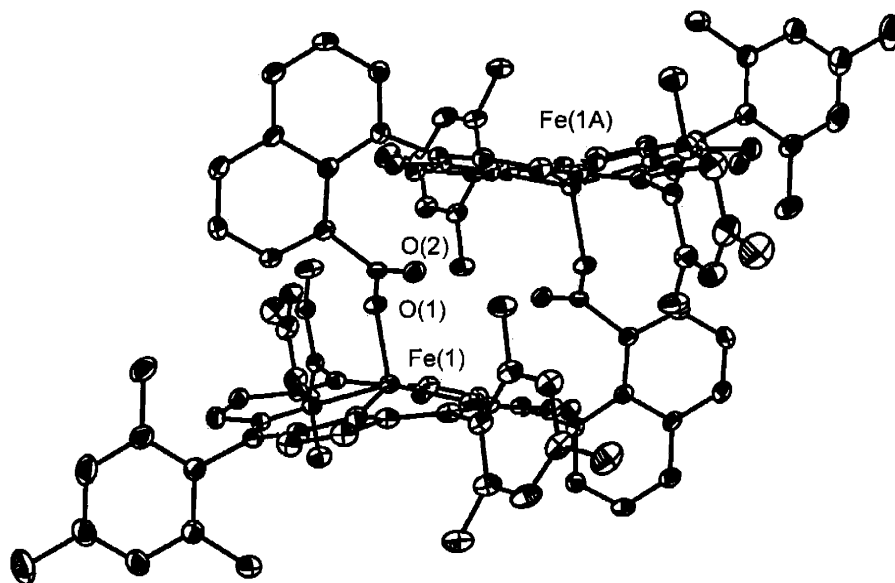
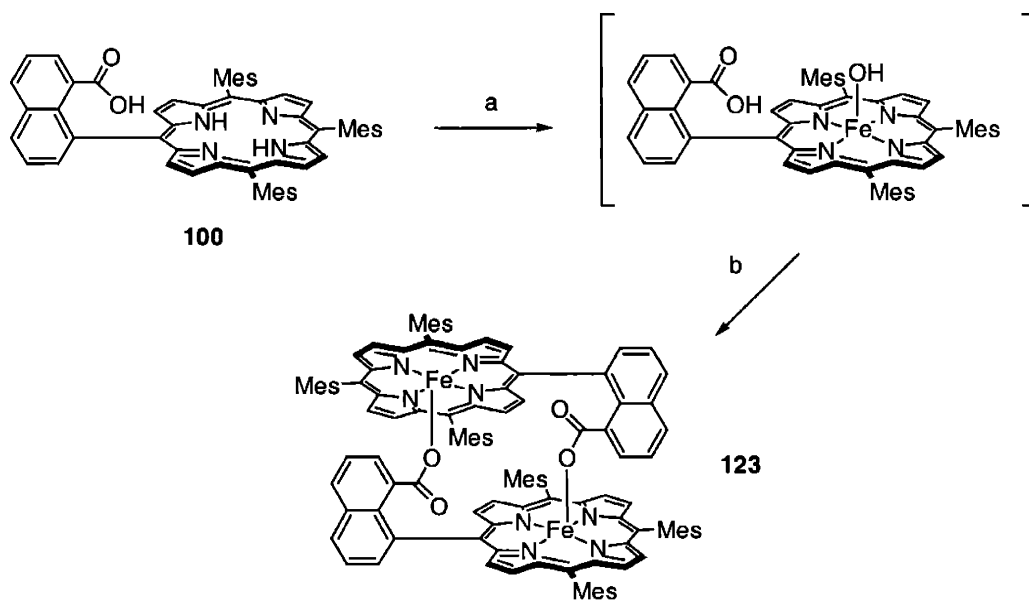


**Figure 10.3.** Crystal structure of  $\text{Fe}_2(\text{HPN-CO}_2)$  (**123**). Thermal ellipsoids are drawn at the 25% probability level. Hydrogen atoms and solvent molecules within the lattice have been omitted for clarity.



**Scheme 10.2.** (a) i.  $\text{FeBr}_2$ , DMF; ii. NaOH; (b)  $-\text{H}_2\text{O}$ .

**Table 10.1.** Crystallographic Data for Compound 123.

	123
Empirical formula	C <sub>122</sub> H <sub>108</sub> N <sub>8</sub> O <sub>4</sub> Fe <sub>2</sub>
Formula weight	1861.86
Temperature	120(2) K
Wavelength	0.71073 Å
Crystal system	Triclinic
Space group	$P\bar{1}$
Unit cell dimensions	$a = 12.2708(3)$ Å $b = 13.6469(4)$ Å $c = 16.0436(5)$ Å $\alpha = 92.8499(11)^\circ$ $\beta = 102.5531(12)^\circ$ $\gamma = 103.1314(14)^\circ$
Volume	2540.14(13) Å <sup>3</sup>
Z	1
Density (calculated)	1.217 Mg/m <sup>3</sup>
Absorption coefficient	0.344 mm <sup>-1</sup>
F(000)	980
Crystal size	0.15 × 0.08 × 0.07 mm <sup>3</sup>
$\theta$ range for data collection	2.62 to 25.00°
Reflections collected	34312
Independent reflections	8783 ( $R_{\text{int}} = 0.0900$ )
Data/restraints/parameters	8783 / 2 / 599
Goodness-of-fit on $F^2$	1.084
Final R indices [ $I > 2\sigma(I)$ ]	$R1 = 0.0738$ $wR2 = 0.1870$
Final R indices (all data)	$R1 = 0.1108,$ $wR2 = 0.2216$
Extinction coefficient	0.0061(18)
Largest diff peak	1.023 eÅ <sup>-3</sup>
Largest diff hole	-0.551 eÅ <sup>-3</sup>

**Table 10.2.** Selected Bond Distances (Å) and Angles (deg) for Compound **123**.

<i>Bond Distances / Å</i>		<i>Bond Angles / deg</i>	
Fe(1)–N(1)	2.041(3)	N(1)-Fe(1)-N(2)	85.92(14)
Fe(1)–N(2)	2.065(4)	N(1)-Fe(1)-N(3)	151.93(14)
Fe(1)–N(3)	2.063(4)	N(2)-Fe(1)-N(3)	87.02(15)
Fe(1)–N(4)	2.036(4)	N(1)-Fe(1)-N(4)	87.66(14)
Fe(1)–O(1)	1.883(3)	N(2)-Fe(1)-N(4)	153.95(14)
O(1)–C(48)	1.314(5)	N(3)-Fe(1)-N(4)	86.88(15)
O(2)–C(48)	1.202(5)	N(1)-Fe(1)-O(1)	103.79(13)
		N(2)-Fe(1)-O(1)	96.55(14)
		N(3)-Fe(1)-O(1)	103.99(13)
		N(4)-Fe(1)-O(1)	109.50(14)

The stability of the unusual carboxylate-bridged HPN dimer offers an opportunity to probe its multielectron redox chemistry for potential catalytic applications, and to establish general physical methodologies for examining redox reactions at fast timescales. Accordingly, the reduction chemistry of bisporphyrin **123** has been thoroughly investigated using a combination of electrochemical, photochemical, and radiolytic techniques. Cyclic voltammograms of **123** in dichloromethane give a single, reversible Fe(III)/Fe(II) reduction wave at  $-0.40$  V (vs Ag/AgCl, Figure 10.4), consistent with non-interacting redox centers. The identity of the reduced diferrous porphyrin species is elucidated using thin-layer spectroelectrochemistry. Thin-layer spectra recorded during the electrochemical reduction of **123** at  $-0.6$  V are shown in Figure 10.5. The final spectrum generated displays a single Soret band at 439 nm and a Q-band absorption at 567 nm with flanking shoulders at 535 and 607 nm. Clean isosbestic points are maintained throughout the electrolysis and reoxidation at 0 V affords **123** in greater than 97% yield according to the intensity of the regenerated Soret maximum at 422 nm. Moreover, the spectrum of reduced **123** is indicative of a five-coordinate iron(II) porphyrin owing to the position and number of Soret bands observed.<sup>2</sup> Taken together, the data establish that the carboxylate-bridged dimer remains intact upon reduction of the metal centers from Fe(III) to Fe(II).



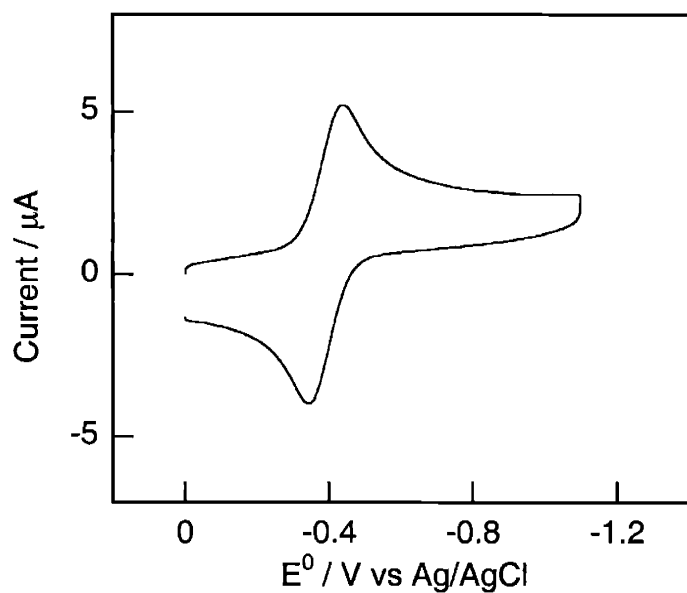


**Figure 10.4.** Cyclic voltammogram of **123** in dichloromethane containing 0.1 M *n*-tetrabutylammonium perchlorate (TBAP) as supporting electrolyte. Scan rate = 100 mV/s, potentials reported vs Ag/AgCl.

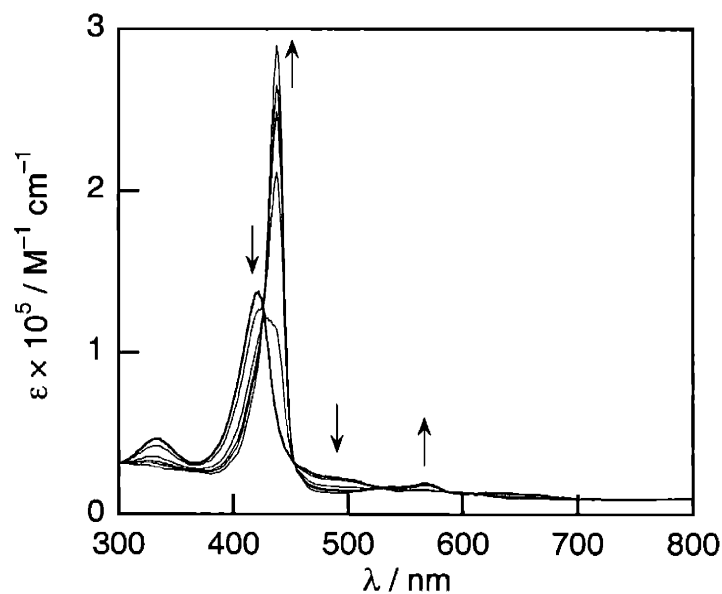
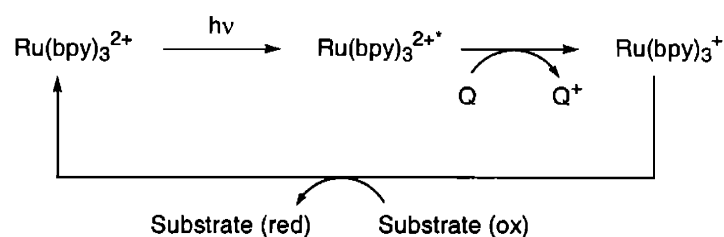


**Figure 10.5.** Thin-layer spectra recorded during the reduction of **123** at  $-0.6$  V in dichloromethane containing 0.1 M tetra *n*-butylammonium perchlorate (TBAP) as supporting electrolyte.

The electron transfer reaction can also be triggered photochemically using a flash-quench technique (Scheme 10.3). Laser excitation of  $\text{Ru}(\text{bpy})_3^{2+}$  in the presence of excess *p*-toluidine

produces  $\text{Ru}(\text{bpy})_3^+$ , a powerful reductant ( $E^0 = -1.24 \text{ V vs NHE}$ ),<sup>88,89</sup> on the order of 50 ns. The formal ruthenium(I) polypyridine species exhibits a positive transient absorption centered at 490 nm. In the absence of porphyrin, the photogenerated  $\text{Ru}(\text{bpy})_3^+$  reacts with the oxidized quencher to restore the starting complexes on a millisecond time scale. The presence of micromolar **123** accelerates the decay of  $\text{Ru}(\text{bpy})_3^+$  and gives rise to absorption changes that are attributable to the formation of the diiron(II) species (Figure 10.6) with no detectable porphyrin-based intermediates. The transient absorption spectrum obtained 5  $\mu\text{s}$  after laser flash photolysis strongly resembles the difference spectrum obtained from thin-layer spectroelectrochemistry (Figure 10.7). The appearance of the five-coordinate  $\text{Fe}^{\text{II}}$  porphyrin signal obeys first-order kinetics (Figure 10.8); the slope of the observed rate constant vs the concentration of **123** (Figure 10.9) yields an apparent second-order rate constant of  $9.5 \times 10^9 \text{ M}^{-1}\text{s}^{-1}$ .



**Scheme 10.3.** Flash-quench method for fast generation of reducing agents; Q = quencher = *p*-toluidine.

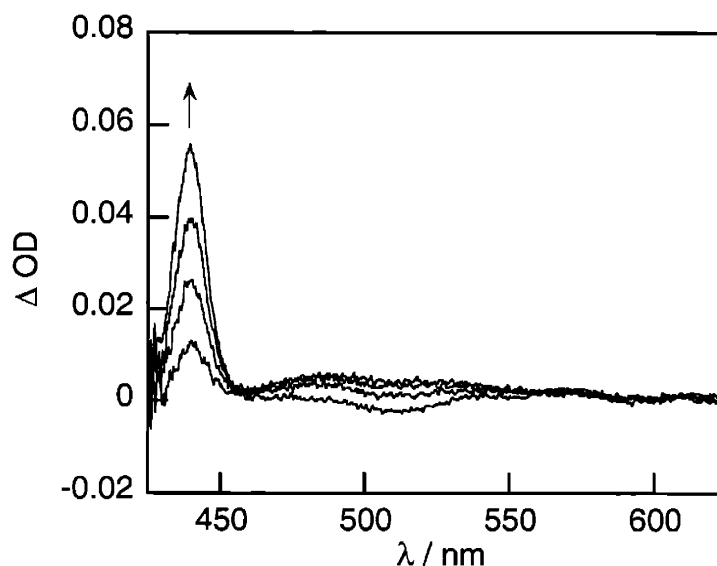


**Figure 10.6.** Transient absorption spectra obtained at 200 ns, 500 ns, 1  $\mu\text{s}$ , and 4  $\mu\text{s}$  after flash photolysis of an  $\text{CH}_3\text{CN}$  solution containing **123** (90  $\mu\text{M}$ ),  $\text{Ru}(\text{bpy})_3^{2+}$  (20  $\mu\text{M}$ ), and *p*-toluidine (20 mM) at 298 K.

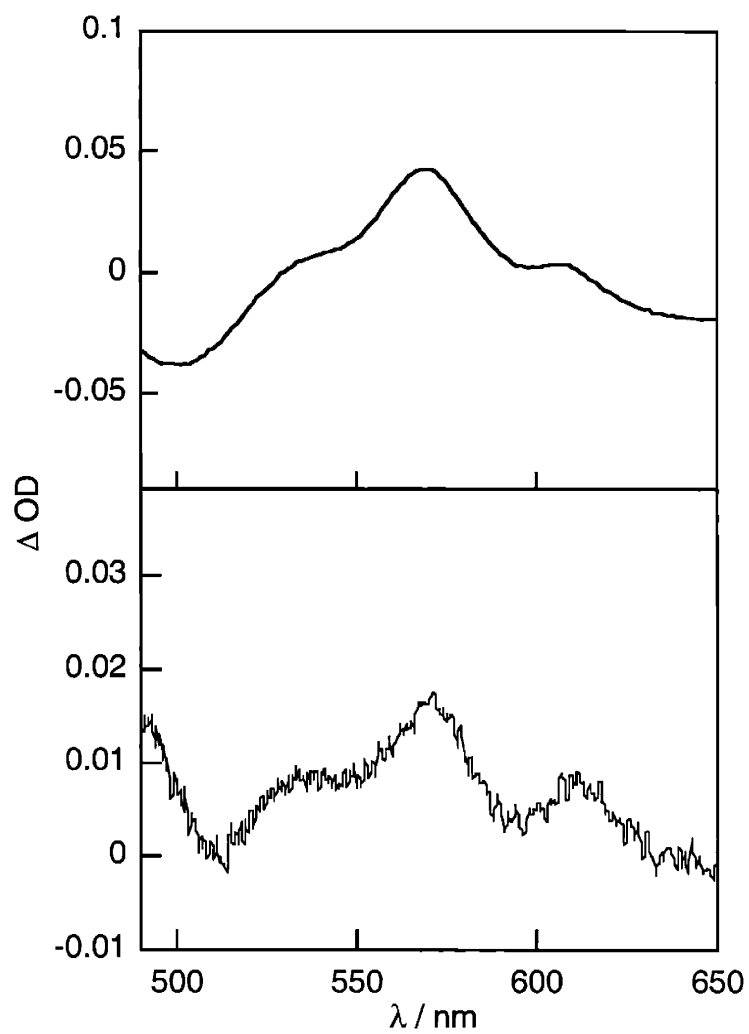


**Figure 10.7.** (a) Q-band region difference spectrum obtained from thin-layer spectroelectrochemistry at 298 K and (b) Q-band region transient absorption spectrum taken 5  $\mu$ s after laser photolysis of an  $\text{CH}_3\text{CN}$  solution containing **123** (100  $\mu\text{M}$ ),  $\text{Ru}(\text{bpy})_3^{2+}$  (20  $\mu\text{M}$ ), and *p*-toluidine (20 mM) at 298 K.

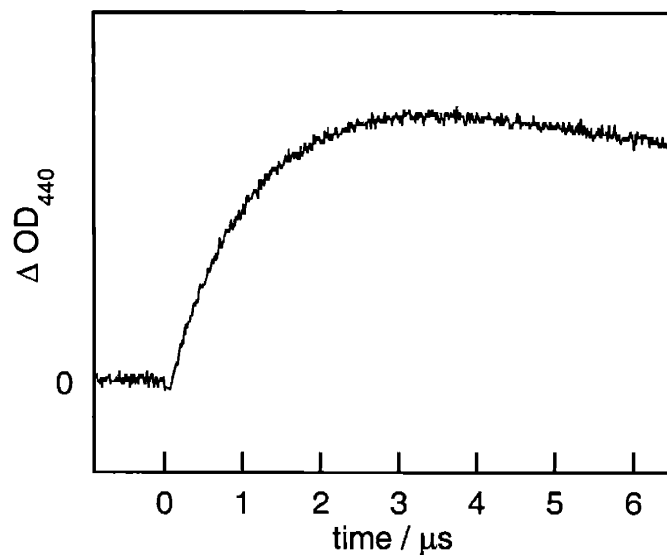


**Figure 10.8.** Single-wavelength transient absorption spectrum at 440 nm obtained after flash photolysis of an  $\text{CH}_3\text{CN}$  solution containing **123** (100  $\mu\text{M}$ ),  $\text{Ru}(\text{bpy})_3^{2+}$  (20  $\mu\text{M}$ ), and *p*-toluidine (20 mM) at 298 K.

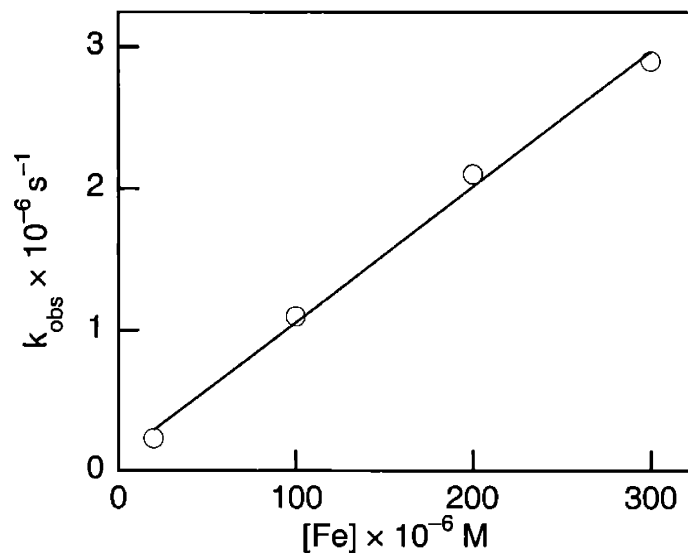


**Figure 10.9.** Plot of observed pseudo-first-order rate constants for reduction of **123** with photogenerated  $\text{Ru}(\text{bpy})_3^+$  as a function of  $[\text{123}]$ . Line is best fit from least-squares fitting.

The multielectron reduction reaction was also initiated using pulse radiolysis. Studies of HPN dimer **123** were performed in THF. Electron adducts were generated by reaction with solvated electrons in THF formed by 30 ps pulses of 8 MeV electrons. These electron adducts react with **123** to produce the reduced diiron(II) dimer with no detectable porphyrin-based intermediates. The transient absorption spectrum obtained within 300 ns after radiolysis (Figure 10.10) agrees well with the difference spectra obtained from thin-layer spectroelectrochemistry and laser flash photolysis. Reaction kinetics were measured by monitoring the decay of the solvated electron adduct transient absorption; the slope of the observed rate constant vs the concentration of **123** (Figure 10.11) yields an apparent second-order rate constant of  $7.9 \times 10^{10} \text{ M}^{-1} \text{ s}^{-1}$ .

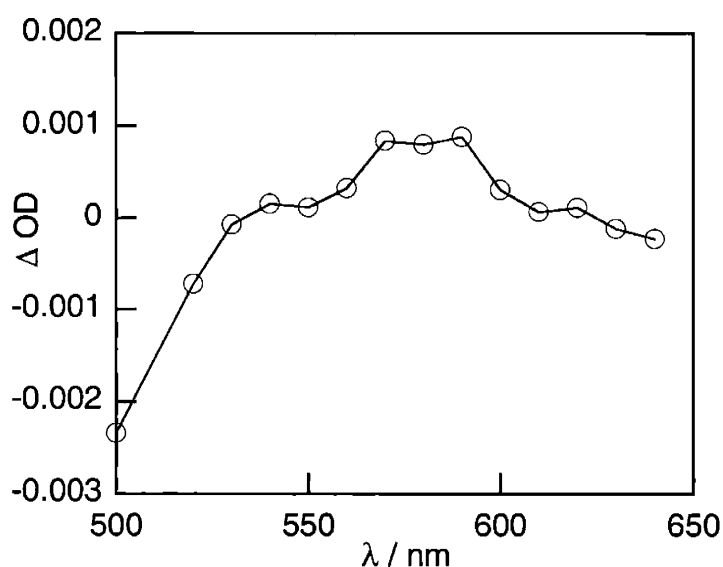


**Figure 10.10.** Q-band region transient absorption spectrum taken 300 ns after pulse photolysis. Sample consists of a 200  $\mu\text{M}$  solution of **123** in tetrahydrofuran at 298 K.

The results establish that the combination of laser flash photolysis and pulse radiolysis techniques allows us to initiate and monitor redox reactions within a nanosecond to microsecond window with high fidelity. Notably, these photolysis and radiolysis triggers are *three to six orders of magnitude* faster than conventional approaches such as stopped-flow spectroscopy (millisecond window), providing a powerful set of physical tools for examining reaction mechanisms at fast timescales. Finally, we note that although reduction reactions have been examined exclusively, the corresponding oxidation processes are also available using these methods.

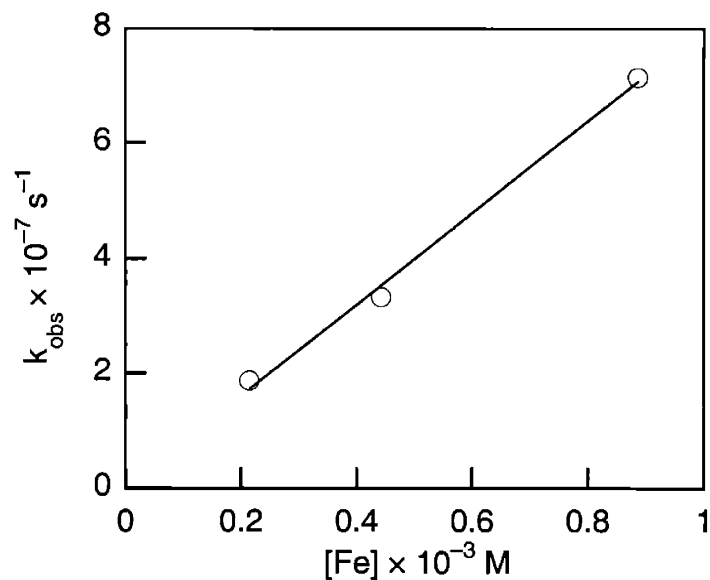
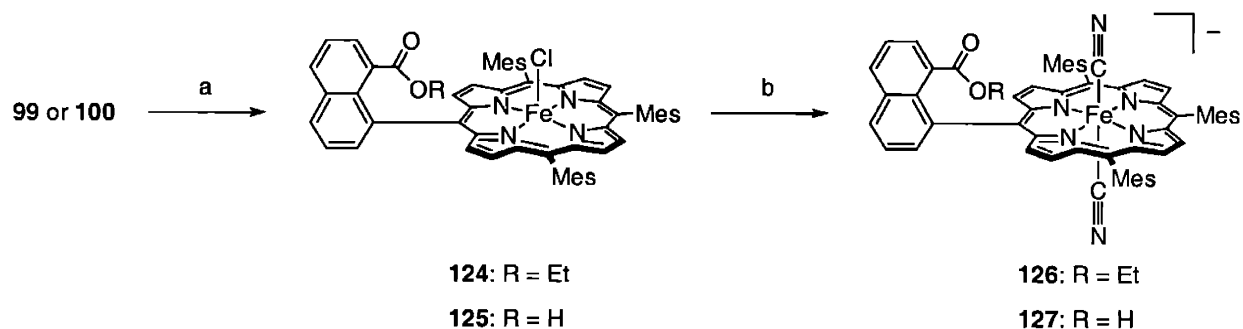


**Figure 10.11.** Plot of observed pseudo-first-order rate constants for radiolytic reduction of **123** as a function of **[123]**. Line is best fit from least-squares fitting.

### 10.3.2 Synthesis and Reduction Chemistry of Dicyanoiron(III) HPN Porphyrins

The proton-facilitated ligand elimination and dimerization of the ferric HPN porphyrins led us to consider alternative axial ligands for examining proton coupling effects on heme redox chemistry. To simplify our investigations, we chose to examine proton-coupling effects on heme redox chemistry using axial cyanide ligands owing to their (i) ability to provide exclusively low-spin iron species to avoid complications arising from spin crossovers and (ii) propensity to form symmetric six-coordinate iron(III) porphyrin complexes to eliminate issues of facial-selective axial ligation. In addition, cyanide has a close structural relationship to a number of biologically relevant diatomics such as dioxygen, carbon monoxide, and nitric oxide. Accordingly, dicyanoiron(III) complexes of the HPN system are prepared as illustrated in Scheme 10.4.

Iron insertion into ester **99** and carboxylic acid **100** followed by acidic workup furnishes the chloroiron(III) porphyrins FeCl(HPN-CO<sub>2</sub>Et) (**124**) and FeCl(HPN-CO<sub>2</sub>H) (**125**), respectively. The ferric porphyrins gave satisfactory high-resolution mass spectral and elemental analyses. Treatment of **124** and **125** with four equiv of *n*-tetrabutylammonium cyanide cleanly generates the corresponding dicyanoiron(III) complexes [NBu<sub>4</sub>][Fe(CN)<sub>2</sub>(HPN-CO<sub>2</sub>Et)] (**126**) and [NBu<sub>4</sub>][Fe(CN)<sub>2</sub>(HPN-CO<sub>2</sub>H)] (**127**), respectively.



**Scheme 10.4.** (a) i.  $\text{FeBr}_2$ , DMF; ii. HCl; (b) *n*-tetrabutylammonium cyanide (TBACN).

Infrared and electronic absorption spectroscopic measurements establish a hydrogen-bonding interaction between the protic carboxylic acid group of **127** and an axial cyanide ligand. Spectral data are collected in Table 10.3. A modest shift in the bound cyanide stretching frequency is observed upon substitution of the carboxylic acid functionality ( $\nu_{\text{CN}} = 2106 \text{ cm}^{-1}$ ) for an ester group ( $\nu_{\text{CN}} = 2110 \text{ cm}^{-1}$ ); the latter exhibits an identical spectral profile to the parent compound  $[\text{NBu}_4][\text{Fe}(\text{CN})_2(\text{TMP})]$  ( $\nu_{\text{CN}} = 2110 \text{ cm}^{-1}$ ). Figure 10.12 displays the electronic absorption spectra for **126** and **127**.

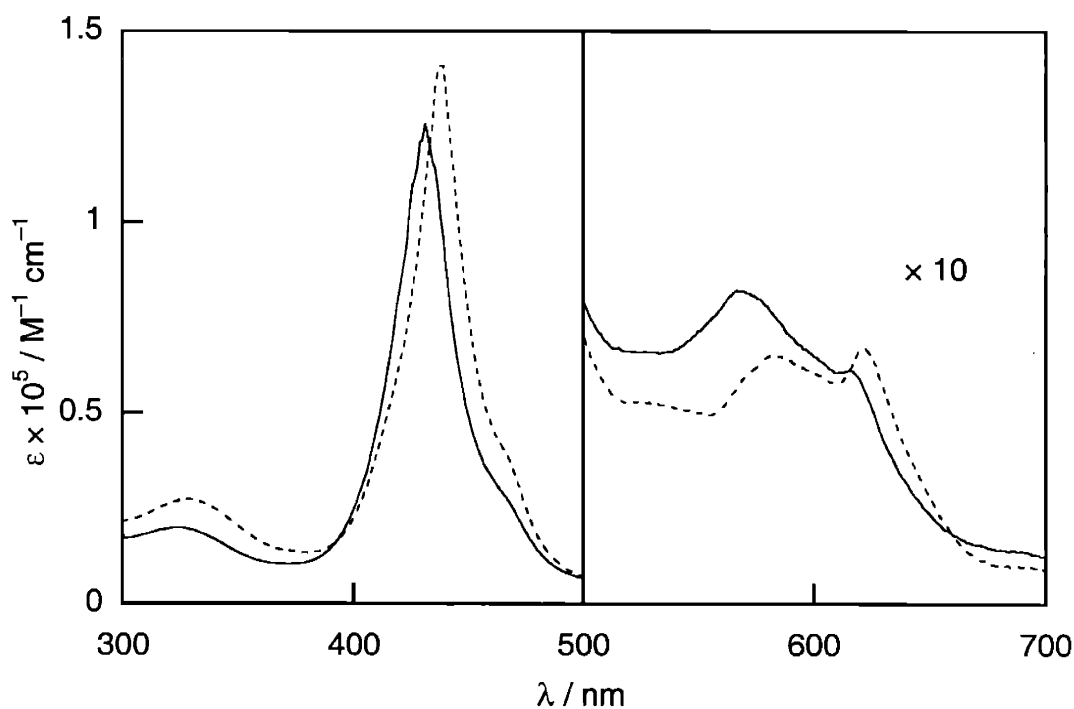


**Figure 10.12.** Absorption spectra of ester **126** (dotted line) and **127** (solid line) in dichloromethane solution at 298 K.

Typical of dicyanoiron(III) porphyrins, complexes **126** and **127** feature a LMCT band in the UV region, an intense Soret band and two Q-band absorptions in the visible region, and a pronounced shoulder to the red of the Soret band. Notably, the Soret and Q band absorption systems of acid **127** are markedly blue-shifted relative to ester **126** and the TMP complex. In addition, the relative intensities of the Q bands for **127** differ from both **126** and [NBu<sub>4</sub>][Fe(CN)<sub>2</sub>(TMP)]. For acid **127**, the Q band lying to the blue is more intense than the one to the red. In contrast, the relative intensities of the Q bands for ester **126** and the TMP compound are reversed from **127**.

**Table 10.3.** Spectroscopic Data for Dicyanoiron(III) Porphyrins in Dichloromethane at 298 K.

Compound	$\nu_{\text{CN}} / \text{cm}^{-1}$	$\lambda_{\text{max}} (\epsilon / \times 10^3 \text{ M}^{-1}\text{cm}^{-1})^a$
[NBu <sub>4</sub> ][Fe(CN) <sub>2</sub> (TMP)]	2110	328(27), 436(164), 463(40 sh), 580(6.4), 618(6.8)
<b>126</b>	2110	328(27), 439(141), 467(39 sh), 583(6.5), 621(6.7)
<b>127</b>	2106	323(24), 431(150), 465(34 sh), 567(8.2), 616(6.2)

<sup>a</sup> sh denotes shoulder

Electrochemical measurements demonstrate the functional consequences of proximate hydrogen bonding and proton coupling to heme redox events (Figure 10.13). Cyclic voltammograms of ester **126** display a quasi-reversible Fe(III)/Fe(II) wave at comparable potentials to [NBu<sub>4</sub>][Fe(CN)<sub>2</sub>(TMP)] ( $E^0 = -0.85 \text{ V vs Ag/AgCl}$ ). In contrast, the ferric/ferrous reduction of carboxylic acid derivative **127** is facilitated by approximately 100 mV ( $E^0 = -0.84 \text{ V vs Ag/AgCl}$ ).

The marked shift in Fe(III)/Fe(II) reduction potential is consistent with the proposal that proton coupling stabilizes the reduced form by attenuating charge density on the cyanide axial ligand. Moreover, the magnitude of the effect is greater than what would be expected for simple acid-base exchange. This last observation offers the tantalizing possibility that proton motion coupled to the redox event is driven by a specific bonding interaction, and that the Hangman motif has isolated this PCET process.





The oxidation chemistry of **128**, **129**, and the reference compound Zn(TMP) were investigated using electrochemical and photochemical techniques. Cyclic voltammograms of carboxylic acid **129** (Figure 10.14) exhibit a quasi-reversible one-electron oxidation wave at +0.71 V, accompanied by an irreversible oxidation at +0.98 V (potentials referenced vs Ag/AgCl). In contrast, voltammograms of the ester derivative **128** and Zn(TMP) are virtually identical, displaying two reversible one-electron oxidations at +0.76 and +1.05 V vs Ag/AgCl (Figure 10.14). Notably, the responses for **128** or Zn(TMP) are unchanged even in the presence of up to 1000 equiv of 1-naphthoic acid.

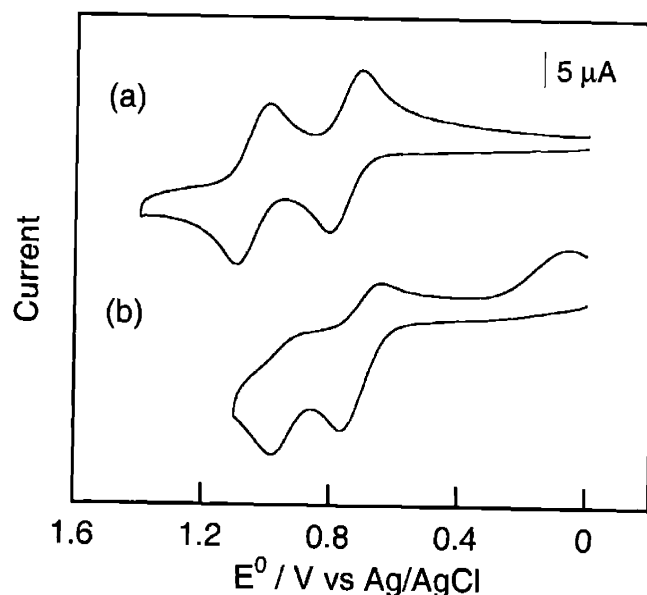


**Figure 10.14.** Cyclic voltammograms of (a) **128** and (b) **129** in dichloromethane containing 0.1 M *n*-tetrabutylammonium perchlorate (TBAP) as supporting electrolyte. Scan rate = 100 mV/s, potentials reported vs Ag/AgCl.

The oxidized species for the triumvirate of zinc(II) porphyrins are characterized using thin-layer spectroelectrochemistry. Thin-layer spectra recorded during the one-electron oxidation of carboxylic acid **129** at +0.9 V are shown in Figure 10.15. Clean isosbestic points are maintained throughout the electrolysis and the oxidation is irreversible; no regeneration of the starting material occurs upon applying a reducing potential. The oxidation occurs with loss of the Soret band at 425 nm and the prominent Q-band feature at 552 nm. The final spectrum generated displays a single band of low intensity at 458 nm in the visible region with a shoulder to the blue at 425 nm. A broad absorption in the near-IR region is observed at 910 nm with a flanking shoulder at 850 nm. The appearance of these near-IR absorptions, together with the

irreversibility of the oxidation process, suggests that the oxidized species is an isoporphyrin.<sup>2</sup> Such a complex is readily produced via nucleophilic attack of the pendant carboxylic acid on the meso carbon connecting the porphyrin and the naphthalene bridge, with one-electron oxidation of the porphyrin macrocycle increasing the electrophilicity of this meso site (Scheme 10.6). It is interesting to note that Saveant and co-workers observed reversible formation of isoporphyrins from the two-electron oxidation of amide-linked porphyrin superstructures.<sup>90</sup>

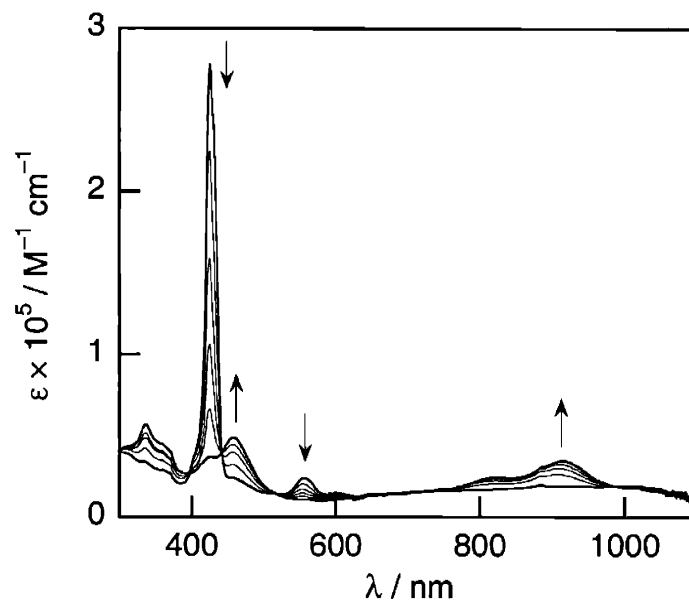
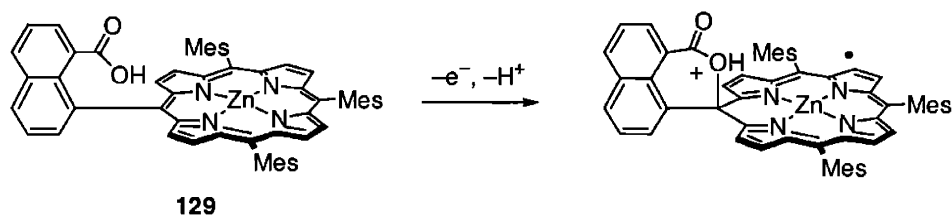


**Figure 10.15.** Thin-layer spectra recorded during the first oxidation of **129** at +0.9 V in dichloromethane containing 0.1 M tetra *n*-butylammonium perchlorate (TBAP) as supporting electrolyte.



**Scheme 10.6.** Formation of isoporphyrin via nucleophilic attack of the hanging carboxylic acid on the porphyrin cation radical species.

The situation for the HPN ester system is more complex. Reaction pathways for the oxidation of **128** are depicted in Scheme 10.7. The one-electron oxidations of ester **128** and Zn(TMP) proceed

in a similar fashion; thin-layer spectra recorded during the one-electron oxidation of ester **128** at +0.9 V are shown in Figure 10.16. Oxidation of Zn(TMP) affords an identical absorption profile. Clean isosbestic points are maintained throughout the electrolysis and re-reduction at 0 V affords **128** in greater than 95% yield according to the intensity of the regenerated Soret maximum at 420 nm. The final spectrum generated features a broad, blue-shifted Soret band of reduced intensity at 412 nm with a weak, tailing absorption centered at 650 nm. No absorptions are observed in the 800 to 900 nm region. The spectral profiles for the one-electron oxidized species of **128** and Zn(TMP) are indicative of porphyrin cation radicals.<sup>2</sup>

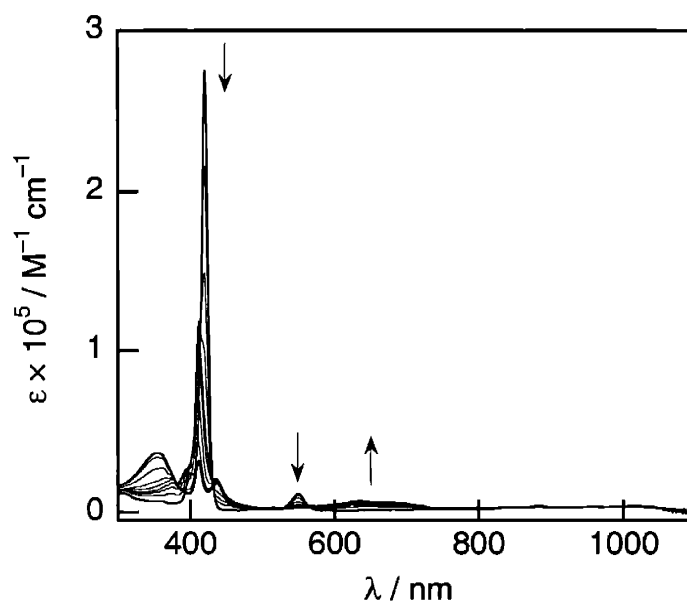
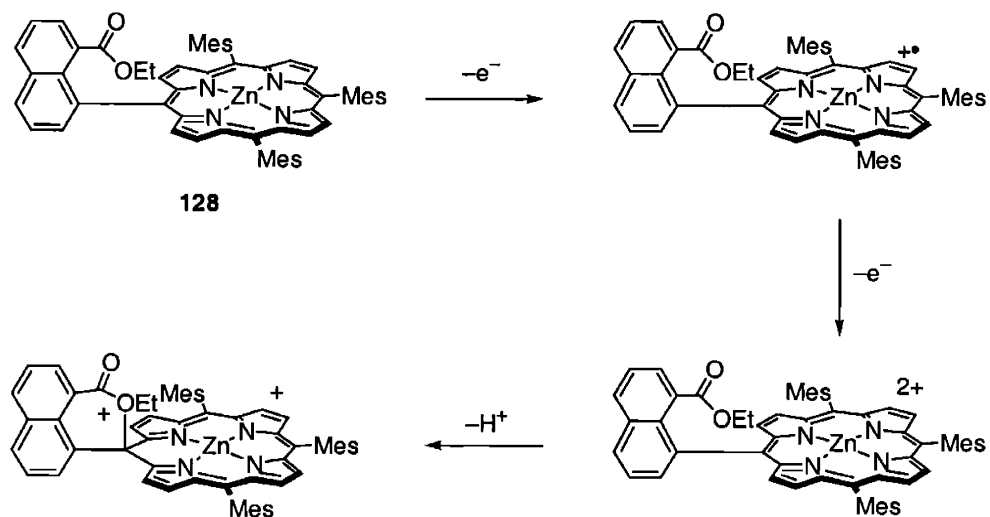


**Figure 10.16.** Thin-layer spectra recorded during the first oxidation of **128** at +0.9 V in dichloromethane containing 0.1 M tetra *n*-butylammonium perchlorate (TBAP) as supporting electrolyte.

The two-electron oxidation of **128** follows a markedly distinct reaction pathway. Thin-layer spectra recorded during the electrochemical oxidation of ester **128** at +1.1 V produces an isoporphyrin species with an absorption spectrum comparable to that obtained by the one-electron oxidation of carboxylic acid **129**; prominent features are at 458 and 910 nm. As observed for the one-electron oxidation of **129**, the two-electron oxidation of **128** is irreversible and the starting material is not regenerated upon applying a reducing potential. The production of an isoporphyrin species is surprising in this regard, demonstrating that the ester functionality is a competent nucleophile when the porphyrin macrocycle is suitably oxidized. Notably, the analogous two-electron oxidation of Zn(TMP) yields only the porphyrin dication, even in the presence of up to 1000 equiv of 1-naphthoic acid or 1-methylnaphthoate.



**Scheme 10.7.** Formation of porphyrin cation radical species and isoporphyrin via nucleophilic attack of hanging ester group on porphyrin dication radical species.

## 10.4 Concluding Remarks

Exquisite control of oxidation-reduction potentials in heme-dependent enzymes is made possible by the ability of proteins to create the exact active site structure necessary for specific and efficient heme function. Although a number of factors, such as ligation and local electrostatics, influence hemoprotein oxidation-reduction chemistry, the role of solvent exposure has received the majority of the attention as the central vehicle by which a hemoprotein modulates its reduction potential. Our findings clearly demonstrate that proton coupling can regulate the reduction potential of model heme systems in which the redox cofactor is fully solvated, and that the magnitude of this contribution can be significant in comparison to solvent exposure effects in biological systems.

Proton coupling can also influence the oxidation chemistry of the heme platform. Comparative electrochemical studies of zinc(II) derivatives shows that the introduction of a single protic group can direct the chemical pathway of porphyrin oxidation. Selective formation of porphyrin cation radicals, dication radicals, or isoporphyrins by macrocycle oxidation is governed by judicious choice of hydrogen-bond functionality. To close, we have demonstrated that proton coupling can direct the oxidation-reduction chemistry of the heme unit. Further studies will focus on Hangman motifs with expanded vertical pocket sizes to allow the binding and PCET-mediated activation of external substrates.

## 10.5 Experimental Section

### 10.5.1 Materials

Silica gel 60 (70-230 and 230-400 mesh, Merck) and aluminum oxide 60 (EM Science) were used for column chromatography. Analytical thin layer chromatography was performed using Merck 60 F254 silica gel (precoated sheets, 0.2 mm thick) or JT Baker IB-F aluminum oxide (precoated sheets, 0.2 mm thick). Solvents for synthesis were of reagent grade or better, and were dried according to standard methods.<sup>91</sup> Porphyrins H<sub>2</sub>(TMP), Zn(TMP), FeCl(TMP), FeOH(TMP), and [NBu<sub>4</sub>][Fe(CN)<sub>2</sub>(TMP)] were prepared according to literature procedures.<sup>2</sup> H<sub>2</sub>(HPN-CO<sub>2</sub>Et) (**99**) and H<sub>2</sub>(HPN-CO<sub>2</sub>H) (**100**) were available according to the methods described in chapter 9.

### 10.5.2 FeOH(HPN-CO<sub>2</sub>Et) (**122**)

In a dry box, **99** (103 mg, 0.12 mmol), 2,6-lutidine (0.2 mL), FeBr<sub>2</sub> (212 mg), THF (15 mL), and benzene (8 mL) were loaded in 100-mL flask equipped with a condenser. The reaction was refluxed under nitrogen for 3 h, opened to air, and brought to dryness under vacuum. The residue was purified using column chromatography (silica gel, dichloromethane to 10% methanol/dichloromethane), redissolved in dichloromethane (50 mL) and stirred with 20% HCl (25 mL) for 1 h. The organic layer was washed with water (5 × 50 mL) and taken to dryness. The resulting solid was redissolved in toluene (50 mL) and stirred with 0.5 M NaOH (50 mL) for 12 h. The organic phase was washed with water (3 × 50 mL), dried over Na<sub>2</sub>SO<sub>4</sub>, and the solvent was removed by rotary evaporation. Recrystallization from pentane furnished analytically pure **122** as a brown powder (97 mg, 87% yield). Anal. Calcd for C<sub>60</sub>H<sub>53</sub>N<sub>4</sub>O<sub>3</sub>Fe: C, 77.19; H, 5.72; N, 6.00. Found: C, 77.47; H, 5.88; N, 5.72. HRFABMS ([M—OH]<sup>+</sup>) calcd for C<sub>60</sub>H<sub>53</sub>N<sub>4</sub>O<sub>3</sub>Fe *m/z* 916.344, found, 916.347.

### 10.5.3 Carboxylate Dimer Fe<sub>2</sub>(HPN-CO<sub>2</sub><sup>-</sup>)<sub>2</sub> (**123**)

A combination of **100** (70 mg, 0.084 mmol), FeBr<sub>2</sub> (100 mg), and DMF (10 mL) was refluxed under nitrogen for 2 h, opened to air, and brought to dryness under vacuum. The solids were redissolved in dichloromethane (50 mL) and washed with water (3 × 25 mL). The organic layer was decanted and purified using column chromatography (silica gel, dichloromethane to 5% methanol/dichloromethane). The iron porphyrin fractions were dissolved in dichloromethane (50 mL) and shaken with 4 N HCl (10 mL). The organic layer was washed with water (5 × 25 mL), dried over Na<sub>2</sub>SO<sub>4</sub>, and the solvent was removed by rotary evaporation. Toluene (50 mL) was added and the solution was stirred with 0.5 M NaOH (50 mL) for 12 h. The organic layer was washed with water (3 × 50 mL), dried over Na<sub>2</sub>SO<sub>4</sub>. Removal of the solvent followed by

recrystallization from hexanes afforded analytically pure **123** as a brown solid (70 mg, 94% yield). Anal. Calcd for  $C_{116}H_{94}N_8O_4Fe_2$ : C, 78.46; H, 5.34; N, 6.31. Found: C, 78.78; H, 5.54; N, 6.19. HRESIMS (M+) calcd for  $C_{116}H_{94}N_8O_4Fe_2$   $m/z$  1774.609, found 1774.619.

#### 10.5.4 Preparation of Model Compound Fe(1-naphthylcarboxylate)(TMP)

Equimolar amounts of 1-naphthoic acid and FeOH(TMP) were combined in dry or toluene solution and stirred for 10 min. The solvent was removed by rotary evaporation to deliver the carboxylate compound in quantitative yield. Solution absorption spectroscopy confirms complete reaction of the starting material.

#### 10.5.5 FeCl(HPN-CO<sub>2</sub>Et) (124)

A combination of **99** (90 mg, 0.104 mmol), FeBr<sub>2</sub> (250 mg), and DMF (35 mL) was refluxed under nitrogen for 3 h, opened to air, and brought to dryness under vacuum. The solids were redissolved in dichloromethane (100 mL), washed with water (4 × 75 mL). The organic layer was stirred with 20% HCl (50 mL) for 75 min, washed with water (5 × 100 mL), and taken to dryness. The resulting residue was purified using column chromatography (silica gel, dichloromethane to 15% methanol/dichloromethane), and retreated with HCl as described above to furnish **124** as a brown powder (86 mg, 87% yield). Anal. Calcd for  $C_{60}H_{52}ClN_4O_2Fe$ : C, 75.67; H, 5.50; N, 5.88. Found: C, 75.20; H, 5.29; N, 6.00. HRFABMS ([M—Cl]<sup>+</sup>) calcd for  $C_{60}H_{52}ClN_4O_2Fe$   $m/z$  916.344, found, 916.345.

#### 10.5.6 FeCl(HPN-CO<sub>2</sub>H) (125)

A combination of **100** (75 mg, 0.090 mmol), FeBr<sub>2</sub> (150 mg), and DMF (15 mL) was refluxed under nitrogen for 2 h, opened to air, and brought to dryness under vacuum. The solids were redissolved in dichloromethane (100 mL), washed with water (4 × 75 mL). The organic layer was stirred with 20% HCl (50 mL) for 75 min, washed with water (5 × 100 mL), and taken to dryness. The resulting residue was purified using column chromatography (silica gel, dichloromethane to 10% methanol/dichloromethane), and retreated with HCl as described above to furnish **125** as a brown powder (70 mg, 84% yield). Anal. Calcd for  $C_{58}H_{48}ClN_4O_2Fe$ : C, 75.37; H, 5.23; N, 6.06. Found: C, 75.45; H, 5.55; N, 5.73. HRFABMS ([M—Cl]<sup>+</sup>) calcd for  $C_{58}H_{48}ClN_4O_2Fe$   $m/z$  888.313, found, 888.313.

#### 10.5.7 Preparation of Dicyanoiron(III) Porphyrins [NBu<sub>4</sub>][Fe(CN)<sub>2</sub>(HPN-CO<sub>2</sub>Et)] (126) and [NBu<sub>4</sub>][Fe(CN)<sub>2</sub>(HPN-CO<sub>2</sub>H)] (127)

Dicyanoiron(III) porphyrins **126** and **127** were obtained by treating dichloromethane solutions of the appropriate chloride complex with *n*-tetrabutylammonium cyanide (4 equiv) at room

temperature. Formation of the dicyano derivatives is evidenced by an instantaneous color change of the solution from yellow-brown to deep green. The low-spin iron(III) dicyano species are readily identified by their characteristic  $^1\text{H}$  NMR spectra; no pyrrole signals corresponding to high-spin chloroiron(III) porphyrin starting materials are observed at ca. 80 ppm.

#### 10.5.8 Zn(HPN-CO<sub>2</sub>Et) (128)

A saturated methanolic solution of Zn(OAc)<sub>2</sub>·2H<sub>2</sub>O (5 mL) and a solution of **99** (50 mg, 0.058 mmol) in 10 mL chloroform were combined and refluxed for 45 min. The solvent was removed by rotary evaporation. The remaining solid was purified by flash column chromatography (silica gel, 3:1 dichloromethane) followed by recrystallization from dichloromethane/methanol to yield **128** as a ruby red solid in quantitative yield.  $^1\text{H}$  NMR (500 MHz, CDCl<sub>3</sub>, 25 °C):  $\delta$  = 8.61-8.70 (m, 8H), 8.30 (d,  $J$  = 7 Hz, 1H), 8.27 (d,  $J$  = 7 Hz, 1H), 8.18 (d,  $J$  = 7 Hz, 1H), 7.84 (t,  $J$  = 7 Hz, 1H), 7.58 (t,  $J$  = 7 Hz, 1H), 7.38 (d,  $J$  = 7 Hz, 1H), 7.32 (s, 1H), 7.23-7.27 (m, 4H), 2.64 (s, 3H), 2.61 (s, 6H), 2.07 (s, 3H), 1.95 (s, 6H), 1.76 (s, 6H), 1.72 (s, 3H), 0.85 (q,  $J$  = 7 Hz, 2H), -0.25 (t,  $J$  = 7 Hz, 3H). Anal. Calcd for C<sub>60</sub>H<sub>52</sub>N<sub>4</sub>O<sub>2</sub>Zn: C, 77.78; H, 5.66; N, 6.05. Found: C, 77.62; H, 5.32; N, 6.33. HRFABMS (M<sup>+</sup>) calcd for C<sub>60</sub>H<sub>52</sub>N<sub>4</sub>O<sub>2</sub>Zn  $m/z$  924.338, found 924.338.

#### 10.5.9 Zn(HPN-CO<sub>2</sub>H) (129)

A saturated methanolic solution of Zn(OAc)<sub>2</sub>·2H<sub>2</sub>O (5 mL) and a solution of **100** (50 mg, 0.060 mmol) in 15 mL chloroform were combined and refluxed for 1 h. The solvent was removed by rotary evaporation. The remaining solid was purified by flash column chromatography (silica gel, 3:1 dichloromethane) followed by recrystallization from dichloromethane/methanol to yield **129** as a ruby red solid in quantitative yield.  $^1\text{H}$  NMR (500 MHz, CDCl<sub>3</sub>, 25 °C):  $\delta$  = 8.70 (d,  $J$  = 4 Hz, 2H), 8.66 (d,  $J$  = 4 Hz, 2H), 8.57 (d,  $J$  = 4 Hz, 2H), 8.48 (d,  $J$  = 4 Hz, 2H), 8.34 (d,  $J$  = 7 Hz, 1H), 8.25 (d,  $J$  = 7 Hz, 1H), 8.15 (d,  $J$  = 7 Hz, 1H), 7.86 (t,  $J$  = 7 Hz, 1H), 7.32 (m, 1H), 7.26 (s, 2H), 7.23 (s, 4H), 2.64 (s, 3H), 2.60 (s, 6H), 1.98 (s, 3H), 1.84 (s, 6H), 1.77 (s, 9H). Anal. Calcd for C<sub>58</sub>H<sub>48</sub>N<sub>4</sub>O<sub>2</sub>Zn: C, 77.54; H, 5.39; N, 6.24. Found: C, 77.53; H, 5.34; N, 6.33. HRFABMS (M<sup>+</sup>) calcd for C<sub>58</sub>H<sub>48</sub>N<sub>4</sub>O<sub>2</sub>Zn  $m/z$  896.307, found 896.308.

#### 10.5.10 General Details of X-ray Data Collection and Reduction

X-ray diffraction data were collected using a Siemens 3 circle diffractometer equipped with a CCD detector. Measurements were carried out at -90° C using Mo K $\alpha$  ( $\lambda$  = 0.71073 Å) radiation, which was wavelength selected with a single-crystal graphite monochromator. Four sets of data were collected using  $\omega$  scans and a -0.3° scan width. All calculations were performed using a Silicon Graphics Indigo 2 or a PC workstation. The data frames were integrated to  $hkl$ /intensity, and final unit cells were calculated by using the SAINT v.4.050



program from Siemens. The structures were solved and refined with the SHELXTL v.5.03 suite of programs developed by G. M. Sheldrick and Siemens Industrial Automation, Inc., 1995.

#### 10.5.11 X-ray Structure of $\text{Fe}_2(\text{HPN-CO}_2^-)_2$ (**123**)

A  $0.15 \times 0.08 \times 0.07$  nm single crystal of **123** suitable for crystallographic analysis was obtained from slow diffusion of ether into a toluene solution of the compound. The crystal was coated in STP and mounted onto a glass fiber. A total of 34312 reflections were collected in the  $\theta$  range 2.62 to 25°, of which 8783 were unique ( $R_{\text{int}} = 0.0900$ ). Hydrogen atoms were placed in calculated positions using a standard riding model and were refined isotropically. The largest peak and hole in the difference map were  $1.023 \text{ e}\text{\AA}^{-3}$  and  $-0.551 \text{ e}\text{\AA}^{-3}$ , respectively. The least squares refinement converged normally giving residuals of  $R_1 = 0.1108$  and  $wR_2 = 0.2216$ , with  $\text{GOF} = 1.084$ .

#### 10.5.12 Physical Measurements

$^1\text{H}$  NMR spectra were collected in  $\text{CDCl}_3$  or  $d_8$ -toluene (Cambridge Isotope Laboratories) at the MIT Department of Chemistry Instrumentation Facility (DCIF) using either a Mercury 300 or an Inova 500 spectrometer at 25 °C. All chemical shifts are reported using the standard  $\delta$  notation in parts-per-million; positive chemical shifts are to higher frequency from the given reference. UV-visible absorption spectra were obtained using a Cary-17 spectrophotometer modified by On-Line Instrument Systems (OLIS) to include computer control or a Spectral Instruments 440 Model spectrophotometer. Infrared absorption spectra were obtained using a Nicolet 860 Magna FT-IR Spectrometer. High-resolution mass spectral analyses were carried out at the University of Illinois Mass Spectrometry Laboratory or the MIT Department of Chemistry Instrumentation Facility (DCIF). Elemental analyses were performed at Michigan State University.

Electrochemical experiments were carried out using a Bioanalytical Systems (BAS) Model CV-50W potentiostat/galvanostat. Cyclic voltammetry was performed in a three-compartment cell using a glassy carbon working electrode, a  $\text{Ag}/\text{AgCl}$  reference electrode, and a platinum-wire auxiliary electrode. A modified Luggin capillary separated the working compartment from the reference electrode. All three compartments were filled with a 0.1 M solution of *n*-tetrabutylammonium perchlorate (TBAP) supporting electrolyte. The working compartment of the cell was bubbled with solvent-saturated nitrogen to deaerate the solution. The working solutions were prepared by recording the background cyclic voltammograms of the electrolyte solution prior to addition of the solid sample. All potentials are reported versus  $\text{Ag}/\text{AgCl}$  and are not corrected for the junction potential. Spectroelectrochemical studies were performed in an optically transparent thin-layer cell using a platinum mesh working electrode, a  $\text{Ag}/\text{AgCl}$

reference electrode, and a platinum-wire auxiliary electrode; absorption spectra were recorded at selected time intervals.

Nanosecond transient absorption measurements were performed using a Coherent Infinity Nd:YAG laser with OPO running at 20 Hz to excite the samples at 480 nm. A 50 W Xe arc lamp (PTI 1000, unpulsed) provided the probe light. A Vincent Associates Uniblitz shutter was used to block the probe light. The signal was dispersed with a Triax 320 spectrometer and detected using an Andor DH520 intensified gated CCD camera (ICCD). The timing of the ICCD, probe light shutter, and laser were controlled using two Stanford DG535 delay generators. Series of four spectra were taken:  $I$  (pump on/probe on),  $I_F$  (pump on/probe off),  $I_0$  (pump off/probe on),  $I_{0F}$  (pump off/probe off). Transient spectra corrected for fluorescence and laser signals were calculated from these spectra:  $\Delta OD = -\log[(I_0 - I_{0F})/(I - I_F)]$ . Spectra reported are the average of 250 of the 4-spectra sequences. Transient kinetics were measured using a Hamamatsu R928 PMT. The signal was averaged for 1000 laser shots and acquired through a LeCroy 9384CM oscilloscope, then transferred to a PC. Instrument control and data analysis were performed using software written in LabView. Luminescence lifetime measurements were obtained using a Hamamatsu C4334-0 Streak Camera. Laser excitation at 480 nm was obtained from a two-stage optical parametric amplifier (Comet 400S, B. M. Industries) which was pumped by a 1 kHz Ti:sapphire based chirped pulse regenerative amplifier system described previously. Samples for photochemical measurements were contained within a cell equipped with a solvent reservoir and a 2-mm clear fused-quartz cell (Starna Cells, Inc.). The two chambers were isolated from each other by a high-vacuum Teflon valve and from the environment with a second high-vacuum Teflon valve. Samples were subject to at least four freeze-pump-thaw cycles ( $10^{-6}$  torr).

Pulse radiolysis experiments were performed at the Brookhaven National Laboratory Laser-Electron Accelerator Facility (LEAF) in collaboration with Drs. James F. Wishart and James P. Kirby. The electron pulse parameters were the following: duration ~30 ps, charge 2-4 nC, and energy 8.5 MeV. Transient absorption data were collected by using a pulsed xenon arc lamp, a selection of 10 and 40 mm wide band-pass filters, silicon (FND-100) or germanium photodiodes, and a Tektronix TDS-680C oscilloscope. Kinetic traces were averaged over 2-8 shots. Samples were prepared under argon in a glovebox in cylindrical Suprasil cells of 5, 10, and 20 mm path lengths.

## 10.6 References and Notes

1. Chapman, S. K.; Daff, S.; Munro, A. W. *Struct. Bonding* **1997**, *88*, 39-70.
2. Kadish, K. M.; Smith, K. M.; Guillard, R. *The Porphyrin Handbook*; Academic Press: San Diego, 2000.
3. Lippard, S. J.; Berg, J. M. *Principles of Bioinorganic Chemistry*; University Science Books: Mill Valley, CA, 1994.
4. Scott, R. A.; Mauk, A. G. *Cytochrome c: a Multidisciplinary Approach*; University Science Books: Sausalito, CA, 1996.
5. Perutz, M. F. *Nature* **1970**, *228*, 726-734.
6. Dickerson, R. E.; Geis, I. *Hemoglobin: Structure, Function, Evolution, and Pathology*; Benjamin/Cummings: Menlo Park, CA, 1983.
7. Sono, M.; Roach, M. P.; Coulter, E. D.; Dawson, J. H. *Chem. Rev.* **1996**, *96*, 2841-2887.
8. Ortiz de Montellano, P. R. *Cytochrome P450: Structure, Mechanism, and Biochemistry*; 2nd ed.; Plenum: New York, 1995.
9. Poulos, T. L. *Curr. Opin. Struct. Biol.* **1995**, *5*, 767-774.
10. Groves, J. T.; Han, Y. In *Cytochrome P450: Structure, Mechanism, and Biochemistry*; 2nd ed.; Ortiz de Montellano, P. R., Ed.; Plenum: New York, 1995, pp 3-48.
11. Ozaki, S.-I.; Roach, M. P.; Matsui, T.; Watanbe, Y. *Acc. Chem. Res.* **2001**, *34*, 818-825.
12. Nicholls, P.; Fita, I.; Loewen, P. C. *Adv. Inorg. Chem.* **2001**, *51*, 51-106.
13. Malmström, B. G. In *Electron Transfer in Chemistry*; Balzani, V., Ed.; Wiley-VCH: Weinheim, Germany, 2001; Vol. 3.1.3, pp 39-55.
14. Michel, H.; Behr, J.; Harrenga, A.; Kannt, A. *Annu. Rev. Biophys. Biomol. Struct.* **1998**, *27*, 329-356.
15. Babcock, G. T.; Wikström, M. *Nature* **1992**, *356*, 301-309.
16. Wasser, I. M.; de Vries, S.; Moeenne-Loccoz, P.; Schroeder, I.; Karlin, K. D. *Chem. Rev.* **2002**, *102*, 1201-1234.
17. Marletta, M. A.; Hurshman, A. R.; Rusche, K. M. *Curr. Opin. Chem. Biol.* **1998**, *2*, 656-663.
18. Chan, M. K. *Curr. Opin. Chem. Biol.* **2001**, *5*, 216-222.
19. Harbury, H. A.; Cronin, J. R.; Fanger, M. W.; Hettinger, T. P.; Murphy, A. J.; Myer, Y. P.; Vinogradov, S. N. *Proc. Natl. Acad. Sci. USA* **1965**, *54*, 1658-1664.
20. Raphael, A. L.; Gray, H. B. *J. Am. Chem. Soc.* **1991**, *113*, 1038-1040.
21. Liu, G.; Shao, W.; Zhu, S.; Tang, W. *J. Inorg. Biochem.* **1995**, *60*, 123-131.
22. Valentine, J. S.; Sheridan, R. P.; Allen, L. C.; Kahn, P. C. *Proc. Natl. Acad. Sci. USA* **1979**, *76*, 1009-1013.

23. Kadish, K. M.; Bottomley, L. A. *Inorg. Chem.* **1980**, *19*, 832-836.
24. Nasset, M. J. M.; Shokhirev, N. V.; Enemark, P. D.; Jacobsen, S. E.; Walker, F. A. *Inorg. Chem.* **1996**, *35*, 5188-5200.
25. Huffman, D. L.; Rosenblatt, M. M.; Suslick, K. S. *J. Am. Chem. Soc.* **1998**, *120*, 6183-6184.
26. Safo, M. K.; Nasset, M. J. M.; Walker, F. A.; Debrunner, P. G.; Scheidt, W. R. *J. Am. Chem. Soc.* **1997**, *119*, 9438-9448.
27. Kennedy, M. L.; Silchenko, S.; Houndonougbo, N.; Gibney, B. R.; Dutton, P. L.; Rodgers, K. R.; Benson, D. R. *J. Am. Chem. Soc.* **2001**, *123*, 4635-4636.
28. Ma, J.-G.; Vanderkooi, J. M.; Zhang, J.; Jia, S.-L.; Shelnut, J. A. *Biochemistry* **1999**, *38*, 2787-2795.
29. Hobbs, J. D.; Shelnut, J. A. *J. Protein Chem.* **1995**, *14*, 19-25.
30. Kassner, R. J. *Proc. Natl. Acad. Sci. USA* **1972**, *69*, 2263-2267.
31. Varadarajan, R.; Zewert, T. E.; Gray, H. B.; Boxer, S. G. *Science* **1989**, *243*, 69-72.
32. Gunner, M. R.; Honig, B. *Proc. Natl. Acad. Sci. USA* **1991**, *88*, 9151-9155.
33. Springs, S. L.; Bass, S. E.; McLendon, G. *Biochemistry* **2000**, *39*, 6075-6082.
34. Stellwagen, E. *Nature* **1978**, *275*, 73-74.
35. Churg, A. K.; Warshel, A. *Biochemistry* **1986**, *25*, 1675-1681.
36. Bixler, J.; Bakker, G.; McLendon, G. *J. Am. Chem. Soc.* **1992**, *114*, 6938-6939.
37. Tezcan, F. A.; Winkler, J. R.; Gray, H. B. *J. Am. Chem. Soc.* **1998**, *120*, 13383-13388.
38. Rivera, M.; Seetharaman, R.; Girdhar, D.; Wirtz, M.; Zhang, X.; Wang, X.; White, S. *Biochemistry* **1998**, *37*, 1485-1494.
39. Lancaster, C. R. D.; Michel, H.; Honig, B.; Gunner, M. R. *Biophys. J.* **1996**, *70*, 2469-2492.
40. Bashford, D.; Karplus, M.; Canters, G. W. *J. Mol. Biol.* **1988**, *203*, 507-510.
41. Shifman, J. M.; Moser, C. C.; Kalsbeck, W. W.; Bocian, D. F.; Dutton, P. L. *Biochemistry* **1998**, *37*, 16815-16827.
42. Rau, H. K.; DeJonge, N.; Haehnel, W. *Angew. Chem. Int. Ed.* **2000**, *39*, 250-253.
43. Low, D. W.; Hill, M. G. *J. Am. Chem. Soc.* **2000**, *122*, 11039-11040.
44. Chen, K.; Hirst, J.; Camba, R.; Bonagura, C. A.; Stout, C. D.; Burgess, B. K.; Armstrong, F. A. *Nature* **2000**, *405*, 814-817.
45. Armstrong, F. A. *J. Chem. Soc. Dalton Trans.* **2002**, 661-671.
46. Kennedy, M. L.; Gibney, B. R. *J. Am. Chem. Soc.* **2002**, *124*, 6826-6827.
47. Yikilmaz, E.; Xie, J.; Brunold, T. C.; Miller, A.-F. *J. Am. Chem. Soc.* **2002**, *124*, 3482-3483.

48. Chang, C. J.; Brown, J. D. K.; Chang, M. C. Y.; Baker, E. A.; Nocera, D. G. In *Electron Transfer in Chemistry*; Balzani, V., Ed.; Wiley-VCH: Weinheim, Germany, 2001; Vol. 3.2.4, pp 409-461.
49. Cukier, R. I.; Nocera, D. G. *Annu. Rev. Phys. Chem.* **1998**, *49*, 337-369.
50. Ramirez, B. E.; Malmström, B. G.; Winkler, J. R.; Gray, H. B. *Proc. Natl. Acad. Sci. USA* **1997**, *92*, 11949-11951.
51. Okamura, M. Y.; Feher, G. *Annu. Rev. Biochem.* **1992**, *61*, 861-896.
52. Takahashi, E.; Maroti, P.; Wraight, C. In *Electron and Proton Transfer in Chemistry and Biology*; Müller, A., Ratajczaks, H., Junge, W. and Diemann, E., Ed.; Elsevier: Amsterdam, 1992, pp 219-236.
53. Burgess, B. K.; Lowe, D. J. *Chem. Rev.* **1996**, *96*, 2983-3011.
54. Feig, A. L.; Lippard, S. J. *Chem. Rev.* **1994**, *94*, 759-805.
55. Stubbe, J. *J. Biol. Chem.* **1990**, *265*, 5329-5332.
56. Stubbe, J.; Riggs-Gelasco, P. *Trends Biochem. Sci.* **1998**, *23*, 438-443.
57. Sjöberg, B.-M. *Structure* **1994**, *2*, 793-796.
58. Uhlin, U.; Eklund, H. *Nature* **1994**, *370*, 533-538.
59. Ostermeier, C.; Harrenga, A.; Ermler, U.; Michel, H. *Proc. Natl. Acad. USA* **1997**, *94*, 10547-10553.
60. Nordlund, P.; Sjöberg, B.-M.; Eklund, H. *Nature* **1990**, *370*, 593-598.
61. Averill, B. A. *Chem. Rev.* **1996**, *96*, 2951-2964.
62. Brzezinski, P. *Biochim. Biophys. Acta* **2000**, *1458*, 1-5.
63. Williams, R. J. P. *J. Solid State Chem.* **1999**, *145*, 488-495.
64. Chang, C. K.; Liang, Y.; Aviles, G.; Peng, S.-M. *J. Am. Chem. Soc.* **1995**, *117*, 4191-4192.
65. Momenteau, M.; Reed, C. A. *Chem. Rev.* **1994**, *94*, 659-698.
66. Matsui, M.; Higashi, M.; Takeuchi, T. *J. Am. Chem. Soc.* **2000**, *122*, 5218-5219.
67. Walker, F. A.; Bowen, J. *J. Am. Chem. Soc.* **1985**, *107*, 7632-7635.
68. Tani, F.; Matsu-Ura, M.; Nakayama, S.; Naruta, Y. *Coord. Chem. Rev.* **2002**, *226*, 219-226.
69. Suzuki, N.; Higuchi, T.; Urano, Y.; Kikuchi, K.; Uekusa, H.; Ohashi, Y.; Uchida, T.; Kitagawa, T.; Nagano, T. *J. Am. Chem. Soc.* **1999**, *121*, 11571-11572.
70. Gupta, R.; MacBeth, C. E.; Young Jr., V. G.; Borovik, A. S. *J. Am. Chem. Soc.* **2002**, *124*, 1136-1137.
71. Wada, A.; Ogo, S.; Nagatomo, S.; Kitagawa, T.; Watanabe, Y.; Jitsukawa, K.; Masuda, H. *Inorg. Chem.* **2002**, *41*, 616-618.

72. Garner, D. K.; Allred, R. A.; Tubbs, K. J.; Arif, A. M.; Berreau, L. M. *Inorg. Chem.* **2002**, *41*, 3533-3541.
73. O'Brien, P.; Sweigart, D. A. *Inorg. Chem.* **1985**, *24*, 1405-1409.
74. Woo, K.; Sweigart, D. A. *Inorg. Chem.* **1993**, *32*, 4979-4981.
75. Chang, C. J.; Yeh, C.-Y.; Nocera, D. G. *J. Org. Chem.* **2002**, *67*, 1403-1406.
76. Yeh, C.-Y.; Chang, C. J.; Nocera, D. G. *J. Am. Chem. Soc.* **2001**, *123*, 1513-1514.
77. Chang, C. K.; Kondylis, M. P. *J. Chem. Soc. Chem. Commun.* **1986**, 316-318.
78. Harmjanz, M.; Scott, M. J. *Inorg. Chem.* **2000**, *39*, 5428-5429.
79. Harmjanz, M.; Gill, H. S.; Scott, M. J. *J. Am. Chem. Soc.* **2000**, *122*, 10476-10477.
80. Harmjanz, M.; Scott, M. J. *Chem. Commun.* **2000**, 397-398.
81. Harmjanz, M.; Gill, H. S.; Scott, M. J. *J. Org. Chem.* **2001**, *66*, 5374-5383.
82. Harmjanz, M.; Bozidarevic, I.; Scott, M. J. *Org. Lett.* **2001**, *3*, 2281-2284.
83. Balch, A. L. *Inorg. Chim. Acta* **1992**, *198-200*, 297-307.
84. Cheng, R.; Latos-Grazynski, L.; Balch, A. L. *Inorg. Chem.* **1982**, *21*, 2412-2418.
85. Goff, H. M.; Shimomura, E. T.; Lee, Y. J.; Scheidt, W. R. *Inorg. Chem.* **1984**, *23*, 315-321.
86. Baldwin, D. A.; Marques, H. M.; Pratt, J. M. *J. Inorg. Biochem.* **1986**, *27*, 245-254.
87. Wang, J. S.; Tsai, A. L.; Heldt, J.; Palmer, G.; Van Wart, H. E. *J. Biol. Chem.* **1992**, *267*, 15310-15318.
88. Kalyanasundaram, K. *Photochemistry of Polypyridine and Porphyrin Complexes*; Academic Press: London, 1992.
89. Roundhill, D. M. *Photochemistry and Photophysics of Metal Complexes*; Plenum Press: New York, 1994.
90. El-Kasmi, A.; Lexa, D.; Maillard, P.; Momenteau, M.; Savéant, J.-M. *J. Am. Chem. Soc.* **1991**, *113*, 1586-1595.
91. Armarego, W. L. F.; Perrin, D. D. *Purification of Laboratory Chemicals*; 4th ed.; Butterworth-Heinmann: Oxford, 1996.

*Chapter 11*

**Proton-Coupled O—O Bond Activation on a Synthetic  
Hydrogen-Bonding Redox Platform**

A portion of the work presented in this chapter has been published:

Yeh, C.-Y.; Chang, C. J.; Nocera, D. G. *J. Am. Chem. Soc.* **2001**, *123*, 1513-1514.

## 11.1 Motivation and Specific Aims

The Hangman porphyrin systems HPX (hanging porphyrin xanthene) and HPD (hanging porphyrin dibenzofuran) described in chapter 9 afford the ability to control both the orientation and acid-base properties of the pendant hydrogen-bonding group, presenting attractive platforms for utilizing proton-coupled electron transfer (PCET) as vehicle for exploring small-molecule activation chemistry. In this chapter, we present the synthesis and characterization of iron and manganese coordination complexes of the HPX and HPD platforms and their subsequent catalytic O—O activation reactivity. In particular, the HPX complexes are remarkably simple models for the heme water channel assemblies found in the cytochrome P450 family of enzymes. These pillared Hangman porphyrins have the distinct ability to orient exogenous water in a controlled fashion using hydrogen bonding in the solid state and in solution, as well as affording the first monomeric iron(III) hydroxide porphyrin to be characterized by single crystal X-ray analysis. Comparative reactivity studies for the catalase-like disproportionation of hydrogen peroxide by iron derivatives and the epoxidation of olefins by manganese complexes reveal that the introduction of a single proton-shuttle group in proper orientation to a redox-active platform can significantly enhance the catalytic activation of O—O bonds. For catalase and epoxidation reactivities, the xanthene-bridged platform with a pendant carboxylic acid group (HPX-CO<sub>2</sub>H) has the highest comparative catalytic activity, establishing that this approach can yield superior catalysts to analogs that do not control both proton and electron currencies.

## 11.2 Background

Many fundamental small-molecule transformations in Nature require the coupled transport of both proton *and* electron equivalents to effect bond-making and bond-breaking catalysis. Consummate examples include the photoinduced oxidation of water to oxygen by photosystem II<sup>1-8</sup> and chemically diametric reduction of oxygen to water by cytochrome *c* oxidase.<sup>9-17</sup> In addition to these enzymes, proton-coupled electron transfer (PCET) events continue to emerge in the structure/function relations of a broad range of other natural systems such as copper-based oxidases,<sup>18-21</sup> flavin and pyrroloquinoline dependent enzymes,<sup>22,23</sup> non-heme iron proteins,<sup>24-30</sup> iron-sulfur proteins,<sup>31-34</sup> and reductases such as hydrogenase<sup>35-38</sup> and nitrogenase<sup>39,40</sup> to name a few.<sup>41</sup>

Within the interiors of the complex tertiary structures of these oxidases and reductases, noncovalent hydrogen-bonding interactions are paramount to dynamically regulating the active site for PCET reactivity. Heme-dependent proteins featuring a conserved iron protoporphyrin IX cofactor are exemplar in their structural control of PCET. From this singular point, hemoproteins have evolved to accommodate a diverse set of functions,<sup>42</sup> including O<sub>2</sub> transport and



storage,<sup>43,44</sup> single outer-sphere electron transfer,<sup>45-47</sup> O<sub>2</sub> reduction,<sup>9-17</sup> small-molecule sensing and signaling,<sup>48-50</sup> and metabolic oxidation reactions.<sup>51-56</sup> In all cases, the specific chemical reactivity of the heme enzyme is dictated by the surrounding polypeptide medium, which encapsulates the redox cofactor within a precise microenvironment for proper delivery of proton and electron equivalents. Figure 11.1 compares the active site structures of peroxidases, catalases, and the cytochrome P450 monooxygenases, highlighting the structural parallels at the distal side of the heme pocket where O—O activation occurs. Through the targeted use of amino acid side chains and/or solvent water as proton shuttles, these proteins react with oxygen or hydrogen peroxide to generate highly reactive iron-oxo species within their active site cavities for substrate oxidation. Such hydrogen-bonding groups participate in directed general acid-base chemistry to provide kinetic control of proton transfer and bond polarization for heterolytic O—O bond cleavage, classically known as the “pull effect”.<sup>55,57-64</sup> The cytochrome P450 family of enzymes are particularly intriguing in their use of internal solvent water channels embedded within the protein superstructure to tune heme electronic structure and redox potential, as well as furnishing a possible proton-relay pathway during catalytic turnover.<sup>52,53,65-67</sup>

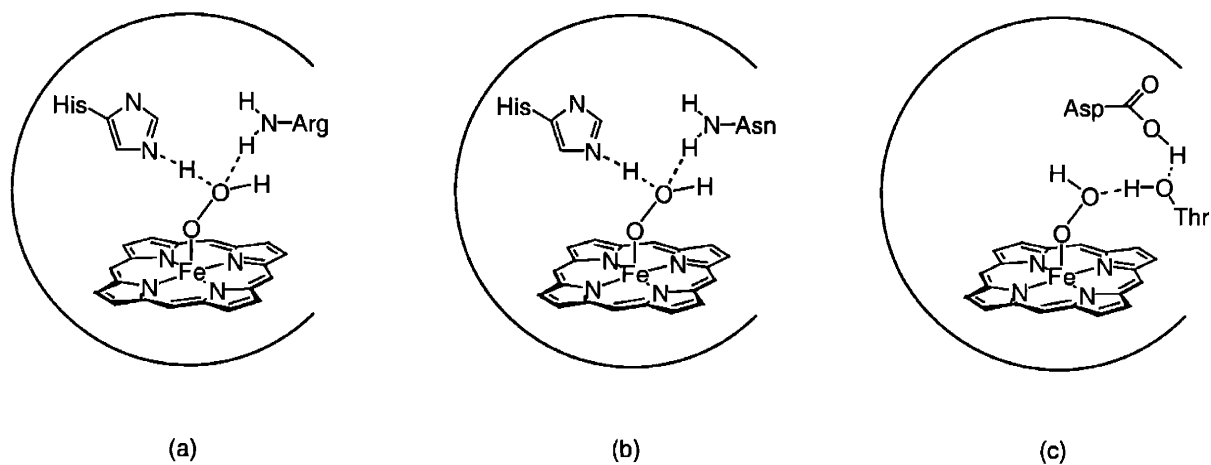


**Figure 11.1.** Comparison of proposed proton-activated O—O bond cleavage for iron-oxo heme formation in (a) peroxidases, (b) catalases, and (c) cytochrome P450 monooxygenases.

With regard to this latter issue, studies with the native P450cam enzyme and its site-directed mutants<sup>51,57,65,68-74</sup> suggest that the active site asparagine and threonine amino acid residues are important in establishing a controlled proton delivery pathway involving solvent water, as well as providing an active-site hydrogen-bond donor to stabilize the oxygen adduct.<sup>66,75-80</sup>

Although the importance of hydrogen bonding and water channels are clearly recognized in the structural biology of heme proteins, neither the origin of protons in the hydrophobic binding

pockets typical of heme enzymes, nor the mechanisms of coupled electron and proton transfer have been definitively established. To this end, several protein- and peptide-based constructs have been designed to probe how oxidative reactivity mediated by proton and electron transfer events is controlled by the heme pocket distal superstructure. Myoglobin has been converted into a peroxidase-like enzyme by alteration of the heme distal pocket via site-directed mutagenesis.<sup>55,81</sup> In a separate strategy, substrates tethered to photoexcitable redox triggers have been employed to scrutinize reactive transient species of cytochrome P450.<sup>82-84</sup> In this same vein, semisynthetic approaches have been utilized to prepare myoglobins with functionalized hemes for generating high-valent ferryl species upon photon absorption.<sup>85-88</sup> Combined with studies of the natural enzymes, these biomolecule-based constructs have sought to exploit the native protein fold to impose the H-bond network required for PCET activation of the O—O bond affixed to the heme active site.

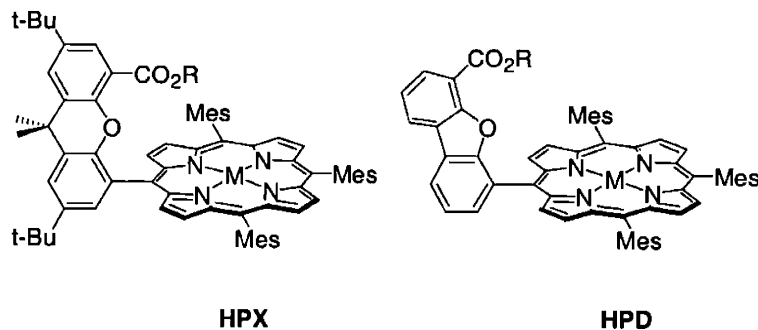
Owing to the challenges associated with isolating and identifying the precise factors governing PCET in complex bioconjugates, we have taken the alternative approach of molecular design by chemical synthesis. We have sought to combine acid-base and redox functionalities onto a single molecular platform. Such simple constructs, in principle, allow for the systematic control of structural and electronic variables through targeted synthetic modification. Initial efforts have explored photoinduced reactions of synthetic donor-acceptor pairs juxtaposed by a hydrogen-bonded interface.<sup>89-99</sup> Our work has focused on PCET reactions mediated by an amidinium-carboxylate scaffold, a noncovalent interaction that models the arginine-aspartate salt bridge found in many biological systems.<sup>100-104</sup> The amidinium-carboxylate interface combines the dipole of an electrostatic ion-pair interaction with a hydrogen-bonding scaffold, allowing us to investigate how proton motion within a hydrogen-bonded interface affects the charge, energetics, and polarity of the electron transport chain. A comparative kinetics study of photoinduced electron transfer through such an asymmetric salt bridge interface shows that the rate of electron transfer through the D---[amidinium-carboxylate]---A system is over 100 times slower than for the donor-acceptor system in which the interface is oriented in the opposite direction, demonstrating that charge transport can be significantly affected by coupled proton motion.<sup>93</sup>

Whereas such systems have been invaluable in elucidating mechanistic details of PCET, they are not suitable scaffolds for exploring PCET as it pertains to small-molecule activation chemistry. Proximate acid-base and redox sites are presented in a side-to-side arrangement, thus orienting the PCET functionalities orthogonal to the catalytic bond-making and bond-breaking processes required to occur at the metal center. Consequently, we sought to create constructs where proton and electron delivery are confined to a face-to-face arrangement, in order to direct PCET along

the metal-ligand coordination axis for catalytic small-molecule activation. Along these lines, we have recently demonstrated that xanthene and dibenzofuran spacers can organize two redox cofactors along the desired face-to-face reaction coordinate. In these DPX (diporphyrin xanthene) and DPD (diporphyrin dibenzofuran) cofacial constructs, neighboring porphyrins display an extensive range of vertical pocket size dimensions and flexibilities with minimal lateral displacements between macrocyclic subunits. Replacement of one of the porphyrin redox subunits with a proton donor converts these cofacial Pacman systems into hybrid proton/redox shuttle platforms (Hangman porphyrins). We have recently shown that a xanthene anchor may be used to “hang” a hydrogen-bond functionality over a redox-active metalloporphyrin platform.<sup>105,106</sup> The compounds are simplified constructs of the biomolecules with engineered distal sites inasmuch as the platforms capture control of both proton and electron transfer without the need for secondary and tertiary protein structure to impose a proton network among structured water or protonated amino acid side chains. In contrast to hydrogen-bonded heme<sup>107-119</sup> and non-heme<sup>120-133</sup> models which have been employed for simple ligand substitution reactions, the Hangman platforms represent a unique approach to exploit hydrogen-bonding motifs for small-molecule activation chemistry.

In this chapter, we report the synthesis, characterization, and catalytic O—O bond activation chemistry of Hangman porphyrin platforms. We stress here that our aim is not to create competitive analogs of existing catalysts, but to demonstrate how the addition of proton control can enhance the reactivity of a redox cofactor. Suzuki cross-coupling methods provide a smooth synthetic inroad towards the preparation of Hangman systems based on xanthene (HPX = hanging porphyrin xanthene) and dibenzofuran (HPD = hanging porphyrin dibenzofuran) scaffolds (Chart 11.1). These simple constructs allow for precise control over the functional nature of the hydrogen-bonding pendant in terms of proton-donating ability and arrangement in relation to the metalloporphyrin redox site. In addition, we have evaluated the catalytic O—O bond activation reactivity of a systematic set of HPX and HPD compounds with varying hydrogen-bonding and proton-transfer abilities. For comparative analysis, we have examined the reactivity of simple redox-only porphyrin analogs with similar steric and electronic properties to our Hangman templates. Two reactivities have been elaborated, namely catalase-like oxygen evolution and cytochrome P450-type epoxidation. Our findings reveal that dramatic enhancement in catalytic reactivity can be obtained with a single well-positioned acid-base functionality, and the design of catalysts that control proton inventory can take a single redox cofactor to make divergent chemical reactivity.

Chart 11.1

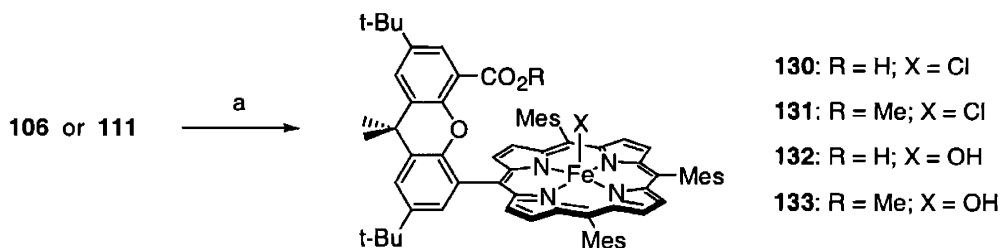


## 11.3 Results and Discussion

### 11.3.1 Iron and Manganese Coordination Complexes of HPX and HPD

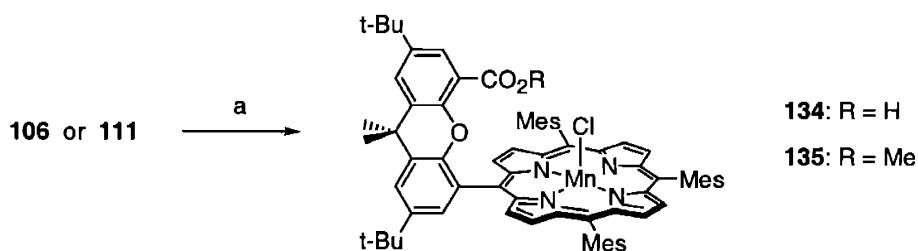
Our interest in the multielectron transformation of small-molecule substrates within a proton-coupled electron transfer (PCET) framework has led us to develop new symmetric cofacial porphyrins based on xanthene (DPX = diporphyrin xanthene) and dibenzofuran (DPD = diporphyrin dibenzofuran) spacers that display an extensive range of vertical pocket size dimensions and flexibilities with minimal lateral displacements between macrocyclic subunits.<sup>134-139</sup> A similar approach may be employed to create asymmetric cofacial porphyrin architectures in which a rigid xanthene or dibenzofuran scaffold is used to “hang” a hydrogen-bonding group over the porphyrin motif (HPX = hanging porphyrin xanthene, HPD = hanging porphyrin dibenzofuran). The substitution of a six-membered center ring for xanthene with a five-membered one for dibenzofuran allows for a large span of vertical distances between ditopic sites.<sup>137</sup>

Transition-metal complexes of the HPX and HPD systems are readily available from direct reaction with metal salts (Schemes 11.1 to 11.3). Iron insertion into HPX porphyrins H<sub>2</sub>(HPX-CO<sub>2</sub>H) (**111**) and H<sub>2</sub>(HPX-CO<sub>2</sub>Me) (**106**) with FeBr<sub>2</sub> followed by treatment with HCl affords the corresponding chloroiron(III) porphyrin complexes FeCl(HPX-CO<sub>2</sub>H) (**130**) and FeCl(HPX-CO<sub>2</sub>Me) (**131**) in excellent yields (89% and 92%, respectively). Compounds **130** and **131** were fully characterized by high-resolution mass spectral and elemental analyses. Alternatively, metalation of **111** and **106** followed by basic workup supplies the monomeric iron(III) hydroxide porphyrins FeOH(HPX-CO<sub>2</sub>H) (**132**) and FeOH(HPX-CO<sub>2</sub>Me) (**133**) in 92% and 90% yield, respectively. The sterically-demanding mesityl groups prevent the formation of bisiron(III)  $\mu$ -oxo dimers.<sup>140-142</sup> Satisfactory high-resolution mass spectral and elemental analyses accompanied **132** and **133**.



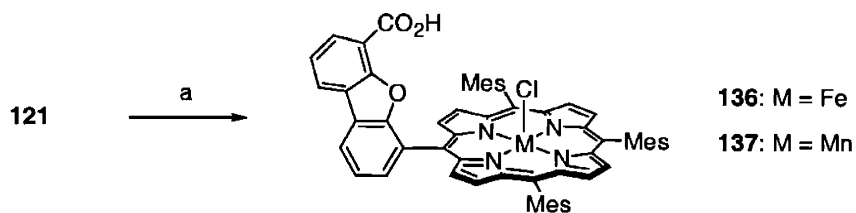
**Scheme 11.1.** (a) i. FeBr<sub>2</sub>, DMF or THF/benzene; ii. HCl or NaOH.

Other metal insertions proceed with equal success. For example, the analogous chloromanganese(III) complexes MnCl(HPX-CO<sub>2</sub>H) (**134**) and MnCl(HPX-CO<sub>2</sub>Me) (**135**) are prepared in excellent yields (90% and 93%, respectively) by reactions of **111** and **106** with Mn(OAc)<sub>2</sub>•4H<sub>2</sub>O under Alder conditions followed by workup with NaCl and HCl. Complexes **134** and **135** gave satisfactory high-resolution mass spectral and elemental analyses.



**Scheme 11.2.** (a) i. Mn(OAc)<sub>2</sub>•4H<sub>2</sub>O, DMF; ii. NaCl/HCl.

Lastly, the chloroiron(III) FeCl(HPD-CO<sub>2</sub>H) (**136**) and chloromanganese(III) MnCl(HPD-CO<sub>2</sub>H) (**137**) complexes of HPD are synthesized in 85% and 90% yield, respectively, from H<sub>2</sub>(HPD-CO<sub>2</sub>H) (**121**). With the ability to control both the protic capability (carboxylic acid vs ester) and orientation (xanthene vs dibenzofuran) of the distal hydrogen-bonding functionality, the HPX and HPD platforms provide a set of well-defined molecular scaffolds for systematic examination of proton-coupled effects on O—O bond activation.



**Scheme 11.3.** (a) i. MX<sub>2</sub>; ii. HCl or NaCl/HCl.

### 11.3.2 Iron(III) Hydroxide HPX Complex Yields a Heme/Water Channel Structure

Remarkably, the HPX system provides a minimalist model platform for the heme water channel assembly found in the cytochrome P450 enzymes as evidenced by the X-ray structure of the iron(III) hydroxide derivative **132** (Figure 11.2). Crystallographic data are given in Table 11.1 and selected bond lengths and angles are collected in Table 11.2.

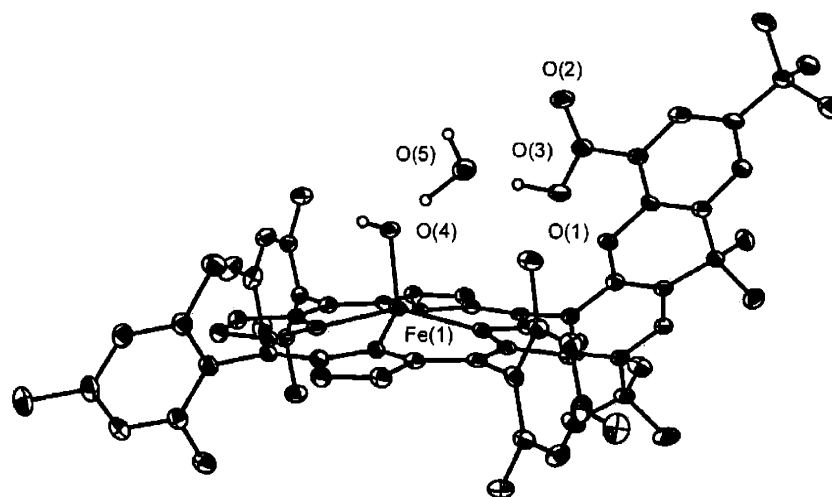


**Figure 11.2.** Crystal structure of FeOH(HPX-CO<sub>2</sub>H)·H<sub>2</sub>O (**132**). Thermal ellipsoids are drawn at the 25% probability level. Hydrogen atoms and solvent molecules within the lattice have been omitted for clarity.

A number of notable features merit discussion here. To the best of our knowledge, we are unaware of another reported crystal structure of a monomeric iron(III) hydroxide porphyrin.<sup>143</sup> Furthermore, it is interesting to note that the hydrogen-bonding network promotes selective binding of the axial hydroxide ligand to the distal side of the HPX platform. The complex adopts a distorted square pyramidal geometry with the pentacoordinate Fe elevated 0.4947 Å out of the N<sub>4</sub> plane and an average Fe—N<sub>pyrrole</sub> bond length of 2.075 Å. The Fe—O<sub>hydroxide</sub> bond length of 1.868 Å is shorter than the Fe—O distances found for Fe(III)-aqua porphyrins (~2.04 Å)<sup>144-146</sup> and Fe porphyrin dimers that contain bent, bridging hydroxo ligands (1.92-1.95 Å),<sup>147,148</sup> but significantly longer than those found in corresponding Fe(III) μ-oxo dimers (1.73-1.82 Å).<sup>144</sup> The values for all these parameters are consistent with data obtained for other five-coordinate high-spin Fe(III) porphyrin derivatives. Even more striking is the water molecule bound between the distal xanthene carboxylic acid and iron porphyrin hydroxide by two hydrogen bonds. The short O—O distances of 2.581 and 2.670 Å from the water to the carboxylic acid and the iron hydroxide, respectively, attest to the stability of this unique hydrogen-bonded scaffold. In order to accommodate the bridging water molecule, the xanthene pillar rotates along the porphyrin macrocycle, forming a dihedral angle of 59.8°.

**Table 11.1.** Crystallographic Data for Compound 132.

<b>132</b>	
Empirical formula	C <sub>76</sub> H <sub>85</sub> N <sub>4</sub> O <sub>5</sub> Fe <sub>2</sub>
Formula weight	1190.33
Temperature	100(2) K
Wavelength	0.71073 Å
Crystal system	Triclinic
Space group	$P\bar{1}$
Unit cell dimensions	$a = 13.348(1)$ Å $b = 15.716(2)$ Å $c = 17.509(2)$ Å $\alpha = 70.287(1)^\circ$ $\beta = 84.608(1)^\circ$ $\gamma = 69.442(1)^\circ$
Volume	3236.2(4) Å <sup>3</sup>
Z	2
Density (calculated)	1.222 Mg/m <sup>3</sup>
Absorption coefficient	0.288 mm <sup>-1</sup>
F(000)	1270
Crystal size	0.19 × 0.15 × 0.09 mm <sup>3</sup>
$\theta$ range for data collection	1.46 to 25.07°
Reflections collected	23746
Independent reflections	11321 ( $R_{\text{int}} = 0.0630$ )
Data/restraints/parameters	11321 / 0 / 599
Goodness-of-fit on F <sup>2</sup>	1.033
Final R indices [ $I > 2\sigma(I)$ ]	$R1 = 0.0545$ $wR2 = 0.1184$
Final R indices (all data)	$R1 = 0.1251$ , $wR2 = 0.1473$
Largest diff peak	0.426 eÅ <sup>-3</sup>
Largest diff hole	-0.549 eÅ <sup>-3</sup>

**Table 11.2.** Selected Bond Distances (Å) and Angles (deg) for **132**.

<i>Bond Distances / Å</i>		<i>Bond Angles / deg</i>	
Fe(1)–N(1)	2.076(3)	N(1)–Fe(1)–N(2)	85.91(12)
Fe(1)–N(2)	2.072(4)	N(1)–Fe(1)–N(3)	152.12(12)
Fe(1)–N(3)	2.081(4)	N(2)–Fe(1)–N(3)	87.32(12)
Fe(1)–N(4)	2.070(4)	N(1)–Fe(1)–N(4)	88.06(12)
Fe(1)–O(4)	1.868(3)	N(2)–Fe(1)–N(4)	152.71(12)
		N(3)–Fe(1)–N(4)	85.67(12)
		N(1)–Fe(1)–O(4)	104.49(12)
		N(2)–Fe(1)–O(4)	106.64(14)
		N(3)–Fe(1)–O(4)	103.37(12)
		N(4)–Fe(1)–O(4)	100.64(14)

Preliminary results suggest that the water remains bound in solution as well as in the solid state, and that this binding is chemically reversible (Figure 11.3). Titration of **132** with a slight excess of various bases results in facile replacement of the carboxylic acid proton with the corresponding cations ( $K^+$  **132b**,  $NMe_4^+$  **132c**,  $NBu_4^+$  **132d**). The solution spectra of carboxylates **132b** and **132c** are nearly identical to that of **132**, displaying Soret absorptions at 419 nm with tailing, low-intensity Q-band shoulders at 490, 550 and 655 nm. In contrast, the spectrum of carboxylate **132d**, containing the sterically bulky  $NBu_4^+$  cation, is distinguished from the rest of the series by a broadened Soret band at 419 nm and a well-defined Q-band doublet at 576 and 622 nm. This absorption profile is identical to  $Fe(TMP)OH$  and to the methyl ester derivative of **133**,  $Fe(HPX-CO_2Me)OH$  (**133**), which does not support a water bound within a hydrogen-bonding network.<sup>142</sup> Compound **132** is recovered quantitatively upon addition of a slight excess of water to **132d**. These solution data are consistent with the reversible binding of a directed water as observed in the crystal structure of **132**.



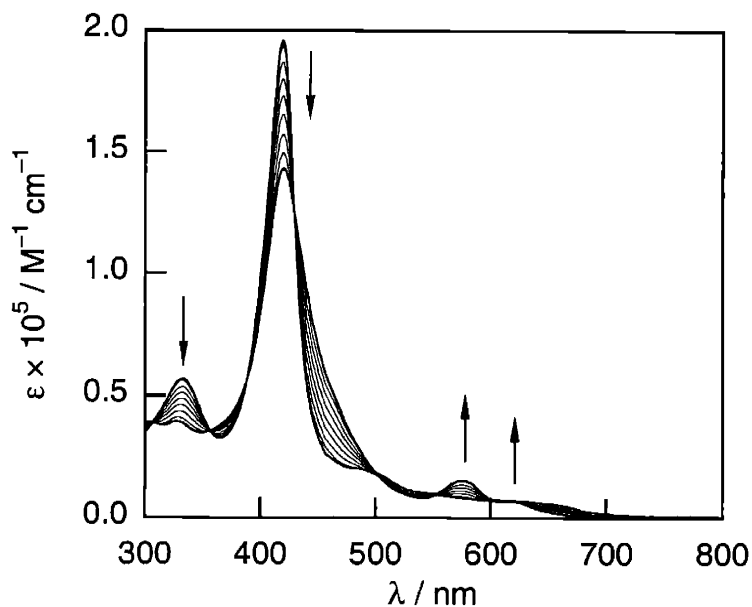


**Figure 11.3.** Absorption spectral changes upon addition of  $[\text{NBu}_4][\text{OH}]$  to a toluene solution of **132**, showing conversion to product **132d**.  $[\text{NBu}_4][\text{OH}]$  added = 0, 0.33, 0.50, 0.67, 0.85, 1.0, 1.5, 2.0 equiv.

The HPX system, with its ability to bind water in a controlled manner via non-covalent hydrogen bond interactions, provides a remarkably minimalist model platform for the heme water channel assembly found in the cytochrome P450 enzymes. Furthermore, the exceptional ability of these Hangman porphyrins to juxtapose water and hydroxy units offers a unique opportunity to explore proton-coupled O—O bond forming and cleavage chemistry using these molecular templates.

### 11.3.3 Thermal Characterization of Water Channel Structure

In addition to providing the first reported crystal structure of a monomeric iron(III) hydroxide porphyrin, the structure of **132** displayed the unprecedented feature of a single water molecule encapsulated by ditopic hydrogen bonding between the distal xanthene carboxylic acid and the terminal hydroxide ligand of the porphyrin. To probe the magnitude of water binding by the hydrogen-bonded scaffold, differential scanning calorimetry (DSC) measurements were carried out on solid samples of **132**. DSC scans exhibit an endothermic peak with an onset of 270 °C (Figure 11.4). Thermal gravimetric measurements coupled to *in-situ* infrared absorption detection confirm that this peak corresponds to a dehydration process. The heat flow associated with the dehydration is 21.8 J/g; integration yields a binding energy of 5.8 kcal/mol for the water to the HPX platform. This value attests to the strength of the matched hydrogen-bonding network for the juxtaposition of two oxygen atoms between the ditopic metalloporphyrin and hydrogen-bonding group sites.

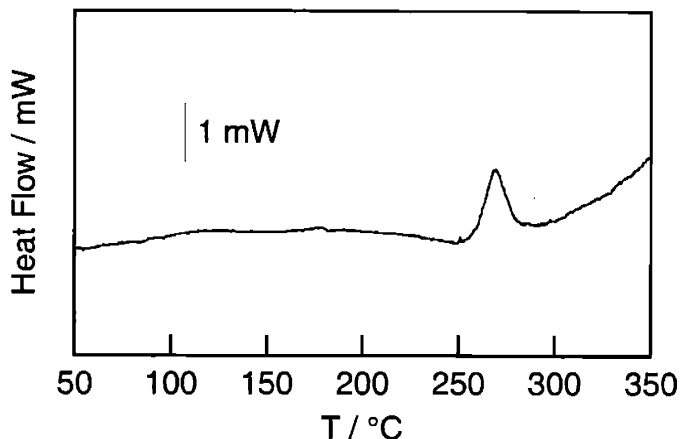


**Figure 11.4.** Differential scanning calorimetry (DSC) scan of a solid sample of **132** under nitrogen.

#### 11.3.4 Chemical Generation of High-Valent Ferryl HPX and HPD Derivatives

We sought to provide direct evidence for the formation of high-valent species in order to establish the suitability of the HPX and HPD platforms to effect oxidation reactions. To this end, iron-oxo complexes of the HPX and HPD frameworks analogous to Compounds I and II of heme enzymes have been prepared at low temperature and spectroscopically interrogated (Figure 11.5). Chemical oxidation to afford the ferryl porphyrin or ferryl porphyrin cation radical species is dependent on the axial ligand, solvent, and reaction temperature. Reactions of iron(III) hydroxide complexes **132** and **133** with mCPBA in THF at  $-61\text{ }^{\circ}\text{C}$  furnish deep red solutions with identical absorption spectra characteristic of neutral iron(IV)-oxo porphyrins, displaying a Soret band at  $418\text{ nm}$  ( $\epsilon = 170,000\text{ M}^{-1}\text{ cm}^{-1}$ ) and a Q-band centered at  $555\text{ nm}$ .<sup>52,141,149,150</sup> In contrast, treatment of the chloroiron(III) derivatives **130**, **131**, and **136** with PhIO in dichloromethane at  $-78\text{ }^{\circ}\text{C}$  occur with the formation of emerald green species that exhibit absorption spectra consistent with their assignment as iron(IV)-oxo porphyrin cation radical species.<sup>52,54,141,150</sup> These spectra exhibit broadened, blue-shifted Soret bands of decreased molar absorptivity ( $\lambda_{\text{max}} \sim 406\text{ nm}$ ,  $\epsilon \sim 70,000\text{ M}^{-1}\text{ cm}^{-1}$ ) with accompanying weak, tailing absorptions at  $600\text{--}700\text{ nm}$  indicative of porphyrin cation radicals.<sup>150</sup> The successful preparation of high-valent ferryl HPX and HPD complexes presages an oxidation reactivity derived from O—O bond activation chemistry.

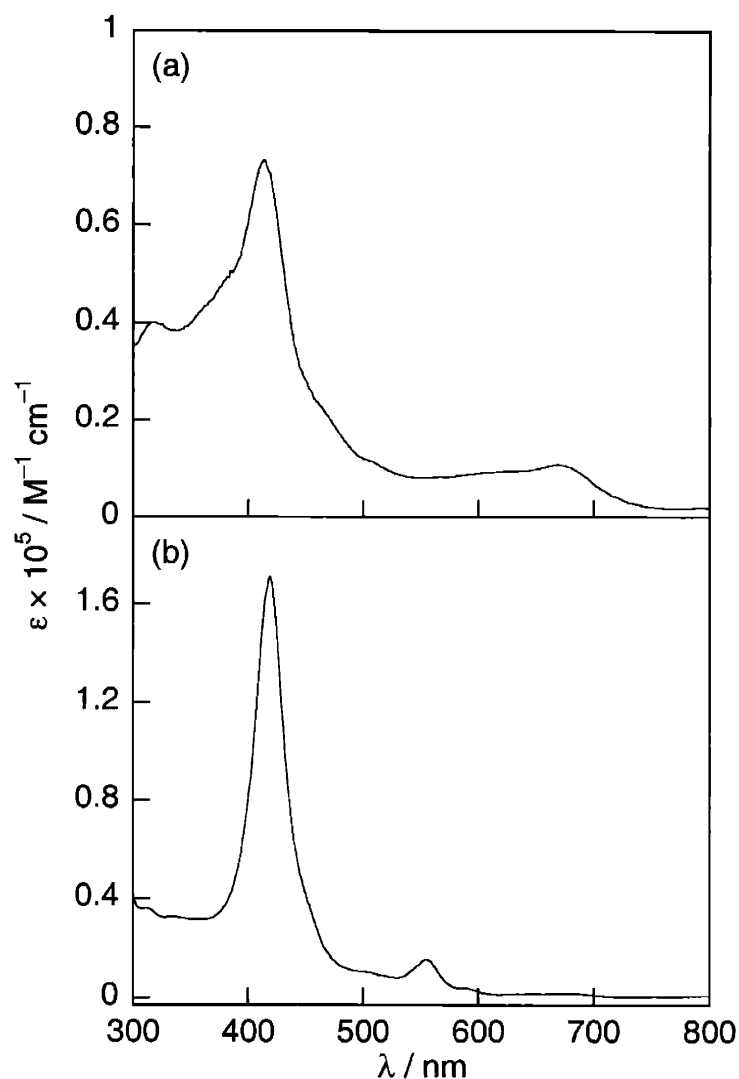
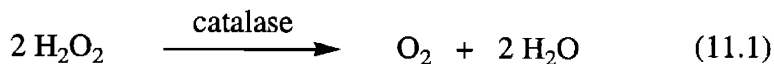


**Figure 11.5.** Absorption spectra of high-valent ferryl-HPX complexes analogous to Compounds I and II of heme oxygenases. Spectrum (a) was obtained by oxidation of  $\text{FeCl}(\text{HPX-CO}_2\text{H})$  (**130**) with PhIO in dichloromethane at  $-78\text{ }^\circ\text{C}$ . Spectrum (b) was obtained by oxidation of  $\text{FeOH}(\text{HPX-CO}_2\text{H})$  (**132**) with mCPBA in THF at  $-61\text{ }^\circ\text{C}$ .

### 11.3.5 Catalase-Like Disproportionation of Hydrogen Peroxide

Peroxide species provide a direct starting point from which to examine the effects of hydrogen bonding and proton transfer on O—O bond activation chemistry.<sup>151</sup> In Nature, the catalase enzymes,<sup>56,57</sup> the majority of which are heme-based, dismutate intracellular hydrogen peroxide to oxygen and water according to the stoichiometry in Equation 11.1:



Because the 2:1  $\text{H}_2\text{O}_2:\text{O}_2$  ratio is characteristic of dismutation, we investigated the  $\text{H}_2\text{O}_2:\text{O}_2$  mass balance of equation 11.1 for the activity of HPX carboxylic acid **130** with  $\text{H}_2\text{O}_2$  under buffered, biphasic conditions (dichloromethane/aqueous phase pH 7) in the presence of 1,5-dicyclohexylimidazole at 25 °C. Figure 11.6 displays the yield of  $\text{O}_2$  as a function of initial  $\text{H}_2\text{O}_2$  concentration in the aqueous layer in the presence of 500  $\mu\text{M}$  of **130**. The yield of  $\text{O}_2$  exhibits a linear dependence on the initial concentration of  $\text{H}_2\text{O}_2$ . The slope of the regression line ( $0.45 \pm 0.03$ ) agrees well with the value of 0.5 expected for a catalase-like stoichiometry.

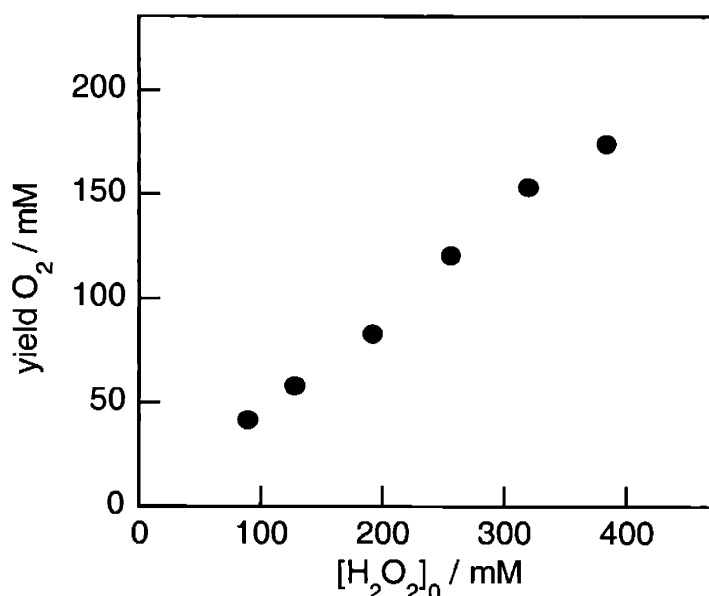


**Figure 11.6.** Oxygen release from  $\text{H}_2\text{O}_2$  dismutation catalyzed by **130** at 25 °C in a biphasic dichloromethane/pH 7 phosphate buffer medium.

A systematic evaluation of catalytic catalase reactivities for the iron HPX and HPD complexes was carried out using the above-mentioned buffered, biphasic conditions. The symmetric porphyrin  $\text{FeCl}(\text{TMP})$  served as a redox-only model compound for baseline comparison. The catalytic results in terms of turnover number (TON), displayed in Figure 11.7, are striking. Complex **130**, containing a xanthene bridge and a carboxylic acid group, is the most reactive, producing almost an order of magnitude more oxygen ( $436 \pm 22$  TON) than any of the catalysts surveyed. Simple replacement of the “hanging” carboxylic acid group on the xanthene backbone with a methyl ester leads to a significant decrease in activity ( $48 \pm 3$  TON for **131**). Similarly,

fixing the carboxylic acid pendant to the vertically-widened dibenzofuran scaffold affords catalytic activities ( $12 \pm 2$  for **136**) comparable to the baseline compound FeCl(TMP) ( $2 \pm 2$ ).

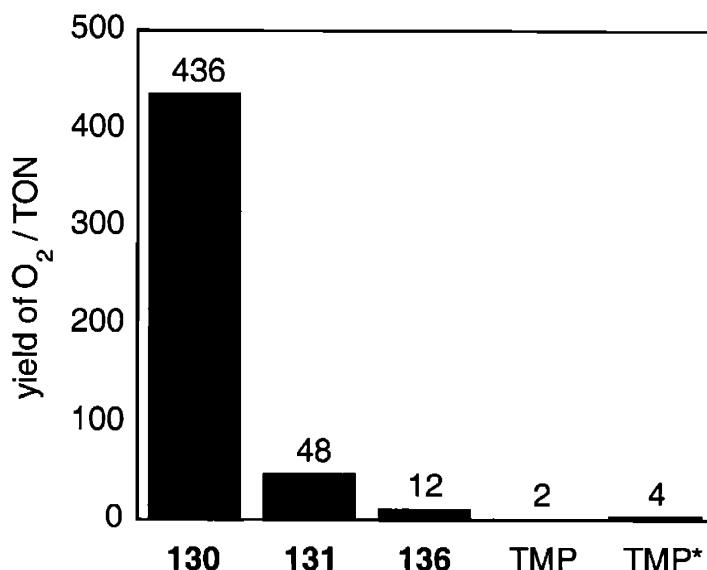
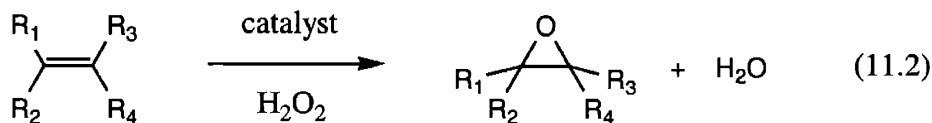


**Figure 11.7.** Turnover numbers (TON) for oxygen release from H<sub>2</sub>O<sub>2</sub> dismutation catalyzed by iron complexes **130**, **131**, **136**, and FeCl(TMP). In the graph, TMP denotes FeCl(TMP), and TMP\* denotes FeCl(TMP) + 1 equiv benzoic acid.

Several control experiments were performed to verify the foregoing findings. Negligible oxygen evolution is observed in the absence of catalyst or in the presence of catalyst without the axial 1,5-dicyclohexylimidazole ligand. Furthermore, the external addition of one equivalent of the molecular analog of the hanging group, either benzoic acid or methyl benzoate, to FeCl(TMP) fails to yield an increase in catalytic catalase activity. Taken together, the data suggest that the protic nature of the hydrogen bonding group and its orientation are critically important for efficient activation of the O—O bond by **130**.

### 11.3.6 Olefin Epoxidation

The success of the HPX-CO<sub>2</sub>H system to enhance relative catalase-like activity provided a compelling imperative to extend the reactivity of Hangman platforms to other processes contingent on O—O bond activation. We targeted the catalytic epoxidation of olefins (Equation 11.2) using hydrogen peroxide as a terminal oxidant<sup>54,151-153</sup> for the following reasons. First, the reaction parallels the peroxide shunt cycle of cytochrome P450 and peroxidase enzymes while building on the results of the observed biomimetic catalase chemistry.<sup>51,52,57</sup> Second, hydrogen peroxide is a green oxidant, yielding water as the sole by-product of catalysis.<sup>151</sup>



Initial catalytic olefin epoxidation studies with the iron Hangman porphyrins using a H<sub>2</sub>O<sub>2</sub>/1,5-dicyclohexylimidazole system were unsuccessful, owing to the electron-rich nature of both the porphyrin and the axial ligand. We thus turned our attention to the reactivity of the manganese HPX and HPD derivatives **134**, **135**, and **137**, with MnCl(TMP) as the standard baseline compound. The common olefins styrene and *cis*-cyclooctene were chosen as substrates. Table 11.3 lists the product yields for olefin epoxidation with H<sub>2</sub>O<sub>2</sub> catalyzed by the manganese complexes at 0.2 mol% catalyst loading, and Figure 11.8 presents a time-course plot for the epoxidation reactions catalyzed by **134**, **135** and MnCl(TMP). Epoxide products are formed in > 95% selectivity with little to no allylic oxidation side products, indicating that the involvement of radical species such as HO• and HOO• are unlikely. The results for epoxidation reactivity of the manganese derivatives follow the same general trend observed for the iron-mediated catalase reactions. Complex **134** bearing a protic carboxylic acid pendant on a xanthene platform is the most active, affording styrene and *cis*-cyclooctene oxides in 70% (350 ± 10 TON) and 92% (460 ± 30 TON), respectively. These values are almost twice as high as those obtained for the ester derivative **135** (191 ± 8 TON for styrene, 208 ± 22 TON for *cis*-cyclooctene). Under these conditions, both HPD complex **137** and MnCl(TMP) yield significantly less epoxide product upon reaction with either styrene or *cis*-cyclooctene (< 10%, < 50 TON).

**Table 11.3.** Epoxidation of Olefins Catalyzed by Manganese Hangman Complexes and MnCl(TMP).<sup>a</sup>

Catalyst	Substrate	
	Styrene (% yield)	<i>Cis</i> -cyclooctene (% yield)
MnCl(HPX-CO <sub>2</sub> H) ( <b>134</b> )	70 ± 2	92 ± 6
MnCl(HPX-CO <sub>2</sub> Me) ( <b>135</b> )	38 ± 2	42 ± 5
MnCl(HPD-CO <sub>2</sub> H) ( <b>137</b> )	4 ± 1	5 ± 1
MnCl(TMP)	4 ± 2	5 ± 1
MnCl(TMP) + 1 equiv PhCOOH	6 ± 1	9 ± 2

<sup>a</sup> Standard catalytic reaction conditions are given in the Experimental Section. Yields were determined by analysis of the epoxide products using GC-MS and <sup>1</sup>H NMR spectroscopy.

As observed for the catalase reactions, negligible olefin epoxidation is detected in the absence of catalyst or in the presence of catalyst without axial ligand. Furthermore, the external addition of one equivalent of either benzoic acid or methyl benzoate to MnCl(TMP) fails to yield an increase in epoxide product. Lastly, we also examined the stereochemistry of the epoxidation of *cis*-stilbene by **134**.<sup>154-157</sup> The high *cis*-epoxide/*trans*-epoxide ratio of  $6 \pm 1$  obtained is consistent with a predominant oxomanganese(V) oxidizing agent.<sup>158-161</sup>

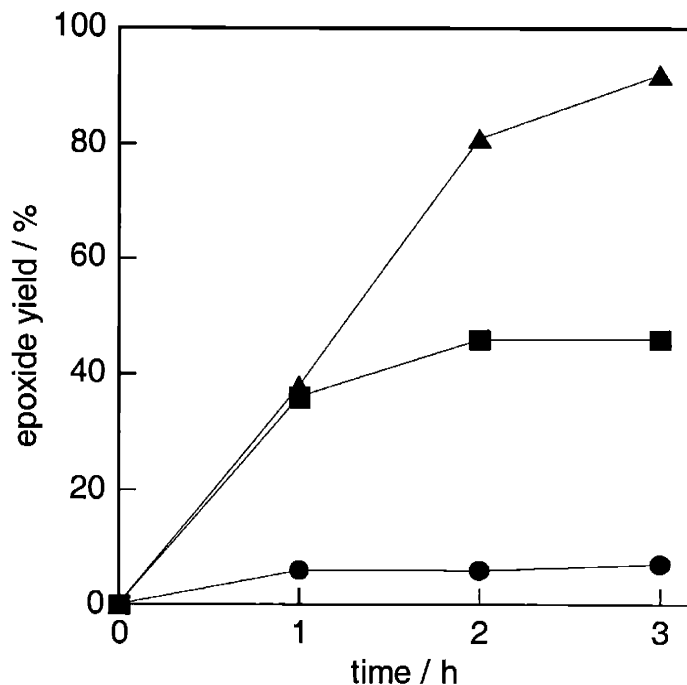


**Figure 11.8.** Time-course plot for the epoxidation of *cis*-cyclooctene with hydrogen peroxide catalyzed by **134** (triangles), **135** (squares), and **137** / MnCl(TMP) (circles). The addition of 1 equiv benzoic acid to MnCl(TMP) shows no detectible enhancement in catalytic epoxidation reactivity.

### 11.3.7 Biological Relevance and Mechanistic Proposals

Specific and efficient catalytic oxidation chemistry in heme-dependent proteins is made possible by the remarkable ability of these enzymes to exquisitely balance proton and electron inventories. In particular, the distal side of the heme microenvironment is crucial for providing a suitable microenvironment surrounding the open coordination site of the heme for the binding of peroxides, molecular oxygen, and other small-molecule substrates, and controlling their subsequent catalytic chemistry by coupled proton and electron transfer steps.<sup>51,52,55-57</sup> For peroxidases, catalases, and the cytochrome P450 monooxygenases, such PCET events facilitate the selective heterolytic cleavage of O—O bonds via the pull effect to form high-valent iron-oxo

porphyrin species such as Compound I for further reaction with external substrates. The key O—O cleavage step itself is driven by proton activation of a hydroperoxide intermediate, which occurs by a hydrogen-bonding shuttle derived from proximate amino acids and/or directed water.

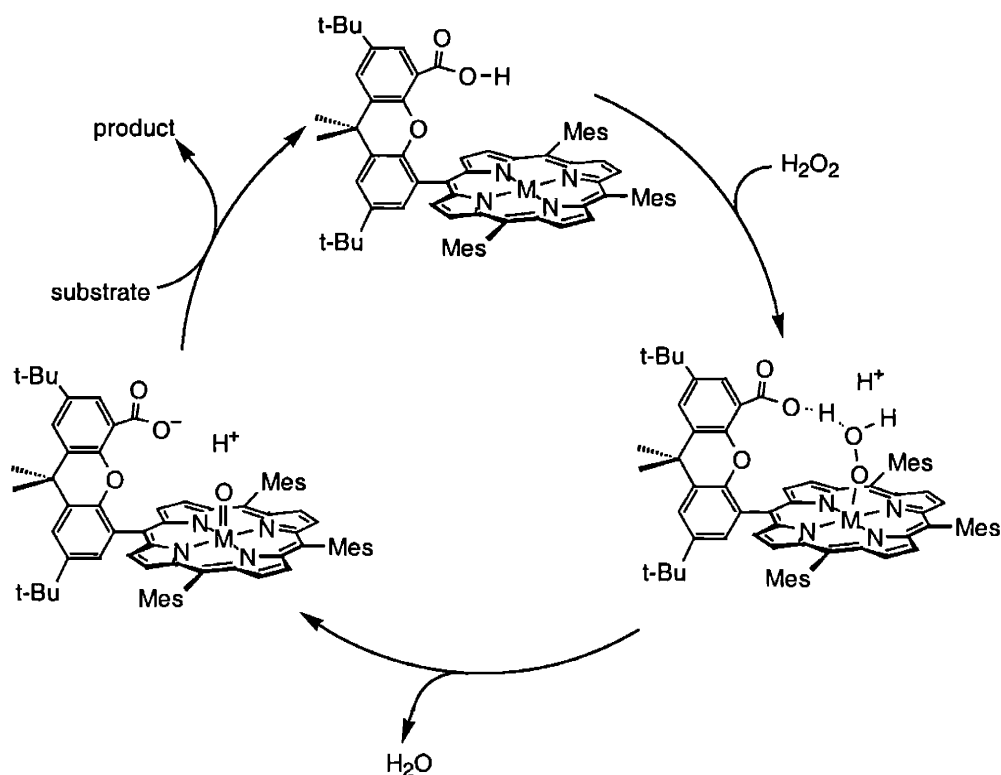
The reaction chemistry of these natural enzymes emphasizes the importance of managing proton inventory in catalytic oxidation processes. Heretofore, metalloporphyrins employed as models for heme-mediated oxidation chemistry have, for the most part, focused on either modifying the redox or steric properties of the macrocycle itself<sup>54,150,151,153,162,163</sup> or changing the electronic identity of the proximal axial ligand.<sup>151-153</sup> With specific regard to catalase, which contains an axial tyrosine ligand, a striking example of the latter approach is work by Meunier and Momenteau that demonstrates selective metalloporphyrin reactivity with H<sub>2</sub>O<sub>2</sub> for dismutation over substrate oxygenation with use of a proximal oxygen ligand. Few intermolecular small-molecule model systems have emerged that attend to issues surrounding the pull effect. In early work, Traylor and co-workers studied the general acid-base effects of added imidazole in the catalytic oxidation of phenols using iron porphyrins and peracid or hydroperoxide oxidants,<sup>164-166</sup> and Bruice has also reported the effects of imidazole and pH on similar O—O cleavage reactions catalyzed by metalloporphyrins in aqueous solution.<sup>167-169</sup> Recent work by Nam has addressed the complexities of hemolytic versus heterolytic O—O bond cleavage pathways in protic and aprotic solvents<sup>170,171</sup> and demonstrated remarkable spectator ligand effects in metalloporphyrin-catalyzed oxidation reactions.<sup>172,173</sup>

Despite this excellent body of work, no simple metalloporphyrin model system to date has utilized an intramolecular approach to control proton inventory for small-molecule activation chemistry. The use of distal intramolecular hydrogen-bonding groups for synthetic porphyrin platforms has focused almost exclusively on the binding and transport of small molecules such as oxygen and carbon monoxide;<sup>107-119</sup> a notable exception is the work of Montanari and Quici, who have prepared a series of metalloporphyrin oxidation catalysts bearing an pendant axial carboxylate ligand.<sup>174-176</sup> In no case, however, has the simple metalloporphyrin model system been intramolecularly controlled in a proton inventory for small-molecule activation. In doing so per a Hangman strategy, catalytic bond-making and bond-breaking chemistry is enhanced on the metalloporphyrin redox platform. These systems isolate the key proton-shuttle attribute of the distal heme cleft in a tunable synthetic platform by scaffolding a single hydrogen-bonding group over a heme core. This small-molecule approach affords the ability to control the acid-base properties of the hydrogen-bond functionality by direct synthetic modification. Moreover, the spatial orientation of this distal hydrogen-bond pendant in relation to the porphyrin redox platform can be modified by choice of either the xantheno or dibenzofuran scaffold.



A structure-reactivity relationship is developed for the HPX and HPD frameworks in catalase-like hydrogen peroxide dismutations and peroxide-mediated olefin epoxidations. The catalytic activities for the systems follow the general trend  $\text{HPX-CO}_2\text{H} \gg \text{HPX-CO}_2\text{Me} > \text{HPD-CO}_2\text{H} \sim \text{TMP}$ , revealing that both the nature of the hydrogen-bonding pendant and its spatial orientation relative to its metalloporphyrin redox partner are critical for selective and efficient catalytic chemistry. For example, the hydrogen-bonding system HPX-CO<sub>2</sub>Me exhibits a marked increase in activity for catalytic dismutation and epoxidation reactions over standard TMP counterparts, and substitution of the aprotic ester group for the protic carboxylic acid on the HPX platform results in catalyst architectures with significantly enhanced activity. The arrangement of acid-base and redox sites is also vital for oxidation reactivity. From the previously reported structure of **132**, the monomeric iron(III) derivative of the HPX-CO<sub>2</sub>H ligand has the unique ability to juxtapose two oxygen atoms between proton (carboxylic acid) *and* electron (metalloporphyrin) shuttle sites. Thus, the HPX template provides a geometrically matched microcavity for the binding and activation of peroxide and other reactive oxygen species. Increasing the distance between the ditopic sites using a dibenzofuran-based HPD scaffold affords a catalyst that has comparable performance to a simple tetramesitylporphyrin counterpart, despite the presence of a pendant protic hydrogen-bonding group in the former.

The divergent oxidation reactivities displayed by the Hangman systems can be grouped into a unified mechanistic model that falls within the context of natural heme enzyme reactivity. A proposed catalytic pathway for the O—O reactivity of the most active xanthene-bridged HPX-CO<sub>2</sub>H platform is shown in Scheme 11.4. Reaction of H<sub>2</sub>O<sub>2</sub> with the porphyrin in the presence of an axial ligand results in a putative metal hydroperoxide complex. The bound HO<sub>2</sub><sup>-</sup> species is then converted into an oxoiron(IV) porphyrin cation radical or an oxomanganese(V) intermediate by proton transfer and subsequent heterolytic O—O bond cleavage; the high-valent metal-oxo species generated are sufficiently reactive to oxidize substrates to product. Alternatively, protonation activates the hydroperoxide for direct reaction with substrates prior to O—O cleavage. In either case, proton transfer to the M—OOH intermediate is the critical step in facilitating reaction with substrate. It is tempting to suggest that the control of proton transfer in these catalytic cycles avoids homolytic cleavage or other peroxide decomposition pathways, but more thorough mechanistic studies are needed to evaluate such issues.



**Scheme 11.4.** Proposed pathways for proton-assisted substrate oxidation by HPX Hangman porphyrins.

The pull-based mechanism provides a working model for assessing the relative reactivities of the Hangman platforms by inspection of the key metal-hydroperoxide intermediate. The HPX-CO<sub>2</sub>H system, which exhibits the highest reactivity, has the capacity to stabilize binding of the oxidant by hydrogen bonding, while the carboxylic acid group provides an intramolecular shuttle to deliver proton equivalents for oxidation chemistry. The ester derivative HPX-CO<sub>2</sub>Me can also stabilize a bound HO<sub>2</sub><sup>-</sup> species via hydrogen bonding through its hanging carbonyl group, but is unable to offer an internal pathway for protons. Finally, the comparable activities of the HPD-CO<sub>2</sub>H and TMP series suggest that hydrogen bonding and intramolecular proton transfer are inefficient in the former owing to the splayed arrangement of redox and acid-base sites.

## 11.4 Concluding Remarks

The present work represents an initial study to utilize PCET as a mechanistic framework for exploring small-molecule activation chemistry. Our findings clearly indicate that the introduction of a single proton-shuttle group onto a redox-active platform in simple chemical model systems can significantly enhance the activation of O—O bonds for disparate catalytic processes. We

have exploited this design feature in the assembly of asymmetric cofacial porphyrin architectures with a pendant hydrogen-bonding functionality.

Suzuki cross-coupling reactions provide a modular synthetic strategy for the facile preparation of Hangman porphyrins anchored to a rigid xanthene or dibenzofuran pillar. The resulting HPX and HPD systems afford the ability to control both the orientation and acid-base properties of the hydrogen-bond pendant. Comparative catalytic oxidation studies with the HPX and HPD systems and simple redox-only porphyrin platforms have been performed to assess the role of proton control in O—O bond activation chemistry. Two distinct reactivities have been elaborated, namely the catalase-like disproportionation of hydrogen peroxide by iron derivatives to oxygen and water and the epoxidation of olefins by manganese complexes. In both cases, a marked activity enhancement is observed for the xanthene-bridged platform with a pendant carboxylic acid group (HPX-CO<sub>2</sub>H), which features a geometrically matched site between proton and electron sources. The reactivity data establish that this Hangman approach can yield superior catalysts to analogs that do not manage both proton and electron inventories.

The results have significant implications from the perspectives of both biological enzymes and catalyst design. First, the Hangman strategy highlights the importance of directing proton transfer pathways for catalytic reactivity. Also, the ability to achieve efficient catalase or epoxidation reactivity using a single metalloporphyrin-based scaffold is evocative of the natural heme-dependent proteins that employ a conserved protoporphyrin IX cofactor. In terms of synthetic catalyst design, the Hangman strategy demonstrates that the addition of proton control to a redox platform can enhance its catalytic performance. We anticipate that the development of hybrid architectures containing both acid-base and redox functionalities will lead to new advances in catalysis. In this vein, current work is directed at the synthesis of platforms that will permit more detailed mechanistic investigations of the effects of hydrogen bonding on these and other O—O activation processes, and expanding the scope of multielectron PCET reactions for catalytic bond-making and bond-breaking chemistry.

## 11.5 Experimental Section

### 11.5.1 Materials

Silica gel 60 (70-230 and 230-400 mesh, Merck) and aluminum oxide 60 (EM Science) were used for column chromatography. Analytical thin layer chromatography was performed using Merck 60 F254 silica gel (precoated sheets, 0.2 mm thick) or JT Baker IB-F aluminum oxide (precoated sheets, 0.2 mm thick). Solvents for synthesis were of reagent grade or better, and were dried according to standard methods.<sup>177</sup> The model porphyrins FeCl(TMP) and

MnCl(TMP) were prepared according to literature procedures. All other reagents were used as received.

### 11.5.2 FeCl(HPX-CO<sub>2</sub>H) (130)

A combination of **111** (218 mg, 0.21 mmol), FeBr<sub>2</sub> (270 mg), and DMF (35 mL) was refluxed under nitrogen for 2 h, opened to air, and brought to dryness under vacuum. The solids were redissolved in dichloromethane (100 mL), washed with water (4 × 75 mL). The organic layer was stirred with 20% HCl (50 mL) for 75 min, washed with water (5 × 100 mL), and taken to dryness. The resulting residue was purified using column chromatography (silica gel, dichloromethane to 5% methanol/dichloromethane), and retreated with HCl as described above to furnish **130** as a brown powder (211 mg, 89% yield). Anal. Calcd for C<sub>71</sub>H<sub>70</sub>ClN<sub>4</sub>O<sub>3</sub>Fe: C, 76.23; H, 6.31; N, 5.01. Found: C, 76.44; H, 6.19; N, 4.82. HRFABMS ([M—Cl]<sup>+</sup>) calcd for C<sub>71</sub>H<sub>70</sub>ClN<sub>4</sub>O<sub>3</sub>Fe *m/z* 1082.4797, found 1082.4773.

### 11.5.3 FeCl(HPX-CO<sub>2</sub>Me) (131)

In a dry box, **106** (50 mg, 0.048 mmol), 2,6-lutidine (0.1 mL), FeBr<sub>2</sub> (100 mg), and THF (15 mL) were loaded in 100-mL flask equipped with a condenser. The reaction was refluxed under nitrogen for 5 h, opened to air, and brought to dryness under vacuum. The residue was purified using column chromatography (silica gel, dichloromethane to 10% methanol/dichloromethane), redissolved in dichloromethane (50 mL) and stirred with 20% HCl (25 mL) for 1 h. The organic layer was washed with water (5 × 50 mL) and taken to dryness. The resulting residue was purified using column chromatography (silica gel, dichloromethane to 5% methanol/dichloromethane), and retreated with HCl as described above to furnish **131** as a brown powder (50 mg, 92% yield). Anal. Calcd for C<sub>72</sub>H<sub>72</sub>ClN<sub>4</sub>O<sub>3</sub>Fe: C, 76.35; H, 6.41; N, 4.95. Found: C, 76.70; H, 6.72; N, 4.62. HRFABMS ([M—Cl]<sup>+</sup>) calcd for C<sub>72</sub>H<sub>72</sub>ClN<sub>4</sub>O<sub>3</sub>Fe *m/z* 1096.4954, found 1096.4969.

### 11.5.4 FeOH(HPX-CO<sub>2</sub>H) (132)

A combination of **111** (218 mg, 0.21 mmol), FeBr<sub>2</sub> (270 mg), and DMF (35 mL) was refluxed under nitrogen for 2 h, opened to air, and brought to dryness under vacuum. The solids were redissolved in dichloromethane (100 mL), washed with water (4 × 75 mL). The organic layer was stirred with 20% HCl (50 mL) for 75 min, washed with water (5 × 100 mL), and taken to dryness. The resulting residue was purified using column chromatography (silica gel, dichloromethane to 1% methanol/dichloromethane), redissolved in toluene (100 mL), and stirred with 0.5 M NaOH (100 mL) for 12 h. The organic layer was washed with water (3 × 50 mL), dried over Na<sub>2</sub>SO<sub>4</sub>. Removal of the solvent followed by recrystallization from pentane afforded

analytically pure **132** as a brown microcrystalline powder (212 mg, 92% yield). Anal. Calcd for  $C_{76}H_{85}N_4O_5Fe$ : C, 76.68; H, 7.20; N, 4.71. Found: C, 76.78; H, 7.19; N, 4.69. HRFABMS ( $[M-OH]^+$ ) calcd for  $C_{71}H_{70}N_4O_3Fe$   $m/z$  1082.4797, found 1082.4824.

#### 11.5.5 FeOH(HPX-CO<sub>2</sub>Me) (133)

In a dry box, **106** (50 mg, 0.040 mmol), 2,6-lutidine (0.1 mL), FeBr<sub>2</sub> (100 mg), and THF (15 mL) were loaded in 100-mL flask equipped with a condenser. The reaction was refluxed under nitrogen for 5 h, opened to air, and brought to dryness under vacuum. The residue was purified using column chromatography (silica gel, dichloromethane to 10% methanol/dichloromethane), redissolved in dichloromethane (50 mL) and stirred with 20% HCl (25 mL) for 1 h. The organic layer was washed with water (5 × 50 mL) and taken to dryness. The resulting solid was redissolved in toluene (50 mL) and stirred with 0.5 M NaOH (50 mL) for 12 h. The organic phase was washed with water (3 × 50 mL), dried over Na<sub>2</sub>SO<sub>4</sub>, and the solvent was removed by rotary evaporation. Recrystallization from pentane furnished analytically pure **133** as a brown powder (48 mg, 90% yield). Anal. Calcd for  $C_{77}H_{87}N_4O_5Fe$ : C, 76.79; H, 7.28; N, 4.65. Found: C, 76.74; H, 7.36; N, 4.72. HRFABMS ( $[M-OH]^+$ ) calcd for  $C_{72}H_{72}N_4O_3Fe$   $m/z$  1096.4954, found 1096.4982.

#### 11.5.6 MnCl(HPX-CO<sub>2</sub>H) (134)

A solution of **111** (103 mg, 0.10 mmol) and Mn(OAc)<sub>2</sub>·4H<sub>2</sub>O (220 mg) in DMF (15 mL) was refluxed in air for 3 h. The reaction was cooled to room temperature and taken to dryness. The residue was taken up in a 1:1 mixture of dichloromethane/water (50 mL). The organic layer was separated, washed with water (3 × 75 mL), and stirred with a 5:1 mixture of saturated aq NaCl and HCl (72 mL) for 90 min. The organic layer was decanted and solvent was removed under vacuum. The remaining solid was purified by column chromatography (silica gel, dichloromethane to 5% methanol/dichloromethane) and retreated with aq NaCl and HCl as described above. The organic phase was separated, washed with water (3 × 75 mL), dried over Na<sub>2</sub>SO<sub>4</sub>, and taken to dryness. Recrystallization from dichloromethane and hexanes afforded pure **134** as a forest green microcrystalline powder (101 mg, 90% yield). Anal. Calcd for  $C_{71}H_{70}ClN_4O_3Mn$ : C, 76.29; H, 6.31; N, 5.01. Found: C, 76.37; H, 6.14; N, 4.93. HRFABMS ( $[M-Cl]^+$ ) calcd for  $C_{71}H_{70}ClN_4O_3Mn$   $m/z$  1081.4828, found 1081.4833.

#### 11.5.7 MnCl(HPX-CO<sub>2</sub>Me) (135)

A solution of **106** (103 mg, 0.098 mmol) and Mn(OAc)<sub>2</sub>·4H<sub>2</sub>O (220 mg) in DMF (15 mL) was refluxed in air for 3 h. The reaction was cooled to room temperature and taken to dryness. The residue was taken up in a 1:1 mixture of dichloromethane/water (50 mL). The organic layer was

separated, washed with water (3 × 75 mL), and stirred with a 5:1 mixture of saturated aq NaCl and HCl (72 mL) for 90 min. The organic layer was decanted and solvent was removed under vacuum. The remaining solid was purified by column chromatography (silica gel, dichloromethane to 5% methanol/dichloromethane) and retreated with aq NaCl and HCl as described above. The organic phase was separated, washed with water (3 × 75 mL), dried over Na<sub>2</sub>SO<sub>4</sub>, and taken to dryness. Recrystallization from dichloromethane and hexanes afforded pure **135** as a hunter green powder (102 mg, 93% yield). Anal. Calcd for C<sub>72</sub>H<sub>72</sub>ClN<sub>4</sub>O<sub>3</sub>Mn: C, 76.41; H, 6.41; N, 4.95. Found: C, 76.32; H, 6.32; N, 5.05. HRFABMS ([M—Cl]<sup>+</sup>) calcd for C<sub>72</sub>H<sub>72</sub>ClN<sub>4</sub>O<sub>3</sub>Mn *m/z* 1095.4985, found 1095.4973.

#### 11.5.8 FeCl(HPD-CO<sub>2</sub>H) (**136**)

Iron insertion into the free base porphyrin was achieved using a standard literature procedure. A mixture of **121** (15 mg, 0.0171 mmol), FeBr<sub>2</sub> (37 mg, 0.171 mmol) and anhydrous DMF (3.5 mL) was refluxed under nitrogen for 2 h, opened to air and brought to dryness under vacuum. The residue was redissolved in dichloromethane (10 mL) and washed with water (3 × 30 mL). The organic layer was stirred with 20% HCl (4 mL) for 75 min, washed with water (3 × 30 mL) and taken to dryness. The residue was purified using column chromatography (silica gel, dichloromethane to 10% methanol/dichloromethane), redissolved in dichloromethane (10 mL) and stirred with 4 N HCl (1.5 mL) overnight. The organic layer was separated, washed with water (3 × 40 mL), dried over Na<sub>2</sub>SO<sub>4</sub>, and evaporated. The iron complex **136** was isolated as a brown powder (14 mg, 85% yield). HRESIMS ([M—Cl]<sup>+</sup>) calcd for C<sub>60</sub>H<sub>48</sub>FeClN<sub>4</sub>O<sub>3</sub> *m/z* 928.3070, found 928.3064.

#### 11.5.9 MnCl(HPD-CO<sub>2</sub>H) (**137**)

A solution of **121** (15 mg, 0.0171 mmol) and Mn(OAc)<sub>2</sub>·4H<sub>2</sub>O (30 mg) in DMF (5 mL) was refluxed in air for 3 h. The reaction was cooled to room temperature and taken to dryness. The residue was taken up in a 1:1 mixture of dichloromethane/water (25 mL). The organic layer was separated, washed with water (3 × 25 mL), and stirred with a 5:1 mixture of saturated aq NaCl and HCl (24 mL) for 90 min. The organic layer was decanted and solvent was removed under vacuum. The remaining solid was purified by column chromatography (silica gel, dichloromethane to 5% methanol/dichloromethane) and retreated with aq NaCl and HCl as described above. The organic phase was separated, washed with water (3 × 25 mL), dried over Na<sub>2</sub>SO<sub>4</sub>, and taken to dryness. Recrystallization from dichloromethane and hexanes afforded pure **137** as a green solid (15 mg, 90% yield). HRESIMS ([M—Cl]<sup>+</sup>) calcd for C<sub>60</sub>H<sub>48</sub>MnN<sub>4</sub>O<sub>3</sub> *m/z* 927.3101, found 927.3093.

### 11.5.10 Physical Measurements

<sup>1</sup>H NMR spectra were collected in *d*<sub>8</sub>-toluene (Cambridge Isotope Laboratories) at the MIT Department of Chemistry Instrumentation Facility (DCIF) using an Inova 500 spectrometer at 25 °C. All chemical shifts are reported using the standard  $\delta$  notation in parts-per-million; positive chemical shifts are to higher frequency from the given reference. Absorption spectra were obtained using either a Cary-17 spectrophotometer modified by On-Line Instruments (OLIS) to include computer control or a Spectral Instruments 440 Series spectrophotometer. Differential scanning calorimetry (DSC) was carried out using a Perkin Elmer Pyris 1 Differential Scanning Calorimeter. Samples were run under a nitrogen atmosphere. Thermal gravimetric analyses with *in-situ* infrared detection were performed using a Perkin Elmer 3000 TG-IR system. High-resolution mass spectral analyses were carried out at the University of Illinois Mass Spectrometry Laboratory or the MIT Department of Chemistry Instrumentation Facility. Elemental analyses were carried out at Quantitative Technologies, Inc. (Whitehouse, New Jersey) and Michigan State University.

### 11.5.11 Hydrogen Peroxide Disproportionation Reactions

Dismutation reactions were performed at room temperature in a 5 mL conical reaction vial with a side port, equipped with a magnetic spinvane stirbar and a capillary gas delivery tube linked to a graduated buret filled with water. The reaction vial was charged with 1  $\mu$ mol of the iron porphyrin, 25  $\mu$ mol of 1,5-dicyclohexylimidazole, 4  $\mu$ mol of benzyldimethyltetradecylammonium chloride, 2 mL of dichloromethane and 1 mL of phosphate buffer, pH 7. The solution was stirred to ensure gas pressure equilibration. An aliquot of 30% H<sub>2</sub>O<sub>2</sub> (0.11 mL) was added to the reaction mixture via syringe through the side port. The oxygen evolution was measured using a buret. The identity of the oxygen gas was confirmed independently using the alkaline pyrogallol test.<sup>178</sup>

### 11.5.12 Olefin Epoxidation Reactions

Epoxidations were carried out at room temperature in air in a 5 mL conical reaction vial equipped with a magnetic spinvane stirbar and a Teflon-lined screw cap. The reaction vial was charged with 1  $\mu$ mol of the manganese porphyrin, 500  $\mu$ mol of styrene or *cis*-cyclooctene, 20  $\mu$ mol of 1,5-dicyclohexylimidazole, 2.75  $\mu$ mol of *n*-dodecane (standard) and 2 mL of dichloromethane. The solution was stirred and at regular intervals of 1 h, an aliquot of 0.23 mL of 30% H<sub>2</sub>O<sub>2</sub> (2940  $\mu$ mol, pH adjusted at 4 – 4.5 with 1% aq NaOH) was added to the reaction mixture. The reactions were stopped after 3 h. An aliquot of the reaction mixture was then withdrawn for gas chromatographic (GC) analyses using *n*-dodecane as a standard. Product

analyses for the styrene and cyclooctene epoxidation reactions were performed using a Hewlett Packard 5890 series II gas chromatograph with a Hewlett-Packard-1 non-polar column (30 m). Retention times for the epoxides prepared in our catalytic reactions are identical to authentic samples. Epoxidation of *cis*-stilbene was carried out as described by Groves and Mansuy.<sup>154,156</sup>



## 11.6 References and Notes

1. Ort, D. R.; Yocum, C. F. *Oxygenic Photosynthesis: The Light Reactions*; Kluwer Academic: Dordrecht, 1996.
2. Tommos, C.; Babcock, G. T. *Acc. Chem. Res.* **1998**, *31*, 18-25.
3. Tommos, C.; Babcock, G. T. *Biochim. Biophys. Acta* **2000**, *1458*, 199-219.
4. Yachandra, V. K.; Sauer, K.; Klein, M. P. *Chem. Rev.* **1996**, *96*, 2927-2950.
5. Yocum, C. F.; Pecoraro, V. L. *Curr. Opin. Chem. Biol.* **1999**, *3*, 182-187.
6. Dismukes, G. C. *Science* **2001**, *292*, 447-448.
7. Ananyev, G. M.; Zaltsman, L.; Vasko, C.; Dismukes, G. C. *Biochim. Biophys. Acta* **2001**, *1503*, 52-68.
8. Vrettos, J. S.; Limburg, J.; Brudvig, G. W. *Biochim. Biophys. Acta* **2001**, *1503*, 229-245.
9. Babcock, G. T.; Wikström, M. *Nature* **1992**, *356*, 301-309.
10. Ferguson-Miller, S.; Babcock, G. T. *Chem. Rev.* **1996**, *96*, 2889-2907.
11. Michel, H.; Behr, J.; Harrenga, A.; Kannt, A. *Annu. Rev. Biophys. Biomol. Struct.* **1998**, *27*, 329-356.
12. Schultz, B. E.; Chan, S. I. *Annu. Rev. Biophys. Biomol. Struct.* **2001**, *30*, 23-65.
13. Malmström, B. G. In *Electron Transfer in Chemistry*; Balzani, V., Ed.; Wiley-VCH: Weinheim, Germany, 2001; Vol. 3.1.3, pp 39-55.
14. Wikström, M. *Biochim. Biophys. Acta* **2000**, *1458*, 188-198.
15. Gennis, R. B. *Proc. Natl. Acad. Sci. USA* **1998**, *95*, 12747-12749.
16. Brzezinski, P. *Biochim. Biophys. Acta* **2000**, *1458*, 1-5.
17. Ramirez, B. E.; Malmström, B. G.; Winkler, J. R.; Gray, H. B. *Proc. Natl. Acad. Sci. USA* **1995**, *92*, 11949-11951.
18. Klinman, J. P. *Chem. Rev.* **1996**, *96*, 2541-2561.
19. Klinman, J. P. *J. Biol. Inorg. Chem.* **2001**, *6*, 1-13.
20. Whittaker, M. M.; Whittaker, J. W. *Biochemistry* **2001**, *40*, 7140-7148.
21. Solomon, E. I.; Chen, P.; Metz, M.; Lee, S.-K.; Palmer, A. E. *Angew. Chem. Int. Ed.* **2001**, *40*, 4570-4590.
22. Silverman, R. B. *Acc. Chem. Res.* **1995**, *28*, 335-342.
23. Davidson, V. L. *Adv. Protein Chem.* **2001**, *58*, 95-140.
24. Feig, A. L.; Lippard, S. J. *Chem. Rev.* **1994**, *94*, 759-805.
25. Guallar, V.; Gherman, B. F.; Lippard, S. J.; Friesner, R. A. *Curr. Opin. Chem. Biol.* **2002**, *6*, 236-242.
26. Lee, S.-K.; Lipscomb, J. D. *Biochemistry* **1999**, *38*, 4423-4432.
27. Wallar, B. J.; Lipscomb, J. D. *Chem. Rev.* **1996**, *96*, 2625-2657.

28. Solomon, E. I. *Inorg. Chem.* **2001**, *40*, 3656-3669.
29. Que Jr., L.; Ho, R. Y. N. *Chem. Rev.* **1996**, *96*, 2607-2624.
30. Knapp, M. J.; Rickert, K.; Klinman, J. P. *J. Am. Chem. Soc.* **2002**, *124*, 3865-3874.
31. Armstrong, F. A. *J. Chem. Soc. Dalton Trans.* **2002**, 661-671.
32. Chen, K.; Hirst, J.; Camba, R.; Bonagura, C. A.; Stout, C. D.; Burgess, B. K.; Armstrong, F. A. *Nature* **2000**, *405*, 814-817.
33. Low, D. W.; Hill, M. G. *J. Am. Chem. Soc.* **2000**, *122*, 11039-11040.
34. Kennedy, M. L.; Gibney, B. R. *J. Am. Chem. Soc.* **2002**, *124*, 6826-6827.
35. Peters, J. W. *Curr. Opin. Struct. Biol.* **1999**, *9*, 670-676.
36. Adams, M. W. W.; Stiefel, E. I. *Curr. Opin. Chem. Biol.* **2000**, *4*, 214-220.
37. Berkessel, A. *Curr. Opin. Chem. Biol.* **2001**, *5*, 486-490.
38. Thauer, R. K.; Klein, A. R.; Hartmann, G. C. *Chem. Rev.* **1996**, *96*, 3031-3042.
39. Burgess, B. K.; Lowe, D. J. *Chem. Rev.* **1996**, *96*, 2983-3011.
40. Rees, D. C.; Howard, J. B. *Curr. Opin. Chem. Biol.* **2000**, *4*, 559-566.
41. Stubbe, J.; van der Donk, W. A. *Chem. Rev.* **1998**, *98*, 705-762.
42. Chapman, S. K.; Daff, S.; Munro, A. W. *Struct. Bonding* **1997**, *88*, 39-70.
43. Perutz, M. F. *Nature* **1970**, *228*, 726-734.
44. Dickerson, R. E.; Geis, I. *Hemoglobin: Structure, Function, Evolution, and Pathology*; Benjamin/Cummings: Menlo Park, CA, 1983.
45. Scott, R. A.; Mauk, A. G. *Cytochrome c: a Multidisciplinary Approach*; University Science Books: Sausalito, CA, 1996.
46. Stellwagen, E. *Nature* **1978**, *275*, 73-74.
47. Gray, H. B.; Winkler, J. R. In *Electron Transfer in Chemistry*; Balzani, V., Ed.; Wiley-VCH: Weinheim, Germany, 2001; Vol. 3.1.1, pp 3-23.
48. Marletta, M. A.; Hurshman, A. R.; Rusche, K. M. *Curr. Opin. Chem. Biol.* **1998**, *2*, 656-663.
49. Wasser, I. M.; de Vries, S.; Moeenne-Loccoz, P.; Schroeder, I.; Karlin, K. D. *Chem. Rev.* **2002**, *102*, 1201-1234.
50. Chan, M. K. *Curr. Opin. Chem. Biol.* **2001**, *5*, 216-222.
51. Sono, M.; Roach, M. P.; Coulter, E. D.; Dawson, J. H. *Chem. Rev.* **1996**, *96*, 2841-2887.
52. Ortiz de Montellano, P. R. *Cytochrome P450: Structure, Mechanism, and Biochemistry*; 2nd ed.; Plenum: New York, 1995.
53. Poulos, T. L. *Curr. Opin. Struct. Biol.* **1995**, *5*, 767-774.
54. Groves, J. T.; Han, Y. In *Cytochrome P450: Structure, Mechanism, and Biochemistry*; 2nd ed.; Ortiz de Montellano, P. R., Ed.; Plenum: New York, 1995, pp 3-48.
55. Ozaki, S.-I.; Roach, M. P.; Matsui, T.; Watanbe, Y. *Acc. Chem. Res.* **2001**, *34*, 818-825.

56. Nicholls, P.; Fita, I.; Loewen, P. C. *Adv. Inorg. Chem.* **2001**, *51*, 51-106.
57. Pond, A. E.; Ledbetter, A. P.; Sono, M.; Goodin, D. B.; Dawson, J. H. In *Electron Transfer in Chemistry*; Balzani, V., Ed.; Wiley-VCH: Weinheim, Germany, 2001; Vol. 3.1.4, pp 56-104.
58. Rodgers, K. R. *Curr. Opin. Chem. Biol.* **1999**, *3*, 158-167.
59. Everse, J.; Everse, K. E.; Grisham, M. B. *Peroxidases in Chemistry and Biology*; CRC Press: Boca Raton, FL, 1991; Vol. I and II.
60. Dawson, J. H. *Science* **1988**, *240*, 433-439.
61. Beyer, W. F. J.; Fridovich, I. *Basic Life Sci.* **1988**, *49*, 651-661.
62. Fujii, H.; Zhang, X.; Tomita, T.; Ikeda-Saito, M.; Yoshida, T. *J. Am. Chem. Soc.* **2001**, *123*, 6475-6484.
63. Rodriguez-Lopez, J. N.; Lowe, D. J.; Hernandez-Ruiz, J.; Hiner, A. N. P.; Garcia-Canovas, F.; Thorneley, R. N. F. *J. Am. Chem. Soc.* **2001**, *123*, 11838-11847.
64. Berglund, G. I.; Carlsson, G. H.; Smith, A. T.; Szöke, H.; Henriksen, A.; Hajdu, J. *Nature* **2002**, *417*, 463-468.
65. Vidakovic, M.; Sligar, S. G.; Li, H.; Poulos, T. L. *Biochemistry* **1998**, *37*, 9211-9219.
66. Schlichting, I.; Berendzen, J.; Chu, K.; Stock, A. M.; Maves, S. A.; Benson, D. E.; Sweet, R. M.; Ringe, D.; Petsko, G. A.; Sligar, S. G. *Science* **2000**, *287*, 1615-1622.
67. Oprea, T. I.; Hummer, G.; García, A. E. *Proc. Natl. Acad. Sci. USA* **1997**, *94*, 2133-2138.
68. Imai, M.; Shimada, H.; Watanbe, Y.; Matsushima-Hubiya, Y.; Makino, R.; Koga, H.; Horiuchi, R.; Ishimura, Y. *Proc. Natl. Acad. Sci. USA* **1989**, *86*, 7823-7827.
69. Martinis, S. A.; Atkins, W. M.; Stayton, P. S.; Sligar, S. G. *J. Am. Chem. Soc.* **1989**, *111*, 9252-9253.
70. Gerber, N. C.; Sligar, S. G. *J. Am. Chem. Soc.* **1992**, *114*, 8742-8743.
71. Benson, D. E.; Suslick, K. S.; Sligar, S. G. *Biochemistry* **1997**, *36*, 5104-5107.
72. Hasemann, C. A.; Kurumbail, R. G.; Boddupalli, S. S.; Peterson, J. A.; Deisenhofer, J. *Structure* **1995**, *3*, 41-62.
73. Poulos, T. L.; Raag, R. *FASEB J.* **1991**, *6*, 674-679.
74. Newcomb, N.; Shen, R.; Choi, S.-Y.; Toy, P. H.; Hollenberg, P. F.; Vaz, A. D. N.; Coon, M. J. *J. Am. Chem. Soc.* **2000**, *122*, 2677-2686.
75. Gerber, N. C.; Sligar, S. G. *J. Biol. Chem.* **1994**, *269*, 4260-4266.
76. Deng, T.-j.; Macdonald, I. D. G.; Simianu, M. C.; Sykora, M.; Kincaid, J. R.; Sligar, S. G. *J. Am. Chem. Soc.* **2001**, *123*, 269-278.
77. Cupp-Vickery, J. R.; Poulos, T. L. *Nat. Struct. Biol.* **1995**, *2*, 144-153.
78. Aikens, J.; Sligar, S. G. *J. Am. Chem. Soc.* **1994**, *116*, 1143-1144.

79. Guallar, V.; Harris, D. L.; Batistia, V. S.; Miller, W. H. *J. Am. Chem. Soc.* **2002**, *124*, 1430-1437.
80. Davydov, R.; Makris, T. M.; Kofman, V.; Werst, D. E.; Sligar, S. G.; Hoffman, B. M. *J. Am. Chem. Soc.* **2001**, *123*, 1403-1415.
81. Matsui, T.; Ozaki, S.-i.; Watanbe, Y. *J. Am. Chem. Soc.* **1999**, *121*, 9952-9957.
82. Dunn, A. R.; Dmochowski, I. J.; Bilwes, A. M.; Gray, H. B.; Crane, B. R. *Proc. Natl. Acad. Sci. USA* **2001**, *98*, 12420-12425.
83. Dmochowski, I. J.; Crane, B. R.; Wilker, J. J.; Winkler, J. R.; Gray, H. B. *Proc. Natl. Acad. Sci. USA* **1999**, *96*, 12987-12990.
84. Wilker, J. J.; Dmochowski, I. J.; Dawson, J. H.; Winkler, J. R.; Gray, H. B. *Angew. Chem. Int. Ed.* **1999**, *38*, 90-92.
85. Hamachi, I.; Tanaka, S.; Shinkai, S. *J. Am. Chem. Soc.* **1993**, *115*, 10458-10459.
86. Hamachi, I.; Tanaka, S.; Tsukiji, S.; Shinkai, S.; Oishi, S. *Inorg. Chem.* **1998**, *37*, 4380-4388.
87. Hamachi, I.; Tsukiji, S.; Shinkai, S.; Oishi, S. *J. Am. Chem. Soc.* **1999**, *121*, 5500-5506.
88. Hu, Y.-Z.; Tsukiji, S.; Shinkai, S.; Oishi, S.; Hamachi, I. *J. Am. Chem. Soc.* **2000**, *122*, 241-253.
89. Chang, C. J.; Brown, J. D. K.; Chang, M. C. Y.; Baker, E. A.; Nocera, D. G. In *Electron Transfer in Chemistry*; Balzani, V., Ed.; Wiley-VCH: Weinheim, Germany, 2001; Vol. 3.2.4, pp 409-461.
90. Cukier, R. I.; Nocera, D. G. *Annu. Rev. Phys. Chem.* **1998**, *49*, 337-369.
91. Turró, C.; Chang, C. K.; Leroi, G. E.; Cukier, R. I.; Nocera, D. G. *J. Am. Chem. Soc.* **1992**, *114*, 4013-4015.
92. Yeh, C.-Y.; Miller, S. E.; Carpenter, S. D.; Nocera, D. G. *Inorg. Chem.* **2001**, *40*, 3643-3646.
93. Kirby, J. P.; Roberts, J. A.; Nocera, D. G. *J. Am. Chem. Soc.* **1997**, *119*, 9230-9236.
94. Roberts, J. A.; Kirby, J. P.; Wall, S. T.; Nocera, D. G. *Inorg. Chim. Acta* **1997**, *263*, 395-405.
95. Deng, Y.; Roberts, J. A.; Peng, S.-M.; Chang, C. K.; Nocera, D. G. *Angew. Chem. Int. Ed.* **1997**, *36*, 2124-2127.
96. Kirby, J. P.; van Dantzig, N. A.; Chang, C. K.; Nocera, D. G. *Tetrahedron Lett.* **1995**, *36*, 3477-3480.
97. Roberts, J. A.; Kirby, J. P.; Nocera, D. G. *J. Am. Chem. Soc.* **1995**, *117*, 8051-8052.
98. Sessler, J. L.; Wang, B.; Springs, S. L.; Brown, C. T. In *Comprehensive Supramolecular Chemistry*; Murakami, Y., Ed.; Pergamon: Oxford, 1997; Vol. 4, pp 311-336.
99. Hayashi, T.; Ogoshi, H. *Chem. Soc. Rev.* **1997**, *26*, 355-364.

100. Crane, B. R.; Siegel, L. M.; Getzoff, E. D. *Science* **1995**, *270*, 59-67.
101. Howell, E. E.; Villafranca, J. E.; Warren, M. S.; Oatley, S. J.; Kraut, J. *Science* **1986**, *231*, 1123-1128.
102. Yoshikawa, S.; Shinzawa-Itoh, K.; Tsukihara, T. *J. Inorg. Biochem.* **2000**, *82*, 1-7.
103. Yoshikawa, S.; Shinzawa-ito, K.; Nakashima, R.; Yaono, R.; Yamashita, E.; Inoue, N.; Yao, M.; Fei, M. J.; Libeu, C. P.; Mizushima, T.; Yamaguchi, H.; Tomizaki, T.; Tsukihara, T. *Science* **1997**, *280*, 1723-1729.
104. Iwata, S.; Ostermeier, C.; Ludwig, B.; Michel, H. *Nature* **1995**, *376*, 660-669.
105. Chang, C. J.; Yeh, C.-Y.; Nocera, D. G. *J. Org. Chem.* **2002**, *67*, 1403-1406.
106. Yeh, C.-Y.; Chang, C. J.; Nocera, D. G. *J. Am. Chem. Soc.* **2001**, *123*, 1513-1514.
107. Chang, C. K.; Kondylis, M. P. *J. Chem. Soc. Chem. Commun.* **1986**, 316-318.
108. Chang, C. K.; Liang, Y.; Aviles, G.; Peng, S.-M. *J. Am. Chem. Soc.* **1995**, *117*, 4191-4192.
109. Collman, J. P.; Wang, Z. *Chemtracts* **1999**, *12*, 229-263.
110. Collman, J. P.; Fu, L. *Acc. Chem. Res.* **1999**, *32*, 455-463.
111. Momenteau, M.; Reed, C. A. *Chem. Rev.* **1994**, *94*, 659-698.
112. Gerothanassis, I. P.; Momenteau, M.; Loock, B. *J. Am. Chem. Soc.* **1989**, *111*, 7006-7012.
113. Momenteau, M.; Loock, B.; Tetreau, C.; Lavalette, D.; Croisy, A.; Schaeffer, C.; Huel, C.; Lhoste, J.-M. *J. Chem. Soc. Perkin Trans. 2* **1987**, 249-257.
114. Wuenschell, G. E.; Tetreau, C.; Lavalette, D.; Reed, C. A. *J. Am. Chem. Soc.* **1992**, *114*, 3346-3355.
115. Walker, F. A.; Bowen, J. *J. Am. Chem. Soc.* **1985**, *107*, 7632-7635.
116. Matsu-ura, M.; Tani, F.; Nakayama, S.; Nakamura, N.; Naruta, Y. *Angew. Chem. Int. Ed.* **2000**, *39*, 1989-1991.
117. Tani, F.; Matsu-ura, M.; Nakayama, S.; Naruta, Y. *Coord. Chem. Rev.* **2002**, *226*, 219-226.
118. Tani, F.; Matsu-ura, M.; Nakayama, S.; Ichimura, M.; Nakamura, N.; Naruta, Y. *J. Am. Chem. Soc.* **2001**, *123*, 1133-1142.
119. Kossanyi, A.; Tani, F.; Nakamura, N.; Naruta, Y. *Chem. Eur. J.* **2001**, *7*, 2862-2872.
120. MacBeth, C. E.; Golombek, A. P.; Young Jr., V. G.; Tang, C.; Kuczera, K.; Hendrich, M. P.; Borovik, A. S. *Science* **2000**, *289*, 938-941.
121. MacBeth, C. E.; Hammes, B. S.; Young Jr., V. G.; Borovik, A. S. *Inorg. Chem.* **2001**, *40*, 4733-4741.
122. Gupta, R.; MacBeth, C. E.; Young Jr., V. G.; Borovik, A. S. *J. Am. Chem. Soc.* **2002**, *124*, 1136-1137.

123. Shirin, Z.; Hammes, B. S.; Young Jr., V. G.; Borovik, A. S. *J. Am. Chem. Soc.* **2000**, *122*, 1836-1837.
124. Hammes, B. S.; Young Jr., V. G.; Borovik, A. S. *Angew. Chem. Int. Ed.* **1999**, *38*, 666-669.
125. Wada, A.; Ogo, S.; Nagatomo, S.; Kitagawa, T.; Watanbe, Y.; Jitsukawa, K.; Masuda, H. *Inorg. Chem.* **2002**, *41*, 616-618.
126. Jitsukawa, K.; Harata, M.; Ariei, H.; Sakurai, H.; Masuda, H. *Inorg. Chim. Acta* **2001**, *324*, 108-116.
127. Ogo, S.; Wada, S.; Watanbe, Y.; Iwase, M.; Wada, A.; Harata, M.; Jitsukawa, K.; Masuda, H.; Einaga, H. *Angew. Chem. Int. Ed.* **1998**, *37*, 2102-2104.
128. Harata, M.; Hasegawa, K.; Jitsukawa, K.; Masuda, H.; Einaga, H. *Bull. Chem. Soc. Jpn.* **1998**, *71*, 1031-1038.
129. Harata, M.; Jitsukawa, K.; Masuda, H.; Einaga, H. *Bull. Chem. Soc. Jpn.* **1998**, *71*, 637-645.
130. Garner, D. K.; Allred, R. A.; Tubbs, K. J.; Arif, A. M.; Berreau, L. M. *Inorg. Chem.* **2002**, *41*, 3533-3541.
131. Berreau, L. M.; Makowska-Grzyska, M. M.; Arif, A. M. *Inorg. Chem.* **2001**, *40*, 2212-2213.
132. Berreau, L. M.; Allred, R. A.; Makowska-Grzyska, M. M.; Arif, A. M. *Chem. Commun.* **2000**, 1423-1424.
133. Berreau, L. M.; Mahapatra, S.; Halfen, J. A.; Young Jr., V. G.; Tolman, W. B. *Inorg. Chem.* **1996**, *35*, 6339-6342.
134. Chang, C. J.; Deng, Y.; Heyduk, A. F.; Chang, C. K.; Nocera, D. G. *Inorg. Chem.* **2000**, *39*, 959-966.
135. Deng, Y.; Chang, C. J.; Nocera, D. G. *J. Am. Chem. Soc.* **2000**, *122*, 410-411.
136. Chang, C. J.; Deng, Y.; Shi, C.; Chang, C. K.; Anson, F. C.; Nocera, D. G. *Chem. Commun.* **2000**, 1355-1356.
137. Chang, C. J.; Baker, E. A.; Pistorio, B. J.; Deng, Y.; Loh, Z.-H.; Miller, S. E.; Carpenter, S. D.; Nocera, D. G. *Inorg. Chem.* **2002**, *41*, 3102-3109.
138. Chang, C. J.; Deng, Y.; Lee, G.-H.; Peng, S.-M.; Yeh, C.-Y.; Nocera, D. G. *Inorg. Chem.* **2002**, *41*, 3008-3016.
139. Pistorio, B. J.; Chang, C. J.; Nocera, D. G. *J. Am. Chem. Soc.* **2002**, *124*, 7884-7885.
140. Balch, A. L. *Inorg. Chim. Acta* **1992**, *198-200*, 297-307.
141. Calderwood, T. S.; Bruce, T. C. *Inorg. Chem.* **1985**, *25*, 3722-3724.
142. Cheng, R.; Latos-Grazynski, L.; Balch, A. L. *Inorg. Chem.* **1982**, *21*, 2412-2418.

143. Buchler, J. W.; Lay, K. L.; Lee, Y. J.; Scheidt, W. R. *Angew. Chem. Int. Ed.* **1982**, *21*, 432.
144. Scheidt, W. R.; Reed, C. A. *Chem. Rev.* **1981**, *81*, 543-555.
145. Evans, D. R.; Reed, C. A. *J. Am. Chem. Soc.* **2000**, *122*, 4660-4667.
146. Cheng, B.; Safo, M. K.; Orosz, R. D.; Reed, C. A.; Debrunner, P. G.; Scheidt, W. R. *Inorg. Chem.* **1994**, *33*, 1319-1324.
147. Scheidt, W. R.; Cheng, B.; Safo, M. K.; Cukiernik, F.; Marchon, J.-C.; Debrunner, P. G. *J. Am. Chem. Soc.* **1992**, *114*, 4420-4421.
148. Evans, D. R.; Mathur, R. S.; Heerwegh, K.; Reed, C. A.; Xie, Z. *Angew. Chem. Int. Ed.* **1997**, *36*, 1335-1337.
149. Gold, A.; Jayaraj, K.; Doppelt, P.; Weiss, R.; Chottard, G.; Bill, E.; Ding, X.; Trautwein, A. X. *J. Am. Chem. Soc.* **1988**, *110*, 5756-5761.
150. Kadish, K. M.; Smith, K. M.; Guillard, R. *The Porphyrin Handbook*; Academic Press: San Diego, 2000.
151. Sheldon, R. A. *Metalloporphyrins in Catalytic Oxidations*; Marcel Dekker: New York, 1994.
152. Mansuy, D. *Coord. Chem. Rev.* **1993**, *125*, 129-142.
153. Meunier, B. *Chem. Rev.* **1992**, *92*, 1411-1456.
154. Groves, J. T.; Stern, M. K. *J. Am. Chem. Soc.* **1988**, *110*, 8628-8638.
155. Bortolini, O.; Meunier, B. *J. Chem. Soc. Perkin Trans. 2* **1984**, 1967-1970.
156. Battoni, P.; Renaud, J. P.; Bartoli, J. F.; Reina-Artiles, M.; Fort, M.; Mansuy, D. *J. Am. Chem. Soc.* **1988**, *110*, 8462-8470.
157. Castellino, A. J.; Bruice, T. C. *J. Am. Chem. Soc.* **1988**, *110*, 158-162.
158. Jin, N.; Bourassa, J. L.; Tizio, S. C.; Groves, J. T. *Angew. Chem. Int. Ed.* **2000**, *39*, 3849-3851.
159. Jin, N.; Groves, J. T. *J. Am. Chem. Soc.* **1999**, *121*, 2923-2924.
160. Nam, W.; Kim, I.; Lim, M. H.; Choi, H. J.; Lee, J. S.; Jang, H. G. *Chem. Eur. J.* **2002**, *8*, 2067-2071.
161. Gross, Z.; Golubkov, G.; Simkovich, L. *Angew. Chem. Int. Ed.* **2000**, *39*, 4045-4047.
162. Dolphin, D.; Traylor, T. G.; Xie, L. Y. *Acc. Chem. Res.* **1997**, *30*, 251-259.
163. Grinstaff, M. W.; Hill, M. G.; Labinger, J. A.; Gray, H. B. *Science* **1994**, *264*, 1311-1313.
164. Traylor, T. G.; Lee, W. A.; Stynes, D. V. *J. Am. Chem. Soc.* **1984**, *106*, 755-764.
165. Traylor, T. G.; Ciccone, J. P. *J. Am. Chem. Soc.* **1989**, *111*, 8413-8420.
166. Traylor, T. G.; Xu, F. *J. Am. Chem. Soc.* **1990**, *112*, 178-186.
167. Lee, W. A.; Bruice, T. C. *J. Am. Chem. Soc.* **1985**, *107*, 513-514.
168. Zippelies, M. F.; Lee, W. A.; Bruice, T. C. *J. Am. Chem. Soc.* **1986**, *108*, 4433-4445.

169. Bruce, T. C.; Balasubramanian, P. N.; Lee, R. W.; Smith, J. R. L. *J. Am. Chem. Soc.* **1988**, *110*, 7890-7892.
170. Nam, W.; Lim, M. L.; Moon, S. K.; Kim, C. *J. Am. Chem. Soc.* **2000**, *122*, 10805-10809.
171. Nam, W.; Han, H. J.; Oh, S.-Y.; Lee, Y. J.; Choi, M.-H.; Han, S.-Y.; Kim, C.; Woo, S. K.; Shin, W. *J. Am. Chem. Soc.* **2000**, *122*, 8677-8684.
172. Nam, W.; Lim, M. H.; Oh, S.-Y.; Lee, J. H.; Lee, H. J.; Woo, S. K.; Kim, C.; Shin, W. *Angew. Chem. Int. Ed.* **2000**, *39*, 3646-3649.
173. Nam, W.; Jin, S. W.; Lim, M. H.; Ryu, J. Y.; Kim, C. *Inorg. Chem.* **2002**, *41*, 3647-3652.
174. Banfi, S.; Legramandi, F.; Montanari, F.; Pozzi, G.; Quici, S. *J. Chem. Soc. Chem. Commun.* **1991**, 1285-1287.
175. Anelli, P. L.; Banfi, S.; Legramandi, F.; Montanari, F.; Pozzi, G.; Quici, S. *J. Chem. Soc. Perkin Trans. 1* **1993**, 1345-1357.
176. Banfi, S.; Montanari, F.; Pozzi, G.; Quici, S. *Gazz. Chim. Ital.* **1993**, *123*, 617-621.
177. Armarego, W. L. F.; Perrin, D. D. *Purification of Laboratory Chemicals*; 4th ed.; Butterworth-Heinmann: Oxford, 1996.
178. Duncan, I. A.; Harriman, A.; Porter, G. *Anal. Chem.* **1979**, *51*, 2206-2208.



*Chapter 12*  
**Perspectives and Future Directions**

## 12.1 Perspectives

The research presented in this thesis represents an initial effort to utilize PCET as a vehicle for designing catalytic cycles for small-molecule activation chemistry. Oxidation and reduction reactions pertaining to O—O bond activation/formation have been explored using synthetic microcavities that scaffold two redox sites (Pacman) or one redox and one acid-base pendant (Hangman) in a face-to-face arrangement. The structure-function relationships of the Pacman and Hangman constructs for oxygen reduction and evolution reactions highlight the importance of controlling both electron and proton inventories to achieve effective catalytic bond-making and bond-breaking reactivity.

The synthetic chemistry of the Pacman motif has been greatly extended from the traditional anthracene- and biphenylene-bridged systems of Chang and Collman. Pillars based on the readily available ethers xanthene, dibenzofuran, and diphenylether afford the ability to tune both the vertical and horizontal sizes and flexibilities of the cofacial bisporphyrin cleft. Comparative reactivity studies for the selective four-electron, four-proton reduction of oxygen to water reveal two significant features for catalyst design: (i) architectures that structurally accommodate reaction intermediates through directed flexibility can lead to catalysts with enhanced reaction selectivities and/or activities over preorganized templates, and (ii) the proton affinity of substrate inclusion complexes is central to determining catalytic reaction pathways.

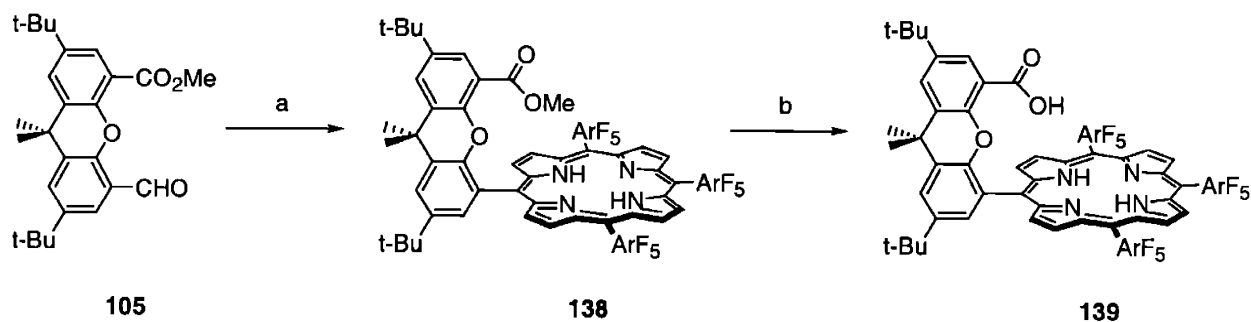
Removal of one of the porphyrins from the Pacman scaffold and replacement with a hydrogen-bond pendant affords the Hangman construct. Naphthalene, xanthene, and dibenzofuran spacers allow for precise control of the spatial orientations between redox and hanging group sites, and the acid-base properties of the hydrogen-bonding functionality can be tuned at will. Comparative reactivity studies for the catalase-like disproportionation of hydrogen peroxide and the epoxidation of olefins by Hangman systems establish that the introduction of a single well-positioned proton-shuttle group onto a redox-active platform can yield superior catalysts to analogs that do not control both proton and electron currencies.

## 12.2 Future Directions

With the field of PCET-catalyzed small-molecule activation in its infancy, new frontiers await exploration and numerous issues remain to be addressed. First and foremost is the continuing search for homogeneous catalysts to effect the oxidation of water to oxygen, with the ultimate goal of triggering such a conversion using light energy. Issues concerning both redox and acid-base chemistry are being considered in current designs. The Hangman motif affords the ability to

directly address both features in a single platform, and hence we will focus the next part of our discussion on these templates.

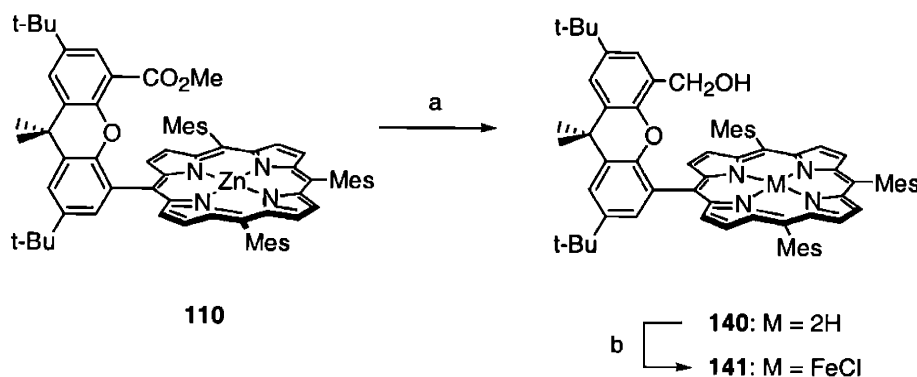
The first-generation HPX and HPD systems employed standard metalloporphyrin subunits to test the idea that adding proton control to a redox center would lead to enhanced catalytic activity. Macrocycles based on TMP substitution were installed to take advantage of the large body of work on these electron-rich metalloporphyrins for oxidation chemistry.<sup>1-4</sup> In principle, however, the porphyrin skeleton affords an unlimited opportunity for steric and electronic tuning.<sup>5</sup> One significant issue is that O—O bond formation requires a high-potential oxometal center, which is not afforded by simple TMP-type macrocycles. Combined with the successes of electronegative substitution on the porphyrin platform to yield oxygenation catalysts with improved activity and selectivity,<sup>2,5-7</sup> we are currently targeting Hangman systems with electron-deficient macrocyclic subunits. Accordingly, recently prepared derivatives feature ancillary rings with pentafluoro substitution (Scheme 12.1). The ester  $H_2(HTPFPPX-CO_2Me)$  (**138**) is furnished using standard Lindsey methods in 25% yield from pyrrole and the appropriate aldehyde and bridge partners. Deprotection proceeds smoothly under harsh acidic conditions to afford  $H_2(HTPFPPX-CO_2H)$  (**139**) in quantitative yield from ester **138**. Iron and manganese insertion into **138** and **139** and reactivity studies are in progress.



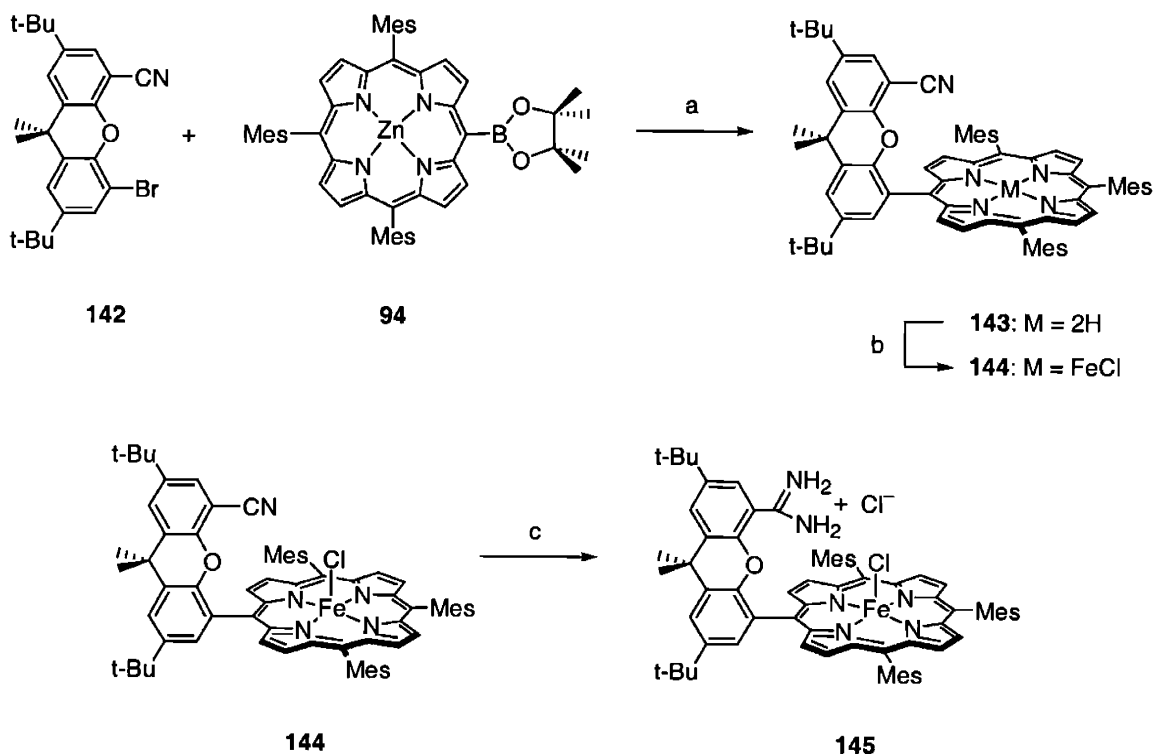
**Scheme 12.1.** (a) i. pyrrole, pentafluorobenzaldehyde,  $BF_3 \cdot OEt_2$ , chloroform/ethanol, ii. 2,3-dichloro-5,6-dicyano-1,4-benzoquinone (DDQ); (b)  $H_2SO_4$ , acetic acid, reflux.

Comparative reactivity studies of HPX and HPD complexes bearing acidic hydrogen-bond pendants with redox-only TMP analogues reveal that proton transfer to a bound metal-hydroperoxide unit facilitates bond-cleavage reactivity for substrate oxygenation. It follows that a metal-hydroperoxide species derived from O—O bond formation may be stabilized by a basic hydrogen-bond pendant. Current work is directed towards the attachment of organic hanging groups spanning a wide range of acidities to the xanthene-based HPX scaffold, while maintaining suitable structural architectures for the juxtaposition of an O—O unit. Examples

based on aliphatic alcohol and amidinium pendants have been recently synthesized (Schemes 12.2 and 12.3). Porphyrin  $H_2(HPX-CH_2OH)$  (**140**) is delivered in 93% yield by reduction of the zinc(II)-protected methyl ester porphyrin **110** with  $LiAlH_4$ . Iron insertion proceeds readily to afford the corresponding chloroiron(III) complex  $FeCl(HPX-CH_2OH)$  (**141**) in virtually quantitative yield.



**Scheme 12.2.** (a)  $LiAlH_4$ , THF, RT; (b) i.  $FeBr_2$ , DMF or THF/benzene; ii. HCl.

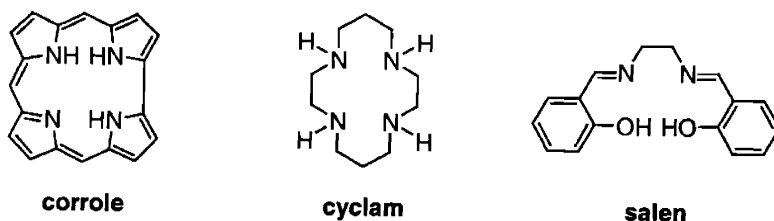


**Scheme 12.3.** (a) i.  $Pd(PPh_3)_4$ ,  $Na_2CO_3$ , DMF, water, reflux, ii. HCl; (b) i.  $FeBr_2$ , DMF or THF/benzene; ii. HCl; (c) chloromethylaluminum amide, toluene,  $80^\circ C$ .

Synthesis of the amidinium congener is based on the cyano Hangman derivative  $H_2(HPX-CN)$  (**143**), which is cleanly delivered in 74% yield by Suzuki cross coupling of zinc(II) boronate porphyrin **94** and the appropriate cyano-bromo xanthene bridge **142**. Metalation of the **143** with iron followed by reaction with Weinreb's amide reagent<sup>8</sup> furnishes the chloroiron(III) Hangman with an amidinium functionality,  $FeCl(HPX-CNH_2NH_2^+Cl^-)$  (**145**), in moderate yield (49%).<sup>9-11</sup> Preliminary catalytic measurements are consistent with the proposal that the O—O bond-activation reactivity of the Hangman platforms loosely correlates with the acidity of the pendant. Alcohol **141** ( $pK_a \sim 17$ ) and amidinium **145** ( $pK_a \sim 12$ ) derivatives catalyze peroxide dismutation with turnover numbers (TON) of  $74 \pm 7$  and  $78 \pm 8$ , respectively. For comparison, carboxylic acid **130** ( $pK_a \sim 4.5$ ) and its corresponding amide congener  $FeCl(HPX-CONH_2)$  ( $pK_a > 25$ ) exhibit activities of  $436 \pm 22$  and  $29 \pm 4$  TON, respectively. Current synthetic targets include the following hanging groups: methyl amine ( $pK_a \sim 9.6$ ), sulfonic acid ( $pK_a \sim 2.5$ ), and boronic acid ( $pK_a \sim 14$ ). Measurements of catalytic activities and O—O cleavage kinetics for a library of Hangman systems should prove intriguing.

Another promising avenue of research is the installation of alternative ancillary frameworks into both the Pacman and Hangman motifs. The closest logical extensions of the planar tetradentate donor set provided by porphyrin ligands are corroles, cyclams, and salens (Chart 12.1).

**Chart 12.1**



Sample architectures are provided in Figure 12.1, and one can envision many other possibilities as well. Corrole-based ligands offer the opportunity to stabilize coordination complexes with metals in high oxidation states,<sup>12-17</sup> and recent results from Gross<sup>14,18-23</sup> and others<sup>24-27</sup> demonstrate the versatility of these formal trianionic ligands for use in a variety of catalytic applications. Also, Guillard, Kadish, and co-workers have recently prepared a series of Pacman biscalcoroles<sup>28-30</sup> and related face-to-face complexes.<sup>31</sup> Cyclams furnish a macrocyclic  $N_4$  set of pure  $\sigma$  donors.<sup>32</sup> These innocent ligand systems are particularly ideal for the direct spectroscopic investigation of PCET activation at an electronically isolated metal center, avoiding complications arising from ancillary ligand-based redox processes.<sup>33-35</sup> Salens provide a salient  $N_2O_2$  framework for transition-metal ions in a variety of oxidation states.<sup>36</sup> These ligands,

derived from the simple Schiff-base condensation of a diamine with a salicylaldehyde, afford an expedient pathway for steric and electronic derivatization.<sup>37-48</sup> The cyclam- and salen-based ligand sets are particularly intriguing because they should be readily accessible by metal-catalyzed cross-coupling methodologies; modified salicylaldehydes have been prepared via Suzuki coupling,<sup>49</sup> and anthracene-bridged cofacial cyclams have been assembled by palladium-catalyzed C—N bond formation.<sup>50</sup>

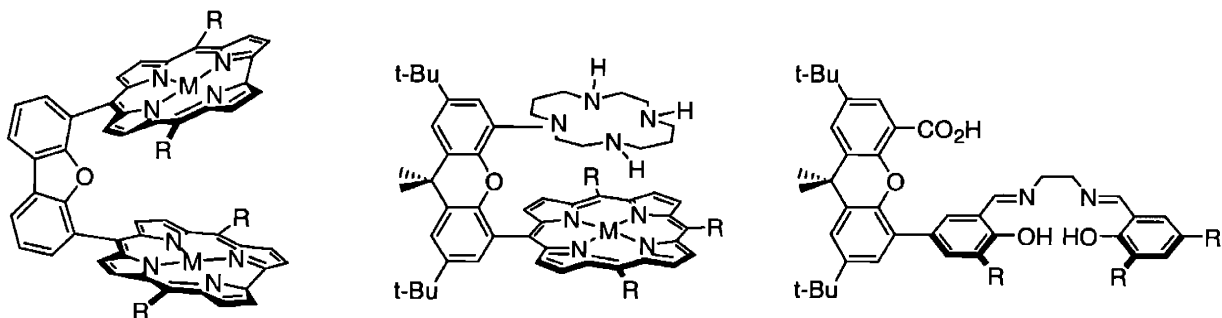


**Figure 12.1.** Examples of Pacman and Hangman systems incorporating alternative ligand sets.

Finally, with the knowledge acquired from studies of O—O bond activation/formation chemistry, future research directions will invariably turn toward defining the mechanisms of coupled electron-proton processes, at a rigorous level, in other small-molecule activation reactions. For example, an intriguing and long-standing problem at the forefront of biological<sup>51-54</sup> and chemical<sup>55-61</sup> research is the catalytic activation and fixation of nitrogen. The chemical conversion of molecular nitrogen to ammonia requires the PCET navigation of six electrons and six protons, with the concomitant activation/formation of three N—N bonds.<sup>56,60</sup> We anticipate that the application of PCET towards the design of discrete molecular systems for the transformation of these and other challenging small-molecule substrates will lead to new advances in catalysis.

## 12.3 Experimental Section

### 12.3.1 Materials

Silica gel 60 (70-230 and 230-400 mesh, Merck) was used for column chromatography. Analytical thin layer chromatography was performed using Merck 60 F254 silica gel (precoated sheets, 0.2 mm thick). Solvents for synthesis were of reagent grade or better, and were dried according to standard methods.<sup>62</sup> Zinc(II) 5,10,15-trimesityl-20-(4',4',5',5'-tetramethyl[1',3',2']dioxaborolan-2'-yl)-porphyrin (**94**) was obtained according to methods presented in Chapter 8. 4-Formyl-5-bromo-2,7-di-*tert*-butyl-9,9-dimethylxanthene (**101**), 4-

formyl-5-methoxycarbonyl-2,7-di-*tert*-butyl-9,9-dimethylxanthene (**105**), and zinc(II) 5-(4-(5-methoxycarbonyl-2,7-di-*tert*-butyl-9,9-dimethylxanthene))-10,15,20-trimesitylporphyrin (**110**), Zn(HPX-CO<sub>2</sub>Me), were synthesized as described in chapter 9. All other reagents were used as received.

### 12.3.2 5-(4-(5-Methoxycarbonyl-2,7-di-*tert*-butyl-9,9-dimethylxanthene))-10,15,20-tripentafluorophenylporphyrin, H<sub>2</sub>(HTPFPPX-CO<sub>2</sub>Me) (**138**)

A solution of aldehyde **105** (0.041 g, 0.1 mmol), pentafluorobenzaldehyde (0.294 g, 1.5 mmol) and pyrrole (0.11 mL, 1.6 mmol) in chloroform (160 mL) was purged with nitrogen for 45 min after which a portion of BF<sub>3</sub>·OEt<sub>2</sub> (0.067 mL, 0.528 mmol) was added via syringe. The solution was stirred at room temperature under nitrogen in the dark for 1 h and 2,3-dichloro-5,6-dicyano-1,4-benzoquinone (0.272 g, 1.2 mmol) was added to the reaction. After stirring for an additional hour under nitrogen, the solvent was removed by rotary evaporation. The dark residue was redissolved in dichloromethane (25 mL) containing 2% triethylamine and filtered. The filtrate was loaded directly onto a silica gel column packed with dichloromethane and eluted with dichloromethane until no more porphyrinic product was detected. Purification by column chromatography (silica gel, 2:1 hexanes/dichloromethane) gave porphyrin **138** as a bright violet microcrystalline solid (29 mg, 25% yield based on bridge **105**). <sup>1</sup>H NMR (500 MHz, CDCl<sub>3</sub>, 25 °C): δ = 8.95 (d, *J* = 8.5 Hz, 2H), 8.90 (br, 4H), 8.78 (d, *J* = 8.5 Hz, 2H), 7.92 (dd, *J*<sub>1</sub> = 10.2 Hz, *J*<sub>2</sub> = 4 Hz, 2H), 7.64 (d, *J* = 4 Hz, 1H), 7.31 (d, *J* = 4 Hz, 1H), 1.95 (s, 6H), 1.54 (s, 9H), 1.26 (s, 9H), -0.04 (s, 3H), -2.76 (s, 2H). HRESIMS (MH<sup>+</sup>) calcd for C<sub>63</sub>H<sub>41</sub>F<sub>15</sub>N<sub>4</sub>O<sub>3</sub> *m/z* 1187.3012, found 1187.3029.

### 12.3.3 5-(4-(5-Hydroxycarbonyl-2,7-di-*tert*-butyl-9,9-dimethylxanthene))-10,15,20-tripentafluorophenylporphyrin, H<sub>2</sub>(HTPFPPX-CO<sub>2</sub>H) (**139**)

Porphyrin **139** (20 mg, 0.0169 mmol) was dissolved in a mixture of acetic acid (5 mL) and sulfuric acid (1 mL). Water (1.5 mL) was added to the green solution and the reaction was refluxed under N<sub>2</sub> in the dark for 7 days. The reaction was cooled to room temperature and extracted with dichloromethane (15 mL). The organic layer was washed with water, dried over Na<sub>2</sub>SO<sub>4</sub>, and the solvent was removed by rotary evaporation. Purification by column chromatography (silica gel, dichloromethane) provided porphyrin **139** as a purple solid in quantitative yield. <sup>1</sup>H NMR (500 MHz, CDCl<sub>3</sub>, 25 °C): δ = 8.91 (m, 5H), 8.79 (d, *J* = 7 Hz, 2H), 8.09 (d, *J* = 4 Hz, 1H), 7.98 (d, *J* = 4 Hz, 1H), 7.72 (d, *J* = 4 Hz, 1H), 7.62 (d, *J* = 4 Hz, 1H), 1.99 (s, 6H), 1.57 (s, 9H), 1.25 (s, 9H), -2.76 (s, 2H). HRESIMS (MH<sup>+</sup>) calcd for C<sub>62</sub>H<sub>39</sub>F<sub>15</sub>N<sub>4</sub>O<sub>3</sub> *m/z* 1173.2855, found 1173.2858.

#### 12.3.4 5-(4-(5-Hydroxymethylene-2,7-di-*tert*-butyl-9,9-dimethylxanthene))-10,15,20-trimesitylporphyrin, H<sub>2</sub>(HPX-CH<sub>2</sub>OH) (140)

Under a nitrogen atmosphere, a solution of LiAlH<sub>4</sub> (0.38 mL, 1.0 M in THF) was added slowly to a solution of **110** (104 mg, 0.0940 mmol) in anhydrous THF (9 mL). The reaction mixture was stirred at room temperature for 1 h and quenched by the addition of ice water. The crude zinc(II) product was extracted with dichloromethane and purified by column chromatography (silica gel, 1:1 hexanes/dichloromethane). The porphyrin was redissolved in dichloromethane and washed with 6 N HCl (5 mL), 20% aq Na<sub>2</sub>CO<sub>3</sub> (20 mL), and water (2 × 30 mL). Drying over Na<sub>2</sub>SO<sub>4</sub> followed by removal of the solvent furnished **140** as a purple powder (89 mg, 93% yield). <sup>1</sup>H NMR (300 MHz, CDCl<sub>3</sub>, 25°C): δ = 8.78 (d, *J* = 5.0 Hz, 2H), 8.63 – 8.64 (m, 6H), 7.88 (d, *J* = 2.4 Hz, 1H), 7.85 (d, *J* = 2.6 Hz, 1H), 7.41 (d, *J* = 2.2 Hz, 1H), 7.27 (s, 2H), 7.25 (s, 4H), 6.79 (d, *J* = 2.2 Hz, 1H), 2.93 (d, *J* = 7.0 Hz, 2H), 2.64 (s, 3H), 2.61 (s, 6H), 2.05 (s, 3H), 1.93 (s, 6H), 1.89 (s, 6H), 1.85 (s, 6H), 1.77 (s, 3H), 1.50 (s, 9H), 1.23 (s, 9H), 0.17 (t, *J* = 7.0 Hz, 1H), -2.44 (s, 2H).

#### 12.3.5 FeCl(HPX-CH<sub>2</sub>OH) (141)

A mixture of **140** (7 mg, 0.00689 mmol), FeBr<sub>2</sub> (15 mg, 0.0696 mmol), and anhydrous DMF (2 mL) was refluxed under nitrogen for 2 h, opened to air and brought to dryness under vacuum. The residue was redissolved in dichloromethane (4 mL) and washed with water (3 × 10 mL), 20% HCl (1 mL), and water again (3 × 10 mL). The solvent was removed and the residue was purified using column chromatography (silica gel, dichloromethane to 5% methanol/dichloromethane). The resulting solid was redissolved in dichloromethane (4 mL) and stirred with 4 N HCl (1 mL) for 1 h. The organic layer was separated, washed with water (3 × 10 mL), dried over Na<sub>2</sub>SO<sub>4</sub> and taken to dryness. Product **141** was afforded in quantitative yield.

#### 12.3.6 4-Cyano-5-bromo-2,7-di-*tert*-butyl-9,9-dimethylxanthene (142)

A combination of **101** (0.944 g, 2.20 mmol) and hydroxylamine hydrochloride (0.160 g, 2.30 mmol) was brought to reflux in a 70:30 (v/v) mixture of chloroform/ethanol (24 mL) in a round-bottom flask fitted with a small Soxhlet extractor topped with a reflux condenser and a drying tube. The thimble contained anhydrous MgSO<sub>4</sub> to remove water formed during the reaction. A solution of pyridine (178 μL) in chloroform (1.10 mL) was added to the reaction mixture and refluxing was continued until complete consumption of the aldehyde starting material was detected by TLC (ca. 2 h). Selenium dioxide (0.488 g, 4.40 mmol) was added slowly to the reaction and the resulting mixture was refluxed overnight. One portion of MgSO<sub>4</sub> (0.328 g, 2.72 mmol) was added to the hot reaction and the mixture was cooled to room temperature with



stirring and then filtered. The filtrate was collected and the solvent was removed. Purification by column chromatography (silica gel, 20% hexanes/dichloromethane) afforded **142** as a white powder (0.656 g, 70% yield).  $^1\text{H NMR}$  (300 MHz,  $\text{CDCl}_3$ ,  $25^\circ\text{C}$ ):  $\delta$  = 7.61 (d,  $J$  = 2.4 Hz, 1H), 7.52 (d,  $J$  = 2.4 Hz, 1H), 7.51 (d,  $J$  = 2.4 Hz, 1H), 7.34 (d,  $J$  = 2.4 Hz, 1H), 1.66 (s, 6H), 1.35 (s, 9H), 1.34 (s, 9H). HRESIMS ( $\text{MNa}^+$ ) calcd for  $\text{C}_{24}\text{H}_{28}\text{BrNNaO}$   $m/z$  448.1246, found 448.1250.

### 12.3.7 5-(4-(5-Cyano-2,7-di-*tert*-butyl-9,9-dimethylxanthene))-10,15,20-trimesitylporphyrin $\text{H}_2(\text{HPX-CN})$ (**143**)

Under a nitrogen atmosphere, the solids **142** (90 mg, 0.211 mmol), **94** (198 mg, 0.232 mmol),  $\text{Na}_2\text{CO}_3$  (89 mg, 0.840 mmol), and  $\text{Pd}(\text{PPh}_3)_4$  (37 mg, 0.0320 mmol) were combined in DMF (45 mL) and deionized water (4.5 mL) and refluxed for 20 h. The solvent was removed under high vacuum and the residue was redissolved in dichloromethane (40 mL) and stirred with 6 N HCl (15 mL) for 15 min. The organic layer was separated and washed with 20% aq  $\text{Na}_2\text{CO}_3$  (20 mL) followed by water ( $2 \times 50$  mL). The solvent was evaporated and the residue was purified by column chromatography (silica gel, 2:1 hexanes/dichloromethane) to yield **143** as a royal purple solid (158 mg, 74% yield).  $^1\text{H NMR}$  (300 MHz,  $\text{CDCl}_3$ ,  $25^\circ\text{C}$ ):  $\delta$  = 8.70 (d,  $J$  = 4.6 Hz, 2H), 8.62 (d,  $J$  = 4.6 Hz, 2H), 8.60 (s, 4H), 7.88 (d,  $J$  = 2.4 Hz, 1H), 7.84 (d,  $J$  = 2.2 Hz, 1H), 7.71 (d,  $J$  = 2.4 Hz, 1H), 7.27 (s, 6H), 7.15 (d,  $J$  = 2.4 Hz, 1H), 2.64 (s, 3H), 2.63 (s, 6H), 2.06 (s, 3H), 1.92 (s, 12H), 1.91 (s, 6H), 1.78 (s, 3H), 1.49 (s, 9H), 1.30 (s, 9H) -2.40 (s, 2H). HRESIMS ( $\text{MH}^+$ ) calcd for  $\text{C}_{71}\text{H}_{72}\text{N}_5\text{O}$   $m/z$  1010.5731, found 1010.5729.

### 12.3.8 $\text{FeCl}(\text{HPX-CN})$ (**144**)

A mixture of **143** (141 mg, 0.140 mmol),  $\text{FeBr}_2$  (301 mg, 1.40 mmol), and anhydrous DMF (30 mL) was refluxed under nitrogen for 2 h, opened to air and brought to dryness under vacuum. The residue was redissolved in dichloromethane (50 mL) and washed with water ( $3 \times 100$  mL), 20% HCl (15 mL), and water again ( $3 \times 100$  mL). The solvent was removed and the residue was purified by column chromatography (silica gel, dichloromethane to 5% methanol/dichloromethane), redissolved in dichloromethane (30 mL) and stirred with 4 N HCl (10 mL) for 1 h. The organic layer was separated, washed with water ( $3 \times 100$  mL), dried over  $\text{Na}_2\text{SO}_4$ , and taken to dryness to produce **144** as a brown powder (149 mg, 97% yield). HRFABMS ( $[\text{M}-\text{Cl}]^+$ ) calcd for  $\text{C}_{71}\text{H}_{69}\text{FeN}_5\text{O}$   $m/z$  1063.4846, found 1063.4857.

### 12.3.9 $\text{FeCl}(\text{HPX-CN}_2\text{NH}_2^+\text{Cl}^-)$ (**145**)

Chloromethylaluminum amide (0.6 mL, 1.0 M in toluene) was added via syringe to a solution of **144** (13.2 mg, 0.0120 mmol) in anhydrous toluene (11 mL) under a nitrogen atmosphere. The

resulting mixture was heated at 80 °C under nitrogen for 7 d. The mixture was cooled to room temperature, poured slowly onto silica gel (2 g) in chloroform (5 mL), and stirred for 10 min. The slurry was filtered and washed with a mixture of chloroform and methanol until the washings became colorless. The solvent was removed and purification by column chromatography (silica gel, dichloromethane to 5% methanol/dichloromethane) furnished the amidinium product **145** as a brown solid (6.8 mg, 49% yield).

### 12.3.10 Physical Measurements

<sup>1</sup>H NMR spectra were collected in CDCl<sub>3</sub> (Cambridge Isotope Laboratories) at the MIT Department of Chemistry Instrumentation Facility (DCIF) using either a Mercury 300 or an Inova 500 spectrometer at 25 °C. All chemical shifts are reported using the standard  $\delta$  notation in parts-per-million; positive chemical shifts are to higher frequency from the given reference. Absorption spectra were obtained using either a Cary-17 spectrophotometer modified by On-Line Instruments (OLIS) to include computer control or a Spectral Instruments 440 Series spectrophotometer. High-resolution mass spectral analyses were carried out at the University of Illinois Mass Spectrometry Laboratory or the MIT Department of Chemistry Instrumentation Facility.

### 12.3.11 Hydrogen Peroxide Disproportionation Reactions

Dismutation reactions were performed at room temperature in a 5 mL conical reaction vial with a side port, equipped with a magnetic spinvane stirbar and a capillary gas delivery tube linked to a graduated buret filled with water. The reaction vial was charged with 1  $\mu$ mol of the iron porphyrin, 25  $\mu$ mol of 1,5-dicyclohexylimidazole, 4  $\mu$ mol of benzyldimethyltetradecylammonium chloride, 2 mL of dichloromethane and 1 mL of phosphate buffer, pH 7. The solution was stirred to ensure gas pressure equilibration. An aliquot of 30% H<sub>2</sub>O<sub>2</sub> (0.11 mL) was added to the reaction mixture via syringe through the side port. The oxygen evolution was measured using a buret. The identity of the oxygen gas was confirmed independently using the alkaline pyrogallol test.<sup>63</sup>

## 12.4 References and Notes

1. Groves, J. T.; Han, Y. In *Cytochrome P450: Structure, Mechanism, and Biochemistry*; 2nd ed.; Ortiz de Montellano, P. R., Ed.; Plenum: New York, 1995, pp 3-48.
2. Sheldon, R. A. *Metalloporphyrins in Catalytic Oxidations*; Marcel Dekker: New York, 1994.
3. Meunier, B. *Chem. Rev.* **1992**, *92*, 1411-1456.
4. Mansuy, D. *Coord. Chem. Rev.* **1993**, *125*, 129-142.
5. Kadish, K. M.; Smith, K. M.; Guillard, R. *The Porphyrin Handbook*; Academic Press: San Diego, 2000.
6. Dolphin, D.; Traylor, T. G.; Xie, L. Y. *Acc. Chem. Res.* **1997**, *30*, 251-259.
7. Grinstaff, M. W.; Hill, M. G.; Labinger, J. A.; Gray, H. B. *Science* **1994**, *264*, 1311-1313.
8. Levin, J. I.; Turos, E.; Weinreb, S. M. *Synth. Commun.* **1982**, *12*, 989-993.
9. Kirby, J. P.; van Dantzig, N. A.; Chang, C. K.; Nocera, D. G. *Tetrahedron Lett.* **1995**, *36*, 3477-3480.
10. Deng, Y.; Roberts, J. A.; Peng, S.-M.; Chang, C. K.; Nocera, D. G. *Angew. Chem. Int. Ed.* **1997**, *36*, 2124-2127.
11. Yeh, C.-Y.; Miller, S. E.; Carpenter, S. D.; Nocera, D. G. *Inorg. Chem.* **2001**, *40*, 3643-3646.
12. De Visser, S. P.; Ogliaro, F.; Gross, Z.; Shaik, S. *Chem. Eur. J.* **2001**, *7*, 4954-4960.
13. Gross, Z. *J. Biol. Inorg. Chem.* **2001**, *6*, 733-738.
14. Gross, Z.; Golubkov, G.; Simkhovich, L. *Angew. Chem. Int. Ed.* **2000**, *39*, 4045-4047.
15. Van Caemelbecke, E.; Will, S.; Autret, M.; Adamian, V. A.; Lex, J.; Gisselbrecht, J.-P.; Gross, M.; Vogel, E.; Kadish, K. M. *Inorg. Chem.* **1996**, *35*, 184-192.
16. Steene, E.; Wondimagegn, T.; Ghosh, A. *J. Phys. Chem. B* **2001**, *105*, 11406-11413.
17. Meier-Callahan, A. E.; Gray, H. B.; Gross, Z. *Inorg. Chem.* **2000**, *39*, 3605-3607.
18. Gross, Z.; Galili, N.; Saltsman, I. *Angew. Chem. Int. Ed.* **1999**, *38*, 1427-1429.
19. Grodkowski, J.; Neta, P.; Fujita, E.; Mahammed, A.; Simkhovich, L.; Gross, Z. *J. Phys. Chem. A* **2002**, *106*, 4772-4778.
20. Golubkov, G.; Bendix, J.; Gray, H. B.; Mahammed, A.; Goldberg, I.; DiBilio, A. J.; Gross, Z. *Inorg. Chem.* **2001**, *40*, 2132-2134.
21. Gross, Z.; Simkhovich, L.; Galili, N. *Chem. Commun.* **1999**, 599-600.
22. Simkhovich, L.; Mahammed, A.; Goldberg, I.; Gross, Z. *Chem. Eur. J.* **2001**, *7*, 1041-1055.
23. Simkhovich, L.; Gross, Z. *Tetrahedron Lett.* **2001**, *42*, 8089-8092.
24. Gryko, D. T. *Eur. J. Org. Chem.* **2002**, 1735-1743.

25. Gryko, D. T. *Chem. Commun.* **2000**, 2243-2244.
26. Gryko, D. T.; Jadach, K. *J. Org. Chem.* **2001**, *66*, 4267-4275.
27. Paolesse, R.; Nardis, S.; Sagone, F.; Khoury, R. G. *J. Org. Chem.* **2001**, *66*, 550-556.
28. Jerome, F.; Gros, C. P.; Tardieux, C.; Barbe, J.-M.; Guillard, R. *Chem. Commun.* **1998**, 2007-2008.
29. Kadish, K. M.; Ou, Z.; Shao, J.; Gros, C. P.; Barbe, J.-M.; Jerome, F.; Bolze, F.; Burdet, F.; Guillard, R. *Inorg. Chem.* **2002**, *41*, 3990-4005.
30. Guillard, R.; Jerome, F.; Barbe, J.-M.; Gros, C. P.; Ou, Z.; Shao, J.; Fischer, J.; Weiss, R.; Kadish, K. M. *Inorg. Chem.* **2001**, *40*, 4856-4865.
31. Jerome, F.; Gros, C. P.; Tardieux, C.; Barbe, J.-M.; Guillard, R. *New. J. Chem.* **1998**, 1327-1329.
32. Lindoy, L. F. *The Chemistry of Macrocyclic Ligand Complexes*; Cambridge University Press: Cambridge, UK, 1992.
33. Grapperhaus, C. A.; Bill, E.; Weyhermueller, T.; Neese, F.; Wieghardt, K. *Inorg. Chem.* **2001**, *40*, 4191-4198.
34. Meyer, K.; Bill, E.; Mienert, B.; Weyhermueller, T.; Wieghardt, K. *J. Am. Chem. Soc.* **1999**, *121*, 4859-4876.
35. Meyer, K.; Bendix, J.; Metzler-Nolte, N.; Weyhermueller, T.; Wieghardt, K. *J. Am. Chem. Soc.* **1998**, *120*, 7260-7270.
36. Wilkinson, G. *Comprehensive Coordination Chemistry*; Pergamon Press: Oxford, UK, 1987.
37. Jacobsen, E. N. *Acc. Chem. Res.* **2000**, *33*, 421-431.
38. Palucki, M.; Finney, N. S.; Pospisil, P. J.; Gueler, M. L.; Ishida, T.; Jacobsen, E. N. *J. Am. Chem. Soc.* **1998**, *120*, 948-954.
39. Jacobsen, E. N. In *Catalytic Asymmetric Synthesis*; Ojima, I., Ed.; VCH: New York, 1993, pp 159-202.
40. Katsuki, T. *Asymmetric Oxidation Reactions*; Oxford University Press: Oxford, UK, 2001.
41. Katsuki, T. *Adv. Syn. Catal.* **2002**, *344*, 131-147.
42. Katsuki, T. *J. Mol. Catal. A* **1996**, *113*, 87-107.
43. Srinivasan, K.; Michaud, P.; Kochi, J. K. *J. Am. Chem. Soc.* **1986**, *108*, 2309-2320.
44. Samsel, E. G.; Srinivasan, K.; Kochi, J. K. *J. Am. Chem. Soc.* **1985**, *107*, 7606-7617.
45. Chang, C. J.; Labinger, J. A.; Gray, H. B. *Inorg. Chem.* **1997**, *36*, 5927-5930.
46. Chang, C. J.; Connick, W. B.; Low, D. W.; Day, M. W.; Gray, H. B. *Inorg. Chem.* **1998**, *37*, 3107-3110.

47. Böttcher, A.; Birnbaum, E. R.; Day, M. W.; Gray, H. B.; Grinstaff, M. W.; Labinger, J. *A. J. Mol. Catal. A* **1997**, *117*, 229-242.
48. Bandini, M.; Cozzi, P. G.; Umani-Ronchi, A. *Chem. Commun.* **2002**, 919-927.
49. Zhuravel, M. A.; Nguyen, S. T. *Tetrahedron Lett.* **2001**, *42*, 7925-7928.
50. Beletskaya, I. P.; Averin, A. D.; Bessmertnykh, A. G.; Denat, F.; Guillard, R. *Tetrahedron Lett.* **2002**, *43*, 1193-1196.
51. Rees, D. C.; Howard, J. B. *Curr. Opin. Chem. Biol.* **2000**, *4*, 559-566.
52. Burgess, B. K.; Lowe, D. J. *Chem. Rev.* **1996**, *96*, 2983-3011.
53. Holm, R. H.; Solomon, E. I. *Chem. Rev.* **1996**, *96*, 2237 (Special Issue: Bioinorganic Enzymology).
54. Lippard, S. J.; Berg, J. M. *Principles of Bioinorganic Chemistry*; University Science Books: Mill Valley, CA, 1994.
55. Fryzuk, M. D.; Johnson, S. A. *Coord. Chem. Rev.* **2000**, *200-202*, 379-409.
56. Yandulov, D. V.; Schrock, R. R. *J. Am. Chem. Soc.* **2002**, *124*, 6252-6253.
57. Hidai, M.; Mizobe, Y. *Chem. Rev.* **1995**, *95*, 1115-1133.
58. Hidai, M. *Coord. Chem. Rev.* **1999**, *185-186*, 99-108.
59. Chatt, J.; Dilworth, J. R.; Richards, R. L. *Chem. Rev.* **1978**, *78*, 589-625.
60. Shilov, A. E. In *Electron Transfer in Chemistry*; Balzani, V., Ed.; Wiley-VCH: Weinheim, Germany, 2001; Vol. 2.2.6, pp 878-904.
61. Peters, J. C.; Cherry, J.-P. F.; Thomas, J. C.; Baraldo, L.; Mindiola, D. J.; Davis, W. M.; Cummins, C. C. *J. Am. Chem. Soc.* **1999**, *121*, 10053-10067.
62. Armarego, W. L. F.; Perrin, D. D. *Purification of Laboratory Chemicals*; 4th ed.; Butterworth-Heinmann: Oxford, 1996.
63. Duncan, I. A.; Harriman, A.; Porter, G. *Anal. Chem.* **1979**, *51*, 2206-2208.

## **Biographical Note**

The author was born in Ames, Iowa on December 17, 1974, and raised in Mount Vernon, Indiana and Palo Alto, California. He graduated from Palo Alto High School in 1993 and received concomitant B.S. and M.S. degrees in Chemistry from the California Institute of Technology in 1997, carrying out undergraduate research with Professor Harry B. Gray on the spectroscopy and reactivity of high-valent metal-salen complexes. The author then spent a year studying molecular knots and catenanes as a Fulbright scholar in the research group of Dr. Jean Pierre Sauvage at the Université Louis Pasteur. His graduate work at the Massachusetts Institute of Technology with Professor Daniel G. Nocera has centered on the use of proton-coupled electron transfer to design catalytic cycles for small-molecule activation chemistry, and he has held predoctoral fellowships from the National Science Foundation and the M.I.T./Merck Foundation. Upon completion of his Ph.D. studies, the author will take a postdoctoral position at M.I.T. as a Jane Coffin Childs fellow in the laboratory of Professor Stephen J. Lippard.

## CHRISTOPHER J. CHANG

### EDUCATION

---

<b>Ph.D.</b>	<b>Massachusetts Institute of Technology</b> <i>Chemistry (Inorganic)</i> Advisor: Professor Daniel G. Nocera Thesis: Small-Molecule Activation Chemistry Catalyzed by Proton-Coupled Electron Transfer	Expected 2002
<b>Fulbright Scholar</b>	<b>Université Louis Pasteur</b> <i>Chemistry</i> Advisor: Dr. Jean-Pierre Sauvage	1997-1998
<b>B.S./M.S.</b>	<b>California Institute of Technology</b> <i>Chemistry</i> Advisor: Professor Harry B. Gray Thesis: Spectroscopy and Reactivity of Metal-Oxo and Metal-Nitrido Schiff-Base Complexes	1997

### PUBLICATIONS

---

- (1) Chang, C. J.; Low, D. W.; Gray, H. B. *Inorg. Chem.* **1997**, *36*, 270-271.
- (2) Chang, C. J.; Labinger, J. A.; Gray, H. B. *Inorg. Chem.* **1997**, *36*, 5927-5930.
- (3) Chang, C. J.; Connick, W. B.; Low, D. W.; Day, M. W.; Gray, H. B. *Inorg. Chem.* **1998**, *37*, 3107-3110.
- (4) Deng, Y.; Chang, C. J.; Nocera, D. G. *J. Am. Chem. Soc.* **2000**, *122*, 410-411.
- (5) Chang, C. J.; Deng, Y.; Heyduk, A. F.; Chang, C. K.; Nocera, D. G. *Inorg. Chem.* **2000**, *39*, 959-966.
- (6) Chang, C. J.; Deng, Y.; Shi, C.; Chang, C. K.; Anson, F. C.; Nocera, D. G. *Chem. Commun.* **2000**, 1355-1356.
- (7) Yeh, C.-Y.; Chang, C. J.; Nocera, D. G. *J. Am. Chem. Soc.* **2001**, *123*, 1513-1514.
- (8) Chang, C. J.; Brown, J. D. K.; Chang, M. C. Y.; Baker, E. A.; Nocera, D. G. In *Electron Transfer in Chemistry*, V. Balzani Ed., Wiley-VCH, Weinheim, Germany, 2001, Vol. 3.2.4., p 409-461.
- (9) Chang, C. J.; Yeh, C.-Y.; Nocera, D. G. *J. Org. Chem.* **2002**, *67*, 1403-1406.
- (10) Chang, C. J.; Deng, Y.; Lee, G.-H.; Peng, S.-M.; Yeh, C.-Y.; Nocera, D. G. *Inorg. Chem.* **2002**, *41*, 3008-3016.
- (11) Chang, C. J.; Baker, E. A.; Pistorio, B. J.; Deng, Y.; Loh, Z.-H.; Miller, S. E.; Carpenter, S. D.; Nocera, D. G. *Inorg. Chem.* **2002**, *41*, 3102-3109.
- (12) Pistorio, B. J.; Chang, C. J.; Nocera, D. G. *J. Am. Chem. Soc.* **2002**, *124*, 7884-7885.

### PRESENTATIONS

---

- (1) Chang, C. J.; Low, D. W.; Gray, H. B. 211<sup>th</sup> ACS National Meeting, New Orleans, LA, Mar 1996.
- (2) Chang, C. J.; Connick, W. B.; Low, D. W.; Gray, H. B. 213<sup>th</sup> ACS National Meeting, San Francisco, CA, Apr 1997.
- (3) Chang, C. J.; Gray, H. B. 214<sup>th</sup> ACS National Meeting, Las Vegas, NV, Sept 1997.
- (4) Chang, C. J. Université Louis Pasteur, Strasbourg, France, Dec 1997.
- (5) Chang, C. J. Oxford University, Oxford, United Kingdom, Feb 1998.
- (6) Chang, C. J.; Dietrich-Buchecker, C.; Sauvage, J. P. 216<sup>th</sup> ACS National Meeting, Boston, MA, Aug 1998.
- (7) Chang, C. J.; Yeh, C.-Y.; Deng, Y.; Miller, S. E.; Carpenter, S. D.; Nocera, D. G. 10<sup>th</sup> International Conference on Bioinorganic Chemistry, Florence, Italy, Aug 2001.
- (8) Chang, C. J. Whiteman Symposium, Massachusetts Institute of Technology, Cambridge, MA, Jan 2002.
- (9) Chang, C. J.; Chng, L. L.; Nocera, D. G. 223<sup>rd</sup> American Chemical Society National Meeting, Orlando, FL, Apr 2002.
- (10) Chang, C. J.; Chng, L. L.; Yeh, C.-Y.; Nocera, D. G. Gordon Research Conference on Organometallics, Newport, RI, July 2002.